# Organic Semiconductors

Edited by

Mohan Jacob

Printed Edition of the Special Issue Published in *Electronics*

www.mdpi.com/journal/electronics

Mohan Jacob (Ed.)

# Organic Semiconductors

This book is a reprint of the special issue that appeared in the online open access journal *Electronics* (ISSN 2079-9292) in 2014 (available at: http://www.mdpi.com/journal/electronics/special_issues/organic-semiconductors).

*Guest Editor*
Mohan Jacob
Electronic Materials Research Lab
School of Engineering and Physical Sciences
James Cook University
Townsville 4811
Australia

*Editorial Office*
MDPI AG
Klybeckstrasse 64
Basel, Switzerland

*Publisher*
Shu-Kun Lin

*Production Editor*
Martyn Rittman

**1. Edition 2015**

MDPI • Basel • Beijing • Wuhan

ISBN 978-3-906980-96-6 (Hbk)
ISBN 978-3-906980-97-3 (PDF)

# Table of Contents

## Section III: Organic Field Effect Transistors



## Section IV: Organic Light Emitting Diodes

## Section V: Solar Cells



## Section VI: Bio-Organic Electronics

# List of Contributors

**Jakaria Ahmad:** Electronic Materials Research Laboratory, School of Engineering and Physical Sciences, James Cook University, Townsville 4811, Australia

**Alberto Aloisio:** Ist. Naz. Fis. Nucl., Sez Napoli and Department of Physics, University of Naples 'Federico II', Via Cintia, I-80125 Naples, Italy

**Hany Aziz:** Department of Electrical and Computer Engineering & Waterloo Institute for Nanotechnology, University of Waterloo, 200 University Avenue, Waterloo, ON, N2L 3G1, Canada

**Christopher Backhouse:** Department of Electrical and Computer Engineering & Waterloo Institute for Nanotechnology, University of Waterloo, 200 University Avenue, Waterloo, ON, N2L 3G1, Canada

**Mario Barra:** CNR-SPIN and Department of Physics, University of Naples 'Federico II', Piazzale Tecchio, 80, I-80125 Naples, Italy

**Kateryna Bazaka:** Electronic Materials Research Laboratory, School of Engineering and Physical Sciences, James Cook University, Townsville 4811, Australia

**Warwick Belcher:** Centre for Organic Electronics, Physics, The University of Newcastle, Callaghan, NSW 2308, Australia

**Joel Bellessa:** Institut Lumière Matière, Université de Lyon, UMR5306 Université Lyon 1-CNRS, Villeurbanne 69622, France

**Jean-Michel Benoit:** Institut Lumière Matière, Université de Lyon, UMR5306 Université Lyon 1-CNRS, Villeurbanne 69622, France

**Jean Christian Bernède:** UNAM, Université de Nantes, MOLTECH-Anjou, CNRS, UMR 6200, 2 rue de la Houssinière, BP 92208, F-44000 Nantes, France

**Beatrice Beyer:** Fraunhofer Institute for Electron Beam, Plasma Technology and COMEDD (FEP), Maria-Reiche-Str. 02, 01109 Dresden, Germany

**Antonio Cassinese:** CNR-SPIN and Department of Physics, University of Naples 'Federico II', Piazzale Tecchio, 80, I-80125 Naples, Italy

**Vittorio Cataudella:** CNR-SPIN and Dipartimento di Fisica, Università "Federico II", Via Cinthia, Napoli I-80126, Italy

**Linda Cattin:** Institut des Matériaux Jean Rouxel (IMN), UMR 6502, Université de Nantes, CNRS, 2 rue de la Houssinière, BP 32229, F-44322 Nantes cedex 3, France

**Fabio Chiarella:** CNR-SPIN and Department of Physics, University of Naples 'Federico II', Piazzale Tecchio, 80, I-80125 Naples, Italy

**Nathan Cooling:** Centre for Organic Electronics, Physics, The University of Newcastle, Callaghan, NSW 2308, Australia

**Paul C. Dastoor:** Centre for Organic Electronics, Physics, The University of Newcastle, Callaghan, NSW 2308, Australia

**Daniel Elkington:** Centre for Organic Electronics, Physics, The University of Newcastle, Callaghan, NSW 2308, Australia

**Fernando Gargiulo:** Institute of Theoretical Physics, École Polytechnique Fédérale de Lausanne (EPFL), Lausanne CH-1015, Switzerland
**Masahiro Hiramoto:** Institute for Molecular Science, 5-1 Higashiyama, Myodaiji, Okazaki, Aichi 444-8787, Japan; JST, CREST, 5, Sanbancho, Chiyoda-ku, Tokyo 102-0075, Japan
**Norihiro Ishiyama:** Institute for Molecular Science, 5-1 Higashiyama, Myodaiji, Okazaki, Aichi 444-8787, Japan; JST, CREST, 5, Sanbancho, Chiyoda-ku, Tokyo 102-0075, Japan
**Masanobu Izaki:** JST, CREST, 5, Sanbancho, Chiyoda-ku, Tokyo 102-0075, Japan; Department of Production System Engineering, Toyohashi University of Technology, Tempaku-cho, Toyohashi, Aichi 441-8580, Japan
**Mohan V. Jacob:** Electronic Materials Research Laboratory, School of Engineering and Physical Sciences, James Cook University, Townsville 4811, Australia
**Toshihiko Kaji:** Institute for Molecular Science, 5-1 Higashiyama, Myodaiji, Okazaki, Aichi 444-8787, Japan; JST, CREST, 5, Sanbancho, Chiyoda-ku, Tokyo 102-0075, Japan
**Masayuki Kubo:** Institute for Molecular Science, 5-1 Higashiyama, Myodaiji, Okazaki, Aichi 444-8787, Japan; JST, CREST, 5, Sanbancho, Chiyoda-ku, Tokyo 102-0075, Japan
**Sandro Lattante:** Dipartimento di Matematica e Fisica "Ennio de Giorgi", Università del Salento, via per Arnesano, Lecce 73100, Italy
**Julien Laverdant:** Institut Lumière Matière, Université de Lyon, UMR5306 Université Lyon 1-CNRS, Villeurbanne 69622, France
**Ning Li:** IBM T. J. Watson Research Center, 1101 Kitchawan Road, Yorktown Heights, NY 10598, USA
**Mustapha Morsli:** UNAM, Université de Nantes, Faculté des Sciences et des Techniques, 2 rue de la Houssinière, BP 92208, F-44000 Nantes, France
**Susan Mühl:** Fraunhofer Institute for Electron Beam, Plasma Technology and COMEDD (FEP), Maria-Reiche-Str. 02, 01109 Dresden, Germany
**Kenta Nishimura:** Department of Materials Science, The University of Shiga Prefecture, 2500 Hassaka, Hikone, Shiga 522-8533, Japan
**Alberto Nocera:** Department of Physics, Northeastern University, Boston, MA 02115, USA
**Toshinobu Ohno:** Osaka Municipal Technical Research Institute, 1-6-50 Morinomiya, Joto-ku, Osaka 536-8553, Japan
**Takeo Oku:** Department of Materials Science, The University of Shiga Prefecture, 2500 Hassaka, Hikone, Shiga 522-8533, Japan
**Carmine Antonio Perroni:** CNR-SPIN and Dipartimento di Fisica, Università "Federico II", Via Cinthia, Napoli I-80126, Italy
**Jean Claude Plenet:** Institut Lumière Matière, Université de Lyon, UMR5306 Université Lyon 1-CNRS, Villeurbanne 69622, France
**Vincenzo Marigliano Ramaglia:** CNR-SPIN and Dipartimento di Fisica, Università "Federico II", Via Cinthia, Napoli I-80126, Italy
**Laura Ricciotti:** Department of Chemistry, University of Naples 'Federico II', Via Cintia, I-80125 Naples, Italy

**Kazuya Sakai:** Graduate School of Engineering, Osaka University, Yamadaoka, Suita, Osaka 565-0871, Japan
**Ken-ichi Sakai:** Department of Advanced Materials Science, Graduate School of Frontier Sciences, University of Tokyo, 5-1-5, Kashiwanoha, Kashiwa-shi, Chiba 277-8561, Japan
**Yusuke Shinmura:** Institute for Molecular Science, 5-1 Higashiyama, Myodaiji, Okazaki, Aichi 444-8787, Japan; JST, CREST, 5, Sanbancho, Chiyoda-ku, Tokyo 102-0075, Japan
**Tze-Bin Song :** Department of Materials Science & Engineering, University of California, Los Angeles, CA 90095, USA; IBM T. J. Watson Research Center, 1101 Kitchawan Road, Yorktown Heights, NY 10598, USA
**Atsushi Suzuki:** Department of Materials Science, The University of Shiga Prefecture, 2500 Hassaka, Hikone, Shiga 522-8533, Japan
**Clementine Symonds:** Institut Lumière Matière, Université de Lyon, UMR5306 Université Lyon 1-CNRS, Villeurbanne 69622, France
**Jun Takeya:** Department of Advanced Materials Science, Graduate School of Frontier Sciences, University of Tokyo, 5-1-5, Kashiwanoha, Kashiwa-shi, Chiba 277-8561, Japan
**Stephane Vignoli:** Institut Lumière Matière, Université de Lyon, UMR5306 Université Lyon 1-CNRS, Villeurbanne 69622, France
**Graeme Williams:** Department of Electrical and Computer Engineering & Waterloo Institute for Nanotechnology, University of Waterloo, 200 University Avenue, Waterloo, ON, N2L 3G1, Canada
**Xiaojing Zhou:** Centre for Organic Electronics, Physics, The University of Newcastle, Callaghan, NSW 2308, Australia

# Preface

## Organic Semiconductors: Past, Present and Future

**Mohan V. Jacob**

Reprinted from *Electronics*. Cite as: Jacob, M.V. Organic Semiconductors: Past, Present and Future. *Electronics* **2014**, *3*, 594-597.

### 1. Introduction

Organic electronics, such as displays, photovoltaics and electronics circuits and components, offer several advantages over the conventional inorganic-based electronics because they are inexpensive, flexible, unbreakable, optically transparent, lightweight and have low power consumption. In particular, organic displays exhibit high brightness, fast response time, wide viewing angle, and low operating voltage.

The past few years have seen a significant and rapid growth of research and development of OSC and Organic Field Effect Transistor (OFET) devices, with promising results [1–3] and diverse range of applications. Organic Field Effect Transistors and Organic Light Emitting Diodes (OLEDs) are the fundamental electronic building blocks of organic electronic circuits. Every display has millions of transistors used for switching the pixels on/off. OFETs are used in displays, human-machine interfaces, electronic artificial skin, and smart digital gadgets. OFETs have been successfully employed in e-inks. One of the main technological advantages of OFET is that all the layers of an OFET can be fabricated and patterned at room temperature by a combination of low-cost solution processing and direct-write printing.

One very exciting prospect of developing devices based on organic materials is the power savings in OLED displays compared to back-light LCDs and plasma displays. Enhancement in applications and the miniaturization of electronics has led to the exploration of many advanced materials including quantum dots [4], organic molecules [5], carbon nanotubes [6], nanowires [7], and single atoms [8] or molecules [9–12].

### 2. The Present Issue

This special issue consists of 13 papers especially covering many important topics including seven reviews in the field of organic semiconductors; Organic Semiconductors [13,14], material fabrication and properties [15–18], OFET [19,20], Sensor [19], OLED [21,22], solar Cells [23,24], Transport Property [17], and Bio-organic electronics [25].

The properties of organic material in strong coupling with plasmon, and delocalized and localized plasmon coupled to aggregated dyes and the material properties in strong coupling is described in [13]. The design constraints of OLEDs and OPDs required to achieve fully organic electronic optical bio-detection systems and lab-on-a-chip (LoC) technologies is described in manuscript [14]. The charge transport properties of materials are critical to optimize organic electronic devices.

The importance of charge transport layers in the development of inverted bulk heterojunction polymer solar cells is the focus of [24] and the intrinsic bulk electron-phonon interaction and the behavior of mobility in the coherent regime of many systems, such as naphthalene, rubrene, and pentacene, is the focus of [17]. Properties of materials that can be used organic semiconductors are reported in references [15–18].

An overview of OFET-based biosensors, pressure sensors and e-nose/vapour sensors is presented in [19]. The charge transport properties of dinaphtho[2,3-*b*:2',3'-*f*]thieno[3,2-*b*]thiophene single crystals in OFET is studied and its nonmonotonic pressure response is demonstrated [20]. The review "Emerging Transparent Conducting Electrodes for Organic Light Emitting Diodes" focuses on the emerging alternative transparent conducting electrodes materials for OLED applications, including carbon nanotubes, metallic nanowires, conductive polymers, and graphene [21]. Improvement in the lifetime of organic photovoltaic cells by using MoO3 in conjunction with *tris*-(8-hydroxyquinoline) aluminum as a cathode buffer layer is analysed [22]. The concept of bandgap science of organic semiconductor films for use in photovoltaic cells, charge control by doping and design of the built-in potential based on precisely-evaluated doping parameters is summarized in the manuscript [23]. The use of electron and hole transport layers in the inverted bulk heterojunction polymer solar cells is the goal of the article [24].

Bio-electronic devices can be used for developing OLEDs, OFETs and organic solar cells and such components have many advantages especially the biodegradable property. The potential opportunities of bio-organic electronics are reviewed in [25].

## 3. Future

New applications are likely to be in areas of biomedicine, lab-on-a-chip biomedical application, optics, OFETs, OLEDs, displays, information technology, smartcards/RFID tags, and sensors for environmental monitoring. The organic electronic devices will be very promising in niche applications, especially due to the cheap manufacturing cost, flexibility, and ease to integrate with other systems. OFETs prove to be important in applications ranging from sophisticated medical diagnostics to "smart" clothes that can display changing images. OFET-based sensors have many advantages over other types of sensors, such as signal amplification, high sensitivity, ease of fabrication, and miniaturisation for multisensory arrays. Organic semiconductors can interact with different chemicals and it is possible to convert the chemical information to electronic information, creating an "electronic nose".

## Acknowledgments

First of all I would like to thank all researchers who published articles to this special issue for their excellent contributions. I am also grateful to all reviewers who helped in the evaluation of the manuscripts and made very valuable suggestions to improve the quality of contributions. I would like to acknowledge Mostafa Bassiouni, the Editor-in-Chief, who invited me to guest edit this special issue. I am also grateful to the Electronics Editorial Office staff who worked thoroughly to maintain the rigorous peer-review schedule and timely publication.

**References**


1. He, Z.; Zhong, C.; Huang, X.; Wong, W.Y.; Wu, H.; Chen, L.; Su, S.; Cao, Y. Simultaneous Enhancement of Open, Circuit Voltage, Short, Circuit Current Density, and Fill Factor in Polymer Solar Cells. *Adv. Mater.* **2011**, *23*, 4636–4643.
2. Jorgensen, M.; Norrman, K.; Krebs, F.C. Stability/degradation of polymer solar cells. *Sol. Energy Mater. Sol. Cells* **2008**, *92*, 686–714.
3. Jacob, M.V.; Bazaka, K.; Weis, M.; Taguchi, D.; Manaka, T.; Iwamoto, M. Fabrication and characterization of polyterpenol as an insulating layer and incorporated organic field effect transistor. *Thin Solid Films* **2010**, *518*, 6123–6129.
4. Schreiber, R.; Do, J.; Roller, E.-M.; Zhang, T.; Schüller, V.J.; Nickels, P.C.; Feldmann, J.; Liedl, T. Hierarchical assembly of metal nanoparticles, quantum dots and organic dyes using DNA origami scaffolds. *Nat. Nanotechnol.* **2014**, *9*, 74–78.
5. Lee, C.H.; Schiros, T.; Santos, E.J.; Kim, B.; Yager, K.G.; Kang, S.J.; Sunwoo Lee, S.; Yu, J.; Watanabe, K.; Taniguchi, T.; *et al*. Epitaxial Growth of Molecular Crystals on van der Waals Substrates for High-Performance Organic Electronics. *Adv. Mater.* **2014**, *26*, 2812–2817.
6. Takahashi, T.; Yu, Z.; Chen, K.; Kiriya, D.; Wang, C.; Takei, K.; Shiraki, H.; Chen, T.;·Ma, B.; Javey, A. Carbon Nanotube Active-Matrix Backplanes for Mechanically Flexible Visible Light and X-ray Imagers. *Nano Lett.* **2013**, *13*, 5425–5430.
7. Park, K.S.; Cho, B.; Baek, J.; Hwang, J.K.; Lee, H.; Sung, M.M. Single-Crystal Organic Nanowire Electronics by Direct Printing from Molecular Solutions. *Adv. Funct. Mater.* **2013**, *23*, 4776–4784.
8. Rolin, C.; Forrest, S.R. Diffusion coefficients of fluorescent organic molecules in inert gases. *Appl. Phys. Lett.* **2013**, *103*, 041911.
9. Robb, M.J.; Ku, S.Y.; Brunetti, F.G.; Hawker, C.J. A renaissance of color: New structures and building blocks for organic electronics. *J. Polym. Sci. Part A Polym. Chem.* **2013**, *51*, 1263–1271.
10. Hanggi, P. Organic electronics: Harvesting randomness. *Nat. Mater.* **2011**, *10*, 6–7.
11. Shinar, J. Organic electronics: Organic thin-film magnetometers. *Nat. Mater.* **2012**, *11*, 663–664.
12. Zhou, Y.; Fuentes-Hernandez, C.; Shim, J.; Meyer, J.; Giordano, A.J.; Li, H.; Winget, P.; Papadopoulos, T.; Cheun, H.; Kim, J.; *et al.* A Universal Method to Produce Low, ÄìWork Function Electrodes for Organic Electronics. *Science* **2012**, *336*, 327–332.
13. Bellessa, J.; Symonds, C.; Laverdant, J.; Benoit, J.-M.; Plenet, J.C.; Vignoli, S. Strong Coupling between Plasmons and Organic Semiconductors. *Electronics* **2014**, *3*, 303–313.
14. Williams, G.; Backhouse, C.; Aziz, H. Integration of Organic Light Emitting Diodes and Organic Photodetectors for Lab-on-a-Chip Bio-Detection Systems. *Electronics* **2014**, *3*, 43–75.
15. Ahmad, J.; Bazaka, K.; Jacob, M. Optical and Surface Characterization of Radio Frequency Plasma Polymerized 1-Isopropyl-4-Methyl-1,4-Cyclohexadiene Thin Films. *Electronics* **2014**, *3*, 266–281.

16. Chiarella, F.; Barra, M.; Ricciotti, L.; Aloisio, A.; Cassinese, A. Morphology, Electrical Performance and Potentiometry of PDIF-$CN_2$ Thin-Film Transistors on HMDS-Treated and Bare Silicon Dioxide. *Electronics* **2014**, *3*, 76–86.
17. Perroni, C.; Gargiulo, F.; Nocera, A.; Ramaglia, V.; Cataudella, V. The Effects of Different Electron-Phonon Couplings on the Spectral and Transport Properties of Small Molecule Single-Crystal Organic Semiconductors. *Electronics* **2014**, *3*, 165–189.
18. Suzuki, A.; Nishimura, K.; Oku, T. Effects of Germanium Tetrabromide Addition to Zinc Tetraphenyl Porphyrin/Fullerene Bulk Heterojunction Solar Cells. *Electronics* **2014**, *3*, 112–121.
19. Elkington, D.; Cooling, N.; Belcher, W.; Dastoor, P.; Zhou, X. Organic Thin-Film Transistor (OTFT)-Based Sensors. *Electronics* **2014**, *3*, 234–254.
20. Sakai, K.-I.; Takeya, J. Anomalous Response in Heteroacene-Based Organic Field Effect Transistors under High Pressure. *Electronics* **2014**, *3*, 255–265.
21. Song, T.-B.; Li, N. Emerging Transparent Conducting Electrodes for Organic Light Emitting Diodes. *Electronics* **2014**, *3*, 190–204.
22. Cattin, L.; Morsli, M.; Bernède, J. Improvement In the Lifetime of Planar Organic Photovoltaic Cells through the Introduction of $MoO_3$ into Their Cathode Buffer Layers. *Electronics* **2014**, *3*, 122–131.
23. Hiramoto, M.; Kubo, M.; Shinmura, Y.; Ishiyama, N.; Kaji, T.; Sakai, K.; Ohno, T.; Izaki, M. Bandgap Science for Organic Solar Cells. *Electronics* **2014**, *3*, 351–380.
24. Lattante, S. Electron and Hole Transport Layers: Their Use in Inverted Bulk Heterojunction Polymer Solar Cells. *Electronics* **2014**, *3*, 132–164.
25. Mühl, S.; Beyer, B. Bio-Organic Electronics—Overview and Prospects for the Future. *Electronics* **2014**, *3*, 444–461.

# Section I: Organic Semiconductors

## Chapter 1

## Strong Coupling between Plasmons and Organic Semiconductors

**Joel Bellessa, Clementine Symonds, Julien Laverdant, Jean-Michel Benoit, Jean Claude Plenet and Stephane Vignoli**

**Abstract:** In this paper we describe the properties of organic material in strong coupling with plasmon, mainly based on our work in this field of research. The strong coupling modifies the optical transitions of the structure, and occurs when the interaction between molecules and plasmon prevails on the damping of the system. We describe the dispersion relation of different plasmonic systems, delocalized and localized plasmon, coupled to aggregated dyes and the typical properties of these systems in strong coupling. The modification of the dye emission is also studied. In the second part, the effect of the microscopic structure of the organics, which can be seen as a disordered film, is described. As the different molecules couple to the same plasmon mode, an extended coherent state on several microns is observed.

Reprinted from *Electronics*. Cite as: Bellessa, J.; Symonds, C.; Laverdant, J.; Benoit, J.-M.; Plenet, J.C.; Vignoli, S. Strong Coupling between Plasmons and Organic Semiconductors. *Electronics* **2014**, *3*, 303-313.

### 1. Introduction

Organic materials have met a growing interest during the past few decades for their various applications in integrated optics and microelectronic. Many of these materials efficiently interact with light due to their large oscillator strength [1,2] and their optical properties can be drastically modified by their environment. In particular, the strong light-matter coupling regime can be reached, inducing dramatic modifications of the energy transition and dynamic behavior. In this regime the plasmon-emitter interaction is predominant compared to the damping in the system leading to the formation of hybrid exciton/plasmon states, associated to an anticrossing of the dispersion lines.

The strong coupling regime with organics has been first demonstrated with microcavities [3]. More recently, polaritons lasing [4] or reversible switching [5] have been evidenced with organics in strong coupling, paving the way of new applications. Beside the studies in microcavities, organic materials have been used for the demonstration of strong coupling with surface plasmons [6]. In this case the molecular excitations interact with surface waves propagating on a metallic interface. The strong coupling with plasmon has been demonstrated with different types of organics [6–8] and plasmon geometries: propagating and localized plasmons [9–11].

The organic layers like dye assemblies present a disordered structure at a microscopic scale. As this structure is smaller than the wavelength, the main properties such as the Rabi splitting can be understood considering a homogeneous film with an effective absorption and refractive index. However, a fine analysis of the emission properties requires taking into account the microscopic structure of the organic layer [12]. The strong coupling modifies the molecules behavior. They are not independent anymore, and a coherent state mixing the plasmon and excitation of a large number of molecules is formed. This coherent state induces coherent emission on micron scale [13].

In this paper we describe some properties of organic materials in strong coupling with plasmons. In a first part the effect of the proximity of a metallic film on the absorption and emission or J-aggregated dye is described. In the second part of the paper, we show that a dramatic increase of the interaction energy occurs for localized plasmons resonances coupled to excitons. In a third part, the influence of the disordered microscopic structure of the plasmons will be studied. We demonstrate that the strong coupling results in the formation of an extended coherent state, mixing excitations in a large number of different molecular sites.

## 2. Strong Coupling between Propagating Plasmons and Organics

The strong coupling between plasmons and excitons occurs when the plasmon-emitter interaction becomes predominant compared to the damping in the system. The strong coupling leads to a characteristic anticrossing in the dispersion lines, and to the formation of mixed exciton/plasmon states, namely polaritons. This regime with delocalized surface plasmons (SPs) has been demonstrated for different organic materials such as J-aggregated dyes [6,14] or laser dyes [7]. In a first approach the microscopic structure of the organic layer can be neglected, and the layer can be considered as a continuous absorbing film. In this part we will give an example of strong coupling with J-aggregated dyes to extract the main properties of the resulting hybrid states.

To demonstrate strong coupling between SPs and organic excitons, we used as the active material a J-aggregated cyanine dye (5,5',6,6'-tetrachloro-1,1'-diethyl-3, 3'-di(4-sulfobutyl)-benzimidazolocarbocyanine (TDBC)). This material is well suited for the observation of strong coupling due to the aggregation of the monomers that occurs when their concentration in water is sufficient, which induces a redshift and a narrowing of the absorption band. Figure 1 presents the monomer absorption band of a solution of TDBC diluted in water (i), as well as the J-band of a solution of aggregated TDBC in water (ii). The J-aggregate absorption spectrum is characterized by a single, narrow and intense band lying at about 590 nm (2.1 eV). This band corresponds to the emission of delocalized excitation in the molecular chain, Frenkel excitons. The same optical behavior is observed for a TDBC layer deposited directly on glass (data not shown). The samples studied were constituted of a 45 nm thick silver film produced by thermal evaporation under a pressure of $10^{-7}$ mbar. The active layer (pure TDBC diluted in water) is then spin-coated onto this stack (see inset of Figure 1).

**Figure 1.** Absorption spectra of a solution of (i) TDBC monomer (black line) and (ii) TDBC J-aggregates in water (red line). The inset presents the chemical formula of TDBC and a sketch of a typical sample.

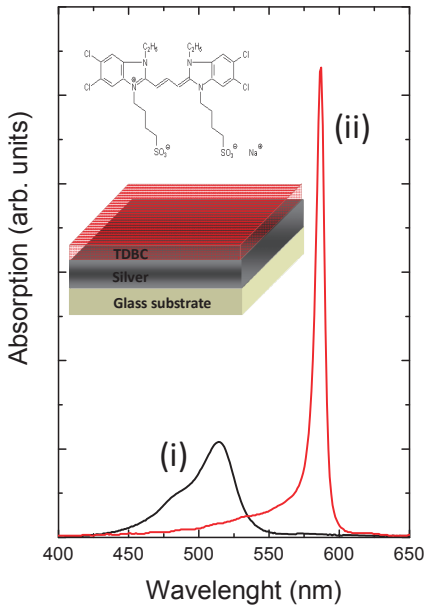


In order to investigate the interactions between silver SPs and excitons, reflectometry under the light cone has to be performed. For this purpose, leakage radiation microscopy [15] or reflectivity in the Kretschmann geometry [16] can be used. The incident light is coupled to the SP mode when the projection of its wavevector on the silver plane matches the wavevector of the SP located at the silver-active layer interface, resulting in a lack of the reflection intensity at the SP energy. The value of the SP wavevector is $k=\frac{2\pi}{\lambda}n_p sin\theta$, where $n_p$ is the refractive index of the incident medium and θ is the incident angle of the light in the prism. The SP energy depends on its wave vector and can be changed by modifying the incident light angle, which enables the SP resonance to be tuned and thus cross the exciton energy.

A typical reflectometry image in leakage radiation microscopy is shown in Figure 2a. In this configuration $k=\frac{2\pi}{\lambda}N.A.$ where $N.A.$ is the numerical aperture of the incident light and is proportional to the sine of the incident angle. It has to be noticed that the $N.A.$ used here is not the total numerical aperture of the microscope objective but a value characterizing the incident angle of the illumination. Two dispersion lines can be seen on the image, one at high wavelength and one less pronounced at lower wavelength. The polariton energies can be calculated using a coupled oscillator model [17] (plasmon and excitons), $E_{U,L}(k)=\left(E_{pl}(k)+E_0\right)/2\pm\sqrt{(\Delta/2)^2+\left(E_{pl}(k)-E_0\right)^2/4}$ where $k$ is the in-plane wavevector, $E_U$ and $E_L$ the energies of the upper and lower polariton states and $E_0$ the energy of the TDBC exciton. $E_{pl}(k)$ is the non interacting plasmon mode energy, calculated using a conventional transfer matrix method with thicknesses of 10 nm for the TDBC layer and 50 nm for the silver film. $\Delta$ is given by the interaction energy between the plasmon and exciton, also called Rabi splitting, and corresponds to the minimum energy separation between the two branches. The solid white lines in Figure 2a represent the calculated polariton dispersion and the dashed lines the

bare plasmon and exciton. A good agreement with experimental data is obtained for a Rabi splitting energy of 300 meV.

**Figure 2.** (**a**) Reflectometry and (**b**) luminescence spectra of a TDBC layer deposited on a 45 nm silver film, displayed as a function of the wavelength and the numerical aperture (*N.A.*). The dashed lines in (**a**) correspond to the bare plasmon and exciton dispersion, and the solid lines to the calculated low energy and high energy polaritonic branches.

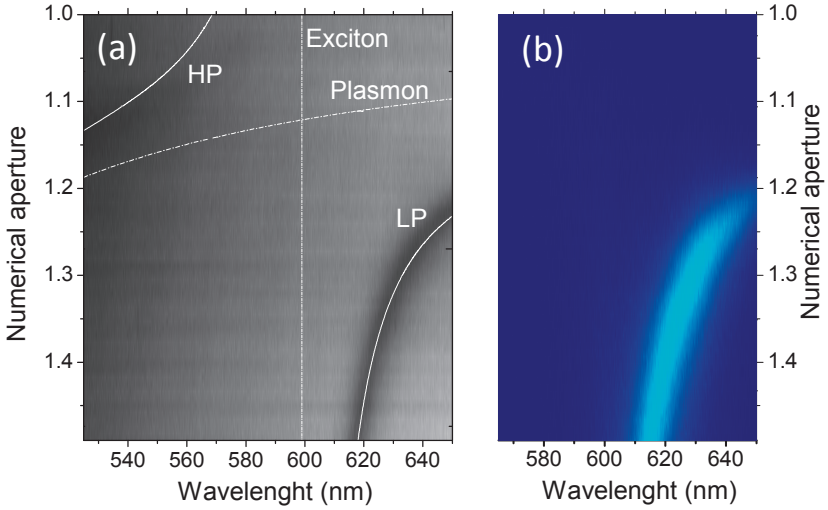


Luminescence experiments are then performed by exciting the top side of the sample (the TDBC side) with a 532 nm diode laser, and by collecting the emitted light trough the silver layer using the same high numerical aperture objective than for the reflectometry experiment. The recorded image of the emission dispersion is presented in Figure 2b. On this image, the intense emission band is clearly related to the emission of the low energy polariton. The emission of the high energy polariton is however not visible. This effect, already reported in the literature, could possibly be attributed to the emission of optical phonons between the two polaritonic branches [17] or to nonradiative decay of the upper polaritonic states towards uncoupled excitonic states [12].

The angle dependence of the polariton energy is more clearly illustrated by the dispersion curves shown in Figure 3a,b where the calculated energy positions of bare excitons and plasmons are also presented as a function of the wavevector or the angle, respectively. The experimental data present a clear anticrossing between the two lines, characteristic of the strong coupling regime occurring between the SP mode and the TDBC exciton. This strong coupling regime leads to the formation of mixed Plasmon-exciton states, that is to say the high- and low-energy polaritonic branches. It has to be noticed that the minimum energy separation between the hybrid states dispersion lines is not the same if the dispersion energies are shown as a function of the wavevector or the angle (300 meV and 780 meV respectively). The good parameter to qualify the polariton is the wavevector: a plasmon with a given wavevector creates two hybrid states with the same wavevector. This difference between curves in angle or wavevector occurs only for the large energy splitting reached for organics and has not to be taken into account for splitting of a few tens of meV usually obtained for inorganic semiconductors [18].

**Figure 3.** Reflectometry dip energy position (open circles) as a function of (**a**) the wavevector and (**b**) the angle. The dashed lines correspond to the calculated bare plasmon and exciton position, the solid lines to the calculated polaritonic branches.

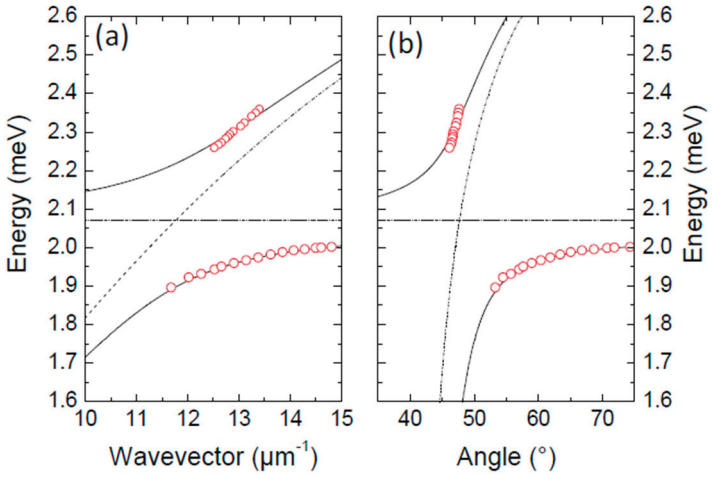


In addition to the dispersion lines anticrossing, an inversion of the dip linewidths is associated with the strong coupling regime [19]. At resonance, the polariton states are formed by an admixture of equal weight of plasmon and exciton, and the widths of the two peaks should be the same.

## 3. Strong Coupling with Localized Plasmons

The values of the Rabi splitting measured for delocalized plasmons in strong coupling with organics reach several hundred of meV. These large values are related to the large oscillator strength of the organic materials as well as the efficient interaction of plasmon spatially confined around the interface. This coupling can be enhanced by using localized plasmons, which present higher spatial confinement of the electric field. This enhanced interaction with localized plasmon has been evidenced in the weak coupling regime, leading to an increase of luminescence [20], but is also present in strong coupling [5,21,22]. Different geometries have been used like nanoshells or nanorods [9,23,24]. Metallic nanodisks (NDs) made by lithography are also good candidates to study the coupling between organics and localized plasmons [10,25]. The main advantage of lithographed structures is that the size of the NDs and their environment (other disks and semiconductor) are well controlled, thereby avoiding a large inhomogeneous broadening of the plasmonic resonances, which could partially mask the plasmon/exciton hybridization. Furthermore, the lithography technique is fully compatible with passive plasmonic devices, such as low-attenuation guides or plasmonic nano cavities developed recently.

In order to study the interaction between localized surface plasmon (LSP) and J-aggregated dyes, Ag NDs have been elaborated on a glass substrate. For this purpose, circular patterns have been defined on a resist layer by e-beam lithography. A 60 nm thick silver film was evaporated on the lithographed structure, and then removed by the lift-off technique hence revealing the silver ND assemblies on the surface. Each assembly consists of a 200 by 200 μm array made of several tens of thousands of NDs separated by 210 nm side to side. Several arrays, with different ND diameters, were fabricated in order to tune the LSP resonance energy. The ND sizes range from 100 nm to 210 nm.

As the localized plasmon resonance can be directly determined with extinction measurements, transmission experiments were done at room temperature on circular regions (50 µm diameter) probing around $2 \times 10^4$ identical NDs. A pronounced transmission dip is observed for each array, associated to the ND LSP resonance. When decreasing the ND diameter, this transmission dip experiences an energy blueshift. Figure 4a shows the experimental variation of the LSP resonance energy as a function of the ND diameter. Transmission spectra were also simulated with 3D FDTD calculations using the silver dielectric constant values reported by Johnson *et al.* [26]. The calculated spectra are shown in color map in Figure 4a and present an excellent agreement with the experimental data.

**Figure 4.** Measured energy of the transmission dips (white circles) as a function of the disk diameter and 3D FDTD calculated transmission spectra for (**a**) a bare sample and (**b**) a sample covered with a TDBC layer.

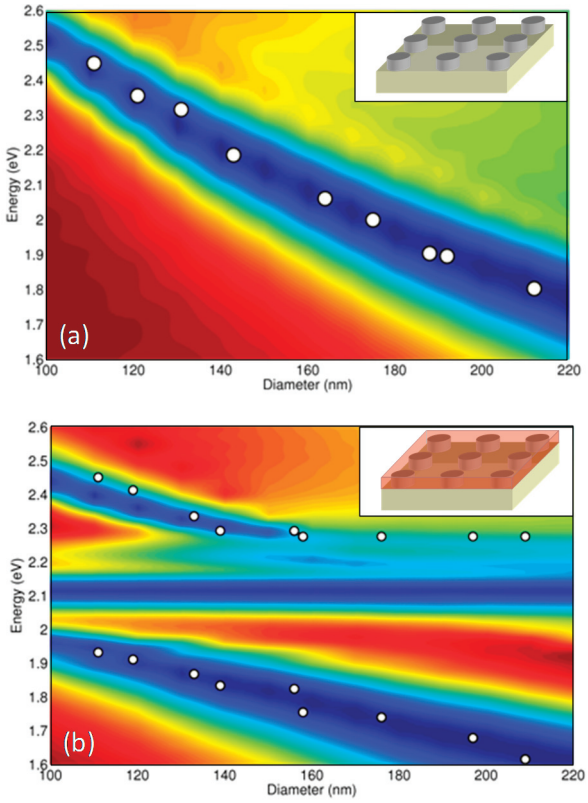


To create hybrid localized plasmons/excitons, an active layer of pure TDBC diluted in water was spin coated onto the whole sample surface. The transmission spectra for this sample show two resonances whose energy positions are dependent of the disk diameter, which is summarized in Figure 4b. A clear anticrossing behavior can be observed in this plot, which is the signature of localized plasmon-exciton strong coupling. For a given disk size, each resonance can thus be associated to a plasmon/exciton mixed state. This result is confirmed by the transmission spectra calculated by 3D FDTD, in which a dye layer of total thickness 22.5 nm has been considered. The calculated and the experimental values are again in excellent agreement. The non dispersive transmission dip lying around 2.1 eV corresponds to the absorption of the uncoupled exciton, originating from the regions between the NDs in which the TDBC cannot interact with the LSP.

From Figure 4a, it can be seen that for ND diameter of about 150 nm the bare plasmon resonance lies at the same energy that the one of the uncoupled excitonic absorption. The minimum energy splitting between the mixed states is obtained for the same ND size in Figure 4b, leading to an estimated Rabi splitting of 450 meV [10]. This value amounts to 20% of the transition energy and metal nanodisks can be considered as a model system to study very strong interaction between a single electromagnetic mode and an optically active medium [27,28].

## 4. Influence of Microscopic Disorder of Organics and Plasmon Induced Coherence

In the previous description of the strong coupling regime with organics, the microscopic structure of the organics was not taken into account. From a microscopic point of view, the organic films are formed by an ensemble of localized independent emitters which can be seen as point dipoles as their size is several orders of magnitude smaller than the wavelength.

The molecular film differs from inorganic semiconductor quantum wells as the in plane wavevector is not conserved in absorption-reemission, which is the case for semiconductor quantum wells (excitons center of mass wavevector equals in-plane photon wavevector). The question which arises is how the coherent absorption/reemission, in other word the Rabi oscillation associated to the strong coupling regime, occurs; or how a dispersive plasmon can hybridize with non-dispersive molecules to form dispersive hybrid states. This problem has been addressed by Agranovich *et al.* [12]. They have shown that a coherent state over a large number of molecules is formed in strong coupling regime. The plasmon/excitons hybrid state is a quantum superposition of a photon and excitations on a large number of molecular sites. The extension of the states is directly correlated to the disorder in the organic film and to the losses of the propagating plasmon. From an experimental point of view, the dependence of the Rabi splitting on the concentration of emitters is a good indication of collective effects; however, the coherence of spatially remote emitters induced by hybridization with a plasmon can also be directly observed [13].

To clearly separate the effect of the plasmon/exciton hybridization from the extension only associated with the plasmon propagation, samples in strong and weak coupling were compared. The active layer of the first sample (sample A) contains a continuous layer of CdSe quantum dots in weak coupling regime (a crossing between plasmon and excitons appears in reflectometry images). The second sample (sample B) contains a TDBC layer on silver and is similar as the sample described in the part 2 (Rabi splitting 300 meV).

To evidence the formation of the extended state mixing a plasmon and excitation of different molecules, coherence experiments using Young slits have been performed. The leakage radiation (LR) microscopy setup already mentioned in part 2 is detailed in Figure 5. The sample is excited with a non-resonant laser at 532 nm. The emission is collected through an immersion oil microscope objective (*N.A.* = 1.49) and imaged on a CCD camera. On a direct image of the surface, the directions of propagation can be selected by inserting beam block in the Fourier plane of the objective [29] collecting either all the propagating directions ($k_{total}$ configuration) or solely the upward propagation as shown in the inset in Figure 5 ($k_{up}$ configuration). To analyze the coherence of the emission, two Young slits can be inserted in an intermediate image plane of the sample and select the emission from two regions of the sample separated by a distance of 2 μm.

**Figure 5.** Sketch of the leakage radiation microscopy setup. BB denotes the position of the removable beam block, FP the Fourier plane, FL the Fourier lens, and Π the intermediate image plane of the sample surface in which are inserted the Young's slits. The black line labeled 1 is devoted to dispersion measurements, and the red line labeled 2 to coherence measurements.

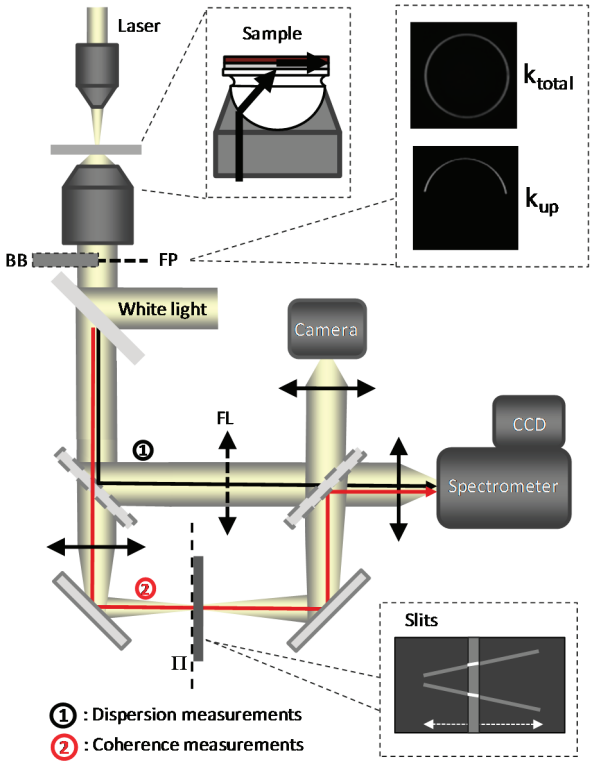


Direct images of the emission as well as the corresponding interference patterns are shown on the left and right side of the panels of Figure 6a–d. A focalized excitation is used corresponding to the white spot at the center of the direct images, which is smaller than the distance between the Young slits (dashed red rectangles). For the sample A in weak coupling regime an upward and downward propagation appear in the direct Image 6a and only an upward propagation in Figure 6b where a Fourier beam block was used. This agrees with a mechanism where each emitter in the excitation spot couples independently to plasmons propagating upwards and downwards in Figure 6a and only upward in Figure 6b. The corresponding interference patterns do not show any fringes, related to the incoherent emission of the different emitters.

The system in strong coupling regime corresponds to the panels Figure 6c and Figure 6d. The shape of the emission in direct images is now similar with Figure 6c and without Figure 6d Fourier filtering. This shows that the emission observed cannot be interpreted as a sum of emission of independent molecules coupled to propagating plasmons. In the interference pattern, clear fringes are present showing a coherent emission over all the luminescence spot. These results show a clear collective behavior, and evidence the formation of a coherent state extended on several microns [13]. In this case the excitation directly relaxes in the extended state with a given wavevector, explaining the large coherent emission spot observed in Figure 6d.

**Figure 6.** Direct imaging of the surface leakage radiation together with the associated interference pattern recorded for two samples: CdSe nanocrystals in weak coupling with the surface plasmon recorded in (**a**) $k_{total}$ and (**b**) $k_{up}$ detection configuration; TDBC in strong coupling regime with the surface plasmon recorded in (**c**) $k_{total}$ and (**d**) $k_{up}$ detection configuration.

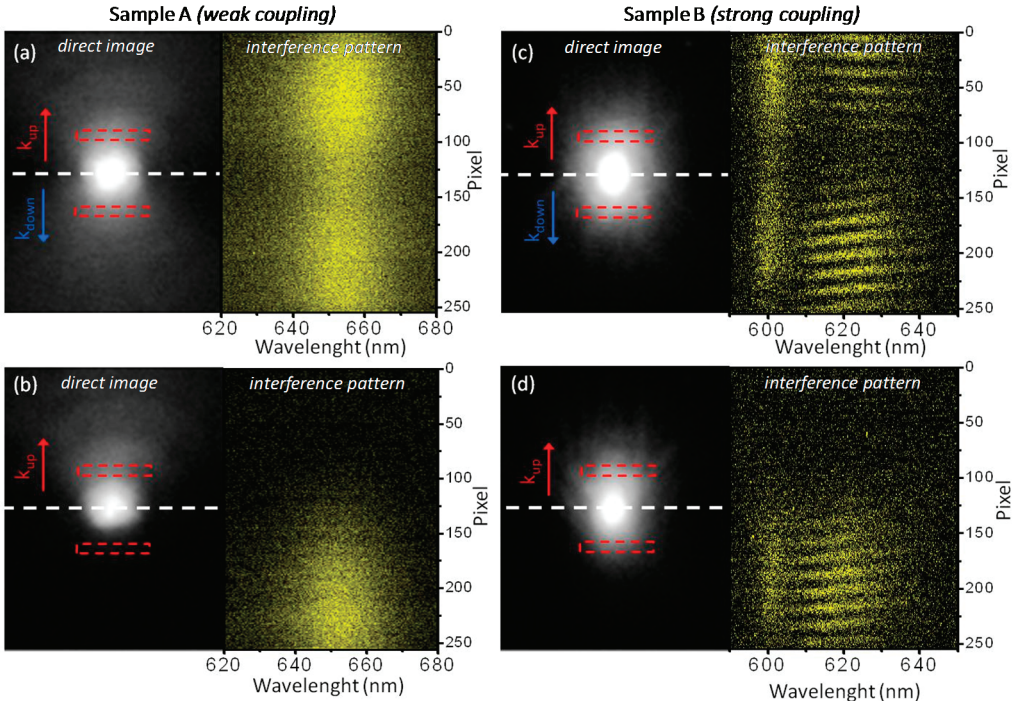


## 5. Conclusions

Organic structures are particularly well suited for the study of the strong coupling with surface plasmons, due to their high oscillator strength. This strong coupling modifies the absorption and emission energies, associated with the formation of hybrid plasmon/excitons states. The detection of the dispersion relation allows a direct determination of the interaction energy and the oscillator strength in these structures. The strong coupling with plasmon couples the different molecules deposited on a metal surface, coupling which leads to a coherent emission over several microns. This coherence can be used for energy transfer mediated by plasmon on a micrometer scale.

## Conflicts of Interest

The authors declare no conflict of interest.

## References

1. Scherer, P.O.J. Molecular aggregate spectra. In *J-aggregate*, 1st ed.; Kobayashi, T., Ed.; World Scientific Publishing: Toh Tuck, Singapore, Singapore, 1996; pp. 95–110.
2. Tischler, J.R.; Bradley, M.S.; Zhang, Q.; Atay, T.; Nurmikko, A.; Bulovic, V. Solid state cavity QED: Strong coupling in organic thin films. *Org. Electron.* **2007**, *8*, 94–113.

3. Lidzey, D.G.; Bradley, D.D.C.; Skolnick, M.S.; Virgili, T.; Walker, S.; Whittaker, D.M. Strong exciton-photon coupling in an organic semiconductor microcavity. *Nature* **1998**, *395*, 53–55.
4. Kena-Cohen, S.; Forrest, S.R. Room-temperature polariton lasing in an organic single-crystal microcavity. *Nat. Photon.* **2010**, *4*, 371–375.
5. Schwartz, T.; Hutchison, J.A.; Genet, C.; Ebbesen, T.W. Reversible switching of ultrastrong light-molecule coupling. *Phys. Rev. Lett.* **2011**, *106*, 196405.
6. Bellessa, J.; Bonnand, C.; Plenet, J.C.; Mugnier, J. Strong coupling between surface plasmons and excitons in an organic semiconductor. *Phys. Rev. Lett.* **2004**, *93*, 036404.
7. Hakala, T.K.; Toppari, J.J.; Kuzyk, A.; Pettersson, M.; Tikkanen, H.; Kunttu, H.; Törmä, P. Vacuum rabi splitting and strong-coupling dynamics for surface-plasmon polaritons and rhodamine 6G molecules. *Phys. Rev. Lett.* **2009**, *103*, 053602.
8. Symonds, C.; Bellessa, J.; Plenet, J.C.; Bréhier, A.; Parashkov, R.; Lauret, J.S.; Deleporte, E. Emission of hybrid organic-inorganic exciton/plasmon mixed states. *Appl. Phys. Lett.* **2007**, *90*, 091107.
9. Fofang, N.T.; Park, T.H.; Neumann, O.; Mirin, N.A.; Nordlander, P.; Halas, N.J. Plexcitonic nanoparticles: Plasmon-exciton coupling in Nanoshell-J-Aggregate complexes. *Nano Lett.* **2008**, *8*, 3481–3487.
10. Bellessa, J.; Symonds, C.; Vynck, K.; Lemaitre, A.; Brioude, A.; Beaur, L.; Plenet, J.C.; Viste, P.; Felbacq, D.; Cambril, E.; *et al.* Giant Rabi splitting between localized mixed plasmon-exciton states in a two-dimensional array of nanosize metallic disks in an organic semiconductor. *Phys. Rev. B* **2009**, *80*, 033303.
11. Wurtz, G.A.; Evans, P.R.; Hendren, W.; Atkinson, R.; Dickson, W.; Pollard, R.J.; Zayats, A.V.; Harrison, W.; Bower, C. Molecular plasmonics with tunable exciton-plasmon coupling strength in J-aggregate hybridized Au nanorod assemblies. *Nano Lett.* **2007**, *7*, 1297–1303.
12. Agranovich, V.M.; Litinskaia, M.; Lidzey, D.G. Cavity polaritons in microcavities containing disordered organic semiconductors. *Phys. Rev. B* **2003**, *67*, 085311.
13. Aberra Guebrou, S.; Symonds, C.; Homeyer, E.; Plenet, J.C.; Gartstein, Y.N.; Agranovich, V.M.; Bellessa, J. Coherent Emission from a disordered organic semiconductor induced by strong coupling with surface plasmons. *Phys. Rev. Lett.* **2012**, *108*, 066401.
14. Dintinger, J.; Klein, S.; Bustos, F.; Barnes, W.L.; Ebbesen, T.W. Strong coupling between surface plasmon-polaritons and organic molecules in subwavelength hole arrays. *Phys. Rev. B* **2005**, *71*, 035424.
15. Hecht, B.; Bielefeldt, H.; Novotny, L.; Inouye, Y.; Pohl, D.W. Local excitation, scattering, and interference of surface plasmons. *Phys. Rev. Lett.* **1996**, *77*, 1889–1892.
16. Raether, H.; Kretschmann, K. Radiative decay of non radiative surface plasmons excited by light. *Z. Naturforsch*. **1968**, *23*, 2135–2136.
17. Lidzey, D.G.; Fox, A.M.; Rahn, M.D.; Skolnik, M.S.; Agranovich, V.M.; Walker, S. Experimental study of light emission from strongly coupled organic semiconductor microcavities following nonresonant laser excitation. *Phys. Rev. B* **2002**, *65*, 195312.

18. Symonds, C.; Bonnand, C.; Plenet, J.C.; Brehier, A.; Parashkov, R.; Lauret, J.S.; Deleporte, E.; Bellessa, J. Particularities of surface Plasmon-exciton strong coupling with large Rabi splitting. *New J. Phys.* **2008**, *10*, 065017.
19. Bonnand, C.; Bellessa, J.; Plenet, J.C. Properties of surface plasmons strongly coupled to excitons in an organic semiconductor near a metallic surface. *Phys. Rev. B* **2006**, *73*, 245330.
20. Furno, M.; Meerheim, R.; Hofmann, S.; Lussem, B.; Leo, K. Efficiency and rate of spontaneous emission in organic electroluminescent devices. *Phys. Rev. B* **2012**, *85*, 115205.
21. Schlather, A.E.; Large, N.; Urban, A.S.; Nordlander, P.; Halas, N.J. Near-Field mediated plexcitonic coupling and giant Rabi Splitting in individual metallic dimers. *Nano Lett.* **2013**, *13*, 3281–3286.
22. Balci, S. Ultrastrong plasmon-exciton coupling in metal nanoprisms with J-aggregates. *Optics Lett.* **2013**, *38*, 4498–4501.
23. Ni, W.; Ambjörnsson, T.; Apell, S.P.; Chen, H.; Wang, J. Observing plasmonic-molecular resonance coupling on single gold nanorods. *Nano Lett.* **2010**, *10*, 77–84.
24. Djoumessi Lekeufack, D.; Brioude, A.; Coleman, A.W.; Miele, P.; Bellessa, J.; de Zeng, L.; Stadelmann, P. Core-shell gold J-aggregate nanoparticles for highly efficient strong coupling applications. *Appl. Phys. Lett.* **2010**, *96*, 253107.
25. Baudrion, A.L.; Perron, A.; Veltri, A.; Bouhelier, A.; Adam, P.M.; Bachelot, R. Reversible strong coupling in silver nanoparticle arrays using photochromic molecules. *Nano Lett.* **2013**, *13*, 282–286.
26. Johnson, P.B.; Christy, R. Optical constants of the noble metals. *Phys. Rev. B* **1972**, *6*, 4370.
27. Ciuti, C.; Bastard, G.; Carusotto, I. Quantum vacuum properties of the intersubband cavity polariton field. *Phys. Rev. B* **2005**, *72*, 115303.
28. Anappara, A.A.; de liberato, s.; Tredicucci, A.; Ciuti, C.; Biasiol, G.; Sorba, L.; Beltram, F. Signatures of the ultrastrong light-matter coupling regime. *Phys. Rev. A* **2009**, *79*, 201303.
29. Drezet, A.; Hohenau, A.; Stepanov, A.L.; Ditlbacher, H.; Steinberger, B.; Galler, N.; Aussenegg, F.R.; Leitner, A.; Krenn, J.R. How to erase surface plasmon fringes. *Appl. Phys. Lett.* **2006**, *89*, 091117.

# Chapter 2

# Integration of Organic Light Emitting Diodes and Organic Photodetectors for Lab-on-a-Chip Bio-Detection Systems

**Graeme Williams, Christopher Backhouse and Hany Aziz**

**Abstract:** The rapid development of microfluidics and lab-on-a-chip (LoC) technologies have allowed for the efficient separation and manipulation of various biomaterials, including many diagnostically relevant species. Organic electronics have similarly enjoyed a great deal of research, resulting in tiny, highly efficient, wavelength-selective organic light-emitting diodes (OLEDs) and organic photodetectors (OPDs). We consider the blend of these technologies for rapid detection and diagnosis of biological species. In the ideal system, optically active or fluorescently labelled biological species can be probed via light emission from OLEDs, and their subsequent light emission can be detected with OPDs. The relatively low cost and simple fabrication of the organic electronic devices suggests the possibility of disposable test arrays. Further, with full integration, the finalized system can be miniaturized and made simple to use. In this review, we consider the design constraints of OLEDs and OPDs required to achieve fully organic electronic optical bio-detection systems. Current approaches to integrated LoC optical sensing are first discussed. Fully realized OLED- and OPD-specific photoluminescence detection systems from literature are then examined, with a specific focus on their ultimate limits of detection. The review highlights the enormous potential in OLEDs and OPDs for integrated optical sensing, and notes the key avenues of research for cheap and powerful LoC bio-detection systems.

Reprinted from *Electronics*. Cite as: Williams, G.; Backhouse, C.; Aziz, H. Integration of Organic Light Emitting Diodes and Organic Photodetectors for Lab-on-a-Chip Bio-Detection Systems. *Electronics* **2014**, *3*, 43-75.

## 1. Introduction

Substantial research efforts have been dedicated to the development of lab-on-a-chip (LoC) technologies, which have matured in parallel with the many advances in the field of microfluidics. LoC offers a miniaturized platform for sample processing and can be used to perform numerous life sciences analyses. The labour intensive steps associated with common detection and biomaterial processing schemes (for example, detection and isolation of specific DNA strands, antibodies or pathogens) can be feasibly simplified to a one-step sample injection into a microfluidic well. The appeal of LoC is thus a combination of the following: a reduction in user error, a decrease in materials/sample usage, fast and low cost analysis, and potential automation of routine techniques.

While there have been numerous breakthroughs in the microfluidics of LoC bio-detection systems [1–3], much of the detection methodologies still rely on external lab-scale systems. However, there is a strong desire for completely portable LoC systems for point-of-care

applications. Given its high degree of sensitivity, many groups have sought to integrate fluorescence/photoluminescence (PL) detection techniques into LoC. In the current review, we examine LoC PL-based detection schemes that use organic light emitting diodes (OLEDs) as an excitation source and/or organic photodiodes (OPDs) as a means of detection.

Since OLEDs and OPDs are comprised of thin films deposited by low temperature techniques, they can be easily integrated with most polymer/plastic microfluidic systems (for example, by depositing on the backside of a polydimethylsiloxane (PDMS) microfluidic channel). The capability to fabricate miniaturized OLED pixels is also ideal for LoC, where the microchannel size can be on the order of an individual pixel size [4,5]. Further, the emission and absorption peaks of OLEDs and OPDs respectively are easily tunable—dependent on the choice of small molecule or polymer—so these organic electronic devices are excellent candidates for more advanced detection systems, such as multiplexed immunoassays using multiple PL peaks. This review is organized as follows: the common OLED and OPD device structures, as well as their principles of operation, are discussed in Section 2. Notable developments in optical excitation and detection methods for non-OLED/OPD LoC technologies are detailed in Section 3, highlighting the potential advantages of OLED and OPD integration. Integrated systems employing OLEDs and/or OPDs in LoC technologies will then be addressed in Section 4.

## 2. Operation Principles of Organic Light Emitting Diodes and Organic Photodetectors

Organic electronic devices employ highly conjugated organic species that are divided into two material subsets: small molecules and polymers. In terms of their implementation, small molecule species are historically insoluble and are thus commonly vacuum-deposited by thermal evaporation techniques. In contrast, polymer materials are more easily synthesized to be soluble in common organic solvents. As an addendum to this point, while they are difficult to synthesize, soluble small molecules are feasible and have recently become the subject of intense research [6–8]. Some of the earliest and most studied OLED materials include tris(quinolinolate) Al ($Alq_3$) and 4,4'-bis[*N*-(1-naphthyl)-*N*-phenylamino]biphenyl (NPB/NPD) for small molecule devices [9,10], and poly(*p*-phenylene vinylene) (PPV) derivatives for polymer devices [11]. As a point of note, $Alq_3$ films electroluminesce with a peak wavelength of 530 nm, whereas poly[2-methoxy-5-(2'-ethylhexyloxy)-*p*-phenylene vinylene] (MEH-PPV), a common PPV derivative, emits at 600 nm with a shoulder emission at 640 nm. As an excitation source for LoC applications, the OLED's peak emission must be chosen appropriately to excite the known fluorophore without substantially overlapping the detector's absorption spectrum. From a fabrication standpoint, this is simple to envision, as there now exist OLED materials with peak emission over the entire visible spectrum—in fact, $Alq_3$ on its own can be tailored to emit over most of the visible spectrum [12]. To this end, the position of each organic material's absorption and emission peak is fundamentally related to its chemical structure (especially its degree of conjugation), which can be altered during its synthesis.

Early and common OPD materials include copper phthalocyanine (CuPc), 3,4,9,10-perylenetetracarboxylic bis-benzimidazole (PTCBI) and fullerene ($C_{60}$) for small molecule OPDs [11], and MEH-PPV and 1-(3-methoxycarbonyl)-propyl-1-phenyl-(6,6)$C_{61}$ (PCBM) for polymer OPDs [13]. In OPDs, the hole transport layer and electron transport layer are commonly

referred to as the donor and acceptor respectively, in light of their typical roles in the device (where the donor "donates" a free electron to the acceptor). The donor and acceptor are commonly mixed together to form a bulk heterojunction (BHJ). In principle, simple OPDs have the same structure as organic solar cells (OSCs)—the difference lies in their mode of operation, where OPDs can be negatively biased to enhance free carrier transport. It is therefore logical that many polymer-based OPDs now make use of the ubiquitous poly3-hexylthiophene (P3HT):PCBM BHJ, which is famous for its use in OSCs [14]. Since OPDs are largely adapted from OSC technologies, they absorb strongly over most of the visible spectrum—for example, P3HT:PCBM OPDs generate substantial photocurrent between 350 nm and 650 nm. For LoC applications, the peak absorption of the OPD should correspond well with the fluorophore's emission spectrum, but it should ideally not overlap with the emission from the excitation source.

Illustrations of the general device structures and energy level diagrams of an OLED, a simple bilayer OPD and a mixed layer/BHJ OPD are provided in Figure 1A–C respectively. Each device comprises an electron transport layer (ETL, or an acceptor in the OPD) and a hole transport layer (HTL, or a donor in the OPD), and the OLED may have an additional emissive layer (EML). Note that the energy levels of the metal and ITO layers are their work functions, whereas the energy levels of the organic layers are their highest occupied molecular orbitals (HOMOs) and lowest occupied molecular orbitals (LUMOs). In an even simpler incarnation of the OLED device—the bilayer OLED—either the hole transport layer or the electron transport layer may serve a dual role as the emissive layer. A simple example of this is the ITO/NPB/$Alq_3$/MgAg bilayer OLED. Devices may also make use of additional hole injection/extraction layers (HILs, HELs) and electron injection/extraction layers (EILs, EELs). These are not illustrated in the energy level diagrams, but they are typically few-nm layers (e.g., 5 nm $MoO_3$, 1 nm LiF) used to adjust the electrode work functions and/or to provide enhanced device stability [15–17].

**Figure 1.** Illustration of the common device structures and associated energy level diagrams for a(n) (**A**) organic light emitting diode (**B**) bilayer organic photodetector (**C**) bulk heterojunction organic photodetector.

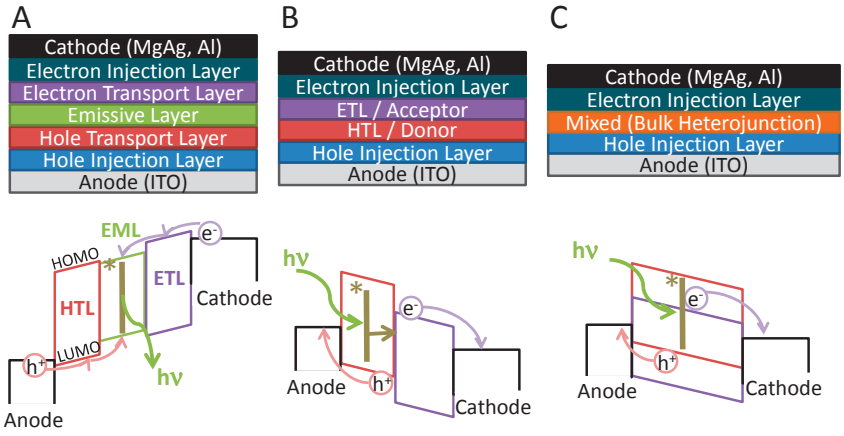

As illustrated in Figure 1A, OLED devices operate as follows:

- A negative bias is applied to the cathode/a positive bias is applied to the anode
- A hole is injected (either by thermionic or field emission) into the HTL and an electron is similarly injected into the ETL
- The electron and hole meet in the EML, form an exciton (denoted as *|), and recombine to emit a photon with energy hν, proportional to the energy gap of the emissive layer.

OPDs operate in approximately the reverse manner, as illustrated in Figure 1B,C, where a photon generates an exciton that is dissociated at a donor-acceptor interface. The specific operation of the OPD is as follows:

- A negative bias is applied to the anode/a positive bias is applied to the cathode
- A photon is absorbed by either the donor or acceptor material (in Figure 1, the photon is absorbed by the donor material) to generate an exciton (denoted as *|)
    - the exciton traverses to the donor/acceptor interface to dissociate into its constituent electron and hole
- The electrons and holes travel along the ETL and HTL to be collected at the cathode and anode respectively.

One of the main limitations to OPD efficiency in the simple bilayer device is the diffusion of the exciton from its point of excitation to the donor/acceptor interface (*i.e.*, before the exciton undergoes recombination). The BHJ architecture serves to minimize exciton diffusion length with an interpenetrating network of donor and acceptor, granting a large number of donor/acceptor interfaces throughout the entire device structure. Unfortunately, this architecture also serves to substantially increase the OPD leakage current since holes can be injected directly from the cathode to the donor HOMO and electrons can be injected directly from the anode to the acceptor LUMO. This effect, however, is avoidable by using a BHJ bordered by neat donor and acceptor layers, referred to as the planar-mixed molecular heterojunction (PM-HJ) [18]. Alternatively, this effect can be minimized through use of carrier-selective extraction layers [19].

The majority of organic electronics research to date has focused on optimization of device performance. For OLEDs, this implies high brightness values through high external quantum efficiencies, with a focus on phosphorescent OLEDs that can show substantial efficiency improvements compared to their fluorescent counter-parts due to electron/hole spin statistics [20]. For OPDs, this implies high “on-off” ratios and, similarly, high external quantum efficiencies, which has been largely addressed with the design of intelligent device architectures [11]. For LoC applications, other critical and less researched device optimizations must also be addressed, such as reducing the full width at half maximum (FWHM) of the OLED emission, and identifying new materials systems for OPDs with narrow regions of absorption. Both efforts should serve to reduce the system dark noise by decreasing light leakage from the excitation source to the detector, ultimately allowing for better detection limits. A final consideration for the use of OLED or OPD detection systems in commercial LoC applications relates to the stabilities of the organic optical elements. However, with proven manufacturability of both OLEDs and OSCs from companies such as Samsung and Heliatek, as well

as a demonstrated potential for extremely long device lifetimes [21,22], it is clear that both OLEDs and OPDs have promise for use in point-of-care LoC systems.

## 3. Early Integration of Optical Excitation and Detection into Lab-on-a-Chip

The vast majority of LoC research to date has been dedicated to finer manipulation of relevant biological species through smart microfluidics. Comprehensive reviews on this particular topic have been presented elsewhere [1–3,23–26]. The culmination of this work is a portfolio of tried and proven microfluidic channels, with a strong understanding of their fabrication methodologies. These channels are generally integrated with larger lab-scale excitation/detection systems. With a greater competency in the control of various biological species, many researchers have now shifted their focus toward integration of these channels with optical manipulation and detection techniques [27–30]. Consider a lab-scale laser-induced fluorescence (LIF) detection setup as it may be incorporated with a microfluidic system, illustrated in Figure 2, and for which numerous research articles have been published [31–34]. In the setup illustrated in Figure 2, the biological species of interest first flow through a microfluidic channel to the relevant point of detection. These species are excited by a blue laser that is focused onto the channel using mirrors and objective lenses. As the excited species relax they emit green light, which is captured by a collection lens, collimated, filtered and routed to a photomultiplier tube (PMT). Some enhancements to this system have been proposed, such as the inclusion of microlenses or wavelength-selective optical waveguides for fine control of the excitation or emitted light [35,36]. While these enhancements allow one to probe multiple channels simultaneously, they also greatly complicate device fabrication.

**Figure 2.** Example laser-induced fluorescence setup when integrated with a microfluidic system for detection of biological species labelled with a fluorescent dye. Figure re-used from Ref. [32] with permission, copyright 2006 American Chemical Society.

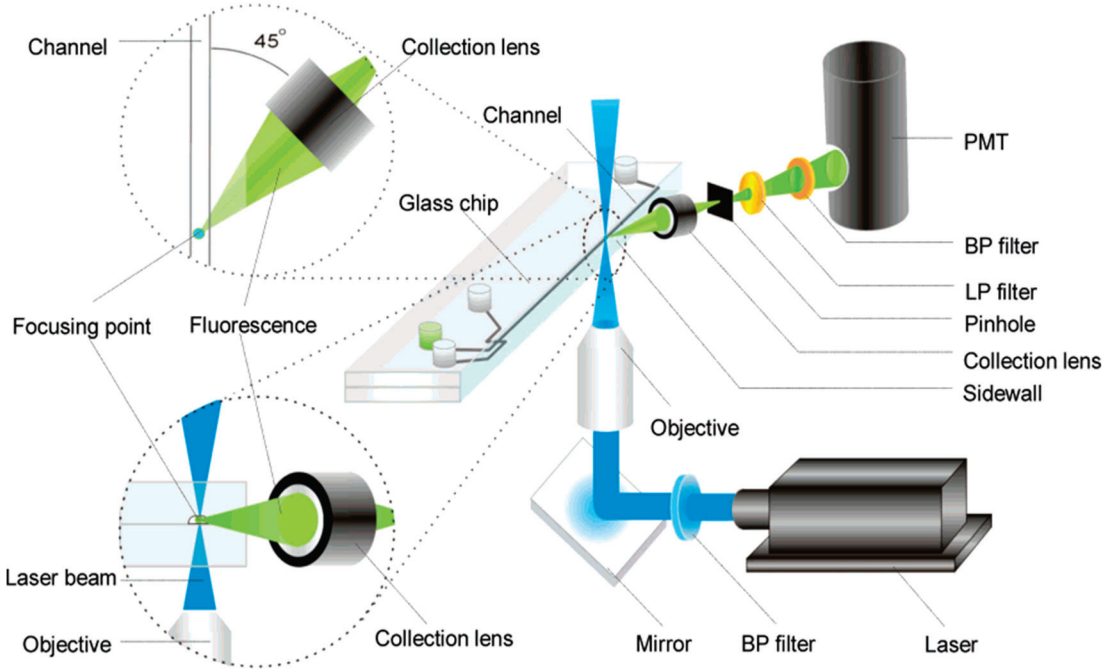

The inherent difficulty with these systems is immediately apparent: each system requires complicated and costly optics for excitation and subsequent photoluminescence detection. Beyond the large size of such a set-up, these systems are extremely sensitive to variations in the positioning of the optical components. Fu *et al.* studied the optimal laser-detector orientation, finding that a 45° light collection angle to the direction of flow (and 90° to the excitation source, as illustrated in Figure 2) offered the best signal to noise ratio (SNR) [32]. While these systems provide impressive results, it is much more desirable to implement the miniaturized LoC technologies with, similarly, miniaturized test platforms. It is worth noting that the adjacent field of optofluidics, which marries optical probing techniques and associated optical phenomena with microfluidics, provides some hints as to how these test platforms may be constructed [37,38]. For example, Gersborg-Hansen and Kristensen developed distributed feedback (DFB) lasers based on third-order Bragg gratings, which also acted as microfluidic channels for their chosen laser dyes [39]. Such a system thus incorporates many of the core aspects of an OLED-/OPD-based LoC system, such as photon generation from organic species and subsequent photon waveguiding.

As a means to better appreciate the advantages of OLED- and OPD-based excitation/detection systems, it is useful to examine current integration schemes that do not employ OLEDs or OPDs. One of the most notable approaches makes use of optical fibres to either route the excitation light to the analyte, or to extract the emitted light from the fluorophore. For example, Chabinyc *et al.* developed a miniaturized test platform where excitation light is fed through optical fibre to PDMS microchannels [40]. Their approach is further unique as it makes use of a micro-avalanche photodiode (μAPD), which is encapsulated in PDMS and placed directly underneath microfluidic channels. Since the μAPD is in such close proximity to the fluorophore, lenses and concentrators are not required. Using this approach, Chabinyc *et al.* were able to detect a minimum concentration of 25 nM fluorescein, and they were able to separate and detect proteins by capillary zone electrophoresis. The main limitation to this approach is the complexity in device fabrication, especially in consideration of the fragile μAPDs and of the difficulty in optical fibre alignment. OLEDs and OPDs may offer a solution to this problem as they can be deposited adjacent to the microchannel and thus do not require any direct physical alignment or manipulation.

Irawan and coworkers also pursued a fibre-coupling scheme to microfluidic devices with some success [33,41,42]. In their preliminary work, the authors made use of a poly(methyl methacrylate) (PMMA) optical fibre and lamination methods to couple blue LED excitation light to their microchannels [41]. Combined with a charge-coupled device (CCD) detector (including relevant filters, lenses and pinhole masks), the researchers managed to detect fluorescein at concentrations of ~3 nM. Irawan *et al.* later improved upon this work, implementing groove-cut PMMA optical fibres to allow for emission from several points along the fibre [33]. As shown in Figure 3, this allows for integration of the fibre into a multi-channel microfluidic device. This research resulted in detection of 30 pM of fluorescein.

**Figure 3.** (**A**) Illustration of the groove-cut optic fibre excitation methodology for PL detection in lab-on-a-chip applications. (**B**) SEM micrograph of the groove-cut optic fibre. Figures re-used from Ref.'s [33,42] with permission, copyright 2007/2009 Springer.

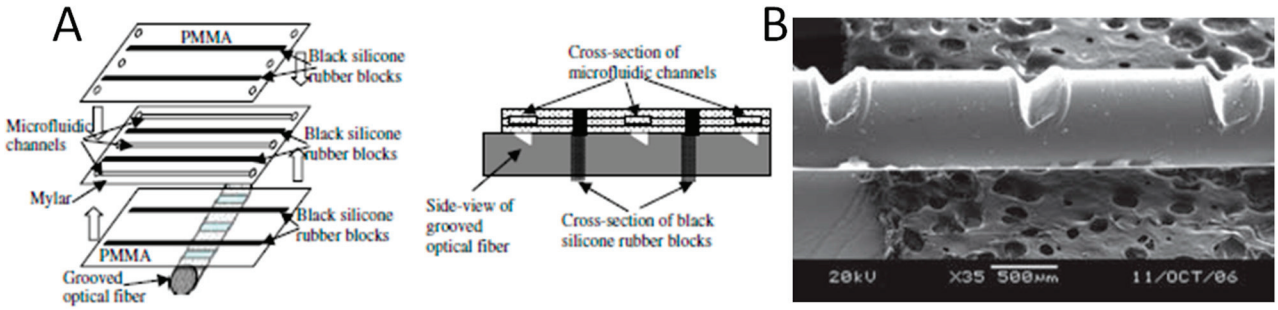


Numerous other approaches to couple light into and out of microfluidic channels have been tested. For example, in order to bypass the difficulty of integrating optical fibres into LoC microfluidics, Seo and Lee instead used 2D-patterned microlenses to couple blue LED excitation light into their microchannels [43]. This follows the work of Roulet and coworkers noted earlier [35], but with a much simpler implementation and without the need for a laser excitation source. Mazurczyk *et al.* fabricated channel optical waveguides with the use of an ion exchange technique in soda lime glass substrates to achieve efficient coupling of light into their microchannels [44]. Instead of coupling light to the microfluidic channels directly, Novak and coworkers aimed to miniaturize the testing platform, effectively achieving a fluorescein detection limit of ~2 nM [45]; however, this approach still requires costly filters and lenses. Ryu *et al.* followed a similar approach, but removed the lenses and used (relatively cheap) dye coated colour filters and linear/reflective polarizers to improve SNR [46], ultimately granting a fluorescein detection limit of ~3 nM. The use of polarizers in LoC systems is a relatively cheap and effective method to remove excitation light before it reaches the detector. This method relies on the placement of orthogonally oriented linear polarizers at both the excitation source and the detector. To this end, linearly polarized light from the excitation source interacts with the fluorescent analyte, resulting in the emission of non-polarized light. While the non-polarized light can pass the second polarizer to reach the detector, the excitation light is blocked due to its orthogonal polarization.

The common theme in all attempts to integrate PL sensing with LoC is the difficulty associated with in-coupling the excitation light and out-coupling the emitted light. In order to achieve a high SNR and a high limit of detection, the intensity of light impingent on the fluorophores must be high. This allows for measurable signals even from highly dilute species. Furthermore, a significant portion of light emitted from the fluorophore must subsequently reach the detector. While the LoC systems studied in this section offer creative and effective methods for light incoupling and outcoupling, these methods largely rely on complicated and, ultimately, costly extra microchannel fabrication steps. For manufacturability, system compatibility and overall simplicity in LoC bio-detection systems, it behooves us to examine easily implementable and more modular designs. In this manner the microfluidics can be fabricated first and then subsequently married to the optimized optical excitation and detection schemes. OLEDs and OPDs may prove to satisfy this requirement, as they can be deposited directly on already-fabricated microchannels, or they may easily be fabricated on separate substrates that can be bonded to PDMS microchannels.

## 4. Integrated Organic Light Emitting Diode and Organic Photodetector Lab-on-a-Chip Systems

The appeal of OLEDs and OPDs for LoC stems from their potential ease of integration. As briefly discussed in Section 2, the most costly aspects of a PL detection system are generally associated with the optics required to have strong excitation output powers and high collection efficiencies. By placing the excitation source and the detector adjacent to the microchannels of interest, one may potentially eliminate the need for lenses, for detectors with internal gain (APDs or PMTs) and for strict alignment. This shifts this technology's realm of applicability from the lab-scale environment to a miniaturized, modular, point-of-care sensing platform.

OLEDs and OPDs, however, are not unique in their ease of linking to adjacent pre-fabricated microchannels. For example, there has been some success making use of hydrogenated amorphous silicon (a-Si:H) photodetectors toward the same goal [47,48]. In this regard, both a-Si:H and organics can be deposited in low temperature environments and can be deposited on top of common microfluidic materials (for example, PDMS). As such, OLEDs, OPDs and a-Si:H PDs can all can be optimized separately and joined to the microfluidics in a modular fashion. Further, all technologies can be miniaturized into individual pixels for sensor array applications. However, OPDs have an added benefit over a-Si:H PDs, as their absorption spectra can be tuned by the use of different organic materials. Combined with the tunable OLED emission spectra, OLED-OPD-LoC systems could feasibly be used to sense multiple PL peaks from different biological species within the same microchannel.

A critical limitation toward integrated PL sensing in any LoC system is the requirement for low noise and thus high SNR. For an OLED-OPD-LoC system, given the proximity of the OLED to the OPD, detection of the OLED excitation light by the OPD can be a significant contribution to noise. There exist several nascent techniques that may be used to minimize or even eliminate this problem. One may:

- use micro-cavity effects (with a semi-reflective anode instead of the transparent anode shown in Figure 1) or distributed Bragg reflectors (DBRs) to substantially narrow the FWHM of the OLED emission peak and remove tail-end emission
    - See, for example, [49,50] for micro-cavities based on metal mirror electrodes and [51] for micro-cavities based on dielectric quarter-wave stack (QWS) mirrors.
- operate the OLED in pulsed mode and exploit differences in electroluminescence (EL) response/decay time *versus* the fluorophore PL response/decay time
    - If the OLED and the fluorophore are selected appropriately, it may be feasible to offset the OLED's emission and the OPD's detection.
    - In some cases, high current pulse operation has allowed for very high brightness values in OLEDs, which may further enhance PL [52].
- use clever design techniques to minimize the excitation light coupled into the OPD

- For example, see Figure 4, which is a suggested back-detection device and is discussed further below. Shinar and coworkers used a much simpler implementation of a back-detection device (with a PMT detector and with no efforts to block or shield excitation light) to some success for their oxygen sensors [53–57].

- incorporate thin film absorbers or polarizers (e.g., following work by Ryu *et al.* [46])
  - While these techniques are the simplest, they also serve to substantially decrease the intensity of the PL signal. They may therefore not be suitable to adequately reduce noise and to provide competitive SNR values that can compete with present lab-scale LIF systems.
  - To minimize the number of components required in the LoC system, it may be feasible to employ excitation sources that emit polarized light without the use of linear polarizers. Such excitation sources have recently been demonstrated with polymer emitting nanofibres, showing the potential for electrical excitation (when incorporated in polymer OLED-like devices) [58], as well as demonstrating reasonable integration into microfluidic systems [59].

**Figure 4.** Illustration of the structural layout of a potential back-detection OLED-OPD lab-on-a-chip system.

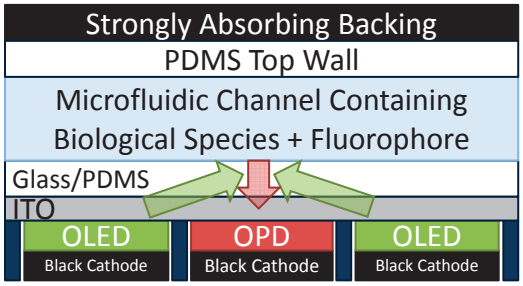


For the back-detection geometry shown in Figure 4, the OLED and OPD are fabricated on the same substrate, which can greatly simplify the fabrication process, and they are separated by opaque spacers. The OLEDs emit green light that interacts with the fluorophore to emit red light as detected by the OPD. By making use of a strongly absorbing backing and black cathodes (see, for example, [60,61]) one may minimize the amount of stray OLED light that reaches the OPD—essentially limiting it to partial reflections and waveguided light.

### *4.1. Organic Light Emitting Diode-Integrated Lab-on-a-Chip Systems*

A summary of the LoC systems employing an OLED excitation source are provided in Table 1 (note: instead of an OLED, ref. [62] uses an organic semiconductor laser). The results have been grouped together by their specific application, which coincides with specific research groups/principal investigators. The intended applications of the various LoC systems in Table 1, and thus the analytes of interest, vary among the different research groups. As such, cross-comparisons on the efficacy of each system are difficult, and so both the analyte and the sensor's dynamic range are listed. For the cases where a dynamic range is not explicitly listed, values have been ascertained from figures within

the publications. For entries with multiple publications, the best dynamic range from the group of publications is listed.

**Table 1.** Summary of lab-on-a-chip systems with OLED excitation sources.

| Application | | Micro-Fluidic | OLED Details | Detector | Analyte | Dynamic Range | Ref. |
|---|---|---|---|---|---|---|---|
| Dye conc | PL | PDMS channel | ITO/α-NPD/$Alq_3$/LiF/Al | CCD w/fibre | RhB | 5–100 μM | [63,64] |
| | | | ITO/α-NPD/ $Alq_3$:C6/$Alq_3$/LiF/Al | | | | |
| Multi-analyte conc | PLq | film (non-MF), PP channel | ITO/CuPc/a-NPD/ DPVBi/$Alq_3$/CsF/Al | PMT, Si PD + pre-amp | glucose, lactate, ethanol | 0.02–0.3 mM | [53–57,65] |
| | | | ITO/CuPc/a-NPD/ $Alq_3$/CsF/Al | | $O_2$ | 0%–100% | |
| | | | ITO/CuPc/NPD/$Alq_3$:C5 45T/$Alq_3$/LiF/Al | | dissolved $O_2$ | 2–40 ppm | |
| EP sep'n, immune assay | PL | etched glass, PDMS channel | ITO/PEDOT:PSS/ (PF or PPV emitter) /LiF/Al | PMT, Si APD w/filter, lens, fibre | fluorescein | 1 μM–10 mM | [66,67] |
| | | | | | HSA | 10–100 mg/L | |
| Dye conc, IEF | PL | PDMS channel | ITO/NPB/$Alq_3$/ Mg:Ag/Ag | PMT, CCD w/filter, lens | rhodamine 6G, Alexa Fluor 532 | 50–700 μM | [68–70] |
| | | | commercial AM-OLED array | | R-phyco-erythrin | 38 ng/mL –50 μg/mL | |
| Dye conc, immune assay | PL | etched glass, PDMS channel | ITO/CuPc/α-NPD/$Alq_3$/LiF/Al | p-i-n, p+n PD | TAMRA | 10–100 μM | [71,72] |
| | | | | | Rh6G | 1–100 μM | |
| Analyte conc | IV | droplet | ITO/TPD/$Alq_3$/Al | N/A | ethanol, methanol | 10–1E3 ppm | [73] |
| Dye conc | PL | PDMS channel | AZO/PEDOT:PSS/ PDY-132/$Alq_3$/Ag | spectro-meter | sulforho-damine 101 | N/A | [74] |
| Dye conc, immuno assay | PL | PDMS channel | ITO/TPD/ CBP:Ir(ppy)$_3$/Bphen/ $Alq_3$/Mg:Ag/Ag | linear CCD w/filter | resorufin | 7.8–80 μM | [75] |
| | | | | | IgA | 17–100 ng/mL | |
| Dye conc | PL | PMMA channel | $Alq_3$:DCM on DFB gratings, pumped w/UV laser | spectro-meter w/filter, lens | fluoro-spheres, Alexa 647 | N/A | [62] |
| Dye conc, immuno assay | PL | droplet | ITO/PEDOT:PSS/ α-NPB/PBD/LiF/Al | CCD w/filter | Alexa 430 | 156–1E4 pg | [76] |
| | | | | | hTG2 antigen | 200–5E3 pg | |

Hofmann and coworkers studied a spincoated PPV-based polymer OLED (500 to 700 nm emission) as an excitation source [67]. The light from the OLED was focused onto a patterned PDMS microchannel using a biconvex lens, allowing for PL detection of labelled urinary human serum albumin (HSA) by a CCD spectrometer. Their efforts allowed for HSA detection from 10 to 100 mg/L. Scholer *et al.* also investigated the use of a polymer OLED as an excitation source for LoC, but they instead used Super Yellow (PDY-132) as their polymer emitter. Combined with a spectrometer detector, they were able to successfully test for the presence of sulforhodamine 101 [74]. Instead of using polymer OLEDs, Camou *et al.* examined a ~530-nm emitting small molecule OLED excitation

source deposited on a glass substrate and bonded back-to-back to a PDMS microchannel for detection of Rhodamine B [63,64]. This simpler approach removed the need for a focusing lens. Their OLED had the structure ITO/*N*,*N*'-di(alpha-naphthyl)-*N*,*N*'-diphenyl-1, 1'-biphenyl-4,4'-diamine (α-NPD) (HTL)/$Alq_3$ (ETL & EML)/LiF (EIL)/Al. The researchers also used an optical fibre to route their fluorescent dye's emitted light to a CCD detector. The fibre was slid into a channel formed in the PDMS directly adjacent to the microchannel. Camou and coworkers were able to detect 10 μM solutions of Rhodamine B visually, and 50 μM solutions by the CCD detector.

Marcello and coworkers employed a similar OLED structure, but replaced the $Alq_3$ ETL with 2-(4-biphenyl)-5-(4-*t*-butylphenyl)-1,3,4-oxadiazole (PBD), which allows for blue light emission from α-NPD. They further chose a fluorophore, Alexa Fluor 430, which has a large Stokes shift (>100 nm), allowing for simpler removal of the excitation signal from their CCD detector. In spite of this deliberate design choice, their test array still required the use of a bandpass filter, thus highlighting the need for further system alterations, such as back-detection device geometries, that reduce the amount of excitation light that reaches the detector. Their system was shown to be capable of detecting 156 pg of Alexa 430 per droplet of solution, and the researchers extended their LoC system to an indirect antibody assay to detect 200 pg of hTG2 with good specificity.

Choudhury, Shinar and Shinar also investigated patterned blue OLED pixels as their excitation source [55]. EL was from 4,4'-bis(2,2'-diphenylvinyl)-1,1'-biphenyl (DPVBi) incorporated into the device: ITO/CuPc (HIL)/α-NPD (HTL)/DPVBi (EML)/$Alq_3$ (ETL)/CsF (EIL)/Al. They also examined green-emitting devices by replacing the DPVBi EML with $Alq_3$, effectively extending the $Alq_3$ ETL already present. 2 mm by 2 mm emitting pixels were formed in a passive matrix by the cross-hatch of patterned ITO and Al strips. Similar to the approach by Camou *et al.* [63,64], the OLED was fabricated on a glass substrate and bonded to the patterned PDMS microchannels. Choudhury and coworkers used their OLED-microchannel setup for the detection of glucose by dissolving glucose oxidase (GOx) in solution with an oxygen-sensitive dye. For blue-emitting OLEDs, tris(4,7-diphenyl-1,10-phenanthroline) Ru chloride (Ru(dpp)) was used, while Pt octaethylporphyrin (PtOEP) was used with the green-emitting OLEDs. At a certain oxygen concentration, PL of the dyes is largely quenched. However, the presence of glucose in the microfluidic channel results in its enzymatic oxidation by GOx and a local reduction in oxygen content. The decrease in oxygen content reduces the quenching of the dye, enabling it to emit, and thus allowing for the highly sensitive detection of glucose.

Cai and Vengasandra *et al.* of the same research group expanded upon this work to test for alcohol and lactate in addition to glucose with alcohol oxidase (AOx) and lactate oxidase (LOx) [56,57,65]. Some key data from this work is shown in Figure 5. The yellow-orange emission is due to the combined emission from the $Alq_3$ OLED as well at the PtOEP dye. As a point of interest, the EL decay time of the presently examined OLEDs is ~30–100 ns, while the decay time of Ru(dpp) PL is ~0.3 to 8 μs and that of PtOEP is on the order of ~100 μs. As noted previously, this difference in EL *vs.* PL decay time can be used to vastly improve SNR by offsetting the excitation and the detection. This system is thus ideal for PL lifetime measurements, which are illustrated in the sub-panels of Figure 5. The decay time of the photoluminescence for each species relates to its concentration by use of a modified Stern-Volmer equation. For the experiment shown in Figure 5, liquid or sol-gel samples containing the relevant biological species were deposited into wells containing a

pre-deposited polystyrene(PS):PtOEP or PS:$TiO_2$:PtOEP film. This is in contrast to earlier work [55], where the dye was simply mixed into the sample solution. Furthermore, when the PS:$TiO_2$:PtOEP film is used without the deposited analyte, it was shown to be capable of $O_2$ gas sensing from 0% to 100% oxygen content.

**Figure 5.** Structurally integrated OLED sensor for loc sensing of oxygen, glucose, alcohol and lactate, with associated photoluminescence decay graphs. Figure re-used from Ref. [56] with permission, copyright 2008 Elsevier B. V.

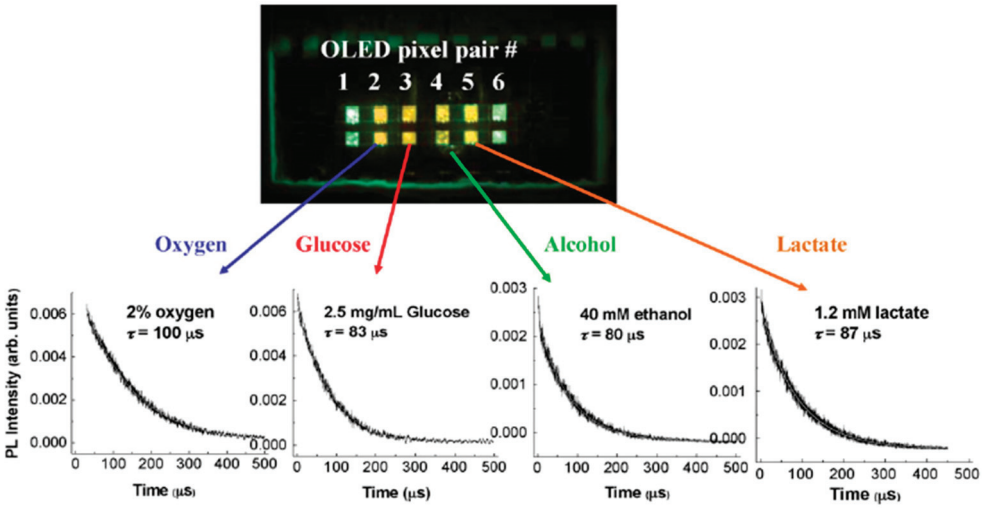


Edel *et al.* pursued a PL-sensing LoC with microchannels etched in glass and a spincoated, blue-emitting fluoropolymer OLED as an excitation source [66]. The authors used their microfluidic channels for electrophoretic separation of fluorescein and 5-carboxyfluorescein. The fluoropolymer was chosen so that its emission spectrum overlapped the absorption spectra of the fluorescein dyes at ~500 nm. Standard filters, lenses and a PMT or a Si APD were used for PL detection. The authors note that higher OLED driving voltages resulted in significantly larger SNRs, with a maximum SNR of 840 for a 10 mM 50 nL fluorescein plug. Detector intensities as well as separation times for the fluorescein dyes were comparable for the OLED excitation source *versus* a standard mercury lamp source.

Yao *et al.* used an NPB/$Alq_3$ bilayer OLED as an excitation source coupled with PDMS microchannels to measure PL from Rhodamine 6 g and Alexa Fluor 532 [69]. In this work, the researchers used an alternating layered $TiO_2$/$SiO_2$ DBR interference filter to block >555 nm light and thus to reduce the noise from the OLED excitation light. This allowed for a 13-times improvement in sensitivity of Rhodamine 6G dye. Yao and coworkers achieved SNR values of 16.9 and 10.2 using 50 μM Rhodamine 6G and 7 mM Alexa 532 respectively. The concentration limit for Alexa 532 was found to be 3 μM with a 0.7 nL injection volume. The researchers also applied their LoC system for separation of bovine serum albumin (BSA) conjugates.

In later work, Yao and coworkers used EL from a long-strip OLED for imaging fluorescently-labelled isoelectrically focused species [70]. This particular approach is a substantial improvement over commercial techniques, which typically use a mobilization step to transport isoelectrically focused zones. This mobilization step is both time-consuming, and can cause

smearing and distortion of the sample bands. While some attempts have been made to perform whole-column PL imaging with more traditional excitation sources [77,78], they generally suffered from non-uniform excitation. In contrast, an OLED can be fabricated adjacent to a linear microchannel with nearly any desired dimensions and relatively uniform emission. It is therefore a perfect candidate as a whole-channel excitation source. Using a CCD detector, the researchers isoelectrically focused R-phycoerythrin (finding 3 bands instead of 1 band due to impurities) within 30 s and note a system sensitivity of ~2.5 nM, as shown in Figure 6.

**Figure 6.** Isoelectric focusing electropherograms of *R*-phycoerythrin from an OLED-LoC system. (**A**) CCD intensity readout at varying concentrations in a 4-cm channel. (**B**) Time evolution of isoelectric focusing for 25 mg/mL in a 2 cm channel. Figures re-used from Ref. [70] with permission, copyright 2006 American Chemical Society.

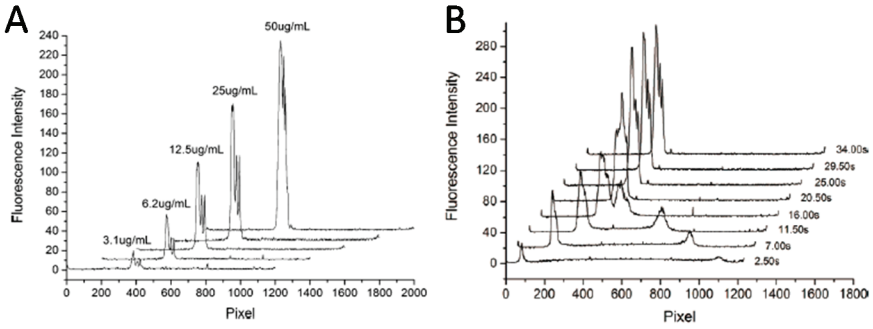


As an alternative approach to OLED-based detection of isoelectric focused species, Ren *et al.* of the same research group examined an active-matrix OLED pixel array as an excitation source [68]. In this manner, the resolution of the fluorescent image of the channel is determined by the size of each individual OLED pixel. In order to generate a full channel image, the pixels are addressed individually from one end of the array to the other. Fluorescent light from the labelled species can be measured by a simple photodiode and the photocurrent readings stitched together. This approach greatly relaxes the requirements of the detector. The researchers successfully applied this system to isoelectrically focus *R*-phycoerythrin to its isoelectric point within ~70–100 s.

Highlighting the need to miniaturize their entire LoC system, Shin and Kim *et al.* investigated a fully integrated microfluidic system with an $Alq_3$ OLED excitation source and a p-i-n Si PD [71,72]. The microchannel itself was etched in glass, and the OLED was deposited onto the same glass substrate. Shin *et al.* also employed an alternating $SiO_2/TiO_2$ interference filter on their p-i-n Si PD, and bonded the PD to the glass substrate. The authors compared the OLED to a laser source, and noted two orders of magnitude poorer PL from rhodamine 6G (by their PD photocurrent) due to excitation with the OLED. This was attributed to the poor OLED emission intensity. It is possible that higher brightness OLEDs could fare better for this LoC system, with state-of-the-art phosphorescent OLEDs granting substantially higher brightness and current efficiency values [79]. Regardless, Shin, Kim and coworkers demonstrated their LoCs to be capable of measuring 10 μM of tetramethylrhodamine and 1 μM of rhodamine 6G.

Following the above reasoning, Nakajima and coworkers studied a LoC system with a *tris*(2-phenylpyridine)iridium ($Ir(ppy)_3$) emitter, using the following OLED structure: ITO/*N*,*N*'-diphenyl-*N*,*N*'-di(m-tolyl)-benzidine (TPD)/4,4'-Di(*N*-carbazolyl)biphenyl

(CBP):Ir(ppy)$_3$/4,7-diphenyl-1,10-pheranthoroline (Bphen)/Alq$_3$/Mg:Ag/Ag. This particular device structure employs an HTL, a guest:host EML and two ETLs, and ultimately allows for very high brightness values. As a first demonstration in a LoC system with a bandpass-filtered CCD detector, Nakajima and coworkers detected 7.8 mM resorufin flowing through PDMS microchannels. They further showed the system to be capable of detecting 16.5 ng/mL of immunoglobulin A (IgA) in an immunoassay experiment.

*4.2. Organic Photodiode-Integrated Lab-on-a-Chip Systems*

A summary of the LoC systems employing an OPD detector are provided in Table 2. Similar to Table 1, the results have been grouped together by their specific application, which coincides with the principal investigators. Also, for the cases where a dynamic range is not explicitly listed, values have been obtained from figures within the publications (best dynamic range noted for groups of publications).

Banerjee *et al.* studied the PL of rhodamine 6G and fluorescein using a PDMS microchannel, a halide lamp excitation source and a CuPc-C$_{60}$ bilayer heterojunction OPD [83]. Their work focused on the ultimate limit of detection of a fully integrated LoC PL system, and thus highlighted the need to prevent excitation light from reaching the OPD. In a similar vein as Ryu *et al.* ([46]), Banerjee and coworkers used polarizers that were aligned orthogonal to each other and placed at the halide lamp and the OPD respectively. The OPD and its polarizer were bonded directly to the PDMS microchannel. By altering the orientation of the polarizer at the halide lamp from 0° offset to 90° offset, the authors noted a decrease in the OPD current (due to the excitation source background) from 5 μA to 19 nA. The dark current of the OPD on its own (with the excitation source off) was found to be 13 nA. This system allowed for detection of Rhodamine 6G at a concentration of 10 nM.

Miyake and coworkers also examined LoC systems based on CuPc-C$_{60}$ photodiodes [93]. Both bilayer and BHJ OPDs were fabricated with the device structures ITO/CuPc/C$_{60}$/bathocuproine (BCP)/Al and ITO/CuPc/CuPc:C$_{60}$ (3:2)/C$_{60}$/BCP/Al respectively. Note that the latter BHJ device is in fact a PM-HJ OSC, which has neat donor and acceptor layers bordering the mixed donor:acceptor layer. The PM-HJ device architecture allows for enhanced absorption and free carrier transport properties due to the neat donor and acceptor layers, while granting efficient exciton separation within the mixed layer. In an optimized device structure, the neat donor and acceptor layer thicknesses are ideally chosen to be equal to the exciton diffusion lengths in the respective materials. The researchers completed their LoC PL detection system by placing a green LED below their PDMS microchannels, and their OPD above the microchannels. In order to minimize excitation light coupled into the OPD, Miyake *et al.* made use of a bandpass filter (in lieu of the polarizers used by Banerjee *et al.* [83]), granting a limit of detection of 1 mM resorufin. They further employed their LoC system in an immunoassay to detect 20 ng/mL IgA. Continuing this work, Ishimatsu *et al.* performed competitive ELISA of alkylphenol polyethoxylates (APnEOs) on magnetic microbeads in PDMS microchannels [92]. To this end, the researchers used a magnet to immobilize anti-APnEO-immobilized beads within the microchannel, and subsequently flowed APnEOs and the secondary sensing antibodies through the same microchannel. Their results showed an APnEO limit of detection of 2 ppb.

**Table 2.** Summary of lab-on-a-chip systems with OPD detectors.

| Application | | Micro-Fluidic | OPD Details | Excitation Source | Analyte | Dynamic Range | Ref. |
|---|---|---|---|---|---|---|---|
| $H_2O_2$/Anti-oxidant conc, TAC assay | CL CLq | PDMS channel | ITO/CuPc/C60/BCP/Al | N/A | $H_2O_2$ | 10 μM–1 M | [80–82] |
| | | | | | β-Carotene | 22–200 μM | |
| | | | ITO/PEDOT:PSS/ P3HT:PCBM/Al | | α-Tocopherol | 10–200 μM | |
| | | | | | Quercetin | 50–200 μM | |
| Dye conc | CL | PDMS channel | ITO/PEDOT:PSS/ CuPc/C60/LiF/Al | m-halide lamp w/polarizer | Rh6g, fluorescein | 10 nM–10 μM | [83] |
| Immuno assay | CL | PDMS channel | ITO/PEDOT:PSS/ P3HT:PCBM/Al | N/A | SEB | 0.1–50 ng/mL | [84] |
| Light scattering, cell counting | abs | PDMS channel | P3HT:PCBM-based OPD (spraycoat) | 488 nm laser | HeLa, NHDF, Jurkat cells | 4E3–3E5 cells/cm$^2$ | [85,86] |
| Multi-analyte conc | PLq abs | film, PDMS channel, pipette | Au/Moo3/CuPc/ PTCBI/Bphen/Ag | LEDs (various) w/aperture | $O_2$, $CO_2$ | 0%–20% | [87–91] |
| | | | | | pH | 5–10 | |
| | | | | | RIU | $n$ = 1.33–1.43 | |
| Dye conc, immune assay | CL PL | PDMS channel | ITO/CuPc/ $C_{60}$/BCP/Al | LEDs (various) w/fibre | resorufin | 1–50 μM | [92,93] |
| | | | | | IgA | 20–120 ng/mL | |
| | | | ITO/CuPc/ CuPc:C60/ $C_{60}$/BCP/Al | | APnEOs | 2–50 ppb | |
| Immuno assay | CL | sol'n in wells, PDMS channel | ITO/PEDOT:PSS/ PCDTBT: PC70BM/LiF/Al | N/A | rhTSH | 30 pg/mL–10 ng/mL | [94–97] |
| | | | | | human cortisol | 0.28–249 nM | |

Hofmann *et al.* similarly examined OPD-microfluidic systems based on both planar heterojunction and BHJ CuPc-$C_{60}$ photodiodes [80]. These OPDs were fabricated on glass substrates and were subsequently bonded to PDMS microchannels. Using their bilayer CuPc/$C_{60}$ OPD, the researchers achieved peak external quantum efficiencies (EQEs) of ~25%–30% at wavelengths near 600–700 nm. Hofmann and coworkers also found a strong limitation to the ultimate limit of detection (LoD) of their system to be due to their OPD's absorption of excitation light. The researchers later developed long-pass thin-film filters based on doping PDMS with lysochrome dyes [98]. The use of PDMS and common biochemical dyes make these filters especially attractive, as they are easily compatible with standard microfluidics fabrication. As a first verification of the capabilities of their integrated OPD-microchannel device, Hofmann *et al.* measured peroxyoxalate chemiluminescence (CL). Both bis (2-carbopentyloxy-3,5,6-trichlorophenyl) oxalate (CPPO) and 9,10-diphenylanthracene dye were introduced into a first sample well, $H_2O_2$ was introduced into a second sample well and 4-dimethylaminopyridine (DMAP, catalyst) was introduced into a third sample well. The three species were hydrodynamically pumped to meet at a channel intersection and then mixed along a 1-cm-long linear segment. The authors noted a limit of detection of ~1 mM $H_2O_2$, and they observed a linear relationship of the OPD current with the $H_2O_2$ concentration up to 1 M.

Wang and coworkers of the same research group studied a similar LoC system, but instead used a P3HT:PCBM-based OPD [82]. Their OPD device structure was ITO/poly(3,4-ethylenedioxythiophene)

poly(styrenesulfonate) (PEDOT:PSS)/P3HT:PCBM (1:1)/Al. As noted previously, P3HT:PCBM absorbs over most of the visible range (~350 m to 700 nm), and so this particular OPD would not be applicable to LoC systems that require absorption over a small bandwidth (e.g., LoC systems with several OPDs to detect multiple PL peaks). In this work, the researchers patterned and miniaturized their OPDs to better align with the geometry of their microchannels to decrease dark current. As a consequence, using a similar CL reaction as described with [80], Wang *et al.* were able to achieve an $H_2O_2$ limit of detection less than 10 μM, with linear OPD photocurrent *vs.* concentration until 1 mM $H_2O_2$. This level of sensitivity is on par with a similar system using an integrated silicon photodiode [99]. Wang *et al.* later applied their P3HT:PCBM OPD-LoC for the evaluation of the antioxidant capabilities of β-carotene, α-tocopherol and quercetin, granting detection limits 10–50 μM [81]. The researchers compared the transient OPD signal to the same system using a PMT detector. They found virtually identical signal profiles for the OPD *versus* the PMT detector, with nearly the same detection limits and precision. This work is therefore a strong evidence for the capability of integrated OPDs to replace the lab-scale detector set-ups in PL/CL measurements.

Wojciechowski *et al.* applied a P3HT:PCBM OPD to detect CL from sandwich immunoassays for detection of Staphylococcal enterotoxin B (SEB) [84]. Similar to the work by Wang *et al.*, the authors note very low (pA) dark currents with fA noise for their P3HT:PCBM OPDs when kept under low reverse bias (0 to 100 mV). OPDs were fabricated on glass substrates, and attachment and assay steps were simply completed on the reverse side of the substrates with a patterned PDMS reservoir. The samples were then fitted with a microfluidic flow chamber and inserted into a custom-made hand-held controller. The components of this system are shown in Figure 7. Their efforts allowed for a limit of detection of 0.5 ng/mL SEB, which is on par with commercially available "portable" PMT-based and CCD-based systems. Furthermore, while these commercially available systems tout portability, they are substantially heavier and costlier than the presently examined OPD-LoC system.

Following the shift in the organic photovoltaics community toward new donor polymers and $C_{70}$-fullerene derivatives (instead of the more common $PC_{60}BM$), Pires *et al.* studied BHJ OPDs based on a poly [*N*-9'-heptadecanyl-2,7-carbazole-alt-5,5-(4',7'-di-2-thienyl-2',1', 3'-benzothiadiazole)] (PCDTBT) donor and a [6,6]-phenyl C71-butyric acid methyl ester ($PC_{71}BM$) acceptor for their LoC systems [94–97]. Such OPDs have been shown to be capable of very high efficiencies [100], and internal quantum efficiencies approaching 100% over a large portion of the visible spectrum [101]. They are thus ideal candidates for LoC systems, where the PL from dilute analyte can be quite weak. The OPD integrated with either micro-wells or PDMS microchannels allowed for detection of CL from 30 pg/mL of recombinant human thyroid stimulating hormone (rhTSH) and 0.28 nM of human cortisol. Pires *et al.* also showed that the PCDTBT:$PC_{71}BM$ OPDs could be used with PMMA microchannels for multiplexed detection of pathogens [97], with the total cost of their detection system estimated at less than $30 USD.

**Figure 7.** Various components of the hand-held OPD PL measurement system by Wojciechowski *et al.* (**A**) From left to right: PMMA holder, PDMS reservoir, glass sensor slide with OPD, opaque microfluidic channel; (**B**) hand-held controller. Figure re-used from Ref. [84] with permission, copyright 2009 American Chemical Society.

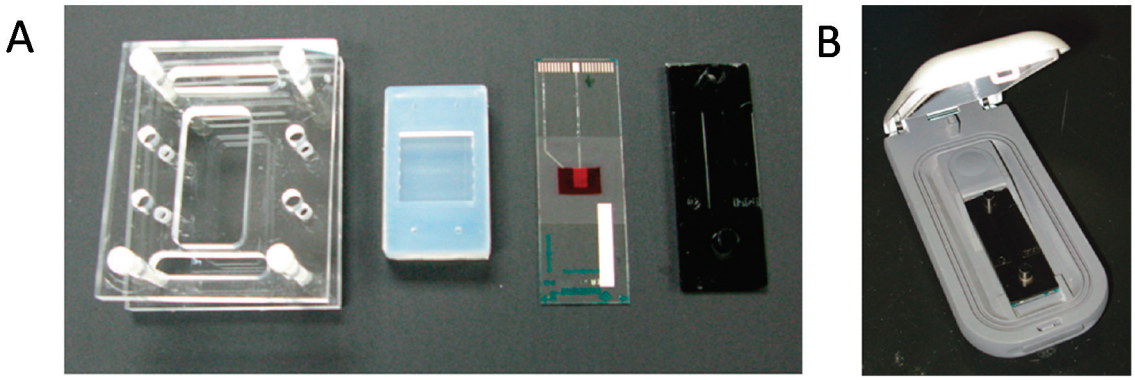


In order to demonstrate the versatility of integrated OPD-LoC technology, Lamprecht, Abel, Sagmeister and coworkers fabricated a number of different multi-analyte sensors to pair with bilayer CuPc/PTCBI OPD detectors [87–91]. Similar to the work by Shinar and coworkers [55–57,65], $O_2$ gas concentration is measured by PL quenching (PLq) of films that employ $O_2$-sensitive phosphorescent materials (e.g., (II) meso-tetra(pentafluorophenyl)porphine (PtTFPP)). This is accomplished by exciting the sensing film with an LED and detecting the change in PL intensity and PL decay dynamics with changing $O_2$ concentration—the PtTFPP triplet state is generally long-lived but prone to quenching by $O_2$. $CO_2$ and pH were also shown to be measurable by changing the sensing film to films based on either 8-hydroxypyrene-1,3,6-trisulfonic acid trisodium salt (HPTS):tetra-*N*-octylammonium hydroxide ($TOA^+OH^-$) or $HTPS(DHA)_3$ respectively. In order to reduce dark noise and improve the sensitivity of their LoC systems, the researchers employ a unique system geometry with ring-shaped OPDs, as shown in Figure 8. This is an extension of the back-detection LoC geometry discussed previously; however, this system further decouples the excitation source and the detector by waveguiding the sensor film's PL to a ring-shaped OPD. To further enhance light coupling to the OPD in this geometry, the researchers also used a scattering ring opposite to the OPD. The use of waveguided light also opens up possibility for surface plasmon resonance test platforms, where the sensor spot is replaced by $Ag/Ta_2O_5$ thin films. Evanescent waves that penetrate the cladding of the waveguide interact with analyte adjacent to the SPR platform, which can then be detected by the OPD. Lamprecht *et al.* employed such a system to test for changes in refractive index in adjacent fluid, allowing for the detection of changes in refractive index with a resolution of 8E-4 RIU. This resolution is on par with similar systems developed by Ratcliff *et al.*, which make use of $Alq_3$/TPD OLED emitters and double pentacene/$C_{60}$ detectors [102].

In their most recent work, Lamprecht *et al.* adapted this same LoC test platform to a glass pipette, placing the sensor film material within the pipette, and then depositing the OPD around the edge of the pipette away from the sensor spot [89]. In this case, the glass walls of the pipette act as the waveguide. This particular application highlights the promise of organic electronic materials and devices in LoC systems. Specifically, OPDs and OLEDs are incredibly adaptable—they are capable

of being deposited on many different substrates at low temperatures, including substrates that are flexible and non-planar.

**Figure 8.** Illustration of the loc system employing a ring-shaped OPD for Reduced dark noise. Figure re-used from Ref. [91] with permission, copyright 2013 Springer.

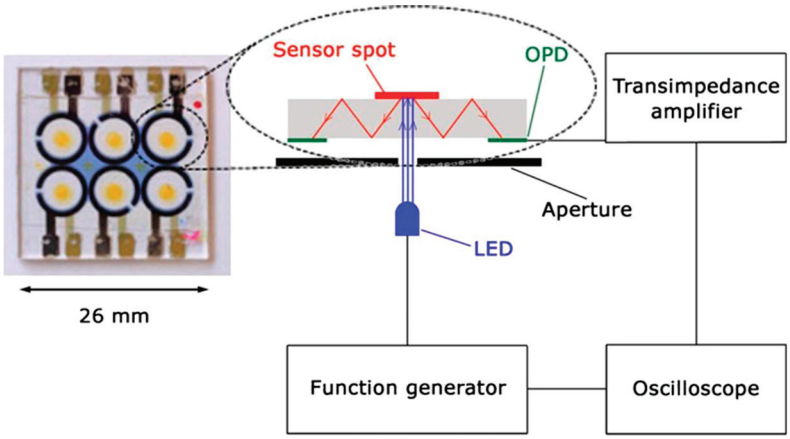


*4.3. Fully Integrated OLED/OPD Lab-on-a-Chip Systems*

A summary of the LoC systems employing both an OLED excitation source and an OPD detector are provided in Table 3. As with the previous tables, the results have been grouped together by their specific application, which coincides with the principal investigators. Also, for the cases where a dynamic range is not explicitly listed, values have been obtained from figures within the publications (the best dynamic range is noted for groups of publications). Furthermore, while the entries in Table 3 and the discussion below primarily focus on experimental OLED-OPD-LoC systems, it is worth noting that some work has been done on modelling these systems to extract ultimate limits of detection [103,104].

Banerjee, Pais and coworkers continued their earlier work by replacing their halide lamp excitation source with a green-emitting $Alq_3$ OLED [105–107]. As with their previous experiments discussed in Section 4.2, the researchers made use of a CuPc-$C_{60}$ bilayer heterojunction OPD as a detector. The authors noted an increase in the limit of detection for rhodamine 6G from 10 nM to 100 nM when switching from the halide lamp to the OLED. The authors also measured a limit of detection of 10 µM fluorescein for their system—much higher than that of rhodamine 6G due to the poor spectral overlap of fluorescein with the $Alq_3$ OLED and the poorer OPD responsivity at ~530 nm (where fluorescein emits light). The authors note that with optimization of channel depth, OPD responsivity and OLED output power, a detection limit of 10 pM should be feasible. By further reducing the noise within the associated system electronics (including connecting wires, the lock-in amplifier, the multimeter and the GPIB-USB connector), even lower detection limits are possible.

**Table 3.** Summary of lab-on–a-chip systems with OLED excitation sources and OPD detectors.

| Application | | Micro-Fluidic | Excitation Source | Detector Details | Analyte | Dynamic Range | Ref. |
|---|---|---|---|---|---|---|---|
| Dye conc | PL | PDMS channel | ITO/EB390/NPB/ Alq3/LiF/Al | ITO/PEDOT: PSS/CuPc/C60/ LiF/Al | Rh6G | 0.1 nM–1 mM | [105–108] |
| | | | | | fluor-escein | 1 µM–1 mM | |
| Multi-analyte conc | PLq | film (non-MF) | Au/CuPc/NPB/ Alq3/LiF/Ag | Au/CuPc/ PTCBI/Alq3/ Ag | $O_2$ | 0%–20% | [109,110] |
| | | | Blue-emitting OLEDs | | $CO_2$ | 0%–10% | |
| | | | | | pH | 3–9 | |
| Multi-analyte conc | PLq | film (non-MF) | ITO/CuPc/NPD/ Alq3:C545T/ Alq3/LiF/Al | ITO/PEDOT: PSS/P3HT: PCBM/Al | $O_2$ | 0%–100% | [111,112] |
| | | | Ag/MoO3/α-NPB/Alq3/LiF/Al | ITO/LiF/CuPc/ C70/Bphen/Al | pH | 4–10 | |
| Cell counting, herbicide conc | PL | PDMS channel | ITO/NPB/DPVBi/ BCP/Alq3/LiF/Al | ITO/PTB3: PCBM/LiF/Al | green algae CC-125 | 2.1E5–3E6 cells/mL | [113] |
| | | | | | DCMU | 7.5 nM–1.5 µM | |
| Immuno assay, Spectro-scopy | abs | PMMA + tape | ITO/PEDOT:PSS/ Ir(mppy)3:PVK :TPD:PBD/Ba/Al | ITO/P3HT: PCBM/Ba/Al w/ etched glass grating | mIgG | N/A | [114] |

Shuai *et al.* of the same research group later improved upon this fully integrated system, replacing the simple bilayer heterojunction OPD with a multiple heterojunction OPD [108]. Both an illustration and a photograph of their experimental setup are shown in Figure 9. The multiple heterojunction OPD is discussed at depth in [11], and uses multiple thin absorbing layers to increase the OPD absorption. If the device is designed correctly, such that the layer thicknesses are smaller than the respective exciton diffusion lengths, the multiple heterojunction can strongly enhance OPD quantum efficiency. Their final OPD device structure is thus ITO/PEDOT:PSS (HIL/HTL)/CuPc (HTL)/$C_{60}$ (ETL)/CuPc (HTL)/$C_{60}$ (ETL)/LiF (EIL)/Al. By using this improved OPD with polarizers to reduce dark noise, the researchers lowered their limit of detection for rhodamine 6G to 1 nM.

**Figure 9.** Illustration and photograph of a fully integrated organic light emitting diode-organic photodetector-lab-on-a-chip PL detection system. Figure re-used from Ref. [108] with permission, copyright 2008 IEEE.

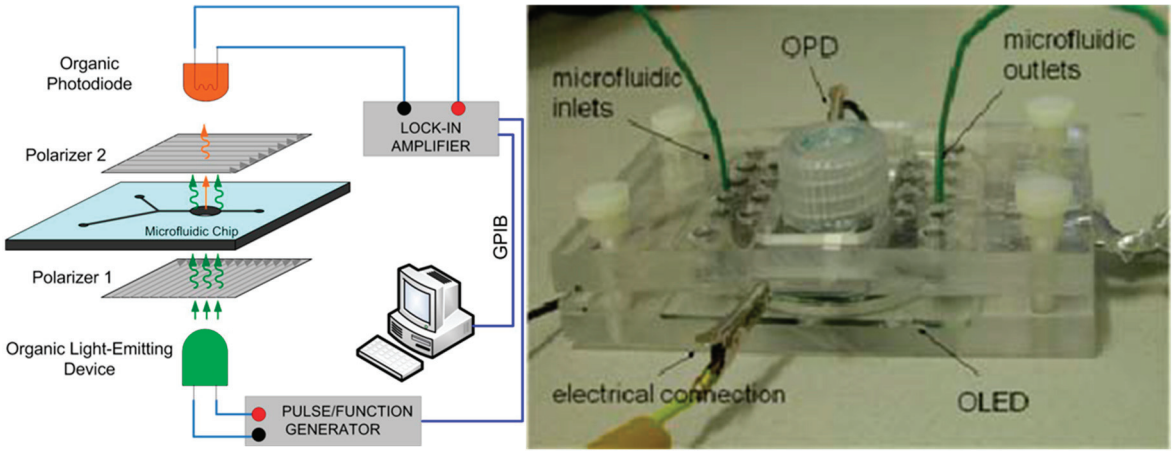


Kraker and coworkers also made use of an $Alq_3$-based OLED and a CuPc-PTCBI OPD with polarizers [109], applying this PL detection scheme to their $O_2$-sensitive films (detailed in

Section 4.2 with Sagmeister, Lamprecht, Abel *et al.* [87–91]). In order to prevent OLED excitation light from reaching the OPD, both the OLED and OPD were fabricated directly on the polarizer foils. A PtTFPP:PS film was then deposited on the reverse-side of the OLED foil for efficient measurement of oxygen content. The authors further employed this system as a pH sensor using fluorescein-isothiocyanate in phosphate buffer. Since organic electronics can be readily deposited on flexible substrates (including polarizer foils), this approach highlights a feasible, and potentially cost/time-saving improvement to the LoC fabrication process. Mayr *et al.* of the same research group instead used blue emitting OLEDs in combination with a CuPc-PTCBI OPD to detect $O_2$ and $CO_2$ gas concentrations [110]. Here the authors employ the ring-OPD geometry described earlier (shown in Figure 8), to detect 0% to 20% $O_2$, 0% to 10% $CO_2$ and 3 to 9 pH with a fast and reversible sensor response. The response of the fully integrated LoC with all-organic optical detection is thus shown to be on par with their previous LoCs, which used inorganic LED excitation sources.

Nalwa, Liu and *et al.* also examined OLED-OPD-LoC systems for $O_2$ and pH sensing [111,112], continuing the progress on multi-analyte detection with Shinar and coworkers. Nalwa *et al.* employed a coumarin 545T (C545T)-doped $Alq_3$ fluorescent OLED as an excitation source and a longpass-filtered P3HT:PCBM OPD for PL detection [112]. The work allowed for the detection of 0% to 16% $O_2$. As such, this system is also capable of similar performance as previously studied LoCs that used inorganic PMT, CCD or Si PD detectors. The combination of this research with that of Kraker *et al.* noted above thus shows that completely organic optical detection for LoC is a practical alternative to more common inorganic detection schemes from both the perspective of the excitation source and the detector. Liu *et al.* focused on further optimizing the sensitivity of their multi-analyte LoCs by addressing the generally large full-width at half-maximum (FWHM) of OLED electroluminescence [111]. To this end, the researchers employed microcavity OLEDs and the back-detection system geometry to substantially reduce the dark noise of their LoC systems by reducing the OLED light detected by their OPD. In this work, the OLED has the following structure: Ag/MoO3/α-NPD/$Alq_3$/LiF/Al, with the silver layer deposited to only 40 nm to remain semi-transparent to the $Alq_3$-emitted light. By fine-tuning the thicknesses of the α-NPD and $Alq_3$ layers, Liu *et al.* showed it was possible to use constructive/deconstructive interference to change the color of their microcavity OLEDs from green to blue. Longpass-filtered CuPc/$C_{70}$ bilayer OPDs were used due to their strong EQE overlap with their PtOEP-based sensing layer absorption. By measuring the PL decay dynamics of PtOEP-based films and the PL intensity variations of solutions containing fluorescein, the researchers achieved sensing of 0% to 100% $O_2$ and 4 to 10 pH respectively.

Lefèvre *et al.* examined a fully integrated OLED-OPD-LoC system for detection of algal chlorophyll [113]. Chlorophyll complex molecules in photosystem II use absorbed energy for photosynthesis, which can be generated from blue photons, and subsequently re-emit excess energy in the far red region. This system is particularly interesting for LoC PL detection, as the absorption and emission bands are spaced ~200 nm apart. The researchers used a blue DPVBi-based OLED for excitation and a polymeric PTB3:PCBM BHJ OPD for detection. The PTB class of polymers was developed for OSCs, and has been shown to yield solar cells with very high performance [115,116]. It is based on alternating ester substituted thieno[3,4-*b*]thiophene and benzodithiophene units and exhibits an absorption peak at 700 nm, with tail-end absorption extending up to 800 nm. It is thus ideal for the present application, as it can absorb the far-red photons emitted by algal chlorophyll.

To further minimize dark noise due to OLED light being detected by the OPD, Lefèvre and coworkers used thin-film filters formed by incorporating dyes into host resin. In fact, the ease of implementation and success of these thin-film absorbing filters follows as a consequence of the large separation between the OLED EL peak and the chlorophyll PL peak. Both the OLED and the OPD were formed on glass substrates and subsequently bonded back-to-back to the PDMS microchannels with their relevant filters. An illustration and photograph of the system layout are shown in Figure 10. Lefèvre *et al.* used this system to identify a limit of detection of ~1900 algal cells within their detection chamber (2.1E5 cells/mL). The researchers further used this system for detection and quantitation of herbicides, with Diuron (DCMU) concentrations as low as 7.5 nM, surpassing the detection limit of portable commercial equipment by an order of magnitude.

**Figure 10.** (**A**/**B**) Illustration of a fully integrated organic light emitting diode(OLED)-organic photodetector(OPD)-lab-on-a-chip PL detection system. (**A**/**B**) (**a**) OPD (**b**) excitation filter (**c**) microfluidic channels (**d**) emission filter (**e**) OLED. (**C**) photograph of the microchannels (colour dyes show channels). Figure re-used from Ref. [113] with permission of The Royal Society of Chemistry.

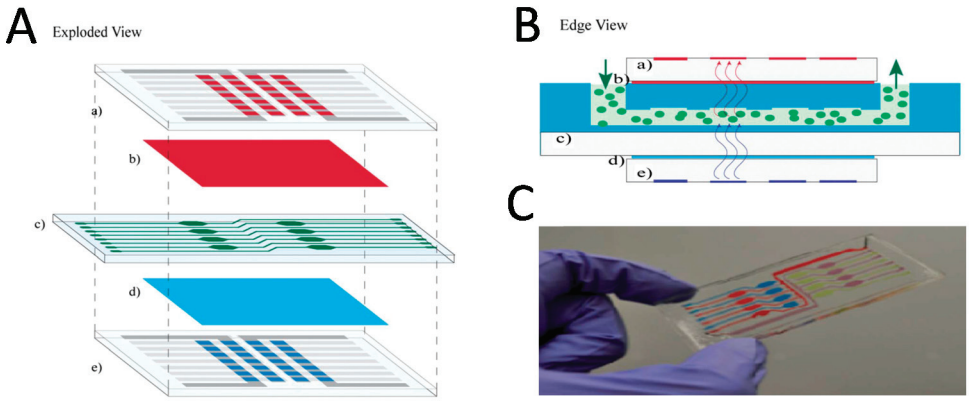


As a final demonstration of the potential for fully integrated organic electronic optical detection schemes for LoC applications, we examine work completed by Ramuz, Leuenberger and Bürgi, who used polymer OLED emitters and OPD spectrometers for flow immunoassays [114]. Their system relies on SPR interaction with analyte in PMMA microchannels by using a $SiO_2/TiO_2/Cr/Au/TiO_2$ SPR sensing platform, with the specific LoC geometry shown in Figure 11. The researchers employed a phosphorescent polymer OLED with the structure ITO/PEDOT:PSS/*tris*[2-(*p*-tolyl)pyridine]iridium(III) ($Ir(mppy)_3$):poly(9-vinylcarbazole) (PVK):TPD:PBD/Ba/Al. The polymer LED pumps a "PL-material", MEH-PPV, to efficiently couple excitation light into the waveguide. The indirect excitation with the MEH-PPV "PL-material" provides better TM mode coupling into the waveguide when compared to direct excitation of the polymer OLED. The second benefit to this method is that the intensity of the light coupled into the waveguide can be scaled with the size of the MEH-PPV PL layer and the size of the polymer OLED. After passing the SPR platform, the waveguided light propagates to a 500 μm grating of etched glass (312 nm period, 12 nm depth), which scatters light into an OPD array (10–50 μm-wide OPD pixels with 5 μm pitch. This approach impressively acts as a spectrometer with 5 nm resolution. Using this

system, Ramuz *et al.* performed an immunoassay for mouse immunoglobulin G (mIgG). Spectra during each stage of the immunoassay were obtained, and clear changes were observed for both the functionalization of the microchannel with mIgG, as well as the subsequent addition of anti-mIgG labelled with the Cy5 fluorescent marker. While this initial demonstration is already impressive, the incorporation of a fully functional organic spectrometer into LoC has incredible potential, and can be easily applied to any number of optical bio-detection experiments.

**Figure 11.** Illustration of a LoC system using SPR-absorption analyte detection with a polymer OLED excitation source and an OPD spectrometer. Figure re-used from Ref. [114] with permission, copyright 2010 Wiley Periodicals, Inc.

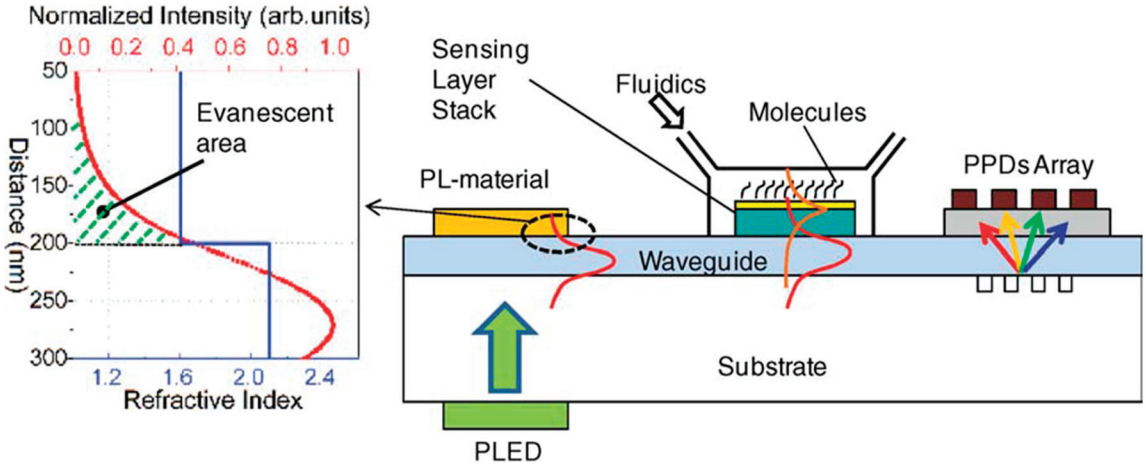


## 5. Conclusions

LoC systems promise substantial improvements in many analytical procedures, especially in those implementing complicated lab-based techniques to simple point-of-care tests. However, LoC systems also suffer in that they are inherently multidisciplinary endeavours, requiring expertise in incredibly varied fields of study. The present review examined the meshing of three core fields of research—organic electronics, microfluidics and life sciences. The entrance difficulty associated with application of all of these fields simultaneously has resulted in a relatively under-developed area of study. To this end, there are only a handful of examples of truly integrated PL LoC systems that do not require external lab space and equipment. In spite of this, the preliminary data from the reviewed research overwhelmingly supports the fact that optimized OLED-OPV-LoC PL systems are certainly capable of surpassing current commercial portable analysis technology, and in some cases may even rival lab-scale set-ups.

Arguably the most critically important parameter to dictate a PL system's realm of applicability is its limit of detection. In most studies, researchers identified the detector's absorption of the excitation light as a hindrance to the limit of detection, since it increases the background or zero-point signal. In lab-scale set-ups, the majority of excitation light can be removed by clever placement of the detector—ideally orthogonal to the excitation source and 45° to the channel. In a scaled down LoC system, this geometry is unwieldy and difficult to implement. As such, researchers have pursued back-detection architectures, waveguide-coupled PL, time-delayed and PL lifetime analysis, interference filters, absorbing filters and polarizer films to varying degrees of success.

The other most significant impediments to the ultimate limit of detection are related to the quality of the OLED and OPD. Namely, most research on this topic to date can be best described as proof-of-concept, using the simplest bilayer $Alq_3$ OLEDs and the most basic CuPc-$C_{60}$ or P3HT:PCBM OPDs. These studies have done well to invigorate and spur new research—the past decade of research has allowed for applications of this technology spanning simple chemical detection, to imaging whole-channel isoelectric focusing, to observing peroxyoxalate CL, to miniaturized organic spectrometers and finally to the measurement of algal PL for herbicide characterization. However, as noted by Banerjee and coworkers [105], the output power of their OLED must be improved by up to 150-times and the responsivity of their OPD must be improved by up to 50-times for their integrated LoC system to reach lab-scale sensitivities. Other improvements can be made in LoC system geometry, as has been observed with the successful use of ring-OPDs and OPDs deposited on circular substrates. It is now necessary to push the OLED-OPV-LoC system to its limits to probe its ultimate capabilities.

## Acknowledgments

Financial support to this work from the Natural Sciences and Engineering Research Council of Canada (NSERC) is gratefully acknowledged. GW acknowledges financial support through NSERC Alexander Graham Bell Canada Graduate Scholarship, Ontario Graduate Scholarship, and WIN Nanofellowship.

## List of Abbreviations

| Abbreviation | Full Name |
|---|---|
| abs | absorbance |
| Alq3 | tris(quinolinolate) Al |
| a-NPD | *N*,*N*'-di(alpha-naphthyl)-*N*,*N*'-diphenyl-1,1'-biphenyl-4,4'-diamine |
| APD | avalanche photodiode |
| APnEOs | alkylphenol polyethoxylates |
| BCP | bathocuproine |
| BHJ | bulk heterojunction |
| Bphen | 4,7-diphenyl-1,10-pheranthoroline |
| C545T | coumarin 545T |
| C60 | fullerene |
| CBP | 4,4'-Di(*N*-carbazolyl)biphenyl |
| CC-125 | chlamydomonas reinhardtii |
| CCD | charge-coupled device |
| CL(q) | chemiluminescence (quenching) |
| CPPO | bis (2-carbopentyloxy-3,5,6-trichlorophenyl) oxalate |
| CuPc | copper phthalocyanine |
| DBR | distributed Bragg reflector |
| DCM | 4-dicyanomethylene-2-methyl-6-(*p*-dimethylaminostyril)-4H-pyrane |
| DCMU | 3(3,4-dichlorophenyl)-1,1-dimethylurea, Diuron |
| DMAP | 4-dimethylaminopyridine |
| DPVBi | 4,4'-bis(2,2'-diphenylvinyl)-1,1'-biphenyl |
| EL | electroluminescence |

| | |
|---|---|
| EP | electrophoretic |
| EQE | external quantum efficiency |
| HPTS | 8-hydroxypyrene-1,3,6-trisulfonic acid |
| IEF | isoelectric focusing |
| Ir(ppy)3 | tris(2-phenylpyridine)iridium |
| IV | current-voltage (measurements) |
| LIF | laser-induced fluorescence |
| LoC | lab-on-a-chip |
| LoD | limit of detection |
| MEH-PPV | poly[2-methoxy-5-(2'-ethylhexyloxy)-*p*-phenylene vinylene] |
| mIgG | mouse immunoglobulin G |
| mKP | m-Cresol purple |
| NHDF | normal human dermal fibroblasts |
| NPB/NPD | 4,4'-bis[*N*-(1-naphthyl)-*N*-phenylamino]biphenyl |
| OLED | organic light emitting diode |
| OPD | organic photodetector |
| OSC | organic solar cell |

| **Abbreviation** | **Full Name** |
|---|---|
| PBD | 2-(4-biphenyl)-5-(4-*t*-butylphenyl)-1,3,4-oxadiazole |
| PC70BM | 1-(3-methoxycarbonyl)-propyl-1-phenyl-(6,6)C71 |
| PCBM | 1-(3-methoxycarbonyl)-propyl-1-phenyl-(6,6)$C_{61}$ |
| PCDTBT | poly [N-9'-heptadecanyl-2,7-carbazole-alt-5,5-(4',7'-di-2-thienyl-2',1',3'-benzothiadiazole)] |
| PDMS | polydimethylsiloxane |
| PDY-132 | Super Yellow |
| PEDOT:PSS | poly(3,4-ethylenedioxythiophene) poly(styrenesulfonate) |
| PF | polyfluorene |
| PL(q) | photoluminescence (quenching) |
| PMT | photomultiplier tube |
| PMMA | poly(methyl methacrylate) |
| PP | polypropylene |
| PPV | poly(*p*-phenylene vinylene) |
| PTCBI | 3,4,9,10-perylenetetracarboxylic bis-benzimidazole |
| PtOEP | Pt octaethylporphyrin |
| PtTFPP | (II) meso-tetra(pentafluorophenyl)porphine |
| PVK | poly(9-vinylcarbazole) |
| Rh6G | rhodamine 6G |
| RhB | rhodamine B |
| rhTSH | recombinant human thyroid stimulating hormone |
| RIU | refractive index unit |
| Ru(dpp) | *tris*(4,7-diphenyl-1,10-phenanthroline) Ru chloride |
| SEB | staphylococcal enterotoxin B |
| SNR | signal to noise ratio |
| SPR | surface plasmon resonance |
| TAC | total antioxidant capacity |
| TAMRA | tetramethylrhodamine |
| TOA+OH- | tetraoctylammonium hydroxide |
| μTPD | *N*,*N*'-diphenyl-*N*,*N*'-di(m-tolyl)-benzidine |
| μc-OLED | microcavity OLED |

## Conflicts of Interest

The authors declare no conflict of interest.

## References


1. Roman, G.T.; Kennedy, R.T. Fully integrated microfluidic separations systems for biochemical analysis. *J. Chromatogr. A* **2007**, *1168*, 170–188.
2. Yi, C.; Li, C.W.; Ji, S.; Yang, M. Microfluidics technology for manipulation and analysis of biological cells. *Anal. Chim. Acta* **2006**, *560*, 1–23.
3. Haeberle, S.; Zengerle, R. Microfluidic platforms for lab-on-a-chip applications. *Lab Chip* **2007**, *7*, 1094–1110.
4. Kajiyama, Y.; Joseph, K.; Kajiyama, K.; Kudo, S.; Aziz, H. Recent Progress on the Vacuum Deposition of OLEDS with Feature Sizes ≤20 μm Using a Contact Shadow Mask Patterned in-situ by Laser Ablation. In *Organic Light Emitting Materials and Devices XVII*, Proceedings of SPIE 8829, San Diego, CA, USA, 25 August 2013; So, F., Adachi, C., Eds.; SPIE International Society for Optical Engineering: Bellingham, WA, USA; p. 882919.
5. Kajiyama, Y.; Wang, Q.; Kajiyama, K.; Kudo, S.; Aziz, H. Vacuum Deposition of OLEDS with Feature Sizes ≤20um Using a Contact Shadow Mask Patterned in-situ by Laser Ablation. In Proceeding of SID Symposium Digest of Technical Papers, 2012; Wiley Online Library: Hoboken, NJ, USA, 1 October 2012; pp. 1544–1547.
6. Mishra, A.; Bäuerle, P. Small molecule organic semiconductors on the move: Promises for future solar energy technology. *Angew. Chem. Int. Edit.* **2012**, *51*, 2020–2067.
7. Mas-Torrent, M.; Rovira, C. Novel small molecules for organic field-effect transistors: Towards processability and high performance. *Chem. Soc. Rev.* **2008**, *37*, 827–838.
8. Duan, L.; Hou, L.; Lee, T.-W.; Qiao, J.; Zhang, D.; Dong, G.; Wang, L.; Qiu, Y. Solution processable small molecules for organic light-emitting diodes. *J. Mater. Chem.* **2010**, *20*, 6392–6407.
9. Tang, C.; VanSlyke, S. Organic electroluminescent diodes. *Appl. Phys. Lett.* **1987**, *51*, 913–915.
10. Van Slyke, S.; Chen, C.; Tang, C. Organic electroluminescent devices with improved stability. *Appl. Phys. Lett.* **1996**, *69*, 2160.
11. Peumans, P.; Yakimov, A.; Forrest, S.R. Small molecular weight organic thin-film photodetectors and solar cells. *J. Appl. Phys.* **2003**, *93*, 3693–3723.
12. Pohl, R.; Montes, V.A.; Shinar, J.; Anzenbacher Jr, P. Red-green-blue emission from tris(5-aryl-8-quinolinolate) al (iii) complexes. *J. Org. Chem.* **2004**, *69*, 1723–1725.
13. Inganäs, O.; Roman, L.S.; Zhang, F.; Johansson, D.; Andersson, M.; Hummelen, J. Recent progress in thin film organic photodiodes. *Synth. Met.* **2001**, *121*, 1525–1528.
14. Reyes-Reyes, M.; Kim, K.; Carroll, D.L. High-efficiency photovoltaic devices based on annealed poly(3-hexylthiophene) and 1-(3-methoxycarbonyl)-propyl-1-phenyl-(6,6)c-61 blends. *Appl. Phys. Lett.* **2005**, *87*, 083506.

15. Williams, G.; Wang, Q.; Aziz, H. The photo-stability of polymer solar cells: Contact photo-degradation and the benefits of interfacial layers. *Adv. Funct. Mater.* **2012**, *23*, 2239–2247.
16. Williams, G.; Aziz, H. In *Insights into Electron and Hole Extraction Layers for Upright and Inverted Vacuum-Deposited Small Molecule Organic Solar Cells*, Proceeding of Organic Photovoltaics XIV, San Diego, CA, USA, 17 October 2013; SPIE International Society for Optical Engineering: Bellingham, WA, USA, 2013; p. 88301.
17. Williams, G.; Aziz, H. The effect of charge extraction layers on the photo-stability of vacuum-deposited *versus* solution-coated organic solar cells. *Org. Electron.* **2013**, *15*, 47–56.
18. Xue, J.G.; Uchida, S.; Rand, B.P.; Forrest, S.R. Asymmetric tandem organic photovoltaic cells with hybrid planar-mixed molecular heterojunctions. *Appl. Phys. Lett.* **2004**, *85*, 5757–5759.
19. Ratcliff, E.L.; Garcia, A.; Paniagua, S.A.; Cowan, S.R.; Giordano, A.J.; Ginley, D.S.; Marder, S.R.; Berry, J.J.; Olson, D.C. Investigating the influence of interfacial contact properties on open circuit voltages in organic photovoltaic performance: Work function *versus* selectivity. *Adv. Energy Mater.* **2013**, *3*, 647–656.
20. Reineke, S.; Baldo, M.A. Recent progress in the understanding of exciton dynamics within phosphorescent oleds. *Phys. Status Solidi* **2012**, *209*, 2341–2353.
21. Birnstock, J.; Lux, A.; Ammann, M.; Wellmann, P.; Hofmann, M.; Stübinger, T. 64.4: Novel Materials and Structures for Highly ‐ Efficient, Temperature ‐ Stable, and Long ‐ Living am OLED Displays. *SIDInt. Symp. Dig. Tech. Pap*. **2006**, *37*, 1866–1869.
22. Uhrich, C.L.; Schwartz, G.; Maennig, B.; Gnehr, W.M.; Sonntag, S.; Erfurth, O.; Wollrab, E.; Walzer, K.; Foerster, J.; Weiss, A. In *Efficient and Long-Term Stable Organic Vacuum Deposited Tandem Solar Cells*, In Proceedings of the SPIE Photonics Europe, Brussels, Belgium, 19 May 2010; International Society for Optics and Photonics: Bellingham, WA, USA, 2010; p. 77220G.
23. Figeys, D.; Pinto, D. Lab-on-a-chip: A revolution in biological and medical sciences. *Anal. Chem.* **2000**, *72*, 330–335.
24. Abgrall, P.; Gue, A. Lab-on-chip technologies: Making a microfluidic network and coupling it into a complete microsystem—A review. *J. Micromech. Microeng.* **2007**, *17*, R15.
25. Mark, D.; Haeberle, S.; Roth, G.; Von Stetten, F.; Zengerle, R. Microfluidic lab-on-a-chip platforms: Requirements, characteristics and applications. *Chem. Soc. Rev.* **2010**, *39*, 1153–1182.
26. Erickson, D.; Li, D. Integrated microfluidic devices. *Anal. Chim. Acta* **2004**, *507*, 11–26.
27. Hunt, H.C.; Wilkinson, J.S. Optofluidic integration for microanalysis. *Microfluid. Nanofluid.* **2008**, *4*, 53–79.
28. Liu, R.; Ishimatsu, R.; Nakano, K.; Imato, T. Optical sensing systems suitable for flow analysis on microchips. *J. Flow Inject. Anal.* **2013**, *30*, 15–20.
29. Capitán-Vallvey, L.F.; Palma, A.J. Recent developments in handheld and portable optosensing—A review. *Anal. Chim. Acta* **2011**, *696*, 27–46.
30. Gai, H.; Li, Y.; Yeung, E.S. Optical Detection Systems on Microfluidic Chips. In *Microfluidics*; Springer: Heidelberg, Germany, 2011; pp. 171–201.

31. Yu, L.; Shen, Z.; Mo, J.; Dong, X.; Qin, J.; Lin, B. Microfluidic chip-based cell electrophoresis with multipoint laser-induced fluorescence detection system. *Electrophoresis* **2007**, *28*, 4741–4747.
32. Fu, J.L.; Fang, Q.; Zhang, T.; Jin, X.H.; Fang, Z.L. Laser-induced fluorescence detection system for microfluidic chips based on an orthogonal optical arrangement. *Anal. Chem.* **2006**, *78*, 3827–3834.
33. Irawan, R.; Tjin, S.C.; Fang, X.; Fu, C.Y. Integration of optical fiber light guide, fluorescence detection system, and multichannel disposable microfluidic chip. *Biomed. Microdevices* **2007**, *9*, 413–419.
34. Gao, J.; Yin, X.F.; Fang, Z.L. Integration of single cell injection, cell lysis, separation and detection of intracellular constituents on a microfluidic chip. *Lab Chip* **2003**, *4*, 47–52.
35. Roulet, J.C.; Völkel, R.; Herzig, H.P.; Verpoorte, E.; de Rooij, N.F.; Dändliker, R. Performance of an integrated microoptical system for fluorescence detection in microfluidic systems. *Anal. Chem.* **2002**, *74*, 3400–3407.
36. Bliss, C.L.; McMullin, J.N.; Backhouse, C.J. Integrated wavelength-selective optical waveguides for microfluidic-based laser-induced fluorescence detection. *Lab Chip* **2008**, *8*, 143–151.
37. Monat, C.; Domachuk, P.; Eggleton, B. Integrated optofluidics: A new river of light. *Nat. Photonics* **2007**, *1*, 106–114.
38. Schmidt, H.; Hawkins, A.R. The photonic integration of non-solid media using optofluidics. *Nat. Photonics* **2011**, *5*, 598–604.
39. Gersborg-Hansen, M.; Kristensen, A. Tunability of optofluidic distributed feedback dye lasers. *Opt. Express* **2007**, *15*, 137–142.
40. Chabinyc, M.L.; Chiu, D.T.; McDonald, J.C.; Stroock, A.D.; Christian, J.F.; Karger, A.M.; Whitesides, G.M. An integrated fluorescence detection system in poly (dimethylsiloxane) for microfluidic applications. *Anal. Chem.***2001**, *73*, 4491–4498.
41. Irawan, R.; Chuan, T.S.; Yaw, F.C. Integration of a fluorescence detection system and a laminate-based disposable microfluidic chip. *Microw. Opt. Technol. Lett.* **2005**, *45*, 456–460.
42. Irawan, R.; Tjin, S.C. Detection of fluorescence generated in microfluidic channel using in-fiber grooves and in-fiber microchannel sensors. *Meth. Mol. Biol.* **2009**, *503*, 403.
43. Seo, J.; Lee, L.P. Disposable integrated microfluidics with self-aligned planar microlenses. *Sensor. Actuat. B* **2004**, *99*, 615–622.
44. Mazurczyk, R.; Vieillard, J.; Bouchard, A.; Hannes, B.; Krawczyk, S. A novel concept of the integrated fluorescence detection system and its application in a lab-on-a-chip microdevice. *Sensor. Actuat. B* **2006**, *118*, 11–19.
45. Novak, L.; Neuzil, P.; Pipper, J.; Zhang, Y.; Lee, S. An integrated fluorescence detection system for lab-on-a-chip applications. *Lab Chip* **2007**, *7*, 27–29.
46. Ryu, G.; Huang, J.; Hofmann, O.; Walshe, C.A.; Sze, J.Y.Y.; McClean, G.D.; Mosley, A.; Rattle, S.J.; Bradley, D.D.C. Highly sensitive fluorescence detection system for microfluidic lab-on-a-chip. *Lab Chip* **2011**, *11*, 1664–1670.
47. Kamei, T.; Paegel, B.M.; Scherer, J.R.; Skelley, A.M.; Street, R.A.; Mathies, R.A. Integrated hydrogenated amorphous Si photodiode detector for microfluidic bioanalytical devices. *Anal. Chem.* **2003**, *75*, 5300–5305.

48. Kamei, T.; Wada, T. Contact-lens type of micromachined hydrogenated amorphous Si fluorescence detector coupled with microfluidic electrophoresis devices. *Appl. Phys. Lett.* **2006**, *89*, 114101.
49. Lin, C.L.; Lin, H.W.; Wu, C.C. Examining microcavity organic light-emitting devices having two metal mirrors. *Appl. Phys. Lett.* **2005**, *87*, 021101.
50. Peng, H.J.; Sun, J.X.; Zhu, X.L.; Yu, X.M.; Wong, M.; Kwok, H.S. High-efficiency microcavity top-emitting organic light-emitting diodes using silver anode. *Appl. Phys. Lett.* **2006**, *88*, 073517.
51. Dodabalapur, A.; Rothberg, L.J.; Jordan, R.H.; Miller, T.M.; Slusher, R.E.; Phillips, J.M. Physics and applications of organic microcavity light emitting diodes. *J. Appl. Phys.* **1996**, *80*, 6954–6964.
52. Tessler, N.; Harrison, N.T.; Friend, R.H. High peak brightness polymer light-emitting diodes. *Adv. Mater.* **1998**, *10*, 64–68.
53. Shinar, J.; Shinar, R. Organic light-emitting devices (OLEDS) and oled-based chemical and biological sensors: An overview. *J. Phys. D* **2008**, *41*, 133001.
54. Liu, R.; Cai, Y.; Park, J.M.; Ho, K.M.; Shinar, J.; Shinar, R. Organic light-emitting diode sensing platform: Challenges and solutions. *Adv. Funct. Mat.* **2011**, *21*, 4744–4753.
55. Choudhury, B.; Shinar, R.; Shinar, J. Glucose biosensors based on organic light-emitting devices structurally integrated with a luminescent sensing element. *J. Appl. Phys.* **2004**, *96*, 2949–2954.
56. Cai, Y.; Shinar, R.; Zhou, Z.; Shinar, J. Multianalyte sensor array based on an organic light emitting diode platform. *Sensor. Actuat. B* **2008**, *134*, 727–735.
57. Cai, Y.; Smith, A.; Shinar, J.; Shinar, R. Data analysis and aging in phosphorescent oxygen-based sensors. *Sensor. Actuat. B* **2010**, *146*, 14–22.
58. Vohra, V.; Giovanella, U.; Tubino, R.; Murata, H.; Botta, C. Electroluminescence from conjugated polymer electrospun nanofibers in solution processable organic light-emitting diodes. *ACS Nano* **2011**, *5*, 5572–5578.
59. Pagliara, S.; Camposeo, A.; Polini, A.; Cingolani, R.; Pisignano, D. Electrospun light-emitting nanofibers as excitation source in microfluidic devices. *Lab Chip* **2009**, *9*, 2851–2856.
60. Aziz, H.; Liew, Y.F.; Grandin, H.M.; Popovic, Z.D. Reduced reflectance cathode for organic light-emitting devices using metalorganic mixtures. *Appl. Phys. Lett.* **2003**, *83*, 186–188.
61. Wong, F.; Fung, M.; Jiang, X.; Lee, C.; Lee, S. Non-reflective black cathode in organic light-emitting diode. *Thin Solid Films* **2004**, *446*, 143–146.
62. Vannahme, C.; Klinkhammer, S.; Lemmer, U.; Mappes, T. Plastic lab-on-a-chip for fluorescence excitation with integrated organic semiconductor lasers. *Opt. Express* **2011**, *19*, 8179–8186.
63. Camou, S.; Kitamura, M.; Gouy, J.-P.; Fujita, H.; Arakawa, Y.; Fujii, T. Organic Light-Emitting Device as a Fluorescence Spectroscopy Light Source: One Step toward the Lab-on-a-Chip Device. In *Applications of Photonic Technology 5*; In Proceedings of the SPIE 4833, Quebec City, Quebec, Canada, 2 June 2002; Lessard, R., Lampropoulos, G., Schinn, G., Eds.; SPIE International Society for Optical Engineering: Bellingham, WA, USA, 2003; pp. 1–8.

64. Camou, S.; Kitamura, M.; Arakawa, Y.; Fujii, T. Integration of Oled Light Source And Optical Fibers on a PDMS Based Microfluidic Device for on-Chip Fluorescence Detection. In Proceedings of Micro Total Analysis Systems 2003 7th International Conference on Miniaturized Chemical and Biochemical Analysis Systems, Squaw Valley, CA, USA, 5–9 October 2003; Northrup, M., Jensen, K., Harrison, D., Eds.; Transducers Research Foundation: Cleveland Heights, OH, USA, 2003; pp. 383–386.
65. Vengasandra, S.; Cai, Y.K.; Grewell, D.; Shinar, J.; Shinar, R. Polypropylene cd-organic light-emitting diode biosensing platform. *Lab Chip* **2010**, *10*, 1051–1056.
66. Edel, J.B.; Beard, N.P.; Hofmann, O.; Bradley, D.D.C. Thin-film polymer light emitting diodes as integrated excitation sources for microscale capillary electrophoresis. *Lab Chip* **2004**, *4*, 136–140.
67. Hofmann, O.; Wang, X.H.; deMello, J.C.; Bradley, D.D.C.; deMello, A.J. Towards microalbuminuria determination on a disposable diagnostic microchip with integrated fluorescence detection based on thin-film organic light emitting diodes. *Lab Chip* **2005**, *5*, 863–868.
68. Ren, K.N.; Liang, Q.L.; Yao, B.; Luo, G.O.; Wang, L.D.; Gao, Y.; Wang, Y.M.; Qiu, Y. Whole column fluorescence imaging on a microchip by using a programmed organic light emitting diode array as a spatial-scanning light source and a single photomultiplier tube as detector. *Lab Chip* **2007**, *7*, 1574–1580.
69. Yao, B.; Luo, G.; Wang, L.; Gao, Y.; Lei, G.; Ren, K.; Chen, L.; Wang, Y.; Hu, Y.; Qiu, Y. A microfluidic device using a green organic light emitting diode as an integrated excitation source. *Lab Chip* **2005**, *5*, 1041–1047.
70. Yao, B.; Yang, H.; Liang, Q.; Luo, G.; Wang, L.; Ren, K.; Gao, Y.; Wang, Y.; Qiu, Y. High-speed, whole-column fluorescence imaging detection for isoelectric focusing on a microchip using an organic light emitting diode as light source. *Anal. Chem.* **2006**, *78*, 5845–5850.
71. Kim, Y.H.; Shin, K.S.; Kang, J.Y.; Yang, E.G.; Paek, K.K.; Seo, D.S.; Ju, B.K. Poly(dimethylsiloxane)-based packaging technique for microchip fluorescence detection system applications. *J. Microelectromech. Syst.* **2006**, *15*, 1152–1158.
72. Shin, K.S.; Kim, Y.H.; Paek, K.K.; Park, J.H.; Yang, E.G.; Kim, T.S.; Kang, J.Y.; Ju, B.K. Characterization of an integrated, fluorescence-detection hybrid device with photodiode and organic light-emitting diode. *IEEE Electron Device Lett.* **2006**, *27*, 746–748.
73. Devabhaktuni, S.; Prasad, S. Nanotextured organic light emitting diode based chemical sensor. *J. Nanosci. Nanotechnol.* **2009**, *9*, 6299–6306.
74. Scholer, L.; Seibel, K.; Panczyk, K.; Bohm, M. An integrated pled—A light source for application specific lab-on-microchips (ALM). *Microelectron. Eng.* **2009**, *86*, 1502–1504.
75. Nakajima, H.; Okuma, Y.; Morioka, K.; Miyake, M.; Hemmi, A.; Tobita, T.; Yahiro, M.; Yokoyama, D.; Adachi, C.; Soh, N.; *et al.* An integrated enzyme-linked immunosorbent assay system with an organic light-emitting diode and a charge-coupled device for fluorescence detection. *J. Sep. Sci.* **2011**, *34*, 2906–2912.
76. Marcello, A.; Sblattero, D.; Cioarec, C.; Maiuri, P.; Melpignano, P. A deep-blue oled-based biochip for protein microarray fluorescence detection. *Biosens. Bioelectron.* **2013**, *46*, 44–47.

77. Wu, X.Z.; Sze, N.S.K.; Pawliszyn, J. Miniaturization of capillary isoelectric focusing. *Electrophoresis* **2001**, *22*, 3968–3971.
78. Cui, H.; Horiuchi, K.; Dutta, P.; Cornelius, F. Isoelectric focusing in a poly (dimethylsiloxane) microfluidic chip. *Anal. Chem.* **2005**, *77*, 1303–1309.
79. Helander, M.; Wang, Z.; Qiu, J.; Greiner, M.; Puzzo, D.; Liu, Z.; Lu, Z. Chlorinated indium tin oxide electrodes with high work function for organic device compatibility. *Science* **2011**, *332*, 944–947.
80. Hofmann, O.; Miller, P.; Sullivan, P.; Jones, T.S.; Demello, J.C.; Bradley, D.D.C.; Demello, A.J. Thin-film organic photodiodes as integrated detectors for microscale chemiluminescence assays. *Sensor Actuators B* **2005**, *106*, 878–884.
81. Wang, X.; Amatatongchai, M.; Nacapricha, D.; Hofmann, O.; de Mello, J.C.; Bradley, D.D.C.; de Mello, A.J. Thin-film organic photodiodes for integrated on-chip chemiluminescence detection–application to antioxidant capacity screening. *Sensor Actuators B* **2009**, *140*, 643–648.
82. Wang, X.; Hofmann, O.; Das, R.; Barrett, E.M.; Bradley, D.D.C. Integrated thin-film polymer/fullerene photodetectors for on-chip microfluidic chemiluminescence detection. *Lab Chip* **2006**, *7*, 58–63.
83. Banerjee, A.; Pais, A.; Papautsky, I.; Klotzkin, D. A polarization isolation method for high-sensitivity, low-cost on-chip fluorescence detection for microfluidic lab-on-a-chip. *IEEE Sens. J.* **2008**, *8*, 621–627.
84. Wojciechowski, J.R.; Shriver-Lake, L.C.; Yamaguchi, M.Y.; Füreder, E.; Pieler, R.; Schamesberger, M.; Winder, C.; Prall, H.J.; Sonnleitner, M.; Ligler, F.S. Organic photodiodes for biosensor miniaturization. *Anal. Chem.* **2009**, *81*, 3455–3461.
85. Charwat, V.; Muellner, P.; Hainberger, R.; Purtscher, M.; Ertl, P.; Tedde, S.; Hayden, O. Monitoring Light Scattering Characteristics of Adherent Cell Cultures Using a Lab-on-a-Chip. In *Information Photonics (IP)*, In Proceedings of the 2011 ICO International Conference, Ottawa, Canada, 18–20 May 2011; IEEE: Piscataway, NJ, USA, 2011; pp. 1–2.
86. Charwat, V.; Purtscher, M.; Tedde, S.F.; Hayden, O.; Ertl, P. Standardization of microfluidic cell cultures using integrated organic photodiodes and electrode arrays. *Lab Chip* **2013**, *13*, 785–797.
87. Abel, T.; Sagmeister, M.; Lamprecht, B.; Kraker, E.; Kostler, S.; Ungerbock, B.; Mayr, T. Filter-free integrated sensor array based on luminescence and absorbance measurements using ring-shaped organic photodiodes. *Anal. Bioanal. Chem.* **2012**, *404*, 2841–2849.
88. Lamprecht, B.; Sagmeister, M.; Kraker, E.; Hartmann, P.; Jakopic, G.; Köstler, S.; Ditlbacher, H.; Galler, N.; Krenn, J.; Ungerböck, B. Integrated Waveguide Sensor Platform Utilizing Organic Photodiodes. In *Plasmonics in Biology and Medicine IX*, Proceedings of SPIE 8234, San Francisco, CA, USA, 21 January 2012; Vo-Dinh, T., Lakowicz, J., Eds.; SPIE International Society for Optical Engineering: Bellingham, WA, USA, 2012; p. 82341.
89. Lamprecht, B.; Tschepp, A.; Cajlakovic, M.; Sagmeister, M.; Ribitsch, V.; Kostler, S. A luminescence lifetime-based capillary oxygen sensor utilizing monolithically integrated organic photodiodes. *Analyst* **2013**, *138*, 5875–5878.

90. Sagmeister, M.; Lamprecht, B.; Kraker, E.; Haase, A.; Jakopic, G.; Kostler, S.; Ditlbacher, H.; Galler, N.; Abel, T.; Mayr, T. Integrated Organic Optical Sensor Arrays Based on Ring-Shaped Organic Photodiodes. In *Organic Semiconductors in Sensors and Bioelectronics IV*, In Proceedings of SPIE 8118, San Diego, CA, USA, 21 August 2011; Shinar, R., Kymissis, I., Eds.; SPIE International Society for Optical Engineering: Bellingham, WA, USA, 2011; p. 811805.
91. Sagmeister, M.; Tschepp, A.; Kraker, E.; Abel, T.; Lamprecht, B.; Mayr, T.; Kostler, S. Enabling luminescence decay time-based sensing using integrated organic photodiodes. *Anal. Bioanal Chem.* **2013**, *405*, 5975–5982.
92. Ishimatsu, R.; Naruse, A.; Liu, R.; Nakano, K.; Yahiro, M.; Adachi, C.; Imato, T. An organic thin film photodiode as a portable photodetector for the detection of alkylphenol polyethoxylates by a flow fluorescence-immunoassay on magnetic microbeads in a microchannel. *Talanta* **2013**, *117*, 139–145.
93. Miyake, M.; Nakajima, H.; Hemmi, A.; Yahiro, M.; Adachi, C.; Soh, N.; Ishimatsu, R.; Nakano, K.; Uchiyama, K.; Imato, T. Performance of an organic photodiode as an optical defector and its application to fluorometric flow-immunoassay for Iga. *Talanta* **2012**, *96*, 132–139.
94. Pires, N.M.; Dong, T. Polycarbazole-Based Organic Photodiodes for highly Sensitive Chemiluminescent Immunoassays. In Proceedings of the 35th Annual International Conference of the IEEE EMBS 2013, Osaka, Japan, 3–7 July 2013; IEEE: Piscataway, NJ, USA, 2013; pp. 1700–1703.
95. Pires, N.M.; Dong, T. Detection of Stress Hormones by a Microfluidic-Integrated Polycarbazole/Fullerene Photodetector. In Proceedings of the 35th Annual International Conference of the IEEE EMBS 2013, Osaka, Japan, 3–7 July 2013; IEEE: Piscataway, NJ, USA, 2013; pp. 4470–4473.
96. Pires, N.M.M.; Dong, T.; Hanke, U.; Hoivik, N. Integrated optical microfluidic biosensor using a polycarbazole photodetector for point-of-care detection of hormonal compounds. *J. Biomed. Opt.* **2013**, *18*, 097001.
97. Pires, N.M.M.; Dong, T. Microfluidic biosensor array with integrated poly (2,7-carbazole)/fullerene-based photodiodes for rapid multiplexed detection of pathogens. *Sensors* **2013**, *13*, 15898–15911.
98. Hofmann, O.; Wang, X.; Cornwell, A.; Beecher, S.; Raja, A.; Bradley, D.D.C. Monolithically integrated dye-doped pdms long-pass filters for disposable on-chip fluorescence detection. *Lab Chip* **2006**, *6*, 981–987.
99. Jorgensen, A.M.; Mogensen, K.B.; Kutter, J.P.; Geschke, O. A biochemical microdevice with an integrated chemiluminescence detector. *Sensor Actuators B* **2003**, *90*, 15–21.
100. Blouin, N.; Michaud, A.; Leclerc, M. A low-bandgap poly (2,7-carbazole) derivative for use in high-performance solar cells. *Adv. Mater.* **2007**, *19*, 2295–2300.
101. Park, S.H.; Roy, A.; Beaupré, S.; Cho, S.; Coates, N.; Moon, J.S.; Moses, D.; Leclerc, M.; Lee, K.; Heeger, A.J. Bulk heterojunction solar cells with internal quantum efficiency approaching 100%. *Nat. Photonics* **2009**, *3*, 297–302.

102. Ratcliff, E.L.; Veneman, P.A.; Simmonds, A.; Zacher, B.; Huebner, D.; Saavedra, S.S.; Armstrong, N.R. A planar, chip-based, dual-beam refractometer using an integrated organic light-emitting diode (OLED) light source and organic photovoltaic (OPV) detectors. *Anal. Chem.* **2010**, *82*, 2734–2742.
103. Krishnaswamy, N.; Srinivas, T.; Rao, G.M. Analysis of Integrated Optofluidic Lab-on-a-Chip Fluorescence Biosensor Based on Transmittance of Light Through a Fluidic Gap. In Proceedings of EMBC 2011 33rd Annual International Conference of the IEEE EMBS, Boston, MA, USA, 30 August–3 September 2011; IEEE: Piscataway, NJ, USA, 2011; pp. 30–34.
104. Krishnaswamy, N.; Srinivas, T.; Rao, G.M.; Varma, M.M. Analysis of integrated optofluidic lab-on-a-chip sensor based on refractive index and absorbance sensing. *IEEE Sens. J.* **2013**, *13*, 1730–1741.
105. Banerjee, A.; Shuai, Y.; Dixit, R.; Papautsky, I.; Klotzkin, D. Concentration dependence of fluorescence signal in a microfluidic fluorescence detector. *J. Lumines.* **2010**, *130*, 1095–1100.
106. Banerjee, A.; Shuai, Y.; Klotzkin, D.; Papautsky, I. High-Sensitivity Mems Based on-Chip Fluorescence Detection System: Measurement and Analysis of Ultimate Sensitivity Limits. In Proceedings of the UGIM 2008 Symposium 17th Biennial University/Government/Industry Micro-Nano Symposium, Louisville, KY, USA, 13–16 July 2008; IEEE: Piscataway, NJ, USA, 2008; pp. 177–182.
107. Pais, A.; Banerjee, A.; Klotzkin, D.; Papautsky, I. High-sensitivity, disposable lab-on-a-chip with thin-film organic electronics for fluorescence detection. *Lab Chip* **2008**, *8*, 794–800.
108. Shuai, Y.; Banerjee, A.; Klotzkin, D.; Papautsky, I. On-Chip Fluorescence Detection with Organic Thin Film Devices for Disposable Lab-on-a-Chip Sensors. In Proceedings of the Seventh IEEE Sensors Conference 2008 IEEE Sensors 2008, Lecce, Italy, 26–29 October 2008; IEEE: Piscataway, NJ, USA, 2008; pp. 122–125.
109. Kraker, E.; Haase, A.; Lamprecht, B.; Jakopic, G.; Konrad, C.; Kostler, S. Integrated organic electronic based optochemical sensors using polarization filters. *Appl. Phys. Lett.* **2008**, *92*, 033302.
110. Mayr, T.; Abel, T.; Kraker, E.; Köstler, S.; Haase, A.; Konrad, C.; Tscherner, M.; Lamprecht, B. An optical sensor array on a flexible substrate with integrated organic opto-electric devices. *Proc. Eng.* **2010**, *5*, 1005–1008.
111. Liu, R.; Xiao, T.; Cui, W.; Shinar, J.; Shinar, R. Multiple approaches for enhancing all-organic electronics photoluminescent sensors: Simultaneous oxygen and pH monitoring. *Anal. Chim. Acta* **2013**, *778*, 70–78.
112. Nalwa, K.S.; Cai, Y.; Thoeming, A.L.; Shinar, J.; Shinar, R.; Chaudhary, S. Polythiophene-fullerene based photodetectors: Tuning of spectral response and application in photoluminescence based (bio) chemical sensors. *Adv. Mater.* **2010**, *22*, 4157–4161.
113. Lefèvre, F.; Chalifour, A.; Yu, L.; Chodavarapu, V.; Juneau, P.; Izquierdo, R. Algal fluorescence sensor integrated into a microfluidic chip for water pollutant detection. *Lab Chip* **2011**, *12*, 787–793.
114. Ramuz, M.; Leuenberger, D.; Burgi, L. Optical biosensors based on integrated polymer light source and polymer photodiode. *J. Polym. Sci. Pt. B* **2011**, *49*, 80–87.

115. Liang, Y.Y.; Feng, D.Q.; Wu, Y.; Tsai, S.T.; Li, G.; Ray, C.; Yu, L.P. Highly efficient solar cell polymers developed via fine-tuning of structural and electronic properties. *J. Am. Chem. Soc.* **2009**, *131*, 7792–7799.
116. Liang, Y.; Xu, Z.; Xia, J.; Tsai, S.; Wu, Y.; Li, G.; Ray, C.; Yu, L. For the bright future—Bulk heterojunction polymer solar cells with power conversion efficiency of 7.4%. *Adv. Mater.* **2010**, *22*, E135–E138.

# Section II: Material Fabrication and Properties

## Chapter 3

# Optical and Surface Characterization of Radio Frequency Plasma Polymerized 1-Isopropyl-4-Methyl-1,4-Cyclohexadiene Thin Films

**Jakaria Ahmad, Kateryna Bazaka and Mohan V. Jacob**

**Abstract:** Low pressure radio frequency plasma-assisted deposition of 1-isopropyl-4-methyl-1,4-cyclohexadiene thin films was investigated for different polymerization conditions. Transparent, environmentally stable and flexible, these organic films are promising candidates for organic photovoltaics (OPV) and flexible electronics applications, where they can be used as encapsulating coatings and insulating interlayers. The effect of deposition RF power on optical properties of the films was limited, with all films being optically transparent, with refractive indices in a range of 1.57–1.58 at 500 nm. The optical band gap ($E_g$) of ~3 eV fell into the insulating $E_g$ region, decreasing for films fabricated at higher RF power. Independent of deposition conditions, the surfaces were smooth and defect-free, with uniformly distributed morphological features and average roughness between 0.30 nm (at 10 W) and 0.21 nm (at 75 W). Films fabricated at higher deposition power displayed enhanced resistance to delamination and wear, and improved hardness, from 0.40 GPa for 10 W to 0.58 GPa for 75 W at a load of 700 μN. From an application perspective, it is therefore possible to tune the mechanical and morphological properties of these films without compromising their optical transparency or insulating property.

Reprinted from *Electronics*. Cite as: Ahmad, J.; Bazaka, K.; Jacob, M.V. Optical and Surface Characterization of Radio Frequency Plasma Polymerized 1-Isopropyl-4-Methyl-1,4-Cyclohexadiene Thin Films. *Electronics* **2014**, *3*, 266-281.

### 1. Introduction

The latest advances achieved in the field of organic electronics have expanded the scope of applications beyond those attainable with conventional silicon (Si) semiconducting technologies to include flexible photovoltaic (PV) and light-emitting devices, flexible displays, chemical and biological sensors, wearable and implantable electronics, to name a few [1–7]. Among these, organic thin film photovoltaics (OPV) is an emerging economically-competitive PV technology that combines manufacturing adaptability, low-cost processing and a lightweight, flexible device end-product. In spite of the significant advances in OPV, commercial use of this technology remains limited, due to both low power conversion efficiency (PCE) and poor overall stability of the devices. Indeed, even though the highest PCE achieved from organic PV has risen from 2.5% to 11% for bulk heterojunction polymer: fullerene solar cells over the last ten years, it falls short of 25%–30% PCE

level offered by established *Si* photovoltaic cells. The lifetime achievable by the most advanced organic solar cells is also far below the 20–25 years lifespan of commercial *Si* photovoltaic cells [8], attributed to relatively low environmental stability of organic photoactive materials.

Most of the research effort to date has concentrated around the photoactive layer, focusing on new, more efficient and stable materials with tailored energy levels and solubility, and a better understanding of the mechanism of photon–to–electron conversion [9]. However, encapsulation with high barrier performance materials has also been recognized as instrumental in significantly improving device lifetime, where device stability is extended by limiting penetration of oxygen and moisture from the environment into device layers [10]. For instance, encapsulation of solar cells based on coating of ZnO layer on top of a photoactive material and subsequent UV resin drop coating resulted in a significant increase in the stability, shelf life of the device, and the cost-effectiveness [11]. Recently synthesized silicon oxide/alumina and parylene layer had an effective water vapor transmission (WVTR) rate of $2.4 \pm 1.5 \times 10^{-5}$ g/m$^2$/day [12]. However, the requirements for high performance encapsulation materials include good processability, high optical transmission, high dielectric constant, low water absorptivity and permeability, high resistance to ultra-violet (UV) degradation and thermal oxidation, good adhesion, mechanical strength, and chemical inertness [13]. While inorganic barrier layers are often used for their sound durability [14], organic encapsulation materials are attracting attention for their synthetic flexibility and resulting property tunability [15].

Organic thin film materials fabricated from renewable precursors using low-cost deposition methods, such as plasma-assisted nanoassembly, have lower environmental and economic costs [16]. Low-temperature plasma deposition is a highly engineering-friendly, economical method of polymer synthesis, that delivers practically pollutant free surface chemistry, and can be easily integrated into manufacturing processes [17,18]. The method offers a level of confidence and deposition quality comparable to and in many cases superior to other widely-used techniques, such as thermal chemical vapor deposition, wet chemistry processing, laser assisted microfabrication, *etc.* [19,20]. Films fabricated using plasma-assisted synthesis are typically smooth, ultrathin and pinhole free, with good spatial uniformity, conformal coverage, and high adhesion to the substrate [21].

1-isopropyl-4-methyl-1,4-cyclohexadiene, also known as γ-terpinene, is a non-synthetic isomeric hydrocarbon derived from *Melaleuca alternifolia essential oil. Earlier*, Jacob and co-workers have successfully used plasma-assisted deposition to fabricate thin films from other renewable precursors for application in electronics and biomedical fields, reporting property variability linked to both deposition conditions and the chemistry of the monomer [22–26]. This paper reports on the plasma-assisted fabrication of new polymer thin films from γ-terpinene, with intention to use these films in OPVs, specifically as encapsulation coatings, and as insulating layers in flexible electronics. Given the proposed application for the plasma polymerized γ-terpinene (pp–GT), the material is studied in terms of optical, surface, mechanical, and adhesion properties as a function of deposition conditions.

## 2. Experimental Section

Thin film samples were deposited on high quality glass microscope slides inside a custom made, cylindrical RF polymerization chamber, 0.75 m in length with an inner diameter of 0.055 m (approximate volume of 0.018 cm$^3$). The slides were thoroughly cleaned using extran, an ultrasonic bath of distilled water, and rinsed with isopropanol prior to deposition. Using the procedure outlined

in [22], plasma polymer films were fabricated from γ-terpinene monomer (Figure 1) at various input RF power levels (10, 25, 50 and 75 W) and at an ambient temperature of 20 °C. The monomer flow rate was estimated to be 1.57 $cm^3$/min by employing the procedure outlined by Gengenbach and Griesser [27].

**Figure 1.** Chemical structure of 1-Isopropyl-4-methyl-1,4-cyclohexadiene ($C_{10}H_{16}$).

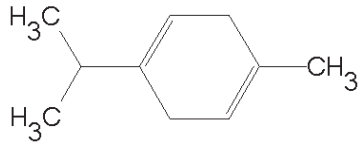


Variable angle spectroscopic ellipsometry (VASE) measurements were performed using a J.A. Woollam Co. Inc. model M-2000D variable angle spectroscopic ellipsometer to estimate sample thickness and optical properties of pp–GT thin films [28]. The refractive index *n*, extinction coefficient *k* and thickness were derived from the experimental $\Delta$ and $\Psi$ data via regression analysis. The relation between *n* and thickness for the polymer samples has also been investigated. UV-Vis spectroscopy measurements were performed using an Avantes Avaspec-2048 spectroscopy unit with an Avalight-DHc light source to measure the absorbance in the ultraviolet and visible region. From those data, values of optical band gap have been derived. Surface morphology and roughness parameters of pp–GT thin films fabricated under different RF powers were determined from atomic force microscope (AFM) images acquired on a NT-MDT NTEGRA Prima AFM operating in semi-contact mode. A Hysitron Triboscope was used to perform the nanoindentation study. During the nanoindentation study, a Berkovich indenter (70.3° equivalent semi-opening angle) was used and instrument compliance was calibrated using fused silica. Preliminary images of the samples under investigations were collected in order to evaluate the roughness of the area to be indented. Twelve indentations were made on each sample and the results presented are an average of these indentations. Typical loads used in the indentation ranged from 100 μN to 2000 μN with fixed loading time and hold time of between 2 and 5 s.

In the load-partial unload (PUL) experiment, several cycles of loading and unloading were performed in a sequence (Figure 2). At a constant rate of loading and unloading (100 μN/s), the Berkovich indenter was first loaded and unloaded two times in succession with each of the unloadings terminated at 10% of the maximum load to assure the contact between the pp–GT thin film sample and the indenter. This was performed to examine the reversibility of the deformation and thus ensure that the unloading data used for analysis purposes were mostly elastic [29]. The load was held constant after the second unloading for a fixed period of time at 10% of the peak value while the displacement was carefully monitored to establish the rate of displacement produced by thermal expansion in the system. Following the hold period, the sample was loaded for the last time to allow any final time dependent plastic effects to diminish, with another fixed hold period inserted at peak load and then the specimen was fully unloaded.

**Figure 2.** Typical load–time sequence used for load–partial unloading experiments.

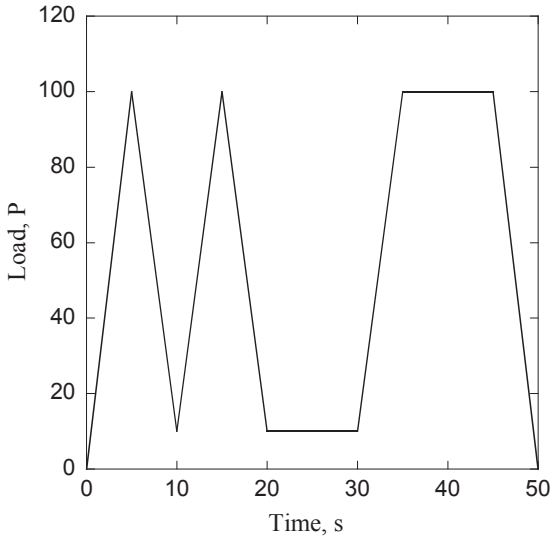


After the indentations were performed, stiffness values and the known modulus for quartz were used to calculate the contact area for each indent. Contact parameters and mechanical properties of the pp–GT thin films are derived from the contact area and load-displacement curve as proposed by Oliver and Pharr [29]. The unloading stiffness was determined after polynomial fitting of 90% of the unloading curve.

The cross-hatch test was performed on pp–GT films fabricated at different power levels using the Elcometer 107 kit to obtain a standardized (ASTM D3359) qualitative assessment of the adhesion between the films and the glass substrate. Crosshatch patterns were made on the polymer film surfaces using the cutting tool (6 teeth, 1 mm spacing). The whole area was then brushed to remove debris and adhesive tape was applied on top of the lattice followed by smoothing out the tape with a pencil eraser across the surface. The tape was then removed by pulling at an angle of 180° and the results were analyzed by comparing the lattice of cuts with ISO standards. Three samples were fabricated for each applied RF power, with three crosshatch tests performed on each sample.

## 3. Results and Discussion

### *3.1. Effect of Time on Film Thickness*

The dependence of pp–GT thin film thickness on the deposition time was studied on samples fabricated for 2, 5, and 10 min at 25 W RF power along with constant monomer flow rate and pressure. A film thickness of 120 nm was obtained with deposition time of 2 min at 25 W. The sample thickness increased linearly with time, approaching 438 nm for deposition time of 10 min. Similar trend was observed for films fabricated at 10, 50, and 75 W RF power. Film thickness is also found to be linearly increasing with higher RF power. This is due to an increase in the densification of electrons with an increased crosslinking. Same phenomenon has also been observed in case of plasma polymerized terpinen-4-ol and linalyl acetate (PLA) thin films [26,30]. Assuming constant deposition conditions (pressure, monomer flow rate, distance between electrodes, *etc.*), the desired film thickness of pp–GT thin film for a potential application can therefore be achieved by controlling the time of deposition.

*3.2. RF Power Dependence of Optical Constants*

The effect of changing the RF power level on the optical constants of pp–GT polymer thin films has been studied using VASE and UV-Vis spectroscopy over the wavelength range of 200–1000 nm. UV-Vis absorption spectrums of samples fabricated at 10, 25, 50, and 75 W RF power level (Figure 3) reveal that the absorption contour is replicable over the RF power range employed during fabrication. Reallocating of the peak position and/or broadening of the peak are not observed with increase in RF power, unlike other studies [31]. The maximum absorption of pp–GT films fabricated at different RF power levels is found to be at 300 nm. It is believed that the main absorption peak may be the result of pi–pi * transitions. The optical transparency of the polymer films is confirmed by these spectra as the maximum absorption peaks are outside of the visible region of the spectrums. The optical transparency of the pp-GT film can be effectively used in applications such OPV, medical imaging, optical sensor and as an encapsulating (protective) layer for the electronic circuits.

**Figure 3.** UV-Vis absorption spectrum of pp–GT thin films.

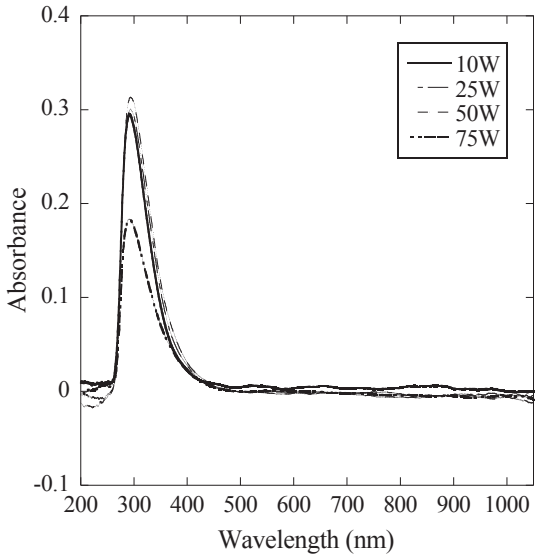


Figure 4 demonstrates the *n* and *k* profiles of pp–GT thin films fabricated at various power levels. Thickness and surface roughness parameters from Cauchy analysis (WVASE software) were used to obtain *n* and *k* profiles. Mean squared error (MSE) values used to assess the quality of the modeling fit were below 3. Considering the profiles, it is observed that the overall shape of the curves was similar across all the samples. At short wavelengths (below 250 nm), a sharp peak in *n* profile was detected. At wavelengths above approximately 250 nm, an increase in RF input power resulted in higher *n* values for the polymer. At 500 nm, the difference in refractive index between 10 and 75 W sample is 0.01, corresponding to a change of less than 1% that is similar to thin films fabricated from linalyl acetate [32].

**Figure 4.** Refractive indices and extinction coefficient of pp–GT thin films.

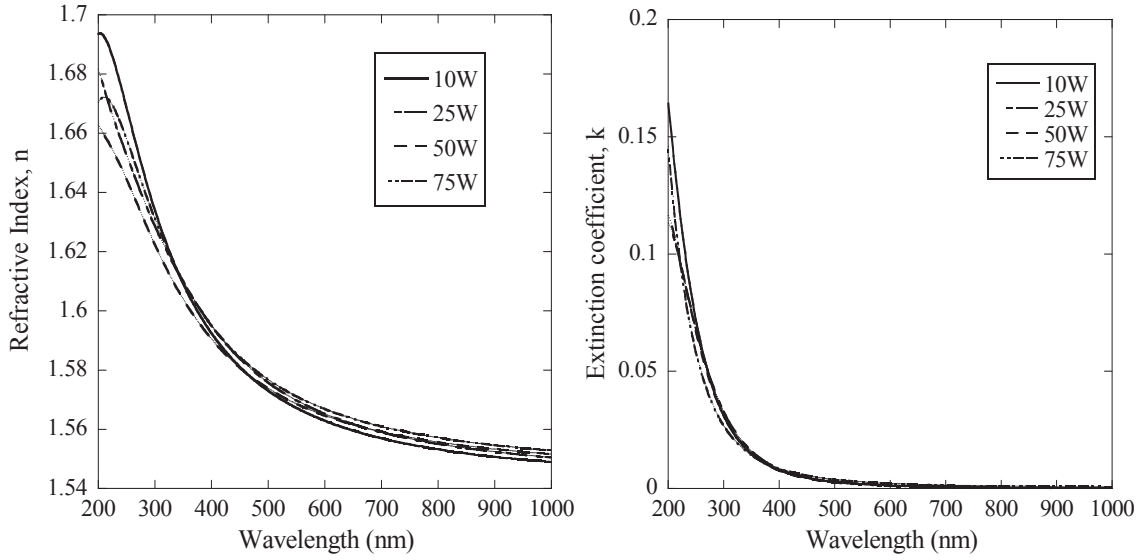


Based on the refractive index values of pp–GT films, it is anticipated that it can be used as a coating on long-period fiber gratings (LPFGs) to enhance its sensitivity, similar to δ-form syndiotactic polystyrene [33]. According to [34], pp–GT can also be used in advanced optoelectronic fabrications, such as high performance substrates for advanced display devices, optical adhesives or encapsulants for OPV devices, antireflective coatings for advanced optical applications or image sensors [4,5,10].

The extinction coefficient ($k$) profiles for pp–GT samples fabricated at various RF power levels illustrate very similar characteristics. These results (optical similarities with glass and transparency in the visible wavelength region) confirm pp–GT thin films as a strong candidate for use as encapsulation coatings in OPV, optical devices, such as LEDs, FETs, and lenses.

Abbe number ($v_D$), a key parameter for the refractive index dispersion, is of great importance for optical materials used in the visible region. It is also defined as $v$-number or refractive efficiency or constringency of the material. The Abbe number is given by following equation [35]:

$$v_D = \frac{n_{d-1}}{n_F - n_c'} \quad (1)$$

where $n_d$, $n_F$, and $n_C$ are the refractive indices of the material at the wavelengths of sodium D (587.6 nm), hydrogen F (486.1 nm), and hydrogen C (656.3 nm), respectively [35]. Materials that have a higher Abbe number ($v_D$) have lower dispersion in the refractive index, whereas highly refractive materials have small Abbe numbers [36,37]. A polymer having low $v_D$ (<30), is therefore not suitable for use in optics [36].

For pp–GT films, $v_D$ increases from 35.37 to 40.35 (Table 1) with increase in RF power (10 W to 75 W), which confirms that films fabricated at 75 W have lower dispersion in the refractive index. These results indicate the well-balanced properties and hence the pp–GT polymer thin films are potential candidates for advanced optical applications.

**Table 1.** Abbe-numbers for pp–GT thin films.

| RF Power (W) | $v_D$ |
|---|---|
| 10 | 35.37 |
| 25 | 35.18 |
| 50 | 37.80 |
| 75 | 40.35 |

*3.3. Thickness Dependence of Optical Constants*

Thickness dependence study was carried out using spectroscopic ellipsometry data taken for pp–GT thin films fabricated at 25 W with different film thicknesses and the corresponding *n* and *k* profiles. With an increase of thickness over the measured wavelength region, a very small increase of *n* is observed. The shift in *n vs.* thickness is comparable to that found for polyparaxylene films [38], which were deemed to not have significant thickness dependence on *n*. The shifts found in pp–GT thin films are therefore insignificant and thus *n* is not dependent on thickness.

*3.4. Determination of the Energy Gap*

To determine the nature of the optical transitions, the optical absorption study was performed for pp–GT thin films. The optical absorption coefficient data were obtained from UV–Vis spectroscopy measurements. The optical absorption dependence of photon energy is expressed by the following relationship [39]:

$$\alpha h\nu = A(h\nu - E_g)^m \quad (2)$$

where $A$ is an energy-independent constant, $E_g$ is the optical band gap and $m$ is a constant which is connected to the density-of-states distribution in the transport gap in the band tails and thus determines the type of transition ($m$ = 1/2 and 3/2 for direct allowed and forbidden transitions, respectively, $m$ = 2 and 3 for indirect allowed and forbidden transitions, respectively) [39].

The optical absorption coefficient data obtained from UV-Vis spectroscopy measurements were converted to a Tauc plot using a MATLAB program. In that curve, a value of $m$ = 3/2 was employed for all the pp–GT thin films studied, as this value provided the most linear plot, indicating direct forbidden transitions. The indirect process is much slower than the direct transitions as it requires three entities to intersect in order to proceed: an electron, a photon, and a phonon. Materials showing direct transition are therefore much more efficient than materials that show indirect transition. Gallium arsenide (*GaAs*) and other direct band gap materials are used in optical devices, such as LEDs and lasers, whereas *Si* that is an indirect band gap material is not used. This study shows that pp–GT, having direct transition has the potential to be used in different optical devices. The optical band gap values (Table 2) remained between 3.14 eV and 3.01 eV, falling within the insulating region of $E_g$. The pp–GT thin films can therefore be used as insulators for the application of flexible coating on electrical apparatus (e.g., printed circuit board, high voltage systems, circuit breakers, *etc.*).

**Table 2.** Optical bandgap of pp–GT thin films for $m$ = 3/2.

| RF power (W) | $E_g$ (eV) |
|---|---|
| 10 | 3.14 |
| 25 | 3.08 |
| 50 | 3.07 |
| 75 | 3.01 |

*3.5. Surface Morphology*

The surface profile of pp–GT thin films fabricated at various input RF power levels were studied to examine surface defects and roughness The topographical features of the investigated films deposited on glass surfaces are shown in Figure 5.

**Figure 5.** AFM images of pp–GT thin films fabricated at 10, 25, 50, and 75 W input RF power levels.

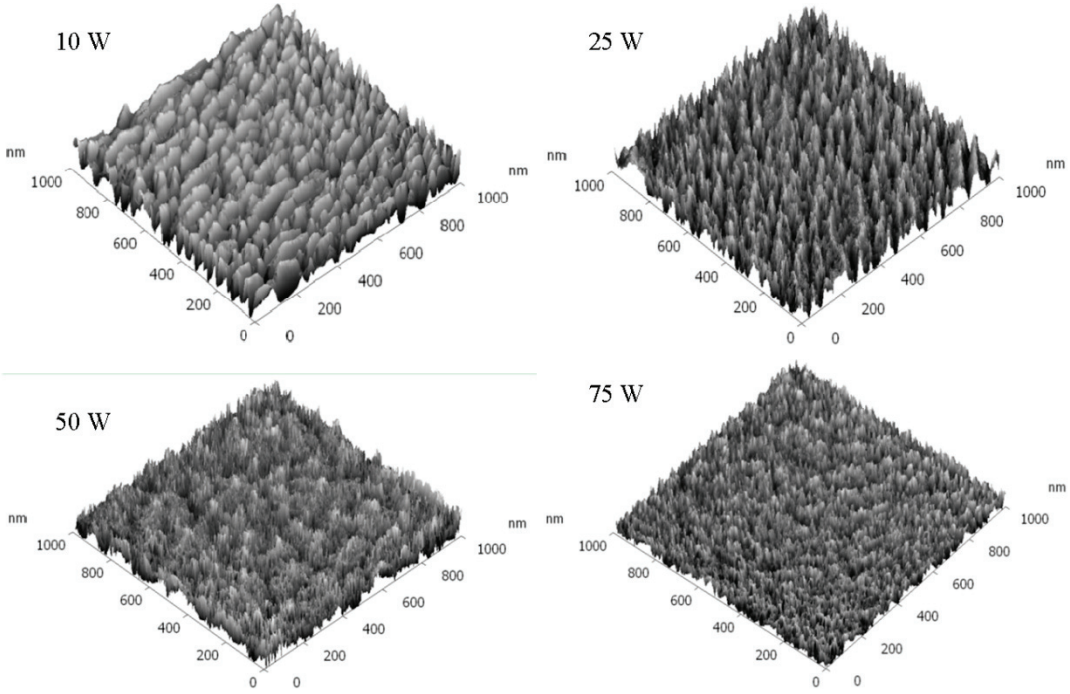


From this study, pp–GT thin films are found to be smooth, uniform and defect-free, exhibiting consistent morphology across film samples. Average roughness values for all samples were approximately 0.3 nm. These roughness values were in agreement with the roughness values found by means of spectroscopic ellipsometry. I Surfaces with RMS roughness values below 0.5 nm have an insignificant effect on its surface and chemical properties and performance [40]. Considering this and the determined roughness of 0.3 nm, the polymerization reactions are confirmed to take place mostly on the surface of the glass substrate rather than in the gas phase [41].

Beside the conventional roughness parameters $R_a$ and $R_q$, the statistical parameters, such as $R_{sk}$ (skewness) and $R_{kur}$ (kurtosis), were determined for the pp–GT thin films. $R_{kur}$ is a quantitative measure of the kurtosis, which is defined as the randomness of profile heights that determines whether the data sets are peaked or flat relative to a normal distribution. $R_{kur}$ values can range from 0 to 8. Surfaces with distinct peaks that decline rather rapidly and have heavy tails exhibit high values;

whereas rough surfaces with flat top near the mean possess lower values. The pp–GT thin film fabricated at 10 W has lower value of $R_{kur}$ (Table 3), whereas sharp peaks and heavier tails are found for samples fabricated at higher RF power levels (Figure 5) that have relatively high values of $R_{kur}$ (Table 3). A surface skewness ($R_{sk}$) greater than 0 is observed for pp–GT films, *i.e.*, the predominance of disproportionate number of peak-like surface features. Furthermore, it was observed that the 75 and 50 W samples have smaller and tapered features (narrow curves) while the 25 and 10 W samples have broad curves. Furthermore, decrease in entropy indicates the surface flatness, *i.e.*, reduction of growth of pores at higher RF power levels [42]. Because of this behavior, $R_{rms}$ and $R_a$ values decreased with increase of RF power. However, higher deposition rate of pp–GT resulted in an increase in the surface roughness values due to the fact that the particles in the growth region were unable to relax fast enough before the next layer of the film is deposited [43]. These surface analysis results clearly indicate the difference between the peak distributions for pp–GT samples fabricated at different RF power that may affect the wettability. Uniformity of films is also confirmed from the analysis, which indicates the less prone to fracture characteristics of the pp–GT films.

**Table 3.** Roughness parameters of pp–GT thin films.

| Roughness parameters | 10 W | 25 W | 50 W | 75 W |
|---|---|---|---|---|
| Maximum peak height $R_{max}$ (nm) | 4.48 | 2.38 | 2.16 | 2.15 |
| Average roughness $R_a$ (nm) | 0.30 | 0.28 | 0.25 | 0.21 |
| Root mean square $R_q$ (nm) | 0.39 | 0.34 | 0.32 | 0.30 |
| Surface skewness $R_{sk}$ | 0.32 | 0.22 | 0.14 | 0.08 |
| Coefficient of kurtosis $R_{kur}$ | 0.06 | 0.54 | 0.63 | 0.77 |
| Entropy | 6.12 | 4.5 | 3.9 | 3.56 |

Surface morphology can also be described in relation to the wetting behavior of the plasma films. Surface roughness generally enhances the hydrophilicity [44]. For pp–GT thin films, the decrease in roughness values with higher deposition power is therefore considered to contribute to the increased hydrophobicity of the surface. Smooth surfaces with greater hydrophobicity are vital for optical and electrical applications, and also for implementing as coating materials for surface protection or buffer layers [45].

### *3.6. Nanoindentation*

Mechanical properties of pp–GT deposited under different RF power conditions were investigated using a single indentation method and a load - partial unload technique. A series of indentations were made in the films with depths ranging from 221.5 nm to 207.2 nm depending on the thickness of the film. Illustrative single indentation curves from 2 μm thick pp–GT film fabricated at 10 W is presented in Figure 6.

The load-unload curve (Figure 6) shows the typical behavior of pp–GT thin films undergoing a nanoindentation test. The initial slope of the unloading process is used to deduce the reduced elastic modulus of the material at the specific contact depth, $h_c$. There are a number of pop-ins in the curve initially and this phenomenon may be attributed to micro-cracking or dislocation nucleation and/or propagation during loading as have been investigated in a wide variety of materials [46].

**Figure 6.** Load–displacement diagram of pp–GT thin film fabricated at 10 W.

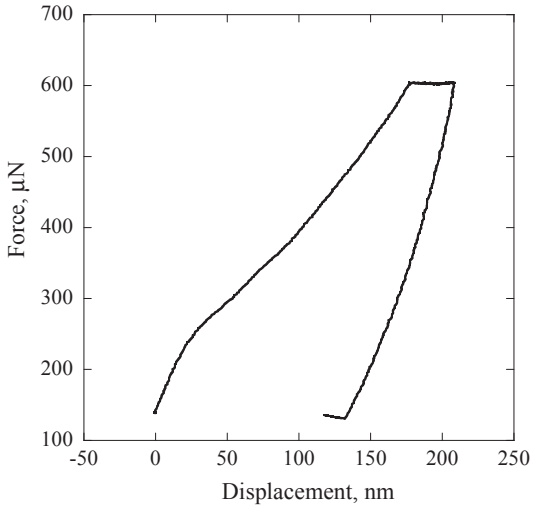


The elastic moduli and hardness of different pp–GT thin film samples increased with the increasing RF power as seen from Table 4. Elastic modulus of pp–GT thin film fabricated at 10 W is 4.22 GPa, while film fabricated at 75 W reaches an elastic modulus of 5.96 GPa. Increase in modulus is also observed with decreasing $h_c$. This may be due to the transition from spherical contact to conical contact behavior occurred at $h_c$ = indenter radius/4 for the Berkovich indenter used in the study [47]. Data at lower depths should be treated with caution as the contact modulus measured varies considerably with tip radius under spherical contact conditions. Hardness of pp–GT thin films also follows the same trend as elastic modulus. The hardness of the materials increases with increase in input RF power and this can be attributed to the higher crosslinking of the polymers fabricated at higher power levels [22]. This results in an increase in resistance against sample deformation. Increase of elastic modulus and hardness with increasing RF power has also been reported in other materials such as linalyl acetate [26]. However, it should be noted that several sources of error may exist in these experiments, which may include the relative non-uniformity of the indent (e.g., pile-up and sink-in phenomena) observed on some samples, and difficulties in precise estimation of the indent area (e.g., possible overestimation in the case of pile-up and underestimation due to sink-in features), respective influences of material properties and sample thicknesses and creep [48]. In addition, artifacts and tip effects affecting the precision of the measurement may possibly be imaged due to the usage of same tip for the actual indentation process and imaging. In a nanoindentation test, very often the stress relaxation is observed at the maximum load during unloading process. This is due to the large strain beneath indenter and the large strain rate at this point (since the loading rate is usually finite during the experiment). Moreover, sudden withdraw of indenter causes oscillations in measurement whereas holding at maximum load may lead to uncertainties in the measured quantities [48]. In addition, the initial portion of unloading is more prone to thermal drift than the loading curve. The values presented in Table 4 are therefore indicative of the evolution of the hardness properties of pp–GT thin films under changing fabrication conditions and may quantitatively differ from the actual material properties due to aforementioned measurement bounds.

**Table 4.** Hardness parameters of pp–GT thin films.

| RF power (W) | Contact depth, $h_c$ (nm) | Hardness, H ± SE (GPa) | Final depth, $h_f$ (nm) | Elastic modulus, E (GPa) |
|---|---|---|---|---|
| 10 | 221.5 | 0.40 ± 0.01 | 137.90 | 4.22 |
| 25 | 218.3 | 0.46 ± 0.02 | 102.53 | 4.61 |
| 50 | 211.7 | 0.51 ± 0.02 | 83.60 | 4.90 |
| 75 | 207.2 | 0.58 ± 0.03 | 69.76 | 5.96 |

Loading time and holding time have significant effect on the indentation behavior of pp–GT thin films. To investigate these effects, single indentations were performed on samples deposited at 75 W at constant load of 1000 μN. Figure 7 shows typical repeat single indentation profiles under increasing indentation load of pp–GT film deposited at 75 W. Hardness value decreased from 0.57 GPa to 0.53 GPa with increasing loading and unloading time with rates (*r*) ranging from 0.5 to 20 nm/s. As creep deformation taking place during the holding time influences the contact depth at maximum load, the hardness values obtained using these maximum contact depth estimates will also be affected [24]. Moreover, the holding time at maximum load affects the unloading portion of the load displacement curve. In this study, an increase in the hold time showed a decrease in the positive slope value of the material. The relationship of decrease in this slope of unloading in the load-displacement curve and modulus of the pp–GT thin films can be explained by the following equation [49]:

$$S = \frac{dP}{dh} = \frac{2}{\sqrt{\pi}} E^* \sqrt{A} \tag{3}$$

The decrease in the slope value means decrease in the d*P*/d*h* value that leads to a decrease in modulus value. Further increase in hold time increases the indentation depth of the indenter tip on the thin film surface, which leads to increase in contact area of the indenter with the film. The increase in the contact area decreases the hardness of the film. In the case of pp–GT thin films, increasing the hold time from 5 to 25 s at constant load of 500 μN resulted in a decrease in the calculated hardness from 0.59 to 0.53 GPa.

To extend the capabilities of quasistatic testing to allow depth profiling of pp–GT thin films, the partial unloading (PUL) technique was used. This investigation revealed that at depths below 190 nm (2 μm thick pp–GT film), the depth profile of the hardness follows a trend similar to that determined using the single indentation approach. The hardness of the system gradually increases above approximately 190 nm due to the stress field no longer being contained within the body of the thin film.

### *3.7. Adhesion Study*

The adhesion behavior of pp–GT thin films deposited on glass is presented in Figure 8. The adhesion improved with higher deposition power. Films fabricated at 10 W showed 5%–15% delamination. However, films fabricated at 50 and 75 W showed no delamination effect with a higher cross hatch rating.

**Figure 7.** Typical AFM image of plastic impressions remaining in pp–GT sample fabricated at 75 W after indentation under different load conditions.

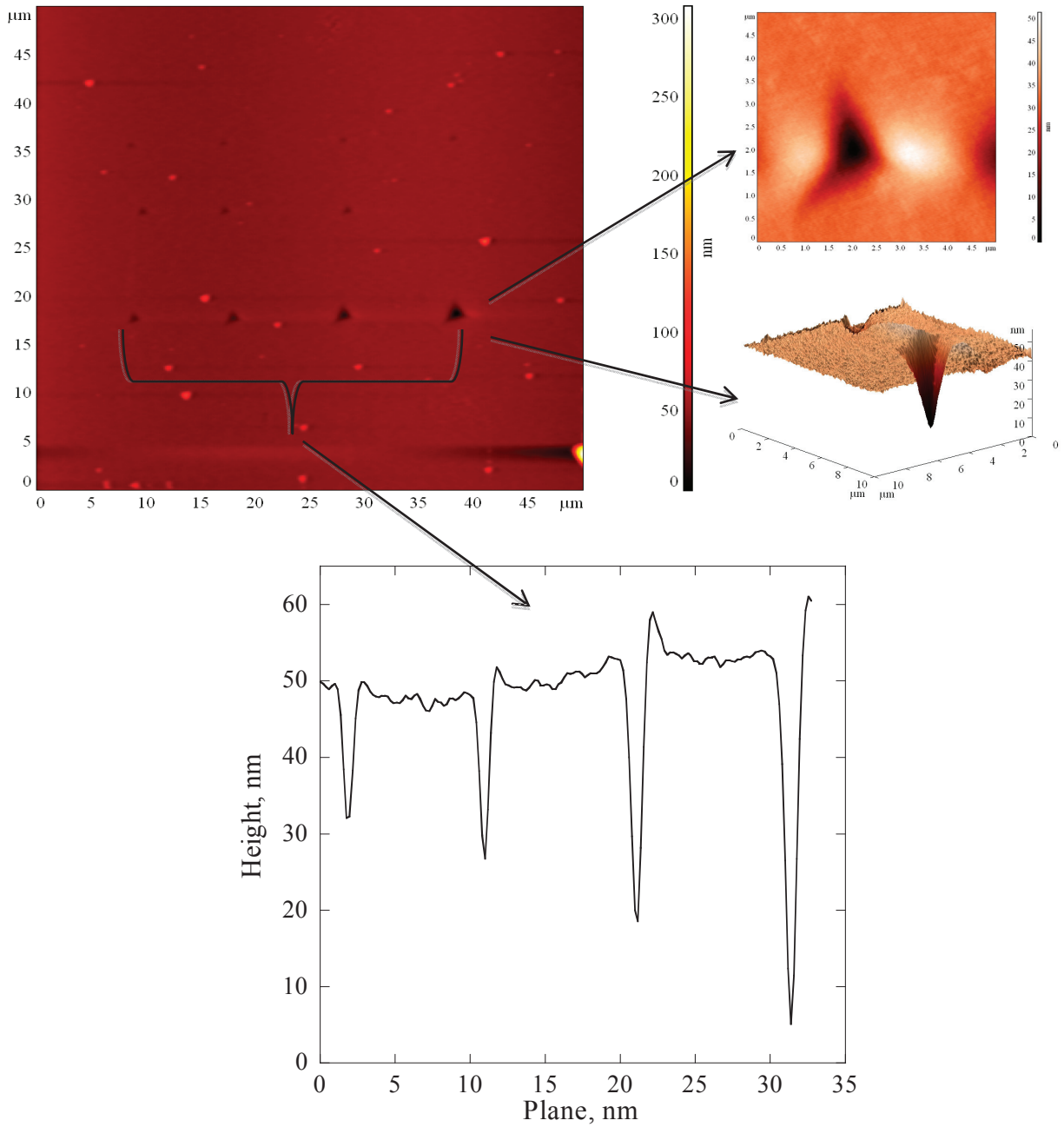


The optical image acquired using the microscope and CCD camera for the 10 W sample showed a significant amount of deformation occurred to the sample upon applying and consequent removal of the adhesive tape. For the thin films deposited at 25 W, the areas that were not affected by the tape test appeared uniform and with the increasing of RF power, this uniformity increased. This trend is attributed to the interfacial bonding that is improved by an increase in cross-link density associated with increasing applied RF power. These findings provide an insight into the reliability of the pp–GT films.

**Figure 8.** Adhesion data for pp–GT thin films at 10, 25, 50, and 75 W.

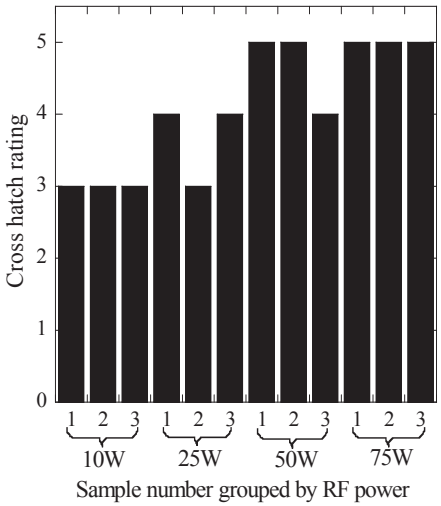


## 4. Conclusions

The basic optical properties and optical constants of the pp–GT thin films were investigated by means of spectroscopic ellipsometry and UV-Vis spectroscopy. The optical constants such as the refractive index ($n$), extinction coefficient ($k$), and optical band gap were determined. The films are confirmed as optically transparent and independent of RF power. The refractive index and extinction coefficient of the pp–GT thin films demonstrated very little dependence on RF power and film thickness. The optical absorption spectra showed that the absorption mechanism is a direct transition. The independence of the refractive index on the RF power level demonstrates the pp–GT thin films as an impending optically stable material for optical applications.

AFM investigation demonstrated that the pp–GT films were smooth, uniform and defect-free. The average roughness parameter decreased with increasing RF power (0.30 for 10 W and 0.21 for 75 W). In the nanoindentation study, combined effects of loading rate and holding time were investigated. For the load rates and hold time considered, pp–GT thin films were found to be a function of both the variables. The unloading portion of the load-displacement curve was found to be strongly dependent on the holding time. The hardness increased from 0.40 GPa for 10 W to 0.58 GPa for 75 W at a load of 700 μN. Elastic modulus of pp–GT thin film fabricated at 10 W was found to be 4.22 GPa, while elastic modulus of 5.96 GPa was found for 75 W film. An adhesion study established that the quality of adhesion is improved for samples fabricated at higher RF power, while the films produced at low RF power adhered poorly to the substrates. These studies demonstrate that the pp–GT polymer is a potential candidate for thin film applications in flexible electronics and OPV that entail smooth and uniform surfaces.

## Acknowledgments

J.A. is grateful to the financial support provided by the JCUPRS scholarship. K.B. acknowledges funding from J.C.U. and A.R.C. (DE130101550).

## Conflicts of Interest

The authors declare no conflict of interest.

## References


1. Jung, K.; Choi, W.-K.; Chae, K.H.; Song, J.-H.; Yoon, S.-J.; Lee, M.-H.; Choi, J.-W. Highly conductive and damp heat stable transparent ZnO based thin films for flexible electronics. *J. Alloys Compd.* **2013**, *554*, 240–245.
2. Dubal, D.P.; Holze, R. All-solid-state flexible thin film supercapacitor based on $Mn_3O_4$ stacked nanosheets with gel electrolyte. *Energy* **2013**, *51*, 407–412.
3. Qian, X.; Wang, T.; Yan, D. Transparent organic thin-film transistors based on high quality polycrystalline rubrene film as active layers. *Org. Electron.* **2013**, *14*, 1052–1056.
4. Ferguson, A.J.; Blackburn, J.L.; Kopidakis, N. Fullerenes and carbon nanotubes as acceptor materials in organic photovoltaics. *Mater. Lett.* **2013**, *90*, 115–125.
5. Kelly, F.M.; Meunier, L.; Cochrane, C.; Koncar, V. Polyaniline: Application as solid state electrochromic in a flexible textile display. *Displays* **2013**, *34*, 1–7.
6. He, H.; Xu, X.-B.; Zhang, D.-F. An aligned macro-porous carbon nanotube/waterborne polyurethane sensor for the detection of flowing organic vapors. *Sens. Actuators B: Chem.* **2013**, *176*, 940–944.
7. Curto, V.F.; Fay, C.; Coyle, S.; Byrne, R.; O'Toole, C.; Barry, C.; Hughes, S.; Moyna, N.; Diamond, D. Real-time sweat pH monitoring based on a wearable chemical barcode micro-fluidic platform incorporating ionic liquids. *Sens. Actuators B: Chem.* **2012**, *171–172*, 1327–1334.
8. Krebs, F.C. Alternative PV: Large scale organic photovoltaics. *Refocus* **2005**, *6*, 38–39.
9. Su, Y.-W.; Lan, S.-C.; Wei, K.-H. Organic photovoltaics—Review article. *Mater. Today* **2012**, *15*, 554–562.
10. Ahmad, J.; Bazaka, K.; Anderson, L.J.; White, R.D.; Jacob, M.V. Materials and methods for encapsulation of OPV: A review. *Renew. Sustain. Energy Rev.* **2013**, *27*, 104–117.
11. Lee, H.-J.; Kim, H.-P.; Kim, H.-M.; Youn, J.-H.; Nam, D.-H.; Lee, Y.-G.; Leeb, J.-G.; Yusoffa, A.R.M.; Jang, J. Solution processed encapsulation for organic photovoltaics. *Sol. Energy Mater. Sol. Cells* **2013**, *111*, 97–101.
12. Kim, N.; Graham, S. Development of highly flexible and ultra-low permeation rate thin-film barrier structure for organic electronics. *Thin Solid Films* **2013**, *547*, 57–62.
13. Cuddihy, E.; Coulbert, C.; Gupta, A.; Liang, R. Electricity from Photovoltaic Solar Cells: Flat-Plate Solar Array Project Final Report. Volume VII: Module Encapsulation; Jet Propulsion Laboratory: 1986. Available online: http://resolver.caltech.edu/JPLpub86-31-volumeVII (accessed on 17 April 2014).
14. Kim, N. Fabrication and Characterization of Thin-Film Encapsulation for Organic Electronics. Ph.D. Thesis, Mechanical Engineering, Georgia Institute of Technology, Atlanta, GA, USA, 2009.
15. Spanggaard, H.; Krebs, F.C. A brief history of the development of organic and polymeric photovoltaics. *Sol. Energy Mater. Sol. Cells* **2004**, *83*, 125–146.
16. Shaheen, S.E.; Ginley, D.S.; Jabbour, G.E. Organic-Based Photovoltaics: Toward Low-Cost Power Generation. *MRS Bull.* **2005**, *30*, 10–19.

17. Forrest, S.R. The path to ubiquitous and low-cost organic electronic appliances on plastic. *Nature* **2004**, *428*, 911–918.
18. Vasilev, K.; Griesser, S.S.; Griesser, H.J. Antibacterial Surfaces and Coatings Produced by Plasma Techniques. *Plasma Process. Polym.* **2011**, *8*, 1010–1023.
19. Ostrikov, K.; Neyts, E.C.; Meyyappan, M. Plasma nanoscience: From nano-solids in plasmas to nano-plasmas in solids. *Adv. Phys.* **2013**, *62*, 113–224.
20. Michelmore, A.; Charles, C.; Boswell, R.W.; Short, R.D.; Whittle, J.D. Defining Plasma Polymerization: New Insight Into What We Should Be Measuring. *ACS Appl. Mater. Interfaces* **2013**, *5*, 5387–5391.
21. Rahman, M.J.; Bhuiyan, A.H. Structural and optical properties of plasma polymerized o-methoxyaniline thin films. *Thin Solid Films* **2013**, *534*, 132–136.
22. Jacob, M.V.; Easton, C.D.; Woods, G.S.; Berndt, C.C. Fabrication of a novel organic polymer thin film. *Thin Solid Films* **2008**, *516*, 3884–3887.
23. Jacob, M.V.; Olsen, N.S.; Anderson, L.; Bazaka, K.; Shanks, R.A. Plasma polymerised thin films for flexible electronic applications. *Thin Solid Films* **2013**, *546*, 167–170.
24. Bazaka, K.; Jacob, M.V. Nanotribological and nanomechanical properties of plasma-polymerized polyterpenol thin films. *J. Mater. Res.* **2011**, *26*, 2952–2961.
25. Bazaka, K.; Jacob, M.V.; Bowden, B.F. Optical and chemical properties of polyterpenol thin films deposited via plasma-enhanced chemical vapor deposition. *J. Mater. Res*. **2011**, *26*, 1018–1025.
26. Xu, Q.F.; Wang, J.N.; Sanderson, K.D. Organic−Inorganic Composite Nanocoatings with Superhydrophobicity, Good Transparency, and Thermal Stability. *ACS Nano* **2010**, *4*, 2201–2209.
27. Berggren, M.; Richter-Dahlfors, A. Organic bioelectronics. *Adv. Mater.* **2007**, *19*, 3201–3213.
28. Li, Y.X.; Yan, L.; Shrestha, R.P.; Yang, D.; Ounaies, Z.; Irene, E.A. A study of the optical and electronic properties of poly (vinylidene fluoride–trifluoroethylene) copolymer thin films. *Thin Solid Films* **2006**, *513*, 283–288.
29. Oliver, W.C.; Pharr, G.M. An improved technique for determining hardness and elastic modulus using load and displacement sensing indentation experiments. *J. Mater. Res*. **1992**, *7*, 1564–1583.
30. Bazaka, K.; Jacob, M.V. Synthesis of radio frequency plasma polymerized non-synthetic Terpinen-4-ol thin films. *Mater. Lett.* **2009**, *63*, 1594–1597.
31. Kim, M.C.; Cho, S.H.; Han, J.G.; Hong, B.Y.; Kim, Y.J.; Yang, S.H.; Boo, J.-H. High-rate deposition of plasma polymerized thin films using PECVD method and characterization of their optical properties. *Surf. Coat. Technol.* **2003**, *169–170*, 595–599.
32. Anderson, L.J.; Jacob, M.V. Effect of RF power on the optical and morphological properties of RF plasma polymerised linalyl acetate thin films. *Appl. Surf. Sci.* **2010**, *256*, 3293–3298.
33. Pilla, P.; Iadicicco, A.; Contessa, L.; Campopiano, S.; Cutolo, A.; Giordano, M.; Guerra, G.; Cusano, A. Optical chemo-sensor based on long period gratings coated with & delta; form syndiotactic polystyrene. *IEEE Photonics Technol. Lett.* **2005**, *17*, 1713–1715.
34. Liu, J.-G.; Ueda, M. High refractive index polymers: Fundamental research and practical applications. *J. Mater. Chem.* **2009**, *19*, 8907–8919.

35. Enlow, J.O.; Jiang, H.; Grant, J.T.; Eyink, K.; Su, W.; Bunning, T.J. Plasma polymerized ferrocene films. *Polymer* **2008**, *49*, 4042–4045.
36. Okubo, T.; Kohmoto, S.; Yamamoto, M. Optical polymer having a high refractive index
37. and high abbe number prepared by radical polymerization using 2,5-BiS(2-Thia-3-Butenyl)-1,4-Dithiane. *J. Macromol. Sci. Part A* **1998**, *35*, 1819–1834.
38. Dislich, H. Plastics as optical materials. *Angew. Chem. Int. Ed. Engl.* **1979**, *18*, 49–59.
39. Gaynor, J.F.; Desu, S.B. Optical properties of polymeric thin films grown by chemical vapor deposition. *J. Mater. Res.* **1996**, *11*, 236–242.
40. You, Z.Z.; Hua, G.J. Refractive index, optical bandgap and oscillator parameters of organic films deposited by vacuum evaporation technique. *Vacuum* **2009**, *83*, 984–988.
41. Fritz, S.E.; Kelley, T.W.; Frisbie, C.D. Effect of dielectric roughness on performance of pentacene TFTs and restoration of performance with a polymeric smoothing layer. *J. Phys. Chem. B* **2005**, *109*, 10574–10577.
42. Hu, X.; Zhao, X.; Uddin, A.; Lee, C.B. Preparation, characterization and electronic and optical properties of plasma-polymerized nitriles. *Thin Solid Films* **2005**, *477*, 81–87.
43. Tien, C.-L.; Lyu, Y.-R.; Jyu, S.-S. Surface flatness of optical thin films evaluated by gray level co-occurrence matrix and entropy. *Appl. Surf. Sci.* **2008**, *254*, 4762–4767.
44. Johnston, E.E.; Ratner, B.D. Surface characterization of plasma deposited organic thin films. *J. Electron Spectrosc. Relat. Phenom.* **1996**, *81*, 303–317.
45. Wenzel, R.N. Resistance of solid surfaces to wetting by water. *Ind. Eng. Chem.* **1936**, *28*, 988–994.
46. Shi, F.F. Recent advances in polymer thin films prepared by plasma polymerization Synthesis, structural characterization, properties and applications. *Surf. Coat. Technol.* **1996**, *82*, 1–15.
47. Bull, S.J. Nanoindentation of coatings. *J. Phys. D* **2005**, *38*, R393.
48. Korsunsky, A.M.; Constantinescu, A. The influence of indenter bluntness on the apparent contact stiffness of thin coatings. *Thin Solid Films* **2009**, *517*, 4835–4844.
49. Zhao, M.; Xiang, Y.; Xu, J.; Ogasawara, N.; Chiba, N.; Chen, X. Determining mechanical properties of thin films from the loading curve of nanoindentation testing. *Thin Solid Films* **2008**, *516*, 7571–7580.
50. Tarefder, R.; Faisal, H. Effects of dwell time and loading rate on the nanoindentation behavior of asphaltic materials. *J. Nanomech. Micromech.* **2013**, *3*, 17–23.

# Chapter 4

# Morphology, Electrical Performance and Potentiometry of PDIF-$CN_2$ Thin-Film Transistors on HMDS-Treated and Bare Silicon Dioxide

**Fabio Chiarella, Mario Barra, Laura Ricciotti, Alberto Aloisio and Antonio Cassinese**

**Abstract:** In this work, the electrical response of n-type organic field-effect transistors, achieved by evaporating PDIF-$CN_2$ films on both bare and Hexamethyldisilazane (HMDS) treated $SiO_2$ substrates, was investigated by standard electrical characterization and potentiometry. Morphological and charge transport characterizations demonstrated that the hydrophobic degree of the substrate surface has a huge impact on the final response of the devices. The PDIF-$CN_2$ transistors on HMDS-treated substrates show a maximum mobility of 0.7 $cm^2$/Volt·s, three orders of magnitude greater than in the case of the device without surface functionalization. The scanning Kelvin probe microscopy technique was used to perform surface potentiometry to image the local surface potential inside the channel during the transistor operation and has allowed us to identify the film morphological disorder as the primary factor that could compromise the effectiveness of the charge injection process from gold contacts to PDIF-$CN_2$ films. For optimized devices on HMDS-treated substrates, SKPM was also used to analyze, over time, the evolution of the potential profile when negative $V_{GS}$ voltages were applied. The findings of these measurements are discussed taking into account the role of $V_{GS}$-induced proton migration towards $SiO_2$ bulk, in the operational stability of the device.

Reprinted from *Electronics*. Cite as: Chiarella, F.; Barra, M.; Ricciotti, L.; Aloisio, A.; Cassinese, A. Morphology, Electrical Performance and Potentiometry of PDIF-$CN_2$ Thin-Film Transistors on HMDS-Treated and Bare Silicon Dioxide. *Electronics* **2014**, *3*, 76-86.

## 1. Introduction

Organic field-effect transistors (OFET) are the key devices for the development of complex analog and digital electronic circuits which, based on low-temperature processed organic semiconductors, can be fabricated through cost-effective techniques [1]. Nowadays, owing to the results of a wide number of accurate experiments, we are fully aware that the quality of the electrical response of an OFET basically relies on the robustness of the charge transport processes taking place across and along the interfaces separating the different device component parts. In particular, severe effects of contact resistance can strongly compromise the device behavior in the presence of a non-optimized charge injection condition. With regard to this last phenomenon, it can be largely dependent on the matching of the Fermi level of the injecting electrode and the LUMO (Low Unoccupied Molecular Orbital) or HOMO (High Occupied Molecular Orbital) level of the organic semiconductor, as well as on the morphological order of the active channel in the proximity of the metal contact [2].

At the same time, a crucial role is also played by the interface between the dielectric barrier and the organic channel, where the charge motion occurs in a very thin region involving few molecular layers [3]. Starting from this consideration, it becomes clear that the chemical and physical nature of the dielectric/organic interface impacts extraordinarily on the final device performances, with the possible occurrence of trapping processes, limiting the carrier mobility and contemporarily giving rise to hysteresis and/or bias-stress effects (namely, the change over time of the drain-source $I_{DS}$ current when the device is driven in the accumulation regime) [4,5].

In the recent past, time and spatial resolved scanning Kelvin probe microscopy (SKPM) allowed us to gain detailed information about the basic mechanisms ruling the charge transport in the OFET [6]. In this context, specific attention was devoted to processes like trapping energy [7], dynamics of trapping and detrapping [8], charge injection at the electrodes [9,10] and charge recombination mechanisms [11]. The near totality of these reports was focused on *p*-type (hole-transporting) organic transistors, while very little experimental data concerning SKPM experiments performed on *n*-type (electron-transporting) OFET are still available today [12]. This occurrence is basically due to the slowness with which organic semiconductors, displaying reliable electron-accumulation effects, have been developed with respect to *p*-type compounds. Indeed, considerable research has been necessary to synthesize conjugated compounds with contemporarily good self-assembling properties and large electron affinity, thus making the formation of radical anions possible, with sufficient insensitivity to oxidative processes by the ambient gases. In particular, within the last 10 years, Perylene diimide molecules functionalized with cyano groups in the bay regions (PDI_CY) have emerged as a new class of *n*-type organic semiconductors, with highly stable electrical performances under ambient conditions and effective charge injection from gold electrodes [13,14]. All these features are basically triggered by the low-lying LUMO levels (down to −4.5 eV) of these compounds, which come from the presence of strong electron-withdrawing moieties in their molecular structure.

Among the PDI_CY molecules, *N*,*N*0-1*H*,1*H*-perfluorobutyl-cyanoperylenediimide (PDIF-$CN_2$) is the compound displaying the highest electron mobility (μ) both in form of thin film [15,16] and single crystal [17,18]. In particular, PDIF-$CN_2$ single-crystal devices have demonstrated μ values up to 6 $cm^2$/Volt·s, band-like transport features (namely, μ increases in a range of temperatures below room temperature) [19] and negligible bias stress effects [20]. On the other hand, very recently, PDIF-$CN_2$ thin-film transistors have also been shown to be able to operate steadily in aqueous environments, opening a new perspective for the use of this compound in the development of bio-sensing devices [21].

In this paper, we analyze the morphological and electrical properties of PDIF-$CN_2$ films deposited by Joule evaporation from Knudsen cells on $SiO_2$ substrates with different surface properties. Our results clearly highlight that the self-assembling properties of PDIF-$CN_2$ molecules and the related electrical performances are strongly improved when hydrophobic surfaces are used for the film growth. SKPM was then applied to investigate basic aspects concerning the charge injection process in the PDIF-$CN_2$ films and the poor operational stability of these devices when operated for a prolonged time in the depletion regime.

## 2. Experimental Section

PDIF-$CN_2$ (Polyera ActivInk N1100) powder was purchased from POLYERA CORPORATION and used without any further purification. Bottom-contact bottom-gate transistors were fabricated by Joule evaporating PDIF-$CN_2$ films on multilayered substrates (Figure 1c) composed of a 500 μm thick layer of highly doped Silicon ($Si^{++}$) acting both as gate and substrate, a 200 nm thin $SiO_2$ dielectric barrier and, finally, interdigitated source/drain gold electrodes (about 130 nm high) (W/L ratio was fixed to 550 where W is the channel width while L is the channel length). These substrates had been recently used to successfully investigate the electrical response of both *p*- and *n*-type molecules [22,23]. Bare substrates were inserted into the evaporation chamber after a basic cleaning by ultrasonic baths in acetone and ethanol. Hexamethyldisilazane (HMDS) treated substrates were obtained with a process lasting 7 days and described in detail in [21]. Water-contact angle ($\theta_C$) was about 60° for the bare substrates, while $\theta_C$ was about 110° after the HMDS treatment, index of the formation of a more hydrophobic surface. During the evaporation, both bare and HMDS-treated substrates were kept at about $T_{sub}$ = 90 °C by warming the entire deposition chamber. The deposition rate was 0.5 nm/min and thickness was fixed to about 30 nm for all films analyzed in this work.

**Figure 1.** Atomic force microscopy (AFM) images (size 5 × 5 $\mu m^2$) of PDIF-$CN_2$ films grown on (**a**) Hexamethyldisilazane (HMDS)-treated and (**b**) bare $SiO_2$ substrates. In the bottom panel (**c**), we report a transversal sketch of the device.

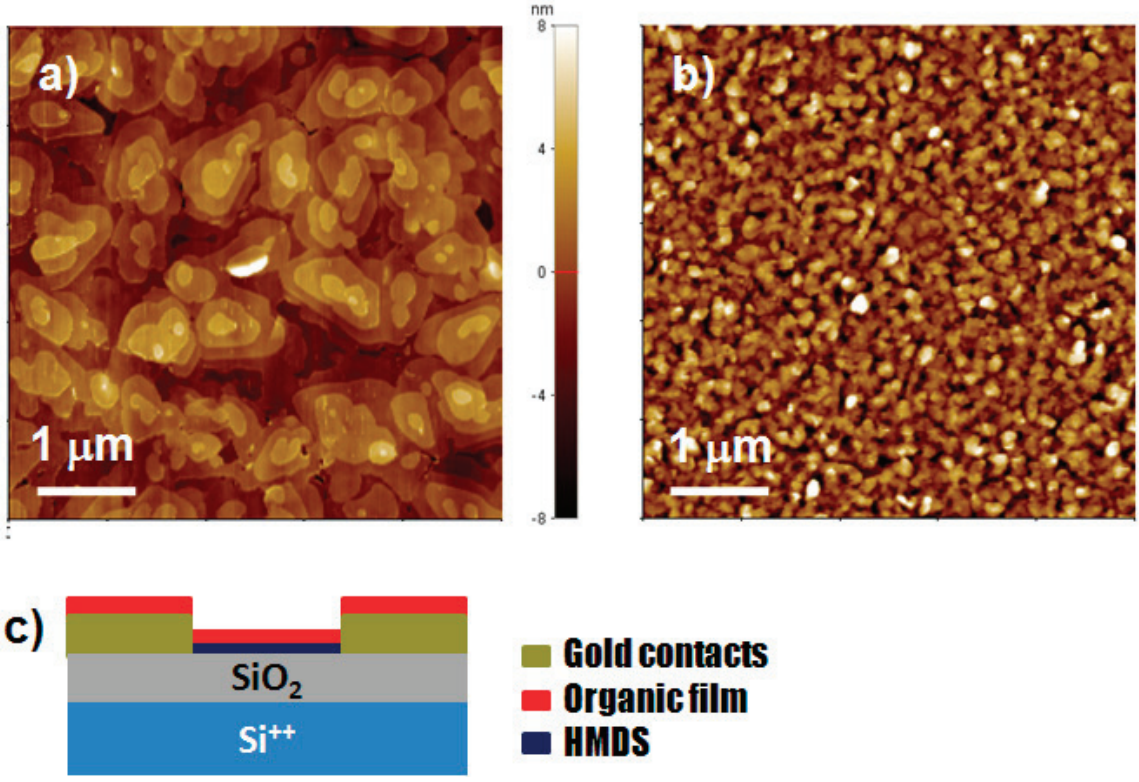


The morphological properties of the film surface were investigated by a XE100 Park AFM operating in air with amplitude regulation and oscillating near the cantilever resonance frequency. Images were acquired using silicon-doped cantilevers (resonance frequency around 300 KHz)

provided by Nanosensor™. The same microscope was used to carry out the SKPM experiments in air and at room temperature, employing conducting cantilevers (NSC14 Cr/Au, MikroMasch™, resonance frequency around 170 KHz). These measurements were performed in a true non contact mode and dual frequency mode, acquiring contemporarily topography and surface potential profiles. We used an AC sinusoidal signal applied to the conductive tip at a frequency of 17 KHz as an electrostatic probe. First harmonic amplitude of the electrostatic force generated by the potential difference between tip and sample, was considered to perform local surface potential measurement [6].

The basic transistor characteristic curves were measured in vacuum ($10^{-4}$ mbar) and darkness using a Janis probe station, connected to a Keithley 2612A Dual-Channel system source-meter instrument. Mobility values were extracted by using the standard MOSFET equations [24].

## 3. Results and Discussion

AFM images in Figure 1 report the surface morphology of PDIF-$CN_2$ films evaporated on bare and HMDS-treated substrates, setting the substrate temperature ($T_{sub}$) at 90 °C. As shown, the film microstructure is strongly affected by the $SiO_2$ functionalization. In particular, on the bare substrates (Figure 1b), the films show a poor morphological order, being composed of small and rounded grains with a lateral size lower than 100 nm. On the other hand, on HMDS substrates (Figure 1a), the long-range order appears to be considerably improved and the films are characterized by the presence of larger circular islands, with diameters approaching 1 μm in the best cases. Moreover, the film surface displays a well-defined terraced structure with molecular steps close to 2 nm, in agreement with previous reports [25], which may indicate an alignment of the long axis of the molecules close to the direction perpendicular to the substrate.

The electrical responses measured for the PDIF-$CN_2$ transistors demonstrate a clear correlation between the film morphological properties and the related charge transport performance. First of all, the output curves reported in Figure 2a for a PDIF-$CN_2$ transistor fabricated on bare $SiO_2$ substrate, evidence the occurrence of peculiar and not ideal electrical features. Indeed, although the current behavior in the low $V_{DS}$ (<10 V) region seems apparently linear, all the $I_{DS}$ current curves overlap for $V_{GS}$ higher than 10 V and no further current modulation is observable.

The transfer-curves reported in Figure 2b,c in the linear and saturation regimes, respectively, confirm the poor electrical performances of this class of devices. In particular, besides the presence of a large hysteresis, the transfer-curve in the linear regime again makes clear that, under the application of small $V_{DS}$ voltages and for $V_{GS}$ exceeding 10 V, the device is not able to work properly, since the $I_{DS}$ current reaches a constant value that $V_{GS}$ is no longer able to modulate.

The inability to further control the channel conductance could be ascribed to the detrimental action of very large contact resistances ($R_C$) at the source and drain electrodes, which, because of their weak dependence on $V_{GS}$, are able to completely dominate the device electrical response in the full accumulation region [26–28].

**Figure 2.** (**a**) Output curves and transfer-curves in (**b**) linear ($V_{DS}$ = 5 V) and (**c**) saturation regions ($V_{DS}$ = 50 V) for a PDIF-$CN_2$ transistor deposited on bare $SiO_2$ substrate. (**d**) Output curves and transfer-curves in (**e**) linear ($V_{DS}$ = 5 V) and (**f**) saturation ($V_{DS}$ = 50 V) regions for a PDIF-$CN_2$ transistor deposited on HMDS-treated $SiO_2$ substrate. In the insets, we show data in a semi-log plot where the current scale is Ampere and the voltage scale is Volt.

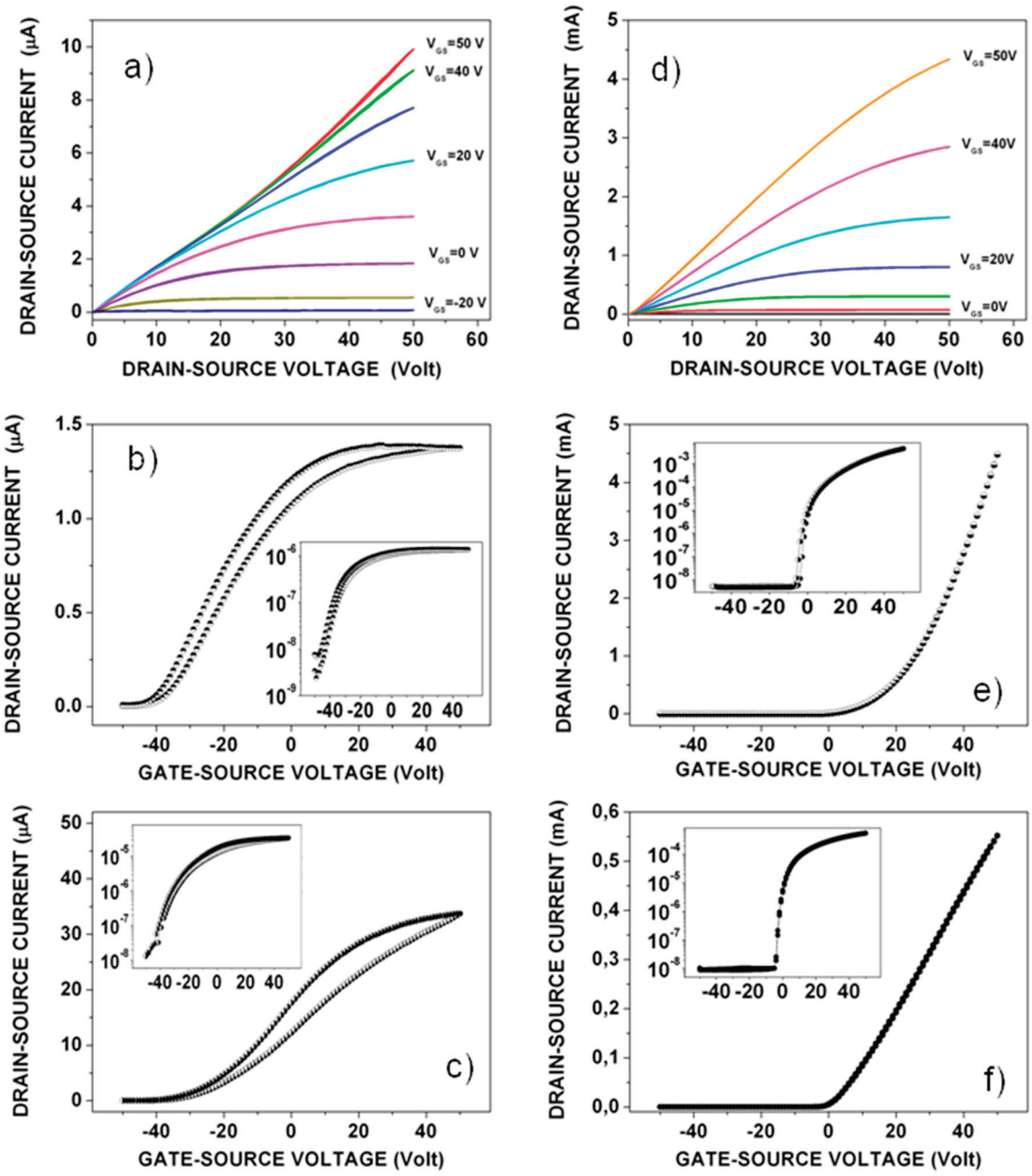


To find an experimental confirmation regarding the $R_C$ role in the electrical behavior of these PDIF-$CN_2$ transistors, we carried out SKPM measurements acquiring the potential profile along a line across the channel of the device in operation with $V_{GS}$ grounded and $V_{DS}$ < 10 V (in the specific, 4.5 Volt for not treated device and 7 Volt for the HMDS-treated one). In these driving conditions, the device works in the linear regime (see the output curve at $V_{GS}$ = 0 V in Figure 2a). Figure 3 depicts the measured potential profile in the transistor channel. As shown, while the

potential follows the predicted linear behavior in the central part of the channel, a large drop ($\Delta V_S$ ~ 1.4 V) appears in the film region (about 2 μm long) close the source electrode. In contrast, only a very small drop of about $\Delta V_D$ ~ 0.1 V can be detected near the drain electrode. This experimental finding reveals that the contact resistance effect is related exclusively to the charge injection process taking place at the source contact and, hence, the $R_C$ value can be simply evaluated by dividing ($\Delta V_S$) for the current flowing in the channel ($I_{DS}$ = 0.44 μA), achieving about 3 MΩ. This value seems to confirm the idea that the device resistance (usually in the range between 3 and 5 MΩ) measured in the $V_{GS}$-independent current region ($V_{GS}$ > 10 V in the transfer-curves), as reported in Figure 2, is completely determined by the contact resistance contribution.

**Figure 3.** Surface potential profile measured by scanning Kelvin probe microscopy (SKPM) across the channel. The colored areas indicate drain (blue light) and source (red light) contacts.

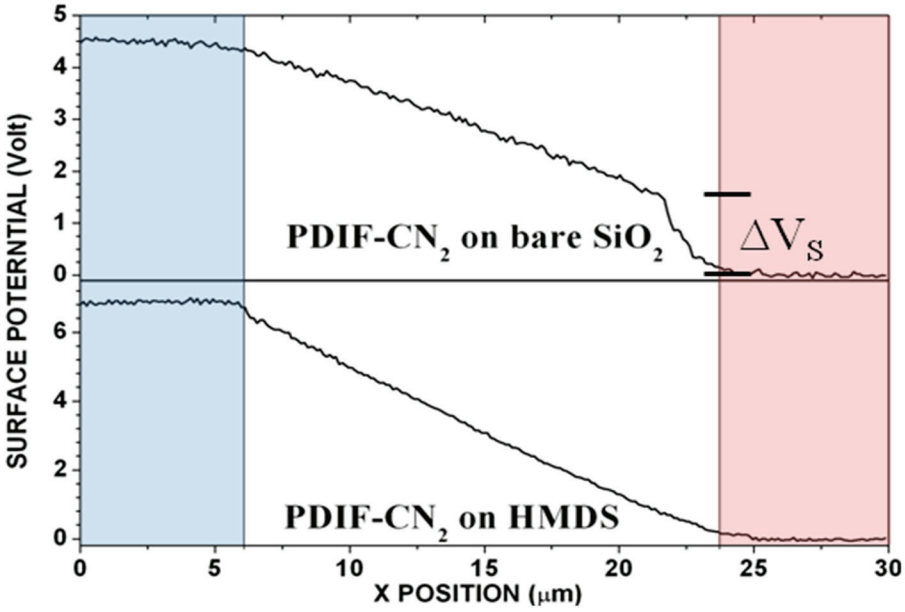


In the saturation regime, the role of contact resistance is still clearly visible and the related transfer-curve shows that the $I_{DS}$ slope strongly reduces at increasing $V_{GS}$. Here, the maximum trans-conductance ($g_m = \partial I_{DS}/\partial V_{GS}$) does not exceed 0.8 μS, while a rough estimation of the charge carrier mobility using the MOSFET equations gives a value of 0.002 $cm^2$/Volt·s. Significantly (see the semi-log plots in the inset of Figure 2b,c), the $I_{DS}$ starts flowing in the channel for highly negative $V_{GS}$, usually comprised between −30 V and −40 V. These $V_{GS}$ values are usually defined as the onset voltages ($V_{on}$) of the transistor and, for PDIF-$CN_2$ films on bare $SiO_2$ substrates, they are even more negative than the corresponding values measured for the parent compound PDI8-$CN_2$ on the same type of $SiO_2$ surface [29]. This occurrence supports the hypothesis that the negative $V_{on}$ in the PDI_CY-based transistors is related to unintentional charge doping effects given by the interaction between the perylene molecules and water molecules absorbed on the substrate surface [29,30]. On the basis of this concept, the larger the electron affinity of the *n*-type compounds the more negative will be the $V_{on}$ values.

Due to the improved morphological order, PDIF-$CN_2$ transistors fabricated on HMDS-treated substrates exhibit noticeably improved electrical performances (Figure 2d–f), and no potential drop related to the $R_C$ effects is appreciable in the SKPM profile reported in Figure 3. In general, the electrical behavior of these devices follows the predictions of the ideal MOSFET model very closely, with the absence of significant hysteresis phenomena.

Mobility values extracted from the curves in the saturation regime are distributed on a homogeneous set of 23 samples, around a mean value of (0.37 ± 0.19) $cm^2$/Volt·s. For one device, we measured a mobility of 0.71 $cm^2$/Volt·s which exceeds the highest value ever reported for an evaporated PDIF-$CN_2$ thin-film transistor [13]. In several cases, the maximum $I_{DS}$ current measured in the saturation regime was higher than 4 mA, while the trans-conductance ($g_m$) came close to the value of 0.2 mS in the best case. It is significant to outline that, according to the experimental data so far reported in literature, mobility values higher than 0.3 $cm^2$/Volt·s have been measured only for films evaporated with $T_{sub}$ ~ 130 °C [14]. Since this temperature is considerably higher than that ($T_{sub}$ = 90 °C) used in this work, we consider that the mobility enhancement obtained in our growth conditions is basically due to the quality of the adopted HMDS treatment, making the $SiO_2$ surface highly hydrophobic with a water contact angle $\theta_c$ close to 110°. The impact of the HMDS surface coverage level on the response of the final transistor was already stressed in [14]. Considering the effect of the $SiO_2$ functionalization on the electrical behavior of the analyzed PDIF-$CN_2$ transistors, it can be also concluded that the contact resistance effect observed for the devices fabricated on bare substrates must be mainly related to the poor structural order of the related films. However, a degradation effect of the injection process, associated to the water electrolysis phenomenon occurring on the metallic surface of the gold source electrode and the consequent protonization of the silanol groups on silicon surface closed to the source electrode, cannot be excluded [4].

Besides the strong influence on mobility and $R_C$ effects, HMDS-treatment also provided a $V_{on}$ shift toward the ideal 0 V, similar to what had recently been observed for PDI8-$CN_2$ devices [29]. This evidence is in agreement with the aforementioned discussion about the role of water molecules absorbed on the $SiO_2$ surface in the $V_{on}$ determination. For most of the pristine PDIF-$CN_2$ devices on HMDS, $V_{on}$ was found to range between −10 and −5 V. However, we also observed that these values can be largely modified during the device operation and, in particular, when the transfer-curves are recorded continuously in air for long periods. More specifically, it was found that a prolonged application of negative $V_{GS}$ voltages is able to induce a considerable shift of the $V_{on}$ values towards more negative values. This phenomenon had already been reported for PDI8-$CN_2$ inkjet-printed OFET and is probably common to n-type devices based on organic semiconductors which have a large electron affinity [30].

While the effect of a continuous application of $V_{GS}$ (positive for n-type OFET) driving the devices into the accumulation regime (*i.e.*, the so-called bias stress effect) can be analyzed in a direct manner through the observation of the $I_{DS}(t)$ behavior, it becomes much more difficult to investigate the time evolution of the device response in the depletion regime, where the $I_{DS}$ current is very low. To approach this interesting task, we have performed SKPM with $V_{GS}$ = −20 V and $V_{DS}$ = 7.5 V along a line across the channel for a time of 10 min. We observe (Figure 4) the presence of a vale in the potential profile inhibiting electron injection for this n-type device.

As shown, this potential well gradually tends to disappear over the time scale of ten minutes, causing the device to move from the depletion regime to that of accumulation and the consequent $V_{on}$ shift. We observe that this time is much shorter than the typical time of recovery as already observed for PDI8-$CN_2$ [29]. This phenomenon agrees very well with the predictions of the so-called proton migration model, which was introduced originally for *p*-type devices [5] based on $SiO_2$ gate dielectric and then applied, in a modified version, also to *n*-type transistors [29]. According to this model, under the application of a negative gate voltage, $H^+$ protons, which are present on the $SiO_2$ surface because of acidification produced by water, can rapidly migrate toward the $SiO_2$ bulk. In this way, as observed in our SKPM measurements, the potential well is gradually screened by the increase of the positive charges localized inside the dielectric.

**Figure 4.** (**top panel**) Time evolution of the potential along a line across the channel, the upper bar is the chromatic scale for the potential values; (**middle panel**) graph of potential of two specific lines at the beginning (red lines) and the end (green lines) of the experiment, the arrow indicates increasing time; (**bottom panel**) topographic profile of the channel acquired contemporarily with potentiometric measure. Vertical dashed lines are guides for eyes to indicate where the gold contacts finish.

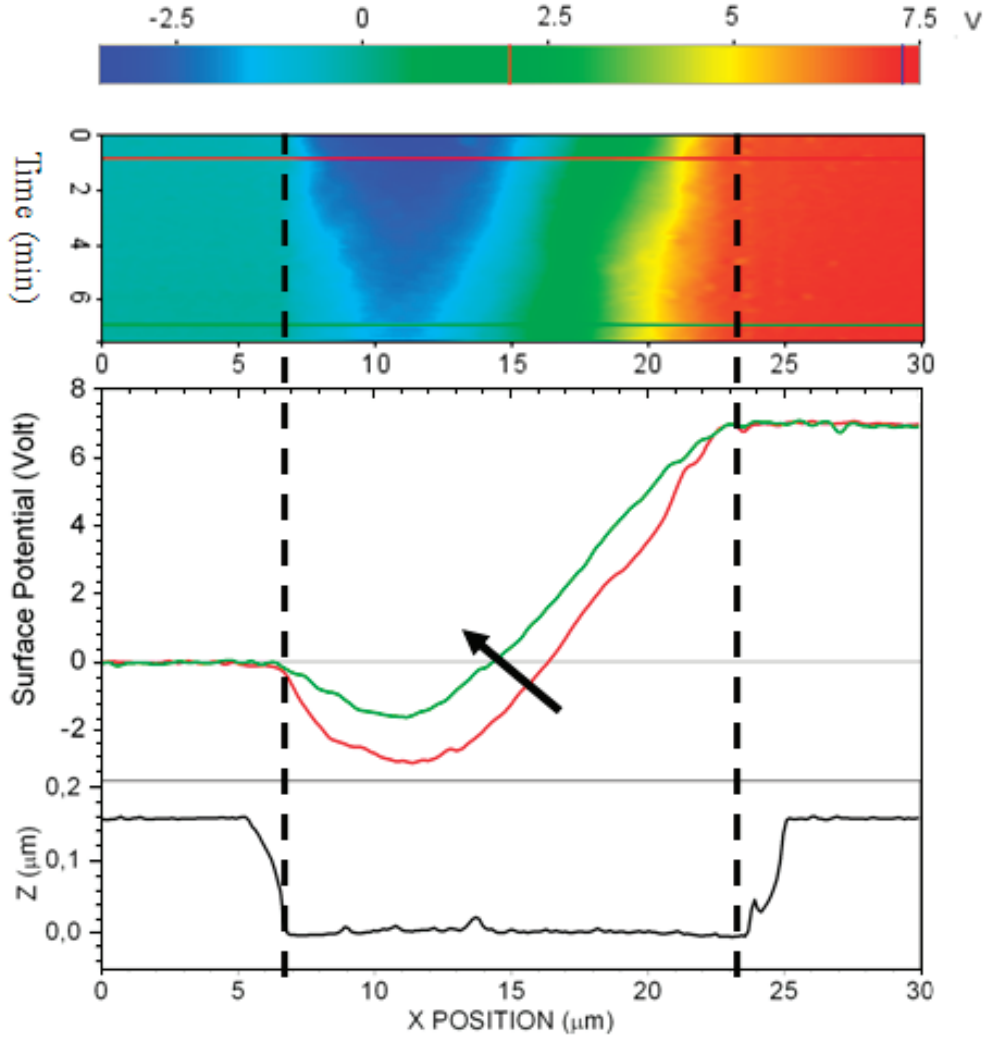

## 4. Conclusions

In conclusion, the experimental work here reported demonstrates that the growth of PDIF-$CN_2$ molecules is extremely sensitive on the hydrophobicity degree of the substrate surface. Indeed, while PDIF-$CN_2$ films on HMDS-treated substrates are characterized by a poly-crystalline structure with a long-range morphological order, very small rounded grains with random spatial orientation characterize the microstructure of PDIF-$CN_2$ films deposited on bare $SiO_2$ substrates. Consequently, the electrical response of these latter devices results to be very poor with μ not exceeding $10^{-3}$ $cm^2$/Volt·s and huge contact resistance effects. On the contrary, charge carrier mobility extracted for PDIF-$CN_2$ transistors grown on HMDS-treated $SiO_2$ surfaces has a mean value of about (0.37 ± 0.19) $cm^2$/Volt·s. The highest mobility value measured in this work for a PDIF-$CN_2$ transistor was higher than 0.7 $cm^2$/Volt·s, which is among the best results ever reported in literature for n-type thin-film transistors. HMDS treatment was found also to shift toward positive values the $V_{on}$ voltages by more than 20 V, approaching in some cases the ideal $V_{on}$ = 0 V condition. In any case, the time stability of the $V_{on}$ values during the device operation remains an open issue also for the transistors fabricated on hydrophobic $SiO_2$ surfaces. In particular, SKPM measurements reveal that the prolonged (of the order of minutes) application of negative $V_{GS}$ is able to change dramatically the channel conducting properties moving rapidly the device from depletion working regime to saturation regime. Further investigation will be needed to further clarify the mechanisms ruling this operational instability in high-mobility PDIF-$CN_2$ transistors.

## Acknowledgments

The authors would like to acknowledge the work of Mary Longrigg in the English editing and of A. Carella (Department of Chemistry, University of Naples) in functionalizing the $SiO_2$ substrates by HMDS treatment. Financial support from EU FP7 project MAMA Grant Agreement No. 264098 is gratefully acknowledged.

## Conflicts of Interest

The authors declare no conflict of interest.

## References

1. Bao, Z.; Locklin, J. *Organic Field-Effect Transistors*; Taylor & Francis: Boca Raton, FL, USA, 2007.
2. Burgi, L.; Richards, T.J.; Friend, R.H.; Sirringhaus, H. Close look at charge carrier injection in polymer field-effect transistors. *J. Appl. Phys.* **2003**, *94*, 6129–6137.
3. Shehu, A.; Quiroga, S.D.; D'Angelo, P.; Albonetti, C.; Borgatti, F.; Scorzoni, A.; Stoliar, P.; Biscarini, F. Layered distribution of charge carriers in organic thin film transitors. *Phys. Rev. Lett.* **2010**, *104*, 246602.
4. Sirringhaus, H. Reliability of organic field-effect transistors. *Adv. Mater*. **2009**, *21*, 3859–3873.
5. Bobbert, P.A.; Sharma, A.; Mathijssen, S.G.J.; Kemerink, M.; de Leuuw, D.M. Operational stability of orgaic field-effect transistors. *Adv. Mater*. **2012**, *24*, 1146–1158.

6. Palermo, V.; Palma, M.; Samori, P. Electronic characterization of organic thin films by Kelvin probe force microscopy. *Adv. Mater.* **2005**, *18*, 145–164.
7. Hallam, T.; Lee, M.J.; Zhao, N.; Nandhakumar, I.; Kemerink, M.; Heeney, M.; McCulloch, I.; Sirringhaus, H. Local charge trapping in conjugated polymers resolved by scanning Kelvin probe microscopy. *Phys. Rev. Lett.* **2009**, *103*, 256803.
8. Mathijssen, S.G.J.; Kemerink, M.; Sharma, A.; Colle, M.; Bobbert, P.; Janssen, R.A.J.; de Leeuw, D.M. Charge trapping at the dielectric of organic transistors visualized in real time and space. *Adv. Mater.* **2008**, *20*, 975–979.
9. Ng, T.N.; Silveira, W.R.; Marohn, J.A. Dependence of charge injection on temperature, electric field, and energetic disorder in an organic semiconductor. *Phys. Rev. Lett*. **2007**, *98*, 066101.
10. Afsharimani, N.; Nysten, B. Electronic properties of dioctylterthiophene-based organic thin-film transistors: A Kelvin probe force microscopy study. *Thin Solid Films* **2013**, *536*, 295–301.
11. Matyba, P.; Maturova, K.; Kemerink, M.; Robinson, N.D.; Edman, L. The dynamic organic p–n junction. *Nat. Mater.* **2009**, *8*, 672.
12. Lüttich, F.; Lehmann, D.; Graaf, H.; Zahn, D.R.T.; von Borczyskowski, C. Kelvin-probe studies of *n*-conductive organic field-effect transistors during operation. *Phys. Status Solidi C* **2010**, *7*, 452–455.
13. Jones, B.A.; Facchetti, A.; Wasielewski, M.R.; Marks, T.J. Tuning orbital energetics in Arylene Diimide semiconductors: Materials design for ambient stability of *n*-Type charge transport. *J. Am. Chem. Soc.* **2007**, *129*, 15259.
14. Jones, B.A.; Facchetti, A.; Wasielewski, M.R.; Marks, T.J. Effects of Arylene Diimide thin film growth conditions on n-channel OFET performance. *Adv. Funct. Mater.* **2008**, *18*, 1329–1339.
15. Jones, B.A.; Ahrens, M.J.; Yoon, M.H.; Marks, A.F.T.J.; Wasielewski, M.R. High-mobility air-stable *n*-Type semiconductors with processing versatility: Dicyanoperylene-3,4:9, 10-bis(dicarboximides). *Angw. Chem. Int. Ed.* **2004**, *43*, 6363–6366.
16. Soeda, J.; Uemura, T.; Mizuno, Y.; Nakao, A.; Nakazawa, Y.; Facchetti, A.; Takeya, J. High electron mobility in air for *N*,*N*'-1*H*,1*H*-perfluorobutyldicyanoperylene carboxydi-imide solution-crystallized thin-film transistors on hydrophobic surfaces. *Adv. Mater.* **2011**, *23*, 3681–3685.
17. Molinari, A.S.; Alves, H.; Chen, Z.; Facchetti, A.; Morpurgo, A.F. High electron mobility in vacuum and ambient for PDIF-$CN_2$ single-crystal transistors. *J. Am. Chem. Soc.* **2009**, *131*, 2462–2463.
18. Willa, K.; Hausermann, R.; Mathis, T.; Facchetti, A.; Chen, Z.; Batlogg, B. Form organic single crystals to solution processed thin-films: Charge transport and trapping with varying degree of order. *J. Appl. Phys.* **2013**, *113*, 133707.
19. Minder, N.A.; Ono, S.; Chen, Z.; Facchetti, A.; Morpurgo, A.F. Band-like electron transport in organic transistors and implication of the molecular structure for performance optimization. *Adv. Mater.* **2012**, *24*, 503–508.

20. Barra, M.; di Girolamo, F.V.; Minder, N.A.; Lezama, I.G.; Chen, Z.; Facchetti, A.; Morpurgo, A.F.; Cassinese, A. Very low bias stress in *n*-type organic single-crystal transistors. *Appl. Phys. Lett.* **2012**, *100*, 133301.
21. Barra, M.; Viggiano, D.; Ambrosino, P.; Bloisi, F.; Girolamo, F.V.D.; Soldovieri, M.V.; Taglialatela, M.; Cassinese, A. Addressing the use of PDIF-$CN_2$ molecules in the development of *n*-type organic field-effect transistors for biosensing applications. *Biochim. Biophys. Acta* **2013**, *1830*, 4365–4373.
22. Riccio, M.; Irace, A.; Breglio, G.; Rossi, L.; Barra, M.; di Girolamo, F.V.; Cassinese, A. Current distribution effects in organic sexithiophene field effect transistors investigated by lock-in thermography: Mobility evaluation issues. *Appl. Phys. Lett.* **2008**, *93*, 243504–245407.
23. Barra, M.; di Girolamo, F.V.; Chiarella, F.; Salluzzo, M.; Chen, Z.; Facchetti, A.; Anderson, L.; Cassinese, A. Transport property and charge trap comparison for *N*-channel perylene diimide transistors with different air-stability. *J. Phys. Chem. C* **2010**, *114*, 20387.
24. Sze, S. *Physics of Semiconductor Devices*; Wiley: New York, NY, USA, 1981.
25. Weitz, R.T.; Amsharov, K.; Zschieschang, U.; Villas, E.B.; Goswami, D.K.; Burghard, M.; Dosch, H.; Jansen, M.; Kern, K.; Klauk, K. Organic n-channel transistors based on core-cyanated perylene carboxylic diimide derivatives. *J. Am. Chem. Soc.* **2008**, *130*, 4637–4645.
26. Necliudov, P.V.; Shur, M.S.; Gundlach, D.J.; Jackson, T.N. Modeling of organic thin film transistors of different designs. *J. Appl. Phys.* **2000**, *88*, 6594–6597.
27. Necliudov, P.V.; Shur, M.S.; Gundlach, D.J.; Jackson, T.N. Contact resistance extraction in pentacene thin film transistors. *Solid State Electron.* **2003**, *47*, 259–262.
28. Dimitrakopoulos, C.D.; Malenfant, P.R.L. Organic thin film transistors for large area electronics. *Adv. Mater.* **2002**, *14*, 99–117.
29. Di Girolamo, F.V.; Ciccullo, F.; Barra, M.; Carella, A.; Cassinese, A. Investigation on bias stress effects in *n*-type PDI8-$CN_2$ thin-film transistors. *Org. Electron.* **2012**, *13*, 2281–2289.
30. Grimaldi, I.A.; Barra, M.; Carella, A.; di Girolamo, F.V.; Loffredo, F.; Minarini, C.; Villani, F.; Cassinese, A. Bias stress effects investigated in charge depletion and accumulation regimes for inkjet-printed perylene diimide organic transistors. *Synthetic Met.* **2013**, *176*, 121–127.

# Chapter 5

# The Effects of Different Electron-Phonon Couplings on the Spectral and Transport Properties of Small Molecule Single-Crystal Organic Semiconductors

**Carmine Antonio Perroni, Fernando Gargiulo, Alberto Nocera ,
Vincenzo Marigliano Ramaglia and Vittorio Cataudella**

**Abstract:** Spectral and transport properties of small molecule single-crystal organic semiconductors have been theoretically analyzed focusing on oligoacenes, in particular on the series from naphthalene to rubrene and pentacene, aiming to show that the inclusion of different electron-phonon couplings is of paramount importance to interpret accurately the properties of prototype organic semiconductors. While in the case of rubrene, the coupling between charge carriers and low frequency inter-molecular modes is sufficient for a satisfactory description of spectral and transport properties, the inclusion of electron coupling to both low-frequency inter-molecular and high-frequency intra-molecular vibrational modes is needed to account for the temperature dependence of transport properties in smaller oligoacenes. For rubrene, a very accurate analysis in the relevant experimental configuration has allowed for the clarification of the origin of the temperature-dependent mobility observed in these organic semiconductors. With increasing temperature, the chemical potential moves into the tail of the density of states corresponding to localized states, but this is not enough to drive the system into an insulating state. The mobility along different crystallographic directions has been calculated, including vertex corrections that give rise to a transport lifetime one order of magnitude smaller than the spectral lifetime of the states involved in the transport mechanism. The mobility always exhibits a power-law behavior as a function of temperature, in agreement with experiments in rubrene. In systems gated with polarizable dielectrics, the electron coupling to interface vibrational modes of the gate has to be included in addition to the intrinsic electron-phonon interaction. While the intrinsic bulk electron-phonon interaction affects the behavior of mobility in the coherent regime below room temperature, the coupling with interface modes is dominant for the activated high temperature contribution of localized polarons. Finally, the effects of a weak disorder largely increase the activation energies of mobility and induce the small polaron formation at lower values of electron-phonon couplings in the experimentally relevant temperature window.

Reprinted from *Electronics*. Cite as: Perroni, C.A.; Gargiulo, F.; Nocera, A.; Ramaglia, V. M.; Cataudella, V. The Effects of Different Electron-Phonon Couplings on the Spectral and Transport Properties of Small Molecule Single-Crystal Organic Semiconductors. *Electronics* **2014**, *3*, 165–189.

## 1. Introduction

In recent years, the interest in plastic electronics has grown considerably. The realization of devices, such as organic field-effect transistors (OFETs), represents a key step in this field. Single-crystal OFETs made of ultra-pure small molecule semiconductors are characterized by mobilities up to one order of magnitude larger then those typical of thin film transistors [1]. The most promising are those based on oligoacenes, such as pentacene and rubrene, which exhibit a strong anisotropy and the largest mobility measured in organic semiconductors [2].

In spite of many applications based on such devices, the intrinsic transport mechanism acting in high mobility organic semiconductors is not fully understood. Transport measurements from $100$ K to room temperature in single crystal semiconductors, such as rubrene, show a behavior of the charge carrier mobility $\mu$ that can be defined as band-like ($\mu \propto T^{-\gamma}$, with the exponent, $\gamma$, close to two), similar to that observed in crystalline inorganic semiconductors [2]. However, the order of magnitude of mobility is much smaller than that of pure inorganic semiconductors, and the mean free path for the carriers has been theoretically estimated to be comparable with the molecular separation at room temperature [3]. Therefore, the Ioffe–Regel limit is reached with increasing temperature. Moreover, in some systems, starting from room temperature, a crossover from band-like to activated hopping behavior can take place [4–6]. The crossover has been interpreted as being due to the formation of the polaron, that is the quasi-particle formed by the electron (or hole) and the surrounding phonon cloud [7]. For example, in naphthalene and anthracene, while the mobility along the $a$- and $b$-axis shows only a slight change with the temperature, that along the $c$-axis is characterized by a temperature activated behavior at higher temperature with an energy barrier of the order of $15$ meV [8–10]. The experimental data in these compounds suggest that the coherent band transport is gradually destroyed and the transport due to polaron hopping evolves as a parallel channel dominating at sufficiently high temperature (which can be larger than room temperature) [8–10].

In systems with polarizable gates, the scaling laws of the mobility as a function of the dielectric constant of solid [11,12] and liquid [13] gates have been discovered, pointing out that the nearby dielectric has a strong influence. Actually, if the difference between the dielectric constant of the organic semiconductor and of the gate is small, at temperatures close or higher than $100$ K, the mobility, $\mu$, of these systems exhibits the power-law band-like behavior. On the other hand, if the dielectric constant mismatch is high, an activated insulating behavior is found with much smaller values of mobility at room temperature [12]. A possible explanation of this behavior is that the injected charge carriers undergo a polaronic localization, due to the interaction with modes at the interface with the polarizable dielectric gate [12,14].

Extended *vs*. localized features of charge carriers appear also in spectroscopic observations. Angle-resolved photoemission spectroscopy (ARPES) supports the extended character of states [15–17], showing that the quasi-particle energy dispersion does exhibit a weak mass renormalization, even if the width of the peaks of the spectral function increases significantly with temperature. For pentacene, the bandwidth is reduced only by about $15\%$, going from $75$ K to $300$

K, indicating moderate values of electron-phonon coupling. On the other hand, some spectroscopic probes, such as electron spin resonance (ESR) [18,19], THz [20], and modulated spectroscopy [21] are in favor of states localized within a few molecules. Actually, in rubrene and in pentacene, to ascribe the presence of localized features to small polarons is not likely, since the electron-phonon coupling is not large enough to justify the polaron formation [4]. Therefore, one of the main theoretical problems is to conciliate band-like with localized features of charge carriers [22].

First-principle calculations have pointed out that charge carriers are affected by the coupling to inter-molecular modes with low frequency in comparison with typical electron hopping [4,23]. A model that is to some extent close to the Su–Schrieffer–Heeger (SSH) [24] Hamiltonian has been recently introduced to take into account this interaction [22]. It is a minimal one-dimensional (1D) system, valid for the most conductive crystal axis of high mobility systems, where the effect of the electron-phonon coupling is reduced to a modulation of the transfer integral [25]. A dynamic approach where vibrational modes are treated as classical variables has been used in 1D and in a recent generalization to two dimensions (2D) [26]. Within this method, the temperature dependence of the computed mobility is in agreement with experimental results. However, the role of the dimensionality of the system is not clear: in fact, in the 1D case, one has $\mu \propto T^{-2}$, while, in the 2D case, the decrease of the mobility with temperature is intermediate between $\mu \propto T^{-2}$ and $\mu \propto T^{-1}$. In any case, the computed mobility is larger than that measured (at least by a factor of two). Moreover, the dynamics of only one charge particle is studied, neglecting completely the role of the chemical potential. Finally, the effects on charge carrier dynamics due to the coupling with vibrational modes are included in an approximate way [27], and the corresponding coupled dynamics do not recover the right thermal equilibrium on long times.

Recently, the transport properties of the 1D SSH model have been analyzed within a different adiabatic approach [28], mapping the problem onto that of a single quantum particle in a random potential (the generalized Anderson problem [29]). Very recently, some of us have made a systematic study of this 1D model, including the vertex corrections into the calculation of the mobility [30]. While finite frequency quantities are properly calculated in this 1D model, the inclusion of vertex corrections leads to a vanishing mobility, unless an *ad-hoc* broadening of the energy eigenvalues is assumed.

It is clear that 1D adiabatic models suffer from severe limitations, of which the main one is that electronic states are always localized [29]. Moreover, features, such as band anisotropy and small but, finite carrier density, are necessary for a correct description of the systems. Therefore, in this review, we first analyze a generic three-dimensional (3D) model, such as the anisotropic Holstein model [31], in order to discuss the relevant issue of the band anisotropy at finite carrier density. This model is studied within the adiabatic approach focusing on the weak to intermediate el-ph coupling regime, which is relevant for high-mobility organic semiconductors [32]. Next, we analyze a realistic model for rubrene, which represents an extension of the 1D SSH model to the quasi 2D case, since this is the relevant geometry for OFETs [33].

Spectral and transport properties calculated within these two models are discussed in this review. The spectral functions show peaks, which are weakly renormalized in comparison with those of the

bare bands. However, with increasing temperature, the width of the spectral functions gets larger and larger, making the quasi-particles less defined. The marked width of the spectral functions gives rise to densities of state with a low energy exponential tail increasing with temperature. At low temperatures, this tail corresponds to localized states and gives rough indications for the energy position of the mobility edge. With increasing temperature, in the regime of low carrier doping appropriate to most OFETs, the chemical potential always enters the energy region of the tail. The features of the spectral function and the behavior of the chemical potential allow one to reconcile the band-like description (ARPES data) with the finding that charge carriers appear more localized at high temperature (ESR and modulated spectroscopy data). The study of spectral properties also clarifies that the states that mainly contribute to the conduction process have low momentum and are not at the chemical potential. The mobility, $\mu$, is studied as a function of the electron-phonon coupling, the temperature and particle density. Not only the order of magnitude and the anisotropy ratio between different directions are in agreement with experimental observations, but also the temperature dependence of $\mu$ is correctly reproduced in the model for rubrene, since it scales as a power law $T^{-\gamma}$, with $\gamma$ close or larger than two. The inclusion of vertex corrections in the calculation of the mobility is relevant, in particular, to get a transport lifetime one order smaller than the spectral lifetime of the states involved in the transport mechanism. Moreover, with increasing temperature, the Ioffe–Regel limit is reached, since the contribution of itinerant states to the conduction becomes less and less relevant.

*Ab initio* calculations have clarified that charge carriers in organic semiconductors are not only coupled to low frequency inter-molecular modes, but also to intra-molecular modes with high frequency in comparison with typical electron hopping [4,34,35] (see Figure 1 for a sketch in a naphthalene crystal). An important point is that the reorganization energy (related to the polaron binding energy) decreases with increasing the number of benzene rings in oligoacenes (for example, going from naphthalene to pentacene). In order to fully explore the effects of the different modes on prototype single crystal organic semiconductors, such as oligoacenes, a model with intermediate coupling to both intra- and inter-molecular modes is analyzed in this review [36]. We will show that the interplay between local and non-local electron-phonon interactions is able to provide a very accurate description of the mobility and to shed light on the intricate mechanism of band narrowing with increasing temperature [17].

When the organic semiconductor is grown on a polarizable gate, it is important to analyze the effects of electron coupling to the surface vibrational modes of the gate at the interface with the semiconductor mediated by a long-range electron-phonon interaction [37,38]. In this review, we analyze a model that combines the effects of interface and intrinsic bulk electron-phonon couplings on the transport properties at finite temperature. We show that the coupling to the organic semiconductor bulk phonon modes affects the behavior of mobility below room temperature, enhancing the coherent contribution, but it is ineffective on the incoherent small polaron contribution dominated by the interface coupling at high temperatures.

In order to improve the modeling of organic semiconductors, the effect of a weak disorder, due to bulk and interface traps, is included [37]. In particular, the interplay between long-range

electron-phonon interactions and disorder effects is investigated within a model. The disorder effects are able to enhance the hopping barriers of the activated mobility and to drive the small polaron formation to lower values of electron-phonon interactions. We point out that disorder is a key factor to get agreement with experimental data in rubrene OFETs grown on polarizable gate dielectrics, such as of a $Ta_2O_5$ oxide [12].

**Figure 1.** Sketch of the interplay between low-frequency inter-molecular and high-frequency intra-molecular vibrational modes in a crystal of naphthalene. The charge carrier deforms the benzene ring when it is on the molecule. Moreover, the charge carrier displaces two neighbor molecules when it jumps.

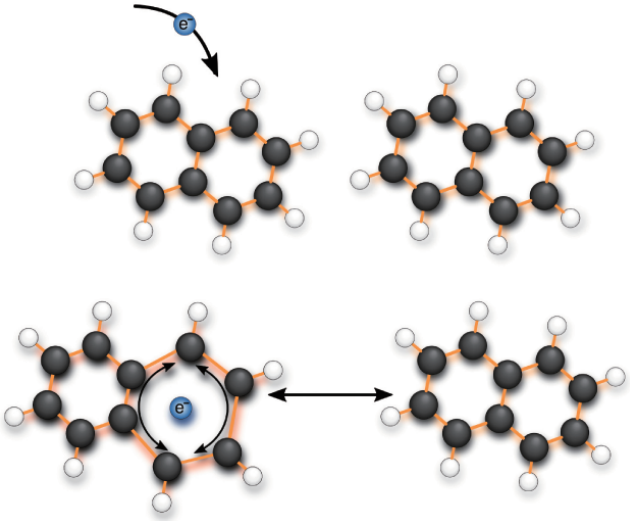

The paper is organized in the following way. In Section 2, the effects of electron coupling to low frequency vibrational modes on the spectral and transport properties are discussed in high-dimensional Holstein-like and SSH-like models. In Section 3, the effects of electron coupling to both low frequency inter-molecular and high frequency intra-molecular modes on the spectral and transport properties are investigated. In Section 4, the influence of gates made of polarizable dielectrics and the interplay between electron-phonon couplings and disorder strength on the transport properties are emphasized. In Section 5, conclusions and final discussions are given.

## 2. Effects of Low-Frequency Vibrational Modes

The anisotropy of the electronic properties is a key ingredient in the description of organic semiconductors [31]. Therefore, in Subsection 2.1, we will introduce a simple anisotropic tight-binding model, including a Holstein-like electron coupling, to low-frequency modes in order to focus on the effects of the electronic structure. However, the results will be discussed later in Subsection 2.4 in comparison with those obtained by a more detailed model based on inter-molecular low frequency modes, which will be introduced in Subsection 2.2.

*2.1. Band Anisotropy*

We assume the following model Hamiltonian:

$$H = -\sum_{\vec{R}_i,\vec{\delta}} t_{\vec{\delta}} c^{\dagger}_{\vec{R}_i} c_{\vec{R}_i+\vec{\delta}} + \sum_{\vec{R}_i} \frac{p^2_{\vec{R}_i}}{2m} + \sum_{\vec{R}_i} \frac{k x^2_{\vec{R}_i}}{2} + H_{el-ph} \tag{1}$$

where $t_{\vec{\delta}}$ is the bare electron hopping toward the nearest neighbors $\vec{\delta}$, $c^{\dagger}_{\vec{R}_i}$ and $c_{\vec{R}_i}$ are the charge carrier creation and annihilation operators, respectively, relative to the site, $\vec{R}_i$ (of a cubic lattice with parameter $a$ for the Holstein model and of an orthorhombic lattice with constants $a$, $b$, $c$ for the rubrene model of the next section), $x_{\vec{R}_i}$ and $p_{\vec{R}_i}$ are the oscillator displacement and momentum, respectively, $m$ the oscillator mass and $k$ the elastic constant. In Equation (1), $H_{el-ph}$ represents the electron-phonon coupling term.

A simple model able to capture the anisotropy of the electronic properties of these materials is the anisotropic Holstein Hamiltonian, which is generic for high mobility organic semiconductors, such as oligoacenes [32]. This model assumes a cubic lattice with the following anisotropic hopping integrals in Equation (1): $t_z \simeq 100$ meV, $t_x \simeq 50$ meV, $t_y \simeq 20$ meV. Moreover, typical values of phonon frequency $\omega_0 = \sqrt{k/m}$ are of the order of $10meV$, leading to a very low adiabatic ratio $\gamma = \omega_0/t_z = 0.1$ (adiabatic regime) [31]. Finally, we assume a very general electron-phonon interaction inspired by the Holstein model [31,39,40]. Therefore, in Equation (1), the electron-phonon Hamiltonian is:

$$H_{el-ph} = \alpha \sum_{\vec{R}_i} x_{\vec{R}_i} c^{\dagger}_{\vec{R}_i} c_{\vec{R}_i} \tag{2}$$

where $\alpha$ is the coupling constant controlling the link between the local electron density and lattice displacement. The following dimensionless quantity, $\lambda_{Hol}$:

$$\lambda_{Hol} = \frac{\alpha^2}{4kt_z} \tag{3}$$

correctly describes the strength of the electron-phonon coupling.

*2.2. Inter-Molecular Vibrational Modes*

In this section, we analyze the influence of the electron coupling of low-frequency inter-molecular modes on the properties of small molecule organic semiconductors.

We consider a realistic quasi-2D model, which simulates the properties of rubrene [33]. Therefore, it not only includes the anisotropy of rubrene crystals (shared with many other small molecule organic semiconductors), but also a more appropriate electron-phonon coupling. First, we derive the effective low-energy electronic model, then the lattice parameters and the appropriate electron-phonon interaction.

**Figure 2.** (**a**) Molecular structure of rubrene. (**b**) Crystal structure along the (a,b) crystallographic plane. The red lines denote the long axis of the molecule.

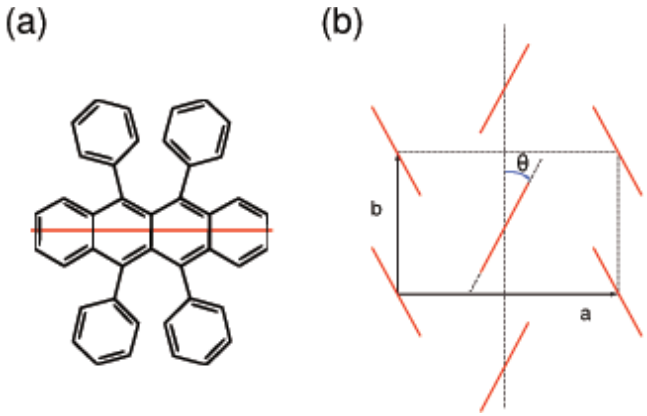


Since we are mostly interested in $dc$ conductivity and low-frequency spectral properties, we need to determine an effective Hamiltonian for the electron degrees of freedom valid for low energy and particle density. We start from the orthorhombic lattice of rubrene with two molecules per unit cell (see Figure 2) and $a$, $b$, $c$ lattice parameter lengths along the three crystallographic vectors of the conventional cell [4]. We follow the ARPES experiments by Ding *et al.* [15] in order to extract the transfer integrals of the highest occupied molecular orbital (HOMO) bands. The dispersion law of the lowest HOMO is accurately fitted with nearest neighbor tight binding parameters for small values of momentum providing the following estimates: $t_a = 118.6$ meV and $t_b = 68.6$ meV [33]. For $t_c$, there is no experimental measure, but theoretical estimates seem to agree that it has to be small compared with other directions, owing to the large interplanar separation of rubrene. In the following, we assume $t_c$ much smaller than $t_a$ and $t_b$ (in the following, we assume $t_c = 0.18\, t_a$). The total volume is $V = L_a * L_b * L_c$ and $L_i$ size along the axis $i = a, b, c$. We consider two crystalline layers along c, because in OFETs, the effective channel of conduction covers only a few planes [41].

In Equation (1), the whole lattice dynamics is ascribed to an effective phononic mode, whose frequency $\omega_0 = \sqrt{K/M}$ is assumed of the order of 5–6 meV [25]. This assumption provides the low adiabatic ratio, $\hbar\omega_0/t_a \simeq 0.05$ (adiabatic regime).

The electron-phonon interacton, $H_{el-ph}$, in Equation (1) is:

$$H_{el-ph} = \sum_{\vec{R}_i,\vec{\delta}} \alpha_{|\vec{\delta}|} \left( x_{\vec{R}_i} - x_{\vec{R}_i+\vec{\delta}} \right) c^{\dagger}_{\vec{R}_i+\vec{\delta}} c_{\vec{R}_i}, \quad \vec{\delta} = \vec{a}, \vec{b}, \vec{c} \tag{4}$$

where $\alpha_{\vec{\delta}}$ is the electron-phonon parameter controlling the effect of the ion displacements in the direction, $\vec{\delta}$, on the transfer integral. Once fixed, $\alpha_a$, we impose $\alpha_b/\alpha_a = t_b/t_a$ and, in the same way, $\alpha_c/\alpha_a = t_c/t_a$. The dimensionless quantity, $\lambda$:

$$\lambda = \frac{\alpha_a^2}{4kt_a} \tag{5}$$

is the relevant parameter to quantify the electron-phonon coupling strength. By comparing *ab initio* calculations and the average properties of a simple 1D model, Troisi *et al.* provided an estimate of

$\lambda \simeq 0.087$ [25,42,43]. However, in our 3D model, the 1D estimate is not correct. Indeed, the hopping, $t_b$, is about half $t_a$, and the average kinetic energy is, then, larger with respect to the one-dimensional case. In order to reproduce the same effective one-dimensional $\lambda$, we have chosen the larger value $\lambda = 0.12$.

In the following part of the section, we use units, such that the lattice parameter $a = 1$, the Planck constant $\hbar = 1$, the Boltzmann constant $k_B = 1$ and the electron charge $e = 1$.

### *2.3. Calculation Method*

For the organic semiconductors studied in this paper, the adiabatic ratio is very low, implying that the adiabatic limit is appropriate for studying low-frequency intermolecular modes. Consequently, it is possible to adopt a semiclassical approach: the electron dynamics is fully quantum, while the ion dynamics is assumed classical. This assumption will limit the temperature range where the results can be considered valid; indeed, all the results are valid for temperatures $T \geq \omega_0 \simeq 100$ K. Finally, we will focus on the weak to intermediate electron-phonon regime that seems to be appropriate for high mobility organic semiconductors [4].

Within the adiabatic regime, the calculation is equivalent to the classical problem of quantum particles in the presence of an external disordered potential given by the ion displacements, $\{x_{\vec{R}_i}\}$, and controlled by electron-phonon coupling. Each configuration of ion displacements is generated according to the probability function of the $P\left(\{x_{\vec{R}_i}\}\right)$, which has to be self-consistently calculated as a function of electron-phonon coupling, temperature and particle density $n = N_p/V$, with $N_p$ number of particles. The adiabatic approach has been also used for the study of molecular junctions and carbon nanotubes at thermodynamical equilibrium and in non-equilibrium conditions [44–48].

In most OFETs, the induced doping is not high; therefore, in the following, we will focus on the regime of low doping (up to $n = 0.01$). For this regime of parameters, the probability function of the lattice displacements, $P\left(\{x_{\vec{R}_i}\}\right)$, shows very tiny deviations from the distribution of free oscillators [30], which is therefore used in the following subsection. Quantities, like spectral function, density of states and conductivity, are calculated through exact diagonalization of the resulting electronic problem at fixed displacements $\{x_{\vec{R}_i}\}$ and through the Monte-Carlo approach for the integration over the distribution, $P\left(\{x_{\vec{R}_i}\}\right)$. In the case of conductivity, for each configuration of the lattice displacements, we calculate the exact Kubo formula [49]:

$$Re\left[\sigma_{\rho,\rho}\left(\omega\right)\left(\{u_{\mathbf{R}_i}\}\right)\right] = \frac{\pi\left(1-e^{-\beta\omega}\right)}{V\omega}\sum_{r\neq s} p_r\left(1-p_s\right)\left|\left\langle r\left|J_\rho\right|s\right\rangle\right|^2\delta\left(E_s-E_r+\omega\right)$$

where $\rho = a, b, c$, $\beta = 1/T$ and $p_r$ is the Fermi distribution:

$$p_r = \frac{1}{1+\exp\left(\beta\left(E_r-\mu_p\right)\right)} \tag{6}$$

corresponding to the exact eigenvalue, $E_r$, at any chemical potential, $\mu_p$. Finally, $\left\langle r\left|J_\rho\right|s\right\rangle$ is the matrix element of the current operator, $J_\rho$, along the direction, $\hat{e}_\rho$, defined as:

$$J_\rho = i\sum_{\vec{R}_i,\vec{\delta}} \bar{t}_{\vec{\delta}}\left(\mathbf{R}_i\right)\left(\vec{\delta}\cdot\hat{e}_\rho\right)c^\dagger_{\vec{R}_i}c_{\vec{R}_i+\vec{\delta}} \tag{7}$$

with:

$$\bar{t}_{\vec{\delta}}(\mathbf{R}_i) = t_{\vec{\delta}} - \alpha_{\vec{\delta}}\left(u_{\mathbf{R}_i} - u_{\mathbf{R}_i+\vec{\delta}}\right), \quad \vec{\delta} = \vec{a}, \vec{b}, \vec{c} \tag{8}$$

We notice that, in contrast with spectral properties, the temperature enters the calculation not only through the displacement distribution, but also directly for each configuration through the Fermi distributions, $p_r$. We point out that the current-current correlator is not evaluated at the lowest order as the convolution of two single-particle Green functions, but the linear response conductivity is exactly calculated within the Kubo formulation presented in Equation (7) [49]. Therefore, the numerical calculation of the conductivity is able to include the vertex corrections (the terms in the correlator beyond the convolution of two Green functions) discarded by previous approaches [49].

Finally, the mobility, $\mu$, is calculated as the ratio between zero-frequency conductivity and carrier density:

$$\mu_\rho = \lim_{\omega \to 0^+} \frac{Re\left[\sigma_{\rho,\rho}(\omega)\right]}{n} \tag{9}$$

Summarizing, the numerical method provides approximation-free results in the adiabatic regime. The only limitation is due to the computational time being controlled by matrix diagonalization.

### *2.4. Results about Spectral and Transport Properties*

Spectral and transport properties, studied within the two models based on Equation (1), will be discussed in this subsection. The study of spectral properties is important to individuate the states that mainly contribute to the conduction process. The spectral properties within the anisotropic Holstein model bear strong resemblance with the rubrene model, so that we will discuss only this last model.

In Figure 3, we report the spectral function at momentum $\mathbf{k} = 0$ for the model parameters of rubrene. We point out that states close to $\mathbf{k} = 0$ are weakly damped. Moreover, with increasing temperature, the peak position of the spectral function is only poorly renormalized in comparison with the bare one, in agreement with results of the 1D SSH model [30]. Therefore, these states keep the itinerant character of the bare ones, and they will be involved in the diffusive conduction process (see the discussion in the next paragraph). We notice that the spectral function at $\mathbf{k} = 0$ is extremely small at the chemical potential, $\mu_p$, for all the temperatures. For example, at $T = 275$ K, the spectral weight is concentrated in an energy region higher than that in which the chemical potential is located ($\mu_p = -3.74t_a$ for $n = 0.002$). Actually, the spectral weight is mainly in the region between $\mu_p + 2T$ and $\mu_p + 3T$.

We have checked that the spectral functions with low momentum are more peaked, while, with increasing $\mathbf{k}$, they tend to broaden. The density of states (DOS) can be calculated as the sum of the spectral functions, $A_\mathbf{k}$, over all the momenta, $\mathbf{k}$. The tail in the DOS is due to the marked width of the high momentum spectral functions. In Figure 4, the DOS is shown for different temperatures at $\lambda = 0.12$ and $n = 0.002$. As shown in logarithmic scale, the DOS has a tail with a low energy exponential behavior. This region corresponds to localized states [50]. We have, indeed, checked, analyzing the wave functions extracted from exact diagonalization, that, actually, states with energies deep in the tail are strongly localized (one or two lattice parameters along the different directions as the localization length). On the other hand, close to the shoulder ($\omega \simeq -3.4t_a$; see Figure 4), the

itinerant nature of states is clearly obtained. This analysis allows one to give an estimation for the mobility edge energy (the energy that divides localized and itinerant states), which can be located very close to the band edge, $E_c$, for free electrons (in our case, $E_c = -3.52t_a$).

**Figure 3.** The spectral function (in units of $1/t_a$) for the rubrene model at momentum $\mathbf{k} = 0$ as a function of the frequency (in units of $t_a/\hbar$) at $\lambda = 0.12$ and $n = 0.002$ for different temperatures, T. We assume the hopping parameter $t_c = 0.18t_a$, with $t_a = 118.6$ meV.

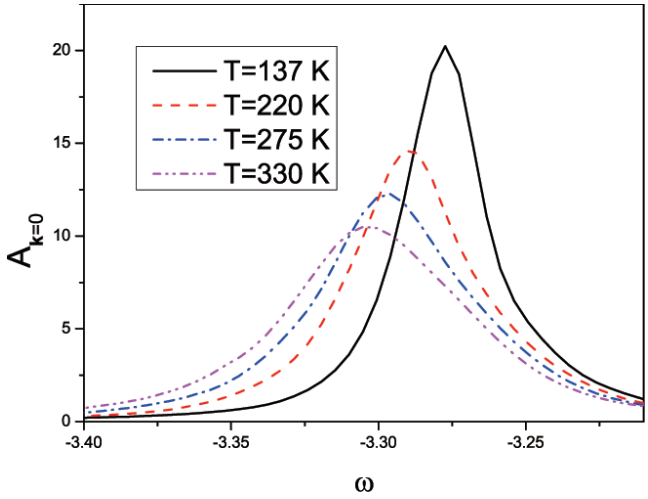


**Figure 4.** The density of states (DOS) (in units of $1/t_a$) for the rubrene model as a function of the frequency (in units of $t_a/\hbar$) at $\lambda = 0.12$ and $n = 0.002$ for different temperatures, T. The squares indicate the chemical potential, $\mu_p$ (in units of $t_a$) at fixed temperature. $E_c$ (dot line, in units of $t_a$) is the free electron band edge close to the mobility edge. We assume the hopping parameter $t_c = 0.18t_a$, with $t_a = 118.6$ meV.

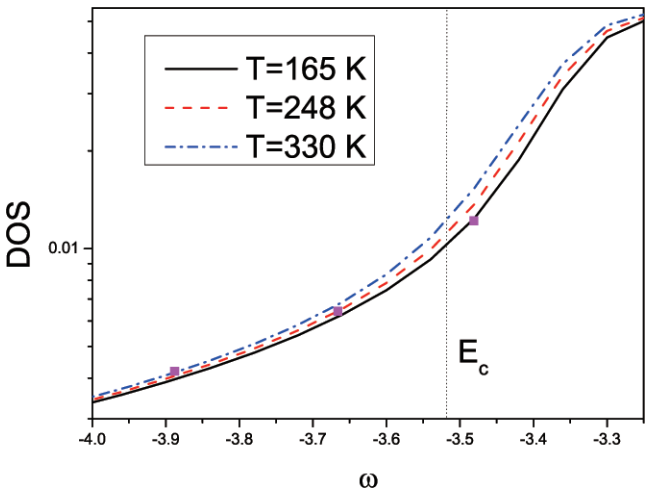


The number of localized states available in the tail increases with temperature. It is important to analyze the role played by the chemical potential, $\mu_p$, with varying the temperature. Actually, $\mu_p$ enters the energy tail and will penetrate into it with increasing temperature. At fixed particle density

$n = 0.002$, for $T = 165$ K, one has $\mu_p = -3.49t_a$, while, for $T = 330$ K, $\mu_p = -3.88t_a$ (see the squares of Figure 4 for the values of the chemical potential). One important point is that the quantity, $E_c$, and the close mobility edge are significantly larger than $\mu_p$. Therefore, in the regime of low density relevant for OFETs, the itinerant states are not at $\mu_p$, but at higher energies. We point out that those are the states relevant for the conduction process. Therefore, the analysis of the properties of a high-dimensional model points out that both localized and itinerant states are present in the system. This is a clear advantage of our work over previous studies in low dimensionality [22,26,28] in which all states are localized: more localized at very low energy and less localized close to the free electron edge. Summarizing, in our system, with increasing temperature, all the states up to $\mu_p$ become localized, and the itinerant states become statistically less effective, due to the behavior of the chemical potential. Eventually, the effect of the penetration of $\mu_p$ in the tail, due to the Fermi statistics, will overcome the effects of available itinerant states around $E_c$. We have checked that the penetration of the chemical potential towards the energy region of the tail is enhanced with increasing the electron-phonon coupling.

We devote the last part of the subsection to analyze the transport properties in both the anisotropic Holstein model and the rubrene model. As shown in the upper panel of Figure 5, we first discuss the mobility of the anisotropic Holstein model along the $z$ direction as a function of temperature with changing of the particle density. Within this model, the carrier density strongly affects the behavior of mobility, showing a cross-over from metallic to insulating behavior at low temperatures. For densities around one percent, the chemical potential at a low temperature is above the mobility edge and, then, the mobility is metallic-like. On the other hand, the situation is different for densities below one percent. At those densities, the chemical potential is below the mobility edge, so that mobility shows an insulating character. Translated in a polaronic framework, this would mean that the single particle sees a potential well, due to electron-phonon coupling; hence, at very low densities, a polaron-like activated mechanism could set in. Actually, the mobility results are consistent with those obtained within the picture of polaron formation [31].

The strong charge density dependence on the mobility is, instead, lost at higher temperatures, where the chemical potential is always in the tail regions for all the charge densities studied, but more states at higher energies (of itinerant nature) get involved, providing the main contribution to mobility. As a consequence of the different behavior with charge densities at low and high temperatures, the mobility changes its character at intermediate temperatures for low-charge carrier densities.

At high temperatures, the mobilities look very similar for all the densities considered in the upper panel of Figure 5. At room temperature, the mobility is about $20$ cm$^2$/(V $\cdot$ s), a value that recovers the right order of magnitude of experimental data in oligoacenes [2]. However, the mobility decreases with the temperature as $1/T$, not in agreement with measurements in oligoacenes, such as rubrene. Moreover, in this model, polaronic localization seems to take place in the low-temperature range for enough low-charge densities, even if experimental data do not seem to support this scenario. Therefore, a more accurate model for the electron-phonon coupling is needed. As already discussed in Subsection $2.2$, the SSH-like coupling with intermolecular vibrational modes is what we need. In the following part of this subsection, we will analyze the transport properties of that model.

In the lower panel of Figure 5, the mobility along the $a$ direction is reported as a function of the temperature at fixed coupling $\lambda = 0.12$ and different concentrations, $n$. The plot shows that the absolute magnitude of the mobility substantially agrees, with the experimental estimates being $\mu \simeq 10\,\mathrm{cm}^2/(\mathrm{V}\cdot\mathrm{s})$ at room temperature. Furthermore, the mobility exhibits a band-like power-law $T^{-\gamma}$ behavior for all the concentrations. The exponent, $\gamma$, is evaluated from the fits of the mobility, providing values in the range 2–2.4, where the highest value is related to the lowest concentration. This trend is in agreement with experimental measures, that for rubrene establish $\gamma \simeq 2$ for temperatures $T > 170 - 180$ K [2]. One feature, in contrast with the Holstein model, is that the mobility increases with decreasing the concentration of carriers. This trend, already found in the 1D SSH model [30], points out that there is no room for a polaronic (bond) localization [51] within the regime of rubrene parameters explored in this review.

**Figure 5.** (**Top**) Mobility along the $z$ direction within the anisotropic Holstein model as a function of temperature T for different particle densities at $\lambda_{Hol} = 0.8$. (**Bottom**) Mobility along the $a$ direction within the rubrene model as a function of temperature T for different particle densities at $\lambda = 0.12$. We assume the hopping parameter $t_c = 0.18 t_a$, $t_a = 118.6$ meV.

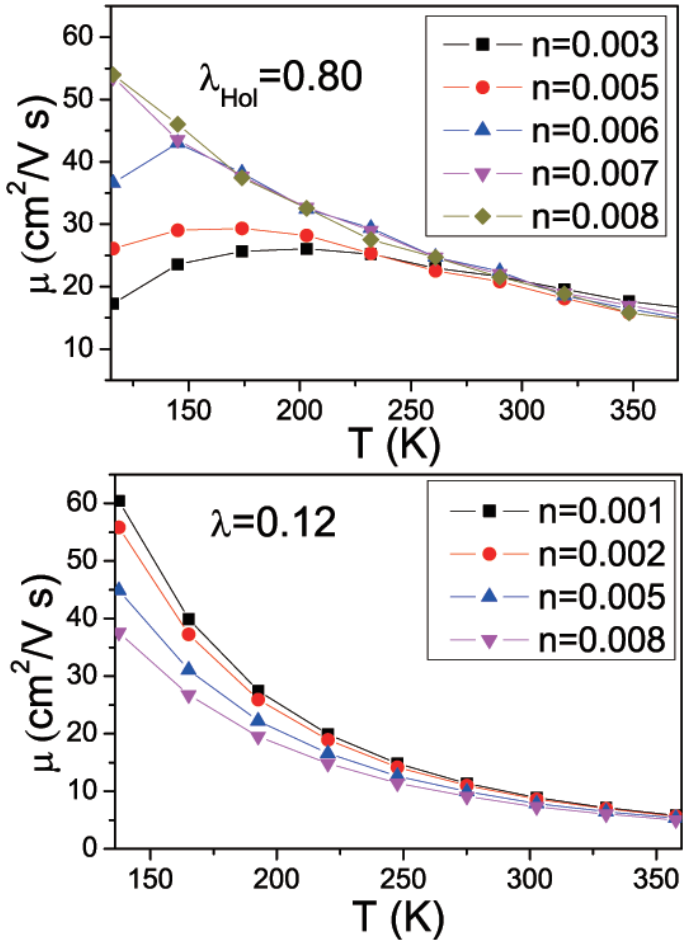

Another important property is the anisotropy of the transport properties along different in-plane directions [53]. In our model for rubrene, the anisotropy of the mobility along different crystallographic directions is essentially the same as the anisotropy of the effective mass. From the estimates of in-plane hopping, $t_a$ and $t_b$, the anisotropy of the mobility is evaluated to be of the order of $(t_b/t_a)^2 = 0.335$. From experiments [2], the anisotropy ratio is about $0.375$ at room temperature; therefore, in agreement with our estimate. However, the experimental data shows that this ratio increases with decreasing temperature. In a recent paper [54], where the electron-phonon coupling is slightly more complex than the SSH-like interaction considered in our model, the anisotropy of the mobility is less marked than that of the mass. Within this paper, the anisotropy ratio between the two in-plane mobilities is calculated to be of the order of 0.44 at room temperature (higher than the experimental value) and 0.5 at $T = 150$ K; therefore, it increases with decreasing temperature in agreement with the experimental trend. Even if the electron-phonon models are slightly different, the conclusions of our work and these recent calculations are qualitatively consistent.

Starting from the mobility, we can determine the scattering time, $\tau_{tr}$, from the relation $\mu = e\tau_{tr}/m$. Since the mass is weakly renormalized from the electron-phonon interaction, one can assume $m$ as the bare mass at $\mathbf{k} = 0$. We point out that $\tau_{tr}$ is on the scale of fs, so that it is one order of magnitude lower than the damping time of the states important for the spectral properties (on the scale of tens of fs). Therefore, the transport processes amplify the effects of the electron-phonon interaction, and the vertex corrections introduced within our approach are fundamental to take into account this effect.

From the scattering time, one can deduce the mean free path as $l_{tr} = v_{av}\tau_{tr}$, where $v_{av}$ is the average velocity of the charge carriers. The quantity, $l_{tr}$, is always on the scale of a few lattice parameters. The most important feature is its temperature behavior. As a consequence of the electron-phonon effects, close to room temperature, it becomes of the order of half lattice parameter $a$. This means that the Ioffe–Regel limit is reached [52]. The decrease of the mobility in the Ioffe–Regel limit is not due to a mass renormalization (dynamic and/or static), but it is due to a reduction of the available itinerant states (the only ones able to transport current) with the temperature. We remark that this result is due to the fundamental role played by vertex corrections (introduced in the previous subsection about the computational methods) in the calculation of the mobility.

## 3. Effects of Combined Low Frequency Inter-Molecular and High Frequency Intra-Molecular Vibrational Modes

For rubrene and pentacene, the carrier mobility is dominated by inter-molecular phonons, since the interaction with intra-molecular modes is almost negligible [25], and then, the model discussed in the previous section is considered adequate. On the other hand, in other oligoacenes with a smaller number of benzene rings, the coupling with local modes cannot be neglected [4].

Indeed, the decrease of the number of benzene rings affects the reorganization energy, which can be related to the binding energy of the polaron, that is the quasi-particle formed by the electron (or hole) and the surrounding phonon cloud. Actually, going from pentacene to naphthalene,

the reorganization energy increases nearly twice, suggesting a much stronger coupling with local modes [4]. Therefore, for systems with a reduced number of benzene rings, like naphthalene, we expect a larger interplay between intra- and inter-molecular modes (see Figure 1) within the intermediate electron-phonon coupling regime for both modes. The next step of the review is to combine the effects of high frequency local vibrational (antiadiabatic) modes with non-local low frequency (adiabatic) ones [36]. For computational ease, we will restrict our analysis to the 1D case, assuming the inter-molecular phonons classical, but considering the intra-molecular modes as fully quantum.

### *3.1. Model Hamiltonian*

We consider a one-dimensional model with coupling to intra- and inter-molecular modes [36,55] similar to the one recently introduced, where the treatment only concerns the study of spectral properties [56]. The coupling to intra-molecular modes is Holstein-like; that to inter-molecular modes is SSH-like (see Figure 1 for a sketch of the two couplings). It can be summarized in the following Hamiltonian:

$$H = H_{el}^{(0)} + H_{Intra}^{(0)} + H_{Inter}^{(0)} + H_{el-Intra} + H_{el-Inter} \tag{10}$$

In Equation (10), the free electronic part, $H_{el}^{(0)}$, is:

$$H_{el}^{(0)} = -t \sum_i \left( c_i^\dagger c_{i+1} + c_{i+1}^\dagger c_i \right) \tag{11}$$

where $t$ is the bare electron hopping between the nearest neighbors on the chain and $c_i^\dagger$ and $c_i$ are the charge carrier creation and annihilation operators, respectively, relative to the site, $i$, of a chain with lattice parameter $a$. For the transfer hopping, the *ab initio* estimate is: $t \simeq 50 - 100$ meV [4]. We consider a single-band one-dimensional electronic structure, since it represents the simplest effective model in anisotropic organic semiconductors to analyze the low energy features responsible for the mobility properties.

In Equation (10), $H_\alpha^{(0)}$, with $\alpha = Intra, Inter$, is the Hamiltonian of the free optical molecular modes:

$$H_\alpha^{(0)} = \sum_i \frac{p_{\alpha,i}^2}{2m_\alpha} + \sum_i \frac{k_\alpha x_{\alpha,i}^2}{2} \tag{12}$$

where $p_{\alpha,i}$ and $x_{\alpha,i}$ are the oscillator momentum and position of the mode, $\alpha$, respectively, $m_\alpha$ the oscillator mass and $k_\alpha$ the elastic constant of the mode, $\alpha$. The inter-molecular modes are characterized by small frequencies ($\hbar\omega_{Inter} \simeq 5 - 10$ meV) in comparison with the transfer hopping [4,22]. On the contrary, the most coupled intra-molecular modes have large frequencies ($\hbar\omega_{Intra} \simeq 130 - 180$ meV) [4].

In Equation (10), $H_{el-Intra}$ is the Holstein-like Hamiltonian describing the electron coupling to intra-molecular modes:

$$H_{el-Intra} = \alpha_{Intra} \sum_i x_i n_i \tag{13}$$

with $\alpha_{Intra}$ the coupling constant to local modes and $n_i = c_i^\dagger c_i$ the local density operator. The dimensionless constant:

$$g_{Intra} = \alpha_{Intra}/\sqrt{2\hbar m_{Intra}\omega_{Intra}^3} \tag{14}$$

is used to describe this electron-phonon coupling [39]. In single crystal organic semiconductors, $g_{Intra}$ is in the weak to intermediate regime (of the order of unity) [4].

Finally, in Equation (10), $H_{el-Inter}$ represents the SSH-like term with electron coupling to inter-molecular modes:

$$H_{el-Inter} = \alpha_{Inter} \sum_i (y_{i+1} - y_i) \left( c_i^\dagger c_{i+1} + c_{i+1}^\dagger c_i \right) \tag{15}$$

with $\alpha_{Inter}$ the coupling constant to non-local modes. In the adiabatic regime for non-local modes ($\hbar\omega_{Inter} \ll t$), the dimensionless quantity:

$$\lambda_{Inter} = \alpha_{Inter}^2/4k_{Inter}t \tag{16}$$

fully provides the strength of the electron coupling to inter-molecular modes. The typical values of $\lambda$ are in the intermediate (of the order of $0.1$) coupling regime [33].

In the following part of this section, we will use units, such that the lattice parameter $a = 1$, the Planck constant $\hbar = 1$, the Boltzmann constant $k_B = 1$ and the electron charge $e = 1$. We will analyze systems in the thermodynamic limit, and we will measure energies in units of $t \simeq 80$ meV. We fix $\omega_{Intra} = 2.0t$ as the model parameter with the highest energy [4].

### *3.2. Calculation Method*

Since a very low carrier density is injected into the organic semiconductor, we will study the case of non-interacting particles. The temperature range where intrinsic effects are relevant is $\omega_{Inter} \leq T \ll t < \omega_{Intra}$. Therefore, the dynamics of intermolecular modes can be assumed to be classical. On the other hand, it is important to retain the quantum nature of high frequency local vibrational modes.

Actually, the electron motion is strongly influenced by the statistical "off-diagonal" disorder that, in the limit of low carrier density, is described by the probability function, $P(\{y_j\})$, of free classical harmonic oscillators. At a fixed configuration of non-local displacements, $\{y_j\}$, Equation (10) is equivalent to a Holstein model with displacements $\{x_i\}$, where the electron hopping depends on the specific nearest neighbor sites throughout the assigned $\{y_j\}$. The resulting inhomogeneous Holstein model can be accurately studied within the modified variational Lang–Firsov approach via a unitary transformation, $U(\{y_j\})$, depending on the non-local displacements, $\{y_j\}$, and appropriate in the anti-adiabatic regime ($\omega_{Intra} > t$) [57,58]. The electron mass is renormalized by the coupling with local modes (polaronic effect), and the Holstein-coupled oscillators $\{x_i\}$ are displaced from their equilibrium position to a distance proportional to the electron-phonon interaction. For each fixed configuration, $\{y_j\}$, one has to calculate quantities, such as spectral function, density of states and mobility (calculated as the ratio between conductivity and carrier density), within the Lang–Firsov

approach. Then, the effect of non-local adiabatic inter-molecular modes can be taken into account, making the integral over the distribution, $P(\{y_i\})$, by means of a Monte-Carlo procedure.

The method exposed above is very accurate in the regime $\omega_{Inter} \ll t$ and $\omega_{Intra} > t$, appropriate for high-mobility organic semiconductors. It properly takes into account the quantum effects of high frequency local vibrational modes. Moreover, the approach is able to include spatial correlations relevant in quasi one-dimensional systems, in particular vertex corrections in the calculation of mobility.

### *3.3. Results on Spectral and Transport Properties*

In Figure 6, we report the density of states (DOS) for $g_{Intra} = 1.3$ and $\lambda_{Inter} = 0.09$ at different temperatures. For all the temperatures, there is a strong renormalization of the bare band, whose width becomes twice smaller (from $4t$ to roughly $2t$) and moves to lower energies (from $-2t$ to roughly $-4t$). Furthermore high energy satellite bands appear at multiples of the vibrational frequency $\omega_{Intra} = 2t$ [49], providing a DOS extending from $-4t$ to $4t$. These effects can be easily ascribed to the local modes, since they survive also at $T = 0$, where the effect of non-local modes is weak. The intrinsic reduction of the bare band due to local modes provides a simple and direct explanation of the difference in the bandwidth evidenced in the series of oligoacenes from naphthalene (an effective band of the order of $40$ meV) to pentacene (an effective band of the order of $80$ meV). Indeed, it can be ascribed to the decrease of the reorganization energy with increasing the benzene rings of the single molecules that, in turn, reduces the renormalization effects [4]. Within the polaron theory [49], the narrowing of the main band is related to the spectral weight, Z, of the quasi-particle, which is estimated to be about $0.5$ from the calculations. Therefore, our estimate of Z compares favorably with recent *ab initio* results for which Z relative to the electron channel is of the order of 0.7 [59].

**Figure 6.** The DOS (in units of $1/t$) as a function of the frequency (in units of $t/\hbar$) for different temperatures, T, at $\lambda_{Inter} = 0.09$ and $g_{Intra} = 1.30$. We consider $\omega_{Intra} = 2t$ (in units of $t$, with $t = 80$ meV).

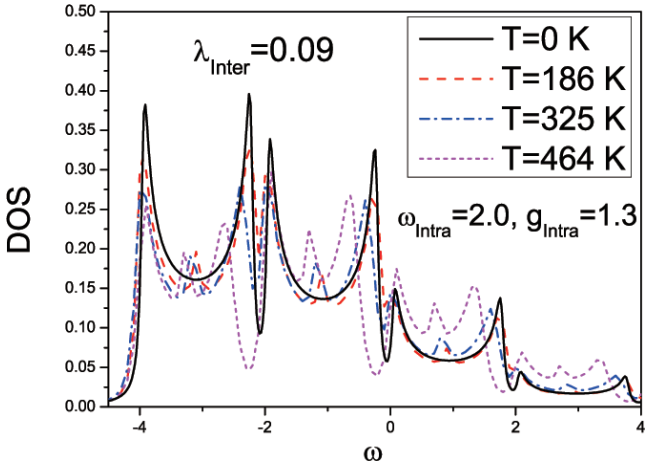

At finite temperature, the shape of the spectra is changed, due to the non-local coupling. Actually, any band shows a new small maximum, due to the coupling to inter-molecular modes. It is well known that, in the polaron theory, the band narrowing increases strongly with temperature. In order to be more quantitative, we notice that, for $\lambda_{Inter} = 0$, the principal band at $T = 325$ K is reduced by about $42\%$ of the band at $T = 0$. On the other hand, for $\lambda_{Inter} = 0.09$, the principal band at $T = 325$ K is reduced by only $7\%$ of the band at $T = 0$. Unexpectedly, in our model, the band narrowing is strongly reduced due to the non-local coupling. The narrowing of the principal band results from a subtle equilibrium between the two opposite tendencies. Actually, the coupling to non-local modes has the main effect of inducing scattering into the single bands of the density of states, preventing the narrowing induced by the coupling to local modes. The interplay between local and non-local modes is able to produce a modest narrowing as function of the temperature, even if the coupling to local modes is not weak. Our prediction is that this effect should be present not only in pentacene [17], but also in naphthalene and anthracene.

Next, we analyze the mobility in the intermediate regime for both intra- and inter-molecular modes (see Figure 7). The mobility can be divided into two contributions: the coherent one, where the scattering of the renormalized electron (the only effect due to local electron-phonon coupling here is the reduction of the bandwidth) with non-local modes is included, and the incoherent one, where, in addition to non-local modes, scattering with multiple real local phonons is considered.

The coherent term of mobility, relevant at low temperatures, bears a strong resemblance with the mobility of the system at $g_{Intra} = 0$, even if, as expected, it is smaller. The local coupling is able to affect, but not to destroy, the low-temperature behavior dominated by the non-local coupling. Actually, for $g_{Intra} = 0$, the mobility scales as $1/T^{1.89}$, while, with increasing $g_{Intra}$, the power-law becomes slightly less pronounced. In the case $g_{Intra} = 1.3$, the mobility goes as $1/T^{1.60}$, still compatible with experiments in naphthalene, and it has the correct order of magnitude [8–10].

**Figure 7.** Mobility and its different contributions as a function of the temperature, T, at $\lambda_{Inter} = 0.09$ and $g_{Intra} = 1.3$. We consider $\omega_{Intra} = 2$ (in units of $t$, with $t = 80$ meV).

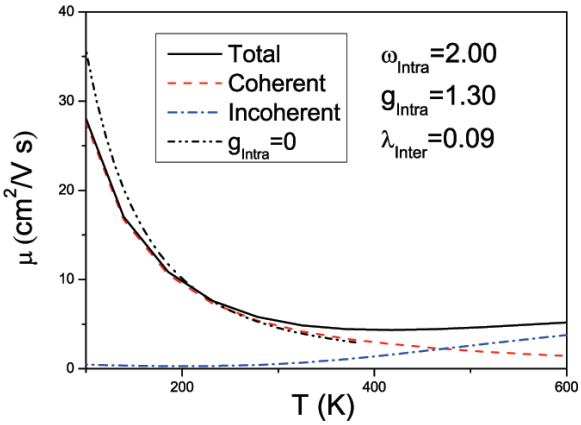


The incoherent term of mobility starts at a temperature of about $T = 230$ K and becomes predominant only at temperatures much higher than room temperature. The role of the local coupling here is to promote an activated behavior in the incoherent regime, which is effective only at high

temperature. Consequently, the local coupling provides a negligible contribution to the mobility up to room temperature. Actually, the combined effect between intra- and inter-molecular modes is able to provide an activation energy, $\Delta$, of only about $20$ meV; therefore, less than one half of that for $\lambda_{Inter} = 0$ and close to that extracted by experimental data in naphthalene (about $15$ meV for mobility along the $c$-axis) [8–10]. We stress that the small activation energy is found even if the reorganization energy related to intra-molecular modes derived from *ab initio* calculations [4] is not small. Actually, the polaronic binding energy is given by $g^2_{Intra}\omega_{Intra}$, which is of the order of $1.7 * 2 * t \simeq 270$ meV. Therefore, the non-local SSH interaction is able to strongly quench the tendency towards localization of the local Holstein coupling. As a result, the activation energy of the transport properties is estimated to be much smaller than the value of the polaronic local energy if other electron-phonon non-local interactions are playing a relevant role.

Summarizing, the proposed model is able to capture many features of the mobility in oligoacenes.

## 4. Effects of Gates Made of Polarizable Dielectrics and Disorder

In the last part of this review, we investigate the effect of a polarizable gate on the transport properties of organic semiconductors [37,38] (see Figure 8 for a sketch about the coupling between charge carrier and polarization in the dielectric). This analysis is important to interpret experimental data in rubrene OFETs grown on polarizable dielectric gates, such as $Ta_2O_5$ oxide [12].

**Figure 8.** Sketch of the effects induced by the charge carrier in the conducting channel on the gate close to the interface. The electron in the organic semiconductor induces a polarization within the dielectric that, in turn, affects the electron dynamics.

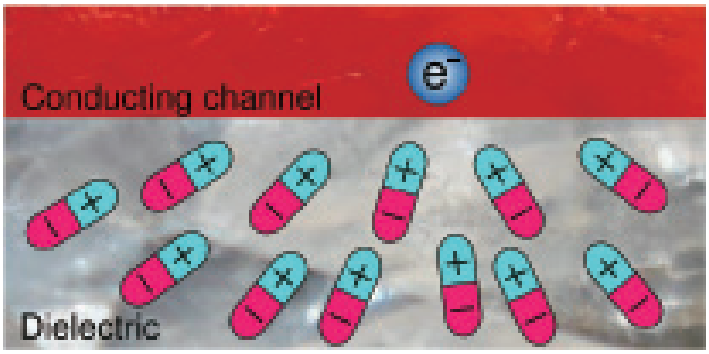


### *4.1. Model Hamiltonian*

We study a one-dimensional Hamiltonian model with coupling to bulk and interface vibrational modes [37]. This model is similar to that of the previous section. Actually, the free electronic Hamiltonian is the same, and the bulk modes of this model correspond to the inter-molecular modes.

The model is described by the following Hamiltonian:

$$H = H_{el} + H^{(0)}_{Bulk} + H_{el-Bulk} + H^{(0)}_{Int} + H_{el-Int} \tag{17}$$

In Equation (17), the electronic part, $H_{el}$, is given by Equation (11) of the previous section, with $t$ bare electron hopping (estimated to be among $80$ meV and $120$ meV) between the nearest neighbors sites.

In Equation (17), $H^{(0)}_{Bulk}$ corresponds to Equation (12) for free intermolecular modes with elastic constant $k$, mass $m$ and $\hbar\omega_{Bulk} \simeq 5 - 10$ meV, much smaller than transfer hopping t [4,22].

In Equation (17), $H_{el-Bulk}$ represents the term similar to the SSH [24] interaction for the coupling to intermolecular modes given in Equation (15). As in the previous section, one can define $\lambda_{Bulk}$, whose typical values are in the intermediate coupling regime (in this section, we take the value $\lambda_{Bulk} = 0.1$, suitable for rubrene) [30].

In Equation (17), $H^{(0)}_{Int}$ is the Hamiltonian of free interface phonons:

$$H^{(0)}_{Int} = \hbar\omega_{Int} \sum_{q} a^{\dagger}_{q} a_{q} \tag{18}$$

where $\omega_{Int}$ is the frequency of optical modes and $a^{\dagger}_{q}$ and $a_{q}$ are creation and annihilation operators, respectively, relative to phonons with momentum $q$.

In Equation (17), $H_{el-Int}$ is the Hamiltonian describing the electron coupling to interface vibrational modes:

$$H_{el-Int} = \sum_{i,q} M_q n_i e^{iqR_i} \left( a_q + a^{\dagger}_{-q} \right) \tag{19}$$

where $n_i$ is the density operator, $M_q$ is the interaction electron-phonon term:

$$M_q = \frac{g\hbar\omega_{Int}}{\sqrt{L}} \sum_{i} e^{iqR_i} \frac{R_0^2}{R_0^2 + R_i^2} \tag{20}$$

with $g$ the dimensionless coupling constant, $L$ the number of lattice sites, $R_i$ position of the site, $i$, and $R_0$ the cut-off length of the order of the lattice spacing, $a$. This electron-phonon coupling describes the long-range interaction induced on the electron at the interface with the dielectric gate. In order to quantify this coupling, we use the dimensionless quantity:

$$\lambda_{Int} = \sum_{q} \frac{M_q^2}{2\hbar\omega_{Int} t} \tag{21}$$

In this work, we take $R_0 = 0.5a$ and $\hbar\omega_{Int} = 0.5t$ [60].

In the following part of this section, we will use units, such that $a = 1$, $\hbar = 1$, $e = 1$, and the Boltzmann constant $k_B = 1$. We will analyze systems in the thermodynamic limit measuring energies in units of $t \simeq 100$ meV. The calculation method is similar to that in the previous section, since the role of intra-molecular modes here is played by interface modes.

### *4.2. Results about Transport Properties*

In Figure 9, we report the mobility as a function of the temperature for different values of $\lambda_{Int}$ at bulk coupling $\lambda_{Bulk} = 0.1$ (appropriate to rubrene). The quantity, $\mu$, shows a coherent band-like behavior at low temperatures, but, with increasing $T$, it goes towards the activated behavior, where

the bulk coupling is not effective. Actually, the mobility interpolates between the behaviors with only bulk and interface phonons. At low temperature, the diffusive contribution is ascribed to the modulation of the electron kinetic energy, due to the bulk modes with SSH interactions. This coherent contribution is weakened with increasing $\lambda_{Int}$, but it does not disappear. This element is in contrast with experimental data, which show a more or less marked insulating behavior from $150$ K to $300$ K [12]. Therefore, the theoretical prediction of mobility is not accurate, even if bulk and interface electron-phonon couplings are active.

**Figure 9.** Mobility $\mu$ as a function of the temperature, T, at $\lambda_{Bulk} = 0.1$ for different values of $\lambda_{Int}$.

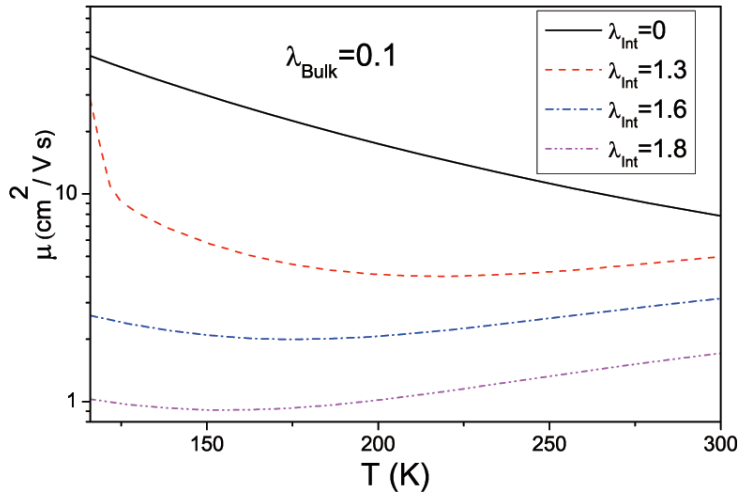


*4.3. Interplay between Electron-Phonon Coupling and Disorder Strength*

In order to explain the experimental data, it is necessary to include also disorder effects. Indeed, there is evidence of traps in the bulk and at the interface with gates [2]. Therefore, it is of paramount importance to investigate the role of disorder on the transport properties.

The model bears a strong resemblance with that of the previous subsections. Actually, the only modification is related to the electronic Hamiltonian, which includes, here, a disorder term. Therefore, in Equation (17), there is a new term given by:

$$H_{dis} = \sum_i \epsilon_i n_i \tag{22}$$

where $\epsilon_i$ is a local energy, whose fluctuations in the range $[-W, W]$ simulates disorder effects in the bulk and at the interface with gate, $n_i = c_i^\dagger c_i$ being the density operator and with $c_i^\dagger$ and $c_i$ the electron creation and annihilation operators, respectively, relative to the site, $R_i$. Due to the presence of shallow traps [2], disorder is not overwhelming, and it is distributed according to a flat probability function. The calculation method is analogous to that of the previous section.

In Figure 10, we show the mobility as a function of the temperature with increasing the strength of disorder for $\lambda_{Int} = 1.3$ and $\lambda_{Bulk} = 0.1$. There are two main results. The first one is related to the suppression of the coherent metallic behavior with increasing $W$. The second one is the

strong enhancement of the activation energy, $\Delta$, up to $67$ meV, even for the small amount of disorder $W = 70$ meV. Furthermore, the decrease of the magnitude of the mobility is not so marked. Therefore, weak disorder effects are able to provide a very accurate description of the mobility, resulting in key quantities for the interpretation of experimental data. Finally, another important effect of disorder is to drive the small polaron formation at lower electron-phonon couplings.

**Figure 10.** Mobility $\mu$ as a function of the temperature for different disorder strengths, $W$, at $\lambda_{Bulk} = 0.1$ and $\lambda_{Int} = 1.3$. The quantity, $\Delta$, is the polaron activation energy.

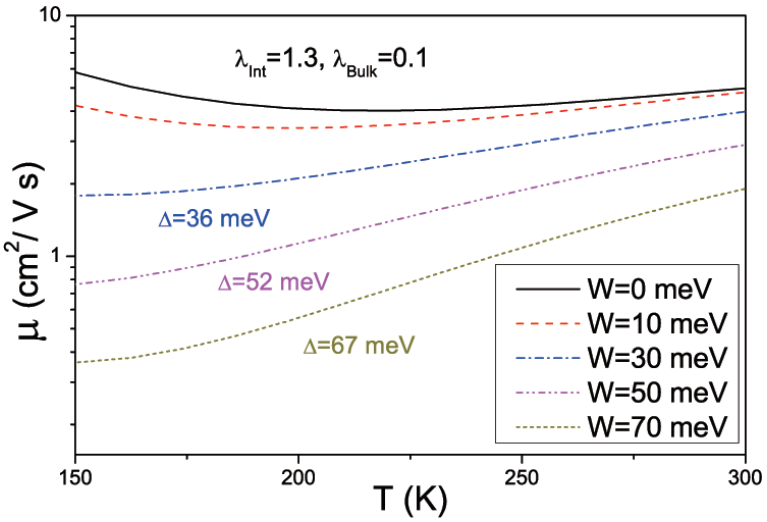


## 5. Conclusions

In this review, we have theoretically analyzed the effects of different electron-phonon couplings on the spectral and transport properties of small molecule single-crystal organic semiconductors. Focus has been on oligoacenes, in particular on the series from naphthalene to rubrene and pentacene.

First, we have discussed the effects of the electron coupling to low-frequency inter-molecular vibrational modes on the spectral and transport properties. The resulting adiabatic models have been studied through numerical approaches with varying electron-phonon coupling and temperature. For rubrene, the model has considered the role of the electron-phonon coupling leading to a modulation of the particle hopping integral. With increasing temperature, the density of states is characterized by a larger exponential tail corresponding to localized states. Consequently, the chemical potential moves into the tail of the density of states, but this is not enough to drive the system into an insulating state. Not only the order of magnitude and the anisotropy ratio between different directions are accurate, but also the temperature dependence of the mobility is correctly reproduced in the model for rubrene. With increasing temperature, the Ioffe–Regel limit is reached, since the contribution of itinerant states to the conduction becomes less and less relevant.

Then, we have analyzed the effects of electron coupling to both low-frequency inter-molecular and high-frequency intra-molecular modes on the spectral and transport properties. The interplay between local and non-local electron-phonon interactions has been able to provide a very accurate description of the mobility of oligoacenes and to shed light on the intricate mechanism of band

narrowing with increasing temperature. The band narrowing is a complicated phenomenon, which could also be affected by the thermal expansion of the crystal structure [61] (an effect that has not been analyzed in this review).

In the last part of the review, we have considered the influence of gates made of polarizable dielectrics on the transport properties. This effect has been studied in a model that has combined bulk and long-range interface electron-phonon couplings. We have pointed out that the bulk coupling affects the behavior of mobility below room temperature, enhancing the coherent contribution, but it is ineffective on the incoherent small polaron contribution dominated by the interface coupling at high temperatures.

Finally, we have emphasized the interplay between electron-phonon couplings and disorder strength on the transport properties. The presence of disorder is important to improve the modeling of the materials studied in this review. In particular, for systems gated with polarizable dielectrics, we have shown that disorder effects are able to enhance the hopping barriers of the activated mobility and to drive the small polaron formation at lower values of electron-phonon interactions. Therefore, disorder represents a key factor to get agreement with experimental data.

Some issues have not been covered in this review. Indeed, the transport properties could be affected by the non-local electron coupling, not only to optical, but also acoustic vibrations [27]. The coupling to acoustic vibrations should be effective at low temperatures, where it would be interesting also to investigate the role of quantum lattice fluctuations. These quantum effects are small in the adiabatic limit; however, they could be important in the regime where the presence of traps also influences the transport properties. Finally, we believe that the concepts and methods discussed in this review can be a starting point for the study of related (such as durene crystals [62]) and more complex systems [63].

## Conflicts of Interest

The authors declare no conflicts of interest.

## References

1. Hasegawa, T.; Takeya, J. Organic field-effect transistors using single crystals. *Sci. Technol. Adv. Mater.* **2009**, *10*, 024314–024329.
2. Gershenson, M.E.; Podzorov, V.; Morpurgo, A.F. Colloquium: Electronic transport in single-crystal organic transistors. *Rev. Mod. Phys.* **2006**, *78*, 973–989.
3. Cheng, Y.C.; Silbey, R.J.; Filho, D.A.; Calbert, J.P.; Cornil, J.; Bredas, J.L. Three-dimensional band structure and bandlike mobility in oligoacene single crystals: A theoretical investigation. *J. Chem. Phys.* **2003**, *118*, 3764–3774.
4. Coropceanu, V.; Cornil, J.; Filho, D.A.d.; Olivier, Y.; Silbey, R.; Bredas, J.-L. Charge Transport in Organic Semiconductors. *Chem. Rev.* **2007**, *107*, 926–952.
5. Cheng, Y.C.; Silbey, R.J. A unified theory for charge-carrier transport in organic crystals. *J. Chem. Phys.* **2008**, *128*, 114713.

6. Ortmann, F.; Bechstedt, F.; Hannewald, K. Charge transport in organic crystals: interplay of band transport, hopping and electron-phonon scattering. *New J. Phys.* **2010**, *12*, 023011.
7. Alexandrov, A.S.; Devreese, J.T. *Advances in Polaron Physics*; Springer Verlag: Berlin/Heidelberg, Germany, 2010.
8. Warta, W.; Karl, N. Hot holes in naphthalene: High, electric-field-dependent mobilities. *Phys. Rev. B* **1985**, *32*, 1172–1182.
9. Karl, N. XIth Molecular Crystal Symposium; Lugano, Switzerland, 1985; p. 135.
10. Karl, N. Charge carrier transport in organic semiconductors. *Synth. Met.* **2003**, *133–134*, 649–657.
11. Stassen, A.F.; de Boer, R.W.I.; Iosad, N.N.; Morpurgo, A.F. Influence of the gate dielectric on the mobility of rubrene single-crystal field-effect transistors. *App. Phys. Lett.* **2004**, *85*, 3899–3901.
12. Hulea, I.N.; Fratini, S.; Xie, H.; Mulder, C.L.; Iossad, N.N.; Rastelli, G.; Ciuchi, S.; Morpurgo, A.F. Tunable Frohlich polarons in organic single-crystal transistors. *Nat. Mater.* **2006**, *5*, 982–986.
13. Ono, S.; Miwa, K.; Seki, S.; Takeya, J. A comparative study of organic single-crystal transistors gated with various ionic-liquid electrolytes. *App. Phys. Lett.* **2009**, *94*, 063301.
14. Fratini, S.; Xie, H.; Hulea, I.N.; Ciuchi, S.; Morpurgo, A.F. Current saturation and Coulomb interactions in organic single-crystal transistors. *New J. Phys.* **2008**, *10*, 033031.
15. Ding, H.; Reese, C.; Makinen, A.J.; Bao, Z.; Gao, Y. Band structure measurement of organic single crystal with angle-resolved photoemission *Appl. Phys. Lett.* **2010**, *96*, 222106.
16. Machida, S.I.; Nakayama, Y.; Duhm, S.; Xin, Q.; Funakoshi, A.; Ogawa, N.; Kera, S.; Ueno, N.; Ishii, H. Highest-Occupied-Molecular-Orbital Band Dispersion of Rubrene Single Crystals as Observed by Angle-Resolved Ultraviolet Photoelectron Spectroscopy. *Phys. Rev. Lett.* **2010**, *104*, 156401.
17. Hatch, R.C.; Huber, D.L.; Höchst, H. Electron-Phonon Coupling in Crystalline Pentacene Films. *Phys. Rev. Lett.* **2010**, *104*, 047601.
18. Marumoto, K.; Kuroda, S.; Takenobu, T.; Iwasa, Y. Spatial Extent of Wave Functions of Gate-Induced Hole Carriers in Pentacene Field-Effect Devices as Investigated by Electron Spin Resonance. *Phys. Rev. Lett.* **2006**, *97*, 256603.
19. Marumoto, K.; Arai, N.; Goto, H.; Kijima, M.; Murakami, K.; Tominari, Y.; Takeya, J.; Shimoi, Y.; Tanaka, H.; Kuroda, S.; *et al*. Microscopic mechanisms behind the high mobility in rubrene single-crystal transistors as revealed by field-induced electron spin resonance. *Phys. Rev. B* **2011**, *83*, 075302.
20. Laarhoven, H.A.V.; Flipse, C.F.J.; Koeberg, M.; Bonn, M.; Hendry, E.; Orlandi, G.; Jurchescu, O.D.; Palstra, T.T.M.; Troisi, A. On the mechanism of charge transport in pentacene. *J. Chem. Phys.* **2008**, *129*, 044704.
21. Sakanoue, T.; Sirringhaus, H. Band-like temperature dependence of mobility in a solution-processed organic semiconductor. *Nat. Mater.* **2010**, *9*, 736–740.

22. Troisi, A.; Orlandi, G. Charge-Transport Regime of Crystalline Organic Semiconductors: Diffusion Limited by Thermal Off-Diagonal Electronic Disorder. *Phys. Rev. Lett.* **2006**, *96*, 086601.
23. Sanchez Carrera, R.S.; Paramonov, P.; Day, G.M.; Coropceanu, V.; Bredas, J.-L. Interaction of Charge Carriers with Lattice Vibrations in Oligoacene Crystals from Naphthalene to Pentacene. *J. Am. Chem. Soc.* **2010**, *132*, 14437–14446.
24. Su, W.P.; Schrieffer, J.R.; Heeger, A.J. Solitons in Polyacetylene. *Phys. Rev. Lett.* **1979**, *42*, 1698–1701.
25. Troisi, A. Prediction of the Absolute Charge Mobility of Molecular Semiconductors: The Case of Rubrene. *Adv. Mat.* **2007**, *19*, 2000–2004.
26. Troisi, A. Dynamic disorder in molecular semiconductors: Charge transport in two dimensions. *J. Chem. Phys.* **2011**, *134*, 034702.
27. Li, Y.; Coropceanu, V.; Bredas, J.-L. Nonlocal electron-phonon coupling in organic semiconductor crystals: The role of acoustic lattice vibrations. *J. Chem. Phys.* **2013**, *138*, 204713.
28. Fratini, S.; Ciuchi, S. Bandlike Motion and Mobility Saturation in Organic Molecular Semiconductors. *Phys. Rev. Lett.* **2009**, *103*, 266601.
29. Anderson, P.W. Absence of Diffusion in Certain Random Lattices. *Phys. Rev.* **1958**, *109*, 1492–1505.
30. Cataudella, V.; de Filippis, G.; Perroni, C.A. Transport properties and optical conductivity of the adiabatic Su-Schrieffer-Heeger model: A showcase study for rubrene-based field effect transistors. *Phys. Rev. B* **2011**, *83*, 165203.
31. Ortmann, F.; Bechstedt, F.; Hannewald, K. Theory of charge transport in organic crystals: Beyond Holstein's small-polaron model. *Phys. Rev. B* **2009**, *79*, 235206.
32. Perroni, C.A.; Nocera, A.; Ramaglia, V.M.; Cataudella, V. Spectral, optical, and transport properties of the adiabatic anisotropic Holstein model: Application to slightly doped organic semiconductors. *Phys. Rev. B* **2011**, *83*, 245107.
33. Gargiulo, F.; Perroni, C.A.; Ramaglia, V.M.; Cataudella, V. Electronic transport within a quasi-two-dimensional model for rubrene single-crystal field effect transistors. *Phys. Rev. B* **2011**, *84*, 245204.
34. Hannewald, K.; Bobbert, P.A. *Ab initio* theory of charge-carrier conduction in ultrapure organic crystals. *Appl. Phys. Lett.* **2004**, *85*, 1535–1537.
35. Hannewald, K.; Stojanović V. M., Schellekens J. M. T., Bobbert, P.A. Theory of polaron bandwidth narrowing in organic molecular crystals. *Phys. Rev. B* **2004**, *69*, 075211.
36. Perroni, C.A.; Ramaglia, V.M.; Cataudella, V. Effects of electron coupling to intramolecular and intermolecular vibrational modes on the transport properties of single-crystal organic semiconductors. *Phys. Rev. B* **2011**, *84*, 014303.
37. Perroni, C.A.; Cataudella, V. Interplay between electron-phonon coupling and disorder strength on the transport properties of organic semiconductors. *Phys. Rev. B* **2012**, *85*, 155205.

38. Perroni, C.A.; Cataudella, V. Bipolaron formation in organic semiconductors at the interface with dielectric gates. *Europhys. Lett.* **2012**, *98*, 47004.
39. Holstein, T. Studies of polaron motion: Part I. The molecular-crystal model. *Ann. Phys.* **1959**, *8*, 325–342.
40. Holstein, T. Studies of polaron motion: Part II. The small polaron. *Ann. Phys.* **1959**, *8*, 343–389.
41. Shehu, A.; Quiroga, S.D.; D'Angelo, P.; Albonetti, C.; Borgatti, F.; Murgia, M.; Scorzoni, A.; Stoliar, P.; Biscarini, F. Layered Distribution of Charge Carriers in Organic Thin Film Transistors. *Phys. Rev. Lett.* **2010**, *104*, 246602.
42. Girlando, A.; Grisanti, L.; Masino, M. Peierls and Holstein carrier-phonon coupling in crystalline rubrene. *Phys. Rev. B* **2010**, *82*, 035208.
43. Venuti, E.; Billotti, I.; della Valle, R.G.; Brillante, A.; Ranzieri, P.; Masino, M.; Girlando, A. Polarized Raman Spectra of a Rubrene Single Crystal. *J. Phys. Chem. C* **2008**, *112*, 17416–17422.
44. Nocera, A.; Perroni, C.A.; Ramaglia, V.M.; Cataudella, V. Stochastic dynamics for a single vibrational mode in molecular junctions. *Phys. Rev. B* **2011**, *83*, 115420.
45. Nocera, A.; Perroni, C.A.; Ramaglia, V.M.; Cataudella, V. Probing nonlinear mechanical effects through electronic currents: The case of a nanomechanical resonator acting as an electronic transistor. *Phys. Rev. B* **2012**, *86*, 035420.
46. Nocera, A.; Perroni, C.A.; Ramaglia, V.M.; Cantele, G.; Cataudella, V. Magnetic effects on nonlinear mechanical properties of a suspended carbon nanotube. *Phys. Rev. B* **2013**, *87*, 155435.
47. Perroni, C.A.; Nocera, A.; Cataudella, V. Single-parameter charge pumping in carbon nanotube resonators at low frequency. *Europhys. Lett.* **2013**, *103*, 58001.
48. Perroni, C.A.; Romeo, F.; Nocera, A.; Ramaglia, V.M.; Citro, R.; Cataudella, V. Noise-assisted Thouless pump in elastically deformable molecular junctions. *arXiv:1307.6834v1 [cond-mat.mes-hall]* **2013**.
49. Mahan, G.D. *Many-Particle Physics*, 2nd ed.; Plenum Press: New York, NY, USA, 1990.
50. Economou, E.N. *Green's Functions in Quantum Physics*; Springer Verlag: Berlin, Germany, 1983.
51. Perroni, C.A.; Piegari, E.; Capone, M.; Cataudella, V. Polaron formation for nonlocal electron-phonon coupling: A variational wave-function study. *Phys. Rev. B* **2004**, *69*, 174301.
52. Gunnarsson, O.; Calandra, M.; Han, J.E. Colloquium: Saturation of electrical resistivity. *Rev. Mod. Phys.* **2003**, *75*, 1085–1099.
53. Hannewald, K.; Bobbert, P.A. Anisotropy effects in phonon-assisted charge-carrier transport in organic molecular crystals. *Phys. Rev. B* **2004**, *69*, 075212.
54. Ishii, H.; Kobayashi, N.; Hirose, K. Strong anisotropy of momentum-relaxation time induced by intermolecular vibrations of single-crystal organic semiconductors. *Phys. Rev. B* **2013**, *88*, 205208.

55. Piegari, E.; Perroni, C.A.; Cataudella, V. Signatures of polaron formation in systems with local and non-local electron-phonon couplings. *Eur. Phys. J. B* **2005**, *44*, 415–421.
56. Ciuchi, S.; Fratini, S. Band Dispersion and Electronic Lifetimes in Crystalline Organic Semiconductors. *Phys. Rev. Lett.* **2011**, *106*, 166403.
57. Lang, I.J.; Firsov, Y.A. Kinetic Theory of Semiconductors with Low Mobility. *Sov. Phys. JETP* **1963**, *16*, 1301.
58. Iorio, A.; Perroni, C.A.; Ramaglia, V.M.; Cataudella, V. Electron-lattice and strain effects in manganite heterostructures: The case of a single interface. *Phys. Rev. B* **2011**, *83*, 085107.
59. Vukmirovic, N.; Bruder, C.; Stojanović, V.M. Electron-Phonon Coupling in Crystalline Organic Semiconductors: Microscopic Evidence for Nonpolaronic Charge Carriers. *Phys. Rev. Lett.* **2012**, *109*, 126407.
60. Kirova, N.; Bussac, M.-N. Self-trapping of electrons at the field-effect junction of a molecular crystal. *Phys. Rev. B* **2003**, *68*, 235312.
61. Li, Y.; Coropceanu, V.; Bredas, J.-L. Thermal Narrowing of the Electronic Bandwidths in Organic Molecular Semiconductors: Impact of the Crystal Thermal Expansion. *J. Phys. Chem. Lett.* **2012**, *3*, 3325–3329.
62. Ortmann, F.; Hannewald, K.; Bechstedt, F. *Ab initio* description and visualization of charge transport in durene crystals. *App. Phys. Lett.* **2008**, *93*, 222105.
63. Ortmann, F.; Hannewald, K.; Bechstedt, F. Charge Transport in Guanine-Based Materials. *J. Phys. Chem. B* **2009**, *113*, 7367–7371.

# Chapter 6

# Effects of Germanium Tetrabromide Addition to Zinc Tetraphenyl Porphyrin/Fullerene Bulk Heterojunction Solar Cells

**Atsushi Suzuki, Kenta Nishimura and Takeo Oku**

**Abstract:** The effects of germanium tetrabromide addition to tetraphenyl porphyrin zinc (Zn-TPP)/fullerene ($C_{60}$) bulk heterojunction solar cells were characterized. The light-induced charge separation and charge transfer were investigated by current density and optical absorption. Addition of germanium tetrabromide inserted into active layer of Zn-TPP/$C_{60}$ as bulk heterojunction had a positive effect on the photovoltaic and optical properties. The photovoltaic mechanism of the solar cells was discussed by experimental results. The photovoltaic performance was due to light-induced exciton promoted by insert of $GeBr_4$ and charge transfer from HOMO of Zn-TPP to LUMO of $C_{60}$ in the active layer.

Reprinted from *Electronics*. Cite as: Suzuki, A.; Nishimura, K.; Oku, T. Effects of Germanium Tetrabromide Addition to Zinc Tetraphenyl Porphyrin/Fullerene Bulk Heterojunction Solar Cells. *Electronics* **2014**, *3*, 112-121.

## 1. Introduction

Electronic applications including electronic devices and solar cell systems based on organic semiconductor of fullerenes as electron accepting material at physical-solid-state have been developed [1–11]. For instance, photovoltaic properties of vapor deposited solar cells using bulk heterojunction film of fullerenes/phthalocyanine have been characterized in regard to light-induced charge separation and photo current behavior [12]. Electronic conductor and optical device of photoactive layer based on porphyrin derivatives have been developed [13–15]. Molecular design and morphological structure of porphyrin is important to control electronic structure with energy levels at highest occupied molecular orbital (HOMO) and lowest unoccupied molecular orbital (LUMO) [16,17]. Donor activity of modified porphyrin in dye-sensitized solar cells is suggested to be one of the key factors in optimizing electronic structure, photovoltaic and optical properties. The effects of the additive in the ternary porphyrin blends on solid-state polymer/fullerene bulk heterojunction solar cells have been focused on improving the photovoltaic performance [18]. The effects of an additive solvent and diiodooctane on the aggregation of a high-efficiency donor polymer and an acceptor molecule of fullerene derivatives have been investigated [19–22]. In addition, the hybrid bulk heterojunction organic solar cells of CdSe-fullerene ($C_{60}$) composite films with insert of quantum dot have been studied for harvesting lighted-excited electrons in the active layer [23]. The quantum dot of CdSe, PbSe and PbS nanocrystal has advantage to promote multiple light-induced charge carriers with high energy excitations in a wide range of optical

absorption [24–28]. In a previous work, fabrication and characterization of bulk heterojunction of 5,10,15,20-tetraphenyl-21*H*,23*H*-porphyrin zinc (Zn-TPP) and $C_{60}$ has been studied [29]. The light-induced charge separation and charge transfer has been investigated by current density and optical absorption. Copper phthalocyanine/fullerene-based solar cells were also fabricated, and the electronic and optical properties were investigated [30]. Effects of germanium addition to the solar cells were also investigated, which resulted in an increase of power conversion efficiencies of the solar cells. Nanostructures of the solar cells were investigated by transmission electron microscopy and electron diffraction, which indicated formation of germanium compound nanoparticles in the copper phthalocyanine layers. Nanodiamond-based solar cells were fabricated and the photovoltaic properties were investigated [31]. The nanostructures of the solar cells were investigated by transmission electron microscopy and X-ray diffractometry, and the electronic property was discussed.

The purpose of this present paper is to investigate additive effect of germanium tetrabromide ($GeBr_4$) on the photovoltaic properties of the Zn-TPP/$C_{60}$ bulk heterojunction solar cells. The relationship between the photovoltaic properties and microstructure on the bulk heterojunction solar cells with insertion of $GeBr_4$ into the active layers has been focused on optimization of the photovoltaic performance. The photovoltaic mechanism will be discussed by experimental results.

## 2. Experimental Section

Fullerene ($C_{60}$, Material Technologies Research, 99.98%), 5,10,15,20-tetraphenyl-21*H*, 23*H*-porphyrin zinc (Zn-TPP, Sigma-Aldrich Japan KK, Tokyo, Japan) were used as received. A mixture of $C_{60}$ and Zn-TPP (10 mg) varied with weight ratio with $GeBr_4$ ($5 \times 10^{-3}$ mL, Sigma-Aldrich Japan KK, Tokyo, Japan) dissolved in o-dichlorobenzene (1 mL, Sigma-Aldrich Japan KK, Tokyo, Japan) was spin-coated on ITO (A11DU80, AGC Fabritech Co. Ltd., 10 Ω/sq., Tokyo, Japan). The thickness of the bulk heterojunction films was approximately 150 nm. The heterojunction film was prepared by vapor deposition process using diffusion vacuum pump ($10^{-3}$ Pa, ULVAC Inc., Tokyo, Japan). Heat treatment of these films on the ITO substrate was carried out at 100 °C for 30 min in $N_2$ atmosphere, aluminum (Al) metal with a thickness of 100 nm was evaporated on a top of electrode. Figure 1 shows schematic diagram of the present $C_{60}$/Zn-TPP solar cells as (a) the bulk heterojunction and (b) heterojunction films. Light and dark current density voltage (J-V) characteristics (Hokuto Denko Corp., HSV-100, Kanagawa, Japan) of the solar cells were measured under AM 1.5 (100 mW $cm^{-2}$) irradiation (Sanei Electric, XES-301S, Tokyo, Japan) in $N_2$ atmosphere. Optical properties of the bulk heterojunction film of $C_{60}$/Zn-TPP at solid state were measured by UV-vis spectroscopy (Hitachi U-4100, Tokyo, Japan) and fluorescence photo spectrometer (F-4500 Hitachi, Tokyo, Japan). Internal microstructure was observed by transmission electron microscope (TEM, 200 kV, Hitachi H-8100, Tokyo, Japan) with electron diffraction. TEM is a useful method for nanostructure analysis. The polycrystal structure in the bulk heterojunction film was measured by thin X-ray reflection patterns (X'Pert-MPD system Philips Co. Ltd., Eindhoven, The Netherlands) using CuKα radiation. The chemical structures were optimized by CS Chem3D (Cambridge Soft, PerkinElmer Inc., Boston, MA, USA). Molecular orbital calculations were carried out by MOPAC (Fujitsu Ltd., Tokyo, Japan). In addition, the isolated molecular structures were optimized by quantum calculation using spin-restricted Hartree-Fock method (RHF) using 6-31G*

as basis set (Gaussian 03, Gaussian Inc., Pittsburgh, PA, USA). The electronic structures of electron densities with energy levels at HOMO and LUMO were investigated.

**Figure 1.** Structure of bulk heterojunction solar cells.

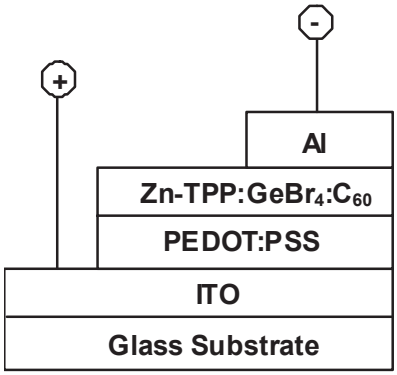


## 3. Results and Discussion

Dark and light induced current density-voltage (J-V) characteristics of the bulk heterojunction solar cells with weight ratio of Zn-TPP and $C_{60}$ with $GeBr_4$ were investigated. The dark J-V curve displayed a gradual increase of current for positive bias to the Zn-TPP electrode. This behavior indicates a light-induced charge separation with charge-transfer at the interface. Table 1 lists measured parameters on the bulk heterojunction solar cell varied with weight ratio of Zn-TPP/$C_{60}$ to $GeBr_4$.

**Table 1.** Measured parameters on bulk heterojunction solar cells of Zn-TPP/$C_{60}$ with $GeBr_4$.

| Zn-TPP:$C_{60}$ | η (%) | FF | $V_{oc}$ (V) | $J_{sc}$ (mA cm$^{-2}$) |
|---|---|---|---|---|
| 3:7 | $2.2 \times 10^{-5}$ | 0.23 | 0.058 | 0.0017 |
| 2:8 | $9.5 \times 10^{-4}$ | 0.20 | 0.25 | 0.019 |
| 1:9 | $1.3 \times 10^{-2}$ | 0.29 | 0.26 | 0.17 |
| **Additive-free** | | | | |
| 1:9 | $6.4 \times 10^{-3}$ | 0.20 | 0.23 | 0.14 |

At weight ratio of Zn-TPP to $C_{60}$ of 3:7 by adding $GeBr_4$, $V_{oc}$, $J_{sc}$, FF, and η were obtained to be 0.058 V, 0.0017 mA cm$^{-2}$, 0.23 and $2.2 \times 10^{-5}$%, respectively. The photovoltaic performance including the measured parameters was gradually improved with increasing weight ratio of $C_{60}$ in Zn-TPP/$C_{60}$ by adding $GeBr_4$. At weight ratio of Zn-TPP/$C_{60}$ in 1:9, the solar cells performance regarded $V_{oc}$, $J_{sc}$, and FF at 0.26 V, 0.17 mA cm$^{-2}$ and 0.29, which could estimate to be conversion efficiency of $1.3 \times 10^{-2}$%. As reference case at weight ratio in 1:9 without addition of $GeBr_4$, the measured parameters, $V_{oc}$, $J_{sc}$, FF, and η were obtained to be 0.23 V, 0.14 mA cm$^{-2}$, 0.20 and $6.4 \times 10^{-3}$%, respectively. Additionally, quantitative analysis of variable amount of $GeBr_4$ was performed on the bulk heterojunction solar cell at weight ratio of Zn-TPP/$C_{60}$ in 1:9. At a fixed amount of $GeBr_4$ in 0.025 mL, the photovoltaic parameters, $V_{oc}$, $J_{sc}$, FF, and η were obtained to be 0.0013 V, 0.0004 mA cm$^{-2}$, 0.25 and $1.3 \times 10^{-7}$%. The exceed addition reduced the photovoltaic performance. The condition of Zn-TPP/$C_{60}$ at weight ratio in 1:9 with additive volume of $GeBr_4$ in 0.005 mL optimized the photovoltaic performance. The photovoltaic properties were due to

light-induced charge separation with charge-transfer from HOMO of Zn-TPP to LUMO of $C_{60}$ in the active layer with insert of $GeBr_4$.

Optical absorptions of the bulk heterojunction solar cells at weight ratio of Zn-TPP/$C_{60}$ in 1:9 with insert of $GeBr_4$ in 0.005 mL are shown in Figure 2. The bulk heterojunction of Zn-TPP/$C_{60}$ had a strong optical absorption in the range of 300 nm–1300 nm. Especially, insertion of $GeBr_4$ in the active layer improved the optical absorption in the range of 300 nm–500 nm and 800 nm–1000 nm. The observed absorption at 350 nm, 480 nm to 1050 nm was converted to energy level of 3.5 eV, 2.6 eV and 1.2 eV, respectively. Enlargement of the optical absorption would be attributed from increase of the light-induced exciton in the active layer with insert of $GeBr_4$.

**Figure 2.** UV-vis absorptions of bulk heterojunction thin films of tetraphenyl porphyrin zinc (Zn-TPP) and $C_{60}$ at weight ratio of 1:9 with insert of $GeBr_4$.

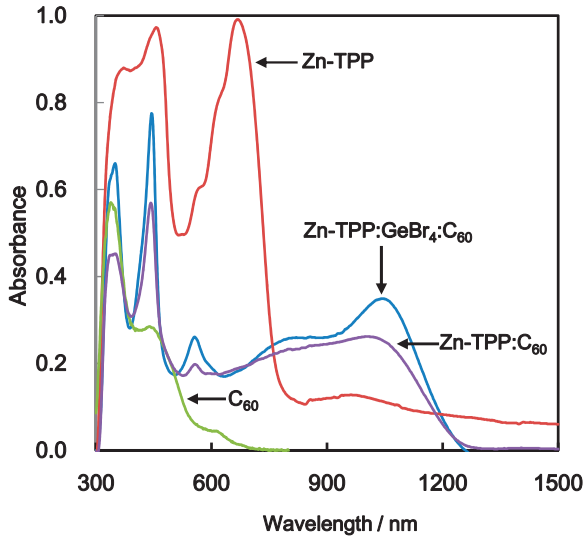


X-ray diffractions of the bulk heterojunction film at weight ratio of Zn-TPP/$C_{60}$ in 1:9 by adding $GeBr_4$ on glass substrate are shown in Figure 3. The X-ray diffraction patterns displayed the crystal order of $C_{60}$, which confirmed tetragonal system noted in crystal index, 111, 220, 311, 220, 420, 422 and 511 in a range of 10° and 33° in 2 θ. There existed a strong peak of Zn-TPP with a small peak at 5° and 22° in 2 θ. The diffraction patterns using the Sherrer's formula suggested that there were about 6 nm of particle sizes in the tetragonal system. The crystal growth of $C_{60}$ was inhibited by insertion of the germanium bromide into the active layer. The germanium crystal was not confirmed around 2 θ in the range of 25°–50° [32].

Figure 4 show (a) TEM image and (b) electron diffraction of the bulk heterojunction film at weight ratio of 1:9 with $GeBr_4$. As shown in Figure 4a, the molecules of $C_{60}$ were coagulated with each other to form the particle as grain size in the range of 10 nm–20 nm. The TEM image displayed the crystal lattice of $C_{60}$ to be about 0.38 nm at 111 in crystal index as tetragonal phase in the polycrystal structure. The electron diffraction patterns through the incident angle at [$\bar{1}$ 1 2] indicated that the polycrystal coagulation of $C_{60}$ had tetragonal structure as noted in crystal index at 111, 210 and 311 with a strong spot as Zn-TPP. The amorphous coagulations were dispersed in the range of 18–30 nm as the particle size. The amorphous coagulations as intrinsic germanium

compound appeared to be semi-conductive behavior with a narrow band-gap in the range of 0.8–2.2 eV [33] as shown in Figure 5.

**Figure 3.** X-ray diffraction patterns of the bulk heterojunction thin films.

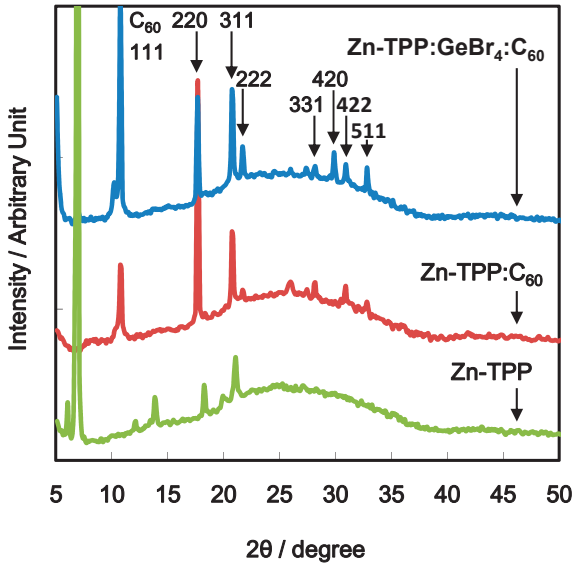


**Figure 4.** (**a**) TEM image and (**b**) electron diffraction pattern of the bulk heterojunction thin film.

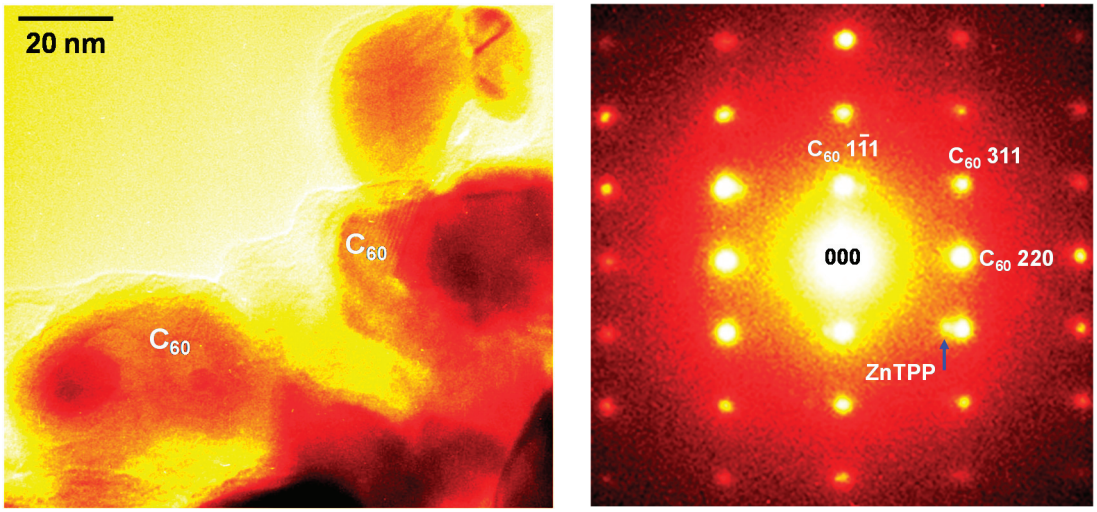


(**a**) (**b**)

As a reference case to support the experiment result, the coagulations of the germanium compound converted from germanium bromide saturated ionic liquid 1-butyl-3-methylimidazolium hexafluorophosphate on Au (111) has been studied with in-situ scanning tunneling microscopy [34]. The tunneling spectrum of an approximately 500 nm thick germanium compound film saturated ionic liquid on Au (111) suggested semiconductive behavior with a typical band gap of 0.7 eV, which made a good agreement with the value of 0.67 eV for intrinsic coagulations of germanium compound.

In the presence work, insert of coagulations of germanium compound into the active layer improved the light-induced exciton with charge transfer near the interface in microstructure. In actual conditions,

energy loss would be generated by the Schottky barrier at the interface between Zn-TPP, $C_{60}$, and $GeBr_4$ on Al substrate. The heat treatment of the internal microstructure near interface between the crystal phase of $C_{60}$ and Zn-TPP with insert of $GeBr_4$ will guide a considerable support to inhibit recombination between electrons and holes, which will improve the photovoltaic performance with increasing $J_{sc}$ and η in the J-V curve.

**Figure 5.** Energy level diagram of the bulk heterojunction solar cell.

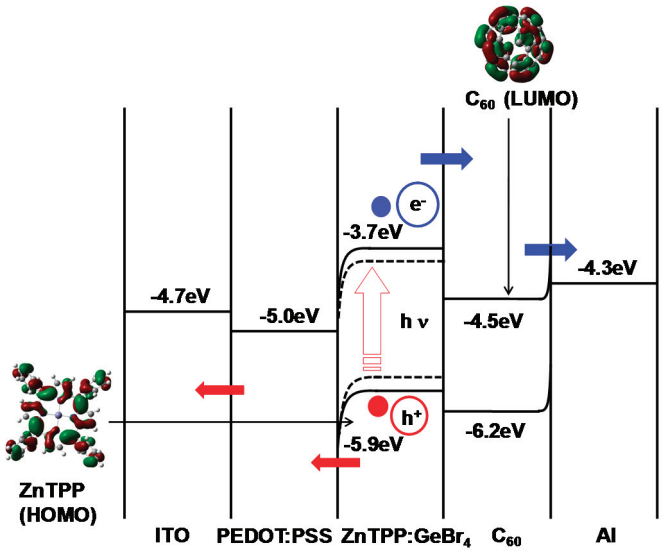


The photovoltaic mechanism of the bulk heterojunction solar cells was discussed by the experimental results. Schematic energy diagrams of the present solar cells with energy levels were summarized as shown in Figure 5. The photovoltaic mechanism of the present solar cells was discussed as follows. The light irradiation immediately generated charge-separation with a band gap between HOMO of Zn-TPP and LUMO of $C_{60}$ with insert of $GeBr_4$. The electrons were excited at a conductive bond, and holes generated at valence band. Suddenly, the excited electrons of Zn-TPP were injected from the conductive band to that of $C_{60}$ at the crystal phase. In addition, the bulk heterojunction solar cell at an excess amount of $C_{60}$ showed improvement in the light-induced exciton with an insert of $GeBr_4$ and the electron diffusion without trapping at interface between inner regions near interface, which suggested an increase of $J_{sc}$ related to carrier mobility, as a result of increasing the conversion efficiency. In contrast, the holes of Zn-TPP at the valence band suddenly charge-transferred to PEDOT:PSS on electrolyte. $V_{oc}$ of the solar cells were related with an energy gap between HOMO of Zn-TPP and LUMO of $C_{60}$ narrowed with an insert of $GeBr_4$. Controlling the electronic structure and the energy gap between HOMO and LUMO is an important factor for improving the photovoltaic performance with the conversion efficiency. Recently, electronic structures with the energy gap between HOMO and LUMO have been studied by quantum chemical calculation using DFT [16,17].

In this present work, the electronic structures of Zn-TPP with the HOMO-LUMO gap were calculated by DFT. The molecular orbital of Zn-TPP and $C_{60}$ at HOMO, LUMO with the energy levels are shown in Figure 5. Modified porphyrin derivatives combined with phenyl group as electron-donating affinity suggests uniformity on electron density distribution, which becomes a strong donor as *p*-type semiconductor with a narrow band gap of energy level between HOMO and

LUMO. The strong affinity to accept substitutions with a low distribution of electron density in the aromatic ring would support the use of an electron acceptor as n-type semiconductor. The chemical modification of porphyrin has a great advantage to generate light-induced charge separation, suggesting improvement of the photovoltaic performance. Improvement of internal structure would promote injection of electron excitation near interface between Zn-TPP and $C_{60}$ in the internal microstructure. The heat treatment of the microstructure would recover the light-induced charge separation, and then the extent of carrier diffusion, which would result in an improvement of the photovoltaic performance. Additionally, insertion of the semi-conductive coagulations based on germanium compound into the active layer would support the promotion of excitation under the Plasmon field effect.

As an advantage, the coagulations with semi-conductive particles of germanium compound converted from $GeBr_4$ had strong absorption with a low-wave length for improvement of photovoltaic performance. In order to incorporate the coagulations with the semi-conductive particles in the active layer, organic solvent with the coagulations of the particles needs to be used in the manufacturing process. For instance, $GeBr_4$ has melting point at 26.1 °C. The material shows melting characteristics at 30 °C above the melting point and easily dissolves in organic solvent. The material has an advantage when used in dispersion in the organic active layer. By annealing treatment, $Ge_3Br_4$ was de-composited with removing bromine atom to form the coagulations of the particles under device fabrication condition. The coagulations of amorphous germanium compound into the active layer were dispersed in a range of 20–30 nm in the size. Addition of the coagulations into the active layer had a positive effect on the photovoltaic and optical properties.

Several points of view from cost, toxicity and hazard will be discussed regarding the use of organic solar cells. Additives of $GeBr_4$ have slightly higher cost associated with their industrial application. If mass production using organic layer with $GeBr_4$ is used for applying the organic solar cell, the production cost and price will be reduced in practical use. In the toxicity and hazard points, organic active layer including a large amount of $GeBr_4$ will cause hydrolysis reaction and inflammation on mucosal tissues. However, the experimental condition with a small amount of the coagulations of the particles converted from $GeBr_4$ will be applied for developing safe devices. The organic active layer including the coagulations of the semi-conductive particles had an advantage in improvement of the photovoltaic performance. The photovoltaic mechanism of the solar cells was discussed by experimental results. The photovoltaic performance was originated in the light-induced carrier separation promoted by insert of $GeBr_4$ and charge transfer from HOMO of Zn-TPP to LUMO of $C_{60}$ in the active layer. Instead of inserting the coagulations of the particles, organic solvent with incorporation of silicon compounds and polysilane derivatives will be used for fabrication of an organic solar cell.

## 4. Conclusions

The effects of germanium tetrabromide addition to Zn-TPP/$C_{60}$ bulk heterojunction organic solar cells were characterized. The light-induced charge separation with charge transfer was investigated by current density and optical absorption. Addition of $GeBr_4$ into active layer of Zn-TPP/$C_{60}$ had a positive effect on the photovoltaic and optical properties. The TEM image, X-ray and electron diffraction patterns showed the crystal lattice of $C_{60}$ to be about 0.38 nm at 111 in crystal index at the

tetragonal phase with a strong spot as crystal structure of Zn-TPP. The coagulations of amorphous germanium compound into the active layer were dispersed in a range of 20–30 nm in size. Addition of the coagulations into the active layer had a positive effect on the photovoltaic and optical properties. The photovoltaic mechanism of the solar cells was discussed by experimental results. The photovoltaic performance was due to the light-induced carrier separation promoted by insert of $GeBr_4$ and charge transfer from HOMO of Zn-TPP to LUMO of $C_{60}$ in the active layer.

## Conflicts of Interest

The authors declare no conflict of interest.

## References


1. Kroto, H.W.; Heath, J.R.; O'Brien, S.C.; Curl, R.F.; Smalley, R.E. $C_{60}$: Buckminsterfullerene. *Nature* **1985**, *318*, 162–163.
2. Steven, C.E.; Warren, E.P. Theoretical Fermi-Surface Properties and Superconducting Parameters for $K_3C_{60}$. *Science* **1991**, *254*, 842–845.
3. Allemand, P.-M.; Khemani, K.C.; Koch, A.; Wudl, F.; Holczer, K.; Donovan, S.; Gruner, G.; Thompson, J.D. Organic Molecular Soft Ferromagnetism in a Fullerene $C_{60}$. *Science* **1991**, *253*, 301–302.
4. Mihailovic, D.; Arcon, D.; Venturini, P.; Blinc, R.; Omerzu, A.; Cevc, P. Orientational and Magnetic Ordering of Buckyballs in TDAE-$C_{60}$. *Science* **1995**, *268*, 400–402.
5. Lappas, A.; Prassides, K.; Vavekis, K.; Arcon, D.; Blinc, R.; Cevc, P.; Amato, A.; Feyerherm, R.; Gygax, F.N.; Schenck, A. Spontaneous Magnetic Ordering in the Fullerene Charge-Transfer Salt (TDAE)$C_{60}$. *Science* **1995**, *267*, 1799–1802.
6. Khlyabich, P.P.; Burkhart, B.; Rudenko, A.E.; Barry, C. Optimization and Simplification of Polymer-Fullerene Solar Cells through Polymer and Active Layer Design. *Polymer* **2013**, *54*, 5267–5298.
7. Marrocchi, A.; Lanari, D.; Facchettibc, A.; Vaccaro, L. Poly(3-hexylthiophene): Synthetic Methodologies and Properties in Bulk Heterojunction Solar Cells. *Energy Environ. Sci.* **2012**, *5*, 8457–8474.
8. Roncali, J. Single Material Solar Cells: The Next Frontier for Organic Photovoltaics? *Adv. Energy Mater.* **2011**, *1*, 147–160.
9. Brabec, C.J.; Gowrisanker, S.; Halls, J.J.M.; Laird, D.; Jia, S.; Williams, S.P. Polymer-Fullerene Bulk-Heterojunction Solar Cells. *Adv. Mater.* **2010**, *22*, 3839–3856.
10. Liao, H.C.; Tsao, C.S.; Lin, T.H.; Jao, M.H.; Chuang, C.M.; Chang, S.Y.; Huang, Y.C.; Shao, Y.T.; Chen, C.Y.; Su, C.J.; *et al*. Nanoparticle-Tuned Self-Organization of a Bulk Heterojunction Hybrid Solar Cell with Enhanced Performance. *ACS Nano* **2012**, *6*, 1657–1666.
11. Chen, W.; Xu, T.; He, F.; Wang, W.; Wang, C.; Strzalka, J.; Liu, Y.; Wen, J.; Miller, D.J.; Chen, J.; *et al*. Hierarchical Nanomorphologies Promote Exciton Dissociation in Polymer/Fullerene Bulk Heterojunction Solar Cells. *Nano Lett.* **2011**, *11*, 3707–3713.

12. Brousse, B.; Ratier, B.; Moliton, A. Vapor deposited solar cells based on heterojunction or interpenetrating networks of zinc phthalocyanine and $C_{60}$. *Thin Solid Films* **2004**, *451–452*, 81–85.
13. Donzello, M.P.; Ercolani, C.; Kadish, K.M.; Ricciardi, G.; Rosa, A.; Stuzhin, P.A. Tetrakis (thiadiazole)porphyrazines. 5. Electrochemical and DFT/TDDFT studies of the free-base macrocycle and its $Mg^{II}$, $Zn^{II}$, and $Cu^{II}$ complexes. *Inorg. Chem.* **2007**, *46*, 4145–4157.
14. David, C.; Hans, G.; Mathieu, O.; Jef, P.; Paul, H. Stacked organic solar cells based on pentacene and $C_{60}$. *Solar Energy Mater. Solar Cells* **2007**, *91*, 399–404.
15. Mauro, M.; Matthias, W.; Alberta, B.; Nikos, K.; Sean, S.; Markus, S.; Zhengguo, Z.; David, W.; Russell, G.; Christoph, B. Bipolar Charge Transport in PCPDTBT-PCBM Bulk-Heterojunctions for Photovoltaic Applications. *Adv. Funct. Mater.* **2008**, *18*, 1757–1766.
16. Park, J.K.; Lee, H.R.; Chen, J.; Shinokubo, H.; Osuka, A.; Kim, D. Photoelectrochemical Properties of Doubly β-Functionalized Porphyrin Sensitizers for Dye-Sensitized Nanocrystalline-$TiO_2$ Solar Cells. *J. Phys. Chem. C* **2008**, *112*, 16691–16699.
17. Ruimin, M.; Ping, G.; Linlin, Y.; Lianshun, G.; Xianxi, Z.; Mohammad, K.N.; Michael, G. Theoretical Screening of $-NH_2$-, $-OH$-, $-CH_3$-, $-F$-, and $-SH$-Substituted Porphyrins As Sensitizer Candidates for Dye-Sensitized Solar Cells. *J. Phys. Chem. A* **2010**, *114*, 1973–1979.
18. Dastoor, P.C.; McNeill, C.R.; Frohne, H.; Foster, C.J.; Dean, B.; Fell, C.J.; Belcher, W.J.; Campbell, W.M.; Officer, D.L.; Blake, I.M.; *et al*. Understanding and Improving Solid-State Polymer/$C_{60}$-Fullerene Bulk-Heterojunction Solar Cells Using Ternary Porphyrin Blends. *J. Phys. Chem. C* **2007**, *111*, 15415–15426.
19. Chen, F.C.; Tseng, H.C.; Ko, C.J. Solvent mixtures for improving device efficiency of polymer photovoltaic devices. *Appl. Phys. Lett.* **2008**, *92*, 103316.
20. Lou, S.J.; Szarko, J.M.; Xu, T.; Yu, L.; Marks, T.J.; Chen, L.X. Effects of Additives on the Morphology of Solution Phase Aggregates Formed by Active Layer Components of High-Efficiency Organic Solar Cells. *J. Am. Chem. Soc.* **2011**, *133*, 20661–20663.
21. Freitas, J.N.D.; Nogueira, A.F. Incorporation of Inorganic Nanoparticles into Bulk Heterojunction Organic Solar Cells. *Nanoenergy* **2013**, doi:10.1007/978-3-642-31736-1_1.
22. Lua, A.J.; Beaupréb, S.; Leclercb, M.; Taoa, Y. Control of the active layer nanomorphology by using co-additives towards high-performance bulk heterojunction solar cells. *Org. Electron.* **2012**, *13*, 1736–1741.
23. Patrick, B.; Prashant, V.K. Quantum Dot Solar Cells. Electrophoretic Deposition of CdSe-$C_{60}$ Composite Films and Capture of Photogenerated Electrons with n$C_{60}$ Cluster Shell. *J. Am. Chem. Soc.* **2008**, *130*, 8890–8891.
24. Nozik, A.J. Quantum dot solar cells. *Phys. E* **2002**, *14*, 115–120.
25. Istvan, R.; Vaidyanathan, S.; Masaru, K.; Prashant, V.K. Quantum Dot Solar Cells. Harvesting Light Energy with CdSe Nanocrystals Molecularly Linked to Mesoscopic $TiO_2$ Films. *J. Am. Chem. Soc.* **2006**, *128*, 2385–2393.
26. Richard, D.S.; Vladimir, M.A.; Victor, C.K. High-efficiency carrier multiplication through direct photogeneration of multi-excitons via virtual single-exciton states. *Nat. Phys.* **2005**, *1*, 189–194.

27. Randy, J.E.; Matthew, C.B.; Justin, C.J.; Pingrong, Y.; Olga, I.M.; Arthur, J.N.; Andrew, S.; Alexander, L.E. Highly efficient multiple exciton generation in colloidal PbSe and PbS quantum dots. *Nano Lett.* **2005**, *5*, 865–871.
28. Luque, A.; Martí, A.; López, N.; Antolín, E.; Cánovas, E.; Stanley, C.; Farmer, C.; Caballero, L.J.; Cuadra, L.; Balenzategui, J.L. Experimental analysis of the quasi-Fermi level split in quantum dot intermediate-band solar cells. *Appl. Phys. Lett.* **2005**, *87*, 083505:1–083505:3.
29. Oku, T.; Noma, T.; Suzuki, A.; Kikuchi, K.; Kikuchi, S. Fabrication and characterization of fullerene/porphyrin bulk heterojunction solar cells. *J. Phys. Chem. Solid.* **2010**, *71*, 551–555.
30. Oku, T.; Kumada, K.; Suzuki; A.; Kikuchi, K. Effects of germanium addition to copper phthalocyanine/fullerene-based solar cells. *Cent. Eur. J. Eng.* **2012**, *2*, 248–252.
31. Nagata, A.; Oku, T.; Kikuchi, K.; Suzuki, A.; Yamasaki, Y.; Osawa, E. Fabrication, nanostructures and electronic properties of nanodiamond-based solar cells. *Prog. Nat. Sci.* **2010**, *20*, 38–42.
32. Vijayarangamuthu, K.; Rath, S.; Kabiraj, D.; Avasthi, D.K.; Kulriya, P.K.; Singh, V.N.; Mehta, B.R. Ge nanocrystals embedded in a $GeO_x$ matrix formed by thermally annealing of Ge oxide films. *J. Vac. Sci. Technol. A* **2009**, *27*, 731–733.
33. Ardyanian, M.; Rinnert, H.; Vergnat, M. Structure and photoluminescence properties of evaporated $GeO_x/SiO_2$ multilayers. *J. App. Phys.* **2006**, *100*, 113106:1–113106:4.
34. Frank, E.; Sherif, Z.E.A. Nanoscale electrodeposition of germanium on Au (111) from an ionic liquid: An *in situ* STM study of phase formation Part I. Ge from $GeBr_4$. *Phys. Chem. Chem. Phys.* **2002**, *4*, 1640–1648.

# Section III: Organic Field Effect Transistors

## Chapter 7

# Organic Thin-Film Transistor (OTFT)-Based Sensors

**Daniel Elkington, Nathan Cooling, Warwick Belcher, Paul C. Dastoor and Xiaojing Zhou**

**Abstract:** Organic thin film transistors have been a popular research topic in recent decades and have found applications from flexible displays to disposable sensors. In this review, we present an overview of some notable articles reporting sensing applications for organic transistors with a focus on the most recent publications. In particular, we concentrate on three main types of organic transistor-based sensors: biosensors, pressure sensors and "e-nose"/vapour sensors.

Reprinted from *Electronics*. Cite as: Elkington, D.; Cooling, N.; Belcher, W.; Dastoor, P.C.; Zhou, X. Organic Thin-Film Transistor (OTFT)-Based Sensors. *Electronics* **2014**, *3*, 234-254.

### 1. Introduction

Organic thin-film transistors (OTFTs) have been the subject of much attention in the scientific research community in recent decades [1,2]. Due to their potential to be low-cost and their ease of fabrication, OTFTs seem ideal for use in sensing applications in which there may be a desire for cheap, single-use or disposable devices that can deliver accurate results. For example, an array of sensing devices can be printed in one device to realize a true "lab-on-chip" proposition for determining the concentration of certain target analytes in a sample. In addition, organic materials are more likely to be compatible with highly selective biological recognition elements, such as enzymes, which can form the basis for effective sensors.

There have already been many review articles in recent years summarizing research into sensing devices that integrate OTFTs into their architecture. This review intends to focus on articles that have reported OTFT-based sensors falling into one of three categories—biosensors, pressure sensors and those detecting vapour-phase analytes for "electronic nose" applications—for the authors feel these three types of sensor are the least explored by other reviews in this highly dynamic field. Some historically significant papers in the chosen areas will be introduced in each section initially, before the focus is turned to papers contributing to the respective fields more recently. This scope was determined both by the interests of the authors and also the desire to avoid repetition through the review of some types of OTFT-based sensors, such as those detecting pH, humidity or certain ionic species, which have been given the most attention in some recent review articles on organic transistor-based sensors as a whole [3,4]. One exception to this scope is biosensors based on proton-liberating enzymatic reactions, which can also be regarded as pH sensors [5], that are included here as enzyme-based biosensors.

*Organic Thin Film Transistors*

OTFTs are three-terminal electrical devices that, much like conventional transistors, allow for the control of the electrical current flowing between two electrodes (source and drain) through the modulation of voltage (or current) at a third electrode (the gate). The term OTFT can be generically used to refer to most types of organic transistor; however (depending on the mechanism used to achieve the current modulation), organic transistors are typically categorized into one of several categories. These categories include (but are not limited to):

- Organic field effect-transistors (OFETs): OFETs operate in a similar way to conventional MOSFET (metal-oxide-semiconductor field effect transistor) or TFT (thin-film transistor) devices in which an electric field is established across a dielectric layer separating the gate electrode from the semiconductor layer (Figure 1a). This electric field can manipulate the size and shape of a region of high conductivity in, and hence, modulate the current flowing through, the semiconductor material, creating a relationship between gate voltage ($V_G$) and drain current ($I_D$).
- Organic electrochemical transistors (OECTs): OECTs operate by inducing a reduction or oxidation reaction, which influences $I_D$, due to a voltage at the gate electrode. Often, these devices can resemble conventional three-terminal electrochemical cells in which the source, drain and gate electrodes play the roles of the working, counter and reference electrodes. Other types of OECTs more closely resemble a standard OFET in which some electrochemical reaction is taking place at an interface of the semiconductor to facilitate current modulation. Many of the other categories of devices listed below could be thought of as sub-categories of OECTs.
- Electrolyte-gated organic field effect transistors (EGOFETs): EGOFETs employ an electrolyte layer (in either a solid or liquid form) to separate the gate electrode from the semiconductor layer (Figure 1b). This electrolyte layer allows for ionic movement within it, and this leads to the build-up of charge at its interfaces and subsequent electrochemical reactions. One advantage of EGOFETs is their low operating voltage; however, they can suffer from poor switching speeds, due to their reliance on electrochemical activity [6]. EGOFETs featuring ion-selective membranes, which could improve their ability to be applied in sensing applications, have also been successfully demonstrated recently [7].
- Ion-sensitive OFETs (ISOFETs): an analogue to the ion-sensitive FET (ISFET) family of silicon-based devices, ISOFETs are similar to EGOFETs in that they have an electrolyte layer adjacent to the gate electrode (Figure 1c). However, unlike EGOFETs, ISOFETs also have a dielectric layer, which isolates the electrolyte from the semiconductor [8].
- Hygroscopic-insulator field effect transistors (HIFETs): HIFETs could be considered a sub-category of both OECTs and EGOFETs. Initially proposed by the group of Österbacka *et al.* [9], HIFETs rely on the hygroscopic nature of their dielectric layer to create a moist environment for the free movement of ions within it. These ions then can interact with the semiconductor at the dielectric/semiconductor interface electrochemically and/or electrostatically to modulate current through the semiconductor (*i.e.*, $I_D$) by varying $V_G$.

- Carbon nanotube FETs (CNTFET or NTFETs): these devices use one or many carbon nanotubes as the material (semiconductor) connecting the source and drain electrodes (Figure 1d). CNTFETs are seen as promising devices for use in all types of electronics, due to the excellent electronic properties of carbon nanotubes (CNTs) [10]. In terms of biosensors, encapsulation by CNTs has been shown as an effective way to immobilise bio-recognition elements [11].
- Organic charge-modulated FETs (OCMFETs): OCMFETs are a relatively new category of organic transistor, which have been proposed by the group of Bonfiglio *et al.* specifically for the purpose of sensing, and are somewhat similar in structure to ISOFETs [12,13]. However, OCMFETs have two gate electrodes: one, a "reference gate", which is held at a fixed electrical potential (biasing the device), as well as a "floating gate", which is coupled to the other gate electrode and to the rest of the device through a common dielectric layer (Figure 1e). The floating gate is electrically connected to the "sensing area" upon which charge is accumulated, depending on the quantity of analyte present. Two of the main claimed advantages of OCMFETs is that they can be miniaturised relative to similar devices implementing a reference electrode and also that the semiconductor is not directly exposed to analyte solution.

**Figure 1.** Simplified diagrams of various types of organic thin-film transistor (OTFT): (**a**) organic field effect-transistor (OFET) (bottom-gate, top-contact version shown); (**b**) electrolyte-gated organic field effect transistor (EGOFET); (**c**) ion-sensitive OFET (ISOFET); (**d**) carbon nanotube FET (CNTFET); and (**e**) organic charge-modulated FET (OCMFET).

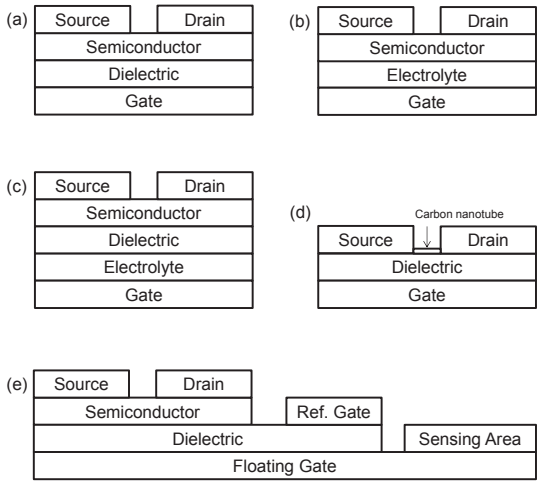


OTFTs are well-suited for use in biosensing applications, due to the biocompatibility of the materials used with biological recognition elements, such as enzymes [14]. Traditional electronic materials, such as silicon and metals, require high processing temperatures and are non-porous and, as such, are not well suited for incorporating enzymes, which denature at high temperatures and require direct contact with their target analyte molecules. In addition, the low-cost fabrication possibilities of organic electronic materials increase their practicality in throw-away applications in which sensors may be desired to be used. Furthermore, the drawbacks of organic semiconductors, such as their relatively low charge carrier mobility, which prevents them from competing with their

conventional counterparts (such as silicon) in applications requiring high switching speeds, for example, are less crucial to many sensing applications, in which taking tens or even hundreds of seconds to generate a detection result is quite acceptable. In addition, organic semiconductors, such as poly(3-hexylthiophene) (P3HT), can be readily modified through the deposition of a thin interfacial layer in order to immobilize biological recognition elements for use in OTFT-based sensors [15].

## 2. Biosensors

Detecting and measuring the concentration of certain biological moieties is critical to many medical and other scientific applications. For example, some of the analytes targeted by sensors discussed below in this review are markers that show the presence or onset of disease or other health problems. However, before examining the existing research in the area of organic transistor-based biosensors, it is worth defining what constitutes a biosensor, since various definitions of a biosensor have been proposed within the existing body of literature. For the purposes of this review, as in the previous review by Kergoat *et al.* [6], we will use the IUPAC's "Gold book" definition, which considers any device that "uses specific biochemical reactions mediated by isolated enzymes, immunosystems, tissues, organelles or whole cells to detect chemical compounds usually by electrical, thermal or optical signals" to be a biosensor [16], and this review will focus on those devices with an electrical output integrated with one of the many varieties of OTFT.

Biosensors have enjoyed steady development since the earliest papers on the subject were published (such as the 1962 report by Clark and Lyons [17]). There have been some excellent review articles summarizing publications on biosensors employing organic electronics in recent years [3,4,6]. However, in this highly dynamic area, improvements to the selectivity and resolution of sensors, as well as the introduction of new materials are often being reported, as research groups gradually develop devices with a view toward commercial use in the not-too-distant future.

This review will summarize the field with a focus on recent advances, and the publications discussed will be organized into three sections. The first section focusses on those sensors detecting glucose enzymatically using glucose oxidase (GOx), since this system has had much attention in the development of new methods and platforms for biosensing. The next section is dedicated to sensors based on enzymes other than glucose oxidase, since the number of publications using non-GOx enzymes has increased recently. Thirdly, sensors that detect biological analytes by non-enzymatic mechanisms will be discussed in the third section. Any types of sensors involving inorganic semiconductor layers in their transistor will not be covered in this review.

### *2.1. Enzymatic Glucose Sensing*

The detection of glucose using GOx has long been used as a model detection system [18] and has been included in biosensor studies going back to the 1960s [17]. This extensive use can be attributed to three reasons. Firstly, the reaction with glucose, which is catalysed by glucose oxidase, has been very clearly defined and well understood for many years, making it ideal for use in situations with other unknown factors, such as newly-developed sensing platforms. Indeed, the high stability and specificity of GOx has led to it being referred to as "the ideal enzyme" [19]. Secondly, $H_2O_2$, a by-product of the glucose-GOx reaction, can electrochemically react with (oxidize) conjugated

polymers, causing a change in conductivity [20], as well as an electrochemical break down when exposed to an electrical potential into by-products, including charge carriers, making for two potential sources of generating an electrical signal (see Equations (1) and (2)). Thirdly, and crucially, the sensing of glucose has many extremely useful medical applications; in particular, for the monitoring of blood-glucose levels in sufferers of diabetes.

$$Glucose \xrightarrow[GOx]{} Gluconic\ acid + H_2O_2 \quad (1)$$

$$H_2O_2 \xrightarrow[0.7\ V\ vs\ SCE]{} O_2 + 2H^+ + 2e^- \quad (2)$$

As early as the 1980s, there have been reports of enzymatic glucose detection using GOx along with organic electronic materials, such as polypyrrole (PPy). Typically, the method reported involved using conventional electrochemical techniques, such as cyclic voltammetry [21,22]. In more recent years, there has been increased attention on developing a more fully integrated sensor using GOx as the detection mechanism and OTFTs to provide the electrical signal to be measured.

In 2004, Zhu *et al.* demonstrated an OECT-based sensor in which PEDOT:PSS was the semiconducting layer of the transistors, and a "well" (constructed from polydimethylsiloxane (PDMS)) was formed above the channel of the devices to hold both the analyte solution and a platinum gate electrode, which was suspended in the analyte solution [23]. In 2007, this work was expanded upon when various concentrations of glucose solutions were mixed with GOx and added to the well of the transistors, after which the change in resistance of the PEDOT:PSS layer was measured [20]. The results indicated that the proposed device structure was more effective than a plain "chemiresistor" (*i.e.*, the same device with no gate electrode), since the sensitivity of the device was greatly improved with a voltage applied to the gate (Figure 2), and sensitivity in the micromolar range was achieved. In a subsequent paper using devices of a similar structure, the "offset voltage" (the difference between the applied $V_G$ and the effective $V_G$ "seen" by the device) was found to depend on glucose concentration and was used as the dependent variable in calibration curves [24].

**Figure 2.** Normalized resistance between the source and drain for Organic electrochemical transistors (OECTs) exposed to different concentrations of glucose solution, at $V_G$ values of 0.1 V and 0.6 V and with no gate connection.

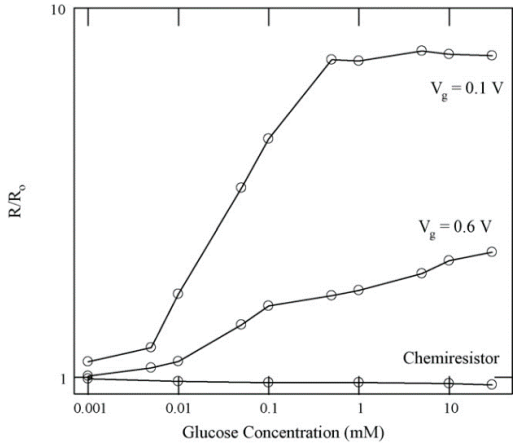


Reprinted from Sensors and Actuators B: Chemical, 123(1), Macaya *et al.*, *Simple glucose sensors with micromolar sensitivity based on organic electrochemical transistors*, 374–378, Copyright (2007), with permission from Elsevier [20].

Another approach used a different design of integrated sensor in which the enzyme was mixed into a phosphate buffer solution and spin-coated to form a film on top of the PEDOT:PSS semiconductor layer joining the source and drain [25]. When $V_G$ and the drain voltage ($V_D$) were fixed at a given value, it was found that $I_D$ increased as a function of the glucose concentration of a solution that was dropped on top of the device. The devices showed a linear relationship between the change in their $I_D$ after analyte addition and glucose concentration in the one to 20 mM range (sensitivity = 1.65 $\mu A \cdot mM^{-1}$), with a response time in the order of 20 s.

More recently, Liao *et al.* have used GOx embedded into graphene or reduced graphene oxide (rGO)-modified gate electrodes with which linear glucose sensing in the range of 10 nM to 1 μM is achieved [26]. The high surface area of the graphene/rGO allowed for a two orders of magnitude increase in the detection limit. The selectivity of the sensors due to the presence of glucose oxidase was demonstrated by presenting analyte solutions of both uric acid and L-ascorbic acid, as well as glucose to devices with and without the enzyme present. The enzyme-containing devices showed a much higher response to glucose, whilst the level of response to the analytes in the enzyme-free devices was comparable. The same group has also gone on to produce dopamine sensors of a similar structure with graphene/rGO, again improving device sensitivity [27]. Furthermore, in 2011, Tang *et al.* showed that the sensitivity of glucose detectors can be improved when GOx is used in conjunction with nanoparticles to improve the effectiveness of how the enzyme is immobilized on the devices [28].

One of the disadvantages of most of the OTFT-based enzymatic glucose sensors reported so far in the body of literature is their relatively slow response speed, often in the tens or hundreds of seconds, and improving this parameter may be a goal of future research in the area. However, for many sensing applications, this may not be an issue, since for applications, such as determining the concentration of glucose in the blood of a diabetes sufferer, these slow response speeds are not important. In addition, response speeds of these prototype devices are likely to improve as the most promising types of sensors undergo further refinements.

### *2.2. Other Enzymatic Sensors*

Although the reaction between glucose and GOx has arguably attracted the majority of attention historically, when it comes to OTFT-based enzymatic biosensors, the majority of recent reports focus on other enzymes, which can be integrated into organic transistors to generate an electrical signal related to the concentration of their target analyte. In this section, some interesting articles from recent years reporting enzymatic sensors with non-GOx recognition elements are introduced. Also included is a short discussion of some publications reporting enzymatic sensors, which, although not incorporating organic transistors into their design, use processing steps or fabrication methods compatible with OTFT-based designs and may be of interest to researchers considering the development of new types of OTFT-based sensors.

Wang and Gao reported in 2010 a method of encapsulating urease into a single-layer PPy membrane for the sensing of urea, a substance present in blood that can be a biomarker for some serious illnesses in humans and other animals, depending on its concentration [29]. The PPy film was electro-polymerized in the presence of the enzyme creating a thin film, which was subsequently used

as the recognition element in a "BioFET", which achieved the linear detection of the analyte from 0.1 μM through to 1 mM in a phosphate buffer solution.

In 2012, Buth *et al.* reported the detection of penicillin using solution-gated organic field effect transistors (dubbed "SGFETs") with a penicillinase-functionalized α-sexithiophene semiconductor, which rely on the pH-sensitive nature of the α-sexithiophene combined with the proton-liberating enzymatic reaction for their operation [30]. The sensitivity is claimed to be at least as good as similar inorganic sensors (as high as 80 $\mu V \cdot \mu M^{-1}$). In 2013, Khodagholy *et al.* demonstrated OECTs with lactose oxidase incorporated into an "ionogel" on top of the devices [31]. The sensors can detect lactate down approximately to 10 mM.

Some other recent publications report enzymatic sensors, which although not employing transistors in their architecture, involve fabrication techniques that could be applicable for use in sensors that do incorporate OTFTs. For example, Phongphut *et al.* reported the sensing of triglyceride, a biomarker for some serious diseases, by immobilizing three different enzymes (lipase, glycerol kinase and glycerol-3-phosphate oxidase) onto a working electrode fabricated using a PEDOT:PSS/gold nanocomposite material [32]. The three enzymes act on triglycerides in subsequent steps to liberate $H_2O_2$, which can be detected electrochemically, and a low detection limit of 7.88 $mg \cdot dL^{-1}$ was achieved. Another example was reported in a 2013 publication from Jia *et al.* in which a novel electrochemical sensor was fabricated in the form of a "temporary-transfer tattoo" capable of continuous sensing lactose levels in human sweat (Figure 3) [33]. Lactate is a biomarker for tissue oxygenation, critical in assessing physical performance in sports and other healthcare areas. High selectivity was displayed, with little or no response to uric acid, glucose, creatinine or ascorbic acid. Although the sensor does not incorporate an OTFT and required a connection to an external potentiostat in the same way as a conventional electrochemical cell, it was fabricated largely from printing techniques and solution-based materials, making it compatible with and perhaps able to be improved by organic transistors. Finally, sub-millimolar sensing of urea (which when found in the body in excessive quantities is a sign of kidney malfunction) using urease-functionalized polyaniline and poly(vinylsulfonic acid) pH-sensitive membranes incorporated onto working electrodes in an electrochemical cell was recently reported by Vieira and co-workers [34]. This type of device is also known as a separative extended gate field-effect transistor (SEGFET), since the gate is separated from the rest of the device by the solution in the cell.

### *2.3. Non-Enzymatic Biosensors*

Enzymes which catalyse charge carrier-liberating reactions are arguably the most well-suited recognition elements for OTFT-based biosensors, due to their inherent selectivity; however, there have also been many non-enzymatic sensors reported recently, which are being shown to be highly effective. Some of the most common recognition elements used in this category of sensors include other (non-enzyme) proteins and antibodies. There are also sensors in this category that do not employ highly specific recognition elements and, instead, rely on electrochemical reduction and/or oxidation reactions induced by an electrical potential. Although such devices by their nature may suffer from poor selectivity, they can have very high sensitivity and may still function as useful sensors if the sensitivity to the target analyte is relatively high compared with other moieties found in typical samples related to the application.

**Figure 3.** (**a**) The intensity profile of an exercise routine; (**b**) a photograph of the lactose-sensing transfer tattoo; and (**c**,**d**) current *versus* time for the devices with (**red**) and without (**blue**) the enzyme present whilst the athlete is performing the exercise routine with the intensity profile shown in (**a**).

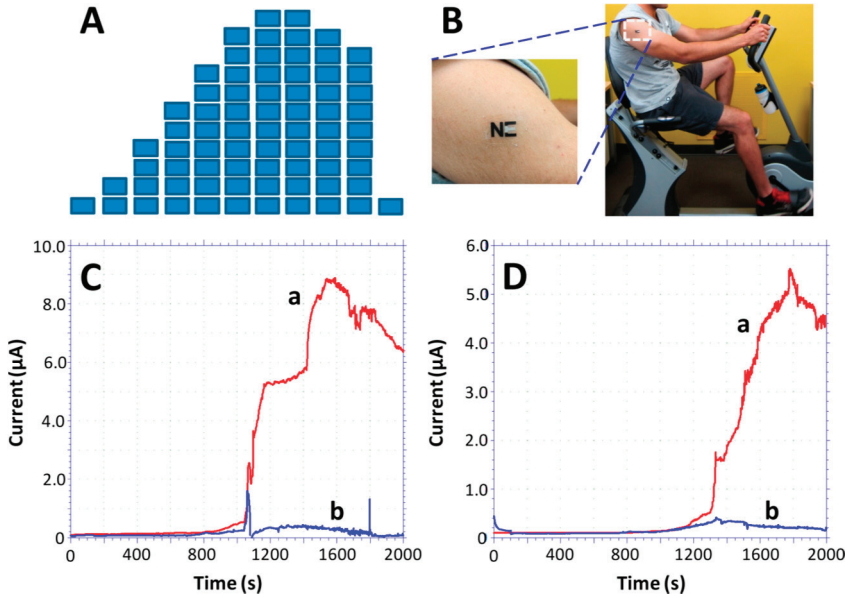


Reprinted with permission from Analytical Chemistry, 85, Jia *et al.*, *Electrochemical tattoo biosensors for real-time non-invasive lactate monitoring in human perspiration*, Copyright (2013) American Chemical Society [33].

In a report from 2002, Someya *et al.* presented an early example of an organic transistor-based biosensor based on electrochemical detection (*i.e.*, no specific receptor/recognition element was used). Lactic acid was detected at concentrations down to 10 μM using organic transistors with α-sexithiophene (α6T) and copper phthalocyanine (CuPc) [35]. Since then, many other types of non-enzymatic biosensor have been reported in the literature.

Biotin detection at concentrations as low as 15 pM has been reported recently by Magliulo *et al.* using OFET-based biosensors employing a "functional bio-interlayer" (FBI) as the material connecting the source and drain (see Figure 4) [36]. The FBI consists of two materials: streptavidin (SA), a protein that has an extremely high affinity to biotin, and the organic semiconductor, P3HT. The protein layer was deposited both by spin-coating and by a self-assembly process, with these two deposition techniques for SA showing comparable performance. When the transfer characteristics of the devices were measured with aqueous solutions of biotin of various concentrations dropped on top of the device, $I_D$ was found to decrease with increasing biotin concentration, due to a change in the P3HT layer's electronic properties upon binding of biotin by the SA. Successful sensing trials were also conducted in which the SA layer was replaced firstly with a biotin antibody and secondly with the enzyme, horseradish peroxidase, showing that the "FBI-OFET" may be a promising platform for a variety of biological recognition elements. In a previous paper from the same group, biotin was also successfully immobilized on an organic semiconductor layer in an EGOFET, and SA was used as the target analyte [37].

**Figure 4.** (**a**) Cross-sectional diagram of functional bio-interlayer (FBI)-OFET with a streptavidin layer for the detection of biotin; (**b**) the output characteristic of the biotin-sensing FBI-OFET. Reproduced from [36].

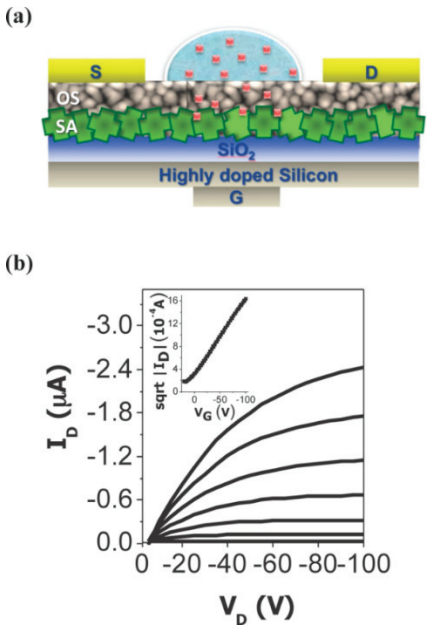


Justino *et al.* have recently reported a C-reactive protein (CRP) detecting NTFET, capable of sensing analyte concentrations of $10^{-4}$ to $10^{2}$ μg·mL$^{-1}$ [11]. This range of concentrations covers the critical range of around one to 10 μg·mL$^{-1}$, in which CRP is an important biomarker for conditions, such as cardiovascular disease. The use of a simple OTFT-based sensor is appealing, as many conventional detection methods (immunoassays) for CRP are expensive. This NTFET-based device utilizes CRP antibodies by immobilizing them on the surface of the CNT joining the source and drain electrodes, and the change in current between the source and drain when different concentrations of CRP were deposited on top of the device was used as the calibration parameter (Figure 5).

Another recent report on an organic biosensor using antibodies as the recognition element published by Chartuprayoon *et al.* employed very thin strips (so-called "nanoribbons") of PPy as a semiconductor layer [38]. Here, the cucumber mosaic virus (CMV) was detected with CMV antibodies. Although the device used in this study could perhaps be most correctly classified as a chemiresistor (rather than an organic transistor), its structure is such that it could easily be adapted to include a gate electrode. This change in architecture could potentially increase performance, as seen with some other sensing systems, which showed an enhanced response when a potential was added at a third electrode in comparison with the chemiresistor case [20].

The detection of DNA, which is important in many medical applications, is also a popular area of research for organic transistor-based biosensors. In 2010, Lin *et al.* showed the detection of DNA using organic field effect devices incorporating single-stranded DNA as the recognition element (ssDNA) [39]. DNA was successfully detected down to concentrations of 1 μM. Furthermore, in 2010, Kahn *et al.* exhibited DNA detection as low as 1 nM using peptide nucleic acid (PNA) as a recognition element [40]. Since then, several other publications have exhibited DNA sensing using a similar detection mechanism incorporated onto different types of transistors [41–43].

**Figure 5.** Calibration curve for the OTFT sensor-based detection of C-reactive protein (CRP).

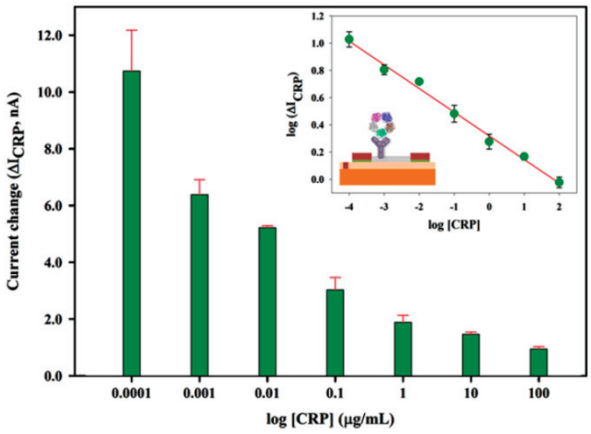


Reprinted from Talanta, 108, Justino et al., Disposable immunosensors for c-reactive protein based on carbon nanotubes field effect transistors, 165–170, Copyright (2013), with permission from Elsevier [11].

Hammock *et al.* have recently reported on a thrombin sensor based on an OFET, capable of detection down to approximately 100 pM [44]. The sensor is comprised of a standard bottom-gate, top-contact OFET, with the sensing layer located adjacent to a polymeric semiconductor layer on top of the devices. The recognition elements in these sensors are gold nanoparticles, which have been functionalized by thrombin-specific DNA aptamers after being deposited on the semiconductor.

In another recent study, Tarabella *et al.* demonstrated that OECTs can be very efficient and reliable sensing devices for detecting liposome-based nanoparticles on a wide dynamic range down to $10^{-5}$ mg·mL$^{-1}$ (with a lowest detection limit, assessed in real-time monitoring, of $10^{-7}$ mg·mL$^{-1}$ [45]. Even more recently, Huang *et al.* have shown that glial fibrillary acidic protein (GFAP), a biomarker associated with brain injury, can be detected with an OTFT-based biosensor in which its antibodies were immobilized on a polymer film on top of the device [46]. Analyte solution is dropped on top of this layer, and changes in $I_D$ were found to be related to the concentration of GFAP. In 2011, Tang *et al.* presented the detection of dopamine down to 5 nM concentrations. The detection mechanism was standard electrochemistry using a platinum gate electrode suspended in the analyte solution [47].

The sensing of *bovine serum albumin (BSA) and BSA antibodies (antiBSA) has been exhibited by Kahn et al. in a duo of papers released in 2011 [48,49]. For the sensing of BSA, antiBSA was used at the detection element and vice versa. Pentacene was used as the semiconductor in these devices, which after passivation with perfluoropolymer, were found to be air and water stable, broadening their potential applications*.

### *2.4. Biosensor Summary*

As was seen in this section, organic transistor-based biosensors come in many different architectures and use different mechanisms to liberate electrical signals in response to the concentration of an analyte. The selectivity of devices that use enzymes, antibodies or other highly selective recognition elements in particular show great promise for high-performance, low-cost sensors. Non-specific electrochemical sensing techniques can also be effective, but suffer from a lack of selectivity. The stability of the materials used in biosensors has received a relatively low amount of

attention in the literature to this point, although some papers have discussed this critical issue, and Kahn *et al.*'s study on the stability of passivized devices shows encouraging results [48].

Table 1 shows a summary of the literature discussed in this section. Included in the table is the target analyte, the material used to detect the analyte, the type of transistor (or otherwise) used in the sensor and the upper and lower concentration limits of analyte detection. The range of concentrations that a sensor can detect is not the parameter by which such devices should be measured. Other critical factors that should be considered in order to determine the practicality of sensors include the selectivity of the devices, their sensitivity and their ease of fabrication, amongst others.

## 3. Pressure Sensors

There have been significant advances in recent years in the development of OTFTs and OTFT-based arrays designed for use in artificial intelligence applications, such as so-called "electronic skin" (e-skin) and "electronic nose" (e-nose). Someya and co-workers at the University of Tokyo were the first to publish reports outlining the development of what they dubbed "e-skin" [51–54]. The principles of e-skin are based on the detection of pressure and force either statically or dynamically. In these initial reports on e-skin, OTFTs, pressure-sensitive rubber and thermal sensors are combined to create fully flexible, pressure and temperature-sensitive artificial skin for use in the robotics industry. However, the pressure sensor arrays in the e-skin are not directly integrated with the transistors, but rather, are formed from a commercially available pressure-sensitive rubber containing carbon particles and a silicone rubber matrix, whilst the OTFTs act simply as signal transducers (see Figure 6). The electrical resistance between the top and bottom surfaces of the carbon-containing rubber material is a function of the mechanical deformation of the sheet and, thus, the pressure applied to it.

**Table 1.** A summary of the biosensor devices discussed in this review. The bounds on detectable analyte concentrations are given in molar ratios where possible. * Denotes the use of a non-specific electrochemical mechanism. CuPc, copper phthalocyanine; SEGFET, separative extended gate field-effect transistor; SGFET, solution-gated organic field effect; NTFET, carbon nanotube FET; BSA, *bovine serum albumin.*

| Analyte(s) | Recognition Element | Device Type | Claimed Lower and Upper Detection Limit | | Year | Ref. |
|---|---|---|---|---|---|---|
| Glucose | Glucose oxidase | OECT | 0.1 mM | 1 mM | 2004 | [23] |
| | | OECT | 1 μM | 30 mM | 2007 | [20] |
| | | OECT | 1 μM | 1 mM | 2007 | [24] |
| | | OTFT | 1.1 mM | 16.5 mM | 2008 | [25] |
| | | OECT (device and analyte in solution) | 5 nM | >1 mM | 2011 | [28] |
| | | OECT | 10 nM | 1 μM | 2013 | [26] |
| Lactic acid | CuPc * | OFET | 10 uM | 2 mM | 2002 | [35] |

**Table 1.** *Cont.*

| Analyte(s) | Recognition Element | Device Type | Claimed Lower and Upper Detection Limit | | Year | Ref. |
|---|---|---|---|---|---|---|
| Urea | Urease | BioFET | 0.1 μM | 1 mM | 2010 | [29] |
| | | SEGFET (device and analyte in solution) | 50 μM | 10 mM | 2013 | [34] |
| Penicillin | Penicillinase | SGFET | 10 μM (approx.) | 600 μM | 2012 | [30] |
| Lactate | Lactose Oxidase | OECT | 10 mM | 100 mM | 2013 | [31] |
| | | Non-transistor electrochemical device | 1 mM | 30 mM | 2013 | [33] |
| Liposome | PEDOT:PSS * | OECT | 10 μg·mL$^{-1}$ | 0.1 mg·mL$^{-1}$ | 2013 | [45] |
| Biotin | Streptavidin | FBI-OFET | 15 pM | 500 nM | 2013 | [36] |
| Streptavidin | Biotin | FBI-OFET | 10 nM | 1 μM | 2013 | [37] |
| C-reactive protein (CRP) | CRP antibodies | NTFET | 0.1 ng·mL$^{-1}$ | 100 μg·mL$^{-1}$ | 2013 | [11] |
| Cucumber mosaic virus (CMV) | CMV antibodies | Chemiresistor | 1 ng·mL$^{-1}$ | 100 μg·mL$^{-1}$ | 2013 | [38] |
| Triglyceride | Lipase, glycerol kinase and glycerol-3-phosphate oxidase | Non-transistor electrochemistry | 7.88 mg·dL$^{-1}$ | 531 mg·dL$^{-1}$ | 2013 | [32] |
| Dopamine | Metal electrode | OECT | 5 nM | | 2011 | [47] |
| Glial fibrillary acidic protein | GFAP antibodies | OTFT | 20 pM | 20 nM | 2014 | [46] |
| BSA | Anti-BSA | OTFT | 1 μM | 10 μM | 2011 | [48] |
| Anti-BSA | BSA | OTFT | 10 nM | 2 μM | 2011 | [49] |
| pH | n/a | Dual-gate OTFT | pH 2 | pH 10 | 2010 | [50] |
| DNA | Single-stranded DNA | OFET | 100 nM | 50 μM | 2010 | [39] |
| | PNA | OTFT | 1 nM | 100 nM | 2010 | [40] |
| | Single-stranded DNA | OECT | 10 pM | >1 μM | 2011 | [43] |
| | PNA | OTFT | ~1 nM | ~100 nM | 2012 | [42] |
| | DNA | Water-gated OFET | 100 nM | n/a | 2012 | [41] |

Similar devices utilizing pressure-sensitive rubber for pressure detection have also been based upon space-charge limited transistors (SCLT) with P3HT as the active layer [55]. An SCLT is a vertically configured transistor with a grid electrode inserted between the source electrode and the drain electrode to control the vertical current flow. As pressure is applied to the pressure-sensitive rubber, the resistance and, therefore, current in the source-drain circuit is systematically modulated, allowing the applied pressure to be monitored. Impressively, the response time of the sensor to the pressure is less than 22 ms. A flexible pressure sensor has also been realized by using transparent plastic foil (Mylar), both as the substrate and gate dielectric [56,57]. Pressure was applied by the

application of compressed air flow, and data analysis suggests that pressure-induced variations in $V_G$, threshold voltage and contact resistance are responsible for the current variations, but the mechanism of detection is not fully understood. Nonetheless, the changes in $I_D$ are reproducible. Moreover, the sensor responds very fast to a mechanical stimulus (tens to hundreds of milliseconds), but the time required to reach the steady state is much higher (tens to hundreds of seconds). A clever solution to pressure sensing has been offered by Kim *et al.* [58]. An OTFT pressure sensor based on soft-contact lamination was fabricated using an elastic polydimethylsiloxane (PDMS) mould with gold electrodes. The effective channel length of the laminated OTFT was controlled by external pressure on the structured PDMS mould; the observed changes in source-drain output currents, therefore, corresponded to these external loads without any change of the material properties. As a result of the elastic properties of the PDMS mould, the laminated device was returned to its former state after the external pressure was released. Based on this device property, reversible and time durable operations of the device were demonstrated. Using PDMS as the dielectric material and a designed microstructure array of pillars in the dielectric layer, Mannsfeld *et al.* demonstrated a highly sensitive, flexible bio-compatible pressure sensor for e-skin application [59]. Similarly, Kim, *et al.* used a nano-needle structured dielectric layer and showed a high sensitivity up to 1.76 $kPa^{-1}$, as determined by the normalized change of capacitance of the dielectric layer [60].

**Figure 6.** The structure of a pressure sensor (**left**) using a pressure-sensitive rubber as a transducer. Shown also is the thermal sensor (**right**) reported in the same publication.

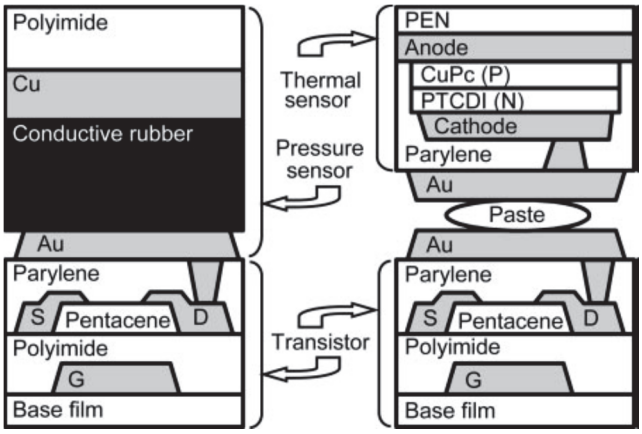




Furthermore, Darlinski *et al.* have shown that organic thin-film transistors are inherently sensitive to applied pressure [61]. The pressure dependence of pentacene transistors with a solution-processed polyvinylphenol gate dielectric on glass substrates was investigated by applying uniaxial mechanical pressure with a needle. The measurements showed a reversible current dependence of the transfer characteristics with $I_D$ reproducibly switching between two states. Experimental and simulation results suggested that turn-on voltage and interface resistance are being affected. However, the change takes of the order of seconds, hinting at charge trap states in the pentacene being responsible for the effect. This work demonstrated a much simpler way of making pressure sensors; however, the mechanism governing the sensitivity is yet to be understood. Cosseddu, Milita and Bonfiglio also showed that pentacene is a better electromechanical material than P3HT for the fabrication of

low-cost pressure sensors, due to the low crystallinity of the P3HT thin film, making it less sensitive to any deformation [62].

More recently, Schwartz and co-workers reported using a micro-structured PDMS dielectric: the pressure-sensitive OTFT achieved a maximum sensitivity of 8.4 $kPa^{-1}$ (in terms of a normalized change in $I_D$). Furthermore, a fast response time of less than 10 ms, high stability (more than 15,000 cycles) and a power consumption of less than 1 mW were achieved. [63]. Lai and co-workers reported the use of a PDMS capacitive sensor and a floating gate, showing that it is also feasible to fabricate a pressure sensor for artificial skin [64]. This type of device works at −2 V for both $V_D$ and $V_G$, making it easily operable from batteries.

Organic transistor-based pressure sensors have shown much promise for e-skin applications, and the mechanisms used are varied. Table 2 summarizes the organic transistor-based pressure sensors presented here, their device structure, sensitivity and the operation mechanism that results in the sensing effects. Few of the discussed papers mention the details about the exact device pressure sensitivity and the response time. There is little known about what the critical criteria are that make effective artificial skin in terms of the sensitivity and response time. In addition, it is still questionable whether large area pressure sensing is achievable under the reported device architectures for e-skin applications. For an OTFT-based pressure sensor, whether it is necessary to demand device operation at low voltages for health, safety and power consumption concerns is dependent on the application.

**Table 2.** A summary of the pressure-sensing devices discussed in this review.

| Device Materials/Structure | Sensitivity | Response Time | Current Modulation Mechanism | Year | Ref. |
|---|---|---|---|---|---|
| Polyimide/pentacene/ conductive rubber network | 30 $kPa^{-1}$ | n/a | Pressure- and thermal-sensitive materials | 2004 | [51] |
| Graphite containing rubber/pentacene | 30 $kPa^{-1}$ | Hundreds of milliseconds | Change in transconductance | 2005 | [52] |
| Single-walled carbon nanotubes as a conducting dopant in a rubber, FET matrix | n/a | n/a | Pressure-sensitive rubber conductor | 2010 | [53] |
| Ionic liquid/conductive rubber/sensor array | 30 $kPa^{-1}$ | n/a | Tension-dependent conductive rubber | 2010 | [54] |
| Pressure-sensitive rubber | n/a | 22 ms | Space charge limited, low voltage operation at ~3 V | 2009 | [55] |
| Plastic foil as dielectric layer (Mylar) | n/a | Tens to hundreds of seconds | Mobility or interface effects | 2007 | [56] |
| Plastic foil as dielectric layer (Mylar) | n/a | Tens to hundreds of seconds | Interface effects | 2006 | [57] |
| PDMS mould on gold | 0.14~0.3 $(N/mm^2)^{-1}$ or 140~300 $kPa^{-1}$ | n/a | Pressure dependent channel length | 2010 | [58] |

**Table 2.** *Cont.*

| Device Materials/Structure | Sensitivity | Response Time | Current Modulation Mechanism | Year | Ref. |
|---|---|---|---|---|---|
| Microstructured PDMS dielectric layer, rubrene semiconducting layer | n/a | Millisecond range | Capacitive effect | 2010 | [59] |
| Nano-needle dielectric layer | 1.76 $kPa^{-1}$ | n/a | The sharpness of the nano-needles | 2012 | [60] |
| PVP/Pentacene | n/a | 20 s | Trapped charges | 2005 | [61] |
| Devices with P3HT and pentacene semiconducting layers | n/a | 100 ms | P3HT layer is less crystalline than pentacene | 2012 | [62] |
| Microstructured PDMS dielectric and polyisoindigobithiophene-siloxane semiconductor | 8.4 $kPa^{-1}$ | Less than 10 ms | Operating device in the sub-threshold regime | 2013 | [63] |
| PDMS dielectric layer with a floating gate | n/a | n/a | Ultra-low voltage operation, variation in the PDMS capacitance | 2013 | [64] |

## 4. Vapour Sensing

In 1982, Persaud and Dodd first proposed the concept of an artificial nose, which operates as a gas sensor for the recognition of odours [65]. Later, the term "e-nose" was used to describe a sensing device resembling a mammalian nose to detect various gases. There is only a very limited amount of work published so far on OTFT-based systems suitable for e-nose applications. Ideally, an e-nose sensor should satisfy the following criteria: high sensitivity to chemical compounds, low sensitivity to humidity and temperature, high stability, high reproducibility, fast response time, robust, easy calibration and small physical dimensions [66]. Most work published on OTFT-based gas sensors have shown that they satisfy one or two aspects of the above criteria, thus making them potential candidates for use in an e-nose.

In 2005, Liao *et al.* reported on a back-gated OTFT in which the sensor material is also the active layer for the transistor itself. Toluene and propanol have been tested, and the OTFT devices are sensitive towards exposure to the gas pressure. The authors also showed the OTFT potentially are able to discriminate between water and milk [67]. Li and Lambeth showed that using a nanostructured rr-P3HT as the active layer, OTFTs show sensitivity to 10 analytes, although the device responses are different for polar and nonpolar gases. The authors attributed the sensing behaviour to the grain boundary effect, which affects OTFT charge transport [68]. Wedge and co-workers using a four-OTFT array structure and an amorphous semiconductor, polytriarylamines (PTAAs), as the active layer and sensing material, combined with a genetic programming pattern recognition, successfully produced a vapour sensor with high sensitivity and specificity [69]. Liao and co-workers tested the effects of the side chain length of polythiophene and the film thickness in the active layer, together with the size of analytes on the sensing responses. They found that the OTFT based sensors can map out different amine gas mixtures [70]. Wang and Swensen proposed a

dual-mode sensing approach by utilizing a set of different and independent transduction signals for vapour detection. They employed luminescent organic semiconductors as the active layer materials, which produce both electrical and optical signals under gate modulation. They demonstrated that these OTFT-based sensors can be used to detect the explosive vapour. However, the operation voltage is quite high (more than 50 V) [71].

Explosive detection has also been explored with encouraging results, firstly by Huang *et al.* in 2010 [72] and also by Kong *et al.* in 2012 [73]. More recently, Kybert *et al.* reported that by using functionalized carbon nanotubes as the active layer and incorporating single-stranded DNA as the sensing agent, so-called "DNA-NT OTFT" gas sensors can be fabricated. The device responds to both the DNA sequence and the analytes, showing a positive response to D-limonene and a negative response to L-limonene, as well as being able to distinguish the isomers of pinene [74].

We propose that one of the reasons for the relatively small number of publications on OTFT-based sensors for "e-nose" applications is due to there being limited options for materials suitable for the semiconducting layer in an OTFT that are also effective for selective gas sensing. Only the bottom gate architecture is feasible if the active layer materials must play these dual roles in the sensors. The sensing signal is triggered by the electrical change in the channel and magnified by the $V_G$ modulation. More exploration on the incorporation of chemically-sensitive elements into the OTFT channel appears to be a desirable line of investigation in the coming years.

## 5. Conclusions

In conclusion, the three types of OTFT-based sensors covered in this review show much promise for their eventual integration into applications outside the laboratory. Two distinct strategies have been used in the development of devices for OTFT-based sensing applications. Firstly, for a multiple-layer, structured OTFT, the organic materials used in the construction of the OTFTs themselves can also probe the analytes and induce changes in the conductivity of the source-drain channel. By measuring the change in the electrical signal in the channel, sensing responses can be quantified in a straightforward manner. The other method requires embedding an extra material, that is a sensitive and selective recognition element, into the device. The former is stricter on the material suitability, and in the latter, material compatibility is more critical. It is also desirable to have the operation voltages below 5 V for a portable, battery-powered device, which is possible for most OTFT-based sensors reported in this review. Progress in recent years has shown both increases in the sensitivity and selectivity of OTFT-based sensors, as well as the range of analytes targeted by such devices. Recent advances, along with the potential for economies of scale in the large-scale fabrication of organic electronic devices in general, gives optimism that reliable, low-cost OTFT-based sensors will be produced in the not-too-distant future.

## Conflicts of Interest

The authors declare no conflict of interest.

## References


1. Dimitrakopoulos, C.D.; Mascaro, D.J. Organic thin-film transistors: A review of recent advances. *IBM J. Res. Dev.* **2001**, *45*, 11–27.
2. Katz, H.E. Recent advances in semiconductor performance and printing processes for organic transistor-based electronics. *Chem. Mater.* **2004**, *16*, 4748–4756.
3. Lin, P.; Yan, F. Organic thin-film transistors for chemical and biological sensing. *Adv. Mater.* **2012**, *24*, 34–51.
4. Liao, C.; Yan, F. Organic semiconductors in organic thin-film transistor-based chemical and biological sensors. *Polym. Rev.* **2013**, *53*, 352–406.
5. Vieira, N.C.S.; Fernandes, E.G.R.; de Queiroz, A.A.A.; Guimarães, F.E.G.; Zucolotto, V. Indium tin oxide synthesized by a low cost route as segfet ph sensor. *Mater. Res.* **2013**, *16*, 1156–1160.
6. Kergoat, L.; Piro, B.; Berggren, M.; Horowitz, G.; Pham, M.-C. Advances in organic transistor-based biosensors: From organic electrochemical transistors to electrolyte-gated organic field-effect transistors. *Anal. Bioanal. Chem.* **2012**, *402*, 1813–1826.
7. Schmoltner, K.; Kofler, J.; Klug, A.; List-Kratochvil, E.J.W. Electrolyte-gated organic field-effect transistor for selective reversible ion detection. *Adv. Mater.* **2013**, *25*, 6895–6899.
8. Loi, A.; Manunza, I.; Bonfiglio, A. Flexible, organic, ion-sensitive field-effect transistor. *Appl. Phys. Lett.* **2005**, *86*, 103512, doi:10.1063/1.1873051.
9. Sandberg, H.G.O.; Bäcklund, T.G.; Österbacka, R.; Stubb, H. High-performance all-polymer transistor utilizing a hygroscopic insulator. *Adv. Mater.* **2004**, *16*, 1112–1115.
10. Deng, J.; Patil, N.; Ryu, K.; Badmaev, A.; Zhou, C.; Mitra, S.; Wong, H.-S. Carbon nanotube Transistor Circuits: Circuit-Level Performance Benchmarking and Design Options for Living with Imperfections. In Proceedings of the IEEE International Solid-State Circuits Conference, 2007, ISSCC 2007, Digest of Technical Papers, San Francisco, CA, USA, 11–15 Febuary 2007; pp. 70–588.
11. Justino, C.I.; Freitas, A.C.; Amaral, J.P.; Rocha-Santos, T.A.; Cardoso, S.; Duarte, A.C. Disposable immunosensors for c-reactive protein based on carbon nanotubes field effect transistors. *Talanta* **2013**, *108*, 165–170.
12. Lai, S.; Demelas, M.; Casula, G.; Cosseddu, P.; Barbaro, M.; Bonfiglio, A. Ultralow voltage, otft-based sensor for label-free DNA detection. *Adv. Mater.* **2013**, *25*, 103–107.
13. Demelas, M.; Lai, S.; Spanu, A.; Martinoia, S.; Cosseddu, P.; Barbaro, M.; Bonfiglio, A. Charge sensing by organic charge-modulated field effect transistors: Application to the detection of bio-related effects. *J. Mater. Chem. B* **2013**, *1*, 3811–3819.
14. Bartic, C.; Campitelli, A.; Borghs, S. Field-effect detection of chemical species with hybrid organic/inorganic transistors. *Appl. Phys. Lett.* **2003**, *82*, 475–477.
15. Magliulo, M.; Pistillo, B.R.; Mulla, M.Y.; Cotrone, S.; Ditaranto, N.; Cioffi, N.; Favia, P.; Torsi, L. PE-CVD of hydrophilic-COOH functionalized coatings on electrolyte gated field-effect transistor electronic layers. *Plasma Process. Polym.* **2013**, *10*, 102–109.
16. IUPAC. *Compendium of Chemical Terminology*, 2nd ed.; Blackwell Scientific Publications: Oxford, UK, 1997.

17. Clark, L.C.; Lyons, C. Electrode systems for continuous monitoring in cardiovascular surgery. *Ann. N. Y. Acad. Sci.* **1962**, *102*, 29–45.
18. Heller, A. Implanted electrochemical glucose sensors for the management of diabetes. *Annu. Rev. Biomed. Eng.* **1999**, *1*, 153–175.
19. Wilson, R.; Turner, A.P.F. Glucose oxidase: An ideal enzyme. *Biosens. Bioelectron.* **1992**, *7*, 165–185.
20. Macaya, D.J.; Nikolou, M.; Takamatsu, S.; Mabeck, J.T.; Owens, R.M.; Malliaras, G.G. Simple glucose sensors with micromolar sensitivity based on organic electrochemical transistors. *Sens. Actuators B* **2007**, *123*, 374–378.
21. Umana, M.; Waller, J. Protein-modified electrodes. The glucose oxidase/polypyrrole system. *Anal. Chem.* **1986**, *58*, 2979–2983.
22. Bartlett, P.N.; Whitaker, R.G. Electrochemical immobilisation of enzymes: Part II. Glucose oxidase immobilised in poly-*n*-methylpyrrole. *J. Electroanal. Chem.* **1987**, *224*, 37–48.
23. Zhu, Z.-T.; Mabeck, J.T.; Zhu, C.; Cady, N.C.; Batt, C.A.; Malliaras, G.G. A simple poly(3,4-ethylene dioxythiophene)/poly(styrene sulfonic acid) transistor for glucose sensing at neutral pH. *Chem. Commun.* **2004**, 1556–1557.
24. Bernards, D.A.; Macaya, D.J.; Nikolou, M.; DeFranco, J.A.; Takamatsu, S.; Malliaras, G.G. Enzymatic sensing with organic electrochemical transistors. *J. Mater. Chem.* **2007**, *18*, 116–120.
25. Liu, J.; Agarwal, M.; Varahramyan, K. Glucose sensor based on organic thin film transistor using glucose oxidase and conducting polymer. *Sens. Actuators B: Chem.* **2008**, *135*, 195–199.
26. Liao, C.; Zhang, M.; Niu, L.; Zheng, Z.; Yan, F. Highly selective and sensitive glucose sensors based on organic electrochemical transistors with graphene-modified gate electrodes. *J. Mater. Chem. B* **2013**, *1*, 3820–3829.
27. Liao, C.; Zhang, M.; Niu, L.; Zheng, Z.; Yan, F. Organic electrochemical transistors with graphene-modified gate electrodes for highly sensitive and selective dopamine sensors. *J. Mater. Chem. B* **2014**, *2*, 191–200.
28. Tang, H.; Yan, F.; Lin, P.; Xu, J.; Chan, H.L. Highly sensitive glucose biosensors based on organic electrochemical transistors using platinum gate electrodes modified with enzyme and nanomaterials. *Adv. Funct. Mater.* **2011**, *21*, 2264–2272.
29. Wang, Z.; Gao, J. Research on the urease biosensor with ppy material as carrier and sensitive membrane. In Proceedings of the 2010 3rd International Conference on Biomedical Engineering and Informatics (BMEI), Yantai, China, 16–18 October 2010; pp. 1574–1576.
30. Buth, F.; Donner, A.; Sachsenhauser, M.; Stutzmann, M.; Garrido, J.A. Biofunctional electrolyte-gated organic field-effect transistors. *Adv. Mater.* **2012**, *24*, 4511–4517.
31. Khodagholy, D.; Curto, V.F.; Fraser, K.J.; Gurfinkel, M.; Byrne, R.; Diamond, D.; Malliaras, G.G.; Benito-Lopez, F.; Owens, R.M. Organic electrochemical transistor incorporating an ionogel as a solid state electrolyte for lactate sensing. *J. Mater. Chem.* **2012**, *22*, 4440–4443.
32. Phongphut, A.; Sriprachuabwong, C.; Wisitsoraat, A.; Tuantranont, A.; Prichanont, S.; Sritongkham, P. A disposable amperometric biosensor based on inkjet-printed au/pedot-pss nanocomposite for triglyceride determination. *Sens. Actuators B* **2013**, *178*, 501–507.

33. Jia, W.; Bandodkar, A.J.; Valdes-Ramirez, G.; Windmiller, J.R.; Yang, Z.; Ramirez, J.; Chan, G.; Wang, J. Electrochemical tattoo biosensors for real-time noninvasive lactate monitoring in human perspiration. *Anal. Chem.* **2013**, *85*, 6553–6560.
34. Vieira, N.C.S.; Figueiredo, A.; Fernandes, E.G.R.; Guimarães, F.E.G.; Zucolotto, V. Nanostructured polyaniline thin films as urea-sensing membranes in field-effect devices. *Synth. Met.* **2013**, *175*, 108–111.
35. Someya, T.; Dodabalapur, A.; Gelperin, A.; Katz, H.E.; Bao, Z. Integration and response of organic electronics with aqueous microfluidics. *Langmuir* **2002**, *18*, 5299–5302.
36. Magliulo, M.; Mallardi, A.; Gristina, R.; Ridi, F.; Sabbatini, L.; Cioffi, N.; Palazzo, G.; Torsi, L. Part per trillion label-free electronic bioanalytical detection. *Anal. Chem.* **2013**, *85*, 3849–3857.
37. Magliulo, M.; Mallardi, A.; Mulla, M.Y.; Cotrone, S.; Pistillo, B.R.; Favia, P.; Vikholm-Lundin, I.; Palazzo, G.; Torsi, L. Electrolyte-gated organic field-effect transistor sensors based on supported biotinylated phospholipid bilayer. *Adv. Mater.* **2013**, *25*, 2090–2094.
38. Chartuprayoon, N.; Rheem, Y.; Ng, J.C.; Nam, J.; Chen, W.; Myung, N.V. Polypyrrole nanoribbon based chemiresistive immunosensor for viral plant pathogen detection. *Anal. Methods* **2013**, *5*, 3497–3502.
39. Lin, T.-W.; Kekuda, D.; Chu, C.-W. Label-free detection of DNA using novel organic-based electrolyte-insulator-semiconductor. *Biosens. Bioelectron.* **2010**, *25*, 2706–2710.
40. Khan, H.U.; Roberts, M.E.; Johnson, O.; Förch, R.; Knoll, W.; Bao, Z. *In situ*, label-free DNA detection using organic transistor sensors. *Adv. Mater.* **2010**, *22*, 4452–4456.
41. Kergoat, L.; Piro, B.; Berggren, M.; Pham, M.-C.; Yassar, A.; Horowitz, G. DNA detection with a water-gated organic field-effect transistor. *Org. Electron.* **2012**, *13*, 1–6.
42. Khan, H.U.; Roberts, M.E.; Johnson, O.; Knoll, W.; Bao, Z. The effect of ph and DNA concentration on organic thin-film transistor biosensors. *Org. Electron.* **2012**, *13*, 519–524.
43. Lin, P.; Luo, X.; Hsing, I.; Yan, F. Organic electrochemical transistors integrated in flexible microfluidic systems and used for label-free DNA sensing. *Adv. Mater.* **2011**, *23*, 4035–4040.
44. Hammock, M.L.; Knopfmacher, O.; Naab, B.D.; Tok, J.B.-H.; Bao, Z. Investigation of protein detection parameters using nano-functionalized organic field-effect transistors. *ACS Nano* **2013**, *7*, 3970–3980.
45. Tarabella, G.; Balducci, A.G.; Coppedè, N.; Marasso, S.; D'Angelo, P.; Barbieri, S.; Cocuzza, M.; Colombo, P.; Sonvico, F.; Mosca, R. Liposome sensing and monitoring by organic electrochemical transistors integrated in microfluidics. *Biochim. Biophys. Acta* **2013**, *1830*, 4374–4380.
46. Huang, W.; Besar, K.; LeCover, R.; Dulloor, P.; Sinha, J.; Hardigree, J.F.M.; Pick, C.; Swavola, J.; Everett, A.D.; Frechette, J. Label-free brain injury biomarker detection based on highly sensitive large area organic thin film transistor with hybrid coupling layer. *Chem. Sci.* **2014**, *5*, 416–426.
47. Tang, H.; Lin, P.; Chan, H.L.; Yan, F. Highly sensitive dopamine biosensors based on organic electrochemical transistors. *Biosens. Bioelectron.* **2011**, *26*, 4559–4563.
48. Khan, H.U.; Jang, J.; Kim, J.-J.; Knoll, W. Effect of passivation on the sensitivity and stability of pentacene transistor sensors in aqueous media. *Biosens. Bioelectron.* **2011**, *26*, 4217–4221.

49. Khan, H.U.; Jang, J.; Kim, J.-J.; Knoll, W. *In situ* antibody detection and charge discrimination using aqueous stable pentacene transistor biosensors. *J. Am. Chem. Soc.* **2011**, *133*, 2170–2176.
50. Spijkman, M.J.; Brondijk, J.J.; Geuns, T.C.; Smits, E.C.; Cramer, T.; Zerbetto, F.; Stoliar, P.; Biscarini, F.; Blom, P.W.; de Leeuw, D.M. Dual-gate organic field-effect transistors as potentiometric sensors in aqueous solution. *Adv. Funct. Mater.* **2010**, *20*, 898–905.
51. Someya, T.; Sekitani, T.; Iba, S.; Kato, Y.; Kawaguchi, H.; Sakurai, T. A large-area, flexible pressure sensor matrix with organic field-effect transistors for artificial skin applications. *Proc. Natl. Acad. Sci. USA* **2004**, *101*, 9966–9970.
52. Someya, T.; Kato, Y.; Sekitani, T.; Iba, S.; Noguchi, Y.; Murase, Y.; Kawaguchi, H.; Sakurai, T. Conformable, flexible, large-area networks of pressure and thermal sensors with organic transistor active matrixes. *Proc. Natl. Acad. Sci. USA* **2005**, *102*, 12321–12325.
53. Sekitani, T.; Someya, T. Stretchable, large-area organic electronics. *Adv. Mater.* **2010**, *22*, 2228–2246.
54. Someya, T.; Dodabalapur, A.; Huang, J.; See, K.C.; Katz, H.E. Chemical and physical sensing by organic field-effect transistors and related devices. *Adv. Mater.* **2010**, *22*, 3799–3811.
55. Chao, Y.-C.; Lai, W.-J.; Chen, C.-Y.; Meng, H.-F.; Zan, H.-W.; Horng, S.-F. Low voltage active pressure sensor based on polymer space-charge-limited transistor. *Appl. Phys. Lett.* **2009**, *95*, 253306, doi:10.1063/1.3266847.
56. Manunza, I.; Bonfiglio, A. Pressure sensing using a completely flexible organic transistor. *Biosens. Bioelectron.* **2007**, *22*, 2775–2779.
57. Manunza, I.; Sulis, A.; Bonfiglio, A. Pressure sensing by flexible, organic, field effect transistors. *Appl. Phys. Lett.* **2006**, *89*, 143502, doi:10.1063/1.2357924.
58. Kim, J.-H.; Sun, Q.; Seo, S. Pressure dependent current-controllable devices based on organic thin film transistors by soft-contact lamination. *Org. Electron.* **2010**, *11*, 964–968.
59. Mannsfeld, S.C.; Tee, B.C.; Stoltenberg, R.M.; Chen, C.V.H.; Barman, S.; Muir, B.V.; Sokolov, A.N.; Reese, C.; Bao, Z. Highly sensitive flexible pressure sensors with microstructured rubber dielectric layers. *Nat. Mater.* **2010**, *9*, 859–864.
60. Kim, J.; Nga Ng, T.; Soo Kim, W. Highly sensitive tactile sensors integrated with organic transistors. *Appl. Phys. Lett.* **2012**, *101*, 103308, doi:10.1063/1.4751354.
61. Darlinski, G.; Bottger, U.; Waser, R.; Klauk, H.; Halik, M.; Zschieschang, U.; Schmid, G.; Dehm, C. Mechanical force sensors using organic thin-film transistors. *J. App. Phys.* **2005**, *97*, 093708, doi:10.1063/1.1888046
62. Cosseddu, P.; Milita, S.; Bonfiglio, A. Strain sensitivity and transport properties in organic field-effect transistors. *IEEE Electron Device Lett.* **2012**, *33*, 113–115.
63. Schwartz, G.; Tee, B.C.-K.; Mei, J.; Appleton, A.L.; Wang, H.; Bao, Z. Flexible polymer transistors with high pressure sensitivity for application in electronic skin and health monitoring. *Nat. Commun.* **2013**, *4*, 1859, doi:10.1038/ncomms2832.
64. Lai, S.; Cosseddu, P.; Bonfiglio, A.; Barbaro, M. Ultralow voltage pressure sensors based on organic fets and compressible capacitors. *IEEE Electron Device Lett.* **2013**, *34*, 801–803.
65. Persaud, K.; Dodd, G. Analysis of discrimination mechanisms in the mammalian olfactory system using a model nose. *Nature* **1982**, *299*, 352–355.

66. Schaller, E.; Bosset, J.O.; Escher, F. “Electronic noses” and their application to food. *LWT—Food Sci. Technol.* **1998**, *31*, 305–316.
67. Liao, F.; Chen, C.; Subramanian, V. Organic tfts as gas sensors for electronic nose applications. *Sens. Actuators B* **2005**, *107*, 849–855.
68. Li, B.; Lambeth, D.N. Chemical sensing using nanostructured polythiophene transistors. *Nano Lett.* **2008**, *8*, 3563–3567.
69. Wedge, D.C.; Das, A.; Dost, R.; Kettle, J.; Madec, M.-B.; Morrison, J.J.; Grell, M.; Kell, D.B.; Richardson, T.H.; Yeates, S. Real-time vapour sensing using an OFET-based electronic nose and genetic programming. *Sens. Actuators B* **2009**, *143*, 365–372.
70. Liao, F.; Yin, S.; Toney, M.; Subramanian, V. Physical discrimination of amine vapor mixtures using polythiophene gas sensor arrays. *Sens. Actuators B* **2010**, *150*, 254–263.
71. Wang, L.; Swensen, J.S. Dual-transduction-mode sensing approach for chemical detection. *Sens. Actuators B* **2012**, *174*, 366–372.
72. Huang, J.; Dawidczyk, T.; Jung, B.; Sun, J.; Mason, A.; Katz, H. Response diversity and dual response mechanism of organic field-effect transistors with dinitrotoluene vapor. *J. Mater. Chem.* **2010**, *20*, 2644–2650.
73. Kong, H.; Jung, B.J.; Sinha, J.; Katz, H.E. Electrical “turn-on” response of poly (3,3‴-didodecylquaterthiophene) and electron donor blend transistors to 2,4,6-trinitrotoluene. *Chem. Mater.* **2012**, *24*, 2621–2623.
74. Kybert, N.J.; Lerner, M.B.; Yodh, J.S.; Preti, G.; Johnson, A.C. Differentiation of complex vapor mixtures using versatile DNA-carbon nanotube chemical sensor arrays. *ACS Nano* **2013**, *7*, 2800–2807.

# Chapter 8

# Anomalous Response in Heteroacene-Based Organic Field Effect Transistors under High Pressure

**Ken-ichi Sakai and Jun Takeya**

**Abstract:** Carrier transport properties of organic field effect transistors in dinaphtho[2,3-*b*:2',3'-*f*]thieno[3,2-*b*]thiophene single crystals have been investigated under high pressure. In contrast to the typical pressure effect of monotonic increase in charge transfer rates according to the application of external hydrostatic pressure, it is clarified that the present organic semiconductor devices exhibit nonmonotonic pressure response, such as negative pressure effect. X-ray diffraction analysis under high pressure reveals that on-site molecular orientation and displacement in the heteroacene molecule is assumed to be the origin for the anomalous pressure effects.

Reprinted from *Electronics*. Cite as: Sakai, K.; Takeya, J. Anomalous Response in Heteroacene-Based Organic Field Effect Transistors under High Pressure. *Electronics* **2014**, *3*, 255-265.

## 1. Introduction

Organic molecular solids, such as organic semiconductors, have been studied intensively due to their considerable scientific and industrial uses. The pristine electronic properties of such material ensures good insulation because of the closed-shell structure of organic molecules, but they can also become electric conducting materials when a charge accumulation layer is formed by the application of an electric field on the surface. The π-electrons, whose interaction is described by weak van-der-Waals interaction, are responsible for the charge transport, in sharp contrast to those in inorganic semiconductors with a well-defined covalent network for charges to transfer. Hence, organic semiconductors have often seemed to provide poor electric conductivity and it appears that the hopping transport mechanism is realized on the basis of localized electronic states. Nevertheless, it has been revealed that some of the organic semiconductor systems show moderate carrier mobility above 1 $cm^2/Vs$ [1–4] and the charge transport mechanism is dominated by a band transport system described by spatially-distributed Bloch waves similar to ordinary metals, but on the verge of self-localization because of the strong molecular fluctuation [5]. From a microscopic viewpoint, the peculiar shape of molecular orbitals in such compounds causes condensation in the corresponding crystal structure at ambient pressure as a result of naïve balance between mutually attracting London force and Coulomb repulsive force. Therefore, considerable impact is expected with the application of external pressure, not only by reducing molecular distance but also by deforming the crystal structure due to freedom of onsite molecular orientation. This is essentially different from inorganic semiconductors composed of atoms which appear as a spherical mass point. Therefore the application of external pressure is expected to induce a striking change in not

only simple reduction of intermolecular molecule distance, but also the deformation of the crystal structure due to the freedom of onsite molecular orientation, and the unanticipated pressure response of electronic properties unlike a simple linear increase in charge transfer rate. Looking at the current progress the electronic industry is making in organic semiconductors, this kind of work becomes necessary for the development of flexible and soft-printed organic devices which is subjected to a bending force behaving like pressure.

In this paper we introduce a method of measuring the effect of hydrostatic pressure on charge carrier conductivity in organic semiconductor crystals, introducing the charge with the application of an electric field on the semiconductor surfaces. In addition to the measurement of common transfer characteristics of drain current as a function of gate voltage shown in former pioneering studies [6,7], we performed four-terminal conductivity measurements to exclude extrinsic influences of metal-to-semiconductor contact resistance [8]. In previous studies, carrier mobility $\mu$ of hydrocarbons, such as rubrene, pentacene, were shown to exhibit a positive pressure response against external pressure $p$, and their pressure coefficient, $d\mu/dp$, is extremely larger than used in inorganic semiconductors. Here we focused on the pressure effect of one of heteroacene-based compounds, dinaphtho[2,3-*b*:2',3'-*f*]thieno[3,2-*b*]thiophene (DNTT). It was found that DNTT shows far larger $d\mu/dp$ values whose sign can even be negative. The result cannot be explained by the simple model: increase in charge transfer rate with decreasing molecular distance. We note that the pressure effect of molecular solids can be explained by taking into account displacement, rotation and other degrees of freedom originating from molecular shapes. From an X-ray diffraction experiment, we constructed a plausible model of the pressure-induced structural deformation. In combination with the measurement of anisotropic charge transfer and structural studies, a route to study the so-called “structure-property relations” is provided [9].

## 2. Experimental Section

### *2.1. Preparation of Single-Crystal Organic Semiconductor*

In the present study, platelet-shaped single crystals of DNTT were employed as the channel material. The DNTT single crystals were prepared by the physical vapor transport method [10]. After purification of crude powder samples supplied from Nipponkayaku Co. by vaporizing at 285 °C and coarse crystallization at 213 °C in a two-zone tube furnace under Ar gas flow (>99.999% for gas purity and 200 ccm for flow rate, respectively), the coarse crystals are slowly recrystallized at the same temperature in three days.

### *2.2. Carrier Transport Measurement under High Pressure*

In order to realize stable and reproducible measurement under high pressure, device structure and pressure cells were newly developed. The charge transport measurements are performed by the four-terminal technique at room temperature to obtain the information about intrinsic charge transfer properties of channel material. All the components of the measured devices are fabricated by polymer materials except for electrodes so that nearly homogeneous shrinkage by pressurization is realized. The field-effect transistor devices with the top-contact and bottom-gate structure are

fabricated as follows. A patterned gate electrode of 20 nm thickness is vapor-deposited through a shadow mask on a polyethylene naphthalete (PEN) substrate. A gate-insulating layer of CYTOP (Asahi Glass Co., Tokyo, Japan) is formed by spin-coating and subsequent heat treatment at 140 °C for 15 h. A single-crystal DNTT flake with a thickness of less than 1 μm is carefully taken and laminated on the position of the gate electrode. DNTT samples with well-defined crystallographic shape are chosen for experiments so that anisotropic effect of transport properties can be discussed (Figure 1). Then Source-drain electrodes and four voltage terminals are formed by vapor deposition of 2,3,5,6-tetrafluoro-7,7,8,8-tetracyanoquinodimethane and over-deposited gold layers through a shadow mask to the thickness of 1 nm and 20 nm, respectively. Carbon past is used to cover the step edges of electrodes on the periphery of DNTT single crystal. The central channel area is finally shaped into Hall-bar structure by laser etching process and just on the top of the gate electrode. The channel size is 100 μm in width and 150 μm in length, respectively. The distance between adjacent voltage terminals along the channel direction is 50 μm. Whole device structure is illustrated in Figure 2a,b. The device is covered with a-few-μm thick parylene for passivation and the completely and then completely filled in epoxy (STYCAST 1266) for the mechanical stability. The devices are introduced in a standard Cu-Be pressure cell and Fluorinert FC70/77 is used for the pressurizing medium (Figure 2c).

**Figure 1.** A photograph of a single crystal dinaphtho[2,3-*b*:2',3'-*f*]thieno [3,2-*b*]thiophene (DNTT) platelet. Crystalline direction for the *a* and *b* axes are indicated by white arrows [9].

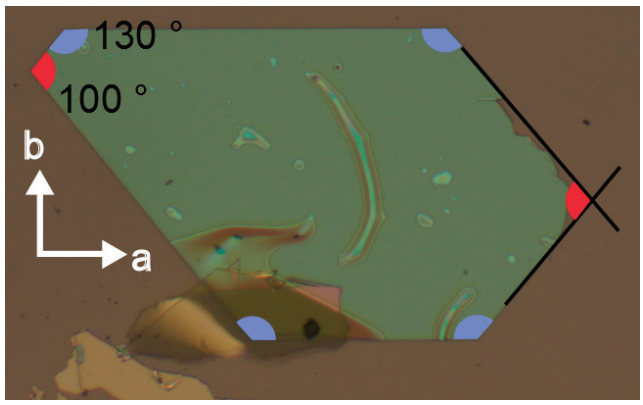


In the present study pressure dependence of the four-terminal carrier mobility at each pressure $\mu(P)$ is taken into account for quantitative argue of pressure effect of the charge transport. $\mu$ is defined as

$$\mu = \frac{1}{C}\frac{\partial \sigma}{\partial V_G} \tag{1}$$

where $C$ is capacitance of the CYTOP gate insulator in a unit area, σ is the four-terminal sheet conductivity and $V_G$ is the applied gate voltage. $C$ is modified as a Pressure-variable number $C(P)$ which is identified in our previous study; we estimated dependent carrier mobility under each pressure by precise Hall-effect measurement using rubrene single-crystal Field-Effect-Transistors (FETs), so that $C$(P) turned out to change by 10% at 0.5 GPa [8]. Carrier mobility is estimated at

$V_G = -100$ V, where field-induced carriers are accumulated at the bottom of the conduction band into avoid contribution of trap-involved pressure effect in the subthreshold regions as is investigated in rubrene single-crystal transistors.

**Figure 2.** (**a**) Side view and (**b**) top view of device structure; (**c**) Schematic illustration of pressure cell used for the present measurement.

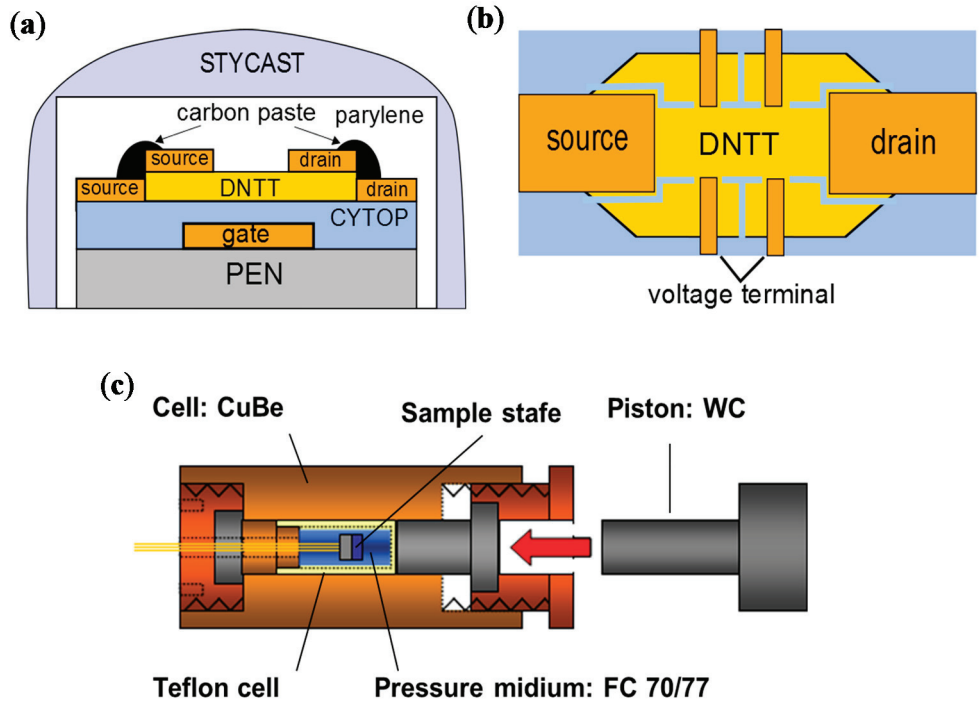


*2.3. Structural Analysis*

X-ray diffraction (XRD) experiments were carried out using well-purified DNTT powder by a synchrotron radiation source on the beamline BL10XU at SPring-8 in order to have an idea of change in unit cells in high pressure. The sample is introduced into a diamond anvil cell with the pressure medium (FC70/77). Applied pressure is measured by a simultaneous ruby fluorescence measurement. The wavelength of X-ray is 0.41413 Å. The diffraction patterns were obtained with an imaging plate detector as a function of 2θ (θ is an incident angle of X-ray). Here we should pay attention that deformation of unit cell observed in powder X-ray diffraction experiment is not precisely consistent with that in our transistors. However, they are somehow comparable due to the fact that the anisotropic behavior of lattice constants in rubrene single crystal under high pressure is consistent with that of carrier mobility [11].

## 3. Results and Discussion

The unit cell of DNTT is monoclinic, meaning that there are four lattice parameters, lattice constants along *a*, *b*, and *c* axes and an angle β, defined as crossing angle of *a* and *c* axes. The XRD patterns as a function of 2θ at each pressure point are shown in Figure 3. No disappearance and emergence of peaks in pressurizing process is observed, indicating that there is no structural phase transition up to 2 GPa. Every peak shifts toward larger angle, indicating the overall shrinkage of

unit cell. We choose four distinctive peaks assigned to (100), (003), (020) and (111) so that the four lattice parameters can be identified. Note that the result is consistent with the positions of all over visible peaks.

**Figure 3.** XRD patterns for pressurized powder DNTT. Red, blue, green and dark arrows indicate (100), (003), (020) and (11-1) reflection peaks, respectively [9].

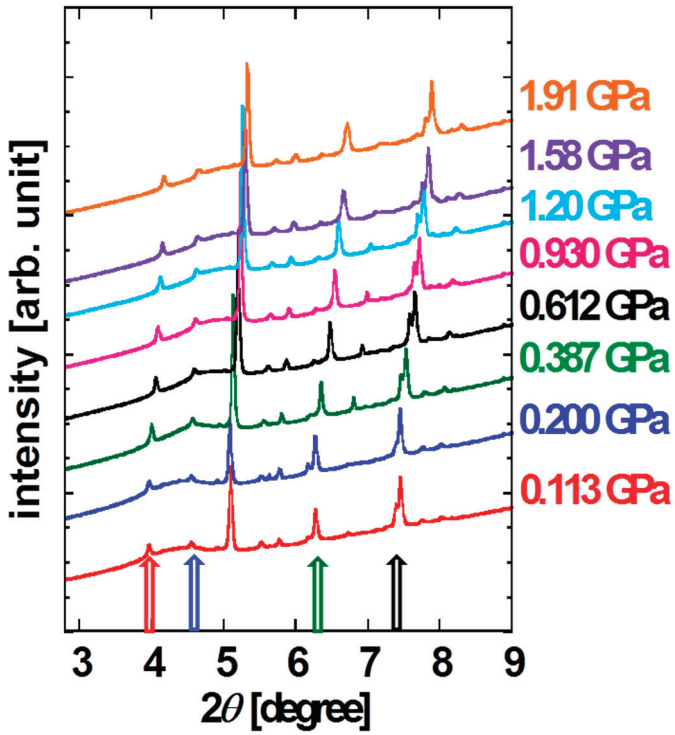


Figure 4a,b indicate the variations of these parameters as a function of pressure. It was found that the lattice parameters $a$, $c$ and β shows rapid variation at the lower pressure range (approximately less than 0.2 GPa) and then moves to more moderate pressure dependency at higher pressure range, in contrast to the variation of $b$ showing an almost constant rate. For further discussion consider the molecular rearrangement in the process of pressurization. Figure 4c shows the ratio of compressibility in $a$ ($\kappa_a$) and $b$ ($\kappa_b$) directions. Here the compressibility is defined as the differential coefficient estimated from two adjacent measurement points,

$$\kappa(P) = \frac{1}{L(P_i)} \frac{L(P_i) - L(P_j)}{P_i - P_j} \tag{2}$$

where $P_i$ and $P_j$ are two adjacent pressure points ($P_i > P_j$). $L(P_i)$ and $L(P_j)$ are the lattice constants evaluated at each pressurized condition and $P$ is the average value between $P_i$ and $P_j$, defined as $(P_i + P_j)/2$ for the sake of convenience since lattice constants plotted in present paper are discrete value; therefore $x$-values of data points in Figure 4a,c are deviated.

**Figure 4.** Pressure dependence of (**a**) lattice constants for three crystallographic directions and (**b**) β, defined as the intersection angle between *a* and *c* axes; (**c**) Compressibility ratio between *a* and *b* axes as a function of applied pressure; (**d**) Schematic diagram of suggested molecular rearrangement in *ab* plane. The two pictures depict the molecular rearrangements in case of shrinkage along the *a* and *b* directions, respectively. Red and blue arrows indicate the rotation direction; (**e**) Crystal structure in *ac* plane. Dark and light molecular images and arrows indicate molecules located on the front and reverse side and corresponding displacement direction in pressurization process, respectively [9].

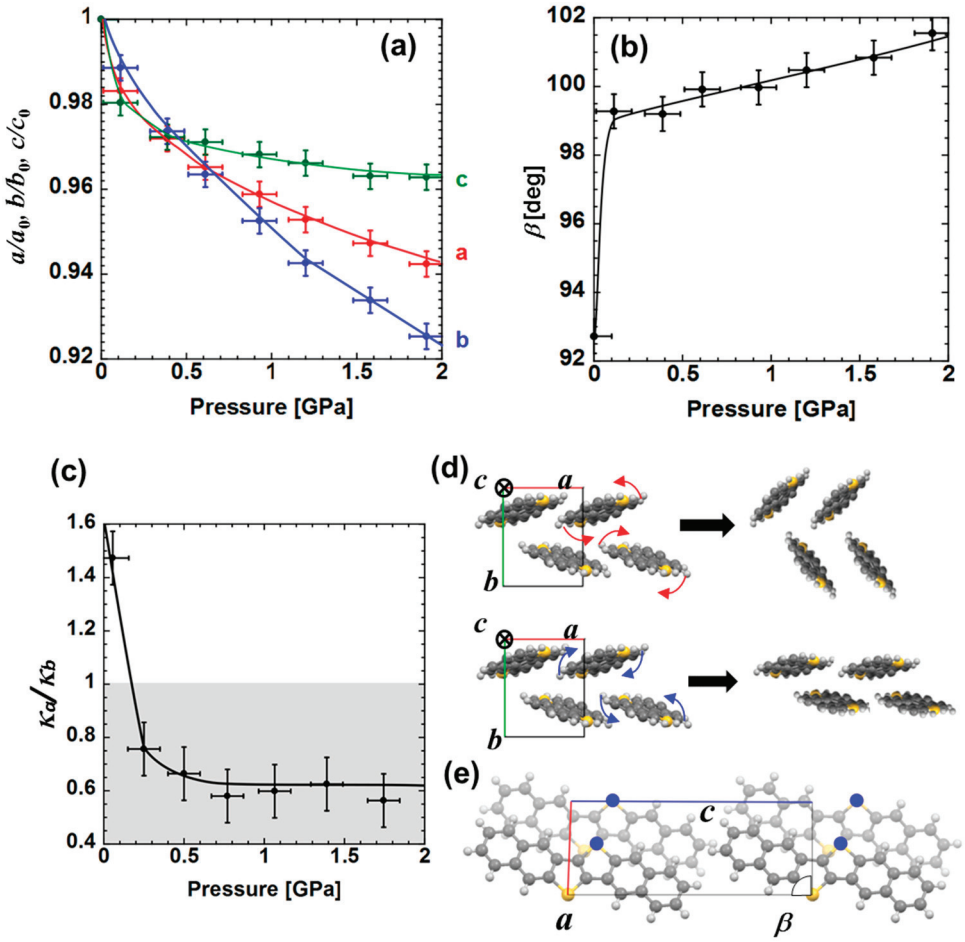


Let us focus on the discussion of the pressure effect below approximately 0.2 GPa. Within this pressure range $\kappa_a/\kappa_b$ is larger than 1, suggesting that the deformation of unit cell in *ab* plane is dominated by the shrinkage along *a*-axis. In this case molecules are supposed to be rearranged with concomitant rotation indicated by the curved red arrows in Figure 4d. For a higher pressure range, the unit cell starts to shrink along *b*-axis since $\kappa_a/\kappa_b < 1$, in which the molecules are supposed to start onsite rotation along the opposite direction to that in the lower pressure range (curved blue arrows in Figure 4d). Note that the relationship between the dominant shrinkage direction of unit cell and the corresponding molecular rearrangement mentioned above is consistent with structural change experimentally observed in the oligoacene system, such as anthracene, pentacene and tetracene under high pressure [12,13].

It is noted that similar pressure dependences are shown among *a*, *c* and β: drastic change in lower pressure region and the following slow change in higher pressure region (Figure 4d). To approach this experimental result let us take into account the molecular rearrangement in *ac* plane which is characterized by these three lattice parameters. As an external mechanical force is added intermolecular interaction is enhanced due to the access of nearest-neighbor molecules. The π-electrons tend to be localized on electro-negative sulfur atoms as compared to carbon and hydrogen sites [14], in addition to the effect of spatially large occupation of the $3p_z$ orbitals on sulfur atoms. Therefore it is expected that intermolecular interaction of nearest-neighbor DNTT molecules are highly dominated by effects between sulfur atoms of different molecules. As the interaction between nearest-neighbor sulfur atoms marked by blue circles in Figure 4e becomes large with increasing pressure, the adjacent molecules tend to displace along *c*-axis to reduce the energy loss of Coulomb repulsion. Because sulfur-to-sulfur interaction is pronounced along *a*-axis, both *c* and β parameters exhibit drastic change under relatively low pressure in the region of $\kappa_a/\kappa_b > 1$ where shrinkage of *a* is dominant, while the values are less sensitive to pressure when shrinkage onn the *b*-axis is dominant at higher pressure. The greater sulfur-to-sulfur interaction along the *a*-axis than the *b*-axis is also consistent with higher carrier mobility on the *a*-axis compared to that along the *b*-axis. Note that the change in β up to 10° at around 2 GPa contrasts that observed in sulfur-free oligoacenes in which only a few degrees of deviation up to 10 GPa is observed for angles, so called α, β and γ [12,13].

Pressure effects of carrier mobility in DNTT-FETs are measured along two distinctive crystallographic directions, *a*- and *b*-axes. Transport and output characters and carrier conductivity as a function of gate voltage are indicated in Figure 5 for each axis. For quantitative discussion of pressure effects on carrier transport properties of DNTT-FETs, let us introduce the increasing rate defined as

$$\frac{\Delta\mu(P)}{\mu(0)} = \frac{[\mu(P) - \mu(0)]}{\mu(0)} \tag{3}$$

where $\mu(P)$ and $\mu(0)$ are four-terminal mobility at a certain pressure *P* and that in the ambient condition. Note that estimated carrier mobility along each axis in ambient conditions is 2.1 $cm^2/Vs$ for *a*-axis and 1.3 $cm^2/Vs$ for *b*-axis respectively. This anisotropic value is in agreement with a previous report [15]. The pressure dependence of carrier mobility is shown in Figure 6 at the drain bias voltage $V_D$ of −10 V. In the present study, the reproducibility of carrier mobility against compression and decompression is confirmed. Simultaneous plots of pressure-dependent carrier mobility of rubrene [8] and pentacene [16] devices reveal that carrier transport of DNTT is much more sensitive to pressurization and, furthermore, shows the nonmonotonous pressure response characterized by the appearance of peak and valley at 0.15 GPa on the *a*-axis and *b*-axis devices, respectively. Note that this is a quite different feature in contrast to two other hydrocarbon FETs with simple linear responses.

**Figure 5.** (**a**) Transport and (**b**) output properties of DNTT-FET for *a*-axis conducting direction; (**c**) transport properties of DNTT-FET for *b*-axis conducting direction. Photographs for each devices are inserted in (**a**) and (**c**); (**d**) four-terminal conductivity in *a* and *b*-axes at ambient condition. The estimated carrier mobility is 2.1 $cm^2\ V^{-1}\ s^{-1}$ for *a*-axis and 1.3 $cm^2\ V^{-1}\ s^{-1}$ for *b*-axis at VG = −100 V, respectively [9].

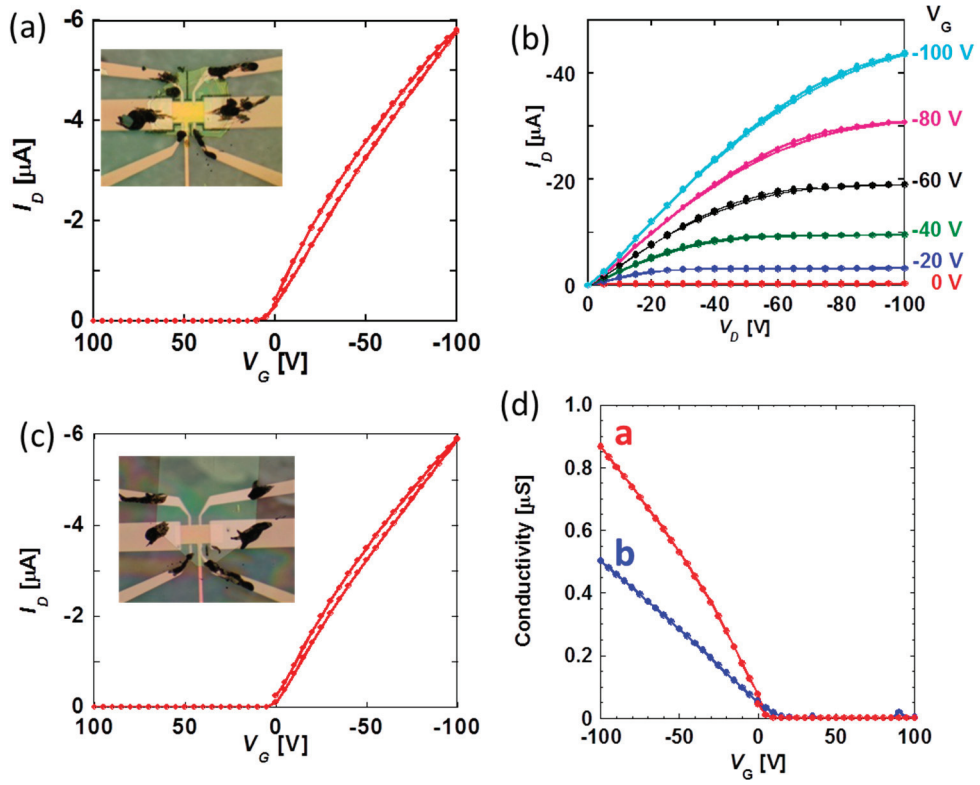


**Figure 6.** Pressure effect on DNTT-FET for *a* and *b*-axes [9]. Those for pentacene [16] and rubrene [8] devices are also plotted for comparison. Open and closed circles indicate the data obtained in compression and decompression processes.

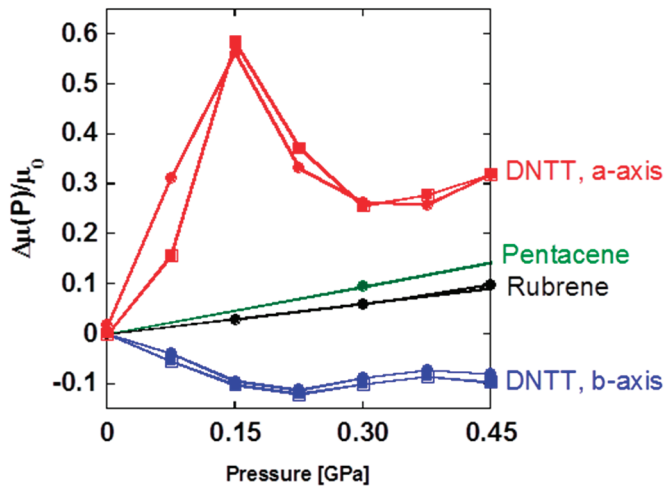


To assist in understanding this phenomenon, it is good to associate this problem with the structural variation by external pressure as shown in Figure 4. The appearance of a peak in $\Delta\mu(P)/\mu(P)$ can be taken that the sign of the derivative $d\mu/dP$ for each axis is converted at 0.15 GPa, which

coincides with the crossover point of $\kappa_a/\kappa_b = 1$, representing a simultaneous change in the anisotropic deformation of unit cell at the same pressure. Therefore the anomalous pressure response of carrier mobility on DNTT-FET seems to be connected with the change in molecular arrangement mentioned above. When $p < 0.15$ GPa, our results suggest that the molecules are likely to rearrange so that face-to-face π–π stacking is enhanced along the *a*-axis, which leads to the increase in carrier mobility on the *a*-axis and decrease on the *b*-axis. In contrast, when $p > 0.15$ GPa, the structural change has the opposite effect, so that carrier mobility decreases on the *a*-axis and increases on the *b*-axis, respectively. Therefore the peak structure results from crossover between the two distinct molecular rotations associated with pressurization. At a higher pressure than 0.30 GPa, a slight increase in carrier mobility on the *a*-axis can be seen due to the predominance of the normal pressure effect from the increase in density of molecular packing. Note that the contribution of molecular rearrangement is suppressed in the profile of $\Delta\mu(P)/\mu(P)$ in this pressure region. We have demonstrated the relationship of carrier transport properties and the structure of DNTT-FETs via their pressure response. However, for further elucidation of structure-property relations of pressure-sensitive organic semiconductors, crystal structure analysis under high pressure should be completed so that we complement the detailed information about the molecular rearrangement. The magnitude of pressure coefficient is up to 3.8 $GPa^{-1}$ along the *a*-axis and is extremely large below 0.15 GPa as compared to those of rubrene (0.2 $GPa^{-1}$) and pentacene (0.4 $GPa^{-1}$), which is already one order larger than typical values for inorganic materials [17]. In conjunction with the significant contribution of the sulfur-to-sulfur interaction which causes peculiar displacement in the *ac* plane, the presence of sulfur atoms in DNTT is responsible for the anomalous pressure dependence in carrier mobility, indicating the significant contribution of $3p_z$ orbital on sulfur to the charge transport in the semiconductors and to the device performance. It is highly expected that the more efficient charge transfer on the *a*-axis is realized in DNTT FETs by pressurization, due to the enhancement of orbital overlap, and especially the presence of more spatially-spread $3p_z$ orbital on sulfur atoms than those for carbon and hydrogen, the main components of rubrene and pentacene.

## 4. Conclusions

Charge transport properties and structures of DNTT have been investigated under high pressure. The crossover of on-site molecular rotation and simultaneous anisotropic deformation of unit cells have been observed. It is suggested that access to nearest-neighbor sulfur atoms as a result of pressurization is responsible for both in order to suppress the repulsive electrostatic interaction between negatively-charged sulfur atoms. Also, the corresponding pressure effect of charge transport on DNTT-FETs can be well-explained by the structural change, indicating the successful observation of so-called structure-property relations. Furthermore the giant pressure effect with extreme pressure response up to 3.8 $GPa^{-1}$ is attributed to the widely-distributed $3p_z$ orbital localized on sulfur atoms. Through this study, we have clarified that the presence of sulfur atom plays an important role for the realization of anomalous and giant pressure effect observed. It is noteworthy that nonmonotonous evolution of structural change and charge transport is attributed to the specific molecule-to-molecule interaction due to the peculiar molecular shape, in sharp contrast to the case of inorganic semiconductors which can be seen as assemblies of more symmetric

atoms. These experimental observations evidence how heteroelement affects the properties of heteroacene-based molecular compounds. It is demonstrated that investigating pressure effects of organic semiconductors is a powerful method to clarify the relationship between charge transport mechanisms and microscopic molecular alignments. The knowledge obtained will assist in designing new compounds and practical devices, such as flexible and soft printed devices in which a mechanical force is applied in the bending process.

## Acknowledgments

Authors thank Y. Okada, T. Uemura, S. Kitaoka and J. Tsurumi for the assistance of device experiment, Y. Ohishi and A. Fujiwara for powder X-ray diffraction experiment at SPring-8 and K. Takimiya and Nippon Kayaku Co., Ltd. for supplying DNTT sample powders. This work is financially supported by Grant-in-Aid for Scientific Research (Grants Nos. 22245032 and 236860050) from MEXT in Japan.

## Conflicts of Interest

The authors declare no conflict of interest.

## References

1. Takeya, J.; Tsukagoshi, K.; Aoyagi, Y.; Takenobu, T.; Iwasa, Y. Hall Effect of Quasi-Hole Gas in Organic Single-Crystal Transistors. *Jpn. J. Appl. Phys*. **2005**, *44*, L1393–L1396.
2. Podzrov, V.; Menard, E.; Rofers, J.A.; Gershenson, M.E. Hall Effect in the Accumulation Layers on the Surface of Organic Semiconductors. *Phys. Rev. Lett*. **2005**, *95*, 226601.
3. Takeya, J.; Kato, J.; Hara, K.; Yamagishi, M.; Hirahara, R.; Yamada, K.; Nakazawa, Y.; Ikehata, S.; Tsukagoshi, K.; Aoyagi, Y.; *et al*. In-Crystal and Surface Charge Transport of Electric-Field-Induced Carriers in Organic Signle-Crystal Semiconductors. *Phys. Rev. Lett*. **2007**, *98*, 196804.
4. Yamagishi, M.; Soeda, J.; Uemura, T.; Okada, Y.; Takatsuiki, Y.; Nishikara, T.; Nakazawa, Y.; Doi, I.; Takimiya, K.; Takeya, J. Free-electron-like Hall effect in high mobility organic shin-film transistors. *Phys. Rev. B* **2010**, *81*, 161306(R).
5. Uemura, T.; Yamagishi, M.; Soeda, J.; Takatsuiki, Y.; Okada, Y.; Nakazawa, Y.; Takeya, J. Temperature dependence of the Hall effect in pentacene field-effect transistors: Possibility of charge decoherence induced by molecular fluctuations. *Phys. Rev. B* **2012**, *85*, 035313.
6. Rang, Z.; Natethan, M.I.; Ruden, P.P.; Chesterfield, R.; Daniel Frisbie, C. Hydrostatic pressure dependence of organic thin-film transistors current *versus* voltage characteristics. *Appl. Phys. Lett.* **2004**, *85*, 5760.
7. Rang, Z.; Natethan, M.I.; Ruden, P.P.; Podzorov, V.; Gershenson, M.E.; Newman, C.R.; Frisbie, C.D. Hydrostatic pressure dependence of charge carrier transport in single-crystal rubrene devices. *Appl. Phys. Lett.* **2005**, *86*, 123501.
8. Okada, Y.; Sakai, K.; Uemura, T.; Nakazawa, Y.; Takeya, J. Charge transport and Hall effect in rubrene single-crystal transistors under high pressure. *Phys. Rev. B* **2011**, *84*, 245308.

9. Sakai, K.; Okada, Y.; Kitaoka, S.; Tsurumi, J.; Ohishi, Y.; Fujiwara, A.; Takimiya, K.; Takeya, J. Anomalous Pressure Effect in Heteroacene Organic Field-Effect Transistors. *Phys. Rev. Lett.* **2013**, *110*, 096603.
10. Klok, C.; Simpkins, P.G.; Siegrist, T.; Laudise, R.A. Physical vapr growth of centimeter-sized crystals of α-hexathiophene. *J. Cryst. Growth* **1997**, *182*, 416.
11. Okada, Y.; Sakai, K.; Kitaoka, S.; Miwa, K.; Ohishi, Y.; Takeya, J. Charge Transport and Srystal Structure in Rubrene Single-Crystal Transistors under High Pressure Proceeding of the 67th Annual Meeting of Physical Society of Japan, Nishinomiya, Hyogo, Japan, 19 March 2012.
12. Oehzelt, M.; Resel, R.; Nakayama, A. High-pressure structural properties of anthracene up to 10 GPa. *Phys. Rev. B* **2002**, *66*, 174104.
13. Oehzelt, M.; Aichholzer, A.; Resel, R.; Heimel, G.; Venuti, E.; Della Valle, R.G. Crystal structure of oligoacenes under high pressure. *Phys. Rev. B* **2006**, *74*, 104103.
14. S-Carrera, R.S.; Atahan, S.; Schrier, J.; A-Guzik, A. Theoretical Characterization of the Air-Stable, High-Mobility Dinaphtho[2,3-*b*:2',3'-*f*]thieno[3,2-*b*]thiophene Organic semiconductor. *J. Phys. Chem. C* **2010**, *114*, 2234–2340.
15. Uno, M.; Tominari, Y.; Yamagishi, M.; Doi, I.; Miyazaki, E.; Takimiya, K.; Takeya, J. Moderately anisotropic field-effect mobility in dinaphtho[2,3-*b*:2',3'-*f*]thiopheno [3,2-*b*]thiophenes single-crystal transistors. *App. Phys. Lett.* **2009**, *94*, 223308.
16. Sakai, K.; Okada, Y.; Kitaoka, S.; Tsurumi, J.; Takeya, J. In Proceeding of the 67th Annual Meeting of Physical Society of Japan, Nishinomiya, Hyogo, Japan, 19 March 2012.
17. Hutson, A.R.; Jayaraman, A.; Coriell, A.S. Effects of High Pressure, Uniaxial Stress, and tempareture on the Electrical Resistibity of *n*-GaAs. *Phys. Rev.* **1967**, *155*, 786–796.

# Section IV: Organic Light Emitting Diodes

## Chapter 9

# Emerging Transparent Conducting Electrodes for Organic Light Emitting Diodes

**Tze-Bin Song and Ning Li**

**Abstract:** Organic light emitting diodes (OLEDs) have attracted much attention in recent years as next generation lighting and displays, due to their many advantages, including superb performance, mechanical flexibility, ease of fabrication, chemical versatility, *etc*. In order to fully realize the highly flexible features, reduce the cost and further improve the performance of OLED devices, replacing the conventional indium tin oxide with better alternative transparent conducting electrodes (TCEs) is a crucial step. In this review, we focus on the emerging alternative TCE materials for OLED applications, including carbon nanotubes (CNTs), metallic nanowires, conductive polymers and graphene. These materials are selected, because they have been applied as transparent electrodes for OLED devices and achieved reasonably good performance or even higher device performance than that of indium tin oxide (ITO) glass. Various electrode modification techniques and their effects on the device performance are presented. The effects of new TCEs on light extraction, device performance and reliability are discussed. Highly flexible, stretchable and efficient OLED devices are achieved based on these alternative TCEs. These results are summarized for each material. The advantages and current challenges of these TCE materials are also identified.

Reprinted from *Electronics*. Cite as: Song, T.-B.; Li, N. Emerging Transparent Conducting Electrodes for Organic Light Emitting Diodes. *Electronics* **2014**, *3*, 190-204.

### 1. Introduction

Organic light emitting diode (OLED) has emerged as a potential candidate for next generation flexible, large-area, high resolution display and solid state lighting panels, because of its high color quality, attractive appearance, ease of fabrication, low manufacturing and materials cost, *etc* [1]. With great efforts from both academia and industry, the OLED has been developed based on small molecule and polymer materials and also fabricated with both vacuum deposition and solution processes [2–5]. In the past few decades, researchers have been focusing on improving the device efficiency and lowering the manufacturing cost. Today, OLED displays are becoming dominant in the high-end market. OLED lighting is also on the verge of becoming widely commercially available, and its performance is competitive with that of its inorganic counterparts.

The basic OLED structure is composed of a stack of several layers: anode/hole transport layer (HTL)/emission layer (EL)/electron transport layer (ETL)/cathode, as shown in Figure 1a. [6] The first OLED was developed by Tang and VanSlyke in 1987 with the structure of an indium tin oxide

(ITO)/aromatic diamine/8-hydroxyquinoline aluminum ($Alq_3$)/Mg-Al metal electrode [7]. Since then, ITO glass has been commonly used as the anode for OLEDs, because ITO simultaneously provides good transparency and conductivity [8]. Moreover, the work function of ITO is around 4.7 eV, which forms a low barrier for hole injection into the emission layer made of commonly used organic materials (Figure 1b) [9]. Despite these advantages, ITO is far from being a perfect candidate for OLED applications for the following reasons. First, it is not ideal for highly flexible electronics, due to its brittleness. Under mechanical bending or stretching, crack generation in the ITO film leads to much deteriorated electrical properties [10]. Second, the sputtering deposition of high quality ITO is a low throughput process and requires elevated temperature. Solution processed ITO also requires high temperature annealing to achieve a good conductivity [11]. It is vital therefore to only use substrates that are stable at high temperatures, which means an increased substrate cost and much reduced performance on plastic substrates. Furthermore, due to the widespread application of ITO as the transparent conducting electrode (TCE) for various optical devices and the limited global reserve of indium, the price of ITO will rise dramatically and further raise the cost of OLEDs. In addition, ITO does not offer ideal performance for OLEDs. It has significant light reflection and also traps the light in the waveguide mode. Its conductivity needs to be further improved, as well, for large area devices.

**Figure 1.** (**a**) Schematic diagram of the organic light emitting diode (OLED) structure; (**b**) engery level diagram of a simple OLED device consisting of *N,N′*-Bis(3-methylphenyl)-*N,N′*-diphenylbenzidine (TPD), *N,N′*-Di(1-naphthyl)-*N, N′*-diphenyl-(1,1'-biphenyl)-4,4'-diamine (NPB), 4,4'-Bis(*N*-carbazolyl)-1,1'-biphenyl (CBP), Bathocuproine (BCP), and Tris-(8-hydroxyquinoline)aluminum (Alq3); (**c**) sheet resistance and transmission chart for various types of transparent conducting electrode (TCE) materials including carbon nanotube (CNT), silver nanowire (AgNW), conductive polymers, and graphene.

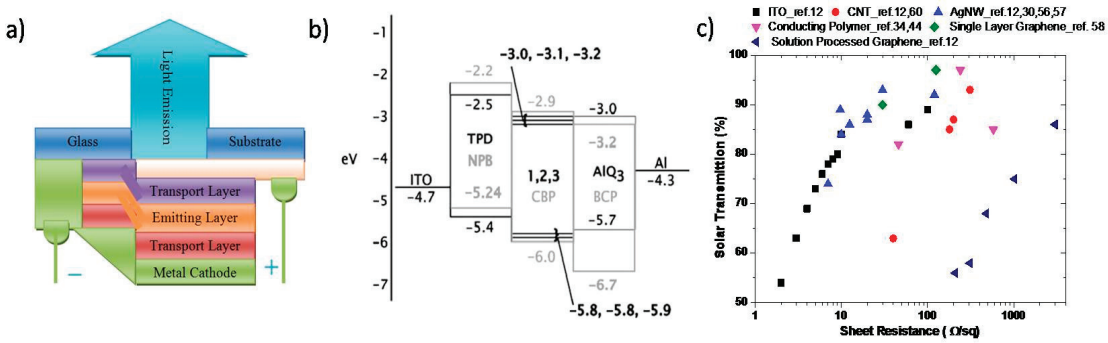


Considering all these factors, there has been increasing interest and an urgent need to look for alternative TCE materials to replace the conventional ITO. These TCE materials should be highly conductive and optically transparent; meanwhile, they should also be low cost and enable new attractive features. Here, we review the recent progress on the promising next generation TCEs. We focus our attention on the following materials: carbon nanotubes (CNTs), metallic nanowires, conducting polymers and graphene. These materials have shown the potential to fulfill standard requirements on the sheet resistance and transmission values of TCE and can be formed by low-cost

processes, such as spin coating, spray coating and even roll-to-roll processes [12]. The sheet resistance and transmittance of these materials is summarized in Figure 1c using the solar spectrum as a reference for transmission evaluation. Moreover, OLED devices demonstrated with these techniques show great potential for future highly flexible, foldable and wearable opto-electronics. We summarize the progress of each of these TCE materials with the device performance achieved and give comparisons between these techniques.

## 2. Carbon Nanotubes

The carbon nanotube (CNT) network is the first nanostructured TCE investigated for OLEDs, leading to a boom of interest in this decade [13]. CNTs exhibit a unique electrical property in that they can be both metallic and semiconducting [14]. Because of this, they are widely applied as high-performance flexible transparent transistors, optical modulators, flexible emitters, as well as TCEs [15–17]. Metallic CNTs have a suitable work function (4.7–5.2 eV) for the application as anodes in OLEDs [18,19]. In addition, the high stability, flexibility and mobility of CNTs make the CNT network a potential candidate to replace the rigid ITO substrate, while avoiding the contamination of the organic layers from the oxygen atoms in ITO.

Zhang *et al.* first developed large area CNT sheets (meter long, 5 cm-wide) as the electrode for OLED, and this nanotube sheet was reported to be as strong as the steel (Figure 2a) [13]. This report demonstrated the huge potential of CNT networks' application in optical electronics and opened a new direction for the nanostructured TCE. Zhang *et al.* tested various CNTs from different growth methods [20]. The arc discharge nanotubes showed better performance compared to high-pressure CO conversion (HiPCO) nanotubes in surface roughness, sheet resistance and transparency. A sheet resistance of ~160 ohm/sq at 87% transparency can be achieved when the CNTs network is treated with $SOCl_2$, as shown in Figure 2b,c. Li *et al.* demonstrated that a poly(3,4-ethylenedioxythiophene) poly(styrenesulfonate) (PEDOT:PSS) layer could play an important role in planarizing the roughness from CNT networks (Figure 2d) and decreasing the hole injection barrier from the CNTs to a polymer blend hole transporting layer poly(9,9-dioctylfluorene-co -*N*-(4-butylphenyl)diphenylamine) (TFB)+ 4,4'-bis[(*p*-trichlorosilylpropylphenyl)phenylamino] biphenyl (TPD-$Si_2$), which could reduce the leakage current [21]. With a PEDOT:PSS layer modified with methanol, a surface roughness less than 1 nm can be achieved, due to better PEDOT:PSS wetting onto the CNT network.

Ou *et al.* further modified the surface of the carbon nanotube network with PEDOT:PSS composite ($PS^C$) coating, which contained polyethylene glycol (PEG) additive in Baytron P500 and used $HNO_3$ acid treatment to improve the conductivity of the CNT network and the band alignment for hole injection [22]. Outstanding performance with a maximum luminance of ~9000 cd/$m^2$ and a luminance efficiency (LE) of ~10 cd/A at 1000 cd/$m^2$ was achieved, which was comparable to devices on ITO substrates. Yu *et al.* explored the capability of CNT transparent electrodes as the cathode and anode for flexible and transparent organic light emitting diodes by a lamination method [23]. Furthermore, stretchable OLEDs based on a CNT network as the TCE was built. The electroluminescent efficiency of the devices can be sustained under a 45% strain, which cannot be achieved for traditional ITO substrates [24]. The device stability with the CNT electrode exhibited

comparable lifetime with that of the ITO electrode, and the acid resistivity of the CNT electrode to PEDOT:PSS is better than that of ITO electrode for long-term operation.

**Figure 2.** (**a**) Photograph of an OLED that uses an multi-wall nanotube (MWNT) sheet as the anode and poly(3,4-ethylenedioxythiophene) poly(styrenesulfonate) (PEDOT:PSS) /Poly[2-methoxy-5-(2-ethylhexyloxy)-1,4-phenylenevinylene] (MEH-PPV)/Ca/Al [13]; (**b**) patterned multilayer single wall CNT/PEDOT:PSS/NPB/$Alq_3$/LiF/Al [20]; (**c**) device performance: photoluminescence spectrum, current density *vs.* voltage bias curve, brightness *vs.* voltage bias and quantum efficiency as a function of current density [20]; (**d**) surface roughness of PEDOT:PSS ~4 nm and methanol-modified PEDOT:PSS ~0.96 nm on a CNT network [21]; (**e**) the luminescence *vs.* the voltage of an OLED with PEDOT:PSS composite ($PS^C$)-modified CNT on Polyethylene terephthalate (PET) substrate [22].

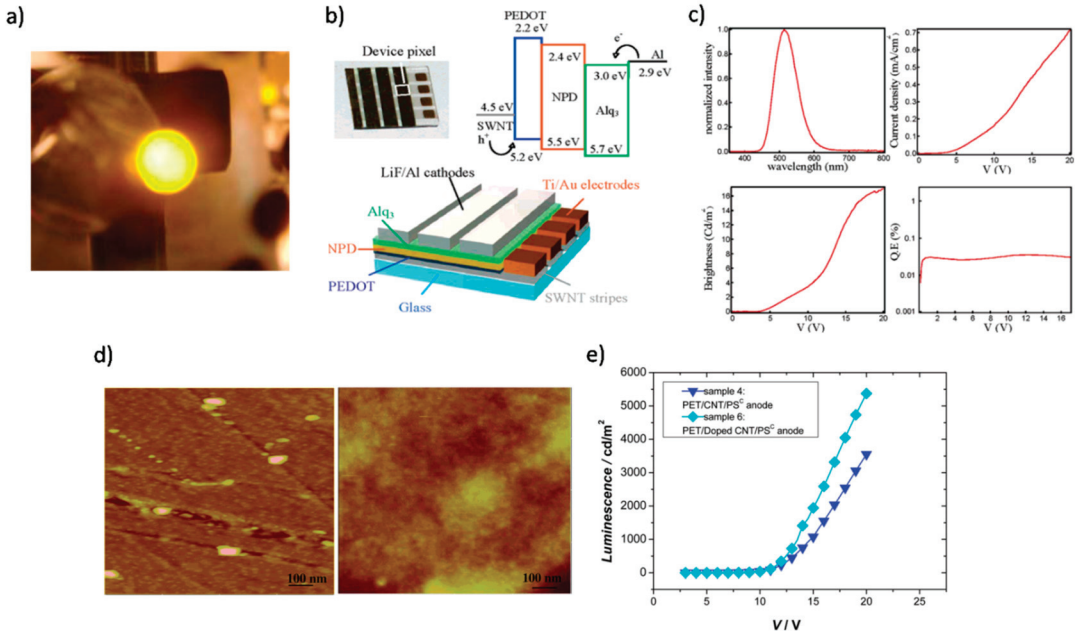


Reproduced with permission from Zhang *et al.*, Science, published by the American Association for the Advancement of Science, 2005 [13]; Zhang *et al.*, Nano Letter, published by the American Chemical Society, 2006 [20]; Li *et al.*, Nano Letter, published by the American Chemical Society, 2006 [21]; and Ou *et al.*, ACS Nano, published by the American Chemistry Society, 2009 [22].

## 3. Metallic Nanowires

Recent studies on the metallic nanowire's application in optical electronics have attracted a lot of attention. Similar to CNTs, high conductivity from the metal material and high transmittance from the open space between nanowires make the metallic nanowire a potential candidate as the TCE. Compared with CNTs, the metallic nanowire network shows better sheet resistance and transmission values, because the wire to wire contact resistance can be reduced by thermal treatment [25]. The low contact resistance between nanowires can significantly reduce the power loss on the electrodes. However, the metallic nanowire network requires PEDOT:PSS or other hole transport materials to ensure efficient hole injection as an anode, which slightly restricts the fabrication process. Lee *et al.*

demonstrated the potential of a silver nanowire network TCE on a glass substrate with a sheet resistance of 16 ohm/sq and an average transmittance of 86% between the wavelengths of 400 and 800 nm, which is comparable to commercial ITO substrates (Figure 3a) [26]. Yu *et al.* first demonstrated a composite electrode in which the silver nanowires were embedded in cross-linkable polyacrylate substrate, which could successfully replace the traditional rigid glass substrate [27]. This result opened up the possibility of realizing the high flexibility and high performance OLEDs by incorporating a solution processed metallic nanowire network.

**Figure 3.** (**a**) Solar photon flux-weighted transmissivity *vs.* sheet resistance for Ag gratings (blue line), ITO (red dotted line), CNT meshes (Δ) and Ag nanowire meshes (■) deposited on a glass substrate. The Ag line width is a 40 nm and a 400 nm grating period [26]. (**b**) Normalized radiant intensity, color coordinates *vs.* viewing angle and photographic image of four operating nanowire (NW)-OLEDs [28]. (**c**) Photographs of a polymer light-emitting electrochemical cell (PLEC) (original emission area, 5.0 × 4.5 $mm^2$) biased at 14 V at specified strains [29]. (**d**) Colors from blue to red can be selected by different period nanowire arrays [32].

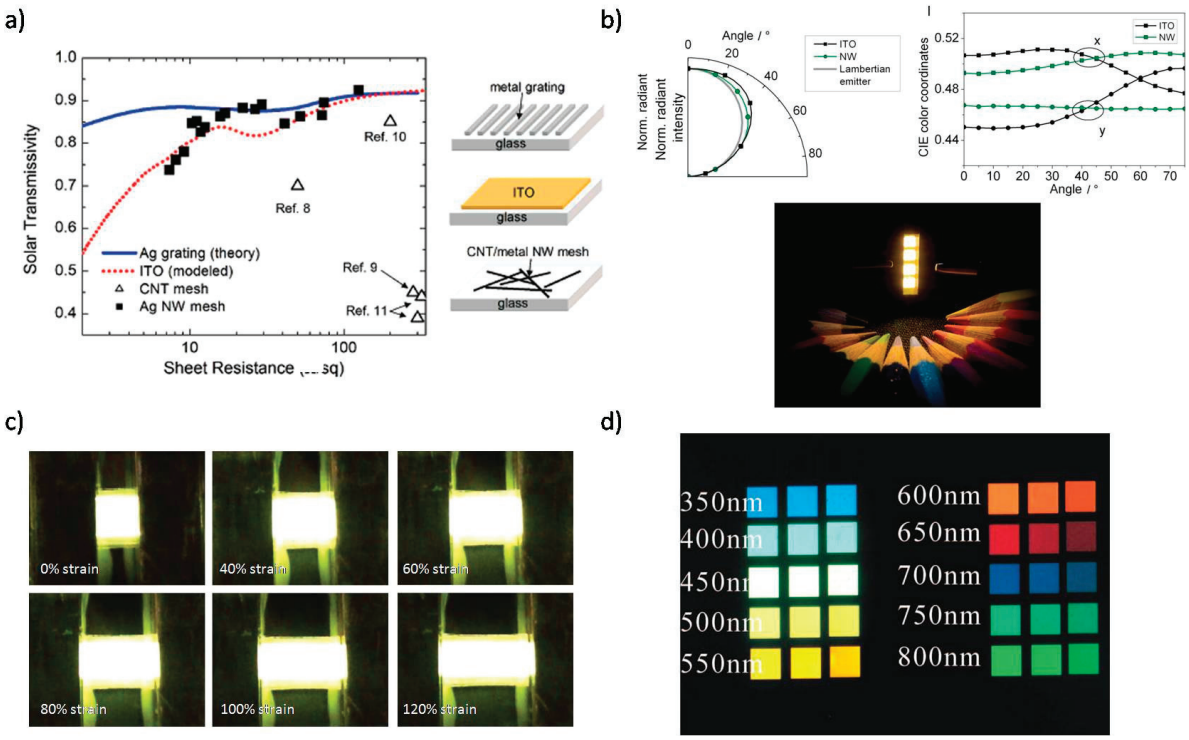


Reproduced with permission from Lee *et al.*, Nano Letter, published by the American Chemical Society, 2008 [26]; Gaynor *et al.*, Advanced Materials, published by John Wiley & Sons, Inc., 2013 [28]; Liang *et al.* Nature Photonics, published by Macmillan Publishers Limited, 2013 [29]; and Hsu *et al.*, Apply Physics Letter, published by the American Institute of Physics, 2008 [32].

Gaynor *et al.* investigated the angular dependence of white OLEDs using silver nanowires embedded in poly(methyl methacrylate) (PMMA) as the electrode [28]. The scattering of the silver nanowire network kept a stabilized viewing angle characteristic with reduced color shift and better Lambertian emission for the OLED. By further incorporation of light outcoupling techniques, a power efficiency of 54 Lm/W was achieved, as shown in Figure 3b. Liang *et al.* reported an

elastomeric polymer (polyurethane acrylate (PUA)) -based silver nanowire substrate with yellow light-emitting polymers consisting of ethoxylated trimethylolpropane triacrylate (ETPTA), polyethylene oxide (PEO) and lithium trifluoromethanesulphonate (LiTf), and the efficiency was kept at 2.5 cd/A under 120% strain (Figure 3c) [29]. The concern for metallic nanowire electrode is the instability, due to Rayleigh instability and contact ripening, resulting in the loss of the conductive path during operation. These might be the challenges for having long lifetime OLED devices [30,31].

The improvement of the silver nanowire TCE provided a platform for OLEDs to reach wider applications on display and lighting. Furthermore, the dimension of the metallic nanowire could affect the light scattering, light coupling and sheet resistance to transmission values of the TCE, providing us with an additional degree of freedom in improving the device performance. Aligned metal nanowire fabricated by a vacuum process was reported to have improved light outcoupling of the OLEDs (Figure 3d) [32]. The optical effect of the metallic nanowire on OLED and the alignment control of the nanowire through fabrication are still under investigation.

## 4. Conductive Polymers

Among various types of conductive polymers, PEDOT:PSS and polyaniline (PANI) are currently the most popular materials to replace the conventional ITO electrode. These two materials are well-studied, conjugated polymers with excellent mechanical stability, flexibility and, more importantly, they can achieve a high conductivity and transparency.

It was shown that PANI has the potential as a solution-processable TCE by Cao *et al.* [33]. They discovered that the camphor-sulfonic acid (CSA) doped PANI (PANI:CSA), which is soluble in m-cresol or chloroform, is conductive (<10 S/cm) and optically transparent. Gustafsson *et al.* successfully fabricated the PANI:CSA film on Polyethylene terephthalate (PET) substrate as the anode and demonstrated the first flexible polymer light emitting diode (PLED) device [5]. However, PANI:CSA film needs to be thicker than 250 nm to achieve 160 ohm/sq, while the transparency is about 70% under such a thickness (Figure 4a) [34]. Fehse *et al.* reported a new dispersion of PANI (D1033), which has a conductivity of 200 S/cm and a lower absorbance at 750 nm in the visible region than that of PANI:CSA (Figure 4b) [35]. Even though the improvement of the PANI properties resulted in better device performance, it is still lower than that of the commercial ITO substrate. PEDOT:PSS was invented in 1991 by Bayer [36] as an antistatic coating material. Cao *et al.* first introduced PEDOT:PSS into the PLED as a TCE with 500 ohm/sq and 75% transmission within the visible light region [37]. After that, PEDOT:PSS became commonly used as the hole injection layer for OLEDs, as well. In order to improve the properties of the PEDOT:PSS, many treatments have been applied to improve the conductivity without losing the transparency. Kim *et al.* investigated different organic solvents, including dimethyl sulfoxide (DMSO), *N*,*N*-dimethyl formamide (DMF) and tetrahydrofuran (THF), and the addition of the high boiling polar solvent DMSO produced the highest conductivity among the three [38]. Ouyang *et al.* reported using ethylene glycol (EG) as a polar additive and acquired PEDOT:PSS thin films with a conductivity up to 160 S/cm, demonstrating a comparable performance to ITO/PEDOT:PSS on Poly[2-methoxy-5-(2-ethylhexyloxy)-1,4-phenylenevinylene] (MEH-PPV) PLED devices [39]. Fehse *et al.* used a commercially available high conductivity PEDOT:PSS Baytron PH500 (conductivity ~500 S/cm) as the TCE in small molecular OLED devices and achieved comparable

or even superior performance (on green and blue emitting devices) than ITO anode devices [40]. Various treatments, like using zwitterionic surfactants, co-solvent system or exposing the films to dichloroacetic acid, were reported to achieve better conductivity in recent years [41–43]. Kim *et al.* demonstrated that with the addition of EG and a solvent post-treatment method, they could remarkably increase the conductivity up to 1418 S/cm, around 65 ohm/sq at 80% transmission [44]. Vosgueritchian *et al.* reported using a combination of DMSO and the fluorosurfactant Zonyl-FS300 (Zonyl) to achieve 46 ohm/sq at 82% transmission [45]. Recently, Xia *et al.* reported a $H_2SO_4$ treatment to reach 2400 S/cm and 3065 S/cm from multiple treatments [46]. These values are close to that of commercially available ITO substrates.

**Figure 4.** (**a**) Transmittance and sheet resistance of different polyaniline (PANI) thicknesses [34]; (**b**) the wavelength dependence of the refractive index and the extinction coefficient of ITO (squares) and PANI (triangles) films [35]; (**c**) the device structure of ITO-free transparent OLEDs based on a PEDOT:PSS TCE; (**d**) the comparison of external quantum efficiencies (EQEs) and corresponding photon fluxes for bottom and top emission and the sum of both (experiment (symbols) and optical simulation (lines) results); (**e**) aging characteristics of PEDOT:PSS-based OLEDs with a different PEDOT:PSS thickness. The encapsulated devices are aged over around 900 h with an initial luminance of around 1500 cd/m$^2$. Constant currents are applied for each sample according to the corresponding luminance [47]. HTL, hole transport layer.

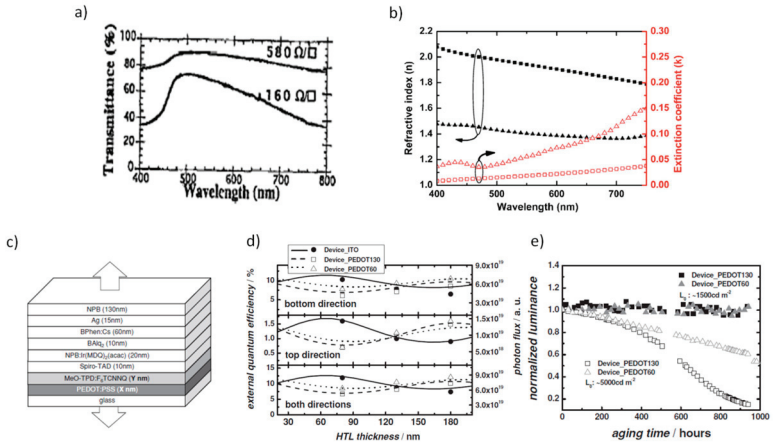


Reproduced with permission from Yang *et al.*, Apply Physics Letter, published by the American Institute of Physics, 1994 [34]; Fehse *et al.*, Journal of Apply Physics, published by the American Institute of Physics, 2007 [35]; and Kim *et al.* Advanced Materials, published by John Wiley & Sons, Inc., 2013 [47].

Kim *et al.* demonstrated long lifetime (over 900 h under 1500 cd/m$^2$) and high performance (over 12% external quantum efficiency (EQE) under a driving current density of 10 mA/cm$^2$) OLEDs on polymer TCE. The results are shown in Figure 4c–d [47], comparing with those made from the ITO substrate. Moreover, from the optical study from Cai *et al*, the PEDOT:PSS anode could be more beneficial to the light outcoupling than ITO substrates, due to the match of the refractive index [48]. At the current stage, however, these polymers still exhibit a lower conductivity and transmission than CNTs and metallic nanowire networks. In order to achieve a better device performance

compared with ITO and other new materials, the properties and stability of the conductive polymers need to be further improved before they can be mass produced as the next generation TCE.

## 5. Graphene

Graphene is another promising candidate as a TCE in OLEDs. A flexible two-dimensional sheet of $sp^2$-hybridized carbon atoms has very high conductivity and is nearly transparent. A single layer of graphene showed a sheet resistance of 125 ohm/sq and 97.4% transmission at the 550 nm wavelength, which is superior to the ITO substrate and other reported TCEs (Figure 5a) [49].

**Figure 5.** (**a**) Transmittance of the roll-to-roll layer-by-layer transferred graphene films on quartz substrates. The inset shows the transmittance spectra of graphene films with and without $HNO_3$ doping and the optical images for the corresponding number of transferred layers (1 × 1 $cm^2$) [49]; (**b**) Current density (filled symbols) and luminance (open symbols) *vs.* applied forward bias for an OLED on graphene (squares) and ITO (circles), with an OLED device structure of anode/PEDOT:PSS/NPD/Alq3/LiF/Al; (**c**) External quantum efficiency (EQE) (filled symbols) and luminous power efficiency (open symbols) for an OLED on graphene film (squares) and ITO glass (circles) [12]; (**d**) Power efficiencies of OLED devices using various graphene layers (doped with $HNO_3$ or $AuCl_3$) and ITO as the anode; (**e**) Photograph of a flexible fluorescent green OLED with a four-layered graphene anode (4L-G) doped with HNO3 (4L-G-HNO3) [51]; (**f**) Power efficiency and current efficiency of white OLED (WOLED) based on ITO and single layer graphene electrode [52].

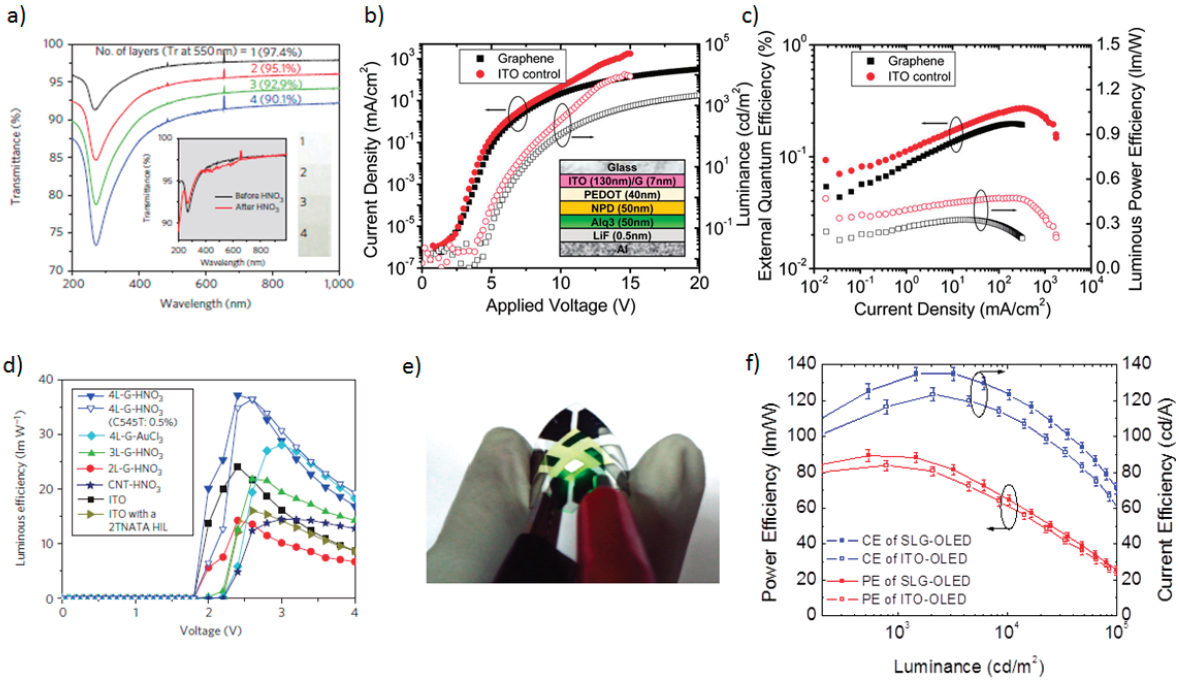


Reproduced with permission from Bae *et al.*, Nature Nanotechnology, published by Macmillan Publishers Limited, 2010 [49]; Wu *et al.* ACS Nano, published by the American Chemical Society, 2010 [12]; Han *et al.* Nature Photonics, published by Macmillan Publishers Limited, 2012 [51]; and Li *et al.* Nature Communication, published by Macmillan Publishers Limited, 2013 [52].

Wu *et al.* demonstrated solution processed graphene oxide thin films fabricated using Hummers' method and the ability to further reduce them to graphene thin films [12,50]. The graphene films were used as the TCE for OLEDs with a film thickness of about 7 nm, a sheet resistance of about 800 ohm/sq and 82% transmission at 550 nm, which is lower than the theoretical value, due to the existence of multiple grain boundaries, lattice defects and oxidative traps formed during the fabrication process. The device performance with a solution processed graphene electrode showed a turn-on voltage of 4.5 V and a luminance of 300 cd/m$^2$ at 11.7 V, which is comparable to those of ITO substrates, which had a turn-on voltage of 3.8 V and a luminance of 300 cd/m$^2$ at 9.9 V bias (Figure 5b,c). Han *et al.* recently reported an extremely efficient flexible OLED by introducing a work function tunable layer [51]. The mismatch of the electrical band alignment between graphene (work function ~4.4 eV) and the hole transport layer, like *N,N′*-Di(1-naphthyl)-*N, N′*-diphenyl-(1,1′-biphenyl)-4,4'-diamine (NPB) (work function ~5.4 eV), needs to be reduced for efficient hole injection. The authors incorporated a self-organized gradient hole injection layer (GraHIL), which was composed of PEDOT:PSS and tetrafluoroethylene-perfluoro-3, 6-dioxa-4-methyl-7-octenesulphonic acid copolymer, one of the perfluorinated ionomers (PFIs). The GraHIL provided a work function gradient throughout the hole injection layer and, in turn, improved the charge injection efficiency. Based on a graphene/GraHIL/NPB/$Alq_3$/LiF/Al structure, the luminance efficiencies with doped graphene TCE as the anode (37.2 Lm/W in fluorescent OLEDs, 102.7 Lm/W in phosphorescent OLEDs) is higher than the devices using conventional ITO as the TCE (24.1 Lm/W in fluorescent OLEDs, 85.6 Lm/W in phosphorescent OLEDs, shown in the Figure 5d,e). Li *et al.* showed that white OLEDs (WOLEDs) on graphene electrode can indeed exhibit performance satisfying general lighting requirements [52]. WOLEDs on graphene with a power efficiency of 80 Lm/W at a high brightness of 3000 cd/m$^2$ are demonstrated (Figure 5f). It is also found that graphene electrodes have the advantage of light extraction over ITO. White ITO has significant light reflection at both the top and bottom interface and also has significant light trapping. In the waveguide mode, Graphene, on the other hand, is so thin that it is optically negligible. There is almost no light reflection and trapping in the graphene layer. Ultimately, more light can be coupled out of the graphene OLED than the ITO OLED [52].

The above high-performance OLEDs on grapheme were all demonstrated using polymer interface layers. In contrast, OLEDs on graphene only electrodes without a polymer interface layers were also reported. In the early work, Sun *et al.* applied multilayered graphene from chemical vapor deposition as the anode for an OLED device and showed working devices without using the polymer interface layer, but with much less performance compared with the ITO reference device. The high leakage current and low efficiency were attributed to the surface roughness and work function mismatch [53]. Hwang *et al.* found that using weak plasma treatment to multilayered graphene can improve the hole injection efficiency and demonstrated high OLED device performance on graphene without polymer interface layers [54]. These works clearly indicate graphene's capability of charge conduction and injection. After optimization, graphene can serve as an excellent electrode by itself or together with a polymer layer.

Besides the high device performance, the stability of graphene is also excellent. Due to the inert material properties, it is not reactive with most chemicals. In addition, it does not have the problem of device degradation caused by electrode material diffusion into OLEDs, which can happen for Ag

and ITO electrodes. The upcoming challenge for the grapheme electrode is to further improve the electrical and optical properties and to make the fabrication process faster, easier and more cost effective.

## 6. Conclusions

Four different types of TCE materials are discussed in this review in terms of their electrical and optical performance as a TCE and the resultant OLED device performance. A comparison of their current status is summarized in Table 1. The performance of CNT TCEs is mainly limited by the contact resistance between adjacent wires, while it provides excellent mechanical properties and stability. The purity and type of CNT will also significantly affect the device performance, due to the difference in conductivity and surface roughness. Metallic nanowire TCEs exhibit better sheet resistance and transmission compared to their CNT counterparts, which resulted in highly efficient and stretchable OLED devices. Optical enhancement by the metallic nanowires is another major advantage for their future application and needs further investigation. Better control of the dimension and alignment of the metallic nanowires also needs to be further investigated. Conducting polymers have a longer developing history comparing with the other mentioned techniques. Their properties are becoming more and more competitive with traditional ITO glass showing similar conductivity values. They can also be tuned to provide optimal refractive index matching for efficient light outcoupling in OLEDs. The search for methods to precisely control the morphologies of the conducting polymers and to further improve the electrical and optical properties is ongoing. Graphene is the latest material to be applied as the TCE for OLEDs. The high transparency and the absence of light trapping from the ultrathin graphene sheet, the high in-plane conductivity and its ability to be solution processed make it a promising candidate as the next generation TCE. Its potential as the TCE in OLEDs has been proven.Outstanding OLED performance comparable to those on ITO glass has been achieved. Surface modification, the reduction of grain boundaries and defects for roll-to-roll processed graphene are some of the key routes towards further improvement.

Although most of these new TCEs still have many challenges in order to replace ITO completely, their performance is improving very rapidly. Even in the current stage, very low sheet resistance can be obtained by combining the new TCEs with a metal grid for large area applications [55]. Light extraction is an aspect that new TCEs can improve over ITO. The light reflection and trapping in most new TCEs are reduced comparing with ITO, due to the porous nature and scattering effect of CNTs and metal nanowires, the tunable index of the polymer, and the ultra-thin thickness of graphene, respectively. Because of this, light-extraction methods can be much simplified, and more light can be coupled out ultimately. In addition, new TCEs do enable many new attractive features, such as high mechanical flexibility and stretchability. High efficiency or reasonably good efficiency devices are demonstrated for most of these TCEs, indicating that the process integration of new TCEs into high performance OLED devices will not be a fundamental hurdle for adopting these new materials. Low cost, high throughput and reliable process development is the key to commercially viability. Once a successful process is established, the impact of a new TCE is not only limited to the field of OLED devices, but can be readily applied to various other opto electronic devices. A myriad of applications can result from the development of one alternative material. These materials and

related techniques are very likely to have a significant impact on optoelectronic research and the industry in the next few decades.

**Table 1.** Comparison of the TCE materials.

| TCE materials for OLEDs | ITO | CNTs | Metal Nanowires | Conductive Polymers | Graphene |
|---|---|---|---|---|---|
| Conductivity/Transparency (at 550 nm) | 10 Ω/sq at 90% | 180 Ω/sq at 85% | 9.7 Ω/sq at 89%<br>30 Ω/sq at 93% | 42 Ω/sq at 82%<br>240 Ω/sq at 97% | 125 Ω/sq at 97%<br>30 Ω/sq at 90% |
| Light Reflection | High | Low | Low | Low | No reflection |
| Light Trapping | High | Low | Low | Low | No Trapping |
| Material Cost | High | Low | Medium | Low | Low |
| Process Cost | High | Potentially Low | Potentially Low | Low | Potentially Low |
| Stability | Good | Excellent | Medium | Medium | Excellent |
| Flexibility | Poor | Flexible | Flexible | Highly flexible | Highly flexible |
| Key OLED Performance Demonstrated | >100 Lm/W (white) | 10 cd/A at 1000 cd/m (green) | 54 Lm/W similar to ITO control device (white) | 12% EQE<br>900 hours<br>(green) | 103 lm/W (green)<br>80 Lm/W at 3000 cd/m$^2$ (white) |
| Advantages over ITO | | Solution process<br>Flexible<br>Stretchable | Solution process<br>Flexible<br>Stretchable<br>Angle uniformity | Solution process<br>Flexible<br>Light extraction | Highly flexible<br>Ultra-thin<br>Light extraction |
| Challenges to Replace ITO | | Conductivity<br>Roughness<br>Cost | Stability<br>Cost | Conductivity<br>Stability | Conductivity<br>Cost |
| Reference | [56] | [23,24,57,58] | [29,30,59,60] | [45–48] | [12,49,61] |

## Acknowledgments

The authors would like to thank Xiaodan Zhu for proof reading.

## Conflicts of Interest

The authors declare no conflict of interest.

## References

1. Tsutsui, T.; Takada, N. Progress in emission efficiency of organic light-emitting diodes: Basic understanding and its technical application. *Jap. J. Appl. Phys.* **2013**, *52*, 110001.
2. Grimsdale, A.C.; Leok Chan, K.; Martin, R.E.; Jokisz, P.G.; Holmes, A.B. Synthesis of light-emitting conjugated polymers for applications in electroluminescent devices. *Chem. Rev.* **2009**, *109*, 897–1091.
3. Li, J.; Liu, D. Dendrimers for organic light-emitting diodes. *J. Mater. Chem.* **2009**, *19*, 7584–7591.

4. Rehmann, N.; Hertel, D.; Meerholz, K.; Becker, H.; Heun, S. Highly efficient solution-processed phosphorescent multilayer organic light-emitting diodes based on small-molecule hosts. *Appl. Phys. Lett.* **2007**, *91*, 103507.
5. Gustafsson, G.; Cao, Y.; Treacy, G.M.; Klavetter, F.; Colaneri, N.; Heeger, A.J. Flexible light-emitting diodes made from soluble conducting polymers. *Nature* **1992**, *357*, 477–479.
6. Islam, A.; Rabbani, M.; Bappy, M.H.; Miah, M.A.R.; Sakib, N. A Review on Fabrication Process of Organic Light Emitting Diodes. *ICIEV* **2013**, doi:10.1109/ICIEV.2013.6572656.
7. Tang, C.W.; VanSlyke, S.A. Organic electroluminescent diodes. *Appl. Phys. Lett.* **1987**, *51*, 913–915.
8. Gordon, R.G. Criteria for choosing transparent conductors. *MRS Bull.* **2000**, *25*, 52–57.
9. Hellstrom, S.L.; Ugolotti, J.; Britovsek, G.J.P.; Jones, T.S.; White, A.J.P. The effect of fluorination on the luminescent behaviour of 8-hydroxyquinoline boron compounds. *New J. Chem.* **2008**, *32*, 1379–1387.
10. Peng, C.; Jia, Z.; Neilson, H.; Li, T.; Lou, J. *In situ* electro-mechanical experiments and mechanics modeling of fracture in indium tin oxide-based multilayer electrodes. *Adv. Eng. Mater.* **2012**, *15*, 250–256.
11. Kim, N.-R.; Lee, J.-H.; Lee, Y.-Y.; Nam, D.-H.; Yeon, H.-W.; Lee, S.-Y.; Yang, T.-Y.; Lee, Y.-J.; Chu, A.; Nam, K.T.; *et al.* Enhanced conductivity of solution-processed indium tin oxide nanoparticle films by oxygen partial pressure controlled annealing. *J. Mater. Chem. C* **2013**, *1*, 5953–5959.
12. Wu, J.; Agrawal, M.; Becerril, H.C.A.; Bao, Z.; Liu, Z.; Chen, Y.; Peumans, P. Organic light-emitting diodes on solution-processed graphene transparent electrodes. *ACS Nano* **2009**, *4*, 43–48.
13. Zhang, M.; Fang, S.; Zakhidov, A.A.; Lee, S.B.; Aliev, A.E.; Williams, C.D.; Atkinson, K.R.; Baughman, R.H. Strong, transparent, multifunctional, carbon nanotube sheets. *Science* **2005**, *309*, 1215–1219.
14. Hu, L.; Hecht, D.S.; Gruner, G. Carbon nanotube thin films: Fabrication, properties, and applications. *Chem. Rev.* **2010**, *110*, 5790–5844.
15. De Volder, M.F.L.; Tawfick, S.H.; Baughman, R.H.; Hart, A.J. Carbon nanotubes: Present and future commercial applications. *Science* **2013**, *339*, 535–539.
16. Dresselhaus, M.; Dresselhaus, G.; Avouris, P.; Ajayan, P.; Zhou, O. Applications of Carbon Nanotubes. In *Carbon Nanotubes*; Springer: Berlin/Heidelberg, Germany, 2001; Volume 80, pp. 391–425.
17. Martel, R.; Schmidt, T.; Shea, H.R.; Hertel, T.; Avouris, P. Single- and multi-wall carbon nanotube field-effect transistors. *Appl. Phys. Lett.* **1998**, *73*, 2447–2449.
18. Zhao, J.; Han, J.; Lu, J.P. Work functions of pristine and alkali-metal intercalated carbon nanotubes and bundles. *Phys. Rev. B* **2002**, *65*, 193401.
19. Suzuki, S.; Bower, C.; Watanabe, Y.; Zhou, O. Work functions and valence band states of pristine and cs-intercalated single-walled carbon nanotube bundles. *Appl. Phys. Lett.* **2000**, *76*, 4007–4009.

20. Zhang, D.; Ryu, K.; Liu, X.; Polikarpov, E.; Ly, J.; Tompson, M.E.; Zhou, C. Transparent, conductive, and flexible carbon nanotube films and their application in organic light-emitting diodes. *Nano Lett.* **2006**, *6*, 1880–1886.
21. Li, J.; Hu, L.; Wang, L.; Zhou, Y.; Gruner, G.; Marks, T.J. Organic light-emitting diodes having carbon nanotube anodes. *Nano Lett.* **2006**, *6*, 2472–2477.
22. Ou, E.C.W.; Hu, L.; Raymond, G.C.R.; Soo, O.K.; Pan, J.; Zheng, Z.; Park, Y.; Hecht, D.; Irvin, G.; Drzaic, P.; *et al.* Surface-modified nanotube anodes for high performance organic light-emitting diode. *ACS Nano* **2009**, *3*, 2258–2264.
23. Yu, Z.; Hu, L.; Liu, Z.; Sun, M.; Wang, M.; Gruner, G.; Pei, Q. Fully bendable polymer light emitting devices with carbon nanotubes as cathode and anode. *Appl. Phys. Lett.* **2009**, *95*, 203304.
24. Yu, Z.; Niu, X.; Liu, Z.; Pei, Q. Intrinsically stretchable polymer light-emitting devices using carbon nanotube-polymer composite electrodes. *Adv. Mater.* **2011**, *23*, 3989–3994.
25. Hu, L.; Wu, H.; Cui, Y. Metal nanogrids, nanowires, and nanofibers for transparent electrodes. *MRS Bull.* **2011**, *36*, 760–765.
26. Lee, J.-Y.; Connor, S.T.; Cui, Y.; Peumans, P. Solution-processed metal nanowire mesh transparent electrodes. *Nano Lett.* **2008**, *8*, 689–692.
27. Yu, Z.; Zhang, Q.; Li, L.; Chen, Q.; Niu, X.; Liu, J.; Pei, Q. Highly flexible silver nanowire electrodes for shape-memory polymer light-emitting diodes. *Adv. Mater.* **2011**, *23*, 664–668.
28. Gaynor, W.; Hofmann, S.; Christoforo, M.G.; Sachse, C.; Mehra, S.; Salleo, A.; McGehee, M.D.; Gather, M.C.; Lüssem, B.; Müller-Meskamp, L.; *et al.* Color in the corners: ITO-free white oleds with angular color stability. *Adv. Mater.* **2013**, *25*, 4006–4013.
29. Liang, J.; Li, L.; Niu, X.; Yu, Z.; Pei, Q. Elastomeric polymer light-emitting devices and displays. *Nat. Photon.* **2013**, *7*, 817–824.
30. Song, T.-B.; Chen, Y.; Chung, C.-H.; Yang, Y.; Bob, B.; Duan, H.-S.; Li, G.; Tu, K.-N.; Huang, Y. Nanoscale joule heating and electromigration enhanced ripening of silver nanowire contacts. *ACS Nano ASAP* **2014**, doi:10.1021/nn4065567.
31. Karim, S.; Toimil-Molares, M.E.; Balogh, A.G.; Ensinger, W.; Cornelius, T.W.; Khan, E.U.; Neumann, R. Morphological evolution of au nanowires controlled by rayleigh instability. *Nanotechnology* **2006**, *17*, 5954–5959.
32. Hsu, S.-Y.; Lee, M.-C.; Lee, K.-L.; Wei, P.-K. Extraction enhancement in organic light emitting devices by using metallic nanowire arrays. *Appl. Phys. Lett.* **2008**, *92*, 013303.
33. Cao, Y.; Treacy, G.M.; Smith, P.; Heeger, A.J. Solutioncast films of polyaniline: Optical quality transparent electrodes. *Appl. Phys. Lett.* **1992**, *60*, 2711–2713.
34. Yang, Y.; Heeger, A.J. Polyaniline as a transparent electrode for polymer lightemitting diodes: Lower operating voltage and higher efficiency. *Appl. Phys. Lett.* **1994**, *64*, 1245–1247.
35. Fehse, K.; Schwartz, G.; Walzer, K.; Leo, K. Combination of a polyaniline anode and doped charge transport layers for high-efficiency organic light emitting diodes. *J. Appl. Phys.* **2007**, *101*, 124509.
36. Bayer, A.G. Europen Patent, 440957, 1991.

37. Cao, Y.; Yu, G.; Zhang, C.; Menon, R.; Heeger, A.J. Polymer light-emitting diodes with polyethylene dioxythiophene-polystyrene sulfonate as the transparent anode. *Synth. Met.* **1997**, *87*, 171–174.
38. Kim, J.Y.; Jung, J.H.; Lee, D.E.; Joo, J. Enhancement of electrical conductivity of poly(3,4-ethylenedioxythiophene)/poly(4-styrenesulfonate) by a change of solvents. *Synth. Met.* **2002**, *126*, 311–316.
39. Ouyang, J.; Chu, C.W.; Chen, F.C.; Xu, Q.; Yang, Y. High-conductivity poly(3,4-ethylenedioxythiophene):Poly(styrene sulfonate) film and its application in polymer optoelectronic devices. *Adv. Funct. Mater.* **2005**, *15*, 203–208.
40. Fehse, K.; Walzer, K.; Leo, K.; Lövenich, W.; Elschner, A. Highly conductive polymer anodes as replacements for inorganic materials in high-efficiency organic light-emitting diodes. *Adv. Mater.* **2007**, *19*, 441–444.
41. Xia, Y.; Zhang, H.; Ouyang, J. Highly conductive PEDOT:PSS films prepared through a treatment with zwitterions and their application in polymer photovoltaic cells. *J. Mater. Chem.* **2010**, *20*, 9740–9747.
42. Xia, Y.; Ouyang, J. PEDOT:PSS films with significantly enhanced conductivities induced by preferential solvation with cosolvents and their application in polymer photovoltaic cells. *J. Mater. Chem.* **2011**, *21*, 4927–4936.
43. Yoo, J.E.; Lee, K.S.; Garcia, A.; Tarver, J.; Gomez, E.D.; Baldwin, K.; Sun, Y.; Meng, H.; Nguyen, T.-Q.; Loo, Y.-L. Directly patternable, highly conducting polymers for broad applications in organic electronics. *Proc. Natl. Acad. Sci. USA* **2010**, *107*, 5712–5717.
44. Kim, Y.H.; Sachse, C.; Machala, M.L.; May, C.; Müller-Meskamp, L.; Leo, K. Highly conductive PEDOT:PSS electrode with optimized solvent and thermal post-treatment for ito-free organic solar cells. *Adv. Funct. Mater.* **2011**, *21*, 1076–1081.
45. Vosgueritchian, M.; Lipomi, D.J.; Bao, Z. Highly conductive and transparent PEDOT:PSS films with a fluorosurfactant for stretchable and flexible transparent electrodes. *Adv. Funct. Mater.* **2012**, *22*, 421–428.
46. Xia, Y.; Sun, K.; Ouyang, J. Solution-processed metallic conducting polymer films as transparent electrode of optoelectronic devices. *Adv. Mater.* **2012**, *24*, 2436–2440.
47. Kim, Y.H.; Lee, J.; Hofmann, S.; Gather, M.C.; Müller-Meskamp, L.; Leo, K. Achieving high efficiency and improved stability in ito-free transparent organic light-emitting diodes with conductive polymer electrodes. *Adv. Funct. Mater.* **2013**, *23*, 3763–3769.
48. Cai, M.; Ye, Z.; Xiao, T.; Liu, R.; Chen, Y.; Mayer, R.W.; Biswas, R.; Ho, K.-M.; Shinar, R.; Shinar, J. Extremely efficient indium-tin-oxide-free green phosphorescent organic light-emitting diodes. *Adv. Mater.* **2012**, *24*, 4337–4342.
49. Bae, S.; Kim, H.; Lee, Y.; Xu, X.; Park, J.-S.; Zheng, Y.; Balakrishnan, J.; Lei, T.; Kim, H.R.; Song, Y.I.; *et al*. Roll-to-roll production of 30-inch graphene films for transparent electrodes. *Nat. Nanotechnol.* **2010**, *5*, 574–578.
50. Hummers, W.S.; Offeman, R.E. Preparation of graphitic oxide. *J. Am. Chem. Soc.* **1958**, *80*, 1339–1339.

51. Han, T.-H.; Lee, Y.; Choi, M.-R.; Woo, S.-H.; Bae, S.-H.; Hong, B.H.; Ahn, J.-H.; Lee, T.-W. Extremely efficient flexible organic light-emitting diodes with modified graphene anode. *Nat. Photon.* **2012**, *6*, 105–110.
52. Li, N.; Oida, S.; Tulevski, G.S.; Han, S.-J.; Hannon, J.B.; Sadana, D.K.; Chen, T.-C. Efficient and bright organic light-emitting diodes on single-layer graphene electrodes. *Nat. Commun*. **2013**, *4*, 2294.
53. Sun, T.; Wang, Z.L.; Shi, Z.J.; Ran, G.Z.; Xu, W.J.; Wang, Z.Y.; Li, Y.Z.; Dai, L.; Qin, G.G. Multilayered graphene used as anode of organic light emitting devices. *Appl. Phys. Lett.* **2010**, *96*, 133301.
54. Hwang, J.; Choi, H.K.; Moon, J.; Kim, T.Y.; Shin, J.-W.; Joo, C.W.; Han, J.-H.; Cho, D.-H.; Huh, J.W.; Choi, S.-Y.; *et al.* Multilayered graphene anode for blue phosphorescent organic light emitting diodes. *Appl. Phys. Lett.* **2012**, *100*, 133304.
55. Zhu, Y.; Sun, Z.; Yan, Z.; Jin, Z.; Tour, J.M. Rational design of hybrid graphene films for high-performance transparent electrodes. *ACS Nano* **2011**, *5*, 6472–6479.
*56.* Ellmer, K. Past achievements and future challenges in the development of optically transparent electrodes. *Nat. Photon.* **2012**, *6*, 809–817.
57. Nirmalraj, P.N.; Lyons, P.E.; De, S.; Coleman, J.N.; Boland, J.J. Electrical connectivity in single-walled carbon nanotube networks. *Nano Lett.* **2009**, *9*, 3890–3895.
58. Gruner, G. Carbon nanotube films for transparent and plastic electronics. *J. Mater. Chem*. **2006**, *16*, 3533–3539.
59. Chung, C.-H.; Song, T.-B.; Bob, B.; Zhu, R.; Duan, H.-S.; Yang, Y. Silver Nanowire Composite Window Layers for Fully Solution-Deposited Thin-Film Photovoltaic Devices. *Adv. Mater.* **2012**, *24*, 5499–5504.
60. Leem, D.-S.; Edwards, A.; Faist, M.; Nelson, J.; Bradley, D.D.C.; De Mello, J.C. Efficient organic solar cells with solution-processed silver nanowire electrodes. *Adv. Mater.* **2011**, *23*, 4371–4375.
61. Eda, G.; Fanchini, G.; Chhowalla, M. Large-area ultrathin films of reduced graphene oxide as a transparent and flexible electronic material. *Nat. Nanotechnol*. **2008**, *3*, 270–274.

# Chapter 10

# Improvement in the Lifetime of Planar Organic Photovoltaic Cells through the Introduction of $MoO_3$ into Their Cathode Buffer Layers

**Linda Cattin, Mustapha Morsli and Jean Christian Bernède**

**Abstract:** Recently, $MoO_3$, which is typically used as an anode buffer layer in organic photovoltaic cells (OPVCs), has also been used as a cathode buffer layer (CBL). Here, we check its efficiency as a CBL using a planar heterojunction based on the CuPc/$C_{60}$ couple. The CBL is a bi-layer *tris*-(8-hydroxyquinoline) aluminum ($Alq_3$)/$MoO_3$. We show that the OPVC with $MoO_3$ in its CBL almost immediately exhibits lower efficiency than those using $Alq_3$ alone. Nevertheless, the OPVCs increase their efficiency during the first five to six days of air exposure. We explain this evolution of the efficiency of the OPVCs over time through the variation in the $MoO_3$ work function due to air contamination. By comparison to a classical OPVC using a CBL containing only $Alq_3$, if it is found that the initial efficiency of the latter is higher, this result is no longer the same after one week of exposure to ambient air. Indeed, this result is due to the fact that the lifetime of the cells is significantly increased by the presence of $MoO_3$ in the CBL.

Reprinted from *Electronics*. Cite as: Cattin, L.; Morsli, M.; Bernède, J.C. Improvement in the Lifetime of Planar Organic Photovoltaic Cells through the Introduction of $MoO_3$ into Their Cathode Buffer Layers. *Electronics* **2014**, *3*, 122-131.

## 1. Introduction

Recent studies show that if current progress is continued, organic photovoltaic cells (OPVCs) will have a unique advantage for large scale power generation [1]. The method often used to increase the efficiency of OPVCs consists of the introduction of buffer layers between the electrodes and the organic films [2,3]. These buffer layers must improve the collection efficiency of one type of carrier and must be selective by opposing the passage of carriers of the opposite sign. Moreover, these buffer layers improve the band matching between the electrodes and the organic materials. In classical OPVCs, the anode buffer layer (ABL) can also smooth the surface of the ITO electrode, while the cathode buffer layer (CBL), often called the exciton blocking layer, protects the electron acceptor from metal diffusion during thermal evaporation of the cathode. However, the lifetime of OPVCs is far from satisfactory. The lifetime is mainly dependent on the environment. Important environmental parameters that influence the lifetime of organic solar cells are the diffusion of oxygen and water into the active layers of the cells through the upper electrode [4–6]. A possible solution to the problem of contaminant diffusion into the active organic layers could be the use of barrier layers with low oxygen and water permeability. The use of buffer layers could contribute to this solution. $MoO_3$ is a very efficient ABL [7,8]. However, there is some controversy about its band structure. It is now well

accepted that its band gap is approximately 3.1 eV and that it is an *n*-type material, yet the values of its ionization potential (IP), its electronic affinity ($\chi$), and its Fermi level (Wf) are still under discussion. These values measured in situ by ultraviolet photoelectron spectroscopy (UPS) after deposition in ultra-high vacuum are IP = 9.7 eV, $\chi$ = 6.7 eV and Wf = 6.9 eV. After air contamination, these values decrease significantly. It is well known that after five minutes or more of air exposure, these values decrease by approximately 1 eV [7,9]. However, as shown in recent studies, these values remain high enough to allow $MoO_3$ to stay an efficient ABL if the highest occupied molecular orbital (HOMO) of the organic material is less than 5.9–6 eV, which is often the case in the typical electron donor materials [7]. It has also been shown that oxygen deficiency promotes hole transfer through the creation of band gap states.

Due to the high values of the IP energy of $MoO_3$, any hole transport via the valence band is prohibited, while the energy alignment between the band conduction minimum, BC, of $MoO_3$ and the HOMO of the organic material is favorable for electron transfer between the two materials. That means that hole injection into the organic film proceeds via an electron transfer from the HOMO of the organic material to the band conduction of $MoO_3$ in the case of organic light emitting diodes, whereas in the case of OPVCs, the photogenerated hole recombines with an electron at the interface between $MoO_3$ and the organic layer, indicating that $MoO_3$ works as a charge recombination layer. From this discussion, $MoO_3$ cannot be an electron blocker because its conduction edge, CB, is too low. Therefore, the proposition of using $MoO_x$ as a CBL is not an incongruous idea, especially because $MoO_x$ tends to be metallic. Moreover, Vasilopoulou *et al*. [10] showed that the electron injection in an OLED based on poly[(9,9-di-*n*-octylfluorenyl-2, 7-diyl)-*alt*-(benzo[2,1,3]thiadiazol-4,8-diyl)] (F8BT) can be significantly improved by inserting a very thin layer (5 nm) of partially reduced molybdenum oxide ($MoO_{2.7}$) between the aluminum cathode and the organic emitting layer. Actually, after measuring the valence band maximum energy of $MoO_x$ by UPS to be equal to 7.1 eV and the band gap of $MoO_3$ to be 3 eV, they conclude that the conduction band minimum is at approximately 4.1 eV, which is in good agreement with the work function of Al (4.3 eV). This energy alignment results in a relatively low electron injection barrier height. In addition, the states present in the band gap of $MoO_x$ may increase both the electron injection from Al and the conductivity of the oxide layer. More recently, Jin *et al*. [11] showed that the efficiency of OPVCs can be improved through the use of bathophenanthroline/molybdenum oxide (Bphen/$MoO_x$) as a compound cathode buffer layer. OPV cells based on planar CuPc/$C_{60}$ diodes were used in this work. It was shown that optimum performances are achieved when the thickness of layers constituting the Bphen/$MoO_x$ CBL is 2 nm/5 nm, respectively. They attributed this improving effect to the fact that the presence of Bphen prevents the formation of a diode at the contact $MoO_3$/$C_{60}$, while $MoO_3$ prevents damage to Bphen during Al deposition. To justify good band matching among Al (Wf = 4.3 eV), $MoO_3$ (Wf = 5.3–6.2 eV depending on the experimental conditions) and $C_{60}$ (lowest unoccupied molecular orbital (LUMO) 3.7 eV), Jin *et al*. proposed a dipole value of 3 eV at the interface of MoOx/Bphen, using a value issued from the bibliography.

As a matter of fact, the work function of $MoO_3$ is not the only important parameter at such complex interfaces; the $Alq_3$/$MoO_3$ interface is also crucial. In the case of conventional CBL, $Alq_3$ protects $C_{60}$ from damage incurred during aluminum deposition onto the organic material. Earlier studies show that there is actually some cathode metal diffusion into the organic under layer [12].

However, if the CBL should be thick enough to protect the electron accepting layer, it should also not block all charge carriers. The HOMO and LUMO values of $Alq_3$ are 5.9 and 3 eV, respectively. Because the LUMO value of the fullerene is 4.4 eV, the offset energy between the LUMO of the fullerene and that of the $Alq_3$ is large, and the electrons must overcome a large energy barrier to reach the Al cathode in the case of electron transport via LUMO levels. To circumvent this difficulty, it has been proposed [13] that the charge transport in the CBL is due to damage induced during deposition of the cathode, which introduces conducting levels below its LUMO and explains why the transport of electrons is not impeded. Therefore, in the case of a double CBL, the relative thickness of both layers will either allow or disallow the presence of these gap states in $Alq_3$. Furthermore, the position of these energy levels relative to the Fermi level of $MoO_3$ will be decisive as regards the passage of electrons.

Thus, because we used nearly similar structures in our laboratory, *i.e.*, planar heterojunctions based on the $CuPc/C_{60}$ junction [14], in the present paper, we probed OPVCs using *tris*-(8-hydroxyquinoline) aluminum ($Alq_3$) as the EBL, leading to an $Alq_3/MoO_3$ compound CBL. Even if our results are not identical to those mentioned above, they converge on those of Jin *et al*. [11], based on the time of exposure in air. These results are discussed in terms of the variation in the $MoO_3$ work function due to air contamination. Moreover, we show that the lifetime of the OPVCs with $MoO_3$ in their CBL is significantly improved.

## 2. Experimental

The OPVCs used were $ITO/MoO_3/CuPc/C_{60}/Alq_3/MoO_3/Al/a\text{-}Se$ with different thicknesses constituting the $Alq_3/MoO_3$ couple. The different films were deposited in thin film form by sublimation under vacuum ($10^{-4}$ Pa), without breaking the vacuum.

The standard substrate dimensions were 25 mm by 25 mm. Because ITO covered the entire glass substrate, some ITO must be removed to obtain the under electrode. After masking a broad band of 25 mm by 20 mm, the ITO was etched using Zn + HCl as the etchant [14]. Before thin film deposition, the ITO coated glass substrate was scrubbed with soap, rinsed with distilled water, dried and then placed in the vacuum chamber.

To test the effect of $MoO_3$ on the performance of the OPVCs when introduced into the CBL, we used the classical planar heterojunction structure $CuPc/C_{60}$; the ABL was, as discussed above, a thin $MoO_3$ film, and the cathode was an aluminum film. The CBL was a double layer of aluminum tris(8-hydroxyquinoline) ($Alq_3$) [14] and $MoO_3$.

Without a protecting layer, the instability of solar cells in ambient air causes rapid deterioration in all performance, and non-encapsulated devices are practically dead after approximately 8 h in air. To mitigate this instability, prior to breaking the vacuum, an encapsulating layer of amorphous selenium (a-Se) approximately 40 nm in thickness was thermally evaporated. The selenium protective coating layer has been proven to be efficient in protecting the under layers from oxygen and water vapor contamination, at least during the early hours of ambient air exposure [14]. This encapsulation hinders, but does not eliminate, the oxygen and water vapor diffusion processes. Therefore, the protective layer, which increases the lifetime of solar cells and prolongs the duration of the process, thus improves the precision of this study on the effect of an EBL on this process.

The thickness of the thin films and deposition rates were estimated *in situ* using a quartz monitor. We used a 3 nm thick $MoO_3$ layer as the ABL because, as discussed above, $MoO_3$ is well known as a very efficient ABL in optoelectronic organic devices. According to a previous study [14], the thickness of the CuPc layer was 35 nm, and that of the $C_{60}$ layer was 40 nm.

The relative thickness of the constituents of the $Alq_3/MoO_3$ CBL was used as a parameter. The cathode was an aluminum film 100 nm thick, deposited by evaporation. The effective area of each cell was 0.16 $cm^2$.

The main focus of this work was to study the influence of the value of the $MoO_3$ work function, when used as the CBL, on the OPV cell performance, *i.e.*, on the band matching at the interface cathode/EA. We varied the thickness of the $Alq_3/MoO_3$ couple from 9 nm/0 nm to 2 nm/7 nm, with intermediary values of 6 nm/3 nm and 3 nm/6 nm. The lifetime of the OPVCs was studied through the protocol proposed in ref [15]. Following this protocol, the procedure used to study the aging process of our OPV cells corresponds to the intermediate level labeled “Level 2” The operational lifetimes have been measured under AM1.5, in air and at room temperature. The experimental conditions during the experiment were quite stable, *i.e.*, the temperature was maintained at $T = 20 \pm 2$ °C and the humidity at 60% ± 5%. Between each measurement, samples were stored in air and in the light of day, without artificial light. Cells were maintained in open circuit conditions. It should be noted that at least nine diodes are used in a cycle of deposit and that three cycles of deposits were used for the aging study.

The work functions of different CBLs have been measured using a Kelvin probe instrument (KPTechnology Model SKP5050). The vibrating probe consists of a stainless steel tip 10 mm in diameter having a work function of 4.947 eV. For the measurements, the tip is calibrated against a gold surface. This calibration value varied by approximately 20–30 meV before and after each measurement, thus keeping the measurement error at 30 meV. The non-scanning mode is used to measure the work function with approximately 500 repetitions for a single point. The work function of the sample is obtained by adding the measured work function (WF) to the correction factor (4.947 eV). The Kelvin method measures the contact potential difference (CPD) between the tip and the surface of the sample that are brought into contact as a result of Fermi energy equalization. The vibrating capacitor consists of the surface of the sample being tested, the reference surface of the electrode and the insulating medium between them. The CPD is evaluated by inducing an AC current flow and by the vibration of one of the surfaces with respect to the other in the vibrating capacitor. The contact potential difference is then measured by determining the compensating voltage required to null this current. The resolution of the measurements is 3 meV.

## 3. Results and Discussion

The measurements made just after the realization of cells show that the presence of $MoO_3$ in the CBL systematically induces degradation of the OPV cell performance, which worsens with increasing thickness of the $MoO_3$ layer (Figure 1). However, when $MoO_3$ is present in the CBL, there is a continuous, systematic improvement in the OPVC efficiency during the first 5–6 days of room air exposure, whereas its efficiency decreases continuously when the CBL contains only $Alq_3$ (Figures 2–4).

**Figure 1.** J-V characteristics of ITO (100 nm)/$MoO_3$ (3 nm)/CuPc (35 nm)/$C_{60}$ (40 nm)/$Alq_3$ (*x* nm)/$MoO_3$ (*y* nm)/Al organic photovoltaic cells (OPVCs) with different thicknesses for the constituents of the $Alq_3/MoO_3$ couple.

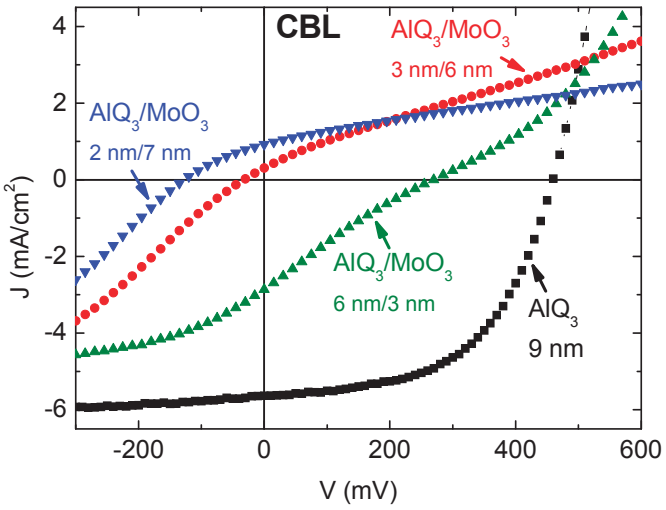


**Figure 2.** Evolution of the J-V characteristics over the duration of room air exposure of an OPVC with $Alq_3$ (3 nm)/$MoO_3$ (6 nm) as the cathode buffer layer (CBL).

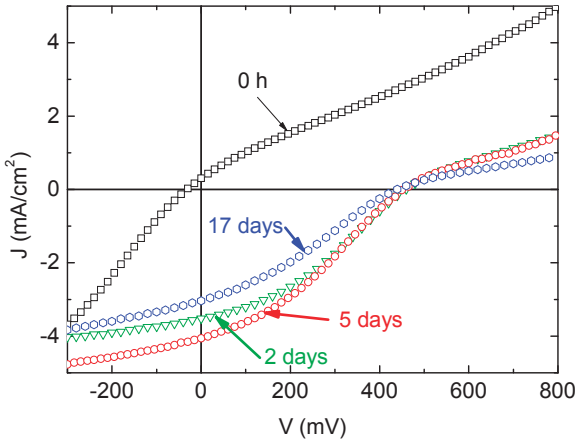


**Figure 3.** Variation with time of the typical performance of an OPVC with $Alq_3$ (3 nm)/$MoO_3$ (6 nm) as the CBL: (■) Jsc, (●) Voc, (▲) FF and (▼) η/2.

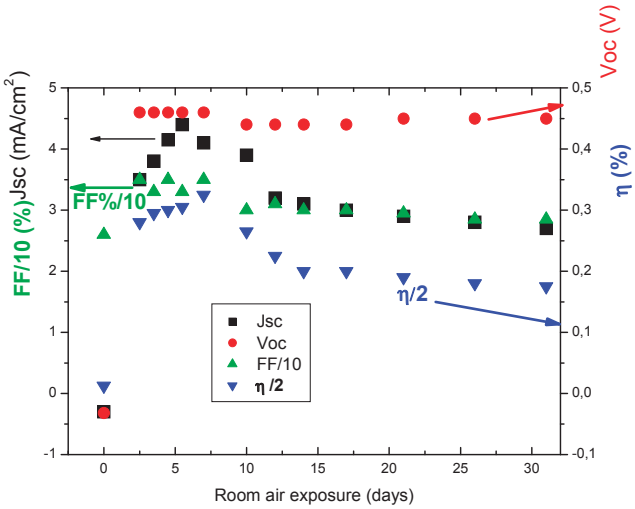

In fact, just after realization, when $MoO_3$ is 3 nm thick (Figure 1), the J-V characteristics are *S*-shaped. This effect increases dramatically with $MoO_3$ thickness (Figure 1) because when the $MoO_3$ thickness is 6 nm, the sign of the photocurrent is inverted, and this effect is accentuated for 7 nm thick $MoO_3$.

Nevertheless, after air exposure, there is progressive improvement of the OPVC performance during the first few days, regardless of the thickness of the $MoO_3$ layer in the CBL.

This improvement is spectacular in the case of the CBL with a $MoO_3$ film thickness of 6 nm because there is an inversion in the direction of the rectifying effect (Figures 2 and 3).

**Figure 4.** Variation with time of the efficiency of OPVCs with different CBLs: (■) CBL = $Alq_3$ (9 nm); (●) CBL = $Alq_3$ (6 nm)/$MoO_3$ (3 nm); (▲) CBL = $Alq_3$ (3 nm)/$MoO_3$ (6 nm).

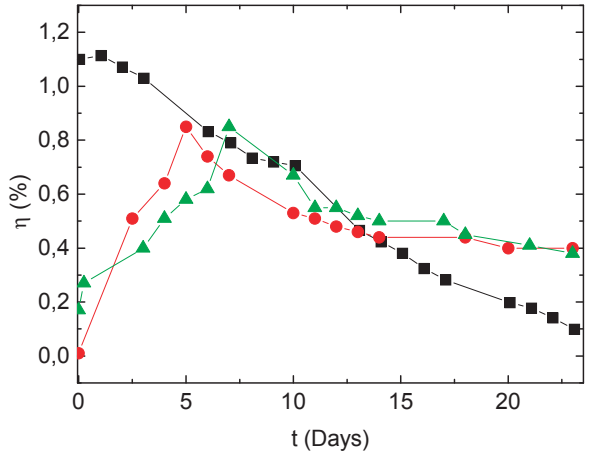


Therefore, ultimately, if we compare the performances of the different OPVCs after approximately 6 days of air exposure, the OPVCs with $MoO_3$ in their CBL exhibit similar efficiencies as those without $MoO_3$, as can be seen in Figure 4. Moreover, the efficiency of the OPVCs with $MoO_3$ in their CBL becomes higher than that obtained with the classical $Alq_3$ CBL after 11–12 days of air exposure.

In Figure 3, we show the typical evolution of the different OPVC parameters as a function of air exposure time for the OPVCs using "$Alq_3$ (3 nm)/$MoO_3$ (6 nm)" as the CBL. The sign of the photocurrent has a striking effect. Immediately after device preparation, there is a positive photocurrent in the second quadrant, but its value is very small (Figures 1 and 2). After aging, the sign of the photocurrent becomes negative, as expected (Figure 2). The absolute values of Jsc and the OPVC efficiency η increase gradually over the first 5–6 days of air exposure. Then, there is a progressive decrease in Jsc and η. After 15 days, η reduces to approximately half its maximum value, which is attributed to degradation of the device from $C_{60}$ contamination [16]. The device then stabilizes for a long time ($t > 4$ months) at a value that is slightly less than half of the initial yield.

Regardless of the $MoO_3$ thickness in the CBL and the duration of aging, the J-V characteristics are *S*-shaped, except when they reach their maximum performance level. It is known that *S*-shaped J-V characteristics are typical for the formation of a reverse diode at the contact electrode/organic material [17,18]. This effect means that in the present structures, band bending occurs not only at the CuPc/$C_{60}$ interface but also at the $C_{60}$/cathode interface (Figure 5).

**Figure 5.** Schematic representation of an OPVC with localization of the active regions.

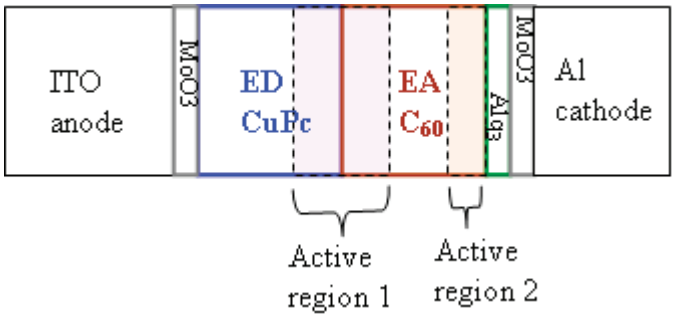


These *S*-shaped J-V characteristics indicate the formation of a barrier at the $C_{60}$/cathode interface. In the case of the J-V characteristics of Figure 1, the band bending near the $C_{60}$/cathode interface must be larger than that at the CuPc/$C_{60}$ interface, resulting in an opposite sign of the short circuit current. The formation of a barrier at the $C_{60}$/cathode interface is due to the presence of $MoO_3$ in the CBL because there are no *S*-shaped characteristics when the CBL is only a film of $Alq_3$ (Figure 1). The formation of this barrier can be explained by the very high work function of $MoO_3$. Actually, it is now well accepted that after deposition under vacuum by sublimation, the work function of $MoO_3$ is approximately 6.2 eV [7]. With this high Wf value, the band structure of the interface is such that at the $C_{60}$/$Alq_3$/$MoO_3$/Al interface, the passage of holes is easier than that of electrons (Figure 6a). This result explains the reversal of the structure when the thickness of the $MoO_3$ layer (6 nm) is such that the probability of charge carriers crossing by the tunnel effect is very low. However, it was also shown that air exposure of $MoO_3$ induces a Wf decrease of approximately 1 eV [9].

**Figure 6.** Band scheme of the $C_{60}$/$Alq_3$/$MoO_3$/Al interface (**a**) just after deposition and (**b**) after five days of air exposure.

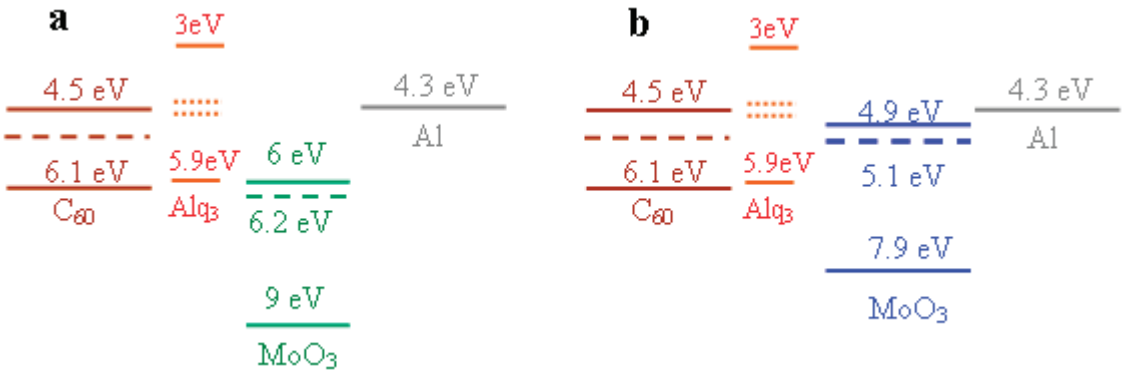


In our case, using a Kelvin probe, we found that the work function of our $MoO_3$ thin films is 5.1–5.2 eV after air exposure, regardless of the CBL, whereas it is 5.6 and 5.9 eV for a fresh CBL containing $Alq_3$ (6 nm)/$MoO_3$ (3 nm) and $Alq_3$ (3 nm)/$MoO_3$ (6 nm), respectively. This result means that the band alignment at the interface $Allq_3$/$MoO_3$ depends on the relative thickness of these layers. Nevertheless, just after deposition, regardless of the value of the $MoO_3$ work function, the work function remains sufficiently high to induce the formation of a barrier at the $C_{60}$/cathode interface.

If, in the present study, the OPVCs were covered with a Se film, it would not prevent progressive air contamination. Furthermore, we have already shown that even if the amorphous selenium film

used as an encapsulation layer stabilizes the OPVCs, it only delays oxygen/water contamination of the cells. Therefore, the evolution of the J-V characteristics of the OPVCs for the duration of air exposure corresponds to the progressive air contamination of the OPVCs. The first layer encountered by the diffused contaminant after crossing the Al polycrystalline film is the $MoO_3$ layer. Therefore, due to this progressive contamination, the Wf of $MoO_3$ will decrease gradually until it reaches its minimal value of 5.1 eV. In parallel, the height of the barrier present at the $C_{60}$/cathode interface decreases, which justifies the progressive improvement in the efficiency of the OPVCs over the first 6 days of air exposure (Figure 6b).

For a longer exposure time, the contamination reaches the $C_{60}$ layer, and the performance of the OPVCs decreases. In fact, the oxygen/water contamination of $C_{60}$ increases its resistivity [16]. However, this contamination is significantly limited by the presence of $MoO_3$ in the ABL because the efficiency of the OPVCs with a classical CBL tends regularly towards 0, whereas that of OPVCs with $MoO_3$ in their CBL tends to stabilize at a value of nearly half their initial efficiency (Figure 4). The greater stability of the OPVCs with an $Alq_3/MoO_3$ bilayer as the CBL can be attributed to the fact that $MoO_3$ deposited by the Joule effect under vacuum is oxygen deficient and tends to trap oxygen, thus preventing the lower organic layer from a high degree of contamination.

The difference between our results and those of reference 6 may be attributed to the facility of the Wf in varying with the history of the $MoO_3$ layer. Indeed, the films deposited by Vasilopoulou *et al*. [10] are strongly oxygen deficient, which ensures that the Wf of their $MoO_3$ is small.

## 4. Conclusions

The presence and height of a barrier at the $C_{60}/Alq_3/MoO_3$/Al interface strongly depends on the Wf function of the $MoO_3$ layer. This value depends on the composition and degree of contamination of the $MoO_3$ layer. In the case of an uncontaminated layer, the Wf is so high that the OPVCs are inverted. When the $MoO_3$ layer is sufficiently oxygen deficient and/or oxygen/air contaminated, its Wf decreases significantly to provide OPVCs with acceptable performance levels. Moreover, except for the first few days, the efficiency of the OPVC with a classical EBL is lower than that with $MoO_3$ in the CBL. This result means that, although the initial performance of the OPVCs without $MoO_3$ in their CBL is greater than that of OPVCs with $MoO_3$, the OPVCs with $MoO_3$ in their CBL become the most promising later on, as their performance quickly exceeds that of the former and tends to remain stable over time.

## Author Contributions

The three authors, Linda Cattin, Mustapha Morsli, and Jean Christian Bernède, contributed equally to the cell realization experiments, characterization and interpretation of the results.

## Conflicts of Interest

The authors declare no conflict of interest.

**References**


1. Darling, S.B.; You, F. The case for organic photovoltaics. *RSC Adv.* **2013**, *3*, 17633–17648.
2. Kumar, P.; Chand, S. Recent progress and future aspects of organic solar cells. *Prog. Photovolt.* **2012**, *20*, 377–415.
3. Nikiforov, M.P.; Strzalka, J.; Jiang, Z.; Darling, S.B. Lanthanides: New metallic cathode materials for organic photovoltaic cells. *Phys. Chem. Chem. Phys.* **2013**, *15*, 13052–13060.
4. Bundgaard, E.; Krebs, F.C. Low band gap polymers for organic photovoltaics. *Sol. Energy Mater. Sol. Cells* **2007**, *91*, 954–985.
5. Krebs, F.C. All solution roll-to-roll processed polymer solar cells free from indium-tin-oxide and vacuum coating steps. *Org. Electron.* **2009**, *10*, 761–768.
6. Nikiforov, M.P.; Strzalka, J.; Darling, S.B. Delineation of the effects of water and oxygen on the degradation of organic photovoltaic devices. *Sol. Energy Mater. Sol. Cells* **2013**, *110*, 36–42.
7. Meyer, J.; Hamwi, S.; Kröger, M.; Kowalsky, W.; Riedl, T.; Kahn, A. Transitionn metal oxides for organic electronics: Energetics, device physics and applications. *Adv. Mater.* **2012**, *24*, 5408–5427.
8. Tseng, Y.-C.; Mane, A.U.; Elam, J.W.; Darling, S.B. Ultrathin molybdenum oxide anode buffer layer for organic photovoltaic cells formed using atomic layer deposition. *Sol. Energy Mater. Sol. Cells* **2012**, *99*, 235–239.
9. Irfan, I.; Ding, H.; Gao, Y.; Small, C.; Kim, D.Y.; Subbiah, J.; So, F. Energy level evolution of air and oxygen exposed molybdenum trioxide films. *Appl. Phys. Lett.* **2010**, *96*, 243307.
10. Vasilopoulou, M.; Palilis, L.C.; Georgiadou, D.G.; Argitis, P.; Kennou, S.; Sygeliou, L.; Kostis, I.; Papadimitropoulos, G.; Konofaos, N.; Liadis, A.A.; *et al*. Reduced molybdenum oxide as an efficient electron injection layer in polymer light-emitting diodes. *Appl. Phys. Lett*. **2011**, *98*, 123301.
11. Jin, F.; Chu, B.; Li, W.; Su, Z.; Zhao, B.; Yan, X.; Zhang, F.; Fan, D.; Zhang, T.; Gao, Y.; *et al*. Improvment in power conversion efficiency and long-term lifetime of organic photovoltaic cells by using bathophenanthroline/molybdenum oxide as compound cathode buffer layer. *Sol. Energy Mater. Sol. Cells* **2013**, *117*, 189–193.
12. Yapi, A.S.; Toumi, L.; Lare, Y.; Soto, G.M.; Cattin, L.; Toubal, K.; Djafri, A.; Morsli, M.; Khelil, A.; del Valle, M.A.; *et al*. On the influence of the exciton-blocking layer on the organic multilayer cells properties. *Eur. Phys. J. Appl. Phys*. **2010**, *50*, 30403:1–30403:8.
13. Rand, B.B.P.; Li, J.; Xue, J.; Holmes, R.J.; Thompson, M.E.; Forrest, S.R. Organic Double-Heterostructure Photovoltaic Cells Employing Thick *Tris*(acetylacetonato)ruthenium(III) Exciton-Blocking Layers. *Adv. Mater.* **2005**, *17*, 2714–2718.
14. Berredjem, Y.; Karst, N.; Boulmokh, A.; Gheid, A.H.; Drici, A.; Bernède, J.C. Optimisation of the interface "organic material/aluminium" of CuPc/$C_{60}$based photovoltaic cell. *Eur. Phys. J.* **2007**, *40*, 163–167.

15. Gevorgyan, S.A.; Medford, A.J.; Bundgaard, E.; Sapkota, S.B.; Schleiermacher, H.-F.; Zimmermann, B.; Würfel, U.; Chafiq, A.; Lira-Cantu, M.; Swonke, T.; *et al*. An inter-laboratory stability study of roll-to-roll coated flexible polymer solar modules. *Sol. Energy Mater. Sol. Cells* **2011**, *95*, 1398–1415.
16. Hamed, A.; Sun, Y.Y.; Tao, Y.K.; Meng, R.L.; Hor, P.H. Effects of oxygen and illumination on the *in situ* conductivity of $C_{60}$ thin films. *Phys. Rev. B* **1993**, *47*, 10873–10880.
17. Kouskoussa, B.; Morsli, M.; Benchouk, K.; Louarn, G.; Cattin, L.; Khelil, A.; Bernède, J.C. On the improvement of the anode/organic material interface in organic solar cells by the presence of an ultra-thin gold layer. *Phys. Status Solidi A* **2009**, *206*, 311–315.
18. Lare, Y.; Kouskoussa, B.; Benchouk, K.; OuroDjobo, S.; Cattin, L.; Morsli, M.; Diaz, F.R.; Gacitua, M.; Abachi, T.; del Valle, M.A.; *et al*. Influence of the exciton blocking layer on the stability of layered organic solar cells. *J. Phys. Chem. Solids* **2011**, *72*, 97–103.

# Section V: Solar Cells

## Chapter 11

# Bandgap Science for Organic Solar Cells

**Masahiro Hiramoto, Masayuki Kubo, Yusuke Shinmura, Norihiro Ishiyama, Toshihiko Kaji, Kazuya Sakai, Toshinobu Ohno and Masanobu Izaki**

**Abstract:** The concept of bandgap science of organic semiconductor films for use in photovoltaic cells, namely, high-purification, *pn*-control by doping, and design of the built-in potential based on precisely-evaluated doping parameters, is summarized. The principle characteristics of organic solar cells, namely, the exciton, donor (D)/acceptor (A) sensitization, and *p-i-n* cells containing co-deposited and D/A molecular blended *i*-interlayers, are explained. "Seven-nines" (7N) purification, together with phase-separation/cystallization induced by co-evaporant 3rd molecules allowed us to fabricate 5.3% efficient cells based on 1 μm-thick fullerene:phthalocyanine ($C_{60}$:$H_2$Pc) co-deposited films. *pn*-control techniques enabled by impurity doping for both single and co-deposited films were established. The carrier concentrations created by doping were determined by the Kelvin band mapping technique. The relatively high ionization efficiency of 10% for doped organic semiconductors can be explained by the formation of charge transfer (CT)-complexes between the dopants and the organic semiconductor molecules. A series of fundamental junctions, such as Schottky junctions, *pn*-homojunctions, $p^+$, $n^+$-organic/metal ohmic junctions, and $n^+$-organic/$p^+$-organic ohmic homojunctions, were fabricated in both single and co-deposited organic semiconductor films by impurity doping alone. A tandem cell showing 2.4% efficiency was fabricated in which the built-in electric field was designed by manipulating the doping.

Reprinted from *Electronics*. Cite as: Hiramoto, M.; Kubo, M.; Shinmura, Y.; Ishiyama, N.; Kaji, T.; Sakai, K.; Ohno, T.; Izaki, M. Bandgap Science for Organic Solar Cells. *Electronics* **2014**, *3*, 351-380.

### 1. Introduction

Organic solar cells consisting of vacuum-deposited small-molecular thin films have been intensively studied [1–3], following the two-layer cell reported by Tang [4]. In 1991, the author proposed *p-i-n* organic solar cells in which the *i*-interlayer is a co-deposited film of *p*- and *n*-type organic semiconductors [5,6]. This is the first organic solar cell having a molecular blend, *i.e.*, the so-called bulk heterojunction [7].

Recently, we have been focused on the establishment of "bandgap science for organic solar cells". We believe that the following features are indispensable. (a) Organic semiconductors purified to sub-ppm level, at least seven nines (7N; 0.1 ppm), should be used; (b) A ppm-level doping technique should be developed; (c) Every individual organic semiconductor should be capable of displaying

both *n*- and *p*-type characteristics by impurity doping alone, *i.e.*, complete *pn*-control should be developed; (d) Unintentional and uncontrollable doping by oxygen and water from air should be completely eliminated; (e) The doping technique should be applicable not only to single organic semiconductor films, but also to co-deposited films consisting of two kinds of organic semiconductors.

*pn*-control by doping are indispensable for the solid-state physics of inorganic semiconductors. It is so-called "bandgap engineering". In the case of organic semiconductors, their genuine potential has been hidden for a long time by the unintentional and unknown impurity contamination typically by oxygen from air. However, the authors have a strong conviction that the organic semiconductors should also be able to be treated similar to the inorganic semiconductors. Simultaneously, the authors strongly expect that the unknown physical phenomena, particular to organic semiconductors will be discovered during the course of research to establish the solid-state physics for organic semiconductors. From these standpoints of view, the authors chose the term "bandgap science". *pn*-control of co-deposited films consisting of D/A organic semiconductors is one of the spin-off of "bandgap science" and particular to organic semiconductors.

In this paper we will first summarize the fundamental principles of organic solar cells, such as the exciton, donor (D)/acceptor (A) sensitization, *p*-*i*-*n* cells containing a co-deposited *i*-interlayer, and nanostructure design of co-deposited layers. Next, factors influencing bandgap science for organic solar cells, such as "seven-nines" purification, *pn*-control by ppm-level doping for both single and for co-deposited organic semiconductor films, and built-in potential design based on precise evaluation of doping parameters, are summarized.

## 2. Principles

### *2.1. Exciton*

The dissociation of photogenerated electron-hole pairs (excitons) is a key factor for carrier generation in organic semiconductors. Exciton dissociation is affected by the relative permittivity of a solid (ε) based on the Coulomb's law; $F = (1/4\pi\varepsilon\varepsilon_0)(q_1q_2/r_2)$ [8]. Here, $\varepsilon_0$, $q_1$, $q_2$, and $r$ are the absolute permittivity, the elementary charges, and the distance between charges. In a solid having a small value of ε, the positive and negative charges experience strong attractive forces. On the contrary, in a solid having a large value of ε, the positive and negative charges experience relatively weak attractive forces. Inorganic semiconductors have large values for ε. For example, Si has a large ε value of 11.9 and the exciton has a large diameter of 9.0 nm and is delocalized over about $10^4$ Si atoms (Figure 1a) [9]. This Wannier-type exciton immediately dissociates to a free electron and a hole from thermal energy at room temperature and generates photocurrent. On the other hand, organic semiconductors have small values for ε. For example, $C_{60}$ has small ε value of 4.4 and the exciton has a very small diameter of 0.50 nm and is localized on a single $C_{60}$ molecule (Figure 1b). These Frenkel-type excitons are hardly dissociated to free electrons and holes by thermal energy of room temperature and can easily relax to the ground state (Figure 2a). Therefore, organic semiconductors can generate few photocarriers. This is the reason why the organic solar cells that were fabricated before the work of Tang [4] showed extremely low photocurrents, of the order of nano- to micro-amperes.

**Figure 1.** Size of excitons for an inorganic semiconductor (Si) and an organic semiconductor ($C_{60}$). The former is Wannier-type and easily dissociates to free carriers. The latter is Frenkel-type and hardly dissociates to free carriers.

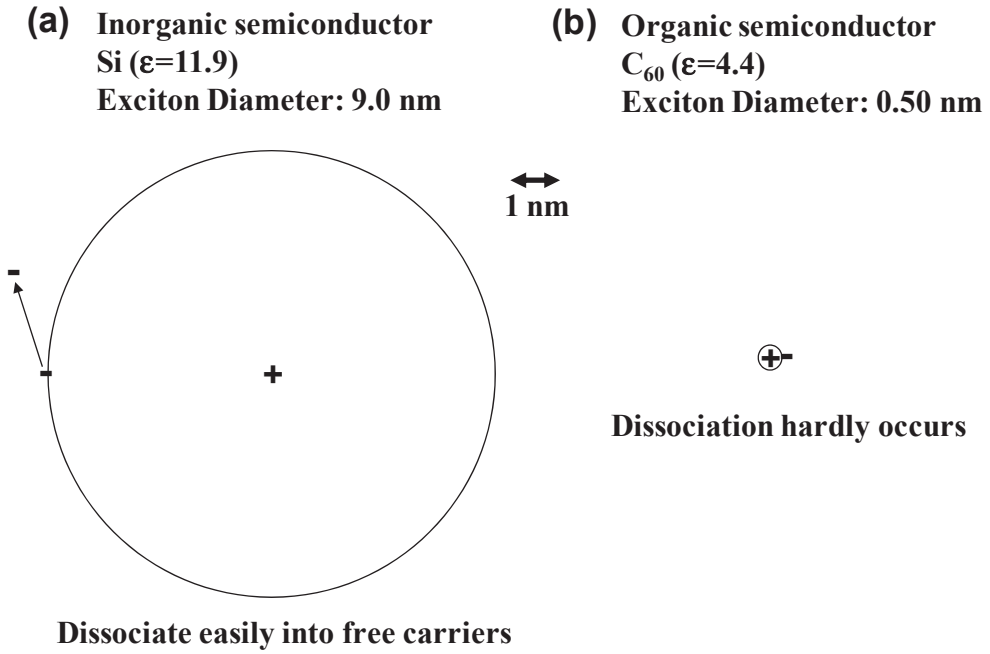


**Figure 2.** Carrier generation in organic semiconductors. (**a**) Single molecular solids; (**b**) Donor (D)/acceptor (A) sensitization of carrier generation by the mixing of two kinds of organic semiconductor molecules. Efficient free carrier generation occurs from the charge transfer (CT) exciton.

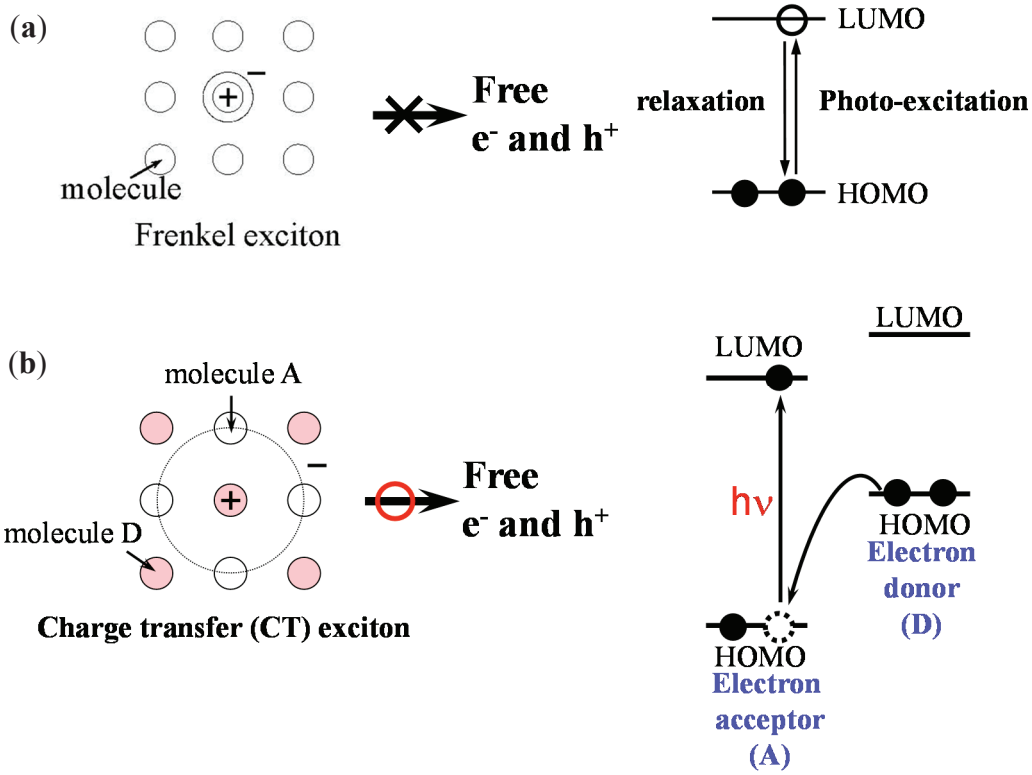

Today's organic solar cells have overcome the above problem by combining two kinds of organic semiconductors. When an electron-donating molecule (D) and an electron-accepting molecule (A), for which the energetic relationship of the highest occupied molecular orbital (HOMO) and the lowest unoccupied molecular orbital (LUMO), are shifted in parallel with each other and are contacted or mixed, then a charge transfer (CT) exciton is formed in which the positive and negative charges are separated on the neighboring D and A molecules due to photoinduced electron transfer (Figure 2b). This CT exciton can dissociate to a free electron and a hole due to thermal energy of room temperature. By utilizing this donor-acceptor (D/A) sensitization, organic semiconductors became capable of generating photocurrents of significant magnitude; of the order of milli-amperes.

A two-layer organic solar cell (Figure 3) [4] utilizes D/A sensitization at the heterojunction. The width of the photoactive region (shaded red) is, however, limited to around 10 nm in the vicinity of the heterojunction due to the extremely small exciton diffusion length of only several nm [10,11]. Thus, when the thickness of the organic layers increases, a dead region that does not generate photocurrent and but absorbs incident solar light develops in front of the active region and, as a result, the magnitude of the photocurrent is severely suppressed. Taking into account the observation that a 10 nm-thick organic film can only absorb a small part of the incident solar light, then in order to increase the efficiency of organic solar cells, the severely contradictory condition, namely, "the whole of the incident solar light shall be absorbed by only a 10 nm-thick active layer", should be satisfied.

**Figure 3.** Schematic illustration of a two-layer cell composed of perylene pigment (Im-PTC) acting as an acceptor molecule (A) and copper phthalocyanine (CuPc) acting as a donor molecule (D). Photocurrent is generated only in the active region (shaded red) close to the heterojunction and all other parts of organic films act as a dead region.

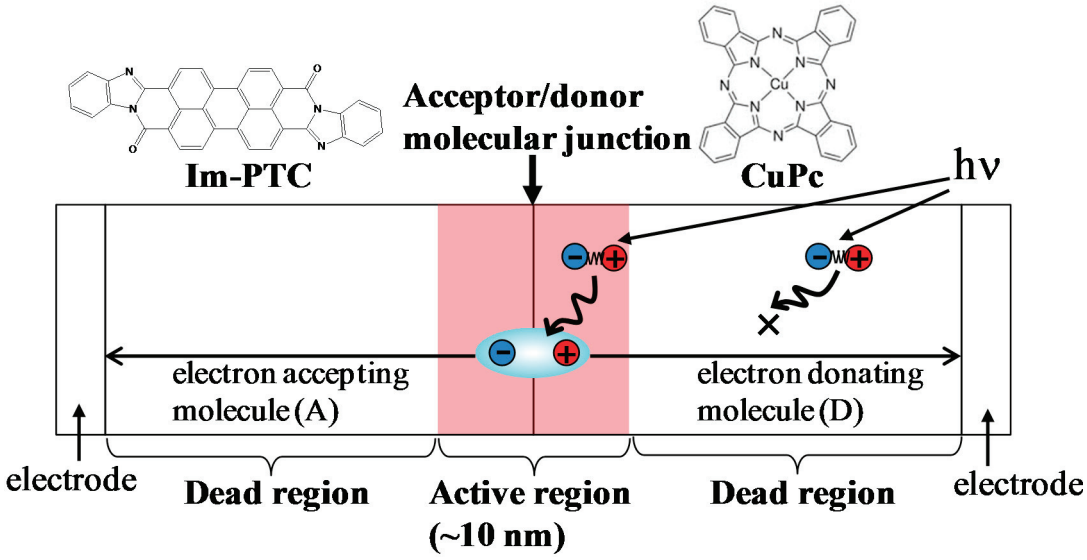


*2.2. Co-Deposited Layer*

In order to overcome this contradiction, in 1991, the authors proposed *p-i-n* organic solar cells in which the *i*-interlayer is a co-deposited film composed of *p*- and *n*-type organic semiconductors (Figure 4a) [5,6]. The original concept is that the positive and negative charges from ionized donors

and acceptors in *n*-type and *p*-type organic semiconductors, respectively, are compensated by each other, and the resulting co-deposited interlayer behaves like an intrinsic semiconductor. From the standpoint of built-in potential formation in a molecular solid, the built-in electric field is distributed across an *i*-interlayer sandwiched by *n*- and *p*-layers, similar to the case of amorphous silicon incorporating a *p*-*i*-*n* junction (Figure 4b). From the standpoint of photocarrier generation occurring at the molecular-level, there are D/A molecular contacts acting as photocarrier generation sites due to the D/A sensitization in the whole of the bulk of the *i*-codeposited layer.

In 1991, the terms *p*-type and *n*-type implied the nature induced by unintentional and uncontrolled doping. The *p*- and *n*-type natures of phthalocyanine and perylene pigments (Figure 3) were induced by unidentified acceptor and donor impurities respectively, and the electron donating molecules (D) and the accepting molecules (A) were recognized as usually showing *p*- and *n*-type natures. It should be noted that the recent *pn*-control technique mentioned in Sections 5 and 6 is based on intentional and controlled impurity doping.

The 'molecular blend' structure became indispensable for organic solar cells. In 1995, a blended junction, *i.e.*, a "bulk heterojunction", was proposed by Heeger's group for the polymer solar cell [7]. Fundamentally, an *i*-codeposited layer has the physical meaning that, by transmitting the incident light through a vast number of heterointerfaces, the severe contradicting conditions, *i.e.*, "the whole of the incident solar light shall be absorbed by only an extremely thin active layer", can be satisfied.

**Figure 4.** (**a**) Concept of *p*-*i*-*n* cell. A mixed *i*-layer co-deposited with *n*- and *p*-type semiconductors is sandwiched between respective *p*- and *n*-type layers. The entire bulk of the *i*-layer acts as an active layer for photocarrier generation; (**b**) Energy structure of the *p*-*i*-*n* cell.

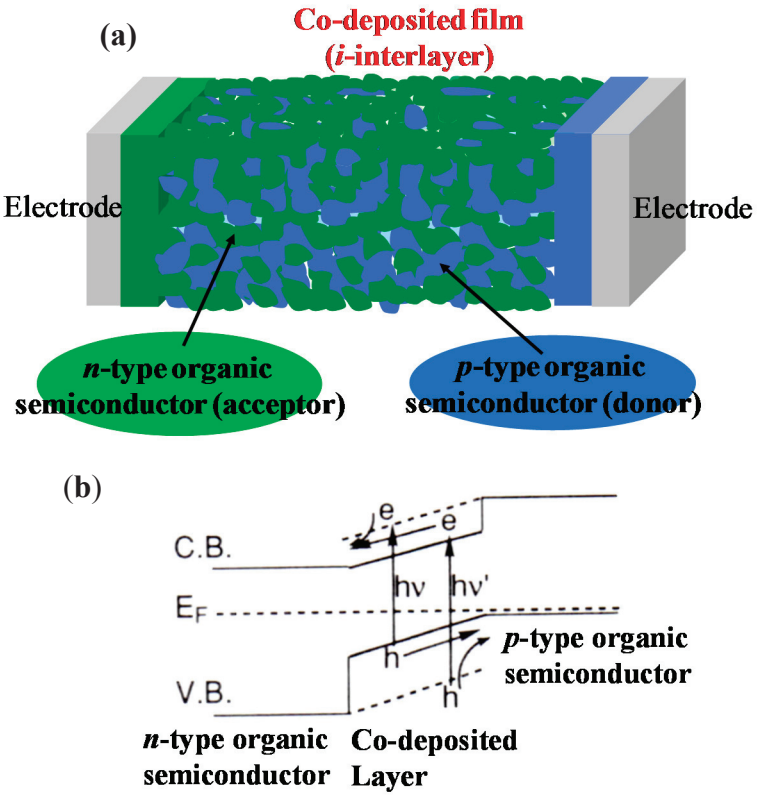

## 3. Nanostructure Design

### *3.1. Vertical Superlattice Structure*

Even if excitonic dissociation occurs, nanostructure control of co-deposited films, *i.e.*, a formation route for electrons and holes generated by excitonic dissociation, is indispensable to extract a significant portion of the photogenerated charges to the external circuit. An ideal nanostructure is the "vertical superlattice" structure (Figure 5b) [11]. This structure enables the efficient dissociation of photogenerated excitons at the D/A interfaces within the exciton diffusion length (5–10 nm) and the transport of electrons and holes to the respective electrodes.

**Figure 5.** (**a**) Co-evaporant 3rd molecule introduction. The balls, plates, and sticks correspond to $C_{60}$, $H_2Pc$, and 3rd molecules, respectively; (**b**) Vertical superlattice structure. Cross sectional SEM images of $C_{60}$:$H_2Pc$ co-deposited films without (**c**) and with (**d**) 3rd molecule. Phase-separation and crystallization occurs by introducing co-evaporant 3rd molecule.

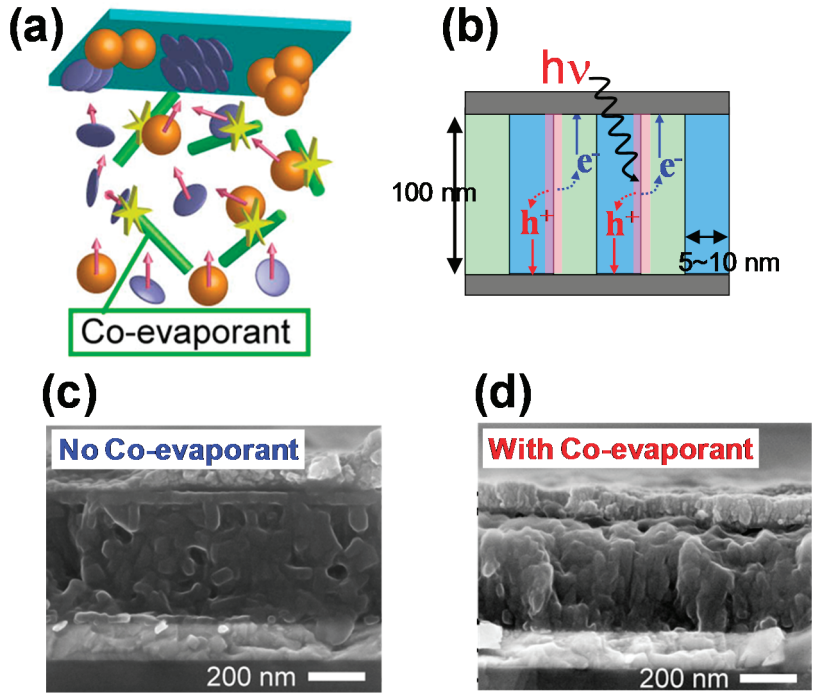


### *3.2. Co-Evaporant 3rd Molecules*

Recently, we developed a fabrication method for a nanostructure similar to Figure 5b by using co-evaporant 3rd molecules that act as a solvent during vacuum deposition [12]. By introducing co-evaporant 3rd molecules onto a substrate heated to +80 °C during film growth, phase-separated and crystallized co-deposited films that improve carrier transport can be fabricated (Figure 5a). The 3rd molecules collide with $C_{60}$ and $H_2Pc$ and decrease the density of the crystalline nucleation sites on the surface and promote the crystallization/phase-separation process. The 3rd molecules are not left in the co-deposited films at elevated substrate temperatures. Columnar structure (Figure 5b)

composed of benzoporphyrin and silylmethylfullerene was also fabricated by Matsuo *et al*. [13] and it was developed to commercialized organic solar cells by Mitsubishi Chemical.

Figure 5c,d show cross-sectional SEM images of a $C_{60}$:$H_2Pc$ (fullerene:metal-free phthalocyanine) co-deposited film. Without the 3rd molecules, an amorphous smooth cross-section was observed for the molecular-level mixture of $C_{60}$ and $H_2Pc$ (Figure 5c). On the other hand, with the 3rd molecules, a columnar structure of phase-separated and crystallized material (Figure 5d) similar to the ideal vertical superlattice (Figure 5b) was formed. The improved crystallinity produced by introducing the 3rd molecules was confirmed by UV-Vis absorption spectra and X-ray diffraction analyses. Photocurrent enhancement was observed, particularly for relatively thick (>400 nm) co-deposited films having greater light absorption (see Section 4). A striking enhancement in photocurrent generation is achieved in organic solar cells without exception, based on a variety of co-deposited films such as $H_2Pc$:$C_{60}$, PbPc:$C_{60}$, AlClPc:$C_{60}$, and rubrene:$C_{60}$. As 3rd molecules, more than 10 kinds of low vapor pressure liquids, such as polydimethylsiloxane (PDMS) and alkyldiphenylether (ADE), can be used. Since ADE is a typical diffusion pump oil, the present effects can often be observed for co-deposition using a chamber evacuated by a diffusion pump (see Section 4). We believe that this method is generally applicable for growing high-quality phase-separated/crystalline co-deposited films by vacuum deposition.

## 4. Seven-Nines (7N) Purification

### *4.1. Single-Crystal Sublimation*

First, in order to establish bandgap science for organic solar cells, we focused on the high purification of organic semiconductors. Conventional *p-i-n* cells (Section 2.2) [5,6] incorporating a quasi-vertical superlattice (Sections 3.1 and 3.2) [12] were used to evaluate the effects of high-purification.

Based on an analogy with inorganic Si, which is usually purified to eleven-nines (11N), the purity of organic semiconductors needs to at least reach the sub-ppm level in order to draw out their essential nature. Based on the above consideration, a more rigorous purification method was applied to organic semiconductors. Conventionally, organic semiconductors are purified by the "train sublimation" method under vacuum [14] and the purified samples are obtained as a powder. Alternatively, when the sublimation is performed at 1 atm, the purified samples are obtained as single crystals that are of extremely high purity due to gas convection [15].

Figure 6a shows a photograph of $C_{60}$ crystals purified by single-crystal sublimation [15]. Crystal growth was performed in a quartz tube surrounded by a three-zone furnace system (Epitech Co., Ltd., Kyoto, Japan) under flowing $N_2$ at 1 atm. The $C_{60}$ sample was set at 720 °C and single crystals with sizes exceeding 2 mm × 2 mm were grown at around 500 °C. X-ray diffraction of the obtained crystals showed precise agreement with the reported crystal structure of $C_{60}$. The obtained $C_{60}$ crystals were used in the next single-crystal sublimation process.

**Figure 6.** (**a**) Photograph of 7N-$C_{60}$ single crystals; (**b**) Structure of organic *p-i-n* solar cell. The $C_{60}$:$H_2$Pc co-deposited layer (thickness: X nm) having a quasi-vertical superlattice structure (Figure 5b,d) is sandwiched between *p*-type $H_2$Pc and *n*-type NTCDA.

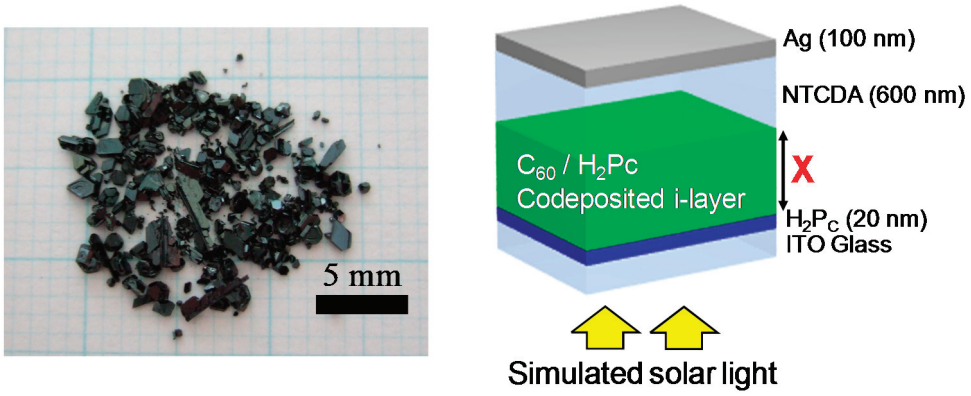


*4.2. One Micrometer-Thick Co-Deposition Cells*

Highly purified organic semiconductors produced by single-crystal sublimation were incorporated in *p-i-n* cells (Figure 6b) (Section 2.2, Figure 4). A *p*-type $H_2$Pc layer (20 nm), a co-deposited $C_{60}$:$H_2$Pc *i*-interlayer, and an *n*-type layer of naphthalene tetracarboxylic anhydride (NTCDA) were successively deposited by vacuum evaporation at $1 \times 10^{-3}$ Pa using a diffusion pump (VPC-260, ULVAC) onto an indium tin oxide (ITO) glass substrate pre-treated in an air plasma. The thick NTCDA layer (600 nm) also acts as a transparent protection layer that prevents electrical shorting of the cells due to metal migration into the organic film during metal deposition [16,17]. The co-deposition was performed on a substrate heated to +80 °C. The optimized $C_{60}$:$H_2$Pc ratio was 1.13:1. ADE, which acted as a co-evaporant 3rd molecule (Section 3.2), was automatically introduced from the diffusion pump. A phase-separated/crystalline nanostructure (Figure 5b,d) was confirmed to be formed for the present $C_{60}$:$H_2$Pc co-deposited film.

Figure 7 shows the current-voltage (J-V) characteristics of the cells in Figure 6b with co-deposited layer thicknesses, *X*, of 250, 600, 960 nm, and 1.2 μm, incorporating a $C_{60}$ sample purified three times by single-crystal sublimation. Figure 8 shows the dependence of the fill-factor (FF) and the short-circuit photocurrent density ($J_{sc}$) on *X*. Surprisingly, FF hardly decreases even for an extremely thick *i*-codeposited layer of 1.2 μm (black open dots). Simultaneously, $J_{sc}$ increases with *X* and reaches a maximum value of 19.1 mAcm$^{-2}$. On the contrary, when the $C_{60}$ is purified by conventional train sublimation under vacuum, FF monotonically decreases with co-deposited layer thickness (Figure 3a, red open squares) [18]. At $X = 960$ nm, a $J_{sc}$ value of 18.3 mAcm$^{-2}$ and a conversion efficiency of 5.3% were observed [19–21]. The internal quantum efficiency reaches around 90% in the region from 400 to 700 nm for the $X = 960$ nm cell (Figure 9a).

**Figure 7.** Current-voltage (J-V) characteristics for *p-i-n* cells with *i*-layer thicknesses (*X*) of 250 nm, 600 nm, 960 nm, and 1.2 μm. Cell parameters (*X* = 960 nm); $J_{sc}$: 18.3 mAcm$^{-2}$, $V_{oc}$: 0.40 V, FF: 0.53, Efficiency: 5.3%. The simulated light intensity transmitted through the ITO glass substrate is 74.2 mWcm$^{-2}$.

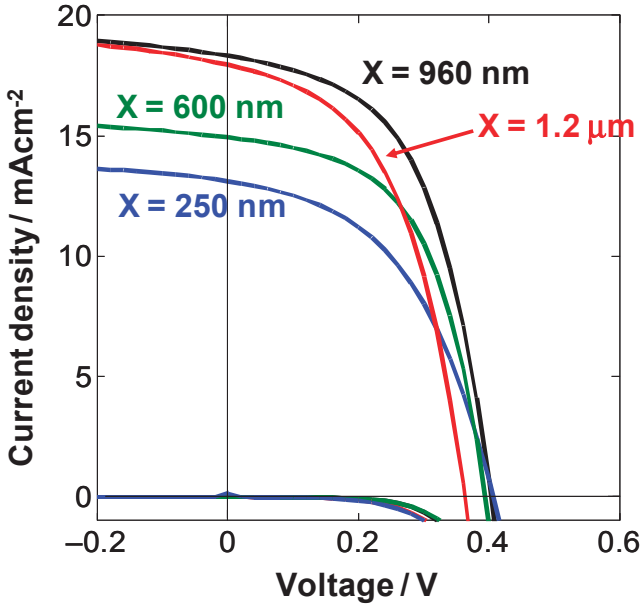


**Figure 8.** (**a**) Dependence of fill factor (FF) on the $C_{60}$:$H_2Pc$ *i*-interlayer thickness (*X*) for *p-i-n* cells incorporating $C_{60}$ purified three times by single-crystal formed sublimation (black open dots) and for *p-i-n* cells incorporating $C_{60}$ purified by conventional train sublimation under vacuum (red open squares); (**b**) Dependence of short-circuit photocurrent density ($J_{sc}$) on *X*.

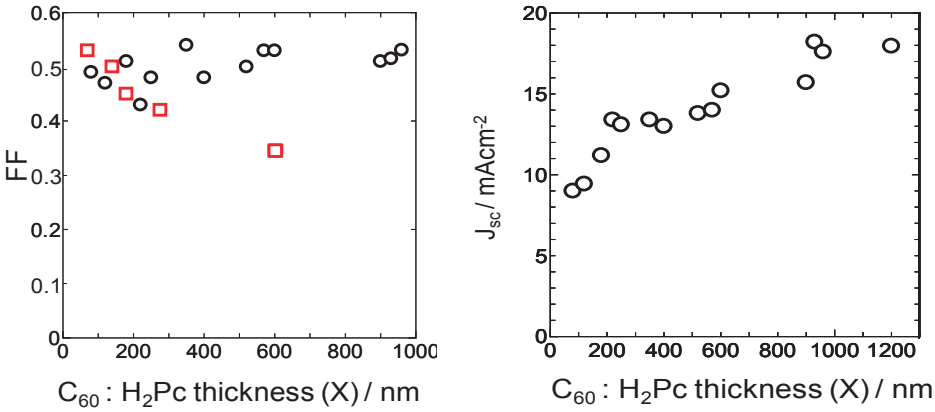


Figure 9b shows the spectral dependence of the absorption ratio of the cells. For a thin $C_{60}$:$H_2Pc$ layer (*X* = 180 nm, curve A), a large portion of the visible light, especially around 500 nm, cannot be absorbed due to the low absorbance of $C_{60}$. For an extremely thick $C_{60}$:$H_2Pc$ layer (*X* = 960 nm, curve C), 95% of the visible light from 300 to 800 nm is absorbed. Figure 9c shows photographs of the cells with *X* = 180 nm (top) and 960 nm (bottom). For *X* = 180 nm, the cell color is a transparent green, *i.e.*, a large portion of the visible light is not absorbed and therefore cannot be utilized. For *X* = 960 nm, the cell color is an opaque dark brown, *i.e.*, almost all of the visible light is absorbed.

The most important feature of the present cells is the incorporation of an extremely thick (1 μm) $C_{60}$:$H_2Pc$ co-deposited layer into the cell without decreasing FF. This allows the utilization of the entire visible region of solar light.

**Figure 9.** (**a**) Spectral dependence of the internal quantum efficiency for a cell with $X$ = 960 nm; (**b**) Spectral dependences of the light absorption ratio of cells with $X$ = 180 nm (curve A), 600 nm (curve B), and 960 nm (curve C); (**c**) Photograph of cells with $X$ = 180 nm (top) and 960 nm (bottom).

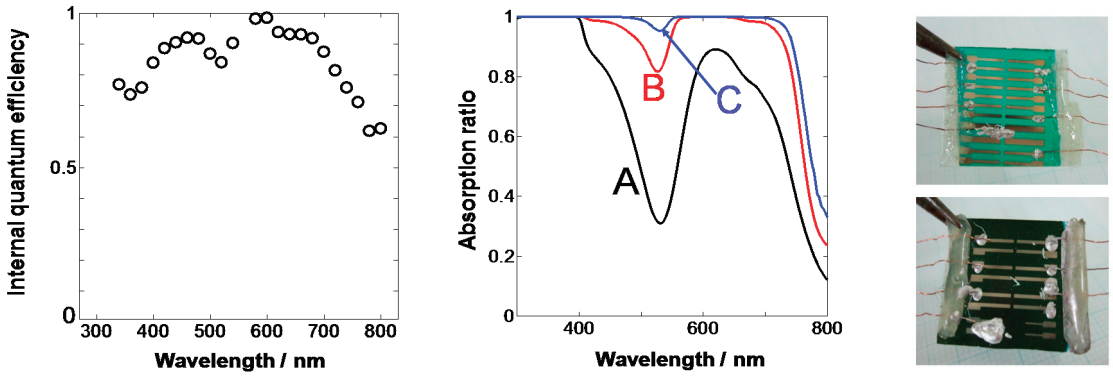


(**a**) (**b**) (**c**)

To evaluate the purity of the $C_{60}$ crystals at the ppm level, secondary ion mass spectroscopy with a $Cs^+$ ion source (SIMS, ULVAC-PHI, 6650M) was used. Figure 10 shows the negative ion mass spectrum (a) and the depth profile (b). Most of the peaks are assigned to carbon ($C_1$, $C_2$, *etc*. and their isotopes). As impurities, only oxygen (O) and hydrogen (H) were detected. The intensity of $10^1$ in the depth profile corresponds to the detection limit for the elements. For O atoms, the detection limit corresponds to a concentration of about $8 \times 10^{15}$ atoms/cm$^3$ [22]. Taking this value into account, we conclude that the purity of the $C_{60}$ has reached at least seven-nines (99.99999%, 7N) [23]. The main impurity is revealed to be oxygen. $C_{60}$ molecules interacting with oxygen seem to be the main impurities. Oxidized $C_{60}$ ($C_{60}O_x$) has been reported to act as an electron trap [24]. It is probable that the absence of $C_{60}O_x$ traps greatly enhances the electron diffusion length ($L = (D\tau)^{1/2}$; $D$: diffusion coefficient, $\tau$: electron lifetime) by increasing the lifetime ($\tau$).

**Figure 10.** Negative ion mass spectrum (**a**) and depth profile (**b**) of SIMS measurements for $C_{60}$ crystal purified three times by single-crystal sublimation.

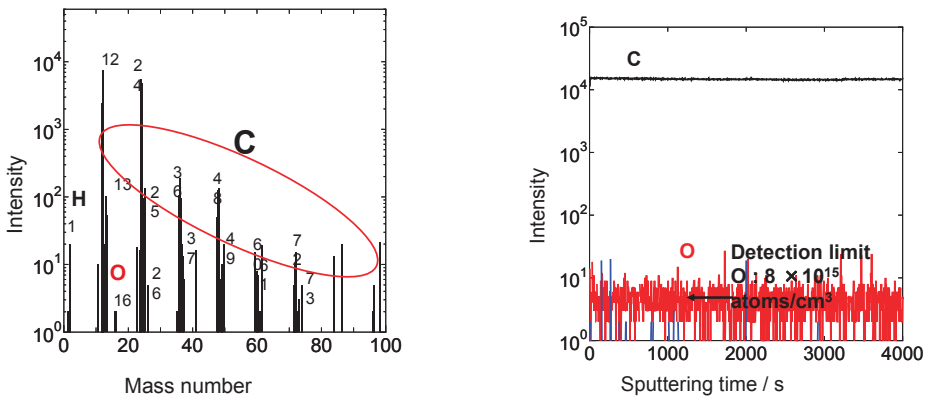


(**a**) (**b**)

The overall results in this Section suggest that both high-purification and phase-separation are necessary to fabricate 1 μm-thick $C_{60}$:$H_2Pc$ co-deposited cells.

## 5. *pn*-Control by Doping

### *5.1. Background*

Organic semiconductors have been recognized as being affected by unintentional contamination from impurities that act as donors, acceptors, traps, *etc*. Uncontrolled impurities due to incomplete purification and due to contamination from air hid the real nature of organic semiconductors for a long time. A typical example is oxygen. Since oxygen from air, which acts as an acceptor impurity, is doped in many kinds of organic semiconductors such as phthalocyanines, they always show *p*-type character. The prevention of exposure to oxygen by the use of ultra-high vacuum during film deposition and subsequent measurements has revealed that phthalocyanines are fundamentally *n*-type in nature [25,26]. A few exceptional kinds of organic semiconductors, such as perylene pigments (for example Im-PTC (Figure 3)) that are not affected by oxygen even in air show *n*-type character.

Though impurity doping into organic semiconductors has already been studied, the types of dopants that were used were very limited. As acceptor dopants, halogen vapors, such as $I_2$ or $Br_2$, were used [27,28]. After $Br_2$-doping, perylene pigment changed its conduction type from *n*- to *p*-type, and *pn*-homojunctions could be formed [29]. On the other hand, as donor dopants, there were few choices except alkaline metals, such as Na and Ca, which are easily oxidized in air.

In the last decade, however, due to spin-offs from organic EL technology, several new kinds of dopants have been identified, firstly for the carrier injection layers. As acceptors, organic dopants such as $F_4$-TCNQ [30,31] and inorganic dopants like $MoO_3$, $V_2O_5$, *etc*. [32,33] were found. In terms of donors that are relatively stable in air, Harada *et al*. found a Ru-complex and applied it to fabricate *pn*-homojunctions in zinc phthalocyanine [34,35] and pentacene [36]. Recently, compounds of alkaline metals, such as $Cs_2CO_3$ [37,38], and Co-complexes [39] acting as donor dopants have been identified. Progress in the search for dopants for organic semiconductors is summarized in reference [40].

We believe that the following points are indispensable for the complete *pn*-control of organic semiconductors. (a) a ppm-level doping technique should be applied to sub-ppm purified organic semiconductors; (b) Complete *pn*-control, *i.e*., the observation that every single organic semiconductor shows both *n*- and *p*-type characteristics by impurity doping alone, should be proved; (c) Uncontrollable doping by oxygen and water from air should be completely avoided to obtain reproducible results; (d) For organic solar cell applications, the doping technique should be applicable not only to single organic semiconductor films, but also to co-deposited films that have D/A sensitization capability.

### *5.2. Method of ppm-Level Doping*

Organic semiconductor samples of at least 7N purity were used. $C_{60}$ (nano purple TL, Frontier Carbon, Tokyo, Japan), $H_2Pc$ (Fastogen Blue EP-101, Dainippon Ink and Chemicals, Inc., Tokyo, Japan), and 6T (sexithiophene; Tokyo Chemical Industry, Tokyo, Japan) samples were purified by growing single-crystals by sublimation, as mentioned in Section 4.1. $MoO_3$ (Alfa Aeser, 99.9995%)

and $V_2O_5$ (Aldrich, 99.99%), and $Cs_2CO_3$ (Aldrich, 99.995%) were used as dopants for acceptors and donors, respectively (Figure 11a).

**Figure 11.** (**a**) Three-sources co-deposition. $MoO_3$ and $V_2O_5$ acting as acceptors and $Cs_2CO_3$ acting as a donor were doped into the $H_2Pc$:$C_{60}$ (1:1) co-deposited film; (**b**) An example of the total-thickness signal from the QCM *vs*. time relationship for 9 ppm doping.

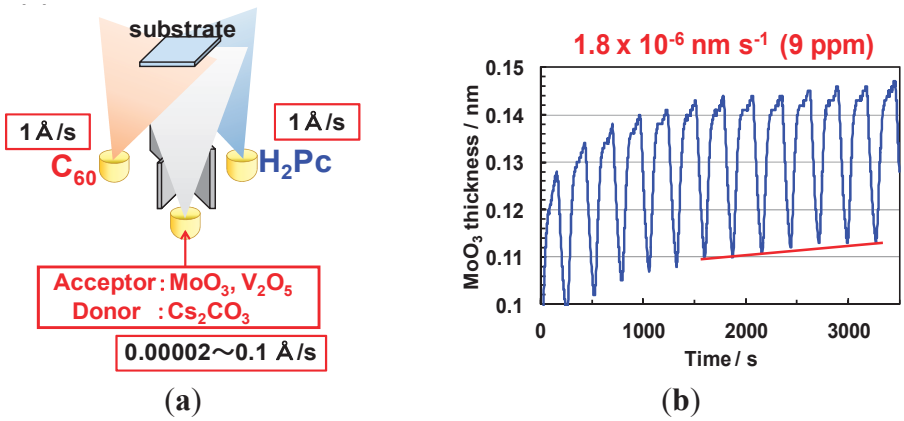


Multiple component co-evaporation techniques were employed to simultaneously evaporate organic semiconductors and dopants. In the case of doping into single organic semiconductor films, a two-component co-evaporation technique was employed. In the case of doping into $C_{60}$:$H_2Pc$ and $C_{60}$:6T co-deposited films, a three-component co-evaporation technique (Figure 11a) was employed. An oil-free vacuum evaporator (ET300-6E-HK, EpiTech Inc., Kyoto, Japan) was used for co-evaporation on indium tin oxide (ITO) glass substrates at a chamber pressure of $10^{-5}$ Pa.

Precise monitoring of the deposition rate using a quartz crystal microbalance (QCM) equipped with a computer monitoring system (ULVAC, CRTM-6000G/Depoview) allowed us to introduce the dopants down to a very low concentration of 10 ppm by volume. Figure 11b shows an example of the total-thickness signal for the QCM *vs*. time relationship as monitored by a PC display for 50 ppm $MoO_3$ doping. There was a very slow cyclical fluctuation in the material due to temperature fluctuations in the cooling water for the QCM caused by on/off cycling of the chiller. However, a reproducible increase in the baseline (red line), which was only observed during $MoO_3$ evaporation for a prolonged timescale of 3500 s, was observed ($1.8 \times 10^{-6}$ nm $s^{-1}$). The evaporation rate of the organic semiconductors was maintained at 0.2 nm $s^{-1}$. Therefore, a doping concentration of 9 ppm in volume can be obtained ($1.8 \times 10^{-6}/0.2 = 9 \times 10^{-6}$).

The Fermi level ($E_F$) of the 100 nm-thick organic semiconductor films was measured using a Kelvin vibrating capacitor apparatus (Riken-Keiki, FAC-1). Both the evaporation chamber and the Kelvin probe were built into a glove-box (Miwa, DBO-1.5) purged with $N_2$ gas ($O_2$ < 0.2 ppm, $H_2O$ < 0.5 ppm). During the film deposition and the $E_F$ and photovoltaic measurements, none of the organic films were exposed to air at any time. Removal of the influence of $O_2$ is indispensable for obtaining accurate $E_F$ measurements of organic semiconductor films. The $E_F$ values were easily perturbed if the organic films were exposed to air even once, especially by the ingress of $O_2$ into the films, and then reproducible results could hardly be obtained.

*5.3. pn-Control of Single $C_{60}$ Films*

In Figure 12, energy diagrams of the $C_{60}$ (left side) and $MoO_3$ (right side) films are shown. The $MoO_3$ showed a remarkably positive value of $E_F$ at 6.69 eV, which is more positive than the upper edge of the valence band of $C_{60}$ (6.4 eV), as determined by X-ray photoelectron spectroscopy [41,42]. The value of $E_F$ for non-doped $C_{60}$ (black line) is located at 4.6 eV, near the lower edge of the conduction band, suggesting that this film is *n*-type in nature. When $MoO_3$ was doped at a concentration of 3000 ppm, the value of $E_F$ shifted toward the positive direction and reached 5.88 eV, which is close to the upper edge of the valence band (6.4 eV). This result strongly suggests that $MoO_3$-doped $C_{60}$ is *p*-type.

**Figure 12.** Energy diagrams of various organic semiconductor films. The black, red, and blue lines show the energetic position of $E_F$ for non-doped, $MoO_3$-doped, and $Cs_2CO_3$-doped films. The doping concentration is 3000 ppm. $E_F$ vales for $MoO_3$ and $Cs_2CO_3$ films (100 nm) are also shown.

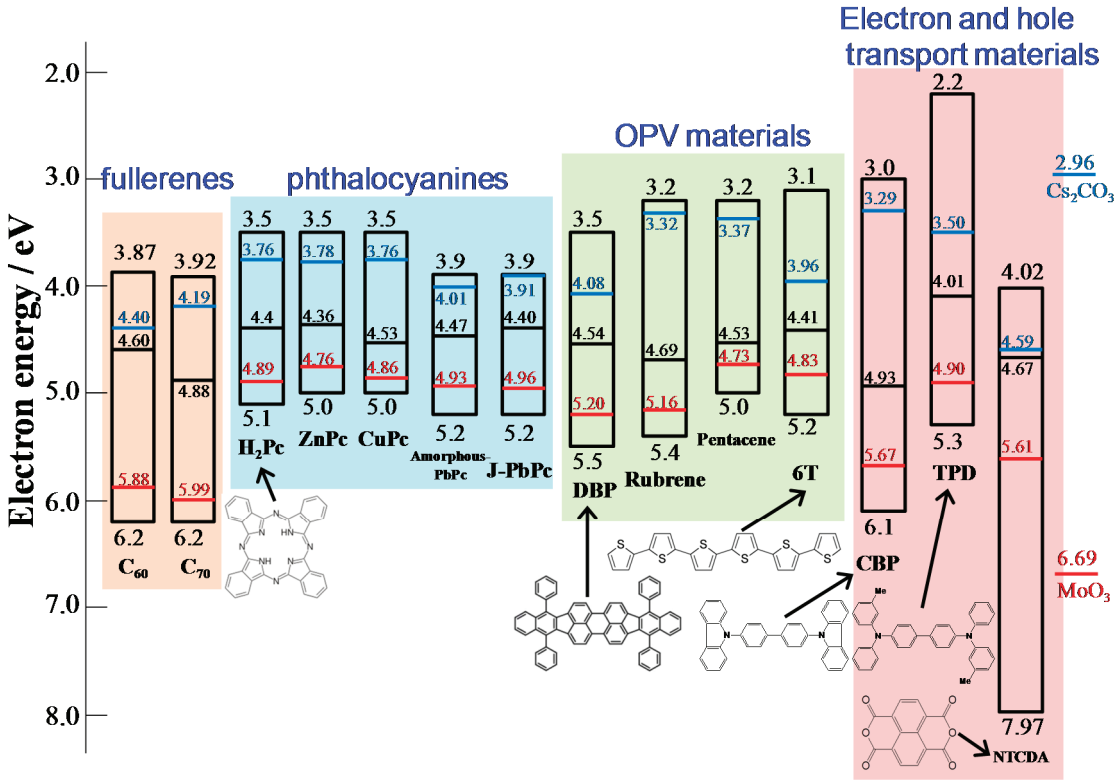


To investigate the kinds of interactions that occur between $C_{60}$ and $MoO_3$, the absorption spectra of a co-deposited film with a ratio of 1:1 were obtained. Though single films of $MoO_3$ and $C_{60}$ are transparent and weak-yellowish transparent respectively, a new strong absorption from 500 to 1800 nm appeared for the co-deposited $MoO_3$:$C_{60}$ (1:1) film and the film color changed to black (Figure 13, left upper photograph). This new absorption can be attributed to charge transfer (CT) absorption between $C_{60}$ and $MoO_3$. Absorption spectrum of CT band is appeared in reference [43]. Based on the energy diagram (Figure 12), it is reasonable to infer that $MoO_3$ extracts electrons from the valence band of $C_{60}$. The left-middle figure in Figure 13 shows the mechanism of *p*-type $C_{60}$ formation. A CT complex, *i.e.*, $C_{60}^{+} - MoO_3^{-}$, is formed. Here, the negative charge on the $MoO_3^{-}$

group can be regarded as a spatially-fixed ion, *i.e.*, an ionized acceptor. On the other hand, the positive charge on $C_{60}^{+}$ can be liberated from the negative charge on the $MoO_3^{-}$ by heat energy at room temperature, and can migrate into the $C_{60}$ film and act as a free hole in the valence band of $C_{60}$. This increase in hole concentration causes the large positive shift of $E_F$ that is observed (Figure 12). This is a process similar to the formation of free holes in *p*-type silicon (Figure 13, left lower). $V_2O_5$ was also confirmed to act as an acceptor in $C_{60}$.

**Figure 13.** (Upper) Photographs of $C_{60}$:$MoO_3$ (1:1) (left) and $C_{60}$:$Cs_2CO_3$ (10:1) (right). Strong CT-absorption was observed. (Middle) Mechanisms of *p*- and *n*-type $C_{60}$ formation by $MoO_3$ (left) and $Cs_2CO_3$ (right) doping. (Lower) Corresponding mechanisms of *p*- and *n*-type Si formation by B (left) and P (right) doping.

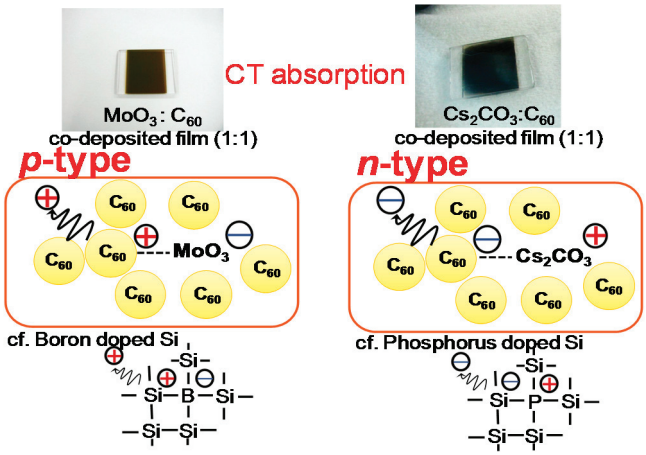


For the 3000 ppm $Cs_2CO_3$-doped $C_{60}$ film, the value of $E_F$ shifted negatively to 4.40 eV, which is close to the lower edge of the conduction band (CB) of $C_{60}$ (4.0 eV) [41]. A thick co-deposited film of $C_{60}$:$Cs_2CO_3$ in the ratio 10:1 changed color to reddish-brown (Figure 13, right upper photograph), *i.e.*, it showed a new broad CT absorption. Since the work function of $Cs_2CO_3$ (2.96 eV) is more negative than the conduction band of $C_{60}$ (4.0 eV), it is reasonable that $Cs_2CO_3$ donates an electron to $C_{60}$ and forms a CT complex, *i.e.*, $C_{60}^{-} - Cs_2CO_3^{+}$. The formation of n-$C_{60}$ by $Cs_2CO_3$ doping is caused by the opposite mechanism to $MoO_3$ doping (Figure 13). The donor ability of $Cs_2CO_3$ did not disappear even after exposure to air.

### *5.4. pn-Homojunction Formation in Single $C_{60}$ Films*

Since both *p*- and *n*-type $C_{60}$ were formed, we tried to fabricate *pn*-homojunctions in the single $C_{60}$ films [44,45]. Three types of cells with different thickness combinations of *p*- and *n*-doped layers, *i.e.*, 250/750 nm (a); 500/500 nm (b); and 750/250 nm (c) were fabricated (Figure 14). The total thickness of the $C_{60}$ was maintained at 1 μm for all cells. Figure 15 shows the action spectra for the three types of cells. Under irradiation onto the ITO electrode (Figure 14a, hν(ITO)) and with the homojunction located at the ITO side (Figures 14a and 15a, curve A), photocurrent mainly appeared between 400 and 500 nm, which corresponds to the visible absorption region of the $C_{60}$ film (black curve). For the homojunction at the center of the cell (Figures 14b and 15a, curve B), the photocurrent decreased and shifted to longer wavelength and the main peak was located at the edge of the $C_{60}$ absorption. Finally, for the homojunction on the Ag side (Figures 14c and 15a, curve C), the low

magnitude photcurrent shifted to a wavelength far longer than 500 nm, where there is little $C_{60}$ absorption. The observed systematic change in the shape of the action spectra with respect to the distance of the homojunction from the light-irradiated electrode can be attributed to the so-called "masking effect". This means that photocarrier generation occurs mainly in the neighboring regions of the *p*/*n*-doped interface (active zone) and that, by retracting this homojunction from the light-irradiated ITO surface, a dead layer is gradually grown in front of this active zone.

**Figure 14.** Three structures of *pn*-homojunction $C_{60}$ cells. The thickness combinations of the $MoO_3$- and Ca-doped layers are 250/750 nm (**a**); 500/500 nm (**b**); and 750/250 nm (**c**). The concentration was kept at 5000 ppm for both dopants. Hν (ITO) and hν (Ag) denote light irradiation onto the ITO and onto Ag electrodes, respectively. The locations of the homojunctions are indicated by the arrows.

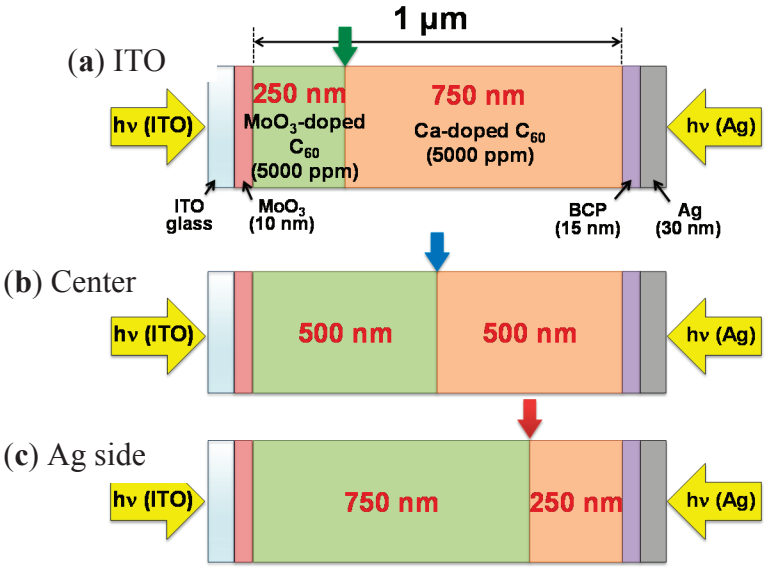


Under light irradiation onto the Ag electrode (Figure 14, hν(Ag)), the homojunction approaches the illuminated electrode in the order of cells (a); (b); and (c). In this case, completely the reverse tendency, namely, an increase in the magnitude of the photocurrent and a shift towards shorter wavelength of the action spectra, were observed (Figure 15b, curves C, B, and A). This means that the dead layer between the active zone and the illuminated Ag electrode gradually disappeared. Apparently, the photoactive zone moves together with the homojunction. Even if the Ca donors were substituted with $Cs_2CO_3$ donors, fundamentally the same result was obtained. Since the width of the depletion layer *pn*-homojunction at the present doping concentrations of 5000 ppm $MoO_3$/5000 ppm $Cs_2CO_3$ is calculated to be only 29 nm, which is far smaller than the total cell thickness of 1 μm, a strong masking effect (Figure 15) was observed.

**Figure 15.** Action spectra of the short-circuit photocurrent density ($J_{sc}$) under irradiation onto the ITO electrode (**a**) (hν(ITO)) and onto the Ag electrode (**b**) (hν(Ag)). Curves A, B, and C are for cells (**a**); (**b**); and (**c**) in Figure 14, respectively. The black curve shows the absorption spectrum of the $C_{60}$ film (150 nm). The monochromatic light intensity irradiated to the electrodes is around 3 $mWcm^{-2}$.

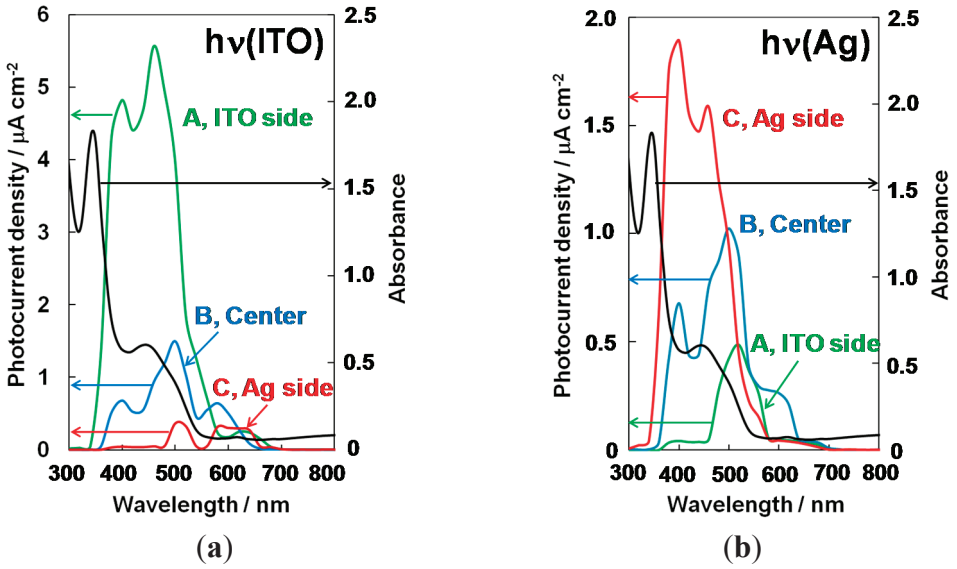


In Figure 16, the energy structure of a *pn*-homojunction (doping concentration: 3000 ppm $MoO_3$/500 ppm $Cs_2CO_3$) as measured by Kelvin-band mapping (see Sections 5.6 and 6.3) is shown. Since there is a significant difference in $E_F$, a built-in potential can be created by contacting the $MoO_3$- and the $Cs_2CO_3$-doped $C_{60}$ films (Figure 12, left side). As a result, a *pn*-homojunction is formed. The observed direction of the photovoltage, whereby ITO/$MoO_3$ is positive and BCP/Ag is negative, is consistent with this energy structure. The present results clearly show that *pn*-homojunctions were fabricated in the single $C_{60}$ films by doping alone. In other words, the photovoltaic properties of organic semiconductor films could be intentionally designed by doping. We also confirmed the formation of *pn*-homojunctions for metal-free phthalocyanine ($H_2Pc$) [46].

**Figure 16.** Energetic structure of *pn*-homojunction formed after contact measured by Kelvin band mapping. The doping concentrations of $Cs_2CO_3$ and $MoO_3$ are 500 ppm and 3000 ppm, respectively.

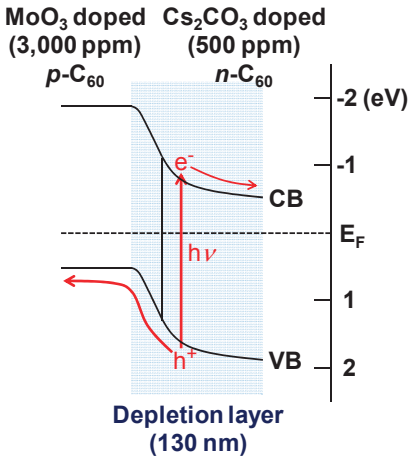

*5.5. Generality*

As shown in Figure 12, other than fullerenes ($C_{60}$ and $C_{70}$), complete *pn*-control was accomplished for various phthalocyanines ($H_2Pc$, ZnPc CuPc, PbPc), other photovoltaic organic semiconductors (rubrene, sexithiophene (6T), pentacene, DBP), and hole transport materials (CBP). In exceptional cases, due to the energy relationship, only *p*- and *n*-type control could be accomplished for TPD and electron transport material (NTCDA), respectively. These results strongly suggest that, in principle, almost all single organic semiconductors can be controlled to both *n*-type and *p*-type by doping alone, similar to the case of inorganic semiconductors. For the cases of $C_{60}$, $H_2Pc$, ZnPc, pentacene, and CBP, *pn*-homojunctions were formed [34,36,38,44,46].

*5.6. Band Mapping by Kelvin Probe*

The concentrations of carriers created by doping can be evaluated by using the Kelvin vibrating capacitor method [47,48]. Figure 17 shows the principle of band mapping by Kelvin probe. When *p*-doped organic semiconductors are in contact with ITO electrodes, the $E_F$ values are aligned. Accordingly, the vacuum level ($E_{VAC}$) is bent upward and the value of the work function, which is defined as the difference between $E_{VAC}$ and $E_F$ (red double arrows), changes with the thickness of the films. Thus, the band-bending can be directly mapped (Figure 17, lower) by measuring the work function using a Kelvin probe for changing thicknesses of doped films (Figure 17, middle). Since the band-bending gives the depletion layer width ($W_{dep}$) and the built-in potential ($V_{bi}$), the carrier concentration ($N$) can be obtained by using the following equation; $W_{dep} = (2\varepsilon\varepsilon_0 V_{bi}/eN)^{1/2}$. Here, $\varepsilon$, $\varepsilon_0$, and e are the relative dielectric constant, the dielectric constant of a vacuum, and the elementary charge.

**Figure 17.** Principle of band-mapping by Kelvin probe. An interface between an ITO and a *p*-type semiconductor film is shown. Work function values (middle figure) corresponding to the double red arrows (lower figure) depending on the thickness of the organic semiconductor film were measured by Kelvin probe. $E_{vac}$, $E_F$, CB, and VB denote the vacuum level, the Fermi level, the conduction band, and the valence band, respectively.

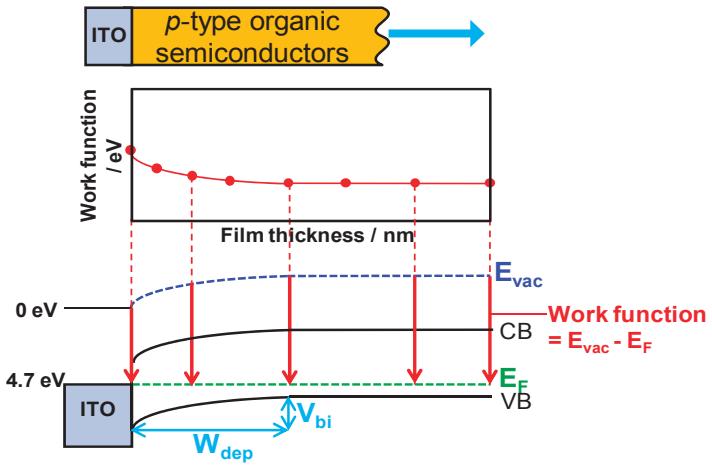

Figure 18 shows the dependences of the work functions of the doped $C_{60}$ films on the film thicknesses. In the case of $Cs_2CO_3$-doping, the work function was shifted toward the negative direction and reached close to the lower edge of the conduction band (CB) (3.9 eV) (triangular dots). In the case of $MoO_3$-doping, the work function was shifted toward the positive direction and reached near the upper edge of the valence band (VB) (6.4 eV) (circular dots). For both dopants, as the doping concentration increased, the film thickness at which the shift in the work function finished became thinner, and the magnitude of the energy shift became larger. Namely, $W_{dep}$ decreased and $V_{bi}$ increased. These band-bendings can be fitted by quadratic curves (Figure 18, solid lines) based on the Poisson equation, and the values of $W_{dep}$ and $V_{bi}$ can be precisely determined. For example, in the cases of the *n*- and *p*-type band-bending of $C_{60}$ films doped with $Cs_2CO_3$ (500 ppm) and with $MoO_3$ (5000 ppm), electron and hole concentrations of $2.5 \times 10^{17}$ $cm^{-3}$ and $9.6 \times 10^{17}$ $cm^{-3}$ [49] were obtained, respectively, from $W_{dep}$ values of 24 nm and 21 nm and $V_{bi}$ values of 0.29 V and 0.87 V using a ε value of 4.4 for $C_{60}$ [50].

**Figure 18.** Work function shifts in $C_{60}$ films doped with $Cs_2CO_3$ and $MoO_3$ on ITO substrates (triangular and circular dots). Band-bending was fitted by a quadratic relationship based on the Poisson equation (solid curves).

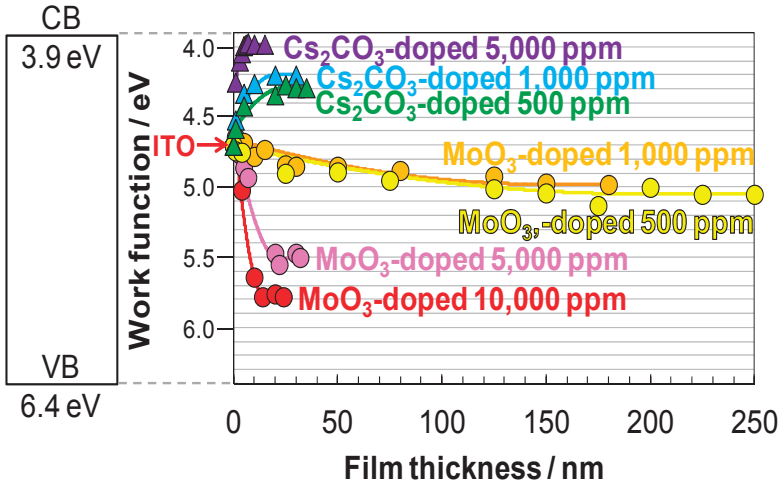


Figure 19a shows the dependence of carrier concentration on the doping concentration. When the $Cs_2CO_3$-doping concentration increased, the electron concentration rapidly increased and reached $10^{19}$ $cm^{-3}$ at a doping concentration of 10,000 ppm. On the other hand, when $MoO_3$ was used as the dopant, the carrier concentration showed a minimum value, *i.e.*, $4.3 \times 10^{15}$ $cm^{-3}$ at 500 ppm, and the hole concentration increased and reached $2.7 \times 10^{18}$ $cm^{-3}$ at 10,000 ppm. The minimum carrier concentration at 500 ppm with $MoO_3$-doping suggests that the holes created by $MoO_3$-doping compensate the inherent *n*-type nature of $C_{60}$.

**Figure 19.** Dependence of carrier concentration (**a**) and doping efficiency (**b**) on doping concentration of $Cs_2CO_3$ or $MoO_3$.

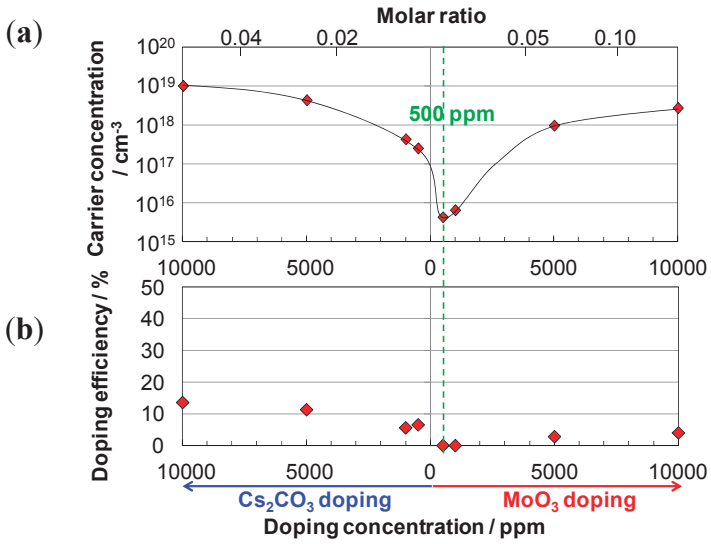


Figure 19b shows the doping efficiency, which is defined as the ratio of the induced carrier concentration to the doped molecular concentration. The doping efficiencies of $Cs_2CO_3$- and $MoO_3$-doping are about 10% and 3%, respectively. The doping process can be explained by the formation of a CT-complex and its subsequent ionization (Figures 13(middle) and 20b). Thus, the doping efficiency is expressed by the product of the rates of CT complex formation and ionization. In the case of $Cs_2CO_3$, since $Cs_2CO_3$ is a substantial molecule, by assuming that $Cs_2CO_3$ evaporates molecularly and the rate of CT complex formation with $C_{60}$ is close to unity [51], the observed doping efficiency of 10% can be regarded as the ionization efficiency, which is significantly smaller than the value of 100% obtained for the donor dopant P in Si at room temperature. The orbitals of the electrons around the positive charge on the ionized donor in the cases of P-doping in Si (a) and of $Cs_2CO_3$-doping in $C_{60}$ (b) are shown in Figure 20. Based on the fact that the ε value of Si is 11.9, the radius of the orbital of the electron around the positive charge of an ionized donor ($P^+$) is calculated to be 3.3 nm. This situation is fundamentally the same to the Wannier exciton (Figure 1a) and the electron is easily liberated from the positive charge by thermal energy at room temperature, and thus the ionization efficiency reaches unity (Figure 20a). The only difference to the exciton is that the positive charge is spatially fixed in the crystal lattice [52]. In the case of $Cs_2CO_3$-doping in $C_{60}$, since the ε value of $C_{60}$ is 4.4, the electron experiences a stronger attractive force from the positive charge. The radius of the Frenkel exciton is only 0.5 nm for $C_{60}$ (Figure 1b). However, a CT complex is formed by employing $Cs_2CO_3$-doping, *i.e.*, [$Cs_2CO_3^+$–$C_{60}^-$] and the charges are separated on the neighboring molecules (Figure 20b). This situation is fundamentally the same as the CT exciton (Figure 2b) and the negative charge on $C_{60}$ can be liberated by thermal energy at room temperature. Thus, significant values for the ionization efficiencies of electrons of about 10% were observed, though they were lower than the case of Si.

**Figure 20.** Orbital of an electron around a positive charge on an ionized donor. (**a**) P-doping in Si. $P^+$ is represented by the red shaded circle. This situation resembles the Wannier exciton (Figure 1a); (**b**) $Cs_2CO_3$-doping in $C_{60}$. $Cs_2CO_3^+$ is represented by the red shaded circle. This situation resembles the CT-exciton (Figure 2b).

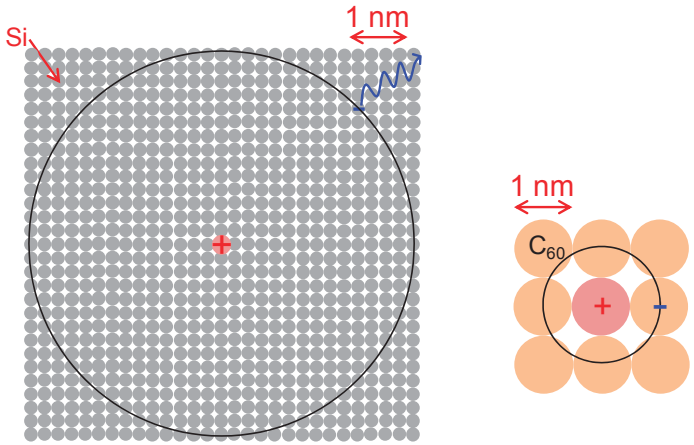


(**a**) (**b**)

In the case of $MoO_3$, a doping efficiency of 3% was obtained under the assumption that $MoO_3$ forms the trimer ($Mo_3O_9$) [53]. Though a similar mechanism to that in Figure 20b can also be applied in this case, in addition, the formation of larger $MoO_x$ clusters lowers the efficiency of CT-complex formation, which seems to lower the total doping efficiency.

*5.7. Organic/Metal Ohmic Junction*

It is very important to make the two organic/metal contacts in a photovoltaic cell ohmic. When the region in the vicinity of a metal electrode is heavily doped, even if there is a Schottky barrier, its width becomes extremely thin allowing charge carrier tunneling and, as a result, an ohmic contact is expected to be formed similar to that on heavily $p^+$- or $n^+$-doped inorganic semiconductors [40,54,55]. Here, + means heavily doped. Moreover, an ohmic contact can be formed irrespective of which electrode material is used, since tunneling is less dependent on the metal work function, enabling the cell structure to be inverted. This technique would allow flexibility in the design of the cell structure.

As a test case, two-layer cells consisting of $C_{60}$ and $H_2Pc$ (Figure 21a,b) were examined [56]. The electrode materials were ITO and Ag. Heavy doping of the order of 10,000 ppm (1%) and 50,000 ppm (5%) was applied to thin 10 nm regions close to the $C_{60}$ and $H_2Pc$/metal interfaces. Figure 21c,d shows the current-voltage (J-V) characteristics for the cells with heavily-doped regions in Figure 21a,b (red curves). For the cell in Figure 21a, the fill factor (FF) reaches a value of 0.59 and clear rectification characteristics can be seen with heavily-doped regions (red broken curve). Without the heavily-doped regions (blue curves), however, FF is only 0.29 and the forward current is significantly suppressed. For the inverted cell (Figure 21b), without heavily-doped regions (Figure 21d, blue curves), photovoltaic and rectification behavior are scarcely perceptible [57]. However, with the heavily-doped regions (red curves), the FF recovers, reaching a value of 0.49, and rectification is clearly observed. Clearly, the photovoltaic properties of the cells with thin heavily-doped regions at

the interfaces are independent of the type of electrode material used. Thus, $H_2Pc/C_{60}$ cells are invertible using this interfacial heavy-doping technique.

**Figure 21.** Structures of invertible two-layered $H_2Pc/C_{60}$ cells with heavily-doped organic/metal interfaces. For the cells in (**a**,**b**), photogenerated holes and electrons are extracted to ITO and Ag, and to Ag and ITO, respectively. The total thicknesses of the $H_2Pc$ and $C_{60}$ films are kept the same; (**c**,**d**) Current-voltage (J-V) characteristics for the cell (**a**,**b**) (red curves). The blue curves are for cells without heavily doped interfaces. The photocurrent and the dark current are shown by the solid and broken curves, respectively. The ITO electrode was irradiated with simulated solar light (AM1.5, 100 $mWcm^{-2}$). Cell performances: (**a**) $J_{sc}$: 3.38 $mAcm^{-2}$, $V_{oc}$: 0.46 V, FF: 0.59, Efficiency: 0.91%; (**b**) $J_{sc}$: 2.70 $mAcm^{-2}$, $V_{oc}$: 0.43 V, FF: 0.49, Efficiency: 0.57%. Copyright© 2012 The Japan Society of Applied Physics.

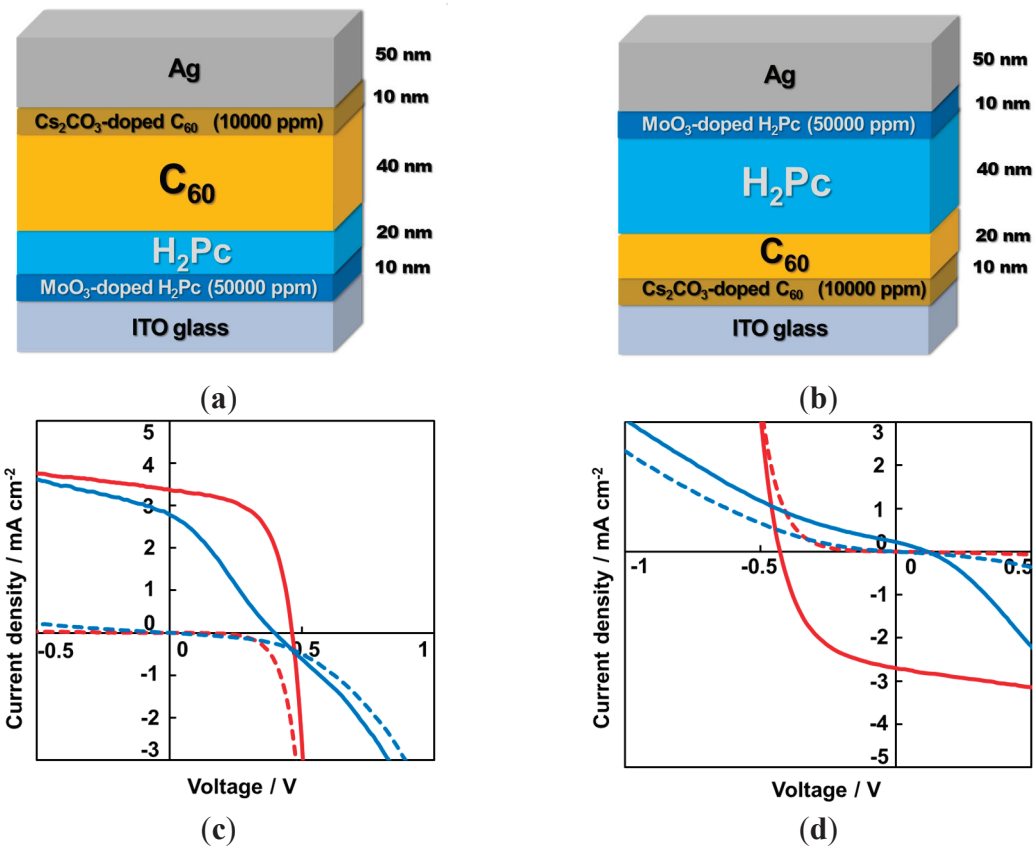


Since electron extraction from $C_{60}$ to the ITO electrode is crucial for the operation of the inverted cell (Figure 21d (red curves)), we estimated the interfacial energy band structure of ITO/10,000 ppm $Cs_2CO_3$-doped $C_{60}$ by Kelvin band mapping (Figure 22) (Section 5.6). There is a distinct barrier to electrons with a height of 0.34 eV from the conduction band of $C_{60}$ to the ITO. However, since the band bends down steeply within 5 nm of the interface, photogenerated electrons can tunnel through this barrier. Heavily-doped $C_{60}$ acts as an $n^+$-type semiconductor and makes the $n^+$-$C_{60}$/ITO junction ohmic. Organic/metal ohmic junctions can be fabricated by making tunneling contacts with heavy interfacial doping.

**Figure 22.** Energy structure for an ITO/$n^+$-$C_{60}$ contact measured by Kelvin band mapping. A tunneling junction for photogenerated electrons is formed. Copyright© 2012 The Japan Society of Applied Physics.

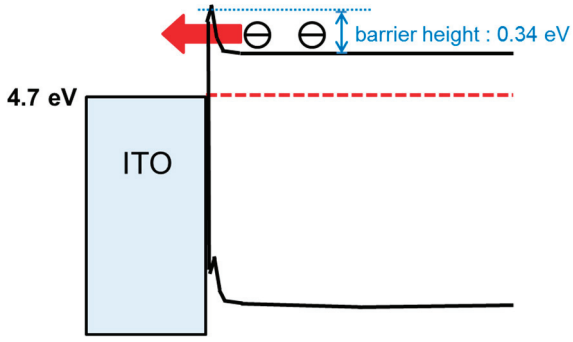


## 6. *pn*-Control of Co-Deposited Films by Doping

### *6.1. pn-Control of Co-Deposited Films*

Co-deposited films consisting of D/A organic semiconductors are essential in order to generate photocurrent densities of significant magnitude based on the dissociation of excitons by the photoinduced electron transfer process (Figures 2b and 4). So, for the application of this doping technique to organic photovoltaic cells, doping should be performed by regarding a co-deposited film consisting two kinds of D/A organic semiconductors as a single semiconductor. We believe that the formation of a built-in potential by direct-doping in the bulk of co-deposited films, where the generation and transport of photocarriers occurs, has the potential to enhance the efficiency of these cells [48]. Moreover, in these types of cells, short exciton diffusion length is no longer a factor that limits cell performance.

Figure 23a shows the energy diagram for $H_2Pc$:$C_{60}$ co-deposited films. With donor ($Cs_2CO_3$) doping, $E_F$ has shifted from the undoped value of 4.48 eV (black broken line) to 4.22 eV (green broken line) and is close to the $C_{60}$ conduction band ($CB_{C60}$). Conversely, for acceptor ($V_2O_5$) doping, $E_F$ has shifted to 4.95 eV (orange broken line) and is close to the $H_2Pc$ valence band ($VB_{H2Pc}$). Clearly, the conduction properties of the co-deposited films are controlled to both *n*- and *p*-type. It should be noted that the $E_F$ shift occurs within the band gap of co-deposited $H_2Pc$ and $C_{60}$ films, *i.e.*, in between $CB_{C60}$ and $VB_{H2Pc}$. For *n*-type doping (Figure 23b), free carriers (electrons) are produced in both $H_2Pc$ and $C_{60}$, and they relax to the conduction band of $C_{60}$. $E_F$ is fixed to 4.22 eV and is constant throughout the $H_2Pc$ and $C_{60}$ (green broken line). For *p*-type doping (Figure 23b), holes are produced that relax to the top of the $H_2Pc$ valence band. $E_F$ is fixed to 4.95 eV and is constant throughout the $H_2Pc$ and $C_{60}$ (orange broken line). As a result, the shifts in $E_F$ are within the "bandgap of the co-deposited film". Thus, control of the doping in the co-deposited film was accomplished [58,59].

**Figure 23.** (**a**) *pn*-control of $H_2Pc$:$C_{60}$ co-deposited films by doping. The $E_F$ shift occurs within the "bandgap of the co-deposited film". (**b**) Mechanism of *n*- and *p*-type formation.

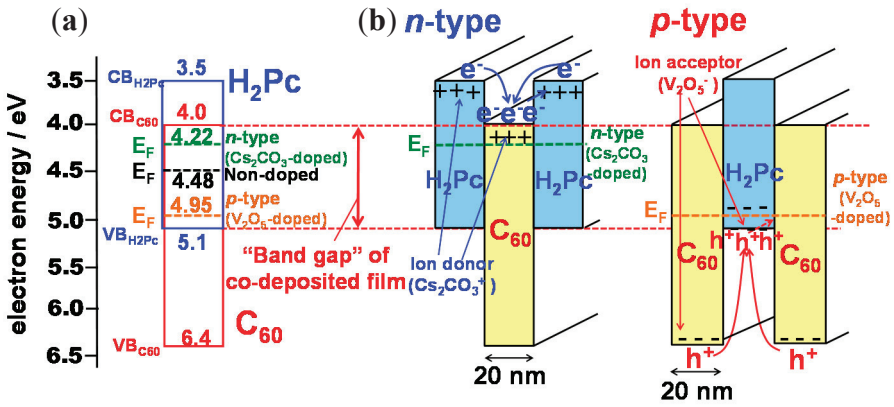


*6.2. Organic/Organic Ohmic Junction*

*pn*-control technique of co-deposited films allows us to fabricate *pn*-homojunction in the uniform co-deposited films. Lightly doped *pn*-homojunction is expected to act as the photovoltaic cells. On the other hand, heavily doped $n^+p^+$-homojunction is expected to act as the organic/organic ohmic junction. In this section, behavior of heavily doped $n^+p^+$-homojunction is mentioned.

Irrespective of whether we use single or co-deposited films, by making an $n^+p^+$ heavily doped double layer, organic/organic ohmic junctions can be fabricated [45,60]. Figure 24a shows an $n^+p^+$-homojunction device fabricated in a $C_{60}$:6T co-deposited film. $MoO_3$ and $Cs_2CO_3$ were heavily doped (50,000 ppm (5%)) for the $p^+$ and $n^+$-regions, respectively. Obviously, the $n^+p^+$-homojunction showed good ohmic properties (Figure 24b).

**Figure 24.** Organic/organic ohmic $n^+p^+$-homojunction (**a**) and its current-voltage characteristics (**b**).

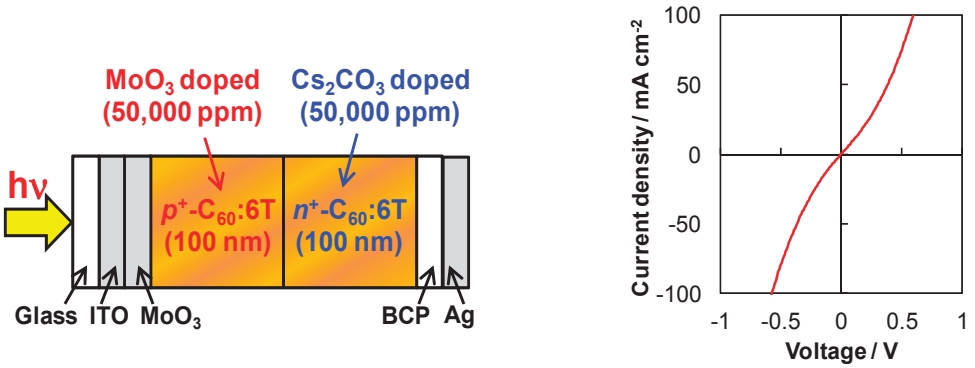


*6.3. Tandem Cells Formed in Co-Deposited Films by Doping*

Tandem organic solar cells were first reported by the authors in 1990 [61] and many types of cells that connect two unit cells have been fabricated [62]. The tandem organic solar cell, in which two single $p^+in^+$-homojunctions are connected by a heavily-doped $n^+p^+$-ohmic interlayer, were formed in

co-deposited films consisting of $C_{60}$ and sexithiophene (6T) simply by doping [60]. Figure 25a,b show the structures of a single $p^+in^+$-homojunction cell and a tandem cell connecting two $p^+in^+$-homojunctions formed in co-deposited $C_{60}$:6T films. The following cell parameters were obtained; $J_{sc}$ of 3.0 mA cm$^{-2}$, $V_{oc}$ of 1.69 V, FF of 0.47, and a conversion efficiency of 2.4% (Figure 25c, red curves B). Compared with the single cell (Figure 25c, blue curves A), $V_{oc}$ has doubled from 0.85 V to 1.69 V. Obviously, the $n^+p^+$-homojunction in the tandem cell acts as an ohmic interlayer to connect the unit cells as shown in Figure 24.

**Figure 25.** (**a**) Structure of a $p^+in^+$-homojunction cell fabricated in a $C_{60}$:6T co-deposited film. A non-doped intrinsic $C_{60}$:6T layer is sandwiched between heavily doped $p^+$ and $n^+$-$C_{60}$:6T layers; (**b**) Structure of a tandem cell connecting two unit $p^+in^+$-homojunction cells via an ohmic $n^+p^+$-homojunction; (**c**) Current voltage (J-V) characteristics for a single $p^+in^+$-homojunction cell (blue curves A) and a tandem cell (red curves B). The photo and dark currents are shown by the solid and the broken curves, respectively. The ITO electrode was irradiated with simulated solar light (AM 1.5, 100 mW cm$^{-2}$). The cell parameters, *i.e.*, $J_{sc}$, $V_{oc}$, FF, and efficiency. Curve A: 4.5 mA cm$^{-2}$, 0.85 V, 0.41, 1.6%. Curve B: 3.0 mA cm$^{-2}$, 1.69 V, 0.47, 2.4%.

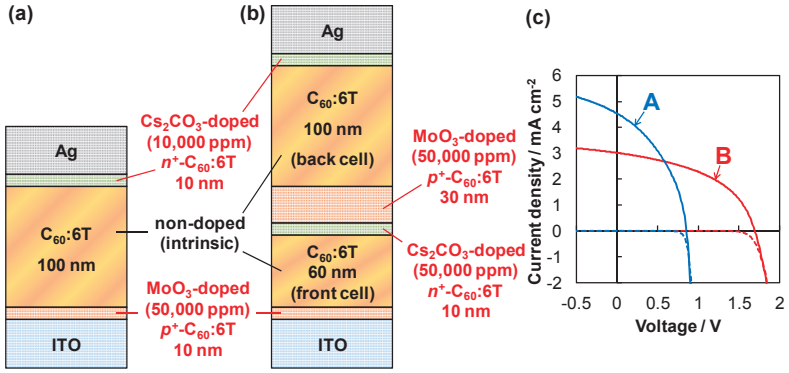


Kelvin energy-band mapping of the homojunctions was performed by measuring from both sides of the homojunction. To illustrate the presence of a $p^+in^+$-homojunction, the $E_F$ values for non-doped $C_{60}$:6T films on doped films were measured (blue curves A in Figure 26a,b). $E_F$ hardly changed and maintained almost constant values on both the $MoO_3$-doped film (Figure 26a) and on the $Cs_2CO_3$-doped (Figure 26b). These constant $E_F$ values indicate that the non-doped $C_{60}$:6T films act as insulators. As a result, when a unit cell having the structure of $MoO_3$-doped (50,000 ppm)/non-doped/$Cs_2CO_3$-doped (50,000 ppm), *i.e.*, a $p^+$/insulator/$n^+$, is fabricated, the built-in electric field generated by the differences in $E_F$ between the $MoO_3$ and $Cs_2CO_3$ doped layers (5.6 − 4.4 = 1.2 eV) (see Figure 26a,b), $C_{60}$:6T thickness = 0 nm) are uniformly distributed across the insulating non-doped $C_{60}$:6T film. Thus, two $p^+in^+$-homojunctions can be depicted in the front and back cells (Figure 27).

**Figure 26.** Energy level mapping of homojunctions using a Kelvin probe. The sample structures and the dependence of the position of the Fermi level ($E_F$) on the thicknesses of the non-doped or doped $C_{60}$:6T films are shown. (**a**) Non-doped (blue curve A) or $Cs_2CO_3$-doped (red curve B) deposited on a $MoO_3$-doped $C_{60}$:6T film; (**b**) Non-doped (blue curve A) or $MoO_3$-doped (red curve B) $C_{60}$:6T film deposited on a $Cs_2CO_3$-doped $C_{60}$:6T film.

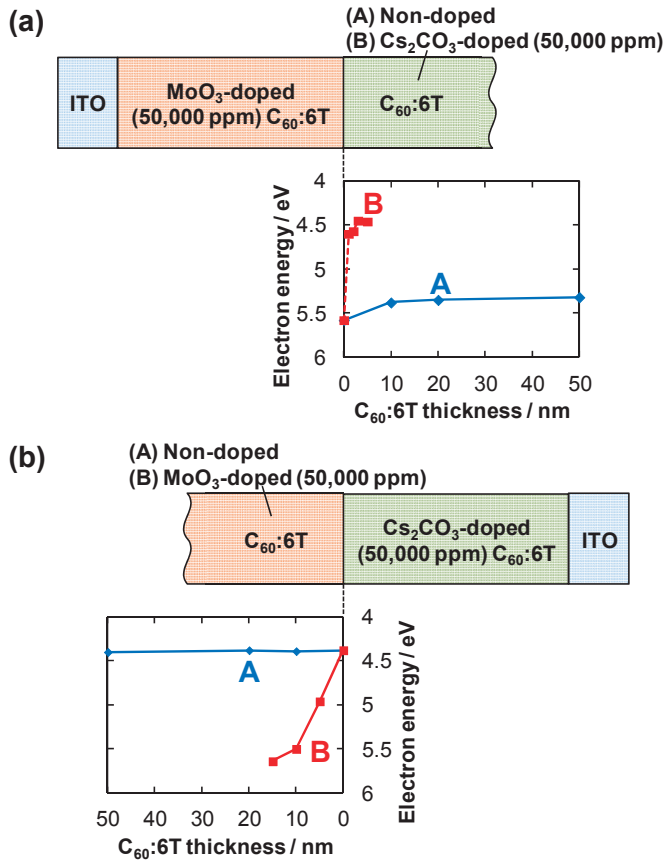


To illustrate the presence of an $n^+p^+$-homojunction, $E_F$ values for $Cs_2CO_3$-doped films on $MoO_3$-doped films (red curve B in Figure 26a) and those for $MoO_3$-doped films on $Cs_2CO_3$-doped films (red curve B in Figure 26b) were measured. All doping concentrations of $MoO_3$ and $Cs_2CO_3$ are 50,000 ppm. In the former case, a rapid negative shift in $E_F$ ended within 3 nm and reached the original $E_F$ position of $Cs_2CO_3$-doped $C_{60}$:6T (4.38 eV, see Figure 26b, $C_{60}$:6T thickness = 0 nm). In the latter case, a quick positive shift in $E_F$ ended within 15 nm and reached the original $E_F$ position of $MoO_3$-doped $C_{60}$:6T (5.58 eV, see Figure 26a, $C_{60}$:6T thickness = 0 nm). Based on these complementary observations, the potential profile of the depletion layer of an $n^+p^+$-homojunction (Figure 27, red shaded region, width: 18 nm) can be drawn.

The overall energy band diagram of a tandem cell is shown in Figure 27. In the case of the $p^+in^+$-homojunction cells formed in co-deposited $C_{60}$:6T films, there are $C_{60}$/6T hetero interfaces where photoinduced electron transfer can occur throughout the whole of the cells. Thus, under light irradiation, electrons and holes are photo-generated in both the front and back cells. Electrons and holes that move toward the $n^+p^+$-ohmic interlayer neutralize each other due to recombination or tunneling. This process is consistent with the observed photovoltaic properties of the present tandem cell (Figure 25). It should be stressed that the present results proved that built-in potentials, like

homojunctions and tandem junctions, can be intentionally formed in bulk co-deposited films induced by doping alone.

**Figure 27.** Energy band diagram of the depicted tandem cell based on Kelvin probe measurements (Figure 26). The red shaded region corresponds to the depletion layer for an $n^+p^+$-homojunction acting as an ohmic interlayer. VB and CB denote the valence band and the conduction band, respectively. The bands for $C_{60}$ and 6T are shown by the black and orange curves, respectively.

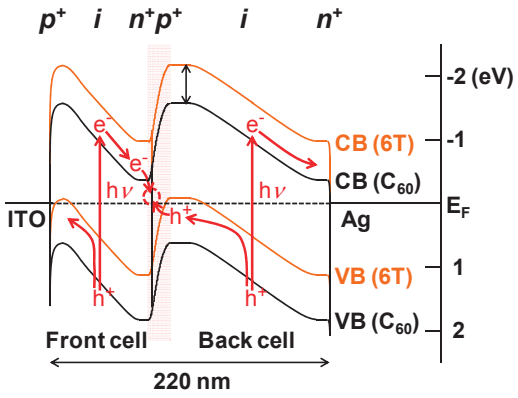


## 7. Conclusions

Factors that determine bandgap science for organic semiconductor films, namely, high-purification, *pn*-control by doping, built-in potential design, and precise evaluation of doping parameters, have been established. 7N-purification together with phase-separation by co-evaporant 3rd molecules allowed us to fabricate organic solar cells incorporating 1 μm-thick co-deposited films. *pn*-control techniques by impurity doping for both single and co-deposited films were established. A series of fundamental junctions, such as Schottky junctions, *pn*-homojunctions, $p^+$, $n^+$-organic/metal ohmic junctions, $n^+$-organic/$p^+$-organic ohmic homojunctions, and tandem cells were formed in single and co-deposited organic semiconductor films by doping alone.

Since conductivity (σ) is the product of the mobility (μ) and the carrier concentration (N), *i.e.*, $\sigma = eN\mu$ [e; electron charge], the cell resistance ($\sigma^{-1}$) can be reduced by increasing both N, by means of doping, and μ, by means of phase-separation of the co-deposited film by using a co-evaporant 3rd molecule, Now, we are trying to combine doping with phase-separation [58].

## Acknowledgments

Financial support from Core Research for Evolutional Science and Technology (CREST) from the Japan Science and Technology Agency (JST) is gratefully acknowledged.

## Conflicts of Interest

The authors declare no conflict of interest.

**References and Notes**


1. *Organic Photovoltaics*, *Mechanisms*, *Materials and Devices*; Sun, S.-S., Sariciftci, N.S., Eds.; CRC Press: New York, NY, USA, 2005.
2. Spanggaard, H.; Krebs, F.C. A brief history of the development of organic and polymeric photovoltaics. *Sol*. *Energy Mater*. *Sol*. *Cells* **2004**, *83*, 125–146.
3. Hoppe, H.; Sariciftci, N.S. Organic solar cells: An overview. *J*. *Mater*. *Res*. **2004**, *19*, 1924–1945.
4. Tang, C.W. Two-layer organic photovoltaic cell. *Appl*. *Phys*. *Lett*. **1986**, *48*, 183–185.
5. Hiramoto, M.; Fujiwara, H.; Yokoyama, M. Three-layered organic solar cell with a photoactive interlayer of codeposited pigments. *Appl*. *Phys*. *Lett*. **1991**, *58*, 1062–1064.
6. Hiramoto, M.; Fujiwara, H.; Yokoyama, M. p-i-n like behavior in three-layered organic solar cells having a co-deposited interlayer of pigments. *J*. *Appl*. *Phys*. **1992**, *72*, 3781–3787.
7. Yu, G.; Gao, J.; Hummelen, J.C.; Wudl, F.; Heeger, A.J. Polymer photovoltaic cells: Enhanced efficiencies via a network if internal donor-acceptor heterojunctions. *Science* **1995**, *270*, 1789–1791.
8. Note: Precisely, since the exciton, *i.e*., the bound electron-hole pair, resembles the hydrogen atom, quantized description is needed. Rydberg levels based on the Bohr's model of hydrogen atom can be expressed by the following equation; $E = E_G - G/n^2$ ($n$ = 1, 2, …). ($E_G$: Ionization energy of the molecule in the solid. $G$: The exciton binding energy.) The exciton binding energy ($G$) is proportional to $\mu/m\varepsilon$. ($\mu$: Reduced mass of exciton. $m$: Mass of electron. $\varepsilon$: Relative permittivity.) Thus, the exciton binding energy becomes large in the organic semiconductor having small value of $\varepsilon$.
9. Note: Exciton radius can be calculated based on the equation expressing the Bohr radius ($r$) including the relative permittivity ($\varepsilon$) and the reduced mass ($m^*$) between the effective mass of an electron ($m_n^*$) and a hole ($m_p^*$), *i.e*., $r = \varepsilon_0\varepsilon h^2/\pi m^* e^2$. Values of $m^*$ are 0.14 and 0.94 for Si and $C_{60}$, respectively.
10. Peumans, P.; Yakimov, A.; Forrest, S.R. Small molecular weight organic thin-film photodetectors and solar cells. *J*. *Appl*. *Phys*. **2003**, *93*, 3693–3723.
11. Hiramoto, M.; Yamaga, T.; Danno, M.; Suemori, K.; Matsumura, Y.; Yokoyama, M. Design of nanostructure for photoelectric conversion using an organic vertical superlattice. *Appl*. *Phys*. *Lett*. **2006**, *88*, 213105.
12. Kaji, T.; Zhang, M.; Nakao, S.; Iketaki, K.; Yokoyama, K.; Tang, C.W.; Hiramoto, M. Co-evaporant induced crystalline donor:acceptor blends in organic solar cells. *Adv*. *Mat*. **2011**, *23*, 3320–3325.
13. Matsuo, Y.; Sato, Y.; Niinomi, T.; Soga, I.; Tanaka, H.; Nakamura, E. Columnar structure in bulk heterojunction in solution-processable three-layered *p-i-n* organic photovoltaic devices using tetrabenzoporphyrin precursor and silylmethyl[60]fullerene. *J*. *Am*. *Chem*. *Soc*. **2009**, *131*, 16048–16050.
14. Wagner, H.J.; Loutfy R.O.; Hsiao, C. Purification and characterization of phthalocyanines. *J*. *Mater*. *Sci*. **1982**, *17*, 2781–2791.

15. Laudise, R.A.; Kloc, Ch.; Simpkins, P.G.; Siegrist, T. Physical vapor growth of organic semiconductors. *J. Cryst. Growth* **1998**, *187*, 449–454.
16. Suemori, K.; Miyata, T.; Yokoyama, M.; Hiramoto, M. Organic solar cells protected by very thick naphthalene tetracarboxylic anhydride films. *Appl. Phys. Lett.* **2004**, *85*, 6269–6271.
17. Surmori, K.; Yokoyama, M.; Hiramoto, M. Electrical shorting of organic photovoltaic films resulting from metal migration. *J. Appl. Phys.* **2006**, *99*, 036109.
18. Suemori, K.; Miyata, T.; Yokoyama, M.; Hiramoto, M.; Three-layered organic solar cells incorporating nanostructure-optimized Phthalocyanine:Fullerene codeposited interlayer. *Appl. Phys. Lett.* **2005**, *86*, 063509.
19. Sakai, K.; Hiramoto, M. Efficient organic p-i-n solar cells having very thick codeposited i-layer consisting of highly purified organic semiconductors. *Mol. Cryst. Liq. Cryst.* **2008**, *491*, 284–289.
20. Hiramoto, M. Efficient organic p-i-n solar cells having very thick codeposited i-layer composed of highly purified organic semiconductors. *Proc. SPIE* **2008**, *7052*, doi:10.1117/12.798120.
21. Note: Thick NTCDA protection against electrical shorting is no longer needed since the *i*-layer has sufficient thickness. So, we could replace NTCDA (600 nm) with $C_{60}$ (80 nm)/bathocuproine (BCP; 15 nm) or $C_{60}$ (80 nm)/NTCDA (80 nm)/bathocuproine (BCP; 15 nm) and obtain similar results. For the latter case, cell parameters are $J_{sc}$: 17.5 $mAcm^{-2}$, $V_{oc}$: 0.44 V, FF: 0.57, efficiency: 5.3% (81.8 $mWcm^{-2}$).
22. Brenninghoven, A.; Rundenauer, F.G.; Werner, H.W. *Secondary Ion Mass Spectrometry*; John Wiley & Sons: New York, NY, USA, 1987.
23. Note: Purity of 7N was also confirmed by temperature programmed desorption mass spectroscopy.
24. Tanaka, Y.; Kanai, K.; Ouchi, Y.; Seki, K. Oxygen effect on the interfacial electronic structure of $C_{60}$ film studied by ultraviolet photoelectron spectroscopy. *Chem. Phys. Lett.* **2007**, *441*, 63–67.
25. Martin, M.; Andre, J.-J.; Simon, J. Influence of dioxygen on the junction properties of metallophthalocyanine based devices. *J. Appl. Phys.* **1983**, *54*, 2792–2794.
26. Tada, H.; Touda, H.; Takada, M.; Matsushige, K. Quasi-intrinsic semiconducting state of titanyl-phthalocyanine films obtained under ultrahigh vacuum conditions. *Appl. Phys. Lett.* **2000**, *76*, 873–875.
27. Akamatsu, H.; Inokuchi, H.; Matsunaga, Y. Electrical conductivity of the perylene-bromine complex. *Nature* **1954**, *173*, 168–169.
28. Hiramoto, M.; Ihara, K.; Fukusumi, H.; Yokoyama, M. Conduction type control from *n*- to *p*-type for organic pigment film purified by reactive sublimation. *J. Appl. Phys.* **1995**, *78*, 7153–7157.
29. Hiramoto, M.; Ihara, K.; Yokoyama, M. Fermi level shift in photoconductive organic pigment films measured by Kelvin vibrating capacitor method. *Jpn. J. Appl. Phys.* **1995**, *34*, 3803–3807.
30. Huang, J.S.; Pfeiffer, M.; Werner, A.; Blochwitz, J., Leo, K.; Liu, S.Y. Low-voltage organic electroluminescent devices using pin structures. *Appl. Phys. Lett.* **2002**, *80*, 139–141.
31. Blochwitz, J.; Pfeiffer, M.; Fritz, T.; Leo, K. Low voltage organic light emitting diodes featuring doped phthalocyanine as hole transport material. *Appl. Phys. Lett.* **1998**, *73*, 729–731.

32. Tokito, S.; Noda, K.; Taga, Y. Metal oxides as a hole-injecting layer for an organic electroluminescent device. *J. Phys. D* **1996**, *29*, 2750–2753.
33. Matsushima, T.; Kinoshita, Y.; Murata, H. Formation of Ohmic hole injection by inserting an ultrathin layer of molybdenum trioxide between indium tin oxide and organic hole-transporting layers. *Appl. Phys. Lett.* **2007**, *91*, 253504:1–253504:3.
34. Harada, K.; Werner, A.G.; Pfeiffer, M.; Bloom, C.J.; Elliott, C.M.; Leo, K. Organic homojunction diodes with a high built-in potential: interpretation of the current-voltage characteristics by a generalized einstein relation. *Phys. Rev. Lett.* **2005**, *94*, 036601:1–036601:4.
35. Chan, C.K.; Zhao, W.; Barlow, S.; Marder, S.; Kahn, A. Decamethylcobaltocene as an efficient *n*-dopant in organic electronic materials and devices. *Org. Electron.* **2008**, *9*, 575–581.
36. Harada, K.; Riede, M.; Leo, K. Pentacene homojunctions: Electron and hole transport properties and related photovoltaic responses. *Phys. Rev. B* **2008**, *77*, 195212:1–195212:9.
37. Liao, H.-H.; Chen, L.-M.; Xu, Z.; Li, G.; Yang, Y. Highly efficient inverted polymer solar cell by low temperature annealing of $Cs_2CO_3$ interlayer. *Appl. Phys. Lett.* **2008**, *92*, 173303.
38. Hamwi, S.; Riedl, T.; Kowalsky, W. An organic *p-i-n* homojunction as ultra violet light emitting diode and visible-blind photodiode in one. *Appl. Phys. Lett.* **2011**, *99*, 053301:1–053301:3.
39. Chan, C.K.; Amy, F.; Zhang, Q.; Barlow, S.; Marder, S.; Kahn, A. N-type doping of an electron-transport material by controlled gas-phase incorporation of cobaltocene. *Chem. Phys. Lett.* **2006**, *431*, 67–71.
40. Walzer, K.; Maennig, B.; Pfeiffer, M.; Leo, K. Highly efficient organic devices based on electrically doped transport layers. *Chem. Rev.* **2007**, *107*, 1233–1271.
41. Falkenberg, C.; Uhrich, C.; Olthof, S.; Maennig, B.; Riede, M.; Leo, K. Efficient *p-i-n* type organic solar cells incorporating 1,4,5,8-naphthalenetetracarboxylic dianhydride as transparent electron transport material. *J. Appl. Phys.* **2008**, *104*, 034506:1–034506:6.
42. Yoshida, H. Low-energy inverse photoemission spectroscopy using a high-resolution grating spectrometer in the near ultraviolet range. *Rev. Sci. Instrum.* **2013**, *84*, 103901:1–103901:5.
43. Kubo, M.; Iketaki, K.; Kaji, T.; Hiramoto, M. Conduction type control of fullerene films from *n*- to *p*-type by molybdenum oxide doping. *Appl. Phys. Lett.* **2011**, *98*, 073311:1–073311:3.
44. Kubo, M.; Kaji, T.; Hiramoto, M. *pn*-homojunction formation in single fullerene films. *AIP Adv.* **2011**, *1*, 032177:1–032177:5.
45. Ishiyama, N.; Ishiyama, K.; Kubo, M.; Kaji, T.; Hiramoto, M. Tandem photovoltaic cells formed in single fullerene films by impurity doping. *Appl. Phys. Lett.* **2012**, *101*, 233303:1–233303:3.
46. Shinmura, Y.; Kubo, M.; Ishiyama, N.; Kaji, T.; Hiramoto, M. *pn*-control and *pn*-homojunction formation of metal-free phthalocyanine by doping. *AIP Adv.* **2012**, *2*, 032145:1–032145:6.
47. Hamwi, S.; Meyer, J.; Winkler, T.; Riedl, T.; Kowalsky, W. *p*-type doping efficiency of $MoO_3$ in organic hole transport materials. *Appl. Phys. Lett.* **2009**, *94*, 253307:1–253307:3.
48. Ishiyama, N.; Kubo, M.; Kaji, T.; Hiramoto, M. Doping-based control of the energetic structure of photovoltaic co-deposited films. *Appl. Phys. Lett.* **2011**, *99*, 133301:1–133301:3.
49. Note: Hole concentration created by $MoO_3$-doping (5000 ppm) was cross-checked by capacitance-voltage measurements. Obtained value of $5 \times 10^{17}$ $cm^{-3}$ was consistent with that measured by Kelvin method ($9.6 \times 10^{17}$ $cm^{-3}$).

50. Hebard, A.F.; Hadon, R.C.; Fleming, R.M.; Kortan, A.R. Deposition and characterization of fullerene films. *Appl*. *Phys*. *Lett*. **1991**, *59*, 2109–2111.
51. Note: There is no evidence of $Cs_2CO_3$ dissociation during vacuum evaporation, since a single $Cs_2CO_3$ film is completely transparent.
52. Note: The radius of an electron orbital around a positively ionized donor can be calculated based on the equation expressing the Bohr radius (r) including the relative permittivity (ε) and the effective mass of an electron ($m_n$*), *i.e*., $r = \varepsilon_0 \varepsilon h^2/\pi m_n^* e^2$.
53. Kröger, M.; Hamwi, S.; Meyer, J.; Riedl, T.; Kowalsky, W.; Kahn, A. P-type doping of organic wide band gap materials by transition metal oxides: A case-study on Molybdenum trioxide. *Org*. *Electron*. **2009**, *10*, 932–938.
54. deMello, J.C.; Tessler, N.; Graham, S.C.; Friend, R.H. Ionic space-charge effects in polymer light-emitting diodes. *Phys*. *Rev*. *B* **1998**, *57*, 12951–12963.
55. Hiramoto, M.; Tomioka, A.; Suemori, K.; Yokoyama, M. Formation of ohmic contacts to perylene molecular crystals. *Appl*. *Phys*. *Lett*. **2004**, *85*, 1852–1854.
56. Kubo, M.; Shinmura, Y.; Ishiyama, N.; Kaji, T.; Hiramoto, M. Invertible organic photovoltaic cells with heavily-doped organic/metal ohmic contacts. *Appl*. *Phys*. *Expr*. **2012**, *5*, 092302:1–092302:3.
57. Note: The inverse photovoltaic effect in Figure 22(d)(blue curve) can be attributed to the *p*-type Schottky junction formation at Ag/$H_2$Pc interface. Absence of $C_{60}$ sensitivity of action spectrum of $J_{sc}$ of inverse photocurrent showed that the inverse photocurrent was generated near $H_2$Pc/Ag electrode.
58. Kubo, M.; Kaji, T.; Hiramoto, M. *pn*-homojunction organic solar cells formed in the thick phase-separated co-deposited films by doping. *Appl*. *Phys*. *Lett*. **2013**, *103*, 263303:1–263303:4.
59. Kubo, M.; Shinmura, Y.; Ishiyama, N.; Kaji, T.; Hiramoto, M. Junction formation by doping in $H_2$Pc:$C_{60}$ co-evaporated films for solar cell application. *Mol*. *Cryst*. *Liq*. *Cryst*. **2013**, *581*, 13–17.
60. Ishiyama, N.; Kubo, M.; Kaji, T.; Hiramoto, M. Tandem organic solar cells formed in co-deposited films by doping. *Org*. *Electron*. **2013**, *14*, 1793–1796.
61. Hiramoto, M.; Suezaki, M.; Yokoyama, M. Effect of thin gold interstitial-layer on the photovoltaic properties of tandem organic solar cell. *Chem*. *Lett*. **1990**, 327–330.
62. Yuan, Y.; Huang, J.; Li, G. Intermediate layers in tandem organic solar cells. *Green* **2011**, *1*, 65–80.

# Chapter 12

# Electron and Hole Transport Layers: Their Use in Inverted Bulk Heterojunction Polymer Solar Cells

**Sandro Lattante**

**Abstract:** Bulk heterojunction polymer solar cells (BHJ PSCs) are very promising organic-based devices for low-cost solar energy conversion, compatible with roll-to-roll or general printing methods for mass production. Nevertheless, to date, many issues should still be addressed, one of these being the poor stability in ambient conditions. One elegant way to overcome such an issue is the so-called "inverted" BHJ PSC, a device geometry in which the charge collection is reverted in comparison with the standard geometry device, *i.e.*, the electrons are collected by the bottom electrode and the holes by the top electrode (in contact with air). This reverted geometry allows one to use a high work function top metal electrode, like silver or gold (thus avoiding its fast oxidation and degradation), and eliminates the need of a polymeric hole transport layer, typically of an acidic nature, on top of the transparent metal oxide bottom electrode. Moreover, this geometry is fully compatible with standard roll-to-roll manufacturing in air and is less demanding for a good post-production encapsulation process. To date, the external power conversion efficiencies of the inverted devices are generally comparable to their standard analogues, once both the electron transport layer and the hole transport layer are fully optimized for the particular device. Here, the most recent results on this particular optimization process will be reviewed, and a general outlook regarding the inverted BHJ PSC will be depicted.

Reprinted from *Electronics*. Cite as: Lattante, S. Electron and Hole Transport Layers: Their Use in Inverted Bulk Heterojunction Polymer Solar Cells. *Electronics* **2014**, *3*, 132–164.

## 1. Introduction

In 1977, Shirakawa, Louis, MacDiarmid, Chiang and Heeger reported on their discovery of electrically conductive polymers [1] (for which, in 2000, the Nobel Prize in Chemistry was awarded jointly to Heeger, MacDiarmid and Shirakawa). From that milestone, a great deal of research activity on conjugated polymer-based optoelectronics has been developed all over the world. To date, organic-based light-emitting diodes (OLED) have become commercially available with good performance, and polymer-based photovoltaics has reached high efficiency: over 9% in lab-scale devices [2,3]. The exploiting of the peculiar properties of conjugated polymers in the photovoltaic (PV) field is more recent than in light emitting devices, and still, a lot of unsolved questions must be addressed in order to really develop a commercial route for polymer PV [4]. Followingthe ideas and the experimental results in the pioneering works on small organic molecule-based photovoltaics [5], in 1993, Sariciftci reported on the evidence of a conjugated polymer/fullerene

heterojunction bilayer solar cell [6,7]. Soon after that, the first polymeric *bulk*heterojunction (BHJ) PV device was described by Yu *et al*. [8]. In 1995, the new soluble fullerene derivatives [9] allowed the boosting of device performances [10]. Starting from those first works, a lot of efforts have been made in order to increase the device power conversion efficiency (PCE) and stability, mainly working on synthesizing new polymers to be used in the active layer and on optimizing the device structure and geometry. The most commonly used device structure for a BHJ organic solar cell comprises a conductive transparent substrate—typically metal oxides, like indium tin oxide (ITO) or fluorine-doped tin oxide (FTO) on glass or plastic substrates—covered by a thin hole conducting layer, such as the polymer, poly(3,4-ethylenedioxythiophene)-poly(styrenesulfonate) (PEDOT:PSS), over which, the active layer is deposited, typically from a solution by means of spin coating, doctor blading, ink-jet printing, spray coating, *etc*. [11–14]. Finally, a thin metal layer is realized (Al, Ca/Al, LiF/Al, for instance), usually by thermal evaporation. This structure has been used in the realization of devices with very good performance, reaching a PCE of around 9% [3]. Despite these good efficiency reports, which, anyway, are far from being general and reproducible [4], such a structure suffers from several drawbacks: due to the required energy level alignment among all the cell components, a low work function metal electrode must be used on top of the device for the electron extraction, like Al. However, low work function metals undergo very fast oxidation when exposed to air, losing their conductivity, suddenly turning a working device into a faulty one. Moreover, the PEDOT:PSS is acidic in nature and is thus detrimental to the underlying metal oxide layer, which undergoes fast degradation [15,16]. Finally, it has been widely reported that polymer/fullerene (as well as polymer/polymer blends [17]) are characterized by a stratified composition (vertical phase separation) during the film formation [18], with the fullerene phase—that is, the electron-conducting phase—mainly concentrated at the bottom of the film and the polymer phase—the hole-conducting one—concentrated mainly at the top of the film. Thus, the film vertical phase structure is opposite to the ideal one, where the electron-conducting phase must face the top low-work function electrode and the hole-conductive phase must face the bottom high work function electrode. All these problems can be avoided by reversing the collection process, *i.e.*, collecting the holes by the top electrode and the electrons by the bottom electrode. In such a structure, the top metal electrode would be a high work function electrode, like silver or gold (Ag or Au), thus eliminating the oxidation problem, while the bottom electrode should be a transparent electron conducting layer (oxides, like zinc oxides (ZnO) or titanium oxide ($TiO_x$) are good examples), eliminating the problem of the acidic PEDOT:PSS on ITO or FTO.

This inverted structure was first exploited in the fabrication of organic light emitting diodes, also initially referred to as an “upside-down” structure [19]; then, it started to be exploited also in the PV field [20,21].

After these pioneering works, it has been demonstrated that the inverted structure allows one to reach performances even better than the standard one [22,23]. Despite this, the research on inverted polymer solar cells (PSCs) is a very small fraction of the total research in the PSC field. As of 14 November 2013, a simple search on the ISI Web of Knowledge using as key words “bulk heterojunction solar cell” (excluding the word “inverted”) gives about 7400 papers, while when the

key words “inverted” AND “bulk heterojunction solar cell” are used, only 207 results are shown, that is less than 3% of the published papers. The situation does not change much if the search string is not limited to bulk heterojunction, but to the more generic “polymer solar cell” (24,700 results) to be compared with the very small number of 514 results when searching for “inverted” AND “polymer solar cell” (less than 2% of the published papers on polymer solar cell), nor would a great variation of this ratio come out if the search were limited to the last two years. This was already pointed out by Krebs and coworkers very recently [4] (they estimated that less than 10% of published results were focused on the inverted structure). This is quite surprising, since the polymeric bulk heterojunction inverted solar cell (BHJ ISC) has by far better stability over time than the standard geometry devices [24].

Among these relative few papers, the review articles are very limited. The most recent and complete, by Zhang *et al*., published in 2011 [25], however, reviews general inverted organic devices, not focusing particularly on the polymer bulk heterojunction concept; while in the one by Hau *et al*. [24], published in 2010, there is no general focus on the electrode interfaces.

The aim of this review is to present a comprehensive description of the most recent results on the improvement in the performances of hole transport layers (HTLs) and electron transport layers (ETLs) used in BHJ ISC in order to tentatively give a strong baseline for further research directions and improvements. On the contrary, this paper will not consider: (1) small molecule-based devices; (2) bi-layered active materials or multi-layered active material devices; and (3) tandem devices; for all of which, there is an excellent scientific literature.

The paper will be structured as follows: first, a very brief and general overview of the working principles of the bulk heterojunction solar cell is given; then, a comparison between the standard geometry device and the inverted one is sketched, highlighting the pros and cons of both, following a detailed review of the various materials and strategies for optimizing the hole transport layer (HTL) and the electron transport layer (ETL); finally, a summary of the major findings is given.

## 2. The Bulk Heterojunction Solar Cell: Working Principles

The working principle of a polymer BHJ solar cell (see Figure 1) could barely be summarized as the creation of an exciton in the active layer, due to light absorption, and the separation of this exciton into two separate charge carriers at the interfaces between the species that constitute the active layer (typically, a binary blend of a polymer and a fullerene or two polymers, which act as the donor phase and the acceptor phase), with subsequent collection by the electrodes [26]. Despite their apparent simplicity, all of these steps must obey very strict limitations in order to be as efficient as one would need. First of all, the generated excitons must hop between the molecules reaching an interface between the two phases before recombining (radiatively or non-radiatively). This means that the two phases should be mixed in an optimal structure, with phase domains usually in the order of 10–30 nm (the average exciton diffusion length in polymers [26]). Then, the position of the energy levels at the interface must be favorable for a fast exciton dissociation followed by charge separation (*i.e.*, the electron in the acceptor phase and the hole in the donor phase without successive recombination [26]). After that, the charges must travel inside the respective phases, reaching the

collecting electrodes again without a charge recombination: at this point, the energetic level structure at the electrode interfaces plays a fundamental role, ideally the interface being an ohmic contact [26].

**Figure 1.** Schematic basic working principle of a polymeric bulk heterojunction solar cell.

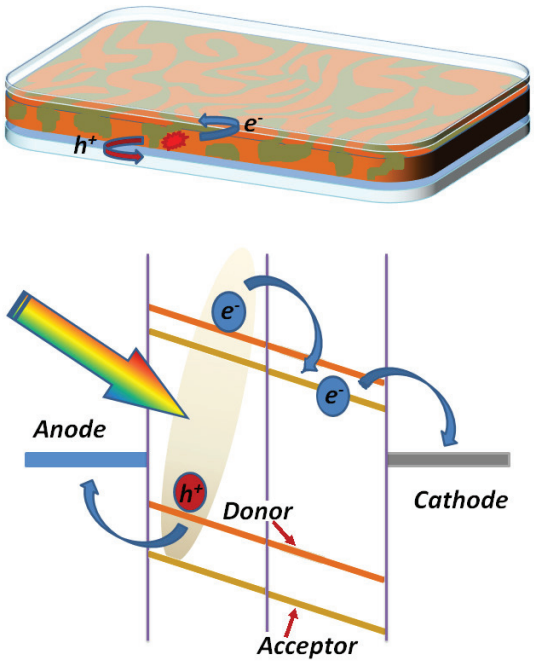


The standard geometry device is sketched in the upper part of Figure 2; as already mentioned in the Introduction, it typically consists of a transparent bottom electrode for the hole collection, a thin layer of active material and a top metal electrode for the electron collection. In the inverted structure (bottom of Figure 2), the role of the electrodes is swapped; thus, the electrons are collected by the bottom transparent electrode and the holes by the top metal electrode. This reversed collection implies that the work function of the top electrode must be high enough in order to match the donor highest occupied molecular orbital (HOMO) energy level, and the work function of the bottom electrode must be low enough in order to match the acceptor lowest unoccupied molecular orbital (LUMO) energy level. If the requirement of the top metal electrode can be simply fulfilled by selecting high work function metals, like gold or silver, the right selection of the bottom electrode is more tricky. In fact, the most used transparent metal oxides, like ITO or FTO, possess high work functions that do not match well with the LUMO level of the acceptors. The matching of the energy levels is obtained by modifying the bottom electrode with the deposition of a thin layer of suitable electron conducting (hole blocking) materials, like, for instance, ZnO or $TiO_x$, which are, moreover, transparent to visible light. The effects of this electrode capsizing are multiple, and the working properties of the devices are strongly influenced, as will be described in the following sections.

**Figure 2.** Schematic geometry for (**top**) a standard bulk heterojunction (BHJ) device and (**bottom**) an inverted BHJ device. The main component layers are sketched. ETL, electron transport layer; HTL, hole transport layer.

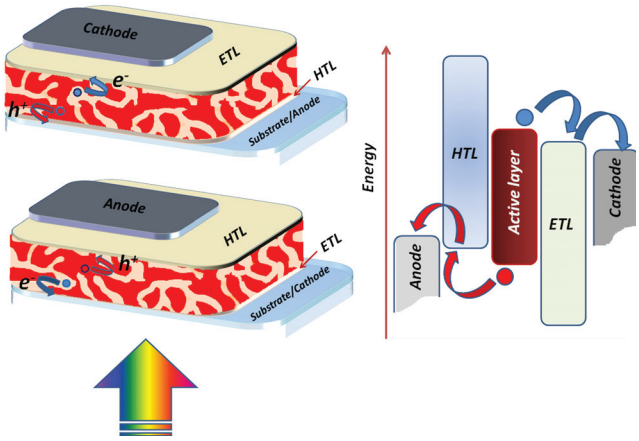


*2.1. Light Absorption and Electromagnetic Field Distribution: Comparison between Standard and Inverted Structure*

The processes of exciton diffusion, exciton dissociation and charge separation, as well as charge recombination in the bulk active layer depend on the active layer properties and are thus expected to be the same for both of the structures. On the contrary, standard and inverted structures present strong differences in the electromagnetic field distribution inside the device.

The main criterion that should be fulfilled in every PV device is that the solar light should be well absorbed by the active layer (that means that, ideally, the main part of the solar spectrum reaching the Earth's surface should be harvested). This is not a well-solved issue yet in organic PV, since each polymer absorbs a narrow range of visible light, and typically, the ones used in BHJ solar cells have no or low absorption in the low energy side of the solar spectrum. Since the open circuit voltage ($V_{oc}$) of a BHJ PSC is believed to be determined mainly by the donor HOMO-acceptor LUMO energy gap [26], the exploitation of low band-gap donors typically decreases the $V_{oc}$, and a trade-off must be reached between good light harvesting and good electrical parameters. Although this is a problem that affects both the standard geometry and the inverted one, it has been demonstrated that the inverted configuration better harvests the incoming light, due to a more favorable electromagnetic field distribution inside the active layer. In fact, Ameri *et al.* [22] considered a poly-3-hexyl thiophene (P3HT):phenyl-C61-butyric acid methyl ester (PCBM) standard geometry solar cell and an inverted analogue; they found that the inverted device performed about 15% better than the standard one. In order to understand the reasons underlying the better performance, they optically modeled the devices. They found that in the inverted structure, the number of absorbed photons by the active layer was increased, thus resulting in an increased number of charge carriers, thanks to the use of a $TiO_x$ bottom layer, which is transparent to visible light, instead of a PEDOT:PSS layer, which absorbs about 20% of the incoming light. With these observations, they were able to explain roughly a 10% increase in performance. The remaining 5% boost was instead ascribed to an unbalanced electron

and hole mobilities that lead to a more efficient charge collection in the inverted structure than in the standard one. Indeed, assuming an exponential absorption profile, the charge carriers are generated mainly closer to the bottom electrode rather than to the top metal electrode; thus in the presence of unbalanced mobilities with the hole mobility lower than the electron one, a better charge collection is expected in the inverted configuration. What was still missing in the discussion was the findings that the P3HT:PCBM blend undergoes a vertical phase separation during the process of film formation, resulting in a stratified structure in which a PCBM-rich layer is formed on the bottom of the film and a P3HT-rich layer is formed on the top [18] (see Figure 3). As the electrons mainly travel inside the PCBM phase and the holes mainly travel inside the P3HT phase towards the respective electrodes, the inverted configuration is the best one, being characterized by a self-assembled ETL (hole blocking) at the electron extraction electrode (bottom) and a HTL (electron-blocking) at the hole extraction electrode (top), thus both increasing the charge extraction efficiency and reducing the bimolecular recombination at the electrodes.

**Figure 3.** Vertical phase separation in a BHJ polymer solar cell (PSC). Reprinted with permission from [18]. PCBM, phenyl-C61-butyric acid methyl ester; PEDOT:PSS, poly(3,4-ethylenedioxythiophene)-poly(styrenesulfonate).

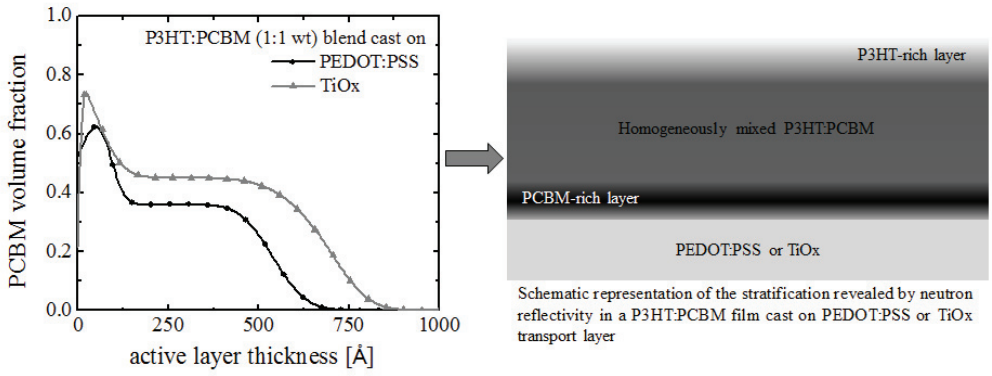


These findings were partially confirmed by Chen *et al.* [27], who modeled a P3HT:PCBM-based inverted device both optically and electrically. They concluded that if one considers only the optical aspects of the structure (*i.e.*, the field distribution inside the active layer), the inverted structure should be better performing than the standard one for the major part of the considered active layer thicknesses. The standard device should, on the contrary, perform better when the active layer thickness is just the ideal one for constructive interference inside the film between the incoming radiation and the reflected one from the top metal electrode. Concerning the electrical aspects, the electrical behavior of the device was modeled as a function of the charge drift length, L, a parameter that accounts for the charge lifetime and mobility, being defined as the maximum length that a charge carrier can drift within its lifetime before any possible recombination. The value of L influences the electromagnetic field distribution and the optical modulation inside the active layer for each thickness. They showed that the inverted structure is better than the standard one, only if the active layer thickness is comparable with L, while the standard geometry performs better if the active layer

thickness is greater than L. This is due to the fact that L induces an "effective area" inside the active layer where the absorbed photons are efficiently transformed into charge carriers, while photons absorbed outside this area are mainly lost, not contributing to the photocurrent. Since the position of this effective area depends on the different charge transport properties peculiar to the active material, the optical field modulation inside the device together with the position of the effective area determine the performance differences between standard and inverted geometry.

This prediction, however, was slightly in contrast with the results of Aziz, Li and coworkers [28], who showed a remarkable difference between standard and inverted devices, especially when analyzing the short circuit current density, $J_{sc}$. In both devices, the $J_{sc}$ increased with increasing the thickness of the active layer, but in their case, the $J_{sc}$ in the standard device started to decrease for an active layer thicker than 300 nm, while the $J_{sc}$ in the inverted one remained constant. They explained their results with a reduced recombination mechanism in the inverted structure (coherently with the conclusions of Ameri *et al.* [22]) and a reduction of the series resistance in the inverted device. This apparent contrast could be, however, explained with the differences in the device structure considering the nature, properties and thicknesses of all the constituent layers, which strongly influence the optical and electrical properties [27].

Even if those reports were based on a P3HT:PCBM active layer, many other research groups reported improved performances of the inverted structure compared to the standard analogue when other active materials were used. For instance, Ma *et al.* reported a boost in performances for an inverted device based on a blend of PBDT-12/PyT2 [23].

Overall, from both the optical and electrical analyses given by those reports, it appears clear that the inverted structure has many advantages with respect to the standard one, at least when thin layers are used, which is actually the standard in realizing organic-based optoelectronic devices. Given the general behavior of the devices, in the next sections, a description of the most recent results for the electrode interfaces is given.

## 3. ETLs and HTLs: Recent Developments

In both the standard and inverted devices, the active material plays the same role, that is, in short, to absorb photons and to convert them into free charge carriers (the influence of optical and electrical parameters on this process has been briefly sketched in the previous section). In order to achieve good performances, however, it is mandatory that a BHJ comprises both an HTL and an ETL.

A list of requirements that a good ETL, as well as a good HTL should fulfill (among which are transparency, good electrical properties and chemical stability) is given in a recent review on the synthesis methods of metal oxides by Litzov and Brabec [29]; although that review focuses on metal oxides only, the general list applies to every material to be used as the electron or hole-transport layer in a BHJ ISC. Here, a summary on the most recent results about different class of materials for the realization of the various ETLs and HTLs in BHJ ISCs is given.

*3.1. Bottom Electrode: Electron Collection*

The main requirements for the bottom electrode are a good electron transport property and, when the light is collected through it, transparency to the solar radiation. This limits the choice to a few materials, among which are the well-known and widely-used ZnO and $TiO_x$ [29] (which have also a good electronic level matching with the LUMOs of most of the polymers used in PV), other less used materials, like $Cs_2CO_3$ [30], and new polymeric materials, like poly(2-(dimethylamino)ethyl methacrylate) (PDMAEMA) [31] and PFEN-Hg [32]. The various realization methods of transparent metal oxides have been described in great detail in a very recent review [29]. In the present work, the attention will be focused on the effects of the ETL and HTL layer properties on the device performances.

3.1.1. ZnO

Very thin layers of ZnO are easily realized by means of several deposition techniques, like sol-gel [33], spray-coating [34] and nanoparticle (NP) deposition [35]. Most of the time, the as-deposited film needs a process of annealing usually at high temperatures in order to optimize the crystalline structure [36], but also, low annealing temperature processes have been recently reported [35,37,38].

Considering the P3HT:PCBM-based devices just as a prototypical PV system, the overall reported power conversion efficiency using ZnO as the ETL spans from about 2% to about 4% [29,35,39]. This quite wide range is due to the differences in several factors, including the chosen HTL, the parameters involved in the active blend preparation and optimization and the properties of the ZnO ETL layer. In this section, the attention will be focused on the possible influences of the ETL layer on the device performances with various active layers.

One of the most important parameters that determines the overall performances of the device is the morphology (and consequently, the roughness) of the ZnO layer. Despite the several methods developed to deposit a thin ZnO layer on substrates, there is no "elective" method to obtain the optimal morphology; each method can afford the best results, once all the deposition parameters have been optimized. Yu *et al*. [40] showed that the power conversion efficiency of a P3HT:PCBM-based ISC was increased from 2.08% to 2.88% by increasing the surface roughness of the ZnO layer. Since the ZnO film realized by the sol-gel technique is affected by three processes during the annealing [41] (solvent evaporation, zinc acetate decomposition and crystallization), they changed the surface roughness of the layer by simply varying the annealing rate of the as-deposited (by sol-gel) ZnO layer, namely a slow annealing rate of 9 °C/min and a fast one of 56 °C/min up to 300 °C. They found both an increase in $J_{sc}$ and in FF for the slowly annealed sample. The boost in the $J_{sc}$ was explained by the enhanced light absorption, due to the rougher ZnO surface, which should provide an efficient light trapping mechanism: once being scattered by the ZnO layer, the light is reflected back by the upper Ag electrode in multiple directions, thus increasing the path length inside the active layer. The higher FF was explained considering the better crystallization of the ZnO, due to the slow annealing rate, which resulted in a more effective electron extraction and hole blocking (it is known

that FF is strongly related to the charge extraction efficiency at the interfaces [42]). Dhibi *et al.* [43] reported the same conclusions in a PCDTBT:PC70BM-based ISC: the absorption of the blend cast onto the ITO/ZnO (sol-gel) substrate was higher than that of the one cast onto the bare ITO substrate. This effect was ascribed both to the light scattering mechanism, as well as to the larger surface area between the ZnO and the active blend. However, they noted that a too pronounced roughness of the sol-gel-derived ZnO films could be, on the other hand, detrimental to the overall device performance when a very thin active layer is needed (that is the case of the PCDTBT:PC70BM blend), due to the rising-up of a high contact resistance and a large leakage current [44]. Moreover, they demonstrated that also the annealing temperature is a key factor in order to determine the morphology of the layer: they annealed the ZnO films at three different temperatures, namely 130 °C, 150 °C and 200 °C, and characterized them by photoluminescence and Raman measurements, showing that the 150 °C annealed film was affected by better crystallization, which could enhance the electron extraction and mobility, as well as suppress the leakage current into the device. Vijila and coworkers [45] showed that the annealing temperature greatly affects the overall crystalline morphology of the ZnO layer. They demonstrated that a ZnO film annealed at 240 °C was characterized by a higher crystallinity compared to a similar layer, but annealed at 160 °C. The device incorporating the 240 °C annealed ZnO layer performed better (with a 40% higher PCE) than the device realized with the 160 °C annealed ZnO layer. They explained these results, observing that the ZnO layer annealed at 240 °C was characterized by a lower trap depth, thus reflecting in higher charge mobility and better ohmic contact and, consequently, higher $J_{sc}$ and $V_{oc}$.

These results indicate that both the annealing temperature and the annealing rate should be taken into account in order to optimize both the crystalline structure and the surface roughness of sol-gel-derived ZnO films, looking for a trade-off between increased light scattering by the surface roughness (thus enhancing the active layer absorption, and, hence, the $J_{sc}$, and increasing the FF, due to the higher interface contact and charge extraction efficiency) and the crystal structure (better charge transport).

A further interesting contribution on this topic is the work by Hu *et al.* [46], showing that the ZnO morphology can also depend on the layer thickness. They realized ZnO layers by the metal organic chemical vapor deposition (MOCVD) technique, finding that the ZnO layer thickness did not influence the energy level alignment at the interfaces, but it had a strong impact on the crystal structure and, hence, on the electrical properties. In particular, with the increase of the thickness, the morphology of the ZnO layer changed from a pure smooth sphere-like structure for a thickness of <100 nm to a rough pyramid-like structure starting from 100 nm and above. They indirectly confirmed the above picture of the need for a trade-off between roughness and crystal structure; in fact, they showed that initially, an increase of the ZnO layer thickness, and hence, of the surface roughness, was beneficial for ISC performances (with PCE increasing from 1.60% for 40 nm of ZnO to 2.93% for 80 nm ZnO), while the PCE started to decrease for the thicker ZnO layer (ISCs were based on the P3HT:PCBM active layer).

It is noteworthy that the above results are commonly characterized by the use of no annealing or a relative low post deposition annealing temperature in order to obtain a good overall film morphology.

This is quite different from the most commonly used high temperature post deposition annealing process; for example, Park *et al.* [47] used a temperature of 450 °C for annealing a sol-gel-derived ZnO layer to be used as the ETL in a P3HT:PCBM- and a P3HT:PCBM:polyoxyethylene tridecyl ether (PTE)-based device; they demonstrated by XRD that the so-annealed film showed two strong crystalline peaks at 30.3 °(100) and 34.3 °(002). .

Nanostructured ZnO layers also appear to be promising as efficient ETL in ISC. Simple ZnO nanoparticles (NPs) are easily deposited onto substrates by spin coating [35,48] or slot-die coating [49]: Alstrup *et al.* [49] realized layers of ZnO starting from an aluminum-doped ZnO NP ink using a roll-to-roll compatible method, the slot-die coating. Their results showed that a very efficient ISC can be realized using low-cost techniques that are feasible for large area device realization, once each layer deposition's parameter has been optimized. Regarding the ZnO layer, they also showed that the overall PCE of the final device is correlated with the thickness of the ZnO layer itself. Ibrahem *et al.* [35] prepared thin layers of ZnO NPs using a simple method that avoids the use of any surfactants in order to stabilize the ZnO particles in solutions, simply dispersing ZnO powder in pure ethylene glycol followed by high energy ball milling at room temperature in a batch-type grinder. They showed that the ZnO particle size decreased with the increasing of the grinding time down to an average particle diameter of 25 nm. The NPs, after grinding, were stable in solution without any precipitation, obtaining very uniform and thin films upon spin coating and final device PCEs over 3.5%. Our group realized all polymer ISC using a thin layer (about 80 nm) of ZnO on fluorine-doped tin oxide (FTO) by simply spin coating a commercial (Sigma Aldrich, St. Louis, MO, USA) aqueous dispersion of ZnO NPs with an average diameter less than 100 nm [50], without any post deposition annealing process. The layer morphology resulted in a very uniform sphere-like texture (see Figure 4) without any cracking or pinholes, with an average surface roughness of 4.53 nm. Thus, it is demonstrated that ZnO NP dispersion in water or common organic solvents can be a convenient and roll-to-roll compatible method for obtaining good ZnO ETLs for efficient inverted solar cells.

**Figure 4.** $1\ \mu\mathrm{m} \times 1\ \mu\mathrm{m}$ atomic force microscopy image of ZnO film on a fluorine-doped tin oxide (FTO) substrate by spin coating from a ZnO nanoparticle (NP) aqueous dispersion.

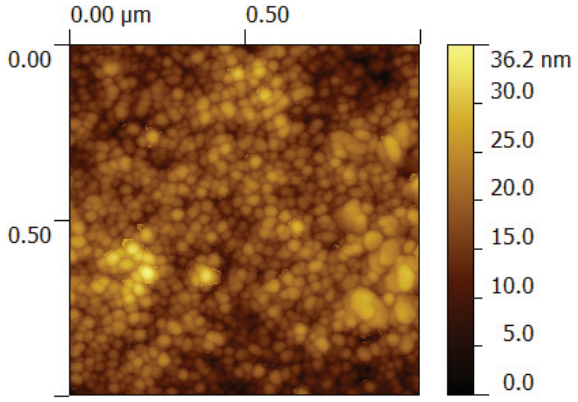

More complex structures have also been reported, like vertically aligned, one-dimensional nanostructures [51] and bi-dimensional nanowalls [52]. The latter, in particular, should theoretically perform better than one-dimensional structures, since it provides a higher contact surface between the ZnO and the active layer (Figure 5). Liang *et al.* [52], however, showed that when compared with ZnO nanorods, the NWs structure does not perform clearly better. They tried to explain their results, observing that the overall growth condition and, hence, the surface chemistry of the two structures are different, thus implying a possible different mechanism of charge recombination and charge transfer through the surface. Nevertheless, their report is quite recent, and there is no systematic optimization of the ZnO NW layer parameters, such as the thickness, etching process and interface modification, in order to improve and promote the diffusion of the active blend inside the nanostructures, thus leaving a large amount of room for future improvement. Electrospun ZnO nanowires (NWs) were incorporated by Vijila *et al.* [53] in a sol-gel-derived ZnO layer to be used as the ETL in ISCs. With the NW plantation, the overall device performance was increased compared to a control device without NW. This was due to a higher FF (both lower series resistance and higher shunt resistance), as well as a beneficial effect on the active layer phase separation morphology (which was reflected in a higher carrier lifetime and a reduced charge recombination).

A proper doping of the ZnO layer [54,55] is another possible route to improve the charge collection efficiency and to reduce the charge recombination, due to charge trapping by defects or oxygen ions [29]. Hu *et al.*, in the already cited work [46], reported an improved overall performance of an ISC when the intrinsic ZnO (i-ZnO) was doped with boron during the MOCVD process, in particular showing that the $J_{sc}$ increased up to 11.31 mA $\mathrm{cm}^{-2}$ when the diborane flow rate was kept at 3 sccm. They explained the results considering a better charge collection at the electrodes (the average resistivity of the ZnO layer decreased from $4.04 \times 10^5\ \Omega/\mathrm{sq}$ of the i-ZnO to $2.46 \times 10^3\ \Omega/\mathrm{sq}$ of the best boron-doped ZnO). Alstrup *et al.* [49] doped ZnO with Al in order to improve the conductivity and quality of the ZnO film deposited by the slot-die coating method. Lithium fluoride (LiF) has been used for a long time as an ultra-thin layer underlying the top Al electrode in standard configuration bulk heterojunction solar cells, since it improves device performances [56] and device stability [57]. Chang *et al.* [58], on the contrary, used it for doping a sol-gel-derived ZnO ETL to be used in ISCs based on a P3HT:PCBM active blend, demonstrating an improvement of the overall PCE of the device from 2.9% to 3.3%. Optimized LiF-doped ZnO showed a very high electron mobility up to 11.2 $\mathrm{cm}^2\mathrm{V}^{-1}\mathrm{s}^{-1}$. They concluded that Li atoms occupy interstitial sites, producing electrons, which results in higher electron mobility. At the same time, F atoms occupied in substitutional oxygen sites reduce the oxygen vacancies in the structure and lower the absorption in the visible region. Their conclusions are indeed supported by the fact that the better performance of the device is correlated with an increase in the $J_{sc}$, all the other cell parameters being almost unchanged.

**Figure 5.** SEM images of (**A**) the ZnO seed layer, (**B**) the as-grown dense ZnO rods, (**C**) the etched ZnO nanowalls and the (**D**) cross-section of the nanowalls. Reprinted with permission from [52].

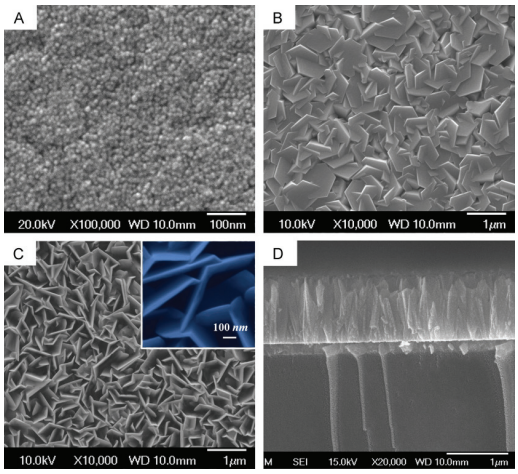


Finally, Du *et al.* [59] showed that UV irradiation of a sol-gel-derived ZnO layer used as the ETL in PBDTTT-C:$PC_{71}BM$-based ISC improved the device performance, due to the increase of the layer conductivity following the reduction of hole traps on ZnO. This is clearly reflected in the higher FF related to a decrease of the device series resistance. The drawback of UV irradiation consisted, however, in a gradual degradation of the polymeric active blend; so, they concluded that, practically, a trade-off between the early stage advantage of UV irradiation and long-term disadvantage due to polymer degradation should be considered in ISCs comprising a ZnO ETL.

Despite the several techniques and the different processes used to date for optimizing ZnO properties, it appears that the final device performance does not depend as much on the technique used for realizing the ZnO layer, but rather on the inner properties of the layer itself, such as the roughness and crystalline structure, both almost independent of the particular deposition method, once optimized.

### 3.1.2. $TiO_x$

Although porous crystalline $TiO_2$ is the standard charge transport layer used in the so-called dye-sensitized solar cell (Grätzel cell) [60], it is, on the contrary, not well suited as the ETL in BHJ ISCs, due to the difficult and tricky deposition of a uniform and homogeneous layer on standard ITO substrates [61,62]. Nevertheless, it has been used by Peng *et al.* [63] in ISCs, showing, in particular, that the overall power conversion efficiency of the device strongly depends on the $TiO_2$ crystalline structure. When the film is characterized by a well-defined morphology (the homogeneity of nanoparticle shapes and distribution) and a maximum crystal size of about 50 nm, the interface between the $TiO_2$ and the active material is characterized by an optimal morphology and interaction, thus favoring both exciton dissociation and charge separation, with improved FF (which means less charge recombination and improved charge transport through the inorganic layer).

However, amorphous $TiO_x$ ($x \leq 2$) is as good as crystalline $TiO_2$ as the ETL, once optimized [64]. Moreover, it is as good as ZnO as the ETL in ISCs, since it is characterized by high electron mobility and high transparency in the visible range [65]. Hadipour *et al.* [66] showed that it is possible to realize a $TiO_x$ ETL layer at room temperature from solution without any post deposition annealing process. They demonstrated that such a layer was as good as calcium in extracting electrons from a bulk heterojunction device, confirming that $TiO_x$ possesses the right energy level to act efficiently as the ETL in combination with several active blends. Finally, they demonstrated that the properties of the deposited $TiO_x$ remain the same when the deposition process occurs both in air and in a glove box, which is important for the possible implementation of their deposition process into roll-to-roll manufacturing.

Inverted devices that utilize amorphous or crystalline $TiO_x$ (usually deposited by the sol-gel method [29]) are characterized by the same range of efficiencies seen in the case of the ZnO [29,66,67].

The performances of devices incorporating an amorphous $TiO_x$ layer can be boosted with proper tuning of the layer's physical and chemical properties. Choulis and co-workers [68] demonstrated that the PCE of inverted devices can be improved once an ultra-thin layer of polyoxyethylene tridecyl ether (PTE) is inserted as the interlayer between the ITO substrate and the $TiO_x$ layer, a mechanism that apparently resembles the improved electron collection in standard devices when an ultra-thin LiF layer is inserted between the active layer and the top aluminum electrode. They showed no variation in the $V_{oc}$ between samples with and without the PTE interlayer, thus suggesting that no recombination or morphological behavior differences should characterize the devices. An increase in the $J_{sc}$ was also indicative of reduced leakage current and series resistance. In order to explain such a result, they take into consideration the possible variation of the hydrophilicity of the $TiO_x$ surface, due to the PTE interlayer underneath. Indeed, they found that the $TiO_x$ layer becomes actually more hydrophilic when coated on top of the PTE layer, instead of directly on top of the ITO substrate, thus enhancing the vertical phase separation of the active blend with more of the fullerene phase (relatively more hydrophilic than P3HT [69]) on the bottom and, hence, the electron transport and collection [26,70]. Their results demonstrate how it is possible to clearly improve the PCE of ISCs simply by adding a suitable interlayer on top of the ITO electrode.

They also demonstrated that, even when processed in air, the $TiO_x$ layer can be unaffected by the so-called "light-soaking effect" [71,72]. This is an unusual "s-shaped" current-voltage curve, translating into an extremely low FF, due to the properties of the ITO/$TiO_x$ interface [73], which sometimes arises for air-processed layers. This effect, however, can be suppressed once the $TiO_x$ layer is exposed to UV light, as shown by Kim *et al.* [73]. They proposed a possible mechanism that is responsible for this process: the work function of the $TiO_x$ slightly changes upon UV irradiation, due to the increase of its charge carrier (electrons) density following the suppression of $O_2^-$ traps (adsorbed by $TiO_x$ during realization processes in air), filled with the holes generated by the absorption of the UV radiation. This change in the work function (increased electron density) induces a rearrangement of the Fermi level at the interface (the decreased energy barrier between

ITO and $TiO_x$, see Figure 6) in a direction favorable to a boost in charge transport and collection, resulting in a strong decrease of the series resistance of the device and improved $J_{sc}$. This mechanism has been exploited to explain also the same findings upon UV irradiation of ZnO layers [59].

**Figure 6.** The energy diagram of the indium tin oxide (ITO)/$TiO_x$ interface before (**a**) and after (**b**) UV irradiation. Reprinted with permission from [73].

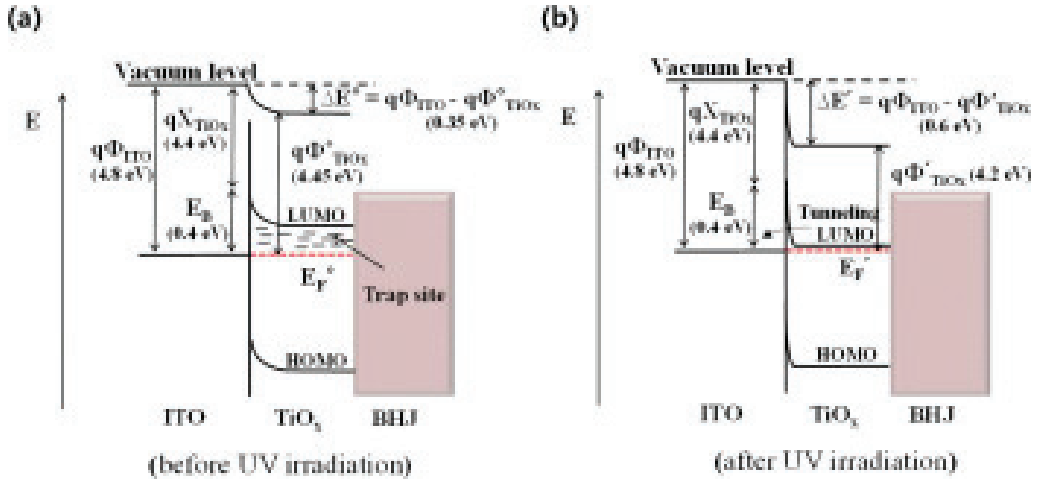


Another elegant way to improve the charge transport and collection and to reduce the charge recombination is by enhancing the vertical phase separation by realizing self-assembled fullerene monolayers (SAM) on top of the $TiO_x$ film [67,74]. Although this seems to be a very good strategy, it is necessary to be careful in the choice of the SAMs: in fact, the deposited layer must resist the subsequent active layer deposition process from solution, which means that the layer should not present at the end of the process localized defects due to the desorption of molecules [75]. Hsu and coworkers [67] joined together the concepts of self-assembling structures and cross-linking, which were separately exploited previously [76–79], in order to overcome the cited drawback of SAMs, synthesizing a new fullerene-derivative, namely the bis(2-(trichlorosilyl)propyl)malonate C60 (TSMC). This new compound was able to both cross-link and self-assemble on top of the $TiO_x$ layer, without the need for annealing or UV irradiation. The modified $TiO_x$ layer was used in ISCs based on both $PC_{61}BM$ and $PC_{71}BM$, showing a clear improvement of the device parameters, which was explained also by an enhanced vertical phase separation of the active blend by the SAM. Their approach seems to be quite interesting in the framework of facile and practical processes for mass production. Quite in parallel, Kim and coworkers [74] synthesized another fullerene derivative able to generate fullerene-based self-assembled monolayers (FSAMs) onto $TiO_x$ to be used as ETL in ISCs, namely bis-4-(2-ethylhexyloxy)-[6,6]-phenyl C61 butyric acid (bis-p-EHO-PCBA). They showed that the bis-FSAM was responsible for the sensible reduction of the series resistance compared to that of the $TiO_x$ layer alone, with an increase both in $J_{sc}$ and FF in polymer:fullerene-based ISC. This confirms the better wetting properties with the organic active layer (responsible, at the end, for the better device performances) when the $TiO_x$ layer is covered with fullerene-based SAMs.

### 3.1.3. $Cs_2CO_3$

The use of $Cs_2CO_3$ as the ETL is more recent: in 2004, a report from the Canon group [80] described its use in organic light emitting diodes. In 2006, Yang *et al*. [30] showed that such a material could be conveniently used as the ETL in BHJ ISCs: a P3HT:PCBM-based ISC exhibited a good PCE of 2.25% using $Cs_2CO_3$ in combination with $V_2O_5$ as the HTL. The interesting result they showed lies in the fact that all the device parameters remained almost unchanged when the $Cs_2CO_3$ layer was realized by thermal evaporation or by spin coating from solution. They proved that the ETL provided an ohmic contact favorable to the device performance. Liao *et al*. [81] showed that the work function of $Cs_2CO_3$ can be tuned by annealing the layer at relatively low temperatures up to 200 °C. This shift in the work function is mainly dependent on the intrinsic properties of the layer more than on some chemical reaction with the underlying ITO layer. They also showed a direct correlation between the annealing temperature and both the device PCE and the $Cs_2CO_3$ surface contact angle, indicating a transition of the ETL from a more hydrophilic-type to a more hydrophobic-type layer, which is beneficial for the subsequent good deposition of the active polymer blend. They explained this work function shift by analyzing the results of XPS experiment, concluding that upon annealing, the $Cs_2CO_3$ decomposes into $Cs_2O$ oxide doped with $Cs_2O_2$, thus lowering the WF, with a better matching with the acceptor LUMO and, consequently, the interface resistance.

Xin *et al*. [82] reported on the effect of UV-ozone treatment of $Cs_2CO_3$ layers on the general performance of BHJ ISCs. They showed that the $V_{oc}$ monotonously decreased with increasing UV-ozone treatment time, while the $J_{sc}$ showed first an increase and then a decrease. The best device performance they obtained was thus attributed to the enhancement of carrier transport and collection by the $Cs_2CO_3$ layer [83,84]. However, while the effects of UV treatment on ZnO or TiOx layers have been widely studied, the precise mechanism underlying the UV-ozone treatment on the $Cs_2CO_3$ layer is still unclear.

Other really interesting and recent results were reported by Barbot and coworkers [83]: they exploited the good ETL properties of both $Cs_2CO_3$ and fullerenes, realizing a $Cs_2CO_3$-doped C60 ETL interlayer. In a previous work, they found that the electrical conductivity of undoped C60 was improved by eight orders of magnitude upon doping with $Cs_2CO_3$ for a molar ratio of 1:0.35 [85]. Indeed, they showed that the best BHJ ISC based on a P3HT:PCBM active blend was exactly the one that incorporated an ETL with such a molar concentration ratio, with an increase of $V_{oc}$ and a decrease of the series resistance.

Finally, Liu *et al*. [86] addressed one drawback of the $Cs_2CO_3$, that is its poor hole blocking ability. By incorporating graphene quantum dots (GQDs) into the $Cs_2CO_3$, they were able to improve the PCE of a BHJ ISC based on P3HT:PCBM from 2.57% for a reference device with a $Cs_2CO_3$ ETL only to 3.17% for a device with a GQDs-$Cs_2CO_3$ ETL. Furthermore, in this case, the better performance was correlated with a better match between the involved energy levels of the ETL and the PCBM, due to a shift of the ETL work function upon incorporation of the GQDs. This minimizes the energy losses at the interface almost without affecting the

overall light absorption in the active blend. Moreover, they proposed that an additional exciton dissociation channel could occur at the P3HT/GQD-$Cs_2CO_3$ interface, facilitating the charge separation. However this could also mean that using such an ETL would affect the vertical phase separation in the active blend, with a non-negligible P3HT phase content on the bottom side of the device that could enhance the charge recombination; this is actually a point that would need to be addressed.

### 3.1.4. $Nb_2O_5$

$Nb_2O_5$ has been used as the ETL in ISCs [87]. A drawback of this metal oxide is that the energy level of its conduction band (about 3.7 eV [88]) is higher than the LUMO level of PCBM (about 3.8 eV [89]); thus, it should not perform as well as ETL in fullerene-based devices. Nevertheless, Cao *et al.* [87] showed that a PCE comparable to that obtained on a similar device, but incorporating a $TiO_2$ layer as the ETL, is achievable (2.7% compared to 2.8%). They explained this counterintuitive effect with an efficient tunneling process from the PCBM LUMO to the $Nb_2O_5$ conduction band. Especially when using this metal oxide, great care should be taken in obtaining the optimal layer thickness: a non-optimized layer thickness can even reduce the device PCE close to 0% [87].

### 3.1.5. Novel Alternatives

Although some of the previous materials dominate the field of electron transport layers in inverted bulk heterojunction solar cells, the surfaces of metal oxides possess hydroxyl groups that are the cause of possible charge trapping [24]. Thus, new materials and concepts have been recently developed as promising alternatives. In particular, towards the development of an all-organic device, the use of polymeric material as ETLs seems to be quite interesting. Huang and coworkers [32] synthesized an amino-functionalized conjugated metallopolymer, namely PFEN-Hg, to be used as an efficient electron transport layer in inverted polymer solar cells. Their polymer was characterized by most of the requirements of an ETL, which are orthogonal solvent processability, transparency to visible light, good electron transport and hole blocking properties, good morphology and effective ITO work function tuning. With the incorporation of such an ETL, they were able to reach about 9% PCE on an ISC based on PTB7:$PC_{71}BM$ as the active material.

Vijila and coworkers [31] used as the ETL in a P3HT:PCBM-based ISC a solution processable cationic biopolymer, poly(2-(dimethylamino)ethyl methacrylate) (PDMAEMA). They compared the device performance with that of a reference device using a standard ZnO ETL layer, finding comparable PCE for a fresh device and a better stability of the polymeric ETL after eight weeks, with a PCE greater than that of the reference device.

Fang *et al.* [90] developed an ETL based on the hybrid material, CdS/2,9-dimethyl-4,7-diphenyl-1,10- phenanthroline (CdS-BCP), which also fulfills most of the cited requirements for good ETLs. They exploited it in PTB7:$PC_{71}BM$- or P3HT:$PC_{60}BM$-based ISCs, showing an improvement in PCE compared to single CdS or BCP-based devices, with improved stability over time.

Jeon and coworkers [91] took advantage of the good electron transport properties of carbon nanotubes (CNTs) by improving their charge selectivity, coating them with an ultra-thin $TiO_x$ layer deposited by atomic layer deposition. The $TiO_x$ coating, due to its good hole-blocking properties, prevents the recombination of holes and electrons at the metallic part of the CNTs during the charge transport-collection process. This results in a final PCE improvement of about 30% compared to the bare CNTs-based ETL. Although being interesting results, the effectiveness of the $TiO_x$-coated CNTs strongly depends on the quality (homogeneity and thickness) of the coating, which, if not optimized, can lead to a large amount of leakage current, due to the coating defects.

Kohlstadt *et al.* [92] demonstrated good PCE in ITO-free PTB7:$PC_{71}BM$-based ISC when a metal-metal oxide multilayer is used as the electrode/ETL. They realized by DC magnetron sputtering a sequence of 25 nm of Al-doped ZnO (AZO), 9 nm of silver and, again, 20 nm of AZO. With such a sequential structure, they demonstrated a PCE of 6.1%, almost comparable with the PCE of a standard geometry device with an ITO/PEDOT:PSS substrate (which was reported to be 6.9%). They pointed out that the possible drawback of such a multilayered structure is an unfavorable field distribution inside the active layer and a lower absorption, issues that still need to be addressed.

Oo *et al.* [93] described a very good ETL, namely a zinc tin oxide (ZTO) layer used on top of FTO in P3HT:PCBM-based ISCs. They explained the better performance of the device incorporating the ZTO layer considering the reduced recombination at the interface, the improved electron transport and the hole blocking properties of the ZTO compared to standard ETL.

#### 3.1.6. ETL: Conclusions

As a brief and overall general conclusion on this section, it appears quite clear that optimized (and possibly doped) ZnO and TiOx represent, to date, the best bet for realizing well performing BHJ ISCs, based on the reported averaged PCE of devices and on their fulfillment of most of the points in the "decalogue" established by Litzov and Brabec [29]. $Cs_2CO_3$, despite its excellent electron transport properties, suffers from poor hole blocking properties [86], while $Nb_2O_5$ possesses a probably unfavorable energy level diagram to be used generically as the ETL with systems that are not based on PCBM. The other novel alternatives seem really interesting and promising, especially the polymeric ETLs to be fully exploited in the framework of an all-polymer device realized by the roll-to-roll technique, but the results are too recent in order to be reasonably able to infer some general conclusion over the near future.

### *3.2. Top Electrode: Hole Collection*

In BHJ ISCs, the top metal electrode is usually either gold or silver, due to their intrinsic stability in air. However, Ag is the most suitable top electrode, since its slow oxidation shifts its work function from about 4.3 eV to about 5 eV [94], favoring hole extraction. It has no absorption in the visible range contrary to the evaporated Au layer (slight absorption in the visible) and a higher reflectivity [95]. In fact, Chen *et al.* [96] showed that, *ceteris paribus*, a device with an Ag top metal electrode performed better compared to Au or Al. This is also due to the better matching of the WF of

Au (5.1 eV [97]) and the oxidized Ag (around 5.0 eV [94]) with the HOMO levels of the commonly used polymer donors, compared to Al (4.28 eV [97]).

Anyway, in order to obtain good performances from an ISC, the introduction of an HTL layer between the organic active layer and the top metal electrode is mandatory; otherwise, the device would show very poor performance or even no operation at all [98]. To date, the most commonly used HTLs in BHJ ISCs are polymers, like PEDOT:PSS, or metal oxides, like $MoO_3$, $V_2O_5$, $WO_3$, NiO.

### 3.2.1. PEDOT:PSS

PEDOT:PSS is the most widely used HTL in standard geometry BHJ solar cells, due to its high work function (matching the HOMO level of commonly used donor polymers well), high transparency in the visible range (higher than 80%), good electrical conductivity and the ability to reduce the ITO surface roughness [99], while increasing its work function. However, PEDOT:PSS is highly hydrophilic; thus, bad film morphology and worse electrical properties have been observed when deposited as the HTL onto the hydrophobic organic layers in inverted devices [100,101]. Nevertheless, it is widely used in BHJ ISCs despite this evident drawback. In order to address the wettability problem on hydrophobic surfaces, several strategies have been reported. First of all, the hydrophilic nature of PEDOT:PSS can be reduced by adding proper additives to the polymer dispersion, like isopropyl alcohol [102], or surfactants, like Zonyl FS-300 [103] and Triton X-100 [104], as well as surfactant mixtures [68]. Moon *et al.* [105] added two amphiphilic surfactants, namely Sulfynol 104 EG or PA (dissolved in ethylene glycol or isopropyl alcohol respectively), showing a clear improvement of the PEDOT:PSS layer morphology. This was reflected in an improved P3HT:PCBM-based device performance of about 60% compared to a reference device incorporating the PEDOT:PSS layer without surfactants. The improvement was mainly due to a higher $J_{sc}$ and a higher FF. Indeed, they showed that upon adding the surfactant, the contact angle between the PEDOT:PSS and the underlying organic layer was decreased from 104° to about 53°. This means a clearly better film forming property, resulting in higher shunt resistance (less charge recombination at the electrode) and a lower series resistance (better charge extraction). They explained the better wettability of the additive-added PEDOT:PSS on the organic layer, observing that the used surfactants consist of a hydrophobic alkyl backbone and a hydrophilic hydroxyl group; thus, a van der Waals-type interaction between the hydrophobic alkyl backbone and the hydrophobic P3HT:PCBM surface occurs, making the organic layer hydrophilic with subsequent good PEDOT:PSS film forming properties on top. Ho and coworkers [106] proposed a novel fluorosurfactants to be used as a substitute to the Zonyl FS-300, since the latter usually needs to be used together with isopropyl alcohol in order to get the best results. The proposed Capstone Dupont FS-31 can be used alone as an additive to the PEDOT:PSS, giving very good results in terms of overall device performance when a relative concentration of about 5% is used. They also showed that the additive concentration in the PEDOT:PSS dispersion greatly affects the final film forming, thus reflecting in better or worse device performances. A concentration below 4% results in a non-uniform layer, due to the still low wettability onto the organic layer. On the contrary, if the concentration

is too high (above 8%), the presence of excess surfactant reduces the charge conduction pathway through the PEDOT molecules, thus resulting in poor charge collection. Moreover, they showed that the surfactant also promotes a phase segregation between PEDOT and PSS, thus resulting in a well-formed PEDOT conduction pathway, while favoring a good physical contact with the underlying organic layer.

Another strategy to improve the PEDOT:PSS adhesion onto the organic layer is to exploit different deposition techniques rather than spin coating. Gupta and coworkers [107] obtained efficient P3HT:PCBM-based inverted OSCs by realizing the top PEDOT:PSS contact by stamp-transfer lamination. They showed that this process does not induce significant losses on the open circuit voltage, nor does it increase the overall resistance of the devices.

However, despite the progresses towards a better adhesion of PEDOT:PSS on top of organic layers, the acidic/hygroscopic nature of the compound is still detrimental for the top-side metal electrode. Indeed, Kim and coworkers clearly showed [108] that PEDOT:PSS is able to promote the corrosion and degradation of a thin layer of Ag as typically used in ISCs. They demonstrated that the hygroscopic nature of PEDOT:PSS promotes a very fast absorption of ambient water inside the layer. This absorbed water becomes corrosive, due to the acidic nature of the PEDOT:PSS, thus slowly corroding the silver layer, first promoting grain boundary grooves, then leading to grain segregation, forming separated particles. They, however, observed that such a process could be slow in a real device configuration and processing, although in the long term, it would cause strong degradation of the performances.

Even if, to date, PEDOT:PSS is still the most used HTL in inverted BHJ PSCs [29], in order to avoid all these drawbacks, in several works, PEDOT:PSS has been replaced by other efficient HTLs, like the following ones.

### 3.2.2. $MoO_3$

A thin HTL of molybdenum trioxide ($MoO_3$) greatly improves the performance of both inverted and conventional OLEDs [109–111]. Early in 2008, Chen and coworkers [96] showed that $MoO_3$ increased the overall efficiency of a BHJ ISC based on both a P3HT:PCBM active layer and a nanocrystalline $TiO_2$ ETL. They reported that the $V_{oc}$ of the device changed only slightly when the top metal electrode was varied from Ag to Au to Al, while the optimal HTL thickness depends on the chosen metal. In particular, with Al as top electrode, an higher thickness of the evaporated $MoO_3$ layer is required in order to obtain the same performances of devices using Ag or Au. This was attributed to the chemical reaction between Al and $MoO_3$ during the evaporation process, forming a $MoO_2$ species, due to the reduction of $MoO_3$.

The dependence of the overall efficiency of devices on the $MoO_3$ thickness has been also detailed by Zheng *et al.* [112] and by Wantz and coworkers [113]. Zheng *et al.* showed that the PIFTBT8:$PC_{71}BM$-based device parameters remained almost unchanged when the thickness of the $MoO_3$ layer was in the range of 10–20 nm, while a drop in both $V_{oc}$ and FF occurred when the thickness was decreased to 5 nm. They correlated such a behavior with the shunt and the series resistance, observing that a decrease of the thickness of the $MoO_3$ layer was followed by both an

increase of the series resistance and a decrease of the shunt resistance. Moreover, increasing the thickness, the $V_{oc}$ changed from 1.00 V to 1.04 V, and the FF varied between 41.9% and 50%. Wantz *et al.* showed that the overall performance of a P3HT:PCBM-based device was only slightly affected by a variation of the $MoO_3$ thickness from 6 nm to 22 nm. Interestingly, they also demonstrated how the post-processing thermal treatment on the device, usually employed to improve the device performance [114], is, on the contrary, detrimental in BHJ ISCs when $MoO_3$ is used as the HTL. In fact, they observed that after 10 min at 170 °C, the cohesion between the $MoO_3$ layer and the silver electrode was lost, and the layer itself evolved into an alloy of silver and molybdenum oxide, with a diffusion of silver ions and oxygen inside the active layer. The thinner the $MoO_3$ layer, the faster and even worse was this process. It should then be concluded that an inverted BHJ incorporating an $MoO_3$ layer should not undergo a thermal treatment after the completion of the device. However, since in the case of P3HT:PCBM, the annealing process promotes the vertical phase separation in a way favorable to the inverted device working principle [115], such an annealing process should be performed *prior* to the deposition of both the HTL and the top metal electrode. Moreover, providing that the post-processing annealing treatment is avoided for the completed device, Gupta and coworkers [116] showed that $MoO_3$ acts as a barrier to the diffusion of metal ions and oxygen inside the active layer, thus preventing fast device degradation. The role of the environment on the effects of the thermal treatment of thin layers of $MoO_3$ was studied by Vijila and coworkers [117]. When the complete device incorporating the $MoO_3$ layer as the HTL is annealed in vacuum, the overall stability and performance are higher compared to a similar device annealed in a nitrogen atmosphere. The difference in the PCE was increased upon aging, with the vacuum annealed device retaining 80% of its initial PCE value after 30 days compared to the 50% of the device annealed in nitrogen atmosphere. They explained this behavior observing that the metal oxide layer annealed in vacuum is characterized by an oxygen deficient structure that is the origin of an enhanced hole-conducting properties.

Jiang *et al.* [118] demonstrated that an interesting way to improve and tune the electrical and the optical properties of a $MoO_3$ layer can be by realizing a composite film with Au. They showed that a $MoO_3$-Au (30%) layer is characterized by very good electrical and optical parameters. They exploited this layer as the HTL in a conventional geometry solar cell, in substitution of PEDOT:PSS. Although there is no report on the use of such a modified $MoO_3$ layer in inverted devices, one can speculate that such a layer could be conveniently exploited also in this type of solar cell.

### 3.2.3. $WO_3$

As shown earlier by Dong *et al.* [97], the high work function of $WO_3$ ($-4.8$ eV) greatly enhances the hole transport and collection at the $WO_3$/Ag interface. They showed that the optimum thickness for $WO_3$ in a P3HT:PCBM-based device is in the range between five and 10 nm. Lower values would results in poor coverage of the film, while higher values would increase the series resistance, thus lowering the overall device performance. They also showed that the $V_{oc}$ of the devices were substantially unaffected by the choice of the top metal electrode (Au, Ag or Al). Kwon *et al.* [119] compared the performances of $MoO_3$ and $WO_3$ inverted devices based on several active layers. They

showed that in all cases, the device incorporating a $WO_3$ HTL layer (5 nm optimum thickness) performed slightly better than those with a $MoO_3$ HTL layer (10 nm optimum thickness). They explained this better behavior of the $WO_3$ layer with: (1) a better film surface morphology (a reduced average roughness measured by atomic force microscopy); (2) a better measured conductivity; and (3) better electron blocking and hole transport properties, due to the higher energy barrier between the donor LUMO and the HTL conduction band and the better matching between the donor HOMO level and valence band of the HTL.

Brabec *et al.* [120] demonstrated that a low temperature (80 °C) solution-processed nanoparticle $WO_3$ HTL was able to perform as well as PEDOT:PSS in a standard geometry device and to give very good performances on an inverted architecture. The solution was alcohol-based and free of any surfactant, and the realized HTL does not need any oxygen-plasma treatment, which is usually required to remove the dispersing agent in the original NP dispersion [121] and to improve its HTL properties. They concluded that the low temperature solution-processed $WO_3$ layer can be easily and conveniently exploited in flexible solar cell production processes.

### 3.2.4. $V_2O_5$ and NiO

Even if $V_2O_5$ has been used as the HTL in inverted devices,-its high toxicity [119] makes it not very suitable for easy and low cost device processing in ambient conditions. Moreover Riedl *et al.* [121] showed that care should be taken when realizing the $V_2O_5$ HTL by the sol-gel process. They compared the performance of P3HT:PCBM-based devices with evaporated $V_2O_5$ HTL or sol-gel-processed $V_2O_5$ HTL, observing that the 10 nm-thick layer of the sol-gel-processed $V_2O_5$ sensibly affects the working device, depending on the initial solution concentration and spin coating speed. In particular, a low concentration of the precursor solution (1:150) spin coated at slow speed formed a film that affected the device positively, showing parameters comparable to those obtained with an evaporated $V_2O_5$ layer. On the contrary, a film with the same thickness, but obtained from a higher concentrated precursor solution (1:70), spin coated at a higher speed, greatly lowered the overall performance of the device. They excluded that such a strange behavior could be attributed to some effect of the solvent onto the active layer, while showing through XPS measurements that the higher concentrated precursor solution leads to a deep penetration of vanadium inside the active layer, up to more than 100 nm. This penetration of the precursor into the active layer (that was by far less evident in the case of the evaporated $V_2O_5$) could damage the P3HT chains and/or lead to the quenching of excitons in the donor phase. This penetration was also indirectly confirmed by Dauskardt and coworkers [115] when comparing the roll-to-roll-processed inverted BHJ PSC incorporating both PEDOT:PSS or $V_2O_5$ HTLs.

NiO has been also used as a good HTL in BHJ ISC. NiO possesses a valence band and a conduction band at $-5.0$ eV and $-1.7$ eV, respectively, thus acting as a good HTL and a good electron blocking layer in combination with a P3HT:PCBM, as shown by Chen and coworkers [122]. The optimal HTL thickness in their case was under 2 nm, above which the device performance starts to decrease. They attributed this behavior to the intrinsic electronic properties of the NiO layer that was deposited in a high vacuum by thermal evaporation, thus

affecting the oxygen concentration in the realized layer. A thin layer was also deposited from solution by Lee *et al*. [123], by simply dissolving NiO powder into various solvents (the best was found to be isopropyl alcohol) and spin coating it onto the P3HT:PCBM active layer. Upon optimization of the active layer thickness, they were able to obtain about 3% PCE, comparable with a reference device incorporating as the HTL a thin layer of PEDOT:PSS. The solution processable NiO layer could be compatible with roll-to-roll manufacturing in air.

### 3.2.5. Novel Alternatives

A solution processable mixture of $V_2O_5$ and $MoO_3$ was exploited by Huang and coworkers [124] as an efficient HTL in a P3HT:PCBM-based inverted solar cell. They showed that the mixed layer causes a significant improvement of the device parameters compared to control devices with $V_2O_5$ or $WO_3$ HTL alone. They explained these results with the efficient hole transport, due to the well matched donor HOMO-valence band of $V_2O_5$ and, concomitantly, to the electron extraction from the top silver electrode through the conduction band of the $WO_3$. This complementary mechanism positively affects the overall device PCE.

Solution-processable triindoles, namely triazatruxene (TAT) and N-trimethyltriindole (TMTI), with tailored HOMO and LUMO levels, in order to be used as the HTL in inverted devices, were presented by Ma *et al*. [125]. They showed an improvement in the $J_{sc}$ and in the overall PCE of a P3HT:PCBM-based inverted device when a thin layer of TAT was spin coated onto the active layer.

Furthermore, graphene oxide has been exploited as the HTL in BHJ PSCs by Dai and coworker [126]. Indeed, graphene is a bidimensional carbon structure that possesses excellent electronic and mechanical properties [127]. Through the neutralization of the –COOH groups of the graphene oxide with $Cs_2CO_3$, they were able to tune the electronic properties of the material, giving both excellent ETL or HTL properties. They exploited these interesting characteristics, showing very good device performances in P3HT:PCBM-based devices with a PCE exceeding 3%.

A 4.4% PCE on a P3HT:PCBM device was achieved by Chen *et al*. [128] by developing a self-assembled HTL strategy. They synthesized a novel fluoroalkyl side-chain diblock copolymer, namely the poly(3-hexylthiophene)-block-poly[3-(4-(3,3,4,4,5,5,6,6,7,7,8,8,8-tridecafluorooctyloxy) phenyl)-decyloxy)thiophene] (P3HT-b-P3FAT), in which, upon spin coating, the fluorinated moiety spontaneously undergoes a segregation on top of the P3HT phase, due to the low surface energy of the fluoroalkyl chains, forming a self-assembled HTL. Exploiting this mechanism and controlling the block ratio into the copolymer, they were able to greatly improve the hole collection and, thus, the overall efficiency of the device.

### 3.2.6. HTLs: Conclusions

Averaging the general results, it should be concluded that the best HTL for BHJ ISCs should be a thin layer of either $MoO_3$ or $WO_3$, due to their intrinsic good electrical and optical properties, their ability to prevent oxygen and metal ion diffusion into the active layer and the almost unchanged

device parameters upon slight variation of their optimum thickness. On the contrary, PEDOT:PSS has to be avoided, due to its evident drawbacks, as mentioned. Dauskardt and coworkers [115] demonstrated how the poor adhesion of PEDOT:PSS onto the active layer results in a general loss of device performance in a roll-to-roll processed device, due to the thermomechanical stress that every "real-life" device would undergo.

However, it appears clear (see, for example, the comparison between $MoO_3$ and $WO_3$ above) that the key factor in choosing the best HTL is the trade-off between the electrical/morphological properties and the energetics involved at the interfaces in the particular device. This means that for each particular donor-acceptor system, the matching between the HOMO and LUMO levels of the organic phases and the valence band and the conduction band of the HTL should be optimum. Not only the HOMO level of the donor should match with the valence band of the HTL, but also the latter should have a conduction band far from the active layers' LUMO level, otherwise resulting in an enhanced charge recombination and poor electron blocking behavior [112]. Finally, when dealing with metal-oxides, it should be also considered (in the proper choosing of the best HTL for the particular system) that the work function of those materials strongly depends on the concentration of defects [129], with a decrease of the WF if oxygen is removed from the material, and an increase in the WF is observed with oxygen addition. Interestingly, Xie and Choy [130] developed a synthesis route for developing low-temperature solution-processed $MoO_3$ or $V_2O_5$ HTL with the ability to control the oxygen vacancies, thus, in the end, controlling the final WF.

Finally, one key motivation in selecting the proper HTL should be the compatibility of its deposition process with standard roll-to-roll or printing techniques for the realization of complete devices in ambient conditions, without the need for vacuum processes, like thermal evaporation. Thus, the choice should come down to solution processable HTLs, which is no longer a limitation, since solution-processed $WO_3$ and $MoO_3$ HTLs have been exploited both in conventional and inverted devices, showing good overall performances [120,131–134]. Furthermore, the very interesting polymeric novel alternatives cited above could be promising.

## 4. Device Stability: A Brief Comment

Considering the environmental stability in the working condition of a BHJ ISC as the *key* parameter, which is the best ETL and HTL choice? Actually it is not possible, to date, to give a precise answer. A detailed discussion on this issue is far beyond the scope of this paper: in one sentence, the stability of BHJ ISCs is still a matter of debate [29]. For example, it is not clear how and to what extent the particular process used for preparing metal oxide layers can affect the final device stability [135], nor which is the particular "best" device structure [136]. One comprehensive study on the stability of several ETL/HTL combinations has recently been performed by Voroshazi and coworkers [137]. They demonstrated that ZnO- and $TiO_x$-based devices were comparably stable in air for over 1000 h, while the analyzed organic ETLs were clearly affected by a lower stability over time. On the HTL side, they surprisingly showed that a PEDOT:PSS-based device was more stable than a $MoO_3$-based device. However, Vijila and coworkers [117] demonstrated that the annealing condition of a MoO3-based device can greatly

affect the final device stability. They demonstrated that a vacuum annealed device was characterized by a 10% increased stability compared to a device annealed in a nitrogen atmosphere, as discussed in the previous section. Furthermore, Sun *et al.* [38] showed that a device incorporating a thin layer of $MoO_3$ as the HTL retained 70% of its initial PCE after 30 days.

Finally, some recent reports on lifecycle analysis (LCA) and energy payback time (EPT) have been published by several groups [138–140]. From the reported results, it can be concluded that it is quite difficult to assess a precise standard, to date, in order to definitively compare different kinds of devices, materials and procedures. Even the same devices are characterized by some variation in their working parameters when measured by different laboratories [136]. A definition of a precise standard in this field should be particularly important to evaluate how much the (sometimes low) increase in the PCE obtained with a particular process/optimization of the ETLs and/or the HTLs is convenient from an economical point of view (considering the energy and time consumption needed for the layer realization/optimization).

## 5. General Conclusions

As a general conclusion, the BHJ ISC appears to be a very promising device structure to be exploited in the mass production of organic solar cells. Aside from the development and optimization of novel active materials, like novel acceptors or low band-gap polymer donors, the correct optimization and choice of the HTL together with the ETL play a fundamental role in order to get the best performance from a device. Many parameters, however, need to be traded off, as has been described. In particular, a necessary trade-off between better HTL and ETL electrical properties and overall device optical properties must be accomplished. Moreover, the right HTL, as well as the right ETL must be chosen, taking into account the energy level structure of the particular active blend used. The ideal optimum is the matching between the donor HOMO and the valence band of the HTL and between the acceptor LUMO and the conduction band of the ETL, together with a proper position of the HTL conduction band and the ETL valence band, in order to provide, at the same time, a good electron blocking or hole blocking behavior, respectively. The same features are also relevant in the case of polymeric or organic HTLs and ETLs (in this case, the matching should be between the HOMO and LUMO levels of the active layer and the HOMO and LUMO levels of the other layers).

As has been pointed out in the previous sections, the ETL and HTL performances can be affected by the realization parameters. Good control and knowledge of all these parameters should be necessary in order to get the maximum performance from a given system.

As a final remark, it is important to stress that novel polymeric alternatives could come in handy for bypassing the depicted criticality typical of the most used metal oxides, being also intrinsically compatible with low-cost device manufacturing processes.

## Acknowledgments

Marco Anni is gratefully acknowledged for useful comments and suggestions.

## Conflicts of Interest

The author declares no conflicts of interest.

## References


1. Shirakawa, H.; Louis, E.J.; MacDiarmid, A.G.; Chiang, C.K.; Heeger, A.J. Synthesis of electrically conducting organic polymers: Halogen derivatives of polyacetylene, (CH)x. *J. Chem. Soc. Chem. Commun.* **1977**, 578–580, doi:10.1039/C39770000578.
2. Service, R.F. Outlook brightens for plastic solar cells. *Science* **2011**, *332*, 293.
3. Scharber, M.; Sariciftci, N.S. Efficiency of bulk-heterojunction organic solar cells. *Prog. Polym. Sci.* **2013**, *38*, 1929–1940.
4. Jorgensen, M.; Carlé, J.E.; Sondergaard, R.R.; Lauritzen, M.; Dagnaes-Hansen, N.A.; Byskov, S.L.; Andersen, T.R.; Larsen-Olsen, T.T.; Böttiger, A.P.; Andreasen, B.; *et al*. The state of organic solar cells—A meta analysis. *Sol. Energy Mater. Sol. Cells* **2013**, *119*, 84–93.
5. Tang, C.W. Two-layer organic photovoltaic cell. *Appl. Phys. Lett.* **1986**, *48*, 183–185.
6. Sariciftci, N.; Smilowitz, L.; Heeger, A.; Wudl, F. Semiconducting polymers (as donors) and buckminsterfullerene (as acceptor): Photoinduced electron transfer and heterojunction devices. *Synth. Met.* **1993**, *59*, 333–352.
7. Sariciftci, N.S.; Braun, D.; Zhang, C.; Srdanov, V.I.; Heeger, A.J.; Stucky, G.; Wudl, F. Semiconducting polymer-buckminsterfullerene heterojunctions: Diodes, photodiodes, and photovoltaic cells. *Appl. Phys. Lett.* **1993**, *62*, 585–587.
8. Yu, G.; Pakbaz, K.; Heeger, A.J. Semiconducting polymer diodes: Large size, low cost photodetectors with excellent visible-ultraviolet sensitivity. *Appl. Phys. Lett.* **1994**, *64*, 3422–3424.
9. Hummelen, J.C.; Knight, B.W.; LePeq, F.; Wudl, F.; Yao, J.; Wilkins, C.L. Preparation and characterization of fulleroid and methanofullerene derivatives. *J. Org. Chem.* **1995**, *60*, 532–538.
10. Yu, G.; Gao, J.; Hummelen, J.C.; Wudl, F.; Heeger, A.J. Polymer photovoltaic cells: Enhanced efficiencies via a network of internal donor-acceptor heterojunctions. *Science* **1995**, *270*, 1789–1791.
11. Tremolet de Villers, B.; Tassone, C.J.; Tolbert, S.H.; Schwartz, B.J. Improving the reproducibility of P3HT:PCBM solar cells by controlling the PCBM/cathode interface. *J. Phys. Chem. C* **2009**, *113*, 18978–18982.
12. Sanyal, M.; Schmidt-Hansberg, B.; Klein, M.F.G.; Colsmann, A.; Munuera, C.; Vorobiev, A.; Lemmer, U.; Schabel, W.; Dosch, H.; Barrena, E. *In Situ* X-ray study of drying-temperature influence on the structural evolution of bulk-heterojunction polymer-fullerene solar cells processed by doctor-blading. *Adv. Energy Mater.* **2011**, *1*, 363–367.
13. Hoth, C.N.; Choulis, S.A.; Schilinsky, P.; Brabec, C.J. On the effect of poly(3-hexylthiophene) regioregularity on inkjet printed organic solar cells. *J. Mater. Chem.* **2009**, *19*, 5398–5404.

14. Nie, W.; Coffin, R.; Liu, J.; MacNeill, C.M.; Li, Y.; Noftle, R.E.; Carroll, D.L. Exploring spray-coating techniques for organic solar cell applications. *Int. J. Photoenergy* **2012**, *2012*, doi:10.1155/2012/175610.
15. Kim, Y.H.; Lee, S.H.; Noh, J.; Han, S.H. Performance and stability of electroluminescent device with self-assembled layers of poly(3,4-ethylenedioxythiophene)-poly(styrenesulfonate) and polyelectrolytes. *Thin Solid Films* **2006**, *510*, 305–310.
16. De Jong, M.P.; van IJzendoorn, L.J.; de Voigt, M.J.A. Stability of the interface between indium-tin-oxide and poly(3,4-ethylenedioxythiophene)/poly(styrenesulfonate) in polymer light-emitting diodes. *Appl. Phys. Lett.* **2000**, *77*, 2255–2257.
17. Yim, K.H.; Zheng, Z.; Friend, R.H.; Huck, W.T.S.; Kim, J.S. Surface-directed phase separation of conjugated polymer blends for efficient light-emitting diodes. *Adv. Funct. Mater.* **2008**, *18*, 2897–2904.
18. Pavlopoulou, E.; Fleury, G.; Deribew, D.; Cousin, F.; Geoghegan, M.; Hadziioannou, G. Phase separation-driven stratification in conventional and inverted P3HT:PCBM organic solar cells. *Org. Electron.* **2013**, *14*, 1249–1254.
19. Baigent, D.R.; Marks, R.N.; Greenham, N.C.; Friend, R.H.; Moratti, S.C.; Holmes, A.B. Conjugated polymer light-emitting diodes on silicon substrates. *Appl. Phys. Lett.* **1994**, *65*, 2636–2638.
20. Arias, A.C.; Granström, M.; Thomas, D.S.; Petritsch, K.; Friend, R.H. Doped conducting-polymer–semiconducting-polymer interfaces: Their use in organic photovoltaic devices. *Phys. Rev. B* **1999**, *60*, 1854–1860.
21. Nyberg, T. An alternative method to build organic photodiodes. *Synth. Met.* **2004**, *140*, 281–286.
22. Ameri, T.; Dennler, G.; Waldauf, C.; Denk, P.; Forberich, K.; Scharber, M.C.; Brabec, C.J.; Hingerl, K. Realization, characterization, and optical modeling of inverted bulk-heterojunction organic solar cells. *J. Appl. Phys.* **2008**, *103*, 084506.
23. Yuan, J.; Huang, X.; Dong, H.; Lu, J.; Yang, T.; Li, Y.; Gallagher, A.; Ma, W. Structure, band gap and energy level modulations for obtaining efficient materials in inverted polymer solar cells. *Org. Electron.* **2013**, *14*, 635–643.
24. Hau, S.K.; Yip, H.L.; Jen, A.K.Y. A review on the development of the inverted polymer solar cell architecture. *Polym. Rev.* **2010**, *50*, 474–510,
25. Zhang, F.; Xu, X.; Tang, W.; Zhang, J.; Zhuo, Z.; Wang, J.; Wang, J.; Xu, Z.; Wang, Y. Recent development of the inverted configuration organic solar cells. *Sol. Energy Mater. Sol. Cells* **2011**, *95*, 1785–1799.
26. Deibel, C.; Dyakonov, V. Polymer-fullerene bulk heterojunction solar cells. *Rep. Prog. Phys.* **2010**, *73*, 096401.
27. Chen, D.; Zhang, C.; Wang, Z.; Zhang, J.; Feng, Q.; Xu, S.; Zhou, X.; Hao, Y. Performance comparison of conventional and inverted organic bulk heterojunction solar cells from optical and electrical aspects. *IEEE Trans. Electron Devices* **2013**, *60*, 451–457.

28. Murphy, L.; Hong, W.; Aziz, H.; Li, Y. Organic photovoltaics with thick active layers (800 nm) using a high mobility polymer donor. *Sol. Energy Mater. Sol. Cells* **2013**, *114*, 71–81.
29. Litzov, I.; Brabec, C.J. Development of efficient and stable inverted bulk heterojunction (BHJ) solar cells using different metal oxide interfaces. *Materials* **2013**, *6*, 5796–5820.
30. Li, G.; Chu, C.W.; Shrotriya, V.; Huang, J.; Yang, Y. Efficient inverted polymer solar cells. *Appl. Phys. Lett.* **2006**, *88*, 253503.
31. Jin Tan, M.; Zhong, S.; Wang, R.; Zhang, Z.; Vijila, C.; Chen, W. Biopolymer as an electron selective layer for inverted polymer solar cells. *Appl. Phys. Lett.* **2013**, *103*, 063303.
32. Liu, S.; Zhang, K.; Lu, J.; Zhang, J.; Yip, H.L.; Huang, F.; Cao, Y. High-efficiency polymer solar cells via the incorporation of an amino-functionalized conjugated metallopolymer as a cathode interlayer. *J. Am. Chem. Soc.* **2013**, *135*, 15326–15329.
33. Kyaw, A.K.K.; Sun, X.W.; Jiang, C.Y.; Lo, G.Q.; Zhao, D.W.; Kwong, D.L. An inverted organic solar cell employing a sol-gel derived ZnO electron selective layer and thermal evaporated MoO3 hole selective layer. *Appl. Phys. Lett.* **2008**, *93*, 221107.
34. Kang, Y.J.; Lim, K.; Jung, S.; Kim, D.G.; Kim, J.K.; Kim, C.S.; Kim, S.H.; Kang, J.W. Spray-coated ZnO electron transport layer for air-stable inverted organic solar cells. *Sol. Energy Mater. Sol. Cells* **2012**, *96*, 137–140.
35. Ibrahem, M.A.; Wei, H.Y.; Tsai, M.H.; Ho, K.C.; Shyue, J.J.; Chu, C.W. Solution-processed zinc oxide nanoparticles as interlayer materials for inverted organic solar cells. *Sol. Energy Mater. Sol. Cells* **2013**, *108*, 156–163.
36. Mahmood, A.; Ahmed, N.; Raza, Q.; Khan, T.M.; Mehmood, M.; Hassan, M.M.; Mahmood, N. Effect of thermal annealing on the structural and optical properties of ZnO thin films deposited by the reactive e-beam evaporation technique. *Phys. Scr.* **2010**, *82*, 065801.
37. Park, H.Y.; Lim, D.; Kim, K.D.; Jang, S.Y. Performance optimization of low-temperature-annealed solution-processable ZnO buffer layers for inverted polymer solar cells. *J. Mater. Chem. A* **2013**, *1*, 6327–6334.
38. Sun, Y.; Seo, J.H.; Takacs, C.J.; Seifter, J.; Heeger, A.J. Inverted polymer solar cells integrated with a low-temperature-annealed sol-gel-derived ZnO film as an electron transport layer. *Adv. Mater.* **2011**, *23*, 1679–1683.
39. Hu, T.; Li, F.; Yuan, K.; Chen, Y. Efficiency and air-stability improvement of flexible inverted polymer solar cells using ZnO/poly(ethylene glycol) hybrids as cathode buffer layers. *ACS Appl. Mater. Interfaces* **2013**, *5*, 5763–5770.
40. Yu, X.; Yu, X.; Hu, Z.; Zhang, J.; Zhao, G.; Zhao, Y. Effect of sol-gel derived ZnO annealing rate on light-trapping in inverted polymer solar cells. *Mater. Lett.* **2013**, *108*, 50–53.
41. Ohyama, M.; Kouzuka, H.; Yoko, T. Sol-gel preparation of ZnO films with extremely preferred orientation along (002) plane from zinc acetate solution. *Thin Solid Films* **1997**, *306*, 78–85.
42. Hu, Z.; Zhang, J.; Liu, Y.; Hao, Z.; Zhang, X.; Zhao, Y. Influence of ZnO interlayer on the performance of inverted organic photovoltaic device. *Sol. Energy Mater. Sol. Cells* **2011**, *95*, 2126–2130.

43. Dhibi, O.; Ltaief, A.; Zghal, S.; Bouazizi, A. Inverted low band gap polymer solar cells integrated with a low-temperature-annealed sol-gel-derived ZnO: Active layer thickness effect on the recombination process. *Superlattices Microstruct.* **2013**, *60*, 548–560.
44. Nickel, F.; Sprau, C.; Klein, M.F.; Kapetana, P.; Christ, N.; Liu, X.; Klinkhammer, S.; Lemmer, U.; Colsmann, A. Spatial mapping of photocurrents in organic solar cells comprising wedge-shaped absorber layers for an efficient material screening. *Sol. Energy Mater. Sol. Cells* **2012**, *104*, 18–22.
45. Elumalai, N.K.; Vijila, C.; Jose, R.; Zhi Ming, K.; Saha, A.; Ramakrishna, S. Simultaneous improvements in power conversion efficiency and operational stability of polymer solar cells by interfacial engineering. *Phys. Chem. Chem. Phys.* **2013**, *15*, 19057–19064.
46. Hu, Z.; Zhang, J.; Zhu, Y. Inverted polymer solar cells with a boron-doped zinc oxide layer deposited by metal organic chemical vapor deposition. *Sol. Energy Mater. Sol. Cells* **2013**, *117*, 610–616.
47. Park, B.; Shin, J.C.; Huh, Y.H. Interface-engineering additives for inverted {BHJ} polymer solar cells. *Sol. Energy Mater. Sol. Cells* **2013**, *110*, 15–23.
48. Liu, Y.; Larsen-Olsen, T.T.; Zhao, X.; Andreasen, B.; Sondergaard, R.R.; Helgesen, M.; Norrman, K.; Jorgensen, M.; Krebs, F.C.; Zhan, X. All polymer photovoltaics: From small inverted devices to large roll-to-roll coated and printed solar cells. *Sol. Energy Mater. Sol. Cells* **2013**, *112*, 157–162.
49. Alstrup, J.; Jorgensen, M.; Medford, A.J.; Krebs, F.C. Ultra Fast and parsimonious materials screening for polymer solar cells using differentially pumped slot-die coating. *ACS Appl. Mater. Interfaces* **2010**, *2*, 2819–2827.
50. Perulli, A.; Lattante, S.; Persano, A.; Cola, A.; di Giulio, M.; Anni, M. On the spatial inhomogeneity of charge generation and collection in inverted all polymer solar cells. *Appl. Phys. Lett.* **2013**, *103*, 053305.
51. Ajuria, J.; Etxebarria, I.; Azaceta, E.; Tena-Zaera, R.; Fernandez-Montcada, N.; Palomares, E.; Pacios, R. Novel ZnO nanostructured electrodes for higher power conversion efficiencies in polymeric solar cells. *Phys. Chem. Chem. Phys.* **2011**, *13*, 20871–20876.
52. Liang, Z.; Gao, R.; Lan, J.L.; Wiranwetchayan, O.; Zhang, Q.; Li, C.; Cao, G. Growth of vertically aligned ZnO nanowalls for inverted polymer solar cells. *Sol. Energy Mater. Sol. Cells* **2013**, *117*, 34–40.
53. Elumalai, N.K.; Jin, T.M.; Vijila, C.; Jose, R.; Palaniswamy, S.K.; Jayaraman, S.; Raut, H.K.; Ramakrishna, S. Electrospun ZnO nanowire plantations in the electron transport layer for high-efficiency inverted organic solar cells. *ACS Appl. Mater. Interfaces* **2013**, *5*, 9396–9404,
54. Bhat, J.S.; Patil, A.S.; Swami, N.; Mulimani, B.G.; Gayathri, B.R.; Deshpande, N.G.; Kim, G.H.; Seo, M.S.; Lee, Y.P. Electron irradiation effects on electrical and optical properties of sol-gel prepared ZnO films. *J. Appl. Phys.* **2010**, *108*, 043513.
55. Ohyama, M.; Kozuka, H.; Yoko, T. Sol-gel preparation of transparent and conductive aluminum-doped zinc oxide films with highly preferential crystal orientation. *J. Am. Ceram. Soc.* **1998**, *81*, 1622–1632.

56. Lee, S.H.; Kim, J.H.; Shim, T.H.; Park, J.G. Effect of interface thickness on power conversion efficiency of polymer photovoltaic cells. *Electron. Mater. Lett.* **2009**, *5*, 47–50.
57. Lattante, S.; Perulli, A.; Anni, M. Study of the series resistance evolution in organic solar cells by use of the Lambert W function. *Synth. Met.* **2011**, *161*, 949–952.
58. Chang, J.; Lin, Z.; Zhu, C.; Chi, C.; Zhang, J.; Wu, J. Solution-processed LiF-doped ZnO films for high performance low temperature field effect transistors and inverted solar cells. *ACS Appl. Mater. Interfaces* **2013**, *5*, 6687–6693.
59. Du, X.; He, D.; Xiao, Z.; Ding, L. The double-edged function of UV light in polymer solar cells with an inverted structure. *Synth. Met.* **2012**, *162*, 2302–2306.
60. Girolamo, V.B.M.; Antonucci, V.; Aricó, A.S. Influence of TiO2 film thickness on the electrochemical behaviour of dye-sensitized solar cells. *Int. J. Electrochem. Sci.* **2011**, *6*, 3375.
61. Sakohara, S.; Ishida, M.; Anderson, M.A. Visible luminescence and surface properties of nanosized ZnO colloids prepared by hydrolyzing Zinc acetate. *J. Phys. Chem. B* **1998**, *102*, 10169–10175,
62. Monticone, S.; Tufeu, R.; Kanaev, A.V. Complex nature of the UV and visible fluorescence of colloidal ZnO nanoparticles. *J. Phys. Chem. B* **1998**, *102*, 2854–2862.
63. Peng, R.; Yang, F.; Ouyang, X.; Liu, Y.; Kim, Y.S.; Ge, Z. Enhanced photovoltaic performance of inverted polymer solar cells by tuning the structures of titanium dioxide. *Thin Solid Films* **2013**, *545*, 424–428.
64. Kuwabara, T.; Sugiyama, H.; Yamaguchi, T.; Takahashi, K. Inverted type bulk-heterojunction organic solar cell using electrodeposited titanium oxide thin films as electron collector electrode. *Thin Solid Films* **2009**, *517*, 3766–3769.
65. Kim, J.Y.; Kim, S.H.; Lee, H.H.; Lee, K.; Ma, W.; Gong, X.; Heeger, A.J. New architecture for high-efficiency polymer photovoltaic cells using solution-based titanium oxide as an optical spacer. *Adv. Mater.* **2006**, *18*, 572–576.
66. Hadipour, A.; Maller, R.; Heremans, P. Room temperature solution-processed electron transport layer for organic solar cells. *Org. Electron.* **2013**, *14*, 2379–2386.
67. Liang, W.W.; Chang, C.Y.; Lai, Y.Y.; Cheng, S.W.; Chang, H.H.; Lai, Y.Y.; Cheng, Y.J.; Wang, C.L.; Hsu, C.S. Formation of nanostructured fullerene interlayer through accelerated self-assembly and cross-linking of trichlorosilane moieties leading to enhanced efficiency of photovoltaic cells. *Macromolecules* **2013**, *46*, 4781–4789.
68. Savva, A.; Neophytou, M.; Koutsides, C.; Kalli, K.; Choulis, S.A. Synergistic effects of buffer layer processing additives for enhanced hole carrier selectivity in inverted organic photovoltaics. *Org. Electron.* **2013**, *14*, 3123–3130.
69. Lu, H.; Akgun, B.; Russell, T.P. Morphological characterization of a low-bandgap crystalline polymer:PCBM bulk heterojunction solar cells. *Adv. Energy Mater.* **2011**, *1*, 870–878.
70. Waldauf, C.; Scharber, M.C.; Schilinsky, P.; Hauch, J.A.; Brabec, C.J. Physics of organic bulk heterojunction devices for photovoltaic applications. *J. Appl. Phys.* **2006**, *99*, 104503.

71. Steim, R.; Choulis, S.A.; Schilinsky, P.; Brabec, C.J. Interface modification for highly efficient organic photovoltaics. *Appl. Phys. Lett.* **2008**, *92*, 093303.
72. Lilliedal, M.R.; Medford, A.J.; Madsen, M.V.; Norrman, K.; Krebs, F.C. The effect of post-processing treatments on inflection points in current–voltage curves of roll-to-roll processed polymer photovoltaics. *Sol. Energy Mater. Sol. Cells* **2010**, *94*, 2018–2031.
73. Kim, J.; Kim, G.; Choi, Y.; Lee, J.; Heum Park, S.; Lee, K. Light-soaking issue in polymer solar cells: Photoinduced energy level alignment at the sol-gel processed metal oxide and indium tin oxide interface. *J. Appl. Phys.* **2012**, *111*, 114511.
74. Choi, H.; Lee, J.; Lee, W.; Ko, S.J.; Yang, R.; Lee, J.C.; Woo, H.Y.; Yang, C.; Kim, J.Y. Acid-functionalized fullerenes used as interfacial layer materials in inverted polymer solar cells. *Org. Electron.* **2013**, *14*, 3138–3145.
75. Goh, C.; Scully, S.R.; McGehee, M.D. Effects of molecular interface modification in hybrid organic-inorganic photovoltaic cells. *J. Appl. Phys.* **2007**, *101*, 114503.
76. Hsieh, C.H.; Cheng, Y.J.; Li, P.J.; Chen, C.H.; Dubosc, M.; Liang, R.M.; Hsu, C.S. Highly efficient and stable inverted polymer solar cells integrated with a cross-linked fullerene material as an interlayer. *J. Am. Chem. Soc.* **2010**, *132*, 4887–4893.
77. Chang, C.Y.; Wu, C.E.; Chen, S.Y.; Cui, C.; Cheng, Y.J.; Hsu, C.S.; Wang, Y.L.; Li, Y. Enhanced performance and stability of a polymer solar cell by incorporation of vertically aligned, cross-linked fullerene nanorods. *Angew. Chem. Int. Ed.* **2011**, *50*, 9386–9390.
78. Cheng, Y.J.; Hsieh, C.H.; He, Y.; Hsu, C.S.; Li, Y. Combination of indene-C60 bis-adduct and cross-linked fullerene interlayer leading to highly efficient inverted polymer solar cells. *J. Am. Chem. Soc.* **2010**, *132*, 17381–17383.
79. Cheng, Y.J.; Cao, F.Y.; Lin, W.C.; Chen, C.H.; Hsieh, C.H. Self-assembled and cross-linked fullerene interlayer on titanium oxide for highly efficient inverted polymer solar cells. *Chem. Mater.* **2011**, *23*, 1512–1518.
80. Hasegawa, T.; Miura, S.; Moriyama, T.; Kimura, T.; Takaya, I.; Osato, Y.; Mizutani, H. Novel Electron-Injection Layers for Top-Emission OLEDs. *Dig. Tech. Papers—Soc. Inf. Disp. Int. Symp.* **2004**, *35*, 154.
81. Liao, H.H.; Chen, L.M.; Xu, Z.; Li, G.; Yang, Y. Highly efficient inverted polymer solar cell by low temperature annealing of $Cs_2CO_3$ interlayer. *Appl. Phys. Lett.* **2008**, *92*, 173303.
82. Xin, Y.; Wang, Z.; Xu, L.; Xu, X.; Liu, Y.; Zhang, F. UV-Ozone treatment on $Cs_2CO_3$ interfacial layer for the improvement of inverted polymer solar cells. *J. Nanomater.* **2013**, *2013*, doi:10.1155/2013/104825.
83. Barbot, A.; Lucas, B.; di Bin, C.; Ratier, B.; Aldissi, M. Optimized inverted polymer solar cells incorporating $Cs_2CO_3$-doped C60 as electron transport layer. *Appl. Phys. Lett.* **2013**, *102*, 193305.
84. Cheng, G.; Tong, W.Y.; Low, K.H.; Che, C.M. Thermal-annealing-free inverted polymer solar cells using ZnO/$Cs_2CO_3$ bilayer as electron-selective layer. *Sol. Energy Mater. Sol. Cells* **2012**, *103*, 164–170.

85. Barbot, A.; Bin, C.; Lucas, B.; Ratier, B.; Aldissi, M. N-type doping and thermoelectric properties of co-sublimed cesium-carbonate-doped fullerene. *J. Mater. Sci.* **2013**, *48*, 2785–2789.
86. Yang, H.B.; Dong, Y.Q.; Wang, X.; Khoo, S.Y.; Liu, B.; Li, C.M. Graphene quantum dots-incorporated cathode buffer for improvement of inverted polymer solar cells. *Sol. Energy Mater. Sol. Cells* **2013**, *117*, 214–218.
87. Wiranwetchayan, O.; Liang, Z.; Zhang, Q.; Cao, G.; Singjai, P. The role of oxide thin layer in inverted structure polymer solar cells. *Mater. Sci. Appl.* **2011**, *2*, 1697–1701.
88. Lenzmann, F.; Krueger, J.; Burnside, S.; Brooks, K.; Grätzel, M.; Gal, D.; Rühle, S.; Cahen, D. Surface photovoltage spectroscopy of dye-sensitized solar cells with TiO2, Nb2O5, and SrTiO3 nanocrystalline photoanodes: Indication for electron injection from higher excited dye states. *J. Phys. Chem. B* **2001**, *105*, 6347–6352,
89. Li, Z.; Dong, Q.; Li, Y.; Xu, B.; Deng, M.; Pei, J.; Zhang, J.; Chen, F.; Wen, S.; Gao, Y.; Tian, W. Design and synthesis of solution processable small molecules towards high photovoltaic performance. *J. Mater. Chem.* **2011**, *21*, 2159–2168.
90. Wu, Y.; Zhang, W.; Li, X.; Min, C.; Jiu, T.; Zhu, Y.; Dai, N.; Fang, J. Solution-processed hybrid cathode interlayer for inverted organic solar cells. *ACS Appl. Mater. Interfaces* **2013**, *5*, 10428–10432.
91. Jin, S.H.; Jun, G.H.; Hong, S.H.; Jeon, S. Conformal coating of titanium suboxide on carbon nanotube networks by atomic layer deposition for inverted organic photovoltaic cells. *Carbon* **2012**, *50*, 4483–4488.
92. Kohlstadt, M.; Grein, M.; Reinecke, P.; Kroyer, T.; Zimmermann, B.; Würfel, U. Inverted ITO- and PEDOT:PSS-free polymer solar cells with high power conversion efficiency. *Sol. Energy Mater. Sol. Cells* **2013**, *117*, 98–102.
93. Oo, T.Z.; Chandra, R.D.; Yantara, N.; Prabhakar, R.R.; Wong, L.H.; Mathews, N.; Mhaisalkar, S.G. Zinc Tin Oxide (ZTO) electron transporting buffer layer in inverted organic solar cell. *Org. Electron.* **2012**, *13*, 870–874.
94. Kim, J.B.; Kim, C.S.; Kim, Y.S.; Loo, Y.L. Oxidation of silver electrodes induces transition from conventional to inverted photovoltaic characteristics in polymer solar cells. *Appl. Phys. Lett.* **2009**, *95*, 183301.
95. Chen, S.; Zhao, Y.; Cheng, G.; Li, J.; Liu, C.; Zhao, Z.; Jie, Z.; Liu, S. Improved light outcoupling for phosphorescent top-emitting organic light-emitting devices. *Appl. Phys. Lett.* **2006**, *88*, 153517.
96. Tao, C.; Ruan, S.; Zhang, X.; Xie, G.; Shen, L.; Kong, X.; Dong, W.; Liu, C.; Chen, W. Performance improvement of inverted polymer solar cells with different top electrodes by introducing a MoO3 buffer layer. *Appl. Phys. Lett.* **2008**, *93*, 193307.
97. Tao, C.; Ruan, S.; Xie, G.; Kong, X.; Shen, L.; Meng, F.; Liu, C.; Zhang, X.; Dong, W.; Chen, W. Role of tungsten oxide in inverted polymer solar cells. *Appl. Phys. Lett.* **2009**, *94*, 043311.

98. Servaites, J.D.; Ratner, M.A.; Marks, T.J. Organic solar cells: A new look at traditional models. *Energy Environ. Sci.* **2011**, *4*, 4410–4422.
99. Carter, S.A.; Angelopoulos, M.; Karg, S.; Brock, P.J.; Scott, J.C. Polymeric anodes for improved polymer light-emitting diode performance. *Appl. Phys. Lett.* **1997**, *70*, 2067–2069.
100. Kemerink, M.; Timpanaro, S.; de Kok, M.M.; Meulenkamp, E.A.; Touwslager, F. J. Three-dimensional inhomogeneities in PEDOT:PSS films. *J. Phys. Chem. B* **2004**, *108*, 18820–18825.
101. Ionescu-Zanetti, C.; Mechler, A.; Carter, S.; Lal, R. Semiconductive polymer blends: Correlating structure with transport properties at the nanoscale. *Adv. Mater.* **2004**, *16*, 385–389.
102. Stubhan, T.; Oh, H.; Pinna, L.; Krantz, J.; Litzov, I.; Brabec, C.J. Inverted organic solar cells using a solution processed aluminum-doped zinc oxide buffer layer. *Org. Electron.* **2011**, *12*, 1539–1543.
103. Lipomi, D.J.; Tee, B.C.K.; Vosgueritchian, M.; Bao, Z. Stretchable organic solar cells. *Adv. Mater.* **2011**, *23*, 1771–1775.
104. Baek, W.H.; Choi, M.; Yoon, T.S.; Lee, H.H.; Kim, Y.S. Use of fluorine-doped tin oxide instead of indium tin oxide in highly efficient air-fabricated inverted polymer solar cells. *Appl. Phys. Lett.* **2010**, *96*, 133506.
105. Heo, S.W.; Baek, K.H.; Lee, T.H.; Lee, J.Y.; Moon, D.K. Enhanced performance in inverted polymer solar cells via solution process: Morphology controlling of PEDOT:PSS as anode buffer layer by adding surfactants. *Org. Electron.* **2013**, *14*, 1629–1635.
106. Lim, F.J.; Ananthanarayanan, K.; Luther, J.; Ho, G.W. Influence of a novel fluorosurfactant modified PEDOT:PSS hole transport layer on the performance of inverted organic solar cells. *J. Mater. Chem.* **2012**, *22*, 25057–25064.
107. Gupta, D.; Wienk, M.M.; Janssen, R.A.J. Efficient polymer solar cells on opaque substrates with a laminated PEDOT:PSS top electrode. *Adv. Energy Mater.* **2013**, *3*, 782–787.
108. Suh, Y.; Lu, N.; Lee, S.H.; Chung, W.S.; Kim, K.; Kim, B.; Ko, M.J.; Kim, M.J. Degradation of a thin Ag layer induced by poly(3,4-ethylenedioxythiophene):polystyrene sulfonate in a transmission electron microscopy specimen of an inverted polymer solar cell. *ACS Appl. Mater. Interfaces* **2012**, *4*, 5118–5124.
109. Meyer, J.; Hamwi, S.; Bülow, T.; Johannes, H.H.; Riedl, T.; Kowalsky, W. Highly efficient simplified organic light emitting diodes. *Appl. Phys. Lett.* **2007**, *91*, 113506.
110. Wang, F.; Qiao, X.; Xiong, T.; Ma, D. The role of molybdenum oxide as anode interfacial modification in the improvement of efficiency and stability in organic light-emitting diodes. *Org. Electron.* **2008**, *9*, 985–993.
111. Tokito, S.; Noda, K.; Taga, Y. Metal oxides as a hole-injecting layer for an organic electroluminescent device. *J. Phys. D* **1996**, *29*, 2750–2753.
112. Yin, Z.; Zheng, Q.; Chen, S.C.; Cai, D. Interface control of semiconducting metal oxide layers for efficient and stable inverted polymer solar cells with open-circuit voltages over 1.0 volt. *ACS Appl. Mater. Interfaces* **2013**, *5*, 9015–9025.

113. Chambon, S.; Derue, L.; Lahaye, M.; Pavageau, B.; Hirsch, L.; Wantz, G. MoO3 thickness, thermal annealing and solvent annealing effects on inverted and direct polymer photovoltaic solar cells. *Materials* **2012**, *5*, 2521–2536.
114. Ng, A.; Liu, X.; To, C.H.; Djurišić, A.B.; Zapien, J.A.; Chan, W.K. Annealing of P3HT:PCBM blend film—The effect on its optical properties. *ACS Appl. Mater. Interfaces* **2013**, *5*, 4247–4259.
115. Dupont, S.R.; Oliver, M.; Krebs, F.C.; Dauskardt, R.H. Interlayer adhesion in roll-to-roll processed flexible inverted polymer solar cells. *Sol. Energy Mater. Sol. Cells* **2012**, *97*, 171–175.
116. Kundu, S.; Gollu, S.R.; Sharma, R.; G, S.; Ashok, A.; Kulkarni, A.; Gupta, D. Device stability of inverted and conventional bulk heterojunction solar cells with MoO3 and ZnO nanoparticles as charge transport layers. *Org. Electron.* **2013**, *14*, 3083–3088.
117. Elumalai, N.K.; Saha, A.; Vijila, C.; Jose, R.; Jie, Z.; Ramakrishna, S. Enhancing the stability of polymer solar cells by improving the conductivity of the nanostructured MoO3 hole-transport layer. *Phys. Chem. Chem. Phys.* **2013**, *15*, 6831–6841.
118. Pan, H.; Zuo, L.; Fu, W.; Fan, C.; Andreasen, B.; Jiang, X.; Norrman, K.; Krebs, F.C.; Chen, H. MoO3–Au composite interfacial layer for high efficiency and air-stable organic solar cells. *Org. Electron.* **2013**, *14*, 797–803.
119. Lampande, R.; Kim, G.W.; Boizot, J.; Kim, Y.J.; Pode, R.; Kwon, J.H. A highly efficient transition metal oxide layer for hole extraction and transport in inverted polymer bulk heterojunction solar cells. *J. Mater. Chem. A* **2013**, *1*, 6895–6900.
120. Stubhan, T.; Li, N.; Luechinger, N.A.; Halim, S.C.; Matt, G.J.; Brabec, C.J. High fill factor polymer solar cells incorporating a low temperature solution processed WO3 hole extraction layer. *Adv. Energy Mater.* **2012**, *2*, 1433–1438.
121. Zilberberg, K.; Trost, S.; Meyer, J.; Kahn, A.; Behrendt, A.; LÃijtzenkirchen-Hecht, D.; Frahm, R.; Riedl, T. Inverted organic solar cells with sol-gel processed high work-function vanadium oxide hole-extraction layers. *Adv. Funct. Mater.* **2011**, *21*, 4776–4783.
122. Yu, W.; Shen, L.; Ruan, S.; Meng, F.; Wang, J.; Zhang, E.; Chen, W. Performance improvement of inverted polymer solar cells thermally evaporating nickel oxide as an anode buffer layer. *Sol. Energy Mater. Sol. Cells* **2012**, *98*, 212–215.
123. Lim, D.C.; Kim, Y.T.; Shim, W.H.; Jang, A.Y.; Lim, J.H.; Kim, Y.D.; Jeong, Y.; Kim, Y.D.; Lee, K.H. Wet-chemically prepared NiO layers as hole transport layer in the inverted organic solar cell. *Bull. Korean Chem. Soc.* **2011**, *32*, 1067–1070.
124. Huang, J.S.; Chou, C.Y.; Lin, C.F. Efficient and air-stable polymer photovoltaic devices with WO3-V2O5 mixed oxides as anodic modification. *IEEE Electron Device Lett.* **2010**, *31*, 332–334.
125. Shelton, S.W.; Chen, T.L.; Barclay, D.E.; Ma, B. Solution-processable triindoles as hole selective materials in organic solar cells. *ACS Appl. Mater. Interfaces* **2012**, *4*, 2534–2540.

126. Liu, J.; Xue, Y.; Gao, Y.; Yu, D.; Durstock, M.; Dai, L. Hole and electron extraction layers based on graphene oxide derivatives for high-performance bulk heterojunction solar cells. *Adv. Mater.* **2012**, *24*, 2228–2233.
127. Allen, M.J.; Tung, V.C.; Kaner, R.B. Honeycomb carbon: A review of graphene. *Chem. Rev.* **2010**, *110*, 132–145.
128. Yao, K.; Chen, L.; Chen, X.; Chen, Y. Self-organized hole transport layers based on polythiophene diblock copolymers for inverted organic solar cells with high efficiency. *Chem. Mater.* **2013**, *25*, 897–904.
129. Greiner1, M.T.; Lu, Z.H. Thin-film metal oxides in organic semiconductor devices: Their electronic structures, work functions and interfaces. *NPG Asia Mater.* **2013**, *5*, e55.
130. Xie, F.; Choy, W.C.H. Hydrogen metal oxide bronzes for efficient hole transport layers. *SPIE Newsroom* **2013**, doi:10.1117/2.1201311.005133.
131. Stubhan, T.; Ameri, T.; Salinas, M.; Krantz, J.; Machui, F.; Halik, M.; Brabec, C.J. High shunt resistance in polymer solar cells comprising a MoO3 hole extraction layer processed from nanoparticle suspension. *Appl. Phys. Lett.* **2011**, *98*, 253308.
132. Choi, H.; Kim, B.; Ko, M.J.; Lee, D.K.; Kim, H.; Kim, S.H.; Kim, K. Solution processed {WO3} layer for the replacement of PEDOT:PSS layer in organic photovoltaic cells. *Org. Electron.* **2012**, *13*, 959–968.
133. Li, N.; Stubhan, T.; Luechinger, N.A.; Halim, S.C.; Matt, G.J.; Ameri, T.; Brabec, C.J. Inverted structure organic photovoltaic devices employing a low temperature solution processed {WO3} anode buffer layer. *Org. Electron.* **2012**, *13*, 2479–2484.
134. Li, N.; Stubhan, T.; Baran, D.; Min, J.; Wang, H.; Ameri, T.; Brabec, C.J. Design of the solution-processed intermediate layer by engineering for inverted organic multi junction solar cells. *Adv. Energy Mater.* **2013**, *3*, 301–307.
135. Yip, H.L.; Jen, A.K.Y. Recent advances in solution-processed interfacial materials for efficient and stable polymer solar cells. *Energy Environ. Sci.* **2012**, *5*, 5994–6011.
136. Angmo, D.; Gonzalez-Valls, I.; Veenstra, S.; Verhees, W.; Sapkota, S.; Schiefer, S.; Zimmermann, B.; Galagan, Y.; Sweelssen, J.; Lira-Cantu, M.; *et al*. Low-cost upscaling compatibility of five different ITO-free architectures for polymer solar cells. *J. Appl. Polym. Sci.* **2013**, *130*, 944–954.
137. Voroshazi, E.; Cardinaletti, I.; Uytterhoeven, G.; Shan, L.; Empl, M.; Aernouts, T.; Rand, B.P. Role of electron- and hole-collecting buffer layers on the stability of inverted polymer: Fullerene photovoltaic devices. *IEEE J. Photovolt.* **2014**, *4*, 265–270.
138. Lizin, S.; van Passel, S.; de Schepper, E.; Maes, W.; Lutsen, L.; Manca, J.; Vanderzande, D. Life cycle analyses of organic photovoltaics: A review. *Energy Environ. Sci.* **2013**, *6*, 3136–3149.
139. Espinosa, N.; Hosel, M.; Angmo, D.; Krebs, F.C. Solar cells with one-day energy payback for the factories of the future. *Energy Environ. Sci.* **2012**, *5*, 5117–5132.
140. Espinosa, N.; Garcia-Valverde, R.; Krebs, F.C. Life-cycle analysis of product integrated polymer solar cells. *Energy Environ. Sci.* **2011**, *4*, 1547–1557.

# Section VI: Bio-Organic Electronics

## Chapter 13

## Bio-Organic Electronics—Overview and Prospects for the Future

**Susan Mühl and Beatrice Beyer**

**Abstract:** In recent years, both biodegradable and bio-based electronics have attracted increasing interest, but are also controversially discussed at the same time. Yet, it is not clear whether they will contribute to science and technology or whether they will disappear without major impact. The present review will address several aspects while showing the potential opportunities of bio-organic electronics. An overview about the complex terminology of this emerging field is given and test methods are presented which are used to evaluate the biodegradable properties. It will be shown that the majority of components of organic electronics can be substituted by biodegradable or bio-based materials. Moreover, application scenarios are presented where bio-organic materials have advantages compared to conventional ones. A variety of publications are highlighted which encompass typical organic devices like organic light emitting diodes, organic solar cells and organic thin film transistors as well as applications in the field of medicine or agriculture.

Reprinted from *Electronics*. Cite as: Mühl, S.; Beyer, B. Bio-Organic Electronics—Overview and Prospects for the Future. *Electronics* **2014**, *3*, 444-461.

### 1. Introduction

Until the 1930s, plastics were almost exclusively fabricated from regrowing resources [1]. Only since the end of the Second World War have raw material sources of non-renewable fossil materials, such as petroleum and natural gas, been generally used. However, within the last 20 years, efforts have continuously increased to enhance the share of bio-based materials in the world of plastics.

Along with the objective to improve the properties of products and to reduce the production cost of materials, the general discussion about greenhouse gases, difficulties in waste management, e.g., the Great Pacific garbage patch in the ocean, and the awareness about the limitation of fossil fuels have contributed considerably to the revived interest and increasing implementation of bio-plastics.

The following paper presents a comprehensive overview of bio-organic electronics and their potential to enable easy waste disposal. At first, essential terms are defined and correlated with standards while summarizing various testing procedures to assess the hazardous risk of potentially biodegradable electronics with regard to the environment.

The principle structure of typical organic electronics is discussed with regard to their separate components. Most progress has so far been achieved in respect to the polymer carrier substrate, which will surely foster further innovation in this novel field. Besides, impressive achievements have

also been demonstrated for the charge carrier transporting organic semiconductors itself. Hence, semi or fully biodegradable devices will be presented and their performance is discussed in more detail. Finally, an outlook to the future market is given.

## 2. Policies and Guidelines

### *2.1. Definitions and Standards*

In recent years, the syllable "*bio*" has become a powerful attribute to attract public attention for designated "green" processes. "*Bio*" is generally used in a broad context which often complicates communication between experts and beginners in this interesting field. Thus, in the following paragraph the use of these common terms shall be clarified in context to this paper.

Products are considered as *bio-based* when they are made of materials derived from living (or once living) organisms. Often they are denoted as biomaterials—but this term is also widely used for any interaction between biological and non-biological systems. Bio-based materials are often biodegradable with a few exceptions (mainly composites where the degradable compound is combined with non-degradable materials). The term *biodegradability*, however, is a more precisely certified performance characteristic. According to EN 13432, compounds are biodegradable if a share of more than 90% converts to $H_2O$, $CO_2$ and biomass under defined temperature, humidity, and oxygen conditions within 180 days in the presence of microorganisms or fungi. However, biodegradable plastics are not inevitably made of bio-based, renewable materials. There are several examples where fossil resources are used, and a closer look into the production volume of biodegradable materials depending on their raw material origins (Figure 1) shows that the share of both types is nearly equal. Thus, the property of biodegradability is only linked to the chemical structure and not in any way related to its origin. In nature, the biodegradation occurs either aerobically or anaerobically. In the latter process, the material is converted without oxygen to methane, $CO_2$, $H_2O$, energy, and biomass [2]. In the presence of oxygen (aerobic), methane is not formed.

**Figure 1.** Global market of bio-based/non-biodegradable (green) and biodegradable (grey) plastics in 2012 with a total volume of 1.4 million tons [3].

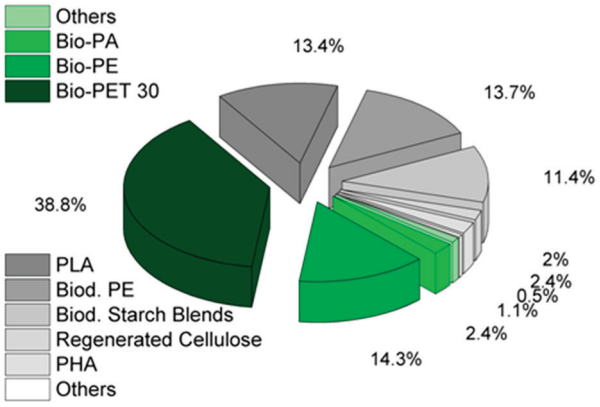


Depending on the molecular weight of the compound, biodegradation begins with chain cleavage by enzymes (e.g., lipases and esterases) released by microorganisms. This mainly occurs on the surface of the biodegradable compound since the enzymes are too large to diffuse into the bulk

material. After the cleavage, these fragments can be absorbed by the cells of the microorganisms. During that metabolism process, the cells can gain energy from this mineralization process [2,4].

Along with the European standard 13432, there is a variety of other standards all over the globe available (ISO 17088, ASTM D 6400 in North America, GreenPla in Japan). The ISO 17088, EN 13432 and ASTM D 6400 define the requirements concerning packaging and choice of materials being considered as "biodegradable" in industrial composting facilities. If a material passes the tests necessary to achieve this status, additional tests might be necessary to get the final product registration according to ISO 17088. After this procedure has been applied, it ensures that nonconforming, potentially toxic additives, colors and package goods are not used, and the products are allowed to have labels as depicted in Figure 2. The requirements of these standards are very strict, which is emphasized by the fact that freshly green leaves or wooden branches as thick as fingers would fail in these tests. Thus, polymeric materials only pass this test when they are sufficiently thin to quickly decompose.

**Figure 2.** Selection of logos which indicate the biodegradability of products, e.g., as used in Belgium (**a**), North America (**b**), Finland (**c**), Japan (**d**), Catalonia (**e**), Germany (**f**), and Italy (**g**).

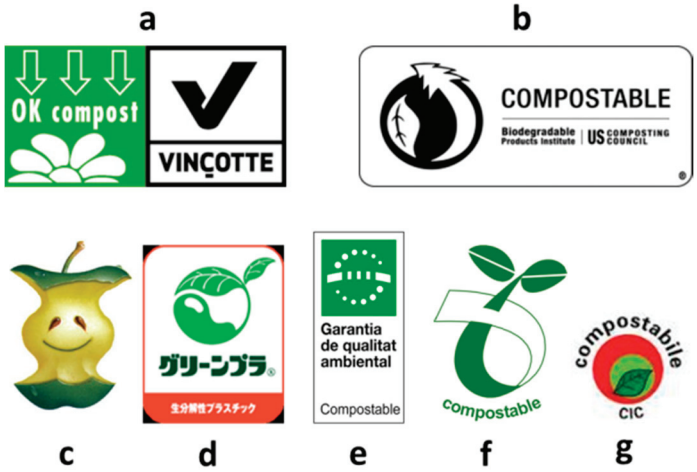


*2.2. Environmental Impact and Biotoxicity*

Sustainable development and economics is one of the greatest challenges mankind has to face in the 21st century [5]. We have to rethink the character and design of our technologies, products and how they are produced. This has to result in changes to marketing patterns, distribution, usage and recycling.

The recycling of discarded products could be a way to save materials and energy. However, a basic requirement of recycling is the collection of the used products. Most (mobile) consumer electronics are small and the majority of people will rather throw them into the waste than collecting and bringing them back to collection facilities [6]. This behavior will show a negative impact particularly in countries with inadequate waste regulations. Thus, the development of non-toxic, biodegradable electronics would be a step forward to diminish the problem.

In order to prevent any negative impact of organic chemicals which are supposed to be introduced into the environment, it is necessary and important to duly assess the environmental and toxicological

safety of these materials. Typically, the material itself as well as its potentially resistant residues (after biodegradation) has to be characterized [4]. Important test procedures comprise the "water-soluble intermediates-Daphnia test" and the "plant growth test". The former one is of great importance because water-soluble intermediates may enter the groundwater and are easily absorbed afterwards by other organisms. The test has to be carried out in accordance to DIN 38412 where 10 water fleas are exposed to different concentrations of the designated pollutant at 20 °C and pH 7.0. In addition, a control stock solution is prepared where the testing material degrades enzymatically. After 24 h, the remaining number of swimming water fleas is evaluated. With this relation of concentration and living fleas, the toxicity can be evaluated.

The plant growth test studies the eco-toxicity of materials and is described in EN 13431, annex E. There, the seedling growth behavior of four plant types (wheat, summer barley, mustard, and mung bean) is investigated both with treated and control soil. Subsequently, the harvest yield is correlated with the different soil mixtures. After these tests have been passed successfully, further experimentation involving higher organisms such as earth worm, rabbits, guinea pig and rats will follow.

According to the chemical structure of classic organic semiconductors, the water solubility will be very low for the majority of this material class due to their extended π-system and the lack of highly polar functional groups. At the same time, there are plenty of aromatic compounds, structurally very similar to organic semiconductors, which are classified as toxic. Thus, it is mandatory to carefully investigate the hazardous impact of each designated "biodegradable" compound.

## 3. Components

Along with organic semiconductors, organic electronics comprise various other components like carrier substrates, electrodes, dielectrics, adhesives, and the organic semiconductor itself. Here, the term "*organic*" is considered according to the chemical definition, thus being mainly composed of hydrogen and carbon. Depending on their use, organic semiconductors are often sensitive against water and moisture and show an increasing number of defect sites over the operational lifetime. Therefore, the organic layers are protected with an encapsulation material (could be the same as the carrier substrate) and an adhesive as shown in Figure 3. It is often recommended that both the adhesive as well as the encapsulation material have to feature a water vapor transmission rate (WVTR) smaller than $10^{-5}$ g/(m$^2$ day) [7]. The controversial requirements of being insensitive against water or oxygen and biodegradable at the same time are very challenging. Thus, for appropriate discussion, each component is described separately.

Depending on the device functionality, the organic device stack is composed of a certain material layer sequence which can result in organic light emitting diodes (OLEDs), organic solar cells (OSCs) or organic thin film transistors (OTFTs). Organic device stacks of these three types are represented in Figure 3.

The layer structures of OLEDs and OSCs are very similar. In the common bottom structure where a transparent anode on a transparent substrate is used, the device fabrication may start with deposition of the electrode on the substrate material. A barrier free charge carrier transport from the anode to the hole transport layer (HTL) is ensured by limiting the difference of the highest occupied molecular orbitals (HOMOs) of the single materials to less than 0.3 eV for the interfaces [8]. Similar requirements exist between HTL and the functional layer, *i.e.*, absorption layer (AL) for OSCs and

emission layer (EL) for OLEDs. In both cases, it is necessary to prevent the electrons from entering the HTL and, *vice versa*, the holes from entering the ETL. This can be realized by implementing materials with favorable energy levels providing transport barriers that block either electrons or holes. On the electron transporting side from AL to ETL, the lowest unoccupied molecular orbitals (LUMOs) of the single materials are used and have to align with the work function of the cathode.

**Figure 3.** Schematic illustration of (**a**) the cross section of an organic device consisting of an organic device stack deposited on a substrate, encapsulated with a barrier material that is fixed with an adhesive (Adh). The composition of the organic device stack defines the properties of an OSC (**b**), an OLED (**c**), or an OTFT (**d**).

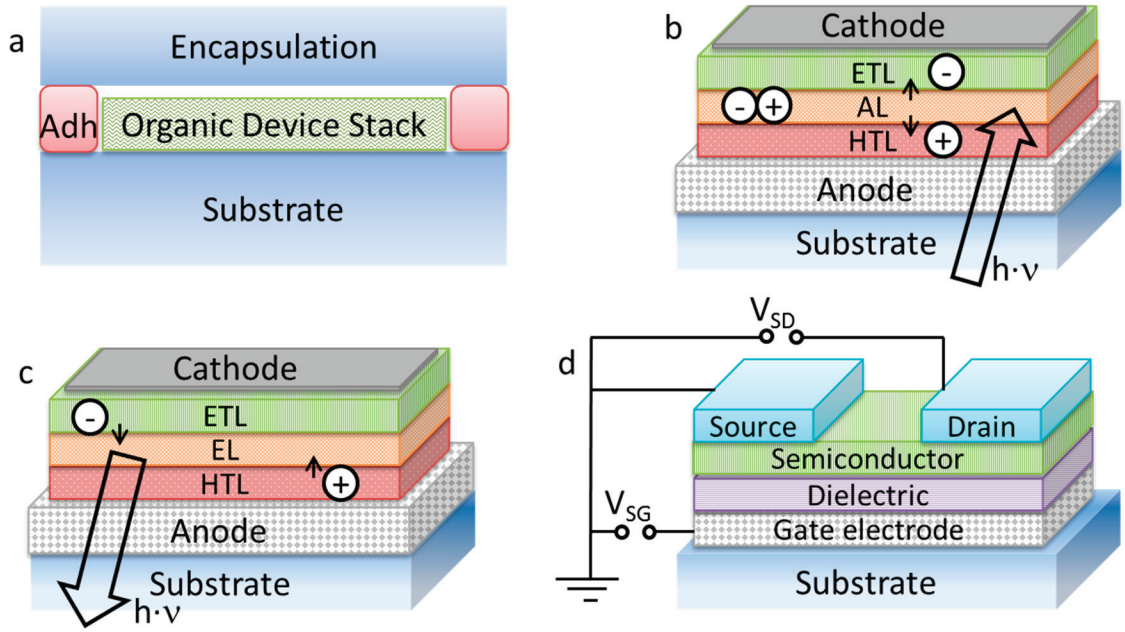


The value of the charge carrier mobility of organic semiconductors has to be high for all organic electronic devices; however, achieving a sufficiently high value is even more important when used in OTFTs. Usually, for organic semiconductors, the hole mobility is larger than the electron mobility. Hence, depending on the electrode polarization, holes are accumulated on the semiconductor/dielectric interface after a voltage is applied between gate and source. Due to the voltage between drain and source, the majority of charge carriers are able to move along the interface.

### *3.1. Substrate Materials*

One of the most decisive properties of organic electronics to successfully enter the future market is their inherent flexibility due to the weak intermolecular forces of organic semiconductors. Along with the ductility allowing new application scenarios, also the possibility to use potentially low cost roll-to-roll processes will enable use of the application in consumer electronics. By defining the mechanical properties and providing certain barrier properties, the substrates highly influence the device lifetime. Conventionally, plastic substrates such as polyethylene terephthalate (PET), polyethylene naphthalate (PEN), polycarbonate (PC), and polyimide (PI) have been widely used. However, decomposition for all these polymer foils may take 30–450 years [9], thus causing a

serious waste problem in some areas of the world. In addition, their production costs are highly dependent on the oil price.

Therefore, new biodegradable, bio-based, flexible and transparent substrates have attracted considerable attention. Depending on their composition, they may derive from earth-abundant renewable materials or still rely on fossil resources. Figures 4 and 5 schematically illustrate the variety of biodegradable plastics.

**Figure 4.** Schematic representation of the diversity of degradable materials.

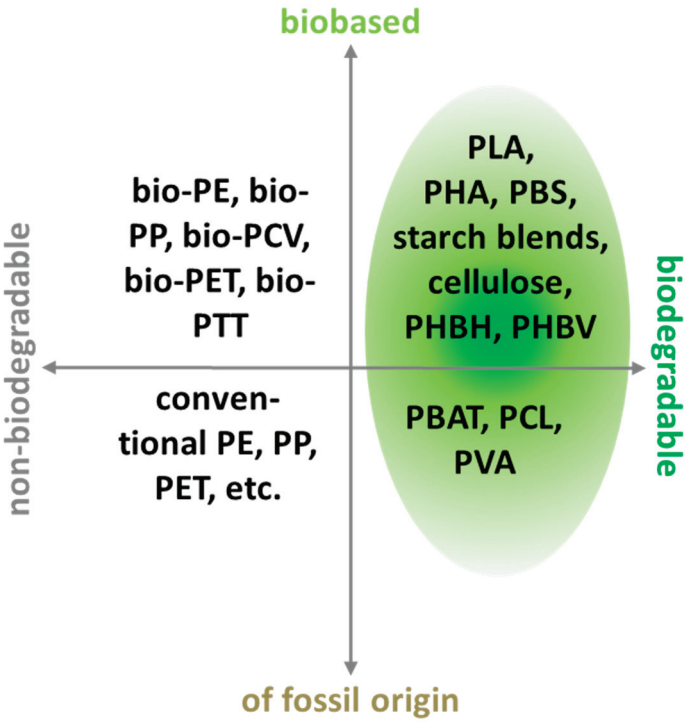


For example, starch is transformed into glucose, which is further used as fermentation feedstock for monomers, e.g., lactic acid for poly lactic acid (PLA) or polyhydroxy alkanoates (PHA) production. Other feedstocks for fermentative monomer production are sucrose, glycerol, or plant oil. Intensive work has been carried out to access cellulose raw materials not only for bioethanol production, but also for different chemical intermediates and monomers such as lactic and succinic acid. Whereas the materials **1**–**7** are derived from these renewable resources, the compounds **8**–**11** originate (partly) from fossil fuels. Aliphatic polyesters (**9**, **10**) are the first completely fossil-based polymers which are biodegradable at the same time. Structures such as polybutylene adipate-co-terephthalate (PBAT) (**8**) represent a mixture of both natural and synthetic origin. The only existing biodegradable polymer with an all-carbon backbone is polyvinyl alcohol (PVA). The main substrate type that has successfully been integrated in organic electronic technology in recent years is cellulose in its various modifications [10–13]. Although the initial roughness of these substrate types is initially challenging, the roughness level could be lowered either by adjusted fabrication parameters or by additional (bio)coatings. Another biodegradable and well investigated polymer for substrate use is poly lactic acid [14]. For further detailed information about this material class, the authors recommend the excellent overview about biodegradable polymers given by Breulmann and co-workers [15].

**Figure 5.** Established biodegradable polymers potentially usable as carrier substrates. Starch originating from potatoes or corn consist of the branched amylopectin (**1**) and linear amylose (**2**). Cellulose (**3**) is structurally similar, but differs from the bonding type between the glucose monomers. Polyhydroxy alkanoates (PHA) (**4**) and polylactic acid (PLA) (**5**) may derive from various sugars, fatty acids or starch. Other typical representatives are polyhydroxybutyrate-co-valerate (PHBV) (**6**) and polyhydroxybutyrate-co-hexanoate (PHBH) (**7**). Polybutylene adipate-co-terephthalate (PBAT) (**8**) is a polymer with aromatic fragments. Polyesters are represented by polycaprolactone (PCL) (**9**), and polybutylene succinate (PBS) (**10**). Polyvinyl alcohol (PVA) (**11**) has a rather simple structure compared to the aforementioned structures.

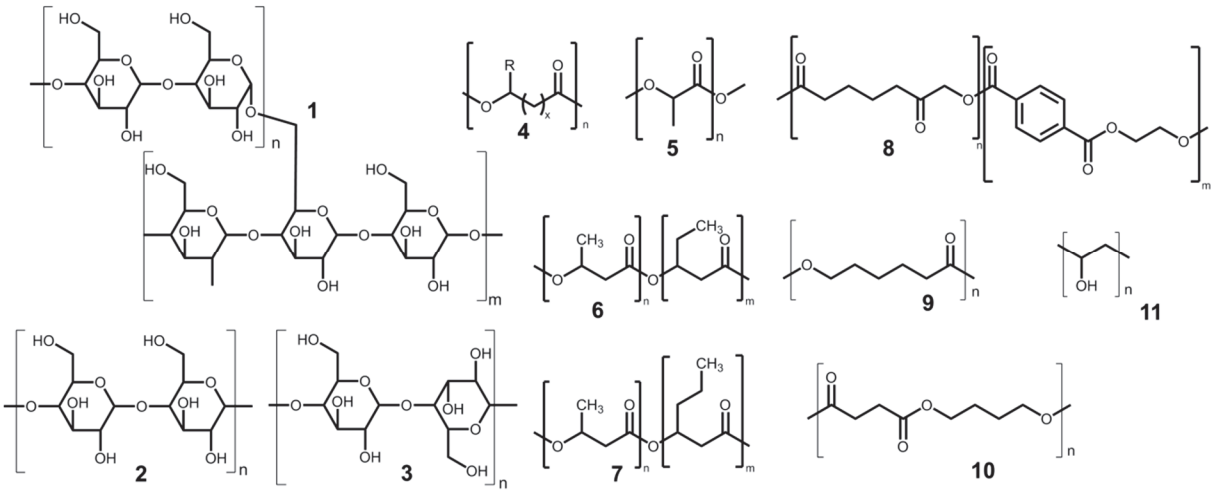


*3.2. Adhesives*

The development of biodegradable adhesives is a very critical issue for achieving biodegradable electronic products. A biodegradable material which is resistant against water appears to be mutually preclusive (exception e.g., shellac). In the subsequent paragraphs, examples are presented which are mainly dedicated for packaging purposes and thus have less distinctive barrier requirements than devices targeted for long term applications like displays—hence, the impermeability against water is usually not evaluated.

In 1996, a biodegradable, polymerizable adhesive consisting of diacrylate with mono- or disaccharide residues was described [16], while later in 2002 an eco-friendly adhesive based on soy protein was developed [17]. In the latter example, additives such as copper naphthenate, o-phenyl phenol or copper-8-quinolate are inserted to improve the moisture stability. An interesting report shows how a biodegradable gecko-inspired tissue adhesive is developed while being resistant to water treatment for a sufficiently long time [18]. Another work combines human serum albumin and organic acid-based crosslinkers with active ester groups, creating solid-liquid type adhesives without the presence of any organic solvents [19].

A water-based conductive adhesive for electrical interconnects and printed circuits was published by Yang and co-workers [20]. This environmentally harmless, but not biodegradable, adhesive based on polyether diol was stable for 1440 h at 85 °C and a relative humidity of 85% and can potentially be used for flexible consumer electronics.

Bettinger *et al.* determined biodegradable adhesives for organic electronics and asserted that they should be highly crystalline, highly hydrophobic and easy to process while maintaining performance under high-salinity environments and at elevated temperatures. Poly-L-lactide turned out to be a promising candidate because it can repel water (and vapour) for several months [21].

While these examples show that a variety of biodegradable adhesives are available and easily accessible, information about their barrier properties and potential applications in organic electronics is still missing.

### *3.3. Organic Semiconductors*

A requisite of organic semiconductors is the existence of a π-conjugated carbon backbone allowing the delocalization of electrons. Along with the delocalization of electrons, also the absorptivity of these molecules increases with the extension of the π-conjugation. Thus, a great variety of natural dyes are existing that can also be considered as organic semiconductors. Such material classes comprise polyenes (like the carotenes), quinones, anthraquinones, indole, pyran and oligopyrrol colorants as well as pteridines, isoquinolines and phenoxazine. Most of them comprise several aromatic structures and functional groups such as hydroxyl-, amine-, imine, or even halide groups. Thus, in order to explore the usage of organic compounds that are both semiconducting and biodegradable, scientists were focusing on these natural dye structures and their derivatives. The most commonly used so far are presented in Figure 6.

**Figure 6.** Chemical structures of biodegradable or biocompatible organic semiconductors (**12**–**19**) and dielectric materials (**20**, **21**).

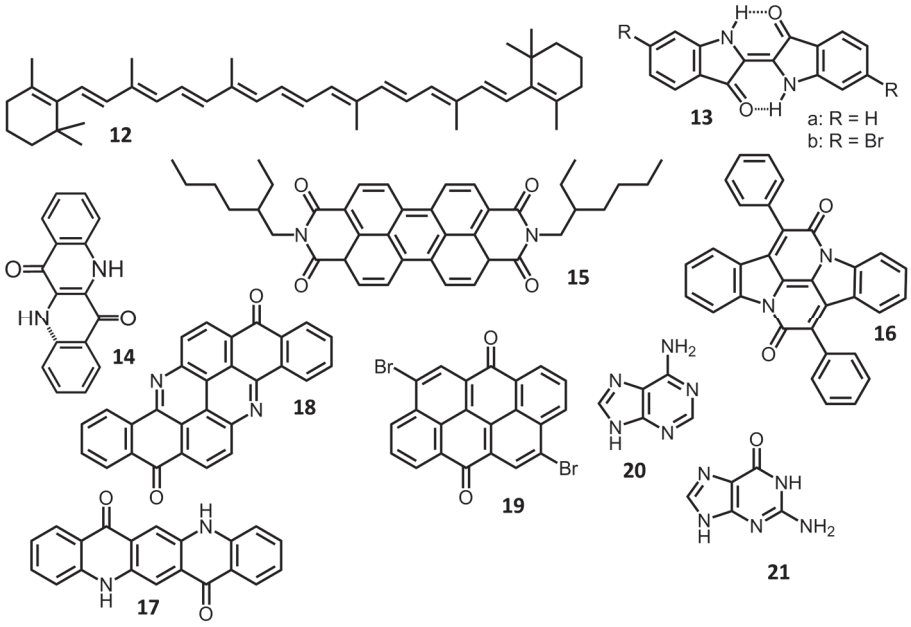


The natural compound melanin has extensively been studied as semiconducting biomaterial. Usually, this compound exhibits low charge carrier mobilities and thus, melanin would not be suitable for electronic devices due to its highly disordered chemical structure [21]. However, evidences have been shown that contradict this hypothesis [22]. Mostert *et al.* has found that free charge carriers

from comproportionation reactions are produced by water absorption. Therefore, melanin is a chemical self-doping polymer and can, in fact, be used for bioelectronics applications.

Furthermore, the focus has turned towards carotenoids as applicable semiconducting materials. The most widely reported examples of these small-molecule polyenes are bixin and β-carotene (**12**). The suitability of biodegradable materials for their utilization in organic electronics, in particular organic thin film transistors, is explored by Irmia-Vladu and his co-workers [21,23–26]. The semiconductors are used as gate-controlled charge transport material between the source and drain electrodes [23]. Additionally, natural chlorophyll, hemin, phenazine, terpenoid molecules and indigo (**13a**) are listed as natural *p*- and *n*-type semiconductors, whereas nature inspired materials such as indanthrene yellow G, brilliant orange RF, epindolidione (**14**), perylene diimide (**15**) and naphthalene diimide are described as biocompatible. These synthetic organic semiconductors have higher field effect mobilities ($4 \times 10^{-4}$–1.5 $cm^2\ V^{-1}{\cdot}s^{-1}$) than the natural organic semiconductors (~$10^{-4}$ $cm^2\ V^{-1}{\cdot}s^{-1}$), are suitable for vacuum processing, highly stable and barely toxic.

In 2011, Głowacki *et al.* evaluated dyes from the material classes acridones, anthraquinones, carotenoids, and indigoids [27] and also determined the charge carrier mobilities in the range of ~$10^{-4}$ $cm^2\ V^{-1}{\cdot}s^{-1}$ when applied in OTFTs. Ambipolar indigoids and quindacridones showed the most promising semiconductor properties due to their long-range order, crystallinity and highly dielectric characteristics. For comparison, the electrical properties are given in Table 1.

**Table 1.** Overview of electrical properties of natural semiconductors comprising the energy levels (HOMO, LUMO), the band gab $E_g$ determined by cyclic voltammetry (CV) or by optical measurements, the charge carrier mobility for holes ($\mu_h$) and electrons ($\mu_e$) as well as the dielectric constant $\varepsilon_r$ [27].

| Material | HOMO (eV) | LUMO (eV) | $E_g$ CV (eV) | $E_g$ Optical (eV) | μ ($cm^2$/VS) | $\varepsilon_r$ |
|---|---|---|---|---|---|---|
| Indigo (**13a**) | −5.5 | −3.8 | 1.7 | 1.7 | $\mu_e = 1 \times 10^{-2}$, $\mu_h = 1 \times 10^{-2}$ | 4.3 |
| Tyrian Purple (**13b**) | −5.8 | −4.0 | 1.8 | 1.9 | $\mu_e = 0.3$ [28], $\mu_h = 0.2$ | 6.2 |
| Cibalackrot (**16**) | −5.6 | −3.5 | 2.1 | 2.0 | $\mu_e = 9.3 \times 10^{-3}$, $\mu_h = 5.3 \times 10^{-3}$ | 4.8 |
| Quinacridone (**17**) | −5.4 | −2.9 | 2.5 | 2.0 | $\mu_h = 0.1$ | 5.2 |
| Vat Yellow 1 (**18**) | −6.3 | −3.6 | 2.7 | 2.3 | $\mu_e = 4.2 \times 10^{-2}$ | 3.8 |
| Vat Orange 3 (**19**) | −6.2 | −3.8 | 2.4 | 2.1 | $\mu_e = 8.8 \times 10^{-3}$ | 3.8 |
| β-carotene (**12**) | −5.84 | −3.54 | NA | 2.3 | $\mu_h = 4 \times 10^{-4}$ | 2.5 |

Along with great electrical properties, thin films of indigo dyes show strong absorption bands (450–730 nm) and are thus highly interesting for other optoelectrical applications like organic solar cells. The thermal and photochemical stability, the low band gap of 1.7–1.8 eV (as tyrian purple **13b**) and high planarity of the molecules are of great advantage for indigo and its derivatives.

While natural organic semiconductors have been evaluated for device fabrication, the classic *n*-type material fullerene $C_{60}$ has been investigated with regard to its toxic nature. For this purpose, $C_{60}$ nanowhiskers have been exposed to macrophage cells and metabolized on average 6 μm long and 660 nm wide (in diameter) $C_{60}$ nanowhiskers. No toxic effects on mammalian cells have been observed [29]. A good overview about toxicity aspects of $C_{60}$ is given by Partha and Conyers, in particular regarding the importance of functionalized fullerenes and its dose dependency [30].

Neither *in vitro* studies on supramolecular structures nor *in vivo* studies on normal "cell" morphology or viability have revealed any toxicity which is in contradiction to listed references [30]. Hence, the toxicity of $C_{60}$ remains under debate.

Additionally, it is noteworthy that the indanthrene dyes biodegrade slowly compared to natural compounds [23], however, perylene diimide and epindolidione show little toxicity, thus, they will not be assigned as "biodegradable" [24,25].

### *3.4. Electrode Materials*

Compared to the components described before, the replacement of conventional electrodes appears to be rather challenging since metals can hardly be metabolized.

The degradation of biocompatible porous silicon nanowire barcodes was shown by Chiappini and co-workers in 2010 [31]. When exposing the barcodes to phosphate buffered saline solution at 20 °C, a complete degradation within 24 h is observed, while the exposure to oxygen plasma resulted in oxidation within 72 h. It has been concluded that the surface influences the degradation rate.

The conductivity of the biological conductor melanin highly depends on its hydration level. Proton conductivity is the mechanism which is responsible for the charge transport. It can be used as thin film for biomedical applications. Synthetic conducting polymers such as polyaniline, polypyrrole, and polythiophene can be used as organic electrode as well, but little is known concerning their biodegradability. Only for PEDOT:PSS does data exist suggesting it is not toxic to living tissue [32].

A good overview about degradable, biocompatible metals for medical applications is, in particular, provided by Hendra Hermawan [33]. The main focus has centred on magnesium- and iron-based alloys. For these examples, the metals degrade in a special physiological environment that is comparable to the human body. The degradation behaviour of Mg, Fe, Mn, and Pd alloys is presented and electrical resistivities ranging from 0.044 $\Omega \cdot mm^2/m$ (Mg) to 0.43 $\Omega \cdot mm^2/m$ (Mn) have been determined.

A comparable article is published by Cheng *et al.* [34]. The suitability of Fe, Mn, Mg, Zn, and W for clinical biomedical applications has been tested and cytotoxic properties have been isolated for manganese and zinc.

### *3.5. Dielectric Materials*

The main function of dielectric materials is to prevent electrical current flow which is needed to insulate different electrical connections. The main requirements for their use in OTFTs are low dielectric losses and leakage currents as well as high breakdown strengths [23,24,26].

Apart from shellac [35], natural dielectrics originating from two material classes have been investigated in 2010. The first group comprises sugar-based small molecules such as fructose or lactose which can be wet-processed from water and/or dimethyl sulfoxide. The second group consisted of various nucleobases like adenine, guanine, cytosine and thymine. Their dielectric properties fulfil the requirements for the use in OTFTs. Nucleobases such as adenine (20) and guanine (21) can easily be purified and evaporated as thin films (up to 2.5 nm) which enable DNA-like sequences [23,24,26]. Moreover, DNA which has been functionalized by a cationic surfactant reaction became soluble in

polar solvents and allowed wet coated thin films. Thus, it can easily be applied as electron blocking layers (EBLs) in OLEDs or as gate dielectrics in OTFTs [23,24,32]. In addition to these materials, polyvinyl acetate which can be cross linked by UV exposure, has been used as gate dielectric, too [21]. Advanced *n*-type organic transistors and light emitting transistors have successfully been built up by using natural silk fibroin, whose degradation lifetime may range from weeks to years [36]. The easily obtainable and inexpensive natural compound chicken albumin is utilized as gate dielectric in OFETs, too [37]. The spin-coated and thermally treated, unmodified material generates high quality thin films for devices with excellent performance. Furthermore, organic thin film transistors implemented in complementary inverters have been presented utilizing spin-coated natural cellulose as high k gate dielectric [38]. The inverters have shown good performance including an excellent switching behavior. Finally, Khor and Chung gave a good overview about the use of different natural materials as dielectrics and discussed the structural and electrical behavior of screen printed, commercially purchased aloe vera gel [39]. In particular, the dependence on the drying temperature, duration and thickness of the thin film on glass substrate is studied.

## 4. Applications and Markets

### *4.1. Consumer Organic Electronics*

In the field of electronics, bio-based materials receive increasing interest because they show potential for having a positive impact on the environment. Already, years ago, IBM investigated bio-based materials like lignin as laminate and demonstrated their potential to save resources [40]. High-tech companies like Samsung and Apple are already using biodegradable components in their electronics as covers for their products such as the Samsung Galaxy S3 or the iPhone 4/4S/5. In addition, a variety of examples have been published where organic electronics have been applied on biodegradable substrates. Zhu and co-workers have used both nanopaper and regenerated cellulose films (RCF) for organic electronics. Both types consist of cellulose nanofibres and differ only in their orientation. As a result of the better scattering properties, an appropriate handling temperature and similar roughness compared to classic PET, green OLEDs have been successfully demonstrated on such substrates [41]. Another work showed that even the deposition of indium tin oxide (ITO) on bacterial cellulose by r.f. sputtering is possible. The resulting OLED device achieved 25% of the reference device performance produced on conventional glass [11]. Although ITO has to be replaced on the long-term time scale, this report shows that common thin film technology can also be applied on biodegradable substrate types with slight adaption of the processing parameters.

Another promising work with bacterial cellulose as carrier substrate demonstrated the proof of concept of developing a dynamic display by using simple electric dopants and inks [12]. With regard to energy storage devices, the conductivity of conventional paper has been increased by depositing carbon nanotubes and silver nanowires [42], whereas cellulose fibers have also been used to improve the mechanical properties of electronically conductive polymers while retaining very high conductivities [43]. Large-area organic electronics on unmodified paper have been fabricated by Barr and co-workers. They have built monolithically integrated OSC on paper with a dimension of $7 \times 7$ cm$^2$ [44]. Although the subcells made on paper achieved lower efficiencies than those fabricated on glass, still a total voltage of 49 V has been realized (compared to 70 V for the sample on

glass). The complete decomposition in water has also been shown for OSC on cellulose nanocrystal substrates, which have achieved efficiency values of 2.7%. However, effects originating from the metal electrodes or the conventional organic semiconductors have not been addressed [9].

In the field of field effect transistors (FETs), flexible devices have been fabricated with cellulose paper as dielectric material and achieved results comparable to conventional PET or glass substrates. Even the application of OTFT on conventional bank notes has been impressively demonstrated [44,45]. With regard to the semiconductor material itself, anthraquinones, perylene bisimides and indigo are applicable as semiconductors in fully "green" OTFTs [16,35].

According to market prediction, the production of biodegradable plastic will increase fivefold from 1102 tons (2010) to 5779 tons by 2016 [3]. On the one hand, a greater availability of biodegradable plastic will increase the research interest in that field resulting in better device performance; on the other hand, the consumer will most likely request more and more green technology. However, it is unlikely that biodegradable organic electronics will enter the market of entertainment electronics where long-term stability is a necessary requirement. The characteristic of biodegradability will be accompanied by short lifetimes due to sensitivity against water and oxygen. However, in the field of smart packaging, this is an advantage due to its intention for single use and fast insertion into the recycling system. At present, the demand for smart packages with sensing and information technology is already continuously rising, though it is very expensive due to used resources.

### *4.2. Medicine*

The need for a healing support is often temporary in the field of medicine [33]. The application of fully biodegradable materials will allow a complete degradation after fulfilling its function which is much better than an additional surgery. Therefore, the use of biodegradable electronics for medical applications like biomedical implant devices for energy harvesting, medical diagnosis, sensing, photonic biomedical devices, tissue engineering scaffolds or drug delivery is highly anticipated [18,19,23,26,31,32,35,46–51]. Benefits for biomedical science, including biocompatible devices, are predicted because of their ability to align to curved, elastic, and soft surfaces. *Biocompatibility* is defined as a sustainable, mutual co-existence of biomaterials and tissues [52]. A comprehensive overview about bio-integrated electronics for medical applications over the last 10 years is given by Koo and co-workers [53].

Biocompatible/biodegradable microelectromechanical systems (MEMS) received growing interest, in particular for biomimetics, tissue engineering and drug delivery [54]. The biodegradable MEMS are fabricated by micromolded polycaprolactone with milimetersized reservoirs, which are filled with water and covered with a gold membrane.

King *et al.* have explored biodegradable polymers for therapeutic medicine [55]. Three dimensional monolithic microdevices are bonded from stacked, microstructured PDMS mold. The resulting microfluidic networks show improved speed, resolution and precision as well as reproducibility, manufacturability and scalability compared to previous methods. A bacterial cellulose membrane is used as flexible substrate for OLEDs for potential photodynamic therapy to treat skin cancer and other skin diseases [11].

Additionally, it has been shown that a combination of organic semiconductors and bioactive molecules have great potential for clinical applications, especially for bioresorbable temporary medical

implants [21]. Muskovich and Bettinger focused on the translation of bioelectric communication between the intra- and inter-cellular environment as well as the important role of material selection and the subsequent quality of the biotic–abiotic interfaces [56].

### *4.3. Agriculture/Horticulture*

In the field of agriculture and horticulture, bio-plastics are already widely used in the form of foils, ribbons and planting pots as displayed in Figure 7. Reasons for their use are the adjustable lifetime and the advantages of fully compostable materials [57]. In order to study the impact of these materials on soil, degradation dynamics of agricultural films have been examined in more detail by IR thermography, SEM analysis and mechanical tensile tests [58]. Further application scenarios for food safety have been discussed such as pesticide and microorganism detection [59].

To the best of the authors' knowledge, there are no publications about the use of biodegradable electronics in horticulture or agriculture. One reason could be that electronics have been generally uncommon in this field. However, the possibility of integrating electronics without negative impact on the environment can open new opportunities. One approach could comprise sensors for nutrients or water in soil that change their shape (hydrogels in polymer micro systems) or color (OLED). Further, the installation of a sensor directly at the plant to measure special surface behavior due to external influences is conceivable.

**Figure 7.** Examples of biodegradable materials: (**a**) plant pot (©Limagrain) and (**b**) mulching film (©BASF).

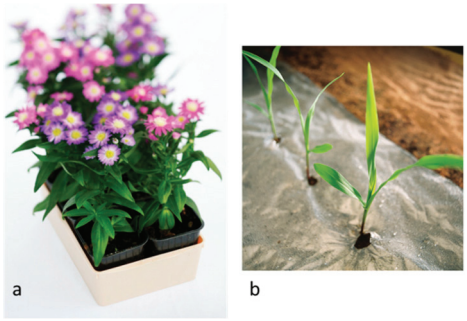


## 5. Conclusions

We have shown the recent progress and great potential of bio-organic electronics for the future consumer market, medical field and agriculture. A survey performed by Theinsthid and co-workers showed that businesses are highly interested in "greener" electronics because they expect economic advantages over their competitors and growth opportunities for their companies, as well as to more easily satisfy customer requirements and receive new opportunities in new markets [60].

These business interests are accompanied by distinctive market growth of cheap, flexible organic electronics which is expected to continuously increase, reaching a market share of approximately 12 billion USD by 2020 [61]. These cheap electronics are supposed to enter the huge market of smart packaging that appears to be the most promising field for biodegradable organic electronics. In addition, it is not too easy to estimate the market benefits of these bio-based electronics for disease

detection or clinic therapy which need to be bio-compatible. These requirements will be more easily achieved if the materials are biodegradable or of bio-based origin.

However, it should be mentioned that there are obstacles before this kind of technology will fulfill the promise of sustainability and wealth. Although tremendous progress has been made to develop biodegradable materials, which completely degrade at the domestic compost heap, often the so-called biodegradable materials used today are still not fully converted in industrial composting plants and significantly disturb the sensitive waste management system. This has led to recommendations from various waste disposal associations to exclude biodegradable plastics from the regular compost bin. In addition, it will remain a matter of discussion if there is a real need for biodegradable electronics when the waste recovery system of a country is effectively working, and then to foster the disposable culture among the citizens further. However, the usage of bio-based materials would bring a different societal value by promoting the development of plastics which originate from regrowing resources ensuring their wide use also after the petroleum age.

Furthermore, scientific proofs about the designated positive ecologic impact of bio-materials are still missing. Examples have been reported, where no evidence is seen for any environmental advantage, by substituting established materials with bio-based and biodegradable ones [32]. Profound life cycle analysis according to DIN EN ISO 14040 and 14044 are strongly requested by the experts to show that the utilization of bio-based and/or biodegradable materials will reduce $CO_2$-emission as well as the consumption of scarce resources and that the development of biodegradable products will have only positive long-term effects.

## Author Contributions

Both authors equally wrote the manuscript, outlined the figures, contributed to discussion and finalized the manuscript.

## Conflicts of Interest

The authors declare no conflict of interest.

## References

1. Seymour, R.B.; Deanin, R.D. *History of Polymer Composites*, 1st ed.; VNU Science Press BV: Utrecht, The Netherlands, 1987.
2. Singh, B.; Sharma, N. Mechanistic implications of plastic degradations. *Polym. Degrad. Stab.* **2008**, *93*, 561–584.
3. BIOPLASTICS—facts and figures. Available online: http://en.european-bioplastics.org /wp-content/uploads/2013/publications/EuBP_FactsFigures_bioplastics_2013.pdf, last (access on 4 March 2014).
4. Shah, A.A.; Hasan, F.; Hameed, A.; Ahmed, S. Biological degradation of plastics: A comprehensive review. *Biotechnol. Adv.* **2008**, *26*, 246–265.
5. Rifkin, J. *The Third Industrial Revolution: How lateral Power is Transforming Energy, the Economy, and the World*, 1st ed.; Palgrave Macmillan: New York, NY, USA, 2011; pp. 1–32.

6. Griese, H.; Stobbe, L.; Middendorf, A.; Reichl, H. Environmental compatibility of electronics—A key towards local and global sustainable development. In Proceedings of the 2004 International IEEE Conference on the Asian Green Electronics AGEC, Hong Kong, China, 5–6 January 2004; pp. 158–163.
7. Fahlteich, J.; Amberg-Schwab, S.; Weber, U.; Noller, K.; Miesbauer, O.; Boeffel, C.; Schiller, N. 29.1: Ultra-high barriers for encapsulation of flexible displays and lighting devices. *SID* **2013**, *44*, 354–357.
8. Tress, T.; Leo, K.; Riede, M. Influence of hole-transport layers and donor materials on open-circuit voltage and shape of I–V curves of organic solar cells. *Adv. Funct. Mater.* **2011**, *21*, 2140–2149.
9. Zhou, Y.; Fuentes-Hernandez, C.; Khan, T.M.; Liu, J.-C.; Hsu, J.; Shim, J.W.; Dindar, A.; Youngblood, J.P.; Moon, R.J.; Kippelen, B. Recyclable organic solar cells on cellulose nanocrystal substrates. *Sci. Rep.* **2013**, *3*, 1–5.
10. Martins, R.F.P.; Ahnood, A.; Correia, N.; Pereira, L.M.N.P.; Barros, R.; Barquinha, P.M.C.B.; Costa, R; Ferreira, I.M.M.; Nathan, A.; Fortunato, E.E.M.C. Recyclable, flexible, low-power oxide electronics. *Adv. Funct. Mater.* **2013**, *23*, 2153–2161.
11. Legnani, C.; Vilani, C.; Calil, V.L.; Barud, H.S.; Quirino, W.G.; Achete, C.A.; Ribeiro, J.L.; Cremona, M. Bacterial cellulose membrane as flexible substrate for organic light emitting devices. *Thin Solid Films* **2008**, *517*, 1016–1020.
12. Shah, J.; Brown, R.M., Jr. Towards electronic paper displays made from microbial cellulose. *Appl. Microbiol. Biotechnol.* **2005**, *66*, 352–355.
13. Kim, D.Y.; Steckl, A.J. Electrowetting on paper for electronic paper display. *ACS Appl. Mater. Interfaces* **2010**, *2*, 3318–3323.
14. Fukuhira, Y.; Kitazonoa, E.; Hayashia, T.; Kanekoa, H.; Tanakab, M.; Shimomurac, M.; Sumi, Y. Biodegradable honeycomb-patterned film composed of poly(lactic acid) and dioleoylphosphatidylethanolamine. *Biomaterials* **2006**, *27*, 1797–1802.
15. Breulmann, M.; Künkel, A.; Philipp, S.; Reimer, V.; Siegenthaler, K.O.; Skupin, G.; Ymamoto, M. Polymers, Biodegradable. In *Ullmann's Encyclopedia of Industrial Chemistry*; Wiley-VCH: Weinheim, Germany, 2009.
16. Oosterhoff, R.H. Biodegradable Diacrylates and Adhesives Based Thereon. U.S. 005580940A, 3 December 1996.
17. Kumar, R.; Choudhary, V.; Mishra, S.; Varma, I.K.; Mattiason, B. Adhesives and plastics based on soy protein products. *Ind. Crop. Prod.* **2002**, *16*, 155–172.
18. Mahdavi, A.; Ferreira, L.; Sundback, C.; Nichol, J.W.; Chan, E.P.; Carter, D.J.D.; Bettinger, C.J.; Patanavanich, S.; Chignozha, L.; Ben-Joseph, E.; *et al*. A biodegradable and biocompatible gecko-inspired tissue adhesive. *Proc. Natl. Acad. Sci. USA* **2008**, *105*, 2307–2312.
19. Taguchi, T.; Saito, H.; Iwasashi, M.; Sakane, M.; Ochiai, N. Biodegradable adhesives composed of human serum albumin and organic acid-based crosslinkers with active ester groups. *J. Bioact. Compat. Pol.* **2009**, *24*, 546–559.
20. Yang, C.; Lin, W.; Li, Z.; Zhang, R.; Wen, H.; Gao, B.; Chen, G.; Gao, P.; Yuen, M.M.F.; Wong, C.P. Water-based isotropically conductive adhesives: Towards green and low-cost flexible electronics. *Adv. Funct. Mater.* **2011**, *21*, 4582–4588.

21. Bettinger, C.J.; Bao, Z. Biomaterials-based organic electronic devices. *Polym. Int.* **2010**, *59*, 563–567.
22. Mostert, A.B.; Powell, B.J.; Pratt, F.L.; Hanson, G.R.; Sarna, T.; Gentle, I.R.; Meredith, P. Role of semiconductivity and ion transport in the electrical conduction of melanin. *Proc. Natl. Acad. Sci. USA* **2012**, *109*, 8943–8947.
23. Irimia-Vladu, M.; Troshin, P.A.; Reisinger, M.; Shmygleva, L.; Kanbur, Y; Schwabegger, G.; Bodea, M.; Schwödiauer, R.; Mumyatov, A.; Fergus, J.W.; *et al*. Biocompatible and biodegradable materials for organic field-effect transistors. *Adv. Funct. Mater.* **2010**, *20*, 4069–4076.
24. Irimia-Vladu, M.; Sariciftcib, N.S.; Bauer, S. Exotic materials for bio-organic electronics. *J. Mater. Chem.* **2011**, *21*, 1350–1361.
25. Głowacki, E.D.; Irimia-Vladu, M.; Kaltenbrunner, M.; Gąsiorowski, J.; White, M.S.; Monkowius, U.; Romanazzi, G.; Suranna, G.P.; Mastrorilli, P.; Sekitani, T.; *et al*. Hydrogen-bonded semiconducting pigments for air-stable field-effect transistors. *Adv. Mater.* **2013**, *25*, 1563–1569.
26. Irimia-Vladu, M.; Troshin, P.A.; Reisinger, M.; Schwabegger, G.; Ullah, M.; Schwoediauer, R.; Mumyatov, A.; Bodea, M.; Fergus, J.W.; Razumov, V.F.; *et al*. Environmentally sustainable organic field effect transistors. *Org. Electron.* **2010**, *11*, 1974–1990.
27. Głowacki, E.D.; Leonat, L.; Voss, G.; Bodea, M.; Bozkurt, Z.; Irimia-Vladu, M.; Bauer, S.; Sariciftci, N.S. Natural and nature-inspired semiconductors for organic electronics. *Proc. SPIE* **2011**, *8118*, 81180M:1–81180M:10.
28. Kanbur, Y.; Irimia-Vladu, M.; Głowacki, E.D.; Voss, G.; Baumgartner, M.; Schwabegger, G.; Leonat, L.; Ullah, M.; Sarica, H.; Erten-Ela, S.; *et al*. Vacuum-processed polyethylene as a dielectric for low operating voltage organic field effect transistors. *Org. Electron.* **2012**, *13*, 919–924.
29. Nudejima, S.-I.; Miyazawa, K.I.; Okuda-Shimazaki, J.; Taniguchi, A. Biodegradation of $C_{60}$ fullerene nanowhiskers by macrophage-like cells. *Adv. Biomed. Res.* **2010**, 89–94.
30. Partha, R.; Conyers, J.L. Biomedical applications of functionalized fullerene-based nanomaterials. *Int. J. Nanomed.* **2009**, *4*, 261–275.
31. Chiappini, C.; Liu, X.; Fakhoury, J.R.; Ferrari, M. Biodegradable porous silicon barcode nanowires with defined geometry. *Adv. Funct. Mater.* **2010**, *20*, 2231–2239.
32. Irimia-Vladua, M.; Głowackib, E.D.; Vossb, G.; Bauera, S.; Sariciftci, N.S. Green and biodegradable electronics. *Mater. Today* **2012**, *15*, 7–8.
33. Hermawan, H. *Biodegradable Metals: From Concept to Application*; Springer: Heidelberg, Germany, 2012; pp. 13–22.
34. Cheng, J.; Liu, B.; Wu, Y.H.; Zheng, Y.F. Comparative *in vitro* study on pure metals (Fe, Mn, Mg, Zn and W) as biodegradable metals. *J. Mater. Sci. Technol.* **2013**, *29*, 619–627.
35. Irimia-Vladu, M.; Głowacki, E.D.; Schwabegger, G.; Leonat, L.; Akpinar, H.Z.; Sitter, H.; Bauer, S.; Sariciftci, N.S. Natural resin shellac as a substrate and a dielectric layer for organic field-effect transistors. *Green Chem.* **2013**, *15*, 1473–1476.

36. Capelli, R.; Amsden, J.J.; Generali, G.; Toffanin, S.; Benfenati, V.; Muccini, M.; Kaplan, D.L.; Omenetto, F.G.; Zamboni, R. Integration of silk protein in organic and light-emitting transistors. *Org. Electron.* **2011**, *12*, 1146–1151.
37. Chang, J.-W.; Wang, C.-G.; Huang, C.-Y.; Tsai, T.-D.; Guo, T.-F.; Wen, T.-C. Chicken albumen dielectrics in organic field-effect transistors. *Adv. Mater.* **2011**, *23*, 4077–4081.
38. Petritz, A.; Wolfberger, A.; Fian, A.; Irimia-Vladu, M.; Haase, A.; Gold, H.; Rothländer, T.; Griesser, T.; Stadlober, B. Cellulose as biodegradable high-k dielectric layer in organic complementary inverters. *Appl. Phys. Lett.* **2013**, *103*, 153303:1–153303:5.
39. Khor, L.Q.; Cheong, K.Y. Aloe vera gel as natural organic dielectric in electronic application. *J. Mater. Sci.: Mater. Electron.* **2013**, *24*, 2646–2652.
40. Kosbar, L.L.; Gelorme, J.D.; Japp, R.M.; Fotorny, W.T. Introducing biobased materials into the electronics industry—Developing a Lignin-based resin for printed wiring boards. *J. Ind. Ecol.* **2001**, *4*, 93–105.
41. Zhu, H.; Xiao, Z.; Liu, D.; Li, Y.; Weadock, N.J.; Fang, Z.; Huang, J.; Hu, L. Biodegradable transparent substrates for flexible organic-light-emitting diodes. *Energy Environ. Sci.* **2013**, *6*, 2105–2111.
42. Hu, L.; Choi, J.W.; Yang, Y.; Jeong, S.; la Mantia, F.; Cui, L.-F.; Cui, Y. Highly conductive paper for energy-storage devices. *Proc. Natl. Acad. Sci. USA* **2009**, *106*, 21490–21494.
43. Nyholm, L.; Nyström, G.; Mihranyan, A.; Strømme, M. Toward flexible polymer and paper-based energy storage devices. *Adv. Mater.* **2011**, *23*, 3751–3769.
44. Barr, M.C.; Rowehl, J.A.; Lunt, R.R.; Xu, J.; Wang, A.; Boyce, C.M.; Im, S.G.; Bulovic, V.; Gleason, K.K. Direct monolithic integration of organic photovoltaic circuits on unmodified paper. *Adv. Mater.* **2011**, *23*, 3500–3505.
45. Zschieschang, U.; Yamamoto, T.; Takimiya, K.; Kuwabara, H.; Ikeda, M.; Sekitani, T.; Someya, T.; Klauk, H. Organic electronics on banknotes. *Adv. Mater.* **2011**, *23*, 654–658.
46. Irimia-Vladu, M.; Głowacki, E.D.; Troshin, P.A.; Schwabegger, G.; Leonat, L.; Susarova, D.K.; Krystal, O.; Ullah, M.; Kanbur, Y.; Bodea, M.A.; *et al*. Indigo—A natural pigment for high performance ambipolar organic field effect transistors and circuits. *Adv. Mater.* **2012**, *24*, 375–380.
47. Kim, D.-H.; Kim, Y.-S.; Amsden, J.; Panilaitis, B.; Kaplan, D.L.; Omenetto, F.G.; Zakin, M.R.; Rogers, J.A. Silicon electronics on silk as a path to bioresorbable, implantable devices. *Appl. Phys. Lett.* **2009**, *95*, 133701:1–133701:3.
48. Barhoumi, H.; Maaref, A.; Rammah, M.; Martelet, C.; Jaffrezic-Renault, N.; Mousty, C.; Cosnier, S.; Perez, E.; Rico-Lattes, I. Insulator semiconductor structures coated with biodegradable latexes as encapsulation matrix for urease. *Biosens. Bioelectron.* **2005**, *20*, 2318–2323.
49. Canham, L. Interview—Nanosilicon for nanomedicine: A step towards biodegradable electronic implants? *Nanomedicine* **2013**, *8*, 1573–1576.
50. Lendlein, A.; Sisson, A. *Handbook of Biodegradable Polymers: Isolation, Synthesis, Characterization and Applications*; Wiley-VCH Verlag GmbH Co. KGaA: Weinheim, Germany 2013; pp. 309–378.
51. Bazaka, K.; Jacob, M.V. Implantable Devices: Issues and Challenges. *Electronics* **2013**, *2*, 1–34.

52. Williams, D.F. On the mechanisms of biocompatibility. *Biomaterials* **2008**, *29*, 2941–2953.
53. Koo, J.H.; Seo, J.; Lee, T. Nanomaterials on flexible substrates to explore innovative functions: From energy harvesting to bio-integrated electronics. *Thin Solid Films* **2012**, *524*, 1–19.
54. Richards-Grayson, A.C.; Scheidt-Shawgo, R.; Li, Y.; Cima, M.J. Electronic MEMS for triggered delivery. *Adv. Drug Deliver. Rev.* **2004**, *56*, 173–184.
55. King, K.R.; Wang, C.C.J.; Kaazempur-Mofrad, M.R.; Vacanti, J.P.; Borenstein, J.T. Biodegradable microfluidics. *Adv. Mater.* **2004**, *16*, 2007–2012.
56. Muskovich, M.; Bettinger, C.L. Biomaterials-based electronics: Polymers and interfaces for biology and medicine. *Adv. Healthcare Mater.* **2012**, *1*, 248–266.
57. Scarascia-Mugnozza, G.; Schettini, E.; Vox, G.; Malinconico, M.; Immirzi, B.; Pagliara, S. Mechanical properties decay and morphological behaviour of biodegradable films for agricultural mulching in real scale experiment. *Polym. Degrad. Stab.* **2006**, *91*, 2801–2808.
58. Mormile, P.; Petti, L.; Rippa, M.; Immirzi, B.; Malinconico, M.; Santagata, G. Monitoring of the degradation dynamics of agricultural films by IR thermography. *Polym. Degrad. Stab.* **2007**, *92*, 777–784.
59. Sozer, N.; Kokini, J.L. Nanotechnology and its applications in the food sector. *Trends Biotechnol.* **2008**, *27*, 82–89.
60. Theinsthid, P.; Chandrachai, A.; Suwannathep, S.; Keeratipibul, S. Bio-based products: Factors that influence their adoption. In Proceeding of the 2010 IEEE International Conference on Management of Innovation and Technology (ICMIT), Singapore, Singapore, 2–5 June 2010; pp. 354–359.
61. Das, R.; Harrop, P. *Printed, Organic & Flexible Electronics Forecasts, Players & Opportunities 2012–2022*; IDTechEx: Cambridge, UK, 2012; pp. 1–58.

MDPI AG
Klybeckstrasse 64
4057 Basel, Switzerland
Tel. +41 61 683 77 34
Fax +41 61 302 89 18
http://www.mdpi.com/

*Electronics* Editorial Office
E-mail: electronics@mdpi.com
http://www.mdpi.com/journal/electronics

MDPI • Basel • Beijing • Wuhan
ISBN 978-3-906980-97-3
www.mdpi.com